Corbett

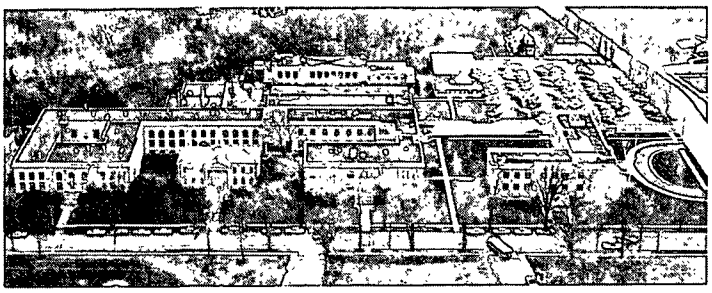

THE INSTITUTE OF PAPER CHEMISTRY, APPLETON, WISCONSIN

PULPING PROCESSES

PROJECT ADVISORY COMMITTEE MEETING

October 20-21, 1987

The Institute of Paper Chemistry

Appleton, WI 54912

NOTICE & DISCLAIMER

The Institute of Paper Chemistry (IPC) has provided a high standard of professional service and has exerted its best efforts within the time and funds available for this project. The information and conclusions are advisory and are intended only for the internal use by any company who may receive this report. Each company must decide for itself the best approach to solving any problems it may have and how, or whether, this reported information should be considered in its approach.

IPC does not recommend particular products, procedures, materials, or services. These are included only in the interest of completeness within a laboratory context and budgetary constraint. Actual products, procedures, materials, and services used may differ and are peculiar to the operations of each company.

In no event shall IPC or its employees and agents have any obligation or liability for damages, including, but not limited to, consequential damages, arising out of or in connection with any company's use of, or inability to use, the reported information. IPC provides no warranty or guaranty of results.

This information represents a review of on-going research for use by the Project Advisory Committees. The information is not intended to be a definitive progress report on any of the projects and should not be cited or referenced in any paper or correspondence external to your company.

Your advice and suggestions on any of the projects will be most welcome.

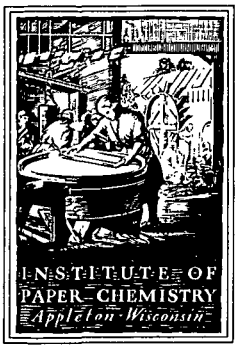

THE INSTITUTE OF PAPER CHEMISTRY
Post Office Box 1039
Appleton, Wisconsin 54912
Phone: 414/734-9251
Telex: 469289

September 25, 1987

TO: Members of the Pulping Processes Project Advisory Committee

The next meeting of the Pulping Processes PAC will be held in Appleton on October 20 and 21, 1987. The meeting will convene Tuesday morning at 8:00 a.m. in the Seminar Room of the Continuing Education Center at The Institute of Paper Chemistry. Accommodations are available for committee members at the Continuing Education Center. Enclosed is a pink "security card" which has instructions for entering the CEC building in the event you find it locked when you arrive. Please confirm that you will attend this meeting at your earliest convenience.

The information enclosed with this letter is for your review for the upcoming meeting. Included are:

(A) a list of current committee members,

(B) the agenda for the October meeting,

(C) lists of current M.S. and Ph.D. student work,

(D) comments on items raised in the minutes of the spring 1987 meeting, and

(E) the status reports for the individual funded projects.

The agenda is similar to that of previous meetings. We will plan on roughly 10 minutes after each presentation for comments from the committee and other attendees. This should expedite the project reviews held at the committee meeting the following morning. The evening session will consist of two student presentations on Ph.D. work plus comments by Dave Clay about Scandinavian recovery research. In addition to the project discussions,

the morning session will review the committee input into our midrange planning effort. This will include results of our most recent exercise in ranking topics from our "Brainstorming Session."

See you in Appleton.

Sincerely,

Earl

Earl W. Malcolm
Director
Chemical Sciences Division

EWM/gmk
Enclosures

PULPING PROCESSES PROJECT ADVISORY COMMITTEE

Dr. Donald C. Johnson (Chairman) -- 6/89
Research Advisor
Weyerhaeuser Paper Company
WTC 2B42
Tacoma, WA 98477
(206) 924-6531

Dr. Glendon W. Brown -- 6/89
Director of Production Technology
Mead Corporation
Publishing Paper Division
P. O. Box 757
Escanaba, MI 49829
(906) 786-1660

Mr. Dean W. DeCrease -- 6/88
Group Leader, Pulping Research
Hammermill Paper Company
1540 East Lake Road
P. O. Box 10050
Erie, PA 16533
(814) 456-8811

Mr. Wendell B. Hammond, Jr. -- 6/89
Resident Manager
Willamette Industries, Inc.
Albany Paper Mill
P. O. Box 339
Albany, OR 97321
(503) 926-2281

Mr. Gerald R. Haw -- 6/88
Assistant Pulp Mill Superintendent
Tennessee River Pulp & Paper Company
Packaging Corporation of America
P. O. Box 33
Counce, TN 38326
(901) 689-3111

Dr. Thomas C. Kisla -- 6/88
Sr. Product Technology Engineer
Stone Container Corporation
2150 Parklake Drive
Suite 400
Atlanta, GA 30345
(404) 621-6700

Dr. Samuel W. McKibbins -- 6/89
Director of Pulping & Bleaching
Champion International Corporation
West Nyack Road
West Nyack, NY 10994
(914) 578-7293

Mr. Michael A. Pikulin -- 6/90
Group Leader
Union Camp Corporation
P. O. Box 3301
Princeton, NJ 08543-3301
(609) 896-1200

Dr. John K. Rogers -- 6/89
Director of Manufacturing Technology
James River Corporation
Neenah Technical Center
1915 Marathon Avenue
P. O. Box 899
Neenah, WI 54956
(414) 729-8340

Dr. Ivan B. Schrodt -- 6/89
Director, Research & Development
Kimberly-Clark Corporation
2100 Winchester Road
Neenah, WI 54956-0056
(414) 721-6136

Dr. James Turnbull -- 6/89
Group Leader, Brightening Research
MacMillan Bloedel Research
3350 East Broadway
Vancouver, BC V5M 4E6
CANADA
(604) 254-5151

Dr. Benjamin F. Ward -- 6/88
Research Director
Charleston Research Laboratory
Westvaco Corporation
5600 Virginia Avenue
Charleston, SC 29406
(803) 745-3505

EWM/gmk
9/87

AGENDA

PULPING PROCESSES PAC MEETING

THE INSTITUTE OF PAPER CHEMISTRY
APPLETON, WISCONSIN

OCTOBER 20-21, 1987

TUESDAY, OCTOBER 20, 1987

CONTINUING EDUCATION CENTER SEMINAR ROOM

7:00	BREAKFAST	
8:00	CONVENE	D. Johnson
8:05	RESEARCH OVERVIEW	E. Malcolm
8:20	PROJECT PRESENTATIONS	
	KRAFT CHEMICAL RECOVERY	
	Fundamental Processes in Alkali Recovery Furnaces (Project 3473-1)	T. Grace J. Cameron S. Lien
	Computer Model of Recovery Furnace (Project 3605)	A. Jones D. Clay
	Smelt-Water Explosions (Project 3456-2)	
10:20	TOUR - DOE Reactor	
10:40	Black Liquor Combustion (DOE Project 3473-6)	D. Clay
	CHEMICAL PULPING	
	Fundamentals of Selectivity in Pulping and Bleaching (Project 3475)	D. Dimmel G. Reed
12:00	LUNCH	

1:00 CHEMICAL PULPING (continued)

Improved Processes for Bleached Pulp (Project 3474)	T. McDonough
Development and Application of Analytical Techniques (Project 3477) FKBG/DOE - On-Line Lignin Sensor (Project 2926-10)	D. Easty
Fine Structure of Wood Pulp Fibers (Projects 3288 and 3521)	R. Atalla

3:15 BREAK

HIGH YIELD PULPS

Fundamentals of Brightness Stability (Project 3524)	U. Agarwal T. McDonough
Strong, Intact High Yield Fibers (Project 3566)	T. McDonough T. Heazel S. Aziz

5:15 SOCIAL HOUR

5:45 DINNER

6:45 EVENING DISCUSSIONS

Student Presentations	
A kinetic analysis of kraft pulp chlorination	S. Pugliese
Development of computer model for black liquor combustion in a recovery furnace	A. Walsh
Scandanavian Highlights	D. Clay

WEDNESDAY MORNING - OCTOBER 21, 1987

7:00 BREAKFAST (CEC)

8:00 COMMITTEE MEETING (Krannert - Rooms K108-109)

Midrange Planning

Project Discussions

12:00 LUNCH (CEC) END OF WEDNESDAY SESSION

NEXT MEETING: MARCH 22-23, 1988

April 30, 1987

A190

MASTERS

INDEPENDENT STUDY

Student	Advisor	Room	Subject
Arnold	Sprague		The effects of nonuniform z-direction density on paper properties.
Bartz	Lavery	1106	Economics of a simulated linerboard mill incorporating the impulse drying process.
Bogenschutz	Becwar		Electroporation-mediated genetic transformation of Norway spruce cells.
Breining, J.	Stratton		Paper sizing with polysoaps.
Burrill	Yeske		Determination of the mechanism of liquid-level corrosion in white liquor storage tanks.
Cedergren	Waterhouse	218	The effect of lignin and hemicellulose removal on the short span compressive strength potential of white spruce.
Christensen	Easty	229	Evaluation of the circular internal reflection unit for the analysis of pulp and paper.
Friese	Stratton	220	Analysis of adsorbed polymer configuration using FTIR spectroscopy with a CIR sample cell.
Fruhwirth	Conners	K100	A comparative study of tension wood and normal wood fibers in the papermaking process.
Ginnow	Jones		Modeling the flow in the headbox and forming zone.
Graf	Malcolm	Carels	The dissociation constant of the hydrogen sulfide ion.
Hamel	Sprague	246	Freeness measurements in refiner control.
Hille	Halcomb		Pulp fiber identification using FLOPS.

Attachment C-1

Student	Advisor	Room	Subject
Jolly	Parker, P.		Dynamic modeling of evaporators using DYSCO.
Kolterjahn	Conners	K100	The load-elongation characteristics of single wood fibers under controlled relative humidity conditions.
Kubale	Cameron		Laser analysis of flugas particles.
LaFond	Yeske		The effect of flowing kraft smelts on corrosion rate.
Lundberg	Easty	227	Static and dynamic headspace analysis of volatiles in paper.
Macdonald	Baum		Effect of the rush-drag ratio on the mechanical properties of paper.
Maule	Cameron		Proposal to formulate a rate equation for the reaction between sulfur dioxide and sodium carbonate fume particles.
Rivard	Jones		Designing and constructing an experimental process control system.
Sell	Wann		Somoclonal variation in conifer tissue culture.
Spielbauer	Farrington		Method to determine object size and three dimensional position from flash x-ray images.
Thomas	Parker, P.		User-friendly interface for MAPPS.
Tracey	Malcolm	44	The effects on pulp properties of changes in the pH profile of a kraft cook.
Willhelm	Habeger	68A	The evaluation of loss tangent as a means to predict mechanical properties of paper.
SPECIAL STUDENT			
Woitkovich	Atalla		Raman studies of delignification of loblolly pine.

April 30, 1987

A490

Ph.D.

THESES IN PROGRESS

Student	Passed to Candidacy	Thesis Approval	Subject	Committee	Room
Bovee	6/11/82	8/9/82	The synthesis and evaluation of an alkali insoluble cellulose model.	Dimmel, chr. (Schroeder)	K213
Geddes (Not in residence Sept. 1983)	9/2/83	1/10/84 & Oct.	Alkaline degradation of amylose: a kinetic model	Halcomb, chr. (Schroeder) Johnson	K209
Heazel (Not in residence summer 1984)	11/29/83	2/14/84	The influence of sulfonation on sulfite CMP properties.	McDonough, chr. Whitsitt Litvay [adjunct member]	K211 K100
Nealey	1/4/84	2/24/84	Isolation and characterization of xyloglucan from suspension cultured loblolly pine cell medium.	Johnson, chr. Easty Becwar	34
Biasca	1/4/84	2/24/84	Oriented fiber refining: application of individual modes of mechanical action to single pulp fibers.	Baum, chr. Habeger McDonough Michael Jackson (Weyerhaeuser) [adjunct member]	71 K27

Attachment C-3

Student	Passed to Candidacy	Thesis Approval	Subject	Committee	Room
Lebo	6/8/84	6/29/84	The rate and quantum yield of the light induced formation of ortho-quinonoid lignin structure.	McDonough, chr.	K219
Pugliese	6/8/84	11/7/84	A kinetic analysis of kraft pulp chlorination.	McDonough, chr. Cameron P. Parker	K211
Byers	9/4/84	10/4/84	An autoradiographic study of the hemicellulose distribution in the cell walls of Pinus Resinosa tracheids.	Atalla, chr. Johnson	K221
Reed	9/4/84	12/11/84	The role of sulfur species in pulping reactions.	Dimmel, chr. Malcolm	K232
Molinarolo, S. (Not in residence Sept. 1984 thru Dec. 1984). (Also July & Aug. 1986).	9/4/84	3/14/85	Sorption of xyloglucan onto cellulose fibers.	Stratton, chr. Johnson	34
Molinarolo, W. (Not in residence Sept. 1984 thru Dec. 1984)	9/4/84	3/14/85	The high temperature alkaline degradation of phenyl β-D-glucopyranoside.	Dimmel, chr. (Schroeder)	K210
Robinson	11/27/84	2/19/85	Characterization of black liquor droplet drying in air, steam, and humid air.	Clay, chr. Grace Lavery	SRB

Attachment C-4

Student	Passed to Candidacy	Thesis Approval	Subject	Committee	Room
Proxmire, P.	11/27/84	2/19/85	The influence of aluminum salts on the retention of titanium dioxide when using cationic polyelectrolyte as a retention aid.	Stratton, chr. Waterhouse Easty	K121
Berger, Brian	3/28/85	3/14/85	The effects of refining and yield on the z-direction elastic properties of paper.	Baum, chr. Habeger Waterhouse	66 K27
Aiken	6/7/85	6/6/85	The use of a char pile reactor to study char bed processes.	Cameron, chr. Grace Parker, P.	So. Res. Lab.
Berger, Bernard	9/10/85	11/14/85	Transient effects of moisture sorption at various temperatures on the ultrasonically measured elastic moduli of cellulosic materials.	Habeger, chr. Stratton Waterhouse Baum (ex officio)	K27
Bither	9/10/85	1/27/86	Strength development through internal fibrillation and wet pressing.	Waterhouse,chr. Baum Farrington	203A
Barkhau	12/6/85	12/16/85	Anthraquinone inhibited lignin condensation.	Dimmel, chr. Malcolm	K106
Wozniak	4/7/86	3/12/86	Preparation and reactions of Diels-Alder adducts of lignin-derived quinones.	Dimmel, chr. Crowe Malcolm	K205
Kulas	3/25/86	4/16/86	An investigation of the fire-side sulfidization of kraft recovery furnace waterwall tubes.	Grace, (co-chr.) Yeske Cameron	Cor. Lab., Rec. Lab.

Attachment C-5

Student	Passed to Candidacy	Thesis Approval	Subject	Committee	Room
Triantafill-opoulos (Not in residence summer 1986)	6/13/86	1/7/87	Investigation of coating flows via flash x-ray.	Farrington,chr. Lindsay Dr. Shands (Beloit)	203A
Crane, K. (Not in residence summer 1986)	6/13/86	12/2/86	An overall model for the combustion of a single droplet of kraft black liquor.	Clay, chr. Grace Atalla	69
Harper (Not in residence summer 1986)	6/13/86	11/24/86	Sulfur release during black liquor burning.	Clay, chr. Grace McDonough	K115
Burns, B.	6/27/86	10/6/86	A kinetic study of m.c. chlorination.	McDonough,chr. Cameron Farrington	168 and 49
Goulet (Not in residence summer 1986)	6/27/86	12/2/86	The effect of pulping, bleaching, and refining processes on the electrokinetic properties of wood fibers.	Stratton, chr. Conners Easty	1225
Uhlin (Not in residence summer 1986)		5/30/86	The influence of hemicelluloses on the structure of bacterial cellulose.	Atalla, chr. Johnson Conners	K216
Jones	9/8/86	9/3/86	A kraft recovery furnace model.	Grace, chr. Cameron Lavery	SR11
Walsh	9/8/86	9/11/86	Development of a computer model for black liquor combustion in a recovery furnace.	Grace, chr. Jones Clay	SR11
Burns, J.	9/23/86	1/7/87	Investigation of the constrained expansion phase of wet pressing.	Lavery, chr. Farrington Sprague	241

Attachment C-6

Student	Passed to Candidacy	Thesis Approval	Subject	Committee	Room
Sumnicht	9/23/86	11/24/86	Computer model of a char bed.	Grace, chr. Clay Farrington	312
Sime	11/7/86	12/11/86	A study of delignification kinetics during alkaline sulfite anthraquinone pulping.	McDonough,chr. Clay Malcolm	67
Goerg	11/7/86	12/18/86	A study of fume particle deposition.	Cameron, chr. Grace Farrington	SR17
Bond	4/2/87				

Attachment C-7

Attachment D-1

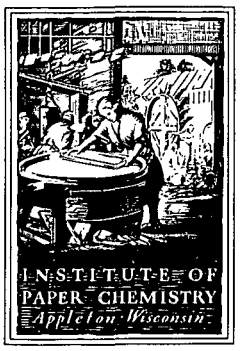

THE INSTITUTE OF PAPER CHEMISTRY
Post Office Box 1039
Appleton, Wisconsin 54912
Phone: 414/734-9251
Telex: 469289

September 23, 1987

TO: Members of the Pulping Processes Project Advisory Committee

SUBJECT: March 1987 Minutes

You all have received the minutes from the March 20-21 PAC meeting. As usual, I feel compelled to make a few brief comments that should serve as a basis for further discussions at the October PAC meeting.

GENERAL COMMENTS

We continue to increase the number of postdoctoral fellows working in various project areas. Our current group includes:

Dr. Bharat Bihani - working with Tom McDonough in oxygen bleaching,

Dr. Jay Hsu - working with David Clay studying fume particles in recovery,

Dr. Niann Shiang - working with Tom Grace on modeling

Dr. Michael Van Lente - Working with Don Dimmel on electrochemistry of pulping reactions.

In addition, Craig Brown is now at IPC as an Industrial Fellow from Weyerhaeuser. Craig is working with Dave Clay studying black liquor combustion. Also, Dr. Tan Zheng is here from China as a visiting scientist working on cellulose structure with Rajai Atalla.

Our search for an organic chemist continues. Concerns on the future location of IPC are a factor in filling this position.

COMMENTS ON SPECIFIC PROJECTS

PROJECT 3475: Fundamentals of Selectivity in Pulping and Bleaching

The question raised concerning the possible use of isolated lignins in place of heterogenous lignin models has been given careful thought. We still feel that there is much to be gained by knowing the exact starting structures. In addition the new "models" are much closer to lignin as it exists in wood than previous ones. This should be discussed at the next meeting.

As far as the carbohydrate work is concerned, once we complete the current set of experiments, it is indeed likely that funded activity in this area will be curtailed.

PROJECT 3474 Improved Process for Bleached Pulp

We have taken the committee's suggestion that, where appropriate, we include chloroform testing as part of any bleach sequence evaluation. The question of routine testing for dioxin also arises. This should be reviewed at the meeting.

PROJECT 3566 Strong, Intact High Yield Fibers

The committee's continued concern as to whether bonding or individual fiber strength limits the strength of products is noted. We have made some efforts to address this point and will continue to do so.

OTHER PROJECTS

No comments.

****

The support expressed for all the projects is appreciated. Your input is of great value to us, not only from a scientific point of view, but also in keeping our research directed at industry needs.

Earl

Earl W. Malcolm

EWM/gmk

Attachment E

STATUS REPORTS

TO THE

PULPING PROCESSES PROJECT ADVISORY COMMITTEE

October 20-21, 1987

The Institute of Paper Chemistry

Appleton, WI 54912

TABLE OF CONTENTS

THE INSTITUTE OF PAPER CHEMISTRY

Appleton, Wisconsin

Status Report

to the

PULPING PROCESSES

PROJECT ADVISORY COMMITTEE

Project 3288

FINE STRUCTURE OF WOOD PULP FIBERS

Project 3521-2

RAMAN MICROPROBE INVESTIGATION OF MOLECULAR STRUCTURE AND ORGANIZATION IN THE NATIVE STATE OF WOODY TISSUE

September 11, 1987

PROJECT SUMMARY FORM

DATE: September 11, 1987

PROJECT No. 3288: FINE STRUCTURE OF WOOD PULP FIBERS

PROJECT LEADER: R. H. Atalla

IPC GOAL:

Develop relationships between the critical paper and board property parameters and the way they are achieved as a combination of raw materials selection, principles of sheet design, and processing.

OBJECTIVE:

Define the structure of wood pulp fibers and relate to ultimate web properties.

CURRENT FISCAL YEAR BUDGET: $75,000

SUMMARY OF RESULTS SINCE LAST REPORT:

The Raman spectra in the OH region of the I_α and I_β forms of native cellulose have been resolved in a manner that is consistent with our hypothesis that the primary difference between the two forms is in the systems of hydrogen bonds which prevail. That is, the skeletal conformations of the molecules in both forms of cellulose I are essentially the same, but the patterns of hydrogen bonding are different.

Studies of the transformation of cellulose I to cellulose III, followed by regeneration of cellulose I, indicate that the I_α form of native cellulose is less stable than the I_β form. This finding is also reflected in published observations of the response of high I_α celluloses to regeneration from their acetylated form, and to treatment in steam at 260 degrees C. All these observations are consistent with our earlier observations that the I_α form is more susceptible to acid hydrolysis than the I_β form.

Studies of structural transformations have shown that the dehydration of celluloses, whether they be regenerated or native, can result in significant stresses within the lattices of the crystalline domains. These effects are clearly related to the complexity of the morphology of the cellulosic samples under investigation. The sample least sensitive to this effect was a fiber of ramie, in which the alignment of the molecular chains is parallel to the fiber axis, and the morphology is quite simple.

Studies of annealing have shown that most handsheet properties are affected negatively by an increase in the crystallinity of pulp fibers. They also revealed that the increase in crystallinity reflects a reduction in the defect content of the lattice structures. The effort to measure conformational changes indicated that the percentage of anhydroglucose units which are transferred from ordered (K_I) to disordered (K_o) chain segments is within the experimental error.

In addition to the above investigations a number of explorations of molecular aggregation of cell wall components have been continued.

PLANNED ACTIVITY THROUGH FISCAL YEAR 1988

Continue the work using solid State ^{13}C NMR, x-ray diffraction, and Raman spectroscopy to define the structure of cellulose and hemicelluloses in native plant tissue. Relate the variations in structure to differences in mechanical properties, chemical reactivities and process response.

In the coming year, additional emphasis will be given to characterizing structural properties that are related to handsheet mechanical properties, and to the effects of cyclic drying and rewetting.

FUTURE ACTIVITY

Progress on several projects, including the new areas of high-yield pulping and moisture tolerant webs, will benefit from a better understanding of the relation between fiber structure and product properties. New information on the fine structure of cellulose and fibers will be helpful in guiding activities in those areas. Future work will focus on the structure of native wood fibers and its modification in both conventional chemical and high yield pulping processes.

STUDENT RESEARCH

Erin Byers, Ph.D.
Ingegard Uhlin, Ph.D. (Gunnar Nicholson Fellow)
Tan Zheng, special student from China

PROJECT SUMMARY FORM

DATE: September 11, 1987

PROJECT No. 3521-2: RAMAN MICROPROBE INVESTIGATION OF MOLECULAR STRUCTURE AND ORGANIZATION IN THE NATIVE STATE OF WOODY TISSUE

PROJECT LEADER: R. H. Atalla

IPC GOAL:

Develop relationships between the critical paper and board property parameters and the way they are achieved as a combination of raw materials selection, principles of sheet design, and processing.

OBJECTIVE:

Develop a better understanding of wood fiber structure through the use of Raman microprobe spectroscopy. Establish the molecular structure present in cell walls of native woody fibers, including cellulose, hemicelluloses, and lignin. Determine the response of structure to process variables.

CURRENT FISCAL YEAR BUDGET: $45,000

SUMMARY OF RESULTS SINCE LAST REPORT:

Again during the most recent period the major component of our effort was devoted to making our new instrumental systems operational. We have encountered an inordinate number of failures of components in the different systems. We believe that we have overcome the major obstacles, and expect to have the systems operational in the near future.

In support of our microprobe program and the parallel effort toward the on-line lignin sensor, we are assessing the correlations between the spectra we observe in lignins and the spectra of the model compounds studied by S. M. Ehrhardt for her doctoral dissertation. Such correlations will enable us to derive the majority of the information in the spectra.

We have continued the studies of luminescence using our older Raman spectrometer. The preliminary results suggest that the primary form is phosphorescence rather than fluorescence. The information will be helpful in the design of gating experiments with the time resolved system.

PLANNED ACTIVITY THROUGH FISCAL YEAR 1988:

We will continue exploration of the spectra of different woods and native fibers with the new microprobe system. The effects of chemical treatments on the architecture of the cell walls will also be investigated.

We will begin calculations, using Ehrhardt's force constants, to help interpretation of the spectra of lignin. We also plan to correlate the changes in band intensities with the results of chemical analyses.

An assessment of the photophysical processes in lignin will be undertaken. We expect to carry out some experiments on fluorescence lifetimes of the excited states at the University of Pennsylvania Laser Laboratory. This will enable us to design a more efficient sequence for the experiments with our own pulsed laser system. Knowledge of the lifetimes of the excited states is essential to design of the gating system we need for the on-line lignin sensor. It will also help us in understanding the photophysics of the interaction of oxygen or other free radical gases with photoexcited lignins. This will be reported under Project 3524.

FUTURE ACTIVITY:

Continuation of the program in conjunction with the DOE-supported effort is anticipated through fiscal year 1989/90. The methods developed under this program may be adapted to explore the effects of mechanical and chemical treatments on structure and organization in high-yield pulp fibers. Some of these methods will also be incorporated into the program directed at development of an on-line lignin sensor.

STUDENT RESEARCH:

J. Wiley, Ph.D. 1986
J. Bond, Ph.D.

Status Report

FINE STRUCTURE OF WOOD PULP FIBERS

INTRODUCTION

Both Projects 3288 and 3521 are concerned with molecular structure and organization in wood pulp and other cellulosic fibers and the relationships between structure and properties. In pulp based materials, as in all other fiber based composites, the mechanical properties of the composite structures are determined by the properties of the fibers. These in turn are determined by the molecular structure of the dominant components and the manner in which these components are aggregated together in the solid state.

In fibrous polymeric materials the state of aggregation is defined by specification of the degrees of molecular orientation and crystallinity; these are among the most often studied parameters for synthetic fibers. In the case of native fibers the state of aggregation is also defined by native morphology and by the manner in which both morphology and molecular organization are changed in isolation and manufacturing processes such as pulping, bleaching, and papermaking.

Project 3288 has focused on questions of structure in chemical pulps and in related native cellulosic fibers since its inception. It has also been concerned with the mechanisms of aggregation of celluloses in both native and regenerated forms and with their interactions with related cell wall polysaccharides.

Project 3521 was initiated with a focus on the structure of cell walls in wood, with particular emphasis on the organization of lignin in the native

state. It is more logically connected to questions of structure in high-yield pulps, though it is also intended to address questions which are relevant to understanding delignification mechanisms in the manufacture of chemical pulps.

Much of the work under both projects has been based on physical methods for structural investigation. The primary tools have been diffractometry and spectroscopy. Although x-ray diffractometry has been a key tool in much of the work, the primary tool has been Raman spectroscopy. Solid State ^{13}C-NMR has also been used through a collaboration with other laboratories, primarily the National Bureau of Standards.

The application of Raman spectroscopy has been pioneered in the work at the Institute, under Project 3288 and its predecessor, and more recently under 3521. In the following sections separate overviews are provided for more recent studies under each of the projects.

OVERVIEW - PROJECT 3288

Under this project our studies continue in two primary areas of emphasis, and are expanding in a new direction, previously covered under exploratory projects. In the first area we continue to pursue a deeper understanding of the natures of the different structures of cellulose, with particular emphasis on the native states. In the second area, in which we are expanding our program, we are investigating the transformations which occur when different celluloses are subjected to conditions which can result in structural modifications. Finally, the third area, in which our studies are extensions of some exploratory projects, is concerned with the factors which dominate the aggregation of cellulose and related cell wall components at the molecular level, particularly in the native state and during biogenesis.

Fundamental Structural Studies

Our most recent structural studies are described in the attached reprint from the Proceedings of the International Symposium on Wood and Pulping Chemistry held in Paris last April. It presents the results of a series of spectral measurements. In the first, the Raman spectra in the OH region of the I_α and I_β forms of native cellulose were derived. This was followed by a series of studies in which an algal cellulose I was transformed into cellulose III by treatment in anhydrous ammonia, and this in turn was treated in boiling water to recover cellulose I, and both the Raman and ^{13}C NMR spectra of all three forms were recorded. This series of transformations is particularly noteworthy because in the cellulose I recovered from the cellulose III, a substantial part of the I_α component characteristic of algal celluloses was transformed into the I_β form.

Our results, including the Raman spectra and the ^{13}C NMR spectra point to a conformational transformation when cellulose I is changed to cellulose III. Reversion to the cellulose I after treatment in boiling water results in recovery of the cellulose I conformation, but with a different pattern of hydrogen bonding between the chains in the lattice. The Raman spectra are particularly important in this series of observations because our interpretation differs from that given by Chanzy et al. and by Harada et al. They looked at electron micrographs of samples of the algal cellulose and of the cellulose I recovered from the cellulose III, and found that the major difference was a significantly smaller lateral dimension to the fibrils after the treatment. They have taken their observation as evidence that the differences between the multiplicities in the ^{13}C NMR spectra of the I_α and I_β forms are a consequence of lateral dimension.

Such an interpretation is possible only if one ignores both the Raman and ^{13}C NMR data on the cellulose III samples.

In the reprint from the ISWPC we have set forth our view that the I_α form of cellulose is more susceptible to acid hydrolysis than the I_β form. This was based on the observation that upon acid hydrolysis of a I_α rich sample of cellulose from Cladophera glomerata a sample rich in the I_β form was recovered. Recently Horii et al. have published two notes suggesting that the I_α form is convertible to the I_β form in the course of other treatments. These include acetylation of algal celluloses under mild conditions, followed by deacetylation, as well as treatment of the algal celluloses with steam at 260 degrees C. Though we are not currently pursuing the differences between the reactivities of the I_α and I_β forms, we believe that the evidence in support of this view is conclusive at this point, particularly in light of the experimental results by Horii et al. It is worthwhile to emphasize that Horii et al. have chosen not to accept the hypothesis of a composite structure to native celluloses, but instead describe their results in terms of the I_α and I_β classification introduced into the discussion of native cellulose by Marinan and Man in 1956, on the basis of the infrared spectra in the OH region. We believe the approach adopted by Horii et al. to be an erroneous one with little foundation.

Studies of Structural Transformations

Two types of transformation have been of particular interest, both involving changes in degree of organization at the molecular level rather than qualitative changes. The first type of transformation investigated is that associated with dehydration of cellulosic materials during drying. The second type of transformation is the change in the degree of crystallinity associated

with annealing at elevated temperatures for extended periods of time in a manner simulating the thermal conditions which prevail during pulping.

Dehydration Effects

The key hypothesis to be derived from the studies of dehydration is that the contraction associated with drying of amorphous domains, when coupled with complexity in the morphology of the cellulosic material, can result in relatively large stresses within the crystalline fibrillar domains. It is likely that the stresses under discussion can result in internal tensile failures of some of the fibrils. Such failures may be in part responsible for the weakening of some fibers when they are recycled.

The effects of dehydration first came to our attention in connection with the differences between the degree of resolution of the ^{13}C NMR spectra of celluloses recorded for wet and dry samples. Though at first we thought the higher resolution for the wet samples may be a manifestation of some accelerated relaxation phenomenon associated with the higher population of protons, a comparison with similar phenomena in starch suggested that the broadening of the resonances of the dry sample results from a limited degree of deformation of the crystalline lattices as a consequence of dehydration.

We then examined the Raman spectra of wet and dry samples of a number of celluloses. The most pronounced effect was seen in the spectra of mercerized and regenerated celluloses. As is seen in Fig. 1, the spectra of the dried samples, when compared with those of the wet samples, reveal small changes in the relative intensities of some of the bands, as well as significant changes in the band width of the majority of the bands. A similar change in the spectra of

wet and dry samples of bleached spruce kraft pulp is shown in Fig. 2. Here again, in addition to the changes in relative intensities of some of the bands, there is a clear indication of broadening of all the bands.

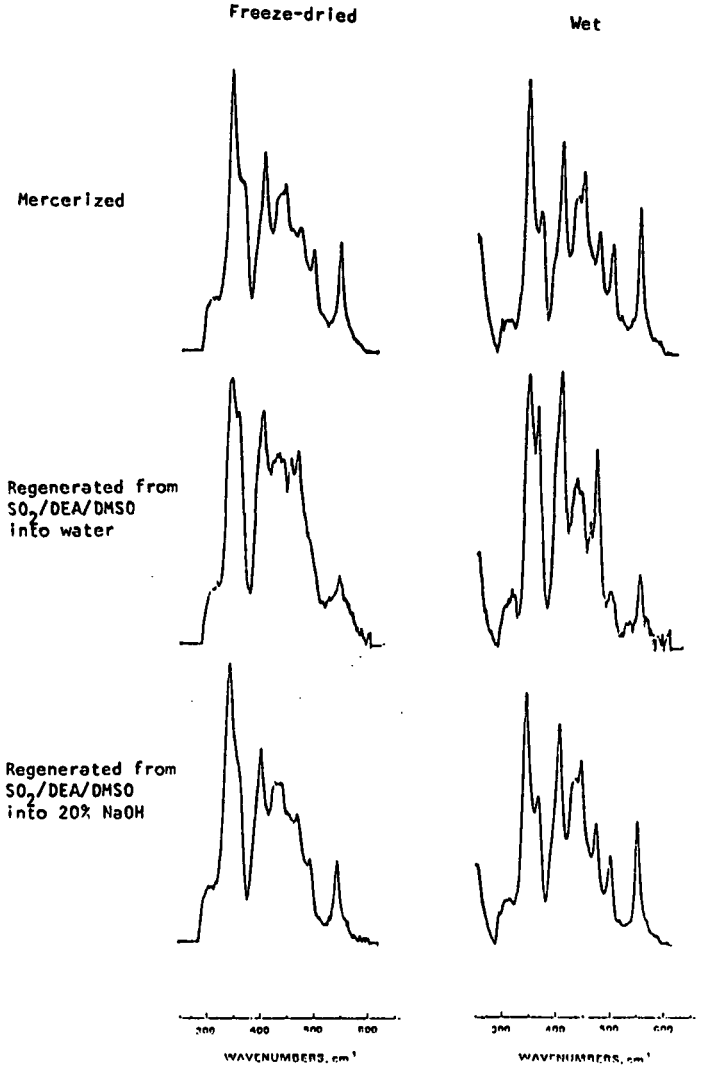

Figure 1. Dehydration of mercerized and regenerated celluloses.

The changes in band shapes seen in Fig. 1 and 2 are precisely the types of change to be expected if the lattices of the crystalline domains are subjected to stresses sufficient to bring about distortions. Such distortions are expected to cause small deformations of the chains which in turn bring about

small departures of the values of the internal coordinates from the uniformity characteristic of an unstressed lattice. These changes in the values of the internal coordinates result in a broadening of the distribution of frequencies for each of the internal modes of vibration in the molecular chain; the direct consequence is a broadening of most of the bands. The key implication of the differences we see between wet and dry samples is that a significant degree of internal stress must arise during the drying; the magnitude of the changes is such that small stresses are unlikely.

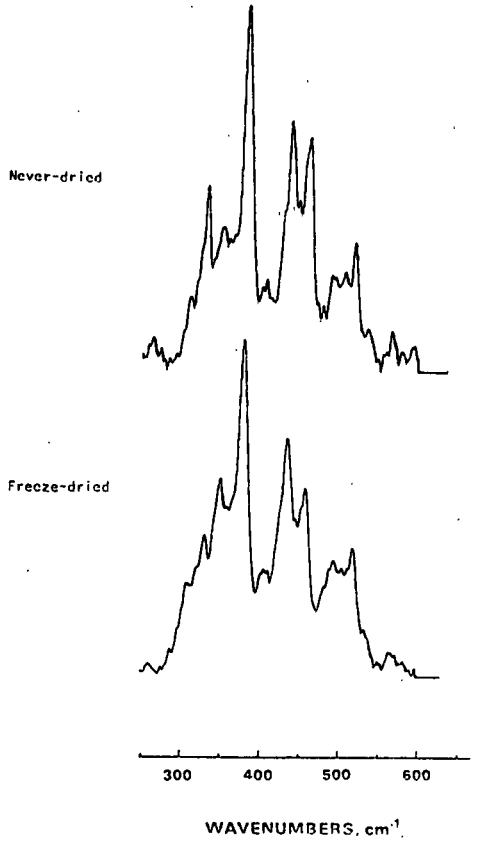

Figure 2. Dehydration of bleached kraft spruce pulp.

In considering the manner in which stresses could come about as a result of drying, it becomes clear that a considerable amount of entanglement of

crystalline and amorphous domains must prevail if the drying is to result in strains of the crystalline domains sufficient for the majority of the bands to become broadened. This would be true in the case of the regenerated celluloses. In the case of the native celluloses, it would not be expected to occur unless the fibers have a morphology complex enough that contraction of some domains would impose stresses on other domains.

To test the hypothesis concerning the role of entanglements we investigated Ramie fibers which have a simple morphology, with all of the molecular chains parallel to the fiber axis. The measurements were made on a single ramie fiber in the never dried-state and after it had been dried. The comparison shown in Fig. 3 showed that the spectra of the wet and dry fiber were quite similar. Because of the distinctive morphology it is not expected that any significant stresses would be generated in the process of drying.

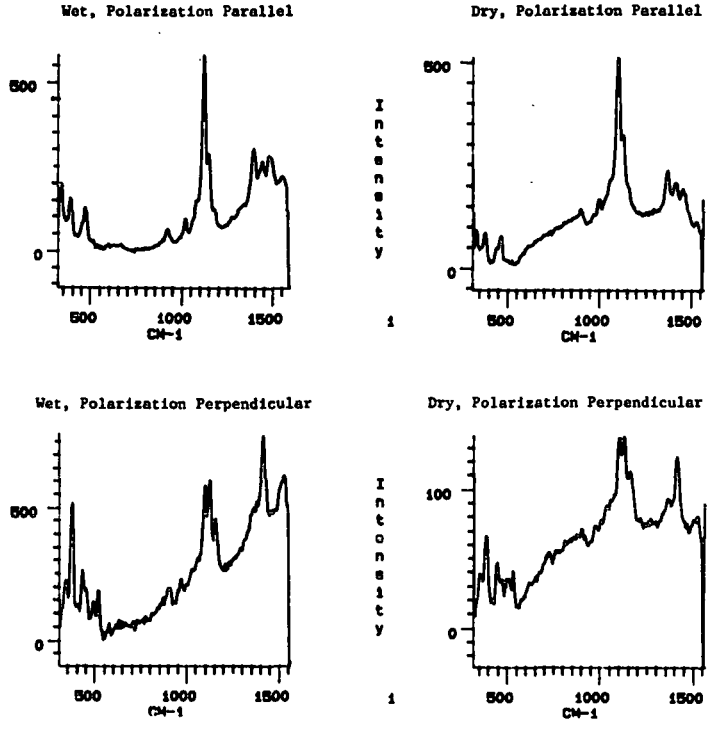

Figure 3. Effect of dehydration on Ramie fiber.

Effects of Annealing

The objective of the annealing studies was an exploration of the effects of differences in crystallinity on mechanical properties of experimental handsheets. The studies were undertaken, in the first instance, to find out whether differences in crystalline structure measureable in terms of differences in conformational distributions have measurable effects on the properties of handsheets.

A holopulp was prepared by an acid chlorite treatment of southern pine chips at 70 degrees C. It was made into handsheets after refining to varying levels of freeness. Some of the never-dried handsheets were heat treated in a humid environment at 125 and 150 degrees C. The sheets were then allowed to dry and the handsheet properties were measured. In addition, x-ray diffractograms were recorded on each of the sheets, and the Raman spectra of selected samples were measured.

The handsheets studied showed a deterioration in every one of the properties investigated as the severity of the thermal treatment increased. The sheets with the poorest properties were those treated at 150 degrees C, while those treated at 125 degrees C were intermediate in every respect. The properties included tensile, tear, and tensile energy absorption.

Correlated with the intensity of thermal treatment, the x-ray diffractograms revealed an increase in the crystallinity of the pulp fibers when it is measured by the width at half height of the 002 reflection in the diffractogram. As the crystallinity increases, the width at half height diminishes. In the case of cellulosic fibers the reduction in the width at half height is usually interpreted in terms of an increase in the average lateral width of crystalline domains.

Based on our prior experience with Raman spectra we had expected that the differences in crystallinity would also show up in differences between the ratios of molecules in the conformations K_I and K_O. We were surprised to find that the spectra of the control pulp and those of the pulps treated at both 125 and 150 degrees were in essence indistinguishable, within experimental error. These results suggest that the effects of heat treatment which we are observing are indeed annealing effects in which the defect content in the crystalline domains is reduced. Under such conditions the net change in the total number of anhydroglucose units in the K_I conformation is quite small relative to the total number already in that conformation in the untreated pulp.

As noted above, the original intent of this series of experiments was to find out if measurable changes in the proportion of cellulose molecules in the K_I conformation have correlated with the difference in the properties of the sheets made from the pulps. It is clear from our results that changes in crystallinity which are too subtle to influence the relative amounts of molecules in the K_I and K_O conformations, are nevertheless sufficient to alter the sheet properties.

The results summarized here are quite recent. We need to reassess the experimental program and carefully consider other implications of our observations before we continue this program.

Studies of Molecular Aggregation

Our studies of molecular aggregation are progressing in a number of areas, all of them intended to provide us with insights concerning the intermolecular interactions which dominate association of the cell wall components in woody tissue. We also seek to use the model systems we develop to assess the

potential response of associated polymers to environments which simulate pulping conditions. Our main goal is to elucidate the interaction between cellulose and the various hemicelluloses that comprise a wood fiber. Here we outline briefly the areas of current investigations.

The first area is an extension of some our earlier studies on blends of cellulose with chitosan. Our intent was to establish whether mixed lattices can be formed when these two components are coprecipitated from solution. We have expanded our investigation to ivory nut mannan. Preliminary indications are that when mannan and cellulose are coprecipitated from solution, a homogeneous blend of the two polymers is formed. We need to investigate the response of these blends to various treatments to establish whether under conditions which simulate pulping environments the association between the polymers is further strengthened, or whether alternatively a dissociation occurs.

In yet another investigation in this area, we expose wood chips from morphologically homogeneous tissue to different thermal environments, and then isolate the cellulose component. By measuring the Levelling Off Degree of Polymerization (LODP) we expect to establish whether cellulose has a tendency to associate in the course of pulping reactions to a degree beyond its degree of association in its native state.

The third class of studies related to the mechanisms of molecular aggregation involves the introduction of various components which simulate cell wall constituents into cultures of Acetobacter xylinum to establish whether their presence during the biogenesis of cellulose can alter the assembly of cellulose microfibrills. We are currently investigating some beta 1,4-linked cell wall polysaccharides, as well as some lignin precursors.

Finally we are continuing our studies of algal celluloses to establish the range of structures of cellulose which occur in these most simple of plant forms. We have so far identified highly crystalline celluloses similar to those previously reported, as well as celluloses of crystallinity similar to that in celluloses isolated from woody tissue. We have also encountered some algae that have cell walls made up entirely of other beta 1,4 hexosans or pentosans.

Related Publications

In addition to the work listed above, a number of publications have been completed in the past year. These include the following papers, all of which were included in the ACS Symposium Series Volume 340, entitled "The Structures of Cellulose" edited by R. H. Atalla:

R. H. Atalla, "The Structures of Cellulose", an overview chapter.

D. L. VanderHart and R. H. Atalla, "Further Carbon-^{13} NMR Evidence for the Coexistence of Two Crystalline Forms in Native Cellulose."

J. H. Wiley and R. H. Atalla, "Raman Spectra of Celluloses."

V. M. Gentile, L. R. Schroeder, and R. H. Atalla, "Physical Structure and Alkaline Degradation of Hydrocellulose."

A. Isogai, A. Ishizu, J. Nakano, and R. H. Atalla, "Intra- and Intermolecular Hydrogen Bonds in Native, Mercerized, and Regenerated Celluloses: Reflections in Patterns of Solubility and Reactivity."

In addition, the following paper has been published:

J. H. Wiley and R. H. Atalla, "Band Assignments in the Raman Spectra of Celluloses," Carbohyd. Res. 160:113(1987).

Copies of the selected papers are appended.

OVERVIEW 3521

Most of our effort under this project has been devoted to assembly of our new instrumental systems; we have encountered an inordinate amount of

failure of components of both systems. We are currently resolving what we believe to be the final problems with the systems, and we expect both to be operational in October. In additon to our work on the new instruments, we have carried out some additonal studies of luminescence phenomena.

The New Instrument Systems

The first of our systems to be assembled was the new microprobe. It consists of a Zeiss microscope, specially modified and interfaced with a Spex triple monochromator, and equipped with a Tracor Northern multichannel detector. We have encountered two major problems with this system. The detector was found defective and was sent back to the manufacturer to be reconstructed. When the detector was returned to us we began our experimental program but encountered another problem; we discovered that samples were moving on the stage of the microscope to a degree that was unacceptable for our work. After many unsuccessful efforts to stabilize the system we concluded that the mechanical coupling of the microscope to the monochromator was inadequate. We have persuaded Spex to redesign the mechanical coupling, and expect them to complete the modification before the end of September. It is perhaps well to note that ours was the first system manufactured by Spex requiring interfacing of the microscope with a triple monochromator.

Our system for time resolved spectroscopy has a similar but somewhat more complicated history. It consists of a scannable triple monochromator equipped with a gatable multichannel detector. The spectra are to be excited by a pulsed laser system. The detector for this system had to be returned for reconstruction as well. In addition, we have had to consider a number of approaches to synchronizing the laser pulses with the gating of the detector.

We have finally zeroed in on using a cavity dumper and a special timing module, both supplied by the laser manufacturer. All the subsystems have now been installed, and we expect the integrated system to be operational by October. Here again it should be noted that the frequency range at which we expect to be operating is not a very common one; it is dictated by the characteristics of the detector we have chosen. When the system is operational we expect to use it, in the first instance, for the FKBG sponsored program to develop an on-line lignin sensor. We will also use it to characterize the sources of luminescence in native woody tissue. Finally, we expect to use the system in photochemical studies in support of the program on Brightness Stability of High-Yield Pulps.

Luminescence Studies

In this area we have continued the studies of the effects of ambient environment on luminescence. We have previously reported that flushing the dry woody tissue samples with oxygen reduces the luminescence. It is now clear that molecular oxygen is quenching the excited states responsible. When other gases were used to flush the samples, a higher level of luminescence was observed.

In additional studies it was found that the presence of molecular oxygen does not affect the luminescence we observe with pure cellulose samples such as CF-1. Two interpretations are possible: I. The species responsible for this luminescence, which we believe to be residues of transition metal ions, are not susceptible to quenching by molecular oxygen. (In the case of woody tissue we believe the luminescence to originate in the excited states of aromatic entities which are known to be susceptible to quenching by molecular oxygen.) II. The alternative interpretation is that in the case of the pure celluloses the luminescence arises from sites imbedded deeply into the cellulosic tissue and not readily accessible to adsorbed gaseous species.

Another series of observations which are quite interesting because they may be relevant to the question of brightness stability were made during the effort to record spectra from samples of woody tissue under oxygen. It was noticed that when cross sections were exposed to the laser beam for extended periods in the presence of oxygen they developed a yellow color. In interesting contrast, when longitudinal sections were exposed, the yellow color did not develop. We speculate that cross sectioning may activate wound response mechanisms to a greater extent than longitudinal sectioning, but an understanding of this effect remains in the future.

On the basis of the studies carried out thus far it seems very likely that the primary luminescence we are dealing with is phosphorescence. We expect to characterize these phenomena in greater detail when the new systems are fully operational. Further details will be given at the October meeting.

The Institute of Paper Chemistry

Rajai H. Atalla
Chemical Sciences Division

ATTACHMENT I

STUDIES ON THE STRUCTURE OF CELLULOSE USING RAMAN SPECTROSCOPY AND SOLID STATE ^{13}C NMR

Rajai H. Atalla
The Institute of Paper Chemistry
Appleton, WI 54912 U.S.A.

and

David L. VanderHart
National Bureau of Standards
Gaithersburg, MD 20899 U.S.A.

ABSTRACT

Studies of cellulose using Raman and ^{13}C NMR spectroscopy reveal new dimensions to the complexity of its structures and their relative stabilities. We present further evidence in support of our hypothesis that native celluloses are composites of two crystalline modifications, I_α and I_β, which coexist in most native forms, and we elaborate on our understanding of these structures and their relative stabilities. We also present studies of the transformation of algal cellulose to cellulose III, and its reversion to cellulose I, which are relevant to the broader question of stability of the native forms of cellulose.

Summary of Prior Results

In our past studies (1,2) the resonance multiplicities in the solid state ^{13}C NMR spectra of native celluloses were examined at high resolution for a variety of native forms as well as samples of regenerated celluloses I and II. These spectra are an important source of new structural information that is complementary to that from other sources.

The spectra of pure samples of cellulose II can be rationalized in terms of nonequivalent sites within a unique unit cell. The spectra of the native celluloses, however, reveal multiplicities that cannot be ascribed to a unique unit cell. In particular, the sharper components of the C-4 and C-6 resonances, as well as the C-1 resonance, possess multiplicities that suggest that they arise from magnetically nonequivalent sites within crystalline domains. The narrow lines observed differ among the samples of native forms; the relative intensities are not constant and they are not in the ratios of small whole numbers as would be expected if they arose from different sites within a single unit cell.

We have found the proposal that native celluloses are composites of two distinct crystalline forms, identified as I_α and I_β, the most plausible basis for interpretation of the spectra. A decomposition of the spectra based on such a model has been described in our earlier reports. The spectra were obtained by taking appropriate linear combinations of the spectra of the regenerated cellulose I and of the cellulose from Acetobacter xylinum; these two celluloses were judged to be the closest to the two extremes on the basis of a two component model.

In studies of the Raman spectra one of us (3) addressed the question of conformational states in the two forms of native cellulose. The question was whether the two forms I_α and I_β represent true solid state allomorphs, with molecules possessing identical conformations, or whether like celluloses I and II they contain molecules with different conformations as well as different lattices.

Comparisons of the Raman spectra in the conformation sensitive region revealed a great deal of similarity in the spectra of the native celluloses included in the previous studies using ^{13}C NMR. In the OH stretching region, on the other hand, there were significant differences. These observations have been described in detail in recent reports by Wiley and Atalla (4,5), and lead to the conclusion that the I_α had I_β forms of cellulose represent lattices with nearly identical conformations of the heavy atom molecular skeletons, but with different hydrogen bonding patterns.

Recent Spectral Studies

The more recent studies undertaken in our laboratories have been directed at understanding the nature of the differences between the I_α and I_β forms. They have included additional Raman spectral studies, NMR relaxation studies, and studies on susceptibility to chemical reactions.

The Raman spectral studies have focused on the OH stretching region of the spectra. As noted earlier, Wiley and Atalla had found significant differences in this region between the spectra of celluloses in which the I_α and I_β forms were dominant. In an extension of this work, the question arose as to whether the different spectra could be resolved into those of the I_α and I_β components.

The spectra used in the resolution were those of the regenerated cellulose I which was known to be essentially of the pure I_β form, and that of *Cladophera glomerata*, an alga which produces celluloses which are very similar to those from *Valonia ventricosa*. Beginning with the proportions of the two forms determined from the Solid State ^{13}C NMR spectra, it was possible to resolve the Raman spectra in the OH stretching region into two component spectra corresponding to the two pure forms.

The two component spectra are shown in Fig. 1, where it is seen that the I_α spectrum possesses bands which do not occur in the I_β spectrum and vice versa. Though in the studies by Wiley and Atalla it was not possible to distinguish the bands seen in Fig. 1, it was clear that the low frequency band in the spectrum of the I_α component does not occur in the spectrum of the I_β component. Similarly, the high frequency shoulder that is pronounced in the spectrum of the I_β component does not occur in the spectrum of the I_α component.

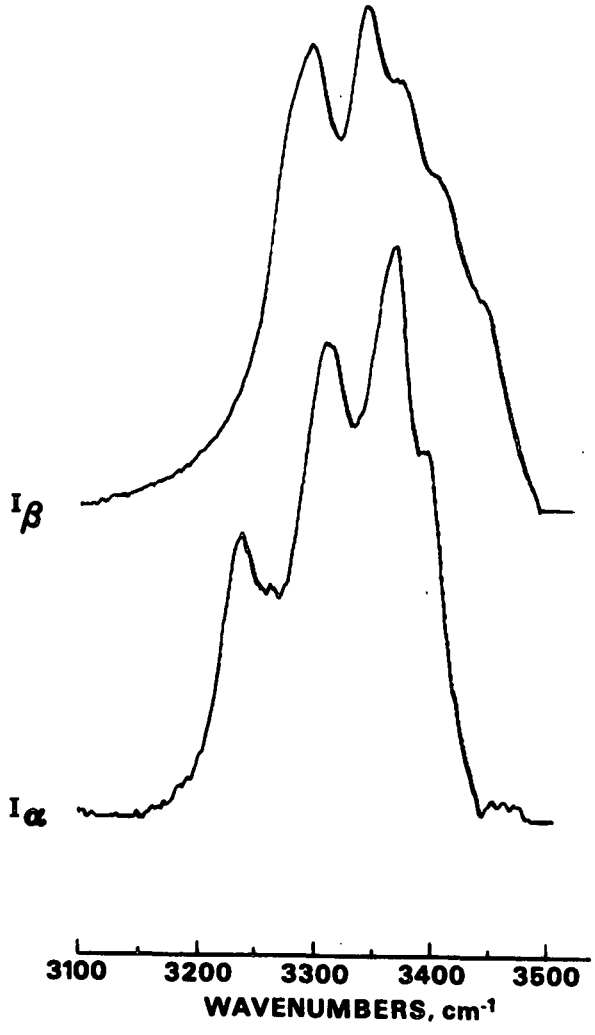

Figure 1. The resolved spectra of the I_α and I_β components of native celluloses in the OH stretching region of the Raman spectra.

In the investigations of Solid State ^{13}C NMR spectra, relaxation studies on both protons and carbon nuclei were used to confirm that unit cell inequivalences rather than crystal surface chain resonances determine the profiles of the sharp multiplets. It was also found that the higher plant celluloses contain a smaller fraction of the I_α component than had previously been proposed.

Experiments based on weak ^{13}C-^{13}C spin exchange were also conducted to probe the spatial environment, within a 0.7-1.0 nm radius, around carbons identified with individual multiplet components, which are assumed to belong exclusively to the I_α or I_β forms. The spectra of "nearest neighbors" were isolated for three different multiplet lines in an algal cellulose and for two lines in a higher plant cellulose. The results rule out the possibility that tertiary morphology can give rise to any multiplicity in these spectra. The results also provide strong support for the hypothesis of multiple crystalline forms in the algal celluloses; however, no clear evidence for multiple crystalline forms in the higher plant cellulose is found by this method.

In the studies of susceptibility to chemical reaction, samples of Cladophera glomerata cellulose were subjected to hydrolysis in boiling acid, and the resulting changes in the ^{13}C NMR spectra investigated. The hydrolysis was carried out in boiling 4N HCl for 44 hours. The mass yield was between 12 and 22%. The Solid State ^{13}C NMR spectra revealed a significant decline in the content of the I_α component. In one instance, shown in Fig. 2, the resulting spectrum suggested proportions of the two components similar to those in higher plants, though the resolution remained typical of the spectra of the algal celluloses.

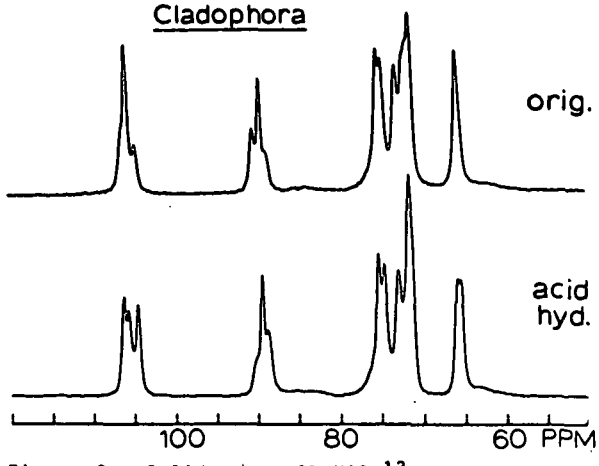

Figure 2. Solid state CP MAS ^{13}C NMR spectra of Cladophera glomerata cellulose before and after acid hydrolysis.

The results of the hydrolysis studies leave very little question that the susceptibility of the I_α form to acid hydrolysis is greater than that of the I_β form. It seems to us quite likely that differences in reactivity will be observed in other contexts as this matter becomes the subject of further studies.

Stability of Native Celluloses

In much of the early literature on polymorphy in cellulose it has been assumed that cellulose I is a less stable form of cellulose than cellulose II because the latter is the form most commonly recovered from solution. Although such an argument is not sound from a thermodynamic view, it has gained wide acceptance. One of us has questioned this on the basis of experimental results of regeneration studies (6,7). For example, it was found that celluloses regenerated at elevated temperatures into the cellulose IV lattice possessed Raman spectra indicating the presence of some cellulose in the conformation corresponding to cellulose I. That work also led to the preparation of regenerated cellulose I under more carefully controlled conditions (8).

In the context of this presentation it is interesting that the regenerated cellulose I has always been the pure I_β form as identified by ^{13}C NMR spectra. We believe this is not unrelated to recent observations of the effects of conversion of cellulose I to cellulose III, and its reversion to cellulose I upon boiling in water, which seem to alter the balance between the I_α and the I_β forms.

In this new series of observations samples of cellulose from Cladophera glomerata were converted to the cellulose III form according to a procedure suggested by Hayashi (9). The x-ray diffractogram of the converted form showed it to be of the highest crystallinity, approaching the same order of crystallinity as that of the native form. The solid state ^{13}C NMR spectra, shown in Fig. 3, differed from any that we had previously recorded for cellulose, in that none of the resonances of the carbons in the anhydroglucose units showed any multiplicities. Thus, the lattice and the molecular conformation were thought likely to be distinct.

Raman spectra confirmed our expectations on the basis of the NMR spectra. As shown in Fig. 4, the conformation sensitive region between 200 and 700 cm^{-1} showed some dramatic differences between the spectra of the cellulose III and that of the Cladophera cellulose from which it was prepared, as well as distinct differences between the cellulose III spectrum from that of cellulose II. These differences point to a change in the conformation of the cellulose skeleton, though not necessarily a very large one.

When the sample of cellulose III was boiled in water, it reverted to cellulose I. However, the Solid State ^{13}C NMR spectra, also shown in Fig. 3, revealed it to have been transformed from a cellulose in which the I_α form was dominant to a cellulose in which the I_β form is dominant. Indeed, the spectra seemed to be quite similar to those expected from a highly crystalline higher plant cellulose. As seen in Fig. 5, the Raman spectrum also reverted, in the conformation sensitive region, to one characteristic of a higher plant crystalline cellulose similar, for example, to that of hydrocellulose from ramie. In the OH stretching region the spectrum of the recovered cellulose I was typical also of the celluloses in which the I_β form is dominant.

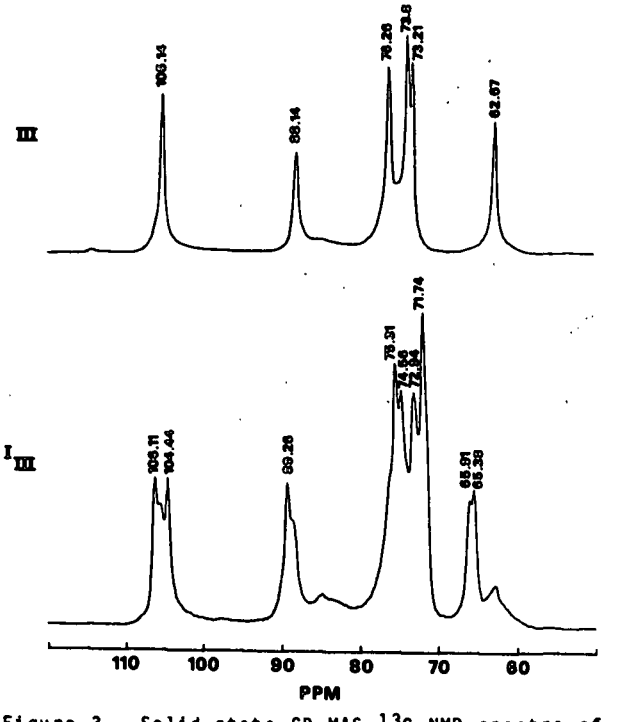

Figure 3. Solid state CP MAS ^{13}C NMR spectra of cellulose III prepared from Cladophera glomerata, and after recovery of cellulose I by boiling in water.

These observations suggest to us that the I_β form may be the more stable of the two native forms of cellulose. But they also suggest that the general assumption that cellulose I is a less stable lattice needs to be reexamined. If cellulose II were the more stable form, one would have expected the treatment in water to result in conversion of the cellulose III to cellulose II, particularly since both the Raman and ^{13}C NMR spectra leave little doubt that the original cellulose I lattice had been completely converted.

ACKNOWLEDGMENTS

The authors wish to acknowledge the help of Ms. Rebecca Whitmore and Mr. Clark Woitkovich in the preparation of some of the samples, and acquisition of the Raman spectra.

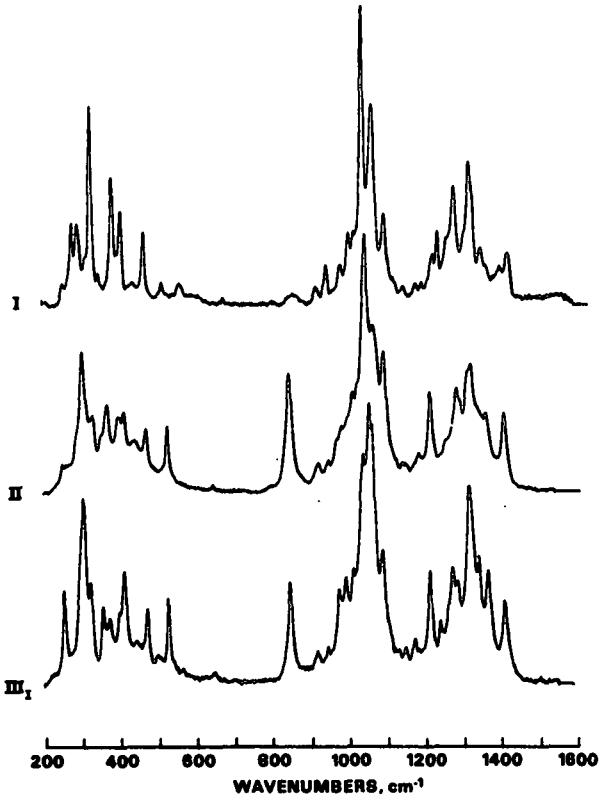

Figure 4. Raman spectra of celluloses I, II, and III, in the conformation sensitive region.

REFERENCES

1. ATALLA, R. H. AND VANDERHART, D. L. Native cellulose: a composite of two distinct crystalline forms. Science 223: 283-5 (Jan. 20, 1984).
2. VANDERHART, D. L. AND ATALLA, R. H. Studies of microstructure in native celluloses using solid state ^{13}C NMR. Macromolecules 17: 1465 (1984).
3. ATALLA, R. H. Polymorphy in native cellulose: recent developments. Structure, Function and Biosynthesis of Plant Cell Walls, W. M. Dugger and S. Bartnicki-Garcia, eds., American Society of Plant Physiologists, Rockville, MD, 1984. p. 381.
4. WILEY, J. H. AND ATALLA, R. H. Raman spectra of celluloses, in "Solid State Characterization of Cellulose." R. H. Atalla, ed., ACS Symposium Series, in press.
5. WILEY, J. H. AND ATALLA, R. H. Raman microprobe studies on cellulose fibers. Carbohydrate Research, special issue on physical chemical studies on macromolecular carbohydrates, in press.
6. ATALLA, R. H. AND NAGEL, S. C. Cellulose: its regeneration in the native lattice. Science 185: 522 (1974).
7. ATALLA, R. H., DIMICK, B. E., AND NAGEL, S. C. Studies of polymorphy in cellulose. Cellulose IV and some effects of temperature. ACS Symposium Series 48: 40-31 (1977). Macromol. 7: 182 (1985).
8. WHITMORE, R. E. AND ATALLA, R. H. Factors influencing regeneration of cellulose I from phosphoric acid solutions. Int. J. Biol. Macromol. 7: 182 (1985).
9. Hayashi, J., personal communication.

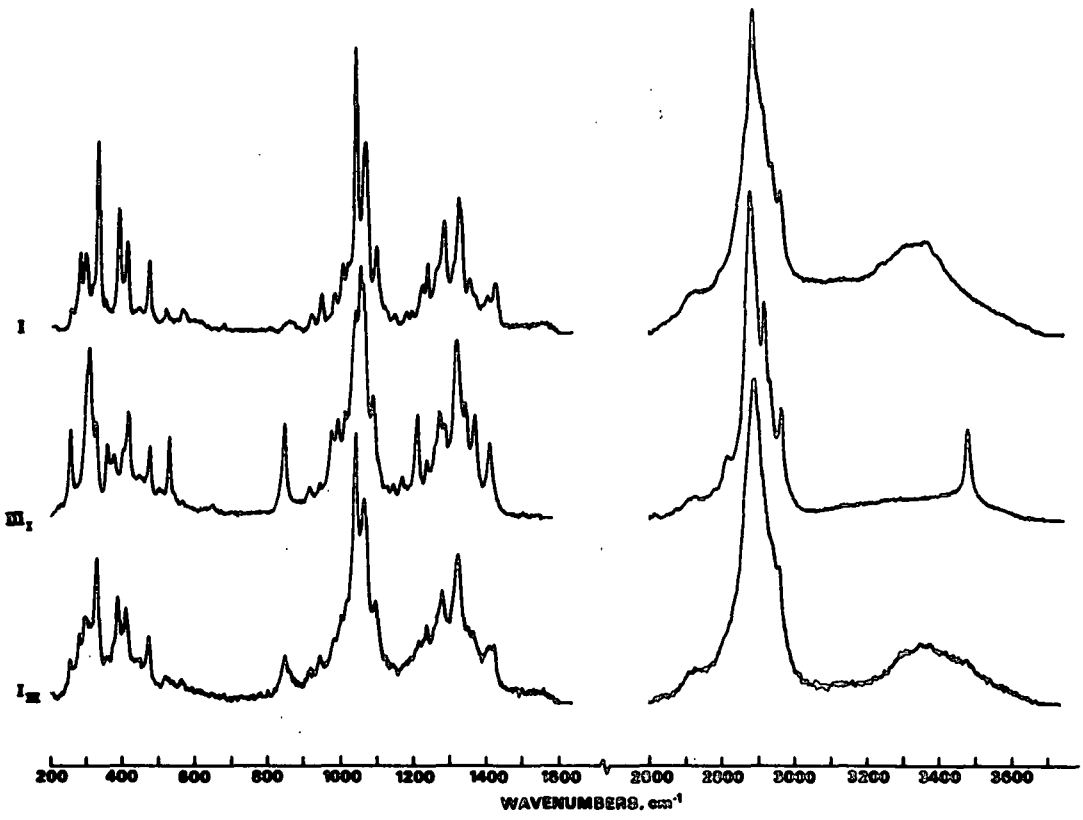

Figure 5. Raman spectra of Cladophera cellulose, in the native form, after conversion to cellulose III, and after reversion to the cellulose I lattice upon boiling in water.

The Structures of Cellulose

Rajai H. Atalla

The Institute of Paper Chemistry
Appleton, Wisconsin 54912

An overview of studies of the structure of cellulose is presented and begins with a historical perspective, developed with particular emphasis on the early diffractometric studies. More recent studies are then described, and the key questions confronted in any analysis of diffractometric data are discussed. The central questions are concerned with the validity of the assumption that the unit cells of cellulose belong to space group $P2_1$, and whether the twofold screw axis associated with this space group coincides with the molecular chain axes. The diversity of the interpretations which occur in the literature and in following chapters is noted. More recent spectroscopic investigations are then discussed, with emphasis on the degree to which they may provide additional information concerning structure. It is noted that although both Raman spectroscopy and CP-MAS ^{13}C NMR cannot provide direct information concerning the positions of molecules in the unit cells, they are sensitive to the values of the internal coordinates. Thus, they provide information complementary to the diffractometric data in that it serves to constrain the acceptable structural models to a smaller subset than that otherwise admissible on the basis of diffractometric observations alone. In this respect, the spectroscopic information complements the diffractometric data in the same way as the assumptions concerning the symmetry of the unit cell. Furthermore, it appears that the structures suggested by the spectroscopic studies represent relatively small although significant departures from those derived on the basis of diffractometry alone. In anticipation of future directions in studies of celluloses, it is noted that multidisciplinary approaches, similar to some described in later chapters, hold great promise for future progress in understanding the structural diversity that is characteristic of cellulose.

Since the occurrence of cellulose as a distinct substance was first recognized by Anselme Payen in 1842 the evolution of ideas concerning its structure has been closely related to advances in structural chemistry and its methodologies. The pattern of close relation continues into the present time and is well reflected in the following chapters which include contributions from most of the major laboratories active in the field. In this chapter, we discuss the structural problem in general and place those of the following chapters which are concerned with the problem in perspective relative to recent developments in the field, with particular emphasis on the past decade.

The procedures for structural studies on cellulose have much in common with investigations of structure in polymers in general. In most instances diffractometric data are not sufficient for a solution of the structure in a manner analogous to that possible for lower molecular weight compounds which can be made to form single crystals. It becomes necessary, therefore, to complement diffractometric data with structural information derived from studies carried out on the monomers or oligomers.

Kakudo and Kasai have summarized the central problem well (1): "There are generally less than 100 independently observable diffractions for all layer lines in the x-ray diagram of a fibrous polymer. This clearly imposes limitations on the precision which can be achieved in polymer structure analysis, especially in comparison with the 2000 or more diffractions observable for ordinary single crystals. However, the molecular chains of the high polymer usually possess some symmetry of their own, and it is often possible to devise a structural model of the molecular chain to interpret the fiber period in terms of the chemical composition by comparison with similar or homologous substances of known structure. Structural information from methods other than x-ray diffraction (e.g., infrared and NMR spectroscopy) are also sometimes helpful in devising a structural model of the molecular chain. The majority of the structural analyses which have so far been performed are based on models derived in this way. This is, of course, a trial and error method". Similar perspectives have been presented by Arnott (2), Atkins (3), and Tadokoro (4,5).

An acceptable fit to the diffractometric data is not the ultimate objective, however. Rather it is the development of a model that possesses a significant measure of validity as the basis for organization, explanation and prediction of experimental observations. With respect to this criterion, the models of cellulose which have been developed so far leave much to be desired, for their capacity to integrate and unify the vast array of information concerning cellulose is limited indeed. One of the objectives of this symposium is to facilitate identification of points of departure for further studies in search of models which are more useful.

To help place the proceedings in perspective we begin with a brief historical review, and continue with a discussion of recent contributions based on the key methodologies which have been used. The methodologies are in three broad, complementary categories, which include diffractometry, spectroscopy, and theoretical model building on the basis of conformational analysis. Although, significant structural information is inferred from patterns of chemical

reactions under a wide range of conditions, we limit this chapter to studies based on physical methods.

In order to achieve greater clarity in the following discussion, it is well to note that questions of structure arise at three different levels. The first, that of the chemical structure, reflects the pattern of covalent bonding in cellulose molecules and is generally well established. While the evolution of concepts at this level is of historical interest, it is not under discussion in these proceedings. The next level of structure is that of the relative organization of the repeat units in an individual molecule, under constraints of conformational energy considerations, as well as considerations of packing of the molecules in a particular state of aggregation. This level of structure is particularly important in spectroscopic studies wherein the energy levels between which transitions are observed are determined by the values of the internal coordinates which define molecular conformations. The final level of structure is that reflecting the arrangement of the molecules relative to each other in a particular state of aggregation, whether it be amorphous, or represents one or another of the crystalline allomorphs which occur because of the polymorphy characteristic of the crystallinity of cellulose. This is the level of structure probed by diffractometric measurements which are inherently most sensitive to the three dimensional organization represented by a particular state of aggregation.

Historical Overview

The evolution of ideas concerning the nature of cellulose and the models of its chemical structure have been described by Purves (6) in an excellent overview, beginning with the first observations by Payen and leading up to those which finally won acceptance of the polymer hypothesis in the decade immediately preceding the Second World War. Another valuable perspective is presented by Flory (7) in his general review of the evolution of the polymeric hypothesis, highlighting investigations of the three common natural homopolymers: starch, cellulose, and natural rubber. Finally, the first chapter in the treatise by Hermans (8) focuses on the physical chemical aspects of the early structural studies, in an account which is an excellent complement to the review by Purves with its emphasis on the classical organic chemical phase in the structural studies.

Among more recent reviews of structure, those by Jones (9), and by Tonessen and Ellefsen (10,11) are the most comprehensive. Preston (12) and Frey-Wyssling (13) in their respective treatises on plant cell walls, have also touched upon the problem of the structure of cellulose. The reader is referred to these sources for comprehensive presentations of the range of proposals concerning the structures of cellulose which have been under discussion in recent decades. A representative subset will be presented here as a point of departure for following discussions.

Quite early in the x-ray diffractometric studies of cellulose it was recognized that its crystallinity is polymorphic. It was established that native cellulose, on the one hand, and both regenerated and mercerized celluloses, on the other, represent two distinct crystallographic allomorphs (14). Little has transpired

since the early studies to change these perceptions. There has been, however, little agreement regarding the structures of the two forms. For example, Petitpas et al. (15) have suggested on the basis of extensive analyses of electron-density distributions from x-ray diffractometric measurements that chain conformations are different in celluloses I and II. In contrast, Norman (16) has interpreted the results of his equally comprehensive x-ray diffractometric studies in terms of similar conformations for the two allomorphs.

At a more basic level than the comparison of celluloses I and II, the stucture of the native form itself has remained in question. Among recent studies, for example, Blackwell and Gardner (17), in their analysis of the structure of cellulose from Valonia ventricosa, assumed a lattice belonging to the $P2_1$ space group, with the twofold screw axis coincident with the molecular chain axis. Hebert and Muller (18), on the other hand, in an electron diffractometric study of a number of celluloses including Valonia, confirmed the findings of earlier investigators who found no systematic absences of the odd order reflec-tions forbidden by the selection rules of $P2_1$, and concluded that the cellulose unit cells do not belong to that space group.

Even when $P2_1$ is taken to be the appropriate space group, the question of chain polarity remains. As noted by Jones (19), and by Howsmon and Sisson (20), the structure initially proposed by Meyer and Mark (21) assumed that the chains were parallel in polarity. The structure later proposed by Meyer and Misch (22) was based on the reasoning that the rapidity of mercerization, and its occurrence without dissolution required that the polarity of the chains be the same in both celluloses I and II. It was reasoned further that regeneration of cellulose from solution is most likely to result in precipitation in an antiparallel form, and that the similarity between x-ray diffraction patterns of mercerized and regenerated cellulose required that they have the same polarity. It was thus inferred that native cellulose must also have an antiparallel structure.

Although the argument that regeneration in the antiparallel mode is more probable was found invalid within a decade of its first presentation (23), the relative organization of molecules suggested by Meyer and Misch remained the point of departure for most subsequent investigators.

When the models incorporating antiparallel arrangement of the chains are extended to native cellulose, they pose serious questions concerning proposed mechanisms for the biosynthesis of cellulose. It is difficult to envision a plausible mechanism for simultaneous synthesis and aggregation of antiparallel chains. It is perhaps for this reason that more recent proposals of parallel structures for native cellulose have been embraced by investigators of the mechanism of biosynthesis.

The contribution of spectroscopy to the early studies of structure was quite limited. An important contribution was made in the studies by Liang and Marchessault (24-26) wherein measurements of dichroism in infrared absorption of oriented specimens led to proposal of a particular hydrogen-bonding scheme. The differences between the spectra of celluloses I and II were explained in terms of differences in the packing of molecular chains and associated

variations in the hydrogen-bonding patterns. In another application, infrared absorption measurements were used as the basis of a crystallinity index by Nelson and O'Connor (27,28).

More recently, a number of new structure sensitive techniques have been developed, and they have been applied to studies of cellulose. These include Raman spectroscopy and Solid State ^{13}C Nuclear Magnetic Resonance, in the experimental arena, and conformational energy calculations in the theoretical domain. These are more recent contributions and are the subjects of subsequent sections in this chapter and later chapters in these proceedings.

Diffractometric Studies

As noted by Kakudo and Kasai, the primary difficulty in structural studies on polymeric fibers is that the number of reflections usually observed in diffractometric studies are quite limited. In the case of cellulose it is generally difficult to obtain more than 50 reflections. Consequently it becomes necessary to minimize the number of structural coordinates to be determined from the data by adopting plausible assumptions concerning the structure of the monomeric entity. The limited scattering data are then used to determine the orientation of the monomer units with respect to each other. In the majority of diffractometric studies of cellulose published so far, the monomeric entity has been chosen as the anhydroglucose unit. Thus, structural information from single crystals of glucose is implicitly incorporated in the analyses of the structure of cellulose. The coordinates which are adjusted in search of a fit to the diffractometric data include those of the primary alcohol group at C6, those of the glycosidic linkage, and those defining the positions of the chains relative to each other.

In addition to selection of the structure of the monomer as the basis for defining the internal coordinates of the repeat unit, the possible structures are usually further constrained by taking advantage of any symmetry possessed by the unit cell. The symmetry is derived from the systematic absence of reflections which are forbidden by the selection rules for a particular space group. In the case of cellulose, the simplification usually introduced is the application of the symmetry of space group $P2_1$, which includes a twofold screw axis parallel to the direction of the chains. The validity of this simplification remains the subject of controversy, however, because the reflections which are disallowed under the selection rules of the space group are in fact frequently observed. In most of the studies these reflections, which are usually weak relative to the other main reflections, are assumed to be negligible. The controversy continues because the relative intensities can be influenced by experimental conditions such as the periods of exposure of the diffractometric plates. Furthermore, the disallowed reflections tend to be more intense in electron diffractometric measurements than in x-ray diffraction measurements. Thus, more often than not, investigators using electron diffraction challenge the validity of the assumption of twofold screw axis symmetry.

The key assumption with respect to symmetry, however, is not the existence of the twofold screw axis as an element of the symmetry of the unit cell, but rather the additional assumption that

this axis coincides with the axis of the molecular chains of cellulose. This latter assumption has, implicit in it, a number of additional constraints on the possible structures which can be derived from the data. It requires that adjacent anhydroglucose units are related to each other by a rotation of 180 degrees about the axis, accompanied by a translation equivalent to half the length of the unit cell in that direction; it is implicit, therefore, that adjacent anhydroglucose units are symmetrically equivalent and, correspondingly, that alternating glycosidic linkages along the chain are symmetrically equivalent.

If the assumption concerning coincidence of the twofold screw axis and the molecular chain axis were excluded for example by locating the twofold screw axis between the molecular chains though still parallel to the chain axes, the diffractometric patterns would admit nonequivalence of alternate glycosidic linkages along the molecular chain, as well as the nonequivalence of adjacent anhydroglucose units. This possibility has been ignored, however, in large part because it requires expansion of the number of internal coordinates which have to be determined from the diffractometric data. Furthermore, it excludes the possibility of antiparallel alignment of chains in the unit cell.

The assumptions that the unit cell possesses the symmetry of space group $P2_1$ and that the twofold axis is coincident with the chain axis, do in fact meet a criterion long honored in scientific studies, namely, William of Ockham's principle of economy, which requires that the most simple hypothesis consistent with observations should always be adopted. Clearly the structure based on the anhydroglucose as the repeat unit is the most simple structure that accounts for the majority of the diffractometric data. Furthermore, the diffractometric data available are not sufficient to allow refinement of a structure possessing many more degrees of freedom, as would be the case if the twofold axis were not assumed coincident with the chain axis.

The assumptions concerning the symmetry of the unit cell noted above have been the basis of recent refinements of the structure of cellulose I. In one such refinement (17) the forbidden reflections were simply assumed negligible, and the intensity data from Valonia cellulose were used to arrive at a final structure. In another study, the inadequate informational content of the diffractometric data was complemented with analyses of lattice packing energies (29); the final structures were constrained to minimize the packing energy as well as optimizing the fit to the diffractometric data. Here the assumptions implicit in the weighting of the potential functions which are used in the energy calculations, further complicate the interpretations. As noted by French, et al. in a subsequent chapter in these proceedings, the structures derived in these two studies, though both based on parallel chain arrangements, are nevertheless very different crystal structures. When the same convention is applied in defining the axes of the crystal lattice, the structure most favored in one analysis is strongly rejected in the other. Furthermore, neither of these is strongly favored over yet a third, antiparallel structure (30).

The structures of oligomers are another important source of relevant information cited by Kakudo and Kasai. The implications of

the structures of the disaccharides have been considered by Atalla (31) and were the basis for reassessment of the second assumption concerning symmetry noted above. Structures with alternating nonequivalent glycosidic linkages were found more consistent with spectroscopic data (32).

Studies of oligomers have been extended in two chapters in the present volume, with the comparisons made primarily with structures proposed for cellulose II. Sakthivel, et al. applied the Rietveld crystal structure method to cellotetraose. Their results favor a parallel arrangement of chains in the unit cell, with individual chains possessing near twofold screw axis symmetry.

In a study of a number of oligomers, Henrissat, et al. used a multidisciplinary approach to examine the matter of the valid repeat unit. Their conformational analyses and ^{13}C NMR spectra were interpreted in terms of nonequivalent glycosidic linkages in the individual chains, but the diffraction data were found most consistent with an antiparallel structure.

Spectroscopy

Spectroscopic studies are useful in structural investigations because they provide information which is complementary to that derived from diffractometric data. The information derived from spectra is not directly related to the coordinates of molecules in the unit cell. The spectra are, however, sensitive to the values of internal coordinates which define molecular structure. Thus they provide a basis for testing the degrees of equivalence of structures. Very often also, specific spectral features can be identified with particular functional groups defined by distinctive sets of internal coordinates.

Two classes of spectral studies have been applied for the first time during the past decade as the basis of structural studies of cellulose. These are Raman spectroscopy, and solid state ^{13}C NMR using the CP/MAS technique. Both have raised questions concerning the assumptions about symmetry incorporated in the diffractometric studies. And while they cannot provide direct information concerning the structures, they establish criteria that any structure must meet to be regarded as an adequate model. The information from spectroscopic studies represents one of the major portions of the phenomenology that any acceptable structural model must rationalize.

Although the new spectral methods have also found application in investigations of structural changes induced by mechanical treatments or by treatments with swelling agents, the following discussion will be limited to studies which have focused on questions of structure. The results of such studies have to be rationalized by any model derived from crystallographic investigations and thus provide tests of consistency complementary to the diffractometric data, in the sense set forth by Kakudo and Kasai.

Raman Spectroscopy. Raman spectroscopy is the common alternative to infrared spectroscopy for investigating molecular vibrational states and vibrational spectra. It has enjoyed a significant revival since the development of laser sources for excitation of the spectra. Its key advantage in the present context is that it is

primarily sensitive to the skeletal vibrations of the cellulose molecule, with the mode of packing in the lattice having only secondary effects. This feature is a consequence of the dependence of Raman spectral activity of molecular vibrations on changes in the polarizability of vibrating bond systems, rather than changes in associated molecular dipoles. The most intense contributions to the spectra are due to bond systems which are predominantly covalent in character, with the more polar systems resulting in much weaker bands.

In the first detailed comparison of the Raman spectra of celluloses I and II, it was concluded that the differences between the spectra, particularly in the low frequency region, could not be accounted for in terms of chains possessing the same conformation but packed differently in the different lattices (33). As noted above, that had been the general interpretation of diffractometric studies of the two most common allomorphs. The studies of the Raman spectra led to the proposal that two different stable conformations of the cellulose chains occur in the different allomorphs.

In order to establish the differences between the conformations, information from other sources was considered. The results of published conformational energy calculations suggested two stable conformations for the glycosidic linkages (34,35). These represent relatively small left-handed and right-handed departures from the conformation of the glycosidic linkage in a twofold helical structure. They are well approximated, respectively, by the experimentally observed conformations of the glycosidic linkages in the crystal structures of the model disaccharides cellobiose (36) and methyl-β-cellobioside (37).

An analysis of the vibrational spectra in the OH stretching region for both the model disaccharides and for celluloses I and II suggested that nonequivalent glycosidic linkages alternate along the molecular chains (31). The solid state ^{13}C NMR spectra were found consistent with this model (38), although alternative interpretations are also possible. Finally the Raman spectra in the methylene bending region indicated that the C6 carbons occur in two nonequivalent environments in cellulose I but appear merged into a single set in cellulose II (39).

The results of the spectroscopic studies were interpreted in terms of nonequivalence of adjacent anhydroglucose units in the molecular chains, requiring the basic repeat unit of structure to be taken as the dimeric anhydrocellobiose unit. The difference between cellulose I and II was associated with the locus of the nonequivalence. In cellulose II it was thought to be at the glycosidic linkages, while in cellulose I it was taken to be centered at C6 and the adjacent segment of the pyranose rings.

To reconcile the conclusions outlined above with the requirements of chain packing, the proposal was made that cellulose chains possess alternate left-handed and right-handed glycosidic linkages in sequence along the chain axes. The left-handed and right-handed linkages were envisioned as representing relatively small departures of the dihedral angles from those prevailing for a twofold helix. The degree of departure from the parameters of a twofold helix was seen as somewhat greater for cellulose II than for cellulose I. The

model is discussed in somewhat more detail in the chapter by Wiley and Atalla, later in this volume.

Solid State ^{13}C NMR Spectra.

The second important spectroscopic method which has been applied in investigating the structure of cellulose during the past decade is high resolution ^{13}C NMR of the solid state based on the CP-MAS technique. In this technique, cross polarization (CP) is used to enhance the ^{13}C signal, high power proton decoupling to eliminate dipolar couplings with protons, and magic angle spinning (MAS) of the sample about a particular axis relative to the field to eliminate chemical shift anisotropy. Application of this method results in acquisition of spectra of sufficiently high resolution so that chemically equivalent carbons which occur in magnetically nonequivalent sites can be distinguished.

Though the technique has been used by a number of different investigators (38,40-43), we focus here on the studies by VanderHart and Atalla as representative of the structural questions addressed (44,45). Some resonance multiplicities for chemically equivalent carbons occur in the spectra of all the celluloses investigated.

The spectra of high crystallinity samples of cellulose II showed clear splittings of the resonances associated with C4 and C1. These have been interpreted as evidence of nonequivalent glycosidic linkages along the molecular chains (38), though it has also been suggested that the splittings may be evidence for nonequivalent chains in the unit cell (43). The latter argument leaves open the question as to why the resonances for carbons 2, 3, 5, and 6 do not display similar splittings.

Perhaps the most significant new information derived from the CP-MAS spectra is that relating to the native celluloses. The spectra reveal multiplicities that cannot be interpreted in terms of a unique unit cell, even though they arise from magnetically nonequivalent sites in crystalline domains. The narrow lines observed have relative intensities which are neither constant among the samples of different native celluloses, nor are they in the ratios of small whole numbers as would be expected if they arose from different sites within a relatively small unit cell. VanderHart and Atalla proposed that native celluloses are composites of two distinct crystalline forms (44,45).

Spectra of the two forms were resolved through linear combination of the spectra of native celluloses possessing the two forms in different proportions. The two types were designated celluloses I_α and I_β. The I_α form was found to be dominant in celluloses from lower plant forms and bacterial celluloses, while the I_β form was found dominant in celluloses from higher plants.

In studies of the Raman spectra of different native celluloses, Atalla (32) concluded that the two forms I_α and I_β consist of molecular chains which have the same molecular conformation. In the chapter by Wiley and Atalla in the present volume, evidence is presented to suggest that though the molecular conformations are the same, the hydrogen-bonding patterns differ in the two forms.

VanderHart and Atalla also present additional ^{13}C NMR CP-MAS experiments in a subsequent chapter. These provide strong evidence for the existence of the I_α and I_β forms in native celluloses,

particularly those from the lower plants and bacterial cellulose. They do raise, however, some questions about the earlier estimates of the amount of I_α form in the native celluloses from the higher plants.

In yet another application of the CP-MAS ^{13}C NMR spectroscopy in studies of the structure of celluloses, Horii, et al. have introduced correlations between the chemical shifts and dihedral angles as the basis of developing new structural information. In a subsequent chapter in these proceedings they provide an overview of their studies correlating the chemical shifts of specific carbons with the values of the dihedral angles about bonds involving those carbons. By examining the values of chemical shifts for monomeric and oligomeric compounds of known structures, they have developed correlations which may be applied in translating the spectral information in a manner that is complementary to the diffractometric studies.

Multidisciplinary Studies

In addition to the studies outlined above, with primary focus on diffractometry or on spectroscopy, there have been, recently, a number of studies which recognize at the outset the type of constraints summarized by Kakudo and Kasai, and which begin with an integrated approach to the investigation of structure. Perhaps the best illustration of this approach is the work of Henrissat and coworkers noted earlier and outlined in a later chapter, focusing on oligomers clearly related to the structure of cellulose II.

In the work of Henrisat, et al., the x-ray diffractometric data of Poppleton and Mathieson (46) on cellotetraose was complemented with structural data on other oligomers, with CP-MAS ^{13}C NMR spectroscopy, with conformational energy calculations, and with molecular orbital calculations to determine some of the favored conformations. The difficulty of the problem of the structures of cellulose is perhaps best illustrated by some of the remaining ambiguities cited in this study.

Yet another set of interdisciplinary studies are represented by the work of Hayashi and coworkers, wherein they attempt to shed light on the questions of reversibility, or lack thereof, in transformations between the allomorphs of cellulose and its derivatives. In addition to their diffractometric studies reported in prior publications, they add in their contribution to the present symposium analyses of the infrared spectra as well as analyses of the CP-MAS ^{13}C NMR spectra. Their thesis is not inconsistent with the proposals of Atalla and coworkers concerning differences between the conformations of celluloses I and II. However, Hayashi and coworkers go beyond this by proposing that the differences in conformation can be preserved in the course of heterogeneous derivatization reactions, and also in the process of generating the other allomorphs of cellulose, namely celluloses III and IV, from the two primary allomorphs I and II.

The adoption of multidisciplinary approaches in the effort to shed light on the complex questions of structures is likely to expand in the future. The proceedings of this symposium are clear evidence both for the need and the value of such approaches.

Future Directions

The studies reviewed briefly above place the problem of the structures of cellulose in a promising perspective. Until the development of the new spectroscopic methods, the crystallographic studies were undertaken with little additional information from other sources, with the exception of some of the conformational energy calculations. These are useful, but they are sensitive to the nature of the potential functions used in the calculations and particularly to the manner in which the different potential functions are weighted.

As noted earlier, the crystallographic studies have sought the most simple model structure consistent with observations. Clearly the structure based on the anhydroglucose as the repeat unit is the most simple structure that accounts for the majority of the diffractometric data. Furthermore, the data available did not provide a basis for introducing departures from the most simple model, nor suggestions for its revision.

The new information from spectroscopic studies sheds new light in two key areas. The first is related to the complexity of the structures of the native celluloses. The second is that of the relationship between the structures of celluloses I and II.

It has been known for some time that the more crystalline native celluloses from algae and from Acetobacter xylinum produce diffraction patterns that have many features in common with those of the crystalline celluloses from the higher plants, such as ramie, but that cannot be indexed as simply or on the basis of the same unit cell. The new information from the CP-MAS ^{13}C NMR spectra, together with that from the Raman spectra, suggests some bases for understanding these differences, and directions for further explorations.

The key conclusion that is relevant here is that the native celluloses are composites of more than one crystaline form, but that the difference between the two forms lies not in the molecular conformation but in the hydrogen bonding patterns. Thus, it is possible that the native celluloses have unit cells with very similar atomic coordinates for the heavy atoms, but with different coordinates for the hydrogens. The similarities in the heavy atom locations could account for the many comonalities in the diffraction patterns, while the differences in the coordinates of the hydrogen atoms could be responsible for the differences between the patterns. This would account for the greater incidence of nonallowed reflections in the electron diffraction patterns.

It is not clear that a polymeric system with a composite structure, such as the one proposed above, represents a tractable crystallographic problem. However, any new insights concerning the discrepancies between the proposed simple structures and the observations are important, for they may suggest departures in new directions for investigation. A very significant implication of the proposal suggested above, to explain the discrepancies between the diffraction patterns, is that the primary determining factor in the structure of the native celluloses may be the shape of the molecules rather than the hydrogen bonding pattern. The proposal clearly implies that more than one hydrogen bonding pattern is consistent

with the organization of the heavy atoms in the molecular skeleton in the unit cell. The proposal has a number of other implications for further investigation, discussion of which is beyond the scope of the present chapter.

With respect to the comparison between celluloses I and II, the spectral data leave little question that the molecular conformations are indeed different. The chapter by Wiley and Atalla sets forth some of the evidence based on Raman spectroscopy. The validity of the theoretical arguments developed in support of the hypothesis that two distinct conformations do indeed occur has been demonstrated through its application in studies of model compounds. The most comprehensive is a study of the vibrational spectra of the inositols (47), wherein spectra of seven of the isomers were investigated and the effects of conformational differences accounted for.

The hypothesis that conformational differences occur is also supported by the differences between the CP-MAS ^{13}C NMR spectra of celluloses I and II. It is indeed not likely that the differences in the chemical shifts of the different carbons and the differences in the degrees of splittings of the C1 and C4 resonances can be accounted for in terms of structures adhering strictly to the assumption that the twofold screw axes coincide with the axes of the molecular chains.

The data arising from both spectroscopic methods clearly point to the need to explore the degree to which the diffraction data can be accounted for in terms of structures wherein the anhydrocellobiose unit is assumed to be the basic repeat unit in the crystallographic structure. The spectroscopic studies and the conformational energy calculations suggest that the departures from equivalence of the two anhydroglucose units need not be very large ones. This may indeed be the reason why the disallowed reflections appear to be weak in the diffraction patterns. On the other hand, the spectroscopic evidence suggests that the nature of these minor departures from symmetric equivalence of adjacent anhydroglucose units may be the key to some of the anomalies encountered in the structural studies.

It is clear that the new information developed from spectroscopic and multidisciplinary studies provides a basis for initiating diffractometric studies with a different set of constraints than those used in the past. The refinements are likely to be more complex, but the expectation is that the structures thus derived will more closely approximate the molecular structure of cellulose. Such models may then provide more comprehensive rationalizations of the phenomenology of cellulose.

Literature Cited

1. Kakudo, M.; Kasai, N. X-ray diffraction by polymers, Elsevier, New York, 1972, p. 285.
2. Arnott, S. In Fiber Diffraction Methods; ACS Symposium Series No. 141, American Chemical Society, Washington, DC, 1980, p. 1.
3. Atkins, E. D. T. In Fiber Diffraction Methods, ACS Symposium Series No. 141, American Chemical Society, Washington, DC, 1980, p. 31.

4. Tadokoro, H. In Fiber Diffraction Methods, ACS Symposium Series No. 141, American Chemical Society, Washington, DC, 1980, p. 43.
5. Tadokoro, H. Structure of crystalline polymers, Wiley, New York, 1979, p. 6.
6. Purves, C. B. In Cellulose and Cellulose Derivatives, Pt. I; Ott, E.; Spurlin, H. M.; Graffline, M. W., Eds., Interscience, New York, 1954, p. 29.
7. Flory, P. J. Principles of polymer chemistry, Cornell University Press, Ithaca, New York, 1953, p. 3.
8. Hermans, P. H. Physics and chemistry of cellulose fibers, Elsevier, New York, 1949, p. 3.
9. Jones, D. W. In Cellulose and Cellulose Derivatives, Pt. IV; Bikales, N. M.; Segal, L.; Eds., Wiley-Interscience, New York, 1971, p. 117.
10. Ellefsen, O.; Tonessen, B. A. In Cellulose and Cellulose Derivatives, Pt. IV, Bikales, N. M.; Segal, L.; Eds., Wiley-Interscience, New York, 1971, p. 151.
11. Tonessen, B. A.; Ellefsen, O. In Cellulose and Cellulose Derivatives, Pt. IV, Bikales, N. M.; Segal, L.; Eds., Wiley-Interscience, New York, 1971, p. 265.
12. Preston, R. D. The physical biology of plant cell walls; Chapman and Hall, London, 1974.
13. Frey-Wyssling, A. The plant cell wall; Gebruder Borntrager, Berlin, 1976.
14. Howsmon, J. A.; Sisson, W. A. In Cellulose and Cellulose Derivatives, Pt. I; Ott, E.; Spurlin, H. M.; Graffline, M. W.; Eds., Interscience, New York, 1954, p. 231.
15. Petipas, T.; Oberlin, M.; Mering, J. J. Polym. Sci. C 1963, 2, 423.
16. Norman, M. Text. Res. J. 1963, 33, 711.
17. Gardner, K. H.; Blackwell, J. Biopolymers 1974, 13, 1975.
18. Hebert, J. J.; Muller, L. L. J. Appl. Polym. Sci. 1974, 18, 3373.
19. Ref. 9; p. 138.
20. Ref. 14; p. 237.
21. Meyer, K. H.; Mark, H. Z. Physik. Chem. 1929, B2, 115.
22. Meyer, K. H.; Misch, L. Helv. Chim. Acta 1937, 20, 232.
23. Pierce, F. T. Trans. Faraday Soc. 1946, 42, 545.
24. Liang, C. Y.; Marchessault, R. H. J. Polym. Sci. 1959, 37, 385.
25. Liang, C. Y.; Marchessault, R. H. J. Polym. Sci. 1959, 39, 269.
26. Marchessault, R. H.; Liang, C. Y. J. Polym. Sci. 1960, 43, 71.
27. Nelson, M. L.; O'Connor, R. T. J. Appl. Polym. Sci. 1964, 8, 1311.
28. Nelson, M. L.; O'Connor, R. T. J. Appl. Polym. Sci. 1964, 8, 1325.
29. Sarko, A.; Muggli, R. Macromol. 1974, 7, 486.
30. French, A. D. Carbohydrate Res. 1978, 61, 67.
31. Atalla, R. H. Advances in Chemistry Series 1979, 181, 55.
32. Atalla, R. H. In Structure, Function and Biosynthesis of Plant Cell Walls, Dugger, W. M.; Bartinicki-Garcia, S.; Eds.,

American Society of Plant Physiologists, Rockville, MD, 1984, p. 381.
33. Atalla, R. H. Appl. Polym. Symp. 1976, 28, 659.
34. Reese, D. A.; Skerrett, R. J. Carbohydrate Res. 1968, 7, 334.
35. Melberg, S.; Rasmussen, K. Carbohydrate Res. 1979, 71, 25.
36. Chu, S. S. C.; Jeffrey, G. A. Acta Crystallogr. 1968, B24, 830.
37. Ham, J. T.; Williams, D. G. Acta Crystallogr. 1970, B29, 1373.
38. Atalla, R. H.; Gast, J. C.; Sindorf, D. W.; Bartuska, V. J.; Maciel, G. E. JACS 1980, 102, 3249.
39. Atalla, R. H. Proceedings of the International Symposium on Wood and Pulping Chemistry, SPCI Rept. No 38, Stockholm 1981, Vol. 1, p. 57.
40. Earl, W. L.; VanderHart, D. L. JACS 1980, 102, 3251.
41. Earl, W. L.; VanderHart, D. L. Macromol. 1981, 14, 570.
42. Maciel, G. E.; Kolodziejski, W. L.; Bertran, M. S.; Dale, B. E. Macromol. 1982, 15, 686.
43. Fyfe, C. A.; Dudley, R. L.; Stephenson, P. J.; Deslandes, Y.; Hamer, G. K.; Marchessault, R. H. JACS 1983, 105, 2469.
44. Atalla, R. H.; VanderHart, D. L. Science 1984, 223, 283.
45. VanderHart, D. L.; Atalla, R. H. Macromol. 1984, 17, 1465.
46. Poppleton, B. J.; Mathieson, A. McL. Nature 1968, 219, 1946.
47. Williams, R. M.; Atalla, R. H. J. Phys. Chem. 1984, 88, 508.

Raman Spectra of Celluloses

James H. Wiley and Rajai H. Atalla

The Institute of Paper Chemistry
Appleton, Wisconsin 54912

An investigation to study molecular orientation and polymorphy in cellulose fibers, and to further assign the bands in the vibrational spectrum of cellulose was conducted utilizing the Raman microprobe. The microprobe allows spectra to be recorded from domains as small as 1 micrometer and thereby greatly increases the potential of Raman spectroscopy as a tool for studying the structure of cellulose fibers. In the band assignment work, spectra were recorded from oriented fibers by varying the polarization of the incident light relative to the fiber axis. Analysis of the band intensities revealed new information about the directional character of the vibrational displacements. This information was used in conjunction with the spectra of deuterated celluloses and normal coordinate analyses of cellulose model compounds to make assignments.

Cellulose polymorphy was studied by comparing the spectra of Valonia, ramie, and mercerized ramie. It appears that the conformation of the cellulose backbone is the same in Valonia and ramie celluloses, but that the hydrogen bonding patterns are different. Mercerized cellulose and native celluloses differ in both their backbone conformations and hydrogen bonding patterns.

Cellulose orientation in the plane perpendicular to the chain axis was studied by recording spectra of ramie cross sections with different polarizations of the incident light relative to the cell wall surface. The intensities are consistent with random cellulose orientation. It appears, however, that the sample preparation techniques can influence the cellulose orientation. Therefore, further studies will be necessary to understand the molecular orientation in cellulose fibers.

Many questions about the molecular organization in plant cell walls remain unanswered. A new instrument, the Raman microprobe, has

provided a novel method for investigating plant cell wall structure. The objective in this work was to study the structure of the principal cell wall component, cellulose, using the Raman microprobe's unique capabilities. The investigation had two phases. In the first phase, the information made acessible by the microprobe was used to advance the assignment of the Raman spectrum of cellulose. In the second phase, the microprobe was used to study molecular orientation and polymorphy in cellulose fibers. The major results from both phases of this investigation will be discussed in this report.

Background

Raman Spectra of Cellulose. In laser excited Raman spectroscopy, a sample is exposed to monochromatic light, and the scattered light is analyzed. The frequency of a small fraction of the scattered light is shifted relative to the exciting light. The magnitude of the frequency shift corresponds to the vibrational frequencies of the molecules in the sample. Therefore, Raman spectroscopy provides information similar to that provided by infrared spectroscopy.

Both Raman and infrared spectroscopy yield information about chemical functionality, molecular conformation, and hydrogen bonding. Raman spectroscopy, however, has some important advantages. Highly polar bond systems, which result in intense infrared bands, have relatively low polarizabilities and, hence, weak Raman intensities. Water, therefore has very weak Raman bands and does not interfere with the spectrum of cellulose. In the Raman technique, control of the polarization of the exciting light coupled with analysis of the polarization of the scattered light can facilitate assignment of the spectra and provide information about molecular orientation. In infrared spectra, the attenuation of the incident beam is measured. This means that any processes other than absorption which cause attenuation of the incident beam are problematic. Since the refractive index of the sample will often go through large excursions in the neighborhood of absorption bands, the scattering losses will vary greatly with frequency over the infrared region. The variations in the refractive index can cause anomalous features in infrared spectra. In Raman spectroscopy, refractive index variations are not a problem, since the excitation frequency is far removed from any absorption bands. Therefore, it is easier to record Raman rather than infrared spectra from samples such as cellulose which scatter light strongly.

Raman Microprobe. A recent innovation in Raman spectroscopy was the development of the Raman microprobe. The microprobe is a specially designed optical microscope coupled with a conventional Raman spectrometer. The microscope performs two key functions. It focuses the exciting light on the sample down to a diameter of one micrometer; then it gathers the scattered light and transmits it to the entrance slit of the spectrometer. Since the microprobe acquires spectra from such small domains, the structural heterogeneity of the domains is greatly reduced relative to the domains examined in conventional Raman spectroscopy. The microprobe makes it possible to identify the morphological features from which

spectra are recorded so that orientation, composition, and structure can be studied as a function of morphology.

The special attributes of the microprobe make new information available. This investigation utilized the ability of the microprobe to record spectra from morphologically homogeneous domains, using polarized light to derive new information for assigning the Raman spectrum of cellulose. These assignments along with other spectral information obtained with the microprobe were then used to study polymorphy within the cellulose I family and cellulose orientation as a function of morphology.

Band Assignments. In order for Raman spectroscopy to provide structural information, the assignment of the spectra must be understood. The large number of vibrational degrees of freedom and low symmetry possessed by the cellulose molecule have made interpretation of the spectrum difficult. Given the complexity of the problem, a series of detailed normal coordinate analyses of model compounds were conducted in our laboratory to provide a basis for interpreting the vibrational spectrum of cellulose (1-8). The calculations showed that, except for the internal vibrations of the methylene groups, the modes below 1500 cm^{-1} are delocalized motions which are not adequately described by the group frequency approximation in which modes are assumed to be localized within certain chemical groups in the molecule.

Polymorphy. The two major allomorphs of cellulose, cellulose I and cellulose II, have been studied extensively. The question of polymorphy within the cellulose I (native cellulose) family has not received as much attention. Evidence has been reported, however, that the structure of native cellulose varies depending on the source. Early x-ray studies of cotton, ramie, linen, algal cellulose, and bacterial cellulose detected significant differences in the unit cell parameters (9). Based on electron diffractograms, Honjo and Watanabe (10) and others (11-13) concluded that the unit cell of algal cellulose is larger and has lower symmetry than the commonly accepted cell for cellulose I. Marrinan and Mann (14-15) and later Liang and Marchessault (16) observed that the infrared spectra of algal and bacterial cellulose differ from the spectra of ramie.

More recently, Atalla and VanderHart (17-18) have studied the solid-state ^{13}C NMR spectra of several forms of native cellulose. They concluded that native celluloses appear to be composites of two distinct crystalline forms of cellulose called I_α and I_β. The proportions of I_α and I_β in the composite varies depending on the source of the cellulose. In algal and bacterial cellulose, the I_α form dominates, whereas the I_β form dominates in ramie, cotton, and wood pulp. These results are consistent with the data from diffractometry and infrared spectroscopy in that algal and bacterial cellulose are similar to each other but different from other native celluloses.

The structural differences between I_α and I_β are not understood yet. Atalla (18) compared the Raman spectra of various native celluloses with different I_α to I_β ratios. He also compared the native cellulose spectra with the spectrum of cellulose II. The spectra of

the native celluloses are all similar to each other in the region most sensitive to cellulose conformation. The spectrum of cellulose II is quite different in this region. Therefore Atalla concluded that celluloses I_α and I_β have similar conformations but are packed in different lattices. In cellulose II, both the conformation and lattice are different from that of cellulose I.

Other workers (19-20) have interpreted these differences in the NMR spectra and other data in alternative ways. They believe that celluloses I and II have the same skeletal conformation but are packed in different lattices. In this theory, the differences within the cellulose I family are derived from the size of the unit cells. Valonia contains a larger 8 chain unit cell, whereas ramie contains a mixture of the 8 chain unit cell and the smaller Meyer and Misch unit cell. Therefore the interpretation of the NMR spectra remains controversial.

Orientation. The orientation of the cellulose chain axis in a number of different fibers has been studied in detail (21-22). Much less is known about the cellulose orientation in the plane perpendicular to the chain axis. The orientation in this plane is determined by the lateral arrangement of the microfibrils relative to each other. In algal celluloses, the evidence from x-ray and electron diffraction indicates that the microfibrils are arranged nonrandomly in the plane perpendicular to the chain axis (21-29). Preston (22) proposed the model shown in Figure 1 to explain his x-ray data. There are two different orientations of the microfibrils. The 002 planes in one set of microfibrils are approximately perpendicular to the 002 planes in the second set. In both sets of microfibrils, the 101 planes are oriented parallel to the cell wall surface (refer to Figure 1). Preston's model has been confirmed in more recent studies (29). In the remainder of this report, the type of orientation shown in Figure 1 will be referred to as alternating orientation.

Direct measurements of cellulose orientation in fibers have yielded conflicting results. Evidence from x-ray diffraction studies of wood samples suggested that the cellulose crystallites are arranged randomly in the plane perpendicular to the fiber axis (30-33). Raman spectroscopic studies of cotton fibers dried under tension, however, demonstrated that the methine C-H bonds are oriented preferentially perpendicular to the surface of the cell wall (34). Since the C-H bonds are perpendicular to the 002 plane, the orientation suggested by the Raman evidence differs from the alternating orientation in algal celluloses.

Overview of Experimental Method

In the spectra of nonrandomly oriented polymers, the intensity and polarization of the Raman scattered light are dependent on the polarization of the exciting light relative to the orientation of the molecules (35). If the orientation of the molecules is known, comparison of spectra recorded with different polarizations of the exciting light yields useful information about the directionality of the vibrational motions. Conversely, information about molecular orientation can be gained if the directionality of the vibrations is

known. In the present work, the major technique employed in the experiments was to compare spectra recorded with different polarizations of the incident laser beam relative to the morphology of the samples.

In all spectra recorded, precautions were taken to avoid complications associated with the dichroism inherent in the optics of the microscope and the monochromator. First, a polarization scrambler was inserted in the path of the Raman scattered light at the coupling between the microscope and the monochromator. Second, we did not change the polarization of the incident light directly but instead used a rotating stage to rotate the sample relative to the plane of polarization of the incident light.

Two classes of experiments were conducted. In both sets of experiments, fibers in which the cellulose chains are oriented parallel to the fiber axis were used. In the first class of experiments, the plane of polarization of the incident light was changed relative to the axis of the fibers by rotating the fibers around the optical axis of the microscope (see Figure 2a). The dependence of the band intensities on the polarization of the incident light was studied to determine the directional character of the vibrational motions. This information was used to advance the assignment of the Raman spectrum of cellulose. Spectra from Valonia, ramie, and mercerized ramie fibers, which have different allomorphic compositions, were compared to study the structural differences between the allomorphs.

In the second class of experiments, spectra were recorded from ramie fiber cross-sections. The plane of polarization of the incident light was changed relative to plane of the cell wall by rotating the cross-sections around the optical axis of the microscope axis (see Figure 2b). The information from these spectra was used to study the orientation of the cellulose in the plane perpendicular to the chain axis.

Results and Discussion

Assignment of the Vibrational Spectrum of Cellulose. Sets of spectra in which the orientation of the electric vector of the incident light was varied in 15 degree increments relative to the fiber axis were recorded. Figure 3 shows the set recorded from a fibrillar aggregate of Valonia macrophysa cellulose. Scanning electron micrographs showed that the aggregates are highly oriented bundles of fibrils. Therefore, the cellulose chains are parallel to the axis of the bundle. A set of spectra recorded from a ramie fiber is shown in Figure 4. In ramie, the cellulose chains are also approximately parallel to the fiber axis (21-22).

From the figures it is clear that the band intensities are strongly dependent on the polarization of the light. The intensities are related to the orientation of the electric vector by the following equation:

$$I = a + b\,(\cos^2\theta) + c\,(\cos^4\theta) \qquad (1)$$

where a, b, and c are constants related to scattering activities, and θ is the angle between the electric vector of the incident light

and the fiber axis. Equation 1 was derived by following Snyder's treatment (35) and assuming that the cellulose chains are parallel to the fiber axis, and that the chains are oriented randomly around their axes. Equation 1 was fitted to the data in Figure 3 and 4 by a linear regression technique. Equation 1 adequately described the observed data for bands which were well resolved. An example of the fit which could be achieved by this analysis is shown in Figure 5, where the observed and predicted peak heights are plotted against θ for the intense band at 1095 cm^{-1}. Bands which were weak and/or poorly resolved could not be fitted as well.

Based on the number and location of the maxima and minima in the intensity vs. θ curves, the bands in the Raman spectrum of native cellulose were divided into four categories. Table 1 summarizes the band classifications for those bands which were resolved well enough to be analyzed. The classifications provide information about the directional character of the vibrations. The four categories are described as follows:

1) A_0 bands are most intense when the incident electric vector is parallel to the cellulose chain axis. Therefore, the maximum change in polarizability associated with the vibrations is parallel to the chain axis. The intensity vs. θ curves contain a single maximum and minimum.
2) A_{90} bands are most intense when the incident electric vector is perpendicular to the chain axis. The maximum change polarizability is perpendicular to the chain axis. These bands also exhibit a single maximum and minimum in the intensity vs. θ curves.
3) B_0 bands are most intense when the incident electric vector is parallel to the chain axis. As was the case with A_0 bands, the maximum change in polarizability is parallel to the chain axis. In the intensity vs. θ curves, however, these bands exhibit two maxima and a single minimum. The multiple maxima may result from accidentally degenerate modes which have maxima at 0 and 90° or from modes in which some of elements of the polarizability decrease during the vibration.
4) B_{90} bands are most intense when the incident electric vector is perpendicular to the chain axis. The maximum change in polarizability is perpendicular to the chain axis. These bands also exhibit two maxima and a single minima in the intensity vs. polarization curves.

As a supplement to the intensity work, the nature of the vibrations was also studied by recording spectra from deuterated celluloses. By comparing the spectrum of fully deuterated cellulose with that of normal cellulose, the vibrations involving the hydrogen atoms can be separated from the pure skeletal motions. Figure 6 is the spectrum of carbon-deuterated bacterial cellulose. This sample was kindly provided by Dr. H. L. Crespi. It was prepared by growing Acetobacter xylinum in deuterated growth media (36). The residual intensity in the O-H and C-H stretching regions indicates that the cellulose is not fully deuterated. We also recorded Raman spectra

of oriented samples of partially deuterated cellulose with the electric vector both parallel and perpendicular to the chain axis. Based on these studies, the deuteration sensitivity for several of the bands was determined. This information is also listed in Table I.

Based on the intensity studies, deuterated cellulose spectra, and normal coordinate analyses of model compounds (7-8), the assignment of the bands in the vibrational spectrum of cellulose was advanced. The information is summarized in Table 1. A detailed discussion of the band assignments is beyond the scope of this report and will be given elsewhere (37). A brief overview of the assignments will be given here. The frequency region between 600 and 250 cm^{-1} is dominated by bending motions of the cellulose skeleton. These are complex modes which are very delocalized and often involve motion at the glycosidic linkage. The frequencies, especially between 400 and 300 cm^{-1}, are sensitive to the conformation of the anhydroglucose residues about the linkage (8). In the modes between 900 and 1200 cm^{-1}, CC and CO stretching motions are dominant. This region contains very intense bands. The modes between 1200 and 1500 cm^{-1} involve methylene, methine, and hydroxyl bending motions. Although the modes in this region are generally delocalized motions, the HCH bending motion is isolated and behaves as a group mode. In the regions between 2700 and 3000 cm^{-1} and 3200 and 3500 cm^{-1}, the C-H and O-H stretching motions occur. These motions behave as pure group vibrations. Although the assignments do not provide a complete description of the vibrational motions, they serve to increase our understanding of the cellulose vibrational spectrum.

Polymorphy. Cellulose polymorphy within the cellulose I family was studied by comparing the Raman spectra of Valonia and ramie cellulose. Solid state NMR spectra indicate that the I_α form predominates in Valonia while the I_β form predominates in ramie (17-18). The cellulose I spectra were also compared with spectra of cellulose II recorded from a mercerized ramie fiber. Figures 7 and 8 show the Raman spectra of these three celluloses. Spectra were recorded with the electric vector of the incident light parallel and perpendicular to the chain axis. These spectra can be divided into two regions. The region below 1600 cm^{-1} (Figure 7) is most sensitive to the conformation of the cellulose backbone (especially below 700 cm^{-1}). The higher frequency region, above 2700 cm^{-1} (Figure 8), is more sensitive to hydrogen bonding.

In the low frequency region (Figure 7), there are only minor differences between the spectra of native ramie and Valonia. The peaks in the Valonia spectra are narrower and better resolved. The reason for this is probably the larger size of the crystallites in Valonia cellulose (38-39). When the crystallites are larger, the environment of the molecules is more homogeneous. Therefore, the vibrational energy of the molecules is more uniform, resulting in narrower bands.

The most significant difference between the two native cellulose spectra in the low frequency region is that the intensity of the peak at 913 cm^{-1} is greater in the ramie spectra. This peak is also more intense in the spectrum of bacterial cellulose than in the

Valonia spectra. Since bacterial cellulose has approximately the same I_α to I_β ratio as Valonia (17-18), the intensity of this peak does not appear to be related to structural differences between I_α and I_β. Instead, the intensity of this peak appears to be inversely correlated with the size of the crystallites. It is very weak in the spectra of Valonia which has very large crystallites, but it is stronger in the spectra of ramie and bacterial cellulose which both have smaller crystallites (38-39).

The differences between the spectra of ramie and Valonia are quite small compared to the differences between native cellulose and cellulose II (see Figure 7). In the spectra of ramie and Valonia, the different peak widths and relative intensities can be attributed to the difference in the crystallite sizes. In the spectrum of cellulose II, however, the frequency and number of peaks is significantly different. In previous publications, the differences between the spectra of celluloses I and II have been interpreted as evidence for different conformations in celluloses I and II (40-41). The spectral differences which are indicative of conformational change are not observed in the spectra of ramie and Valonia. Since ramie and Valonia have different I_α to I_β ratios, it would appear that celluloses I_α and I_β must have similar molecular conformations.

In the C-H stretching region (Figure 8, 2700-3000 cm^{-1}), the primary difference between the spectra of ramie and Valonia is the broadness of the peaks. The peaks in the ramie spectra are broader as was the case in the low frequency region presumably due to the smaller crystallite size. In the spectra of mercerized ramie, the C-H stretching region differs slightly from that in the native celluloses but the differences are not as large as those in the low frequency region.

In the O-H stretching region (3200-3600 cm^{-1}), however, significant differences are observed between all three celluloses. These differences are most prominent in the spectra recorded with the electric vector parallel to the fiber axis (Figure 8a-c). The frequency as well as the broadness of the peaks varies in this region. The spectra of Valonia cellulose have a peak at 3231 cm^{-1} that is not observed in the ramie spectra. The spectra of native ramie on the other hand, have a peak at 3429 cm^{-1} that is not observed in Valonia. The spectrum of mercerized ramie recorded with the electric vector parallel has two sharp peaks at frequencies above those observed in the native celluloses. The differences in the O-H region between Valonia, ramie, and mercerized ramie suggest that the hydrogen bonding patterns are different in each of these celluloses. In summary, the Raman spectra indicate that celluloses I_α and I_β exhibit different hydrogen bonding patterns but have similar molecular conformations. Celluloses I and II have different molecular conformations as well as different hydrogen bonding patterns.

Cellulose Orientation. The orientation of the cellulose molecules in the plane perpendicular to the chain axis was studied by using the microprobe to record spectra of ramie fiber cross sections. Figure 9 shows spectra recorded with the electric vector of the exciting light tangential, perpendicular, and at 45° to the cell wall surface. If the cellulose orientation in the plane perpendicular to the fiber axis is anisotropic, then the intensities

should differ in the cross-section spectra recorded with different orientations of the incident electric vector. With the exception of the peaks at 1095 and 1123 cm^{-1}, the relative peak intensities in the cross-section spectra did not vary noticeably as the polarization of the incident light was changed (see Figure 9). The insensitivity of the majority of the bands to the orientation of incident electric vector is not consistent with either a preferential orientation of the methines perpendicular to the cell wall surface or the alternating type of orientation found in algal celluloses.

The variation in the relative intensities of the 1095 and 1123 cm^{-1} bands between the 0° and 45° spectra suggests anisotropy in the cellulose orientation. Table I shows that these peaks are skeletal stretching modes that are most intense when the electric vector of the incident light is parallel to the chain axis. Since the 1095 cm^{-1} peak is very sensitive to the orientation of the incident electric vector relative to the chain axis, the intensity variation suggests that the plane of sectioning was not exactly perpendicular to the cellulose chain axes so that the chains are tilted relative to the plane of sectioning.

If the cellulose is oriented randomly in the plane perpendicular to the chain axis, then the band intensities would be the same regardless of whether the incident electric vector was parallel, perpendicular, or 45° to the cell wall surface. The cross-section spectra, therefore, are consistent with random cellulose orientation in the plane perpendicular to the chain axis. These results conflict with our earlier spectra of tension dried cotton fibers (34) that indicated the methines were oriented preferentially perpendicular to the cell wall surface. More recent spectra of cotton fibers have shown that if the fibers are not dried under tension, the methine orientation is random in the plane perpendicular to the chain axis. Therefore, it appears the cellulose orientation can be influenced by the sample preparation methods. Since microtoming exerts large forces on the fibers, it is also possible that the cellulose orientation could have been disrupted during the preparation of the cross-sections. Further experiments will be necessary to understand the factors which influence the cellulose orientation.

Conclusions

Based on the number and location of the maxima and minima in the relationship between the band intensities and the polarization of the incident light relative to the chain axis, the bands in the Raman spectrum of cellulose could be divided into four groups. The about the direction of the vibrational motions in cellulose. The directions of the vibrations are such that the major change in polarizability associated with the motions is either parallel or perpendicular to the chain axis. Raman spectra recorded from deuterated celluloses allowed the vibrational modes involving C-H and O-H motions to be identified. These spectra demonstrated that most of the modes are complex coupled vibrations. Normal coordinate analyses of cellulose model compounds were done to determine the types of motion most likely to occur in each region of the spectrum. The calculations also suggested that the vibrational motions are very complex. The information from the normal coordinate calculations,

intensity studies, and spectra of deuterated celluloses was used to advance the assignment of the cellulose vibrational spectrum.

Comparison of the Raman spectra of Valonia, ramie, and mercerized ramie indicates that the conformation of the cellulose backbone is similar in Valonia and native ramie but different in mercerized ramie. The hydrogen bonding patterns, however, are different in Valonia and native ramie as well as in mercerized ramie.

Spectra recorded from ramie cross-sections suggest that the cellulose is oriented randomly in the plane perpendicular to the chain axis. It appears, however, that the sample preparation methods can influence the cellulose orientation. Therefore, further studies will be necessary to characterize the molecular orientation in cellulose fibers.

Acknowledgment

The authors wish to thank Dr. H. L. Crespi for furnishing the sample of deuterated bacterial cellulose and for his advice concerning the growth of algae in heavy water, and Dr. U. P. Agarwal for the many helpful discussions he contributed to this work. Portions of this work were used by J. H. Wiley as partial fulfillment of the requirements for the Ph.D. degree at The Institute of Paper Chemistry.

References

1. Pitzner, L. J. An investigation of the vibrational spectra of the 1,5-anhydropentitols. Doctoral Dissertation. Appleton, WI, The Institute of Paper Chemistry, Jan. 1973. 402 p.
2. Pitzner, L. J.; Atalla, R. H. Spectrochimica Acta 1975, 31A, 911-29.
3. Watson, G. M. An investigation of the vibrational spectra of the pentitols and erythritol. Doctoral Dissertation. Appleton, WI, The Institute of Paper Chemistry, June 1974. 178 p.
4. Edwards, S. L. An investigation of the vibrational spectra of the pentose sugars. Doctoral Dissertation. Appleton, WI, The Institute of Paper Chemistry, Jan. 1976. 245 p.
5. Williams, R. M. An investigation of the vibrational spectra of the inositols. Doctoral Dissertation. Appleton, WI, The Institute of Paper Chemistry, June 1977. 377 p.
6. Williams, R. M.; Atalla, R. H. J. Phys. Chem. 1984, 88, 508-19.
7. Wells, H. A. An investigation of the vibrational spectra of glucose, galactose, and mannose. Doctoral Dissertation. Appleton, WI, The Institute of Paper Chemistry, Jan. 1977. 431 p.
8. Carlson, K. P. An investigation of the vibrational spectra of the cellodextrins. Doctoral Dissertation. Appleton, WI, The Institute of Paper Chemistry, Nov. 1978. 153 p.
9. Wellard, H. J. J. Polym. Sci. 1954, 13, 471-6.
10. Honjo, G.; Watanabe, M. Nature 1958, 181, 326-8.
11. Fisher, D. G.; Mann, J. J. Polym. Sci. 1960, 42, 189-94.
12. Nieduszynski, I. A.; Atkins, E. D. T. Biochim. et Biophys. Acta 1970, 222, 109-18.
13. Hebert, J. J.; Muller, L. L. J. Appl. Polym. Sci. 1974, 18, 3373-7.

14. Marrinan, H. J.; Mann, J. J. Polym. Sci. 1956, 21, 301-11.
15. Mann, J.; Marrinan, H. J. J. Polym. Sci. 1958, 32, 357-70.
16. Liang, C. Y.; Marchessault, R. H. J. Polym. Sci. 1959, 37, 385-95.
17. VanderHart, D. L.; Atalla, R. H. Macromolecules 1984, 17, 1465-72.
18. Atalla, R. H. Polymorphy native in cellulose: recent developments. Function and Biosynthesis of Plant Cell Walls. W. M. Dugger; S. Bartnicki-Garcia, eds., Am. Soc. Plant Physiologists, Rockville, MD., 1984:381.
19. Dudley, R. L.; Fyfe, C. A.; Stephenson, P. J.; Deslandes, Y.; Hamer, G. K.; Marchessault, R. H. J. Am. Chem. Soc. 1983, 105, 2469-72.
20. Cael, J. J.; Kwoh, D. L. W.; Bhattacharjee, S. S.; Patt, S. L. Macromolecules 1985, 18, 819-21.
21. Frey-Wyssling, A. The Plant Cell Wall. Gebruder Borntraeger, Berlin, Stuttgart, 1976.
22. Preston, R. D. Physical Biology of Plant Cell Walls. Chapman and Hall, 1974.
23. Goto, T.; Harada, H.; Saiki, H. J. Japan Wood Res. Soc. 1973, 19(10), 463-8.
24. Revol, J.-F. Carbohyd. Polym. 1982, 2, 123-34.
25. Preston, R. D. Disc. Faraday Soc. 1951, 11, 165-70.
26. Schurz, J. Phyton 1955, 5(2), 53-66.
27. Tanaka, F.; Okamura, K. J. Polym. Sci. Polym. Phys. Ed. 1977, 15, 897-906.
28. Okamura, K. Memoirs of the College of Agriculture, Kyoto Univ. 1980, 115, 63-7.
29. Revol, J.-F.; Goring, D. A. I. Polymer 1973, 24, 1547-50.
30. Revol, J.-F.; Gancet, C.; Goring, D. A. I. Wood Sci. 1982, 14(3), 120-6.
31. Tanaka, F.; Takaki, T.; Okamura, K.; Koshijima, T. Wood Res. 1980, 66, 17-22.
32. Tanaka, F.; Koshijima, T. J. Japan Wood Res. Soc. 1983, 29(1), 1-7.
33. Tanaka, F.; Koshijima, T. Wood Sci. Technol. 1984, 18, 177-86.
34. Atalla, R. H.; Whitmore, R. E.; Heimbach, C. J. Macromolecules 1980, 13, 1717.
35. Snyder, R. G. J. Mol. Spect. 1971, 37, 353-65.
36. Crespi, H. L. Biosynthesis with deuterated microorganisms. Technical Committee Meeting on Modern Trends in the Biological Applications of Stable Isotopes., Leipzig, Germany., Dec. 6-10, 1976. p. 1-15.
37. Wiley, J. H.; Atalla, R. H. Carbohyd. Res. in press.
38. Nieduszynski, I.; Preston, R. D. Nature 1970, 225, 273-4.
39. Boylston, E. K.; Hebert, J. J. J. Appl. Polym. Sci. 1980, 25, 2105-7.
40. Atalla, R. H. Appl. Polym. Symp. 1976, 28, 659-69.
41. Atalla, R. H. Spectroscopic studies of polymorphy in cellulose: a new structural model. Proceedings of the International Symposium on Wood and Pulping Chemistry, Stockholm, June, 1981. SPCI Report, 1981, 38(1), 57.

Figure 1. The cellulose orientation in the plane perpendicular to the chain axis found in algal celluloses.

Figure 2. Microprobe experiments in which the polarization of the exciting light was varied relative to the geometry of the samples.

Figure 3. Polarized Raman spectra from a fibrillar aggregate of Valonia cellulose. The angle between the electric vector and the chain axis was varied from 0° to 90°.

Figure 4. Polarized Raman spectra from a ramie fiber. The angle between the electric vector and the chain axis was varied from 0° to 90°.

Figure 5. The dependence of intensity on the polarization of the incident light for the band at 1095 cm^{-1} in the spectra of Valonia.

Figure 6. Raman spectrum of deuterated bacterial cellulose.

Figure 7. Comparison of the Raman spectra from Valonia, ramie, and mercerized ramie (low frequency region). Spectra were recorded with the electric vector at both 0° and 90°.

Figure 8. Comparison of the Raman spectra from Valonia, ramie, and mercerized ramie (high frequency region). Spectra were recorded with the electric vector at both 0° and 90°.

Figure 9. Polarized Raman spectra of a ramie cross section. The angle between the electric vector and the cell wall surface was varied from 0° to 90°.

Table 1. Summary of intensity maxima, deuteration sensitivities, and band assignments for the Raman spectra of Valonia and ramie.

Band Frequency[a] (cm^{-1})		Intensity Classification	Deuteration Sensitivity	Assignment
Valonia	Ramie			
331	331	A_0	weak	heavy atom bending, some
344	344	$B_?$	"	heavy atom stretching
381	380	$B_?$	"	"
437	437	$B_?$	"	"
459	458	B_0	"	"
520	519	A_{90}	"	"
913	910	B_0	?	HCC and HCO bending at C6
968	969	B_{90}	?	heavy atom (CC and CO)
997	995	A_0	?	stretching
1034	1035	A_0	?	"
1057	1057	A_0	?	"
1095	1095	A_0	weak	"
1118	1117	B_0	"	"
1123	1121	A_0	"	"
1152	1151	$B_?$	?	heavy atom stretching plus HCC and HCO bending
1279	1275	A_0	?	HCC and HCO bending
1292	1291	?	?	"
1334	1331	A_0	strong	"
1337	1337	A_0	"	HCC, HCO, and HOC bending
1378	1378	$B_?$	"	"
1406	1407	A_0	"	"
1455	1456	B_{90}	"	HCH and HOC bending
1477	1475	A_{90}	"	"
2868	2866	B_{90}	"	C-H and CH2 stretching
2885	2889	B_{90}	"	"
2941	2943	$B_?$	"	"
2965	2963	B_0	"	"
3291	3286	B_0	"	O-H stretching
3334	3335	$?_0$	"	"
3261	3363	$?_0$	"	"
3395	3402	B_0	"	"

[a]Only the bands resolved in both the Valonia and ramie are included in the table.

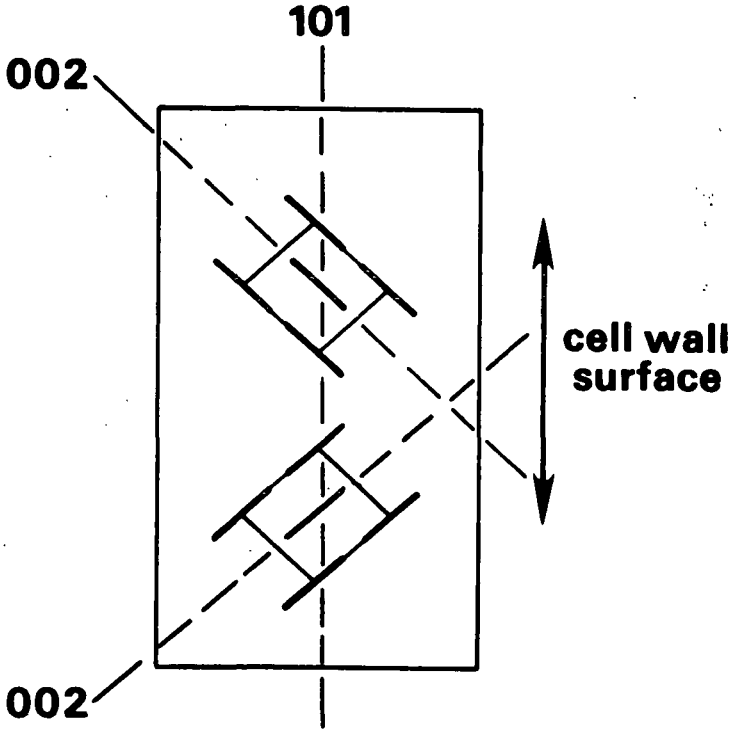

Figure 1. The cellulose orientation in the plane perpendicular to the chain axis found in algal celluloses.

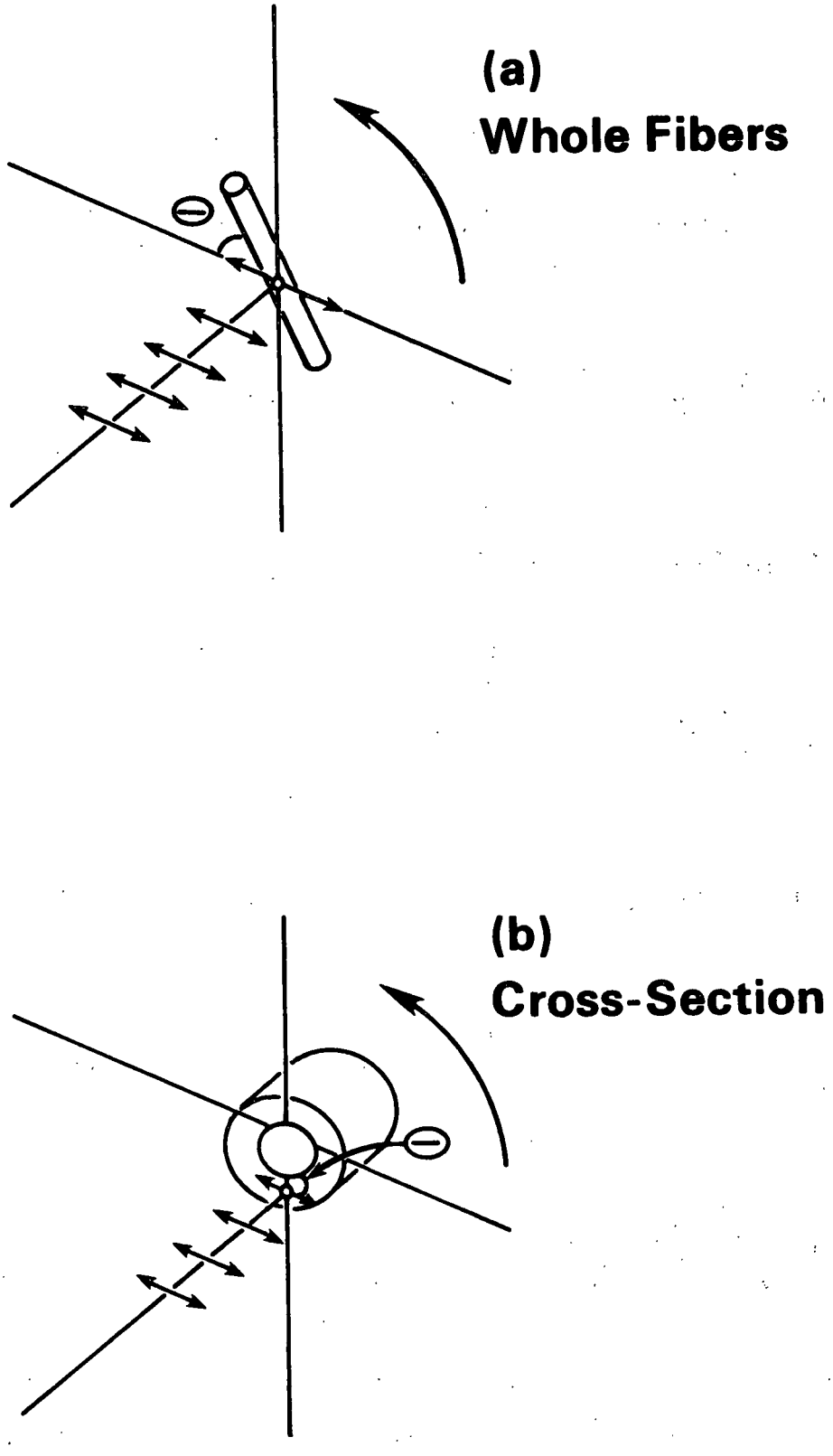

Figure 2. Microprobe experiments in which the polarization of the exciting light was varied relative to the geometry of the samples.

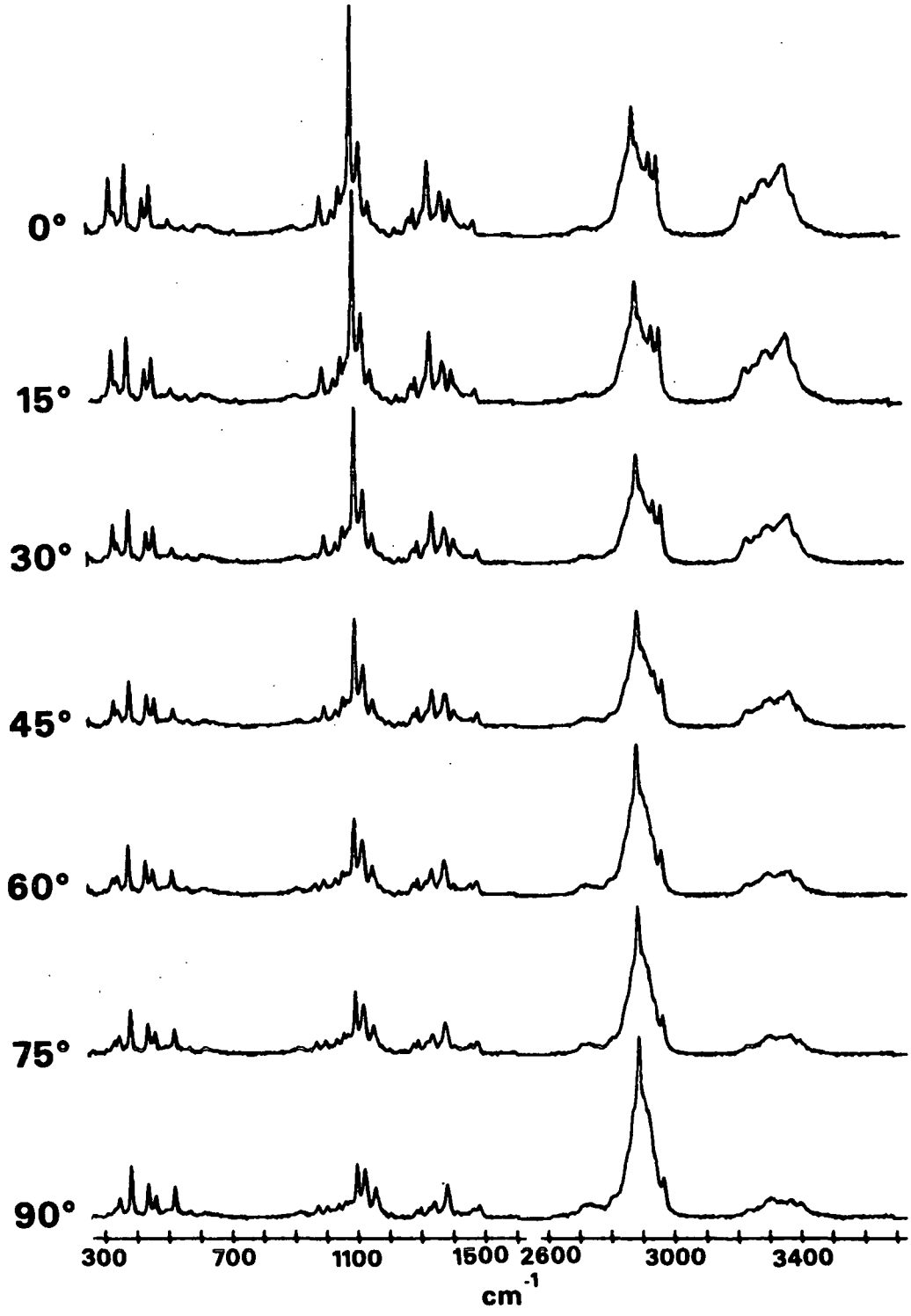

Figure 3. Polarized Raman spectra from a fibrillar aggregate of Valonia cellulose. The angle between the electric vector and the chain axis was varied from 0° to 90°.

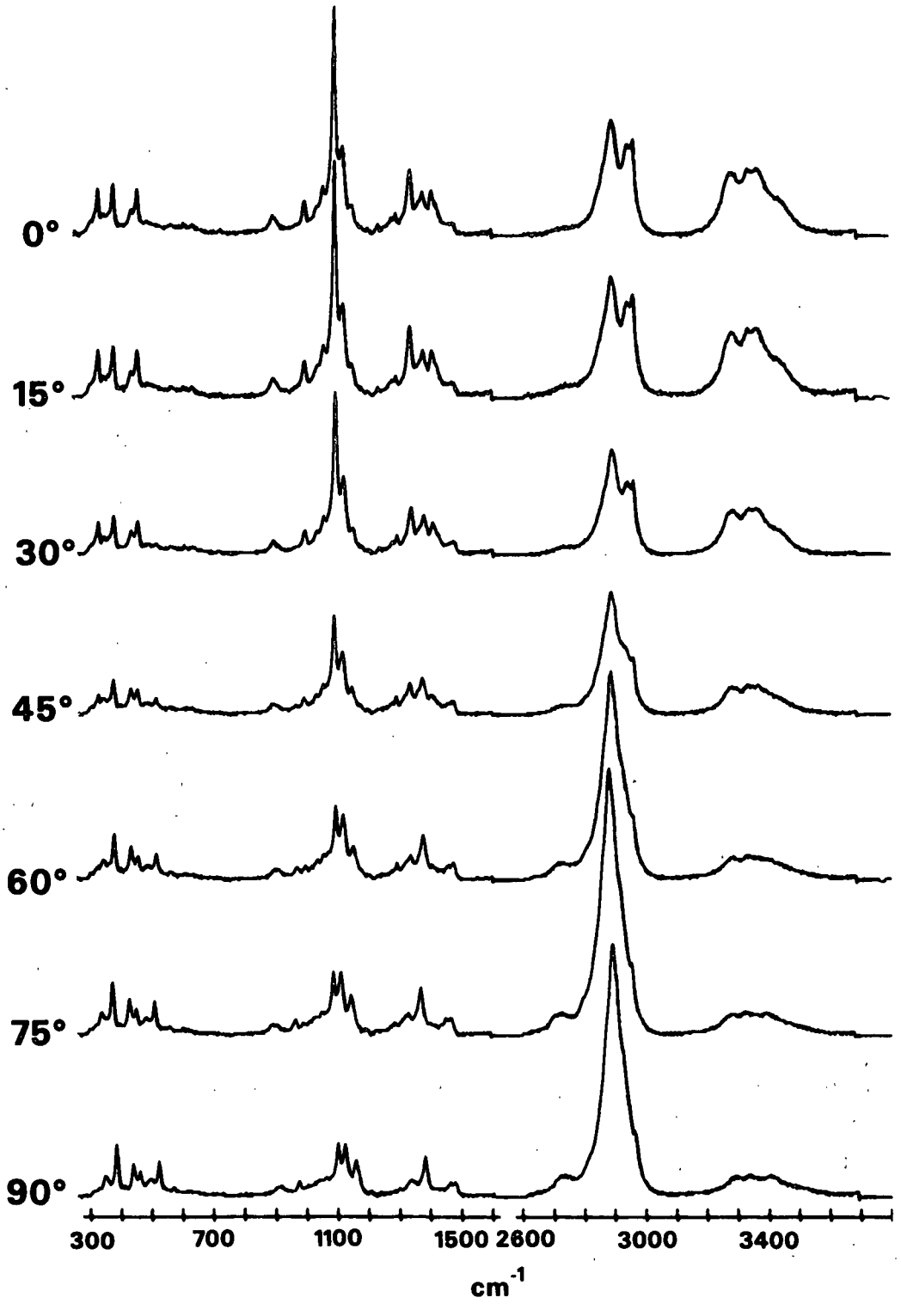

Figure 4. Polarized Raman spectra from a ramie fiber. The angle between the electric vector and the chain axis was varied from 0° to 90°.

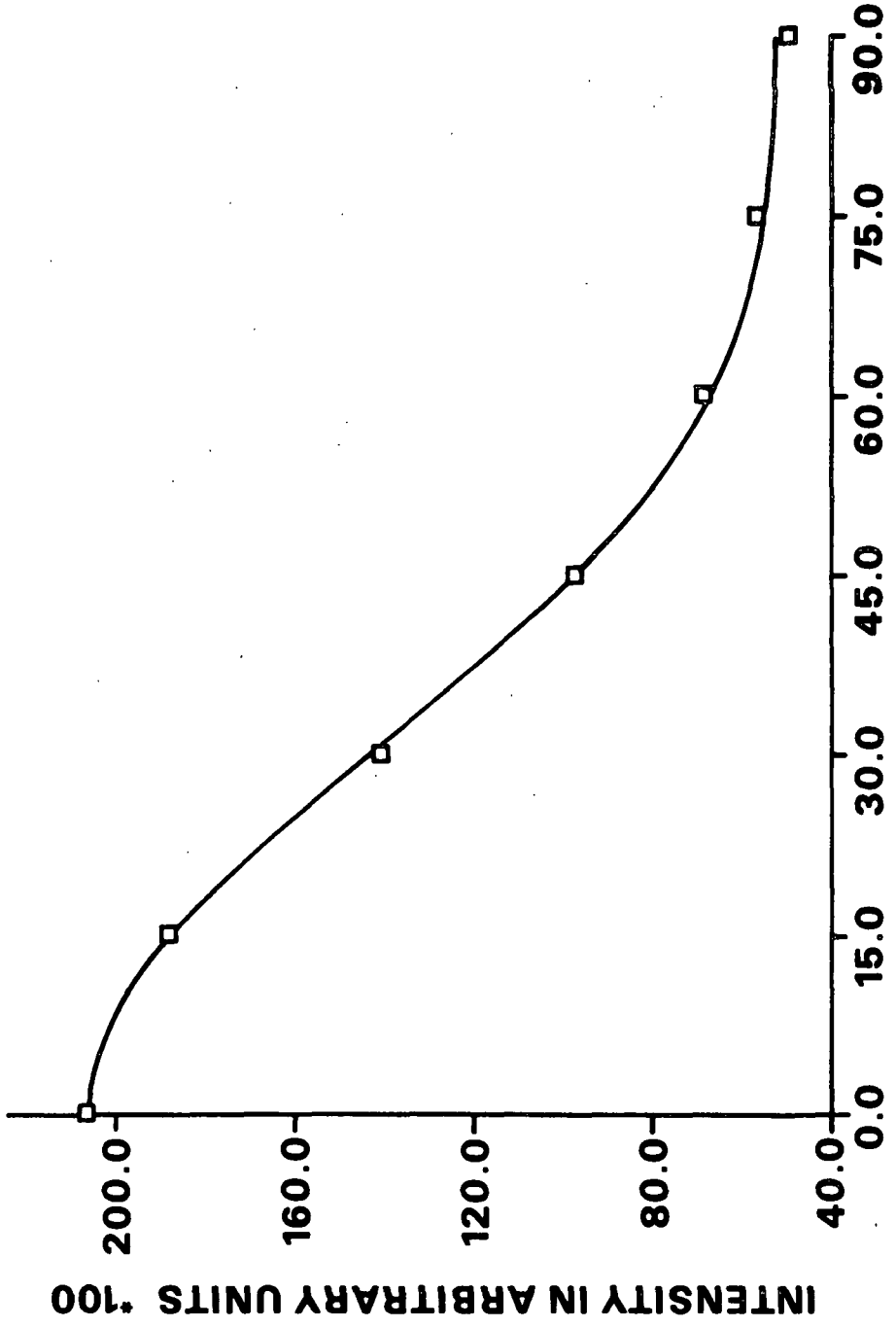

Figure 5. The dependence of intensity on the polarization of the incident light for the band at 1095 cm^{-1} in the spectra of Valonia.

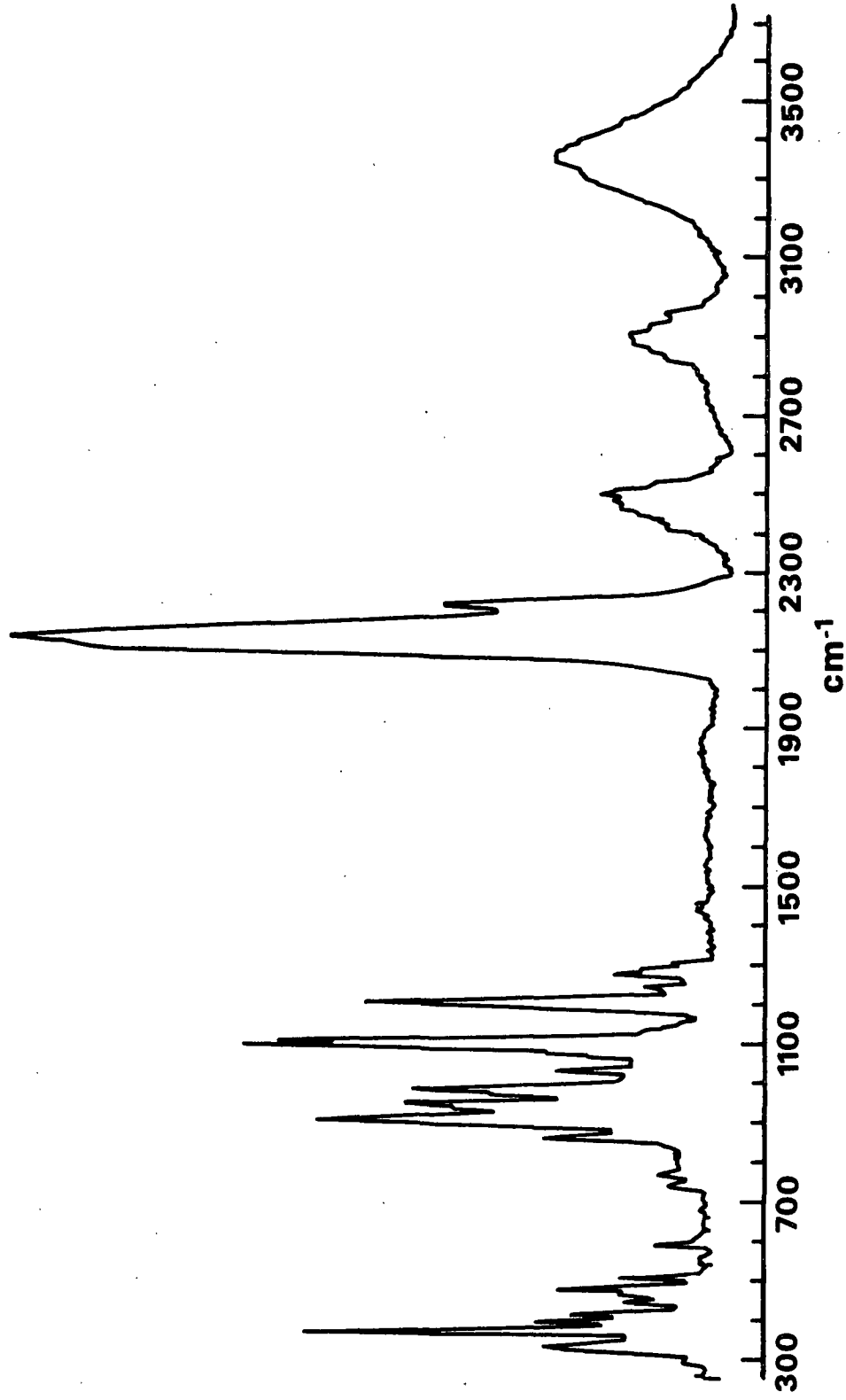

Figure 6. Raman spectrum of deuterated bacterial cellulose.

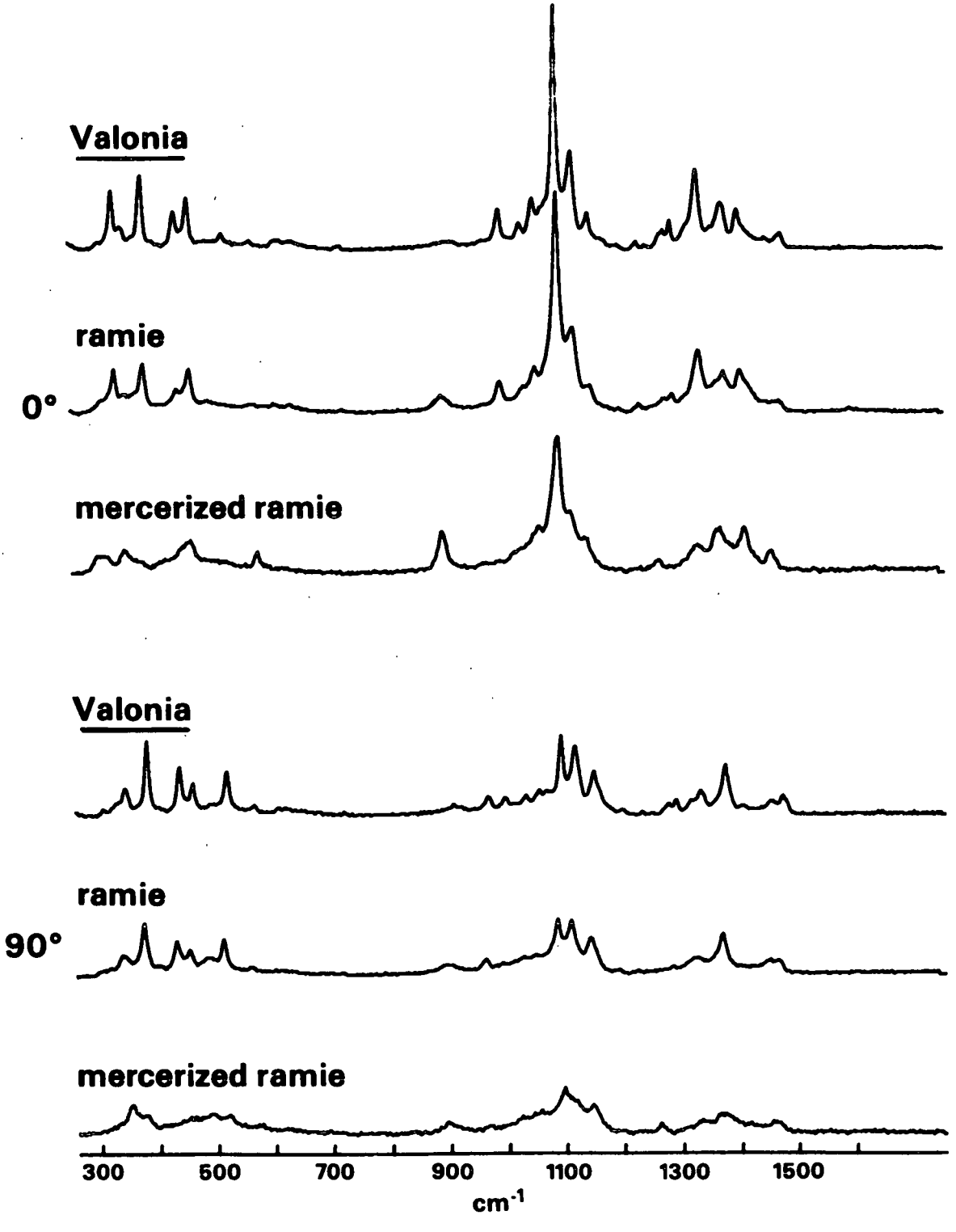

Figure 7. Comparison of the Raman spectra from Valonia, ramie, and mercerized ramie (low frequency region). Spectra were recorded with the electric vector at both 0° and 90°.

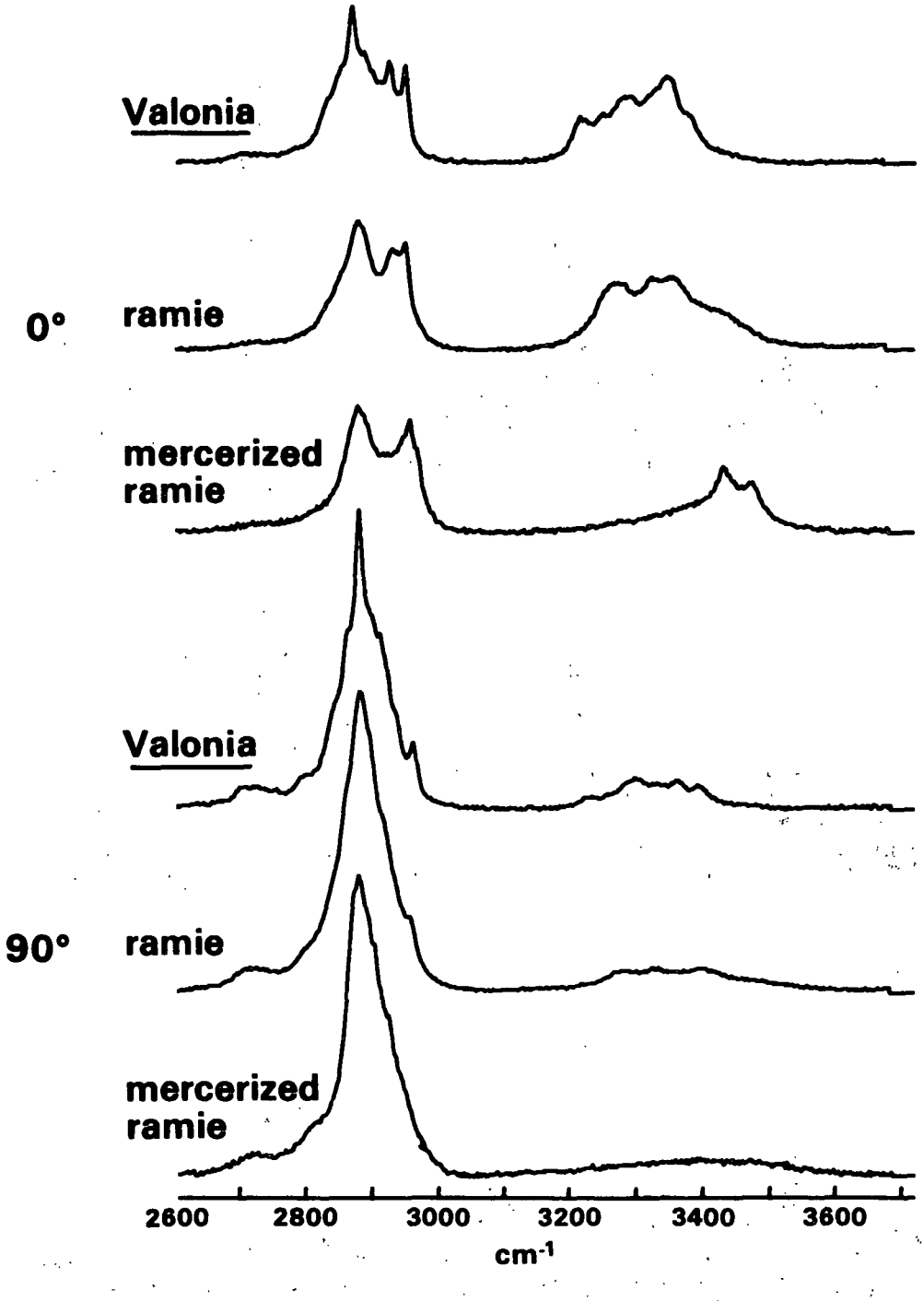

Figure 8. Comparison of the Raman spectra from Valonia, ramie, and mercerized ramie (high frequency region). Spectra were recorded with the electric vector at both 0° and 90°.

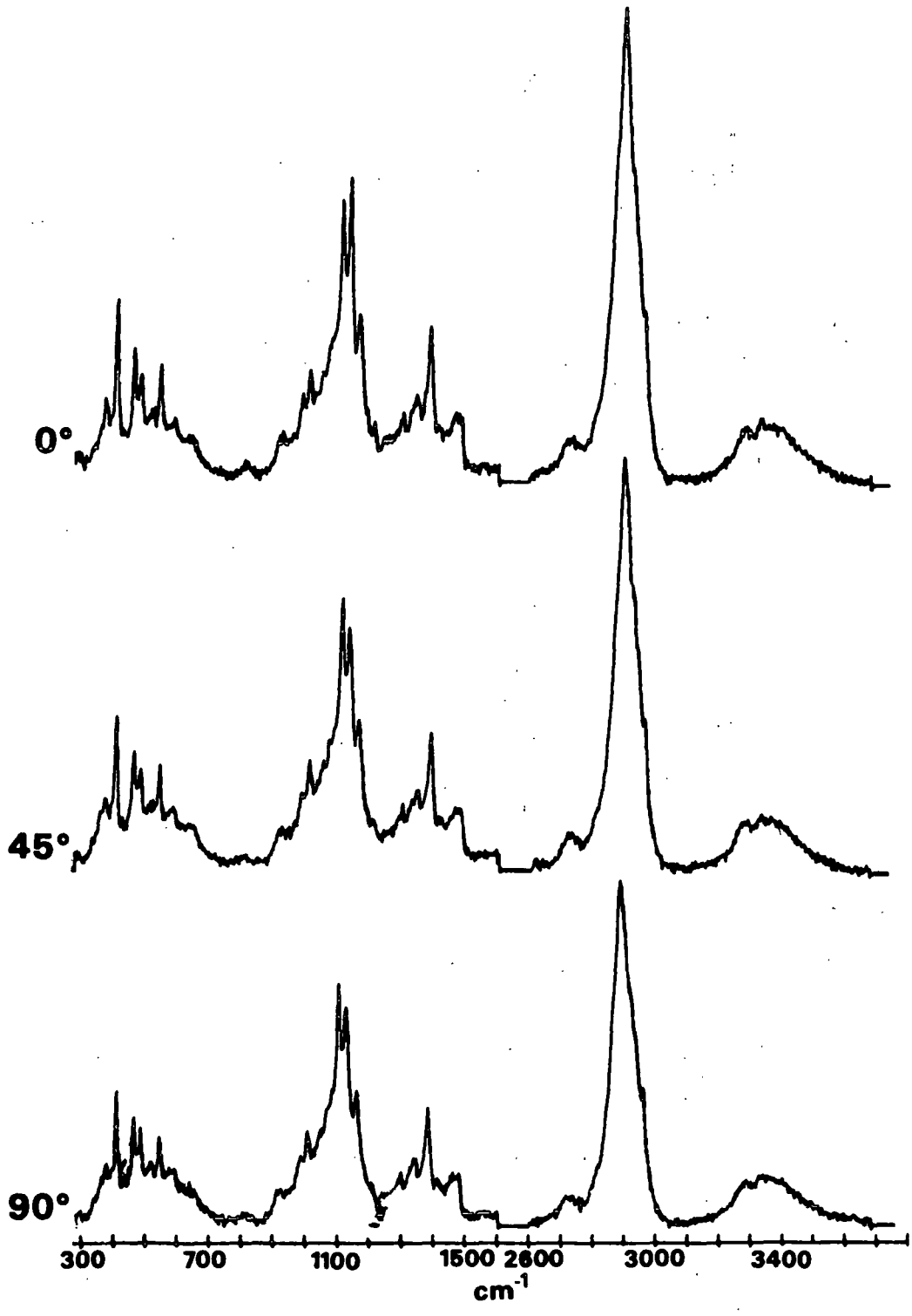

Figure 9. Polarized Raman spectra of a ramie cross section. The angle between the electric vector and the cell wall surface was varied from 0° to 90°.

Effects of Physical Structure on the Alkaline Degradation of Hydrocellulose

Victor M. Gentile, Leland R. Schroeder, and Rajai H. Atalla

The Institute of Paper Chemistry
Appleton, Wisconsin 54912

Degradations of fibrous cotton hydrocellulose and an amorphous hydrocellulose were conducted in oxygen-free 1.0M NaOH at 60 and 80°C. The physical structure of the fibrous hydrocellulose was not significantly altered, while the amorphous hydrocellulose underwent partial recrystallization into the cellulose II form and some loss of amorphous material through degradation. Endwise depolymerization (peeling) and formation of stable carboxylic acid endgroups (chemical stopping) were more rapid and extensive with the amorphous substrate. Both peeling and chemical stopping were inhibited by the more highly ordered physical structure of the fibrous hydrocellulose and the majority of degrading molecules terminated to stable inaccessible reducing endgroups, that is, by physical stopping. In contrast, chemical stopping was the dominant stabilization mechanism in the amorphous hydrocellulose. The rate of chemical stopping relative to peeling increased with temperature for both substrates. In addition, random chain cleavage, normally believed to be important only at much higher temperatures, was detected in the amorphous hydrocellulose.

Alkaline degradation of cellulose occurs by random cleavage of glycosidic linkages and by stepwise elimination of monomer units from the reducing end (peeling) (1,2). These reactions occur in competition with another reaction which stabilizes cellulose against alkaline degradation by converting the reducing endgroup to an alkali-stable, carboxylic acid endgroup (chemical stopping).

Though the major alkaline reactions of cellulose have been relatively well defined, the role of cellulose physical structure in those reactions has not been clearly established. Cellulose molecules have been reported to undergo physical stopping of the peeling reaction when a molecule is peeled back to a crystalline region in the cellulose structure, with the result that the reducing endgroup

becomes inaccessible to the alkaline medium (3-5). It is also reported that for native cellulose the rate of peeling relative to chemical stopping is higher than for mercerized cellulose (3,6-8). Furthermore, random chain cleavage occurs more rapidly in mercerized cellulose than in native cellulose (6). These findings suggest that both molecular accessibility and conformation (i.e., cellulose I or II) influence the susceptibility of cellulose molecules to alkaline reactions. However, separating the different effects of physical structure from the inherent reactivity of the cellulose molecule (in an alkaline environment) is made difficult by its limited solubility in alkaline solutions.

In the present study, the role of cellulose physical structure in alkaline reactions was investigated by comparing the alkaline degradation of highly crystalline (cellulose I) fibrous hydrocellulose with that of amorphous (noncrystalline) hydrocellulose. The amorphous substrate was taken as a cellulose model the reactivity of which would most closely approximate that of alkali-soluble cellulose. The availablity of such an approximation to the inherent reactivity of cellulose allowed evaluation of the effects of the more highly ordered structure of the fibrous hydrocellulose.

Results and Discussion

Experimental Approach. The experimental study was a comparison of the alkaline degradations of fibrous and amorphous hydrocelluloses in oxygen-free 1.0M NaOH, at 60 and 80°C. The fibrous hydrocellulose was predominantly crystalline (cellulose I) and therefore served as a substrate which would undergo alkaline reactions with significant physical structure effects. In contrast, the amorphous hydrocellulose was noncrystalline (9,10). Thus, it was a substrate which would experience substantially less structural constraint during its alkaline reactions.

The fibrous hydrocellulose was prepared by mild acid hydrolysis of cotton fibers to provide sufficient numbers of reducing endgroups for peeling and stopping to occur at measurable rates. The amorphous hydrocellulose was prepared by dissolving the fibrous hydrocellulose in the dimethylsulfoxide-paraform-aldehyde (DMSO-PF) solvent (9-12) and then regenerating the hydrocellulose with a sodium methoxide-isopropoxide solution (9,10). Both hydrocelluloses were freeze-dried during preparation and after degradation to minimize drying-induced structural changes. Thus, structural changes caused by the alkaline medium and the degradation reactions could be detected more readily.

Data on endgroup contents and number-average degrees of polymerization ($\overline{DP}_n$) for the hydrocellulose substrates are presented in Table I. The hydrocelluloses have similar numbers of carboxylic acid endgroups formed during purification of the cotton fibers. But only the amorphous hydrocellulose contained no inaccessible reducing endgroups, demonstrating the capacity of the dissolution/regeneration process to enhance accessibility (9,10). On the other hand, the total reducing endgroup content of the amorphous hydrocellulose was greater than that of the fibrous hydrocellulose. This, together with the lower $\overline{DP}_n$ of the amorphous substrate, indicates that some chain cleavage occurred during regeneration. The chain cleavage was

apparently related to the scale-up of the process, since no cleavage was detected when relatively small samples (≤ 2 g) were regenerated (9). For this reason, in comparisons of the peeling and stopping reactions of the two substrates, reaction rates were corrected for the different accessible (reactive) reducing endgroup contents.

Table I. Endgroup[a] and $\overline{DP}_n$[b] Data for Hydrocellulose Substrates

	Fibrous Hydrocellulose	Amorphous Hydrocellulose
Carboxylic acid endgroups	1.09×10^{-3}	1.02×10^{-3}
Accessible reducing endgroups	1.13×10^{-3}	3.42×10^{-3}
Inaccessible reducing endgroups	0.15×10^{-3}	0
Total reducing endgroups	1.28×10^{-3}	3.42×10^{-3}
$\overline{DP}_n$	422	225

[a]Endgroup values expressed as mole fractions of total monomer units.
[b]Calculated from the total endgroups content^{-1}.

During the course of the alkaline degradations, both physical and chemical structures of the hydrocelluloses were monitored. Hydroxyl accessibility (13) was determined as a practical measure of the fraction of molecules accessible to the alkaline medium. The crystalline structure was characterized by x-ray diffraction (14). In addition, Raman (15) and solid-state carbon-13 nuclear magnetic resonance (^{13}C-NMR) (16,17) spectra were utilized to assess conformational changes. Yield loss was determined gravimetrically and taken as a measure of anhydroglucose units lost due to peeling. The chemical stopping reaction was monitored by measuring carboxylic acid endgroup formation, using methylene blue absorption values (10). The reactive species for both peeling and stopping, that is, the accessible reducing endgroups, were detected by selective reduction with tritium-labeled sodium borohydride (9,10). Inaccessible (nonreactive) reducing endgroups were also detected by reduction with sodium borohydride-^{3}H after they were made accessible via the previously discussed regeneration technique (9). It was therefore possible to detect the so-called "physical stopping" of the peeling reaction as evidenced in the formation of inaccessible or unreactive reducing endgroups.

The physical structure data together with the alkaline reaction data permitted evaluation of the effects of physical structure on alkaline degradation of cellulose.

Alkaline Degradations - Change in Physical Structure. The hydroxyl accessibility of the fibrous hydrocellulose was initially 51.4 ± 0.8%. In contrast, the amorphous substrate had an accessibility of 99.2 ± 1.0%. Exposure of the fibrous hydrocellulose to the alkaline media caused the accessibility to decrease slightly to 50.7 ± 1.0% and 49.1 ± 1.2% at 60 and 80°C, respectively, but accessibility did not change significantly during the reaction periods (0-168 hr).

The accessibility of the amorphous hydrocellulose, however, did decline, both upon exposure to the alkaline media and during the reaction periods (Figure 1). This indicates both recrystallization and selective removal of amorphous material.

X-ray diffractograms of the fibrous hydrocellulose (Figure 2) exhibit the characteristic 002, 101, and $10\bar{1}$ reflections of the cellulose I crystalline lattice (14,18). The sharply defined peaks indicate a high degree of crystallinity. Although there appears to be a slight increase in peak intensity in the diffractogram of the zero-time sample relative to that of the initial substrate, no further change is evident in the diffractogram of the 48-hour sample. Thus, x-ray diffraction confirms that the fibrous hydrocellulose does not undergo significant change in physical structure during degradation.

The diffuse diffractogram of the initial amorphous substrate (Figure 3) is indicative of noncrystalline cellulose (19). The diffractogram of the zero-time sample exhibits a set of weak reflections corresponding to the 002, 101, and $10\bar{1}$ planes of the cellulose II crystalline lattice (14,18). The poorly defined peaks indicate a relatively low degree of crystallinity. Since the diffractogram of the 48-hour sample displays slightly more intense reflections, a small increase in the cellulose II content occurred during the reaction period. This is consistent with the hydroxyl accessibility data.

Raman spectra of the fibrous hydrocellulose in the conformation sensitive 250 to 650 cm^{-1} region have relatively intense cellulose I bands (Figure 4), indicating that the molecules are predominantly in the cellulose I conformation (15). This is best demonstrated by the intense band at 378 cm^{-1}. The lack of sigificant differences in the spectra of the initial substrate, zero-time sample, and 48-hour sample confirm that no significant changes in physical structure occurred during degradation.

In contrast, the same region in the Raman spectrum of the initial amorphous substrate exhibits broad bands (Figure 5) indicative of irregular sequences of conformations along the cellulose chains (15). The emergence of a band at 355 cm^{-1} in the spectrum of the zero-time sample indicates the presence of the cellulose II allomorph. The additional, small increase in band intensity in the spectrum of the 48-hour sample again demonstrates a further slight increase in cellulose II content during degradation.

The solid-state ^{13}C-NMR spectra of the fibrous hydrocellulose also demonstrate the predominance of the cellulose I allomorph (Figure 6). All three spectra contain the sharp resonances associated with the cellulose I conformation and the broader C-4 and C-6 resonances indicative of regions of three-dimensional disorder and crystallite surfaces (16,17). The relative intensities of the sharp and broad resonances of the three spectra are similar, again demonstrating the lack of change in physical structure during degradation.

In comparison, the ^{13}C-NMR spectrum of the initial amorphous subsrate exhibits only broad resonances (Figure 7) characteristic of regions of three-dimensional disorder (16,17). The progressive appearance of sharper resonances in the spectra of the zero-time and 48-hour samples indicates increasing conformational order.

Resonance locations and multiplicities are characteristic of the cellulose II allomorph, confirming the results of x-ray diffraction and Raman spectroscopy.

The absence of change in the physical structure of the fibrous hydrocellulose during degradation suggests three alternative hypotheses. First, selective degradation of amorphous cellulose could have occurred but to an extent not detectable by the methods applied. Second, removal of amorphous material could have been accompanied by a comparable amount of decrystallization of cellulose I domains. Finally, cellulose removed during degradation may have displayed partial cellulose I character. This would involve molecules in slightly distorted cellulose I domains (tilted or twisted segments of elementary fibril) and at crystallite surfaces (20), since removal of either would not result in detectable changes in physical structure. Alkaline reaction data presented in the following section tend to support the latter hypothesis.

The increase in cellulose II character and decrease in accessibility of the amorphous hydrocellulose upon exposure to the alkaline medium and during the reaction interval definitely indicate partial recrystallization. However, selective removal of amorphous cellulose may have occurred simultaneously. This additional possibility is consistent with the alkaline reaction data.

Peeling and Stopping Reactions. The yield loss during alkaline degradation was more rapid and extensive for the amorphous hydrocellulose than for the fibrous hydrocellulose, at both 60 and 80°C (Figure 8). However, the evolution of yield loss with time was different at 60 and 80°C. While at 60°C yield loss occurred throughout the time interval studied (168 hr), the yield of both substrates leveled off after ca. 48 hours at 80°C. While small amounts of pectic material are probably lost during the degradations, such losses are insignificant relative to yield losses due to peeling (10).

Direct comparison of yield data for the two substrates is not possible due to the differences in initial accessible reducing endgroup contents (Table I). The kinetic model used by Haas, et al. (5) was therefore employed to provide a basis for comparison of reaction rates of molecules within the two substrates. This model incorporates pseudo-first-order rate expressions for peeling (Equation 1), chemical stopping (Equation 2), and physical stopping (Equation 4); our notation differs from that of Haas, et al. In all three rate expressions, the reaction rates are related to the number of accessible reducing endgroups by pseudo-first-order rate coefficients. Thus, the rate coefficients reflect the reactivities of accessible reducing endgroups occupying different structural environments.

Since the yield losses were predominantly due to peeling (10), the pseudo-first-order rate expression for peeling can be written:

$$d[Y_l]/dt = k_p[ARE_t] \qquad (1)$$

where $[Y_l]$ = Yield loss, as mole fraction of total monomer units at zero-time

t = Time, hr
k_p = Rate coefficient for peeling, hr^{-1}
$[ARE_t]$ = Accessible reducing endgroup content at time "t," as mole fraction of total monomer units at zero-time

The derivative in Equation 1 was evaluated at selected reaction times from the slopes of plots of yield loss versus reaction time. Values of k_p, calculated from Equation 1, are listed in Table II.

Table II. Rate Coefficients for Peeling[a]

Reaction Time, hr	60°C		80°C	
	Fibrous	Amorphous	Fibrous	Amorphous
0	4.13	6.16	27.9	40.4
2	3.28	5.52	8.91	13.6
4	2.74	4.16	8.06	6.23
48	0.48	0.60	1.38	0.19
96	0.38	0.53	0.60	0.14

[a] k_p, hr^{-1}.

In all cases, k_p decreased with reaction time. Thus, the accessible reducing endgroups in both hydrocelluloses were more reactive initially, apparently due to their location in less ordered regions of the respective physical structures. As the less ordered material was removed, the accessible reducing endgroups occupied increasingly ordered regions of the structures and were therefore less reactive.

The higher k_p values for the amorphous hydrocellulose throughout the 60°C reaction and during the initial period of the 80°C reaction indicate that the accessible reducing endgroups were more reactive than those in the fibrous hydrocellulose. This coincides with the periods during which the accessibility decreased (Figure 1), suggesting that selective removal (peeling) of amorphous material did occur. Thus, the less ordered environment occupied by the degrading molecules in the amorphous hydrocellulose clearly rendered them more susceptible to peeling.

During the later period of the 80°C reaction, the amorphous hydrocellulose exhibited a lower value of k_p than the fibrous hydrocellulose. Since this corresponds to the period during which the hydroxyl accessibility of the amorphous hydrocellulose leveled-off (Figure 1), it appears that the population of degradable chains with accessible reducing endgroups had been depleted. Consequently, peeling was probably occurring close to cellulose II domains where it was significantly inhibited. In contrast, peeling progressed more slowly toward the cellulose I domains of the fibrous hydrocellulose, for example, in slightly distorted cellulose I domains, but was also strongly inhibited at the faces of more perfect cellulose I crystallites. The degree of inhibition of peeling is evidenced by the convergence of 60 and 80°C k_p values for both substrates at longer reaction times.

In the case of chemical stopping, the rate of formation of carboxylic acid endgroups is also proportional to the number of accessible reducing endgroups. The pseudo-first-order rate expression is given by:

$$[AE]/dt = k_{cs}[ARE_t] \quad (2)$$

where [AE] = Carboxylic acid endgroup content, as mole fraction of total monomer units at zero-time
k_{cs} = Rate coefficient for chemical stopping, hr^{-1}

Carboxylic acid endgroup contents were first corrected for losses of carboxylic acid groups associated with pectic material lost during the reactions (10). Values of k_{cs} were then determined at specific time intervals by the same graphical procedure as outlined for k_p; the values of k_{cs} are given in Table III.

Table III. Rate Coefficients for Chemical Stopping[a]

Reaction time, hr	60°C		80°C	
	Fibrous	Amorphous	Fibrous	Amorphous
0	0.0142	0.0302	0.106	0.262
2	0.0112	0.0271	0.0338	0.107
4	0.0094	0.0204	0.0305	0.0808
48	0.0015	0.0057	0.0119	0.0225
96	0.0010	0.0055	0.0073	0.0205

[a] k_{cs}, hr^{-1}.

The rate coefficients for chemical stopping decreased with time for both substrates in a pattern similar to that for peeling. Thus, as the accessible reducing endgroups occupied progressively more ordered regions of the structures, their reactivity toward chemical stopping also decreased.

The amorphous hydrocellulose exhibited higher values of k_{cs} throughout both the 60 and 80°C reactions. During the early period of the 80°C reaction and throughout the 60°C reaction, when the rate coefficient for peeling was higher for the amorphous substrate (Table II), its higher k_{cs} value can be primarily attributed to the reaction occurring in less ordered regions of the structure. However, this could not account for the behavior in the later period of the 80°C reactions, where peeling was apparently hindered to similar extents by the crystalline regions of both structures. Therefore, it is concluded that the cellulose II domains in the amorphous substrate did not inhibit chemical stopping as drastically as the cellulose I domains in the fibrous substrate.

Further clarification of these differences is provided by comparing the relative rates of peeling and chemical stopping for the two substrates. Average values of k_p/k_{cs} (Table IV) were calculated using Equation 3, derived by dividing Equation 1 by Equation 2.

$$d[Y_1]/d[AE] = k_p/k_{cs} \quad (3)$$

The relative rates of peeling and chemical stopping were higher for the fibrous hydrocellulose throughout the reactions. For the amorphous substrate, the values of k_p/k_{cs} were lower at the outset, and decreased substantially, at longer reaction times. Since k_p/k_{cs} remained constant throughout the fibrous hydrocellulose reactions, the relative reactivity of its accessible reducing endgroups toward both reactions appears not to change as the reactions progress from regions of lower order to regions of higher order. This is consistent with the less ordered regions exhibiting some cellulose I character; reference here is to slightly distorted cellulose I domains and crystallite surfaces (20). In the later periods of the amorphous hydrocellulose reactions, however, peeling was inhibited much more than chemical stopping. This is consistent with the earlier proposal that cellulose II domains do not hinder chemical stopping as effectively as cellulose I domains, while both crystalline forms are highly resistant to peeling. Thus, the physical presence of the crystalline domains appears to deter the progression of peeling along a cellulose molecule, while both the degree of structural order and the particular molecular conformation dictate the reactivity of an accessible reducing endgroup toward chemical stopping.

Table IV. Relative Rates of Peeling and Chemical Stopping

Reaction	k_p/k_{cs}
Fibrous 60°C (0-168 hr)	291
Fibrous 80°C (0-96 hr)	264
Amorphous 60°C (0-48 hr)	204
(48-168 hr)	84
Amorphous 80°C (0-4 hr)	154
(4-96 hr)	23

These findings are consistent with results of comparative alkaline degradation studies of native (cellulose I) and mercerized (cellulose II) cellulose (3,6-8). In addition, decreases in k_p/k_{cs} for both substrates with increasing temperature are in agreement with the higher activation energy reported for chemical stopping versus peeling in hydrocellulose (5).

In addition to undergoing chemical stopping reactions, cellulose molecules also are thought to terminate in reducing endgroups which are physically incapable of reacting due to their inaccessbility to the alkaline medium (3-5). The term "physical stopping" has been used to characterize the formation of inaccessible reducing endgroups (nonreactive) on molecules which previously contained accessible (reactive) reducing endgroups. The pseudo-first-order rate expression for physical stopping is written:

$$d[IRE]/dt = k_{ps}[ARE_t] \quad (4)$$

where [IRE] = Inaccessible reducing endgroup content, as mole fraction of total monomer units at zero-time
k_{ps} = Psudo-first-order rate coefficient for physical stopping

Although physical stopping is not a chemical reaction, per se, k_{ps} values determined using Equation 4 may be compared to k_{cs} values, providing a measure of the relative importance of the two modes of stopping. Furthermore, comparison of k_{ps} values for two substrates gives an indication of the relative extent of structural hindrance to peeling.

In both the 60 and 80°C reactions, the fibrous hydrocellulose exhibited higher k_{ps} values than the amorphous hydrocellulose (Table V). This appears to be due to the involvement of more molecules in crystalline domains of the fibrous substrate. The greater inhibition of chemical stopping by cellulose I than cellulose II domains may also have contributed to this effect by allowing more molecules in the fibrous hydrocellulose to peel to a point where the reducing endgroup would be inaccessible.

Table V. Rate Coefficients for Physical Stopping[a]

Reaction Time, hr	60°C		80°C	
	Fibrous	Amorphous	Fibrous	Amorphous
0	0.0410	0.0142	0.363	0.154
2	0.0218	0.0137	0.0812	0.0700
4	0.0157	0.0132	0.0543	0.0195
48	0.0032	0.0021	0	0
96	0.0028	0.0019	0	0

[a] k_{ps}, hr^{-1}.

At 80°C and for longer reaction times, both hydrocelluloses ceased physical stopping. This may be an indication that each physical structure has some maximum number of potential physical stopping sites. As a consequence, inaccessible reducing endgroups could become accessible as adjacent molecules are removed by peeling, giving rise to a steady state distribution of accessible and inacessible reducing endgroups.

Except for the later period of the 80°C reactions, the fibrous hydrocellulose exhibited a higher value of k_{ps} (Table V) than k_{cs} (Table IV). Consequently the degradation of a majority of the molecules in the fibrous hydrocellulose was terminated by physical rather than chemical stopping processes. In contrast, chemical stopping was the dominant mechanism of stabilization in the amorphous hydrocellulose.

Random Chain Cleavage Reaction. In addition to peeling, cellulose is also reported to undergo random cleavage of glycosidic linkages in alkaline media (1,2). This reaction results in the formation of

one reducing and one nonreducing endgroup. Since reducing endgroups can also be involved in peeling and stopping reactions, it is not possible to monitor directly their formation due to random chain cleavage. However, the rate of chain cleavage can be characterized by monitoring increases in the total number of endgroups. Accurate characterization of the reaction does require that no other changes in the total number of endgroups occur, as for example, from loss of molecules by complete peeling or dissolution.

During degradation of the fibrous hydrocellulose, no changes in total endgroup content were detected (Table VI). This is consistent with results of previous studies (6,7) in which chain cleavage was found to be important in native cellulose only above 100°C.

Table VI. Total Endgroup Contents[a] of Hydrocelluloses

Reaction Time, hr	60°C		80°C	
	Fibrous	Amorphous	Fibrous	Amorphous
0	1.94	4.13	1.88	4.51
2	1.94	3.57	1.90	4.28
4	1.92	3.44	1.96	4.35
8	2.04	3.52	1.96	4.44
24	1.95	3.59	1.89	4.96
48	1.92	3.65	1.89	5.05
96	1.86	3.76	1.90	5.35
168	1.89	4.09	--	--

[a]Expressed as 10^3 x mole fraction of total monomer units at zero-time.

In contrast, the amorphous hydrocellulose underwent initial decline in total endgroup content (Table VI) which may be attributed to complete peeling and/or dissolution of low DP molecules. After the initial periods, total endgroup contents increased gradually at both 60 and 80°C, indicating that random chain cleavage occurred. Random chain cleavage must also have occurred during the initial periods but was probably masked by the more substantial negative effects of complete peeling or dissolution on the total endgroup contents.

The amorphous substrate suffered the most rapid decline in hydroxyl accessibility (Figure 1) during the same periods in which total endgroup losses occurred. This indicates that complete peeling or dissolution primarily involved molecules existing entirely within amorphous regions and became insignificant once the majority of highly accessible chains had been removed or chemically stabilized. Further support is thus provided for the hypothesis that selective peeling of amorphous material contributes to the higher rate coefficient of peeling in the case of the amorphous hydrocellulose (Table II). The comparative lack of similar losses from the fibrous substrate suggests that the large majority of molecules were embedded to some extent in crystalline regions.

Because endgroup losses occurred simultaneously with random chain cleavage during the initial periods, analysis of the total endgroup data for kinetics of chain cleavage was confined to the later reaction periods. Since the total number of monomer units, or yield, is essentially equal to the number of glycosidic linkages, the pseudo-first-order rate expression for random chain cleavage can be written as:

$$d[TE]/dt = k_{cc}[Y_t] \quad (5)$$

where [TE] = Total endgroup content, as mole fraction of total monomer units at zero-time
k_{cc} = Rate coefficient for random chain cleavage, hr^{-1}
$[Y_t]$ = Yield, as mole fraction of total monomer units at time "t"

Rate coefficients for random chain cleavage in the 60°C amorphous hydrocellulose reaction decreased gradually from 8 to 168 hours (Table VII). At 80°C, the decrease in k_{cc} occurred more rapidly between 2 and 48 hours, with a more gradual decline up to 96 hours. This reflects the more rapid decline in accessibility of the amorphous hydrocellulose at 80°C (Figure 1). Thus, random chain cleavage appears to be inhibited by the larger cellulose II fraction that formed in the amorphous substrate at 80°C.

Table VII. Rate Coefficients[a] for Random Chain Cleavage

Reaction Time, hr	60°C		80°C	
	Fibrous	Amorphous	Fibrous	Amorphous
0	0	ND	0	ND
2	0	ND	0	5.78×10^{-5}
8	0	8.42×10^{-6}	0	5.31×10^{-5}
48	0	8.38×10^{-6}	0	0.82×10^{-5}
96	0	8.34×10^{-6}	0	0.49×10^{-5}
168	0	7.53×10^{-6}	--	--

[a] k_{cc}, hr^{-1}.
ND = Rate coefficients not determined due to simultaneous complete peeling or dissolution

The absence of chain cleavage in the fibrous hydrocellulose suggests that its disordered regions were more highly structured than the corresponding regions of the amorphous hydrocellulose. This is consistent with the results of a previous study (6) in which mercerized cellulose was found to be more susceptible to random chain cleavage than native cellulose. Another implication is that the disordered regions associated with the two crystalline polymorphs display different degrees of structural order, giving rise to differences in reactivity. Thus, in addition to molecular mobility and accessibility, the particular molecular conformation

appears to influence susceptibility to the random chain cleavage reaction.

Conclusions

Alkaline peeling and chemical stopping occur more rapidly in the amorphous regions of amorphous hydrocellulose than in the disordered regions of fibrous hydrocellulose. In addition, random chain cleavage at 60 and 80°C occurs only in amorphous hydrocellulose. Therefore, it is proposed that the disordered regions of the fibrous hydrocelluose consist of less reactive molecules at crystallite surfaces and in slightly distorted crystalline domains, as previously suggested (20).

Peeling is inhibited to similar extents by the crystalline order of both cellulose I and II allomorphs, while chemical stopping is significantly more inhibited in the cellulose I allomorph. This is consistent with the higher ratio of the rate of chemical stopping to that of peeling typically reported for mercerized cellulose in comparison to native cellulose (3,6-8).

Physical stopping, that is, formation of inaccessible reducing endgroups, occurs when peeling of molecular chains reaches the crystalline domains in both cellulose I and II. The relative rates of physical and chemical stopping are dictated by the number of molecules involved in crystalline domains. In a previous study (5), cellulose molecules were reported to maintain constant reactivity toward peeling and chemical stopping unless physical stopping occurred. However, the results of the present study indicate that reactivity diminishes gradually as reactions approach more highly ordered regions of physical structure. Simultaneously, abrupt physical stopping can occur.

The rate of chemical stopping increases with temperature relative to peeling in both fibrous and amorphous hydrocellulose. This observation is consistent with previous findings (5).

Experimental

Cellulose Substrates. Raw cotton fiber cut in ca. 0.25 inch lengths was purified by extraction with chloroform, 95% ethanol, boiling 1% (w/w) sodium hydroxide (oxygenfree), and diethylene triaminepentaacetic acid (0.15% w/v, pH 9) (10). Fibrous hydrocellulose was prepared by treating the purified fibers (60 g) with 0.1M hydrochloric acid (6L) at 40°C for 20 hours, washing with distilled water (until neutral), and then freeze-drying. Amorphous hydrocellulose was prepared by dropwise addition of a DMSO-PF solution of the fibrous hydrocellulose (0.2%, w/v, cellulose/DMSO, 3.5L) to 0.2M sodium methoxide-isopropoxide solution (1:1, v/v, methanol:isopropanol, 14L) (9,10). The resulting precipitate was washed with 0.2M sodium methoxide-isopropoxide, methanol (until neutral), 0.1M hydrochloric acid, and distilled water (until neutral), and then freeze-dried. Both the fibrous and amorphous hydrocelluloses were further dried in vacuo over phosphorus pentoxide to constant weight.

Degradation Procedure. Alkaline degradations were conducted in 316 stainless steel laboratory digesters (10). Hydrocellulose substrate

(400 mg) and oxygen-free 1.0M sodium hydroxide (40 mL) were sealed in the reaction vessels under nitrogen, and the vessels were rotated end-over-end at ca. 3 rpm in a constant temperature oil bath. The reaction mixtures were maintained at 60 or 80°C for the specified time interval, cooled to 20°C, and neutralized with 1.0M hydrochloric acid. Zero-time samples were prepared by limiting the time at the reaction temperature to ca. one minute. Degraded hydrocellulose was washed with 0.1M hydrochloric acid and distilled water (until neutral), and then freeze-dried. Yield was determined after further drying in vacuo over phosphorus pentoxide to constant weight.

Analytical Methods. Carboxylic acid endgroup contents were determined by methylene blue absorption using TAPPI Standard Method T237 su-63 with minor modifications (10). Accessible reducing endgroups were detected by reduction with sodium borohydride-^{3}H, and total reducing endgroups were determined similarly after regenerating the cellulose from the DMSO-PF solvent (9,10). Inaccessible reducing endgroup contents were calculated as total less accessible reducing endgroup contents.

Cellulose hydroxyl accessibility was measured by the deuteration method of Rouselle and Nelson (13), but the deuteration time (in liquid D_2O) was extended to 12 hours (10). X-ray diffractograms were collected on a Norelco diffractometer, using nickel-filtered, CuKα radiation. Raman spectra were acquired with a Jobin Yvon Ramanor Spectrometer, utilizing the 5145 Å line of an argon laser operated, at 100 mw, as the exciting source. Solid-state ^{13}C-NMR spectra were obtained on a General Electric S-100 instrument employing the combined techniques (16,17) of proton-carbon cross polarization, high power proton decoupling, and magic-angle sample spinning.

Acknowledgments

The authors wish to thank Dr. T. Early of GE-NMR Instruments Company, Inc. for obtaining the solid-state ^{13}C-NMR spectra and Mr. C. Woitkovich for acquiring the Raman spectra. V. M. Gentile sincerely appreciates fellowship support from The Institute of Paper Chemistry during this work.

References

1. Meller, A. Holzforschung 1960, 14, 78 and references cited therein.
2. Richards, G. N. In Cellulose and Cellulose Derivatives; Part V, p. 1007 and references cited therein, N. Bikales and L. Segal (Eds.), Wiley-Interscience, New York, 1971.
3. Machell, G.; Richards, G. N. Tappi 1958, 41, 12.
4. Colbran, R. L.; Davidson, G. F. J. Textile Inst. 1961, 52, T73.
5. Haas, D. W.; Hrutfiord, B. F.; Sarkanen, K. V. Appl. Polymer Sci. 1967, 11, 587.
6. Lai, Y.-Z.; Sarkanen, K. V. Cellulose Chem. Technol. 1967, 1, 517.

7. Franzon, O.; Samuelson, O. Svensk Papperstid. 1957, 60, 872.
8. Christofferson, K.; Samuelson, O. Svensk Papperstid. 1962, 65, 571.
9. Gentile, V. M.; Schroeder, L. R.; Atalla, R. H. J. Wood Chem. 1986, 6, 1.
10. Gentile, V. M. Doctoral Dissertation, The Institute of Paper Chemistry, Appleton, Wisconsin (1986).
11. Nicholson, M. D.; Johnson, D. C.; Haigh, F. C. Appl. Polymer Symp. 1976, 28, 931.
12. Baker, T. J.; Schroeder, L. R.; Johnson, D. C. Cellulose Chem. Technol. 1981, 15, 311.
13. Rouselle M. A.; Nelson, M. L. Textile Res. J. 1971, 41, 599.
14. Wadsworth, L.C.; Cuculo, L. C. In Modified Cellulosics, Part III, p. 117, R. M. Rowell and R. A. Young (Eds.), Academic Press, New York, 1978.
15. Atalla, R. H. J. Appl. Polymer Sci. (Appl. Polymer Symp.) 1983, 37, 295.
16. Earl, W. L.; VanderHart, D. L. Macromolecules 1981, 14, 570.
17. VanderHart, D. L.; Atalla, R. H. Macromolecules 1984, 17, 1465.
18. Tripp, V. M. In Cellulose and Cellulose Derivatives, Part IV, p. 305, N. Bikales and L. Segal (Eds.), Wiley-Interscience, New York, 1981.
19. Howsmon, J. A.; Sisson, W. A. In Cellulose, Part I, 2nd Ed., p. 231, E. Ott and H. M. Spurlin (Eds.), Interscience Publishers, New York, 1954.
20. Rowland, S. P. In Modified Cellulosics, Part III, p. 162, and references cited therein, R. M. Rowell and R. A. Young (Eds.), Academic Press, New York, 1978.

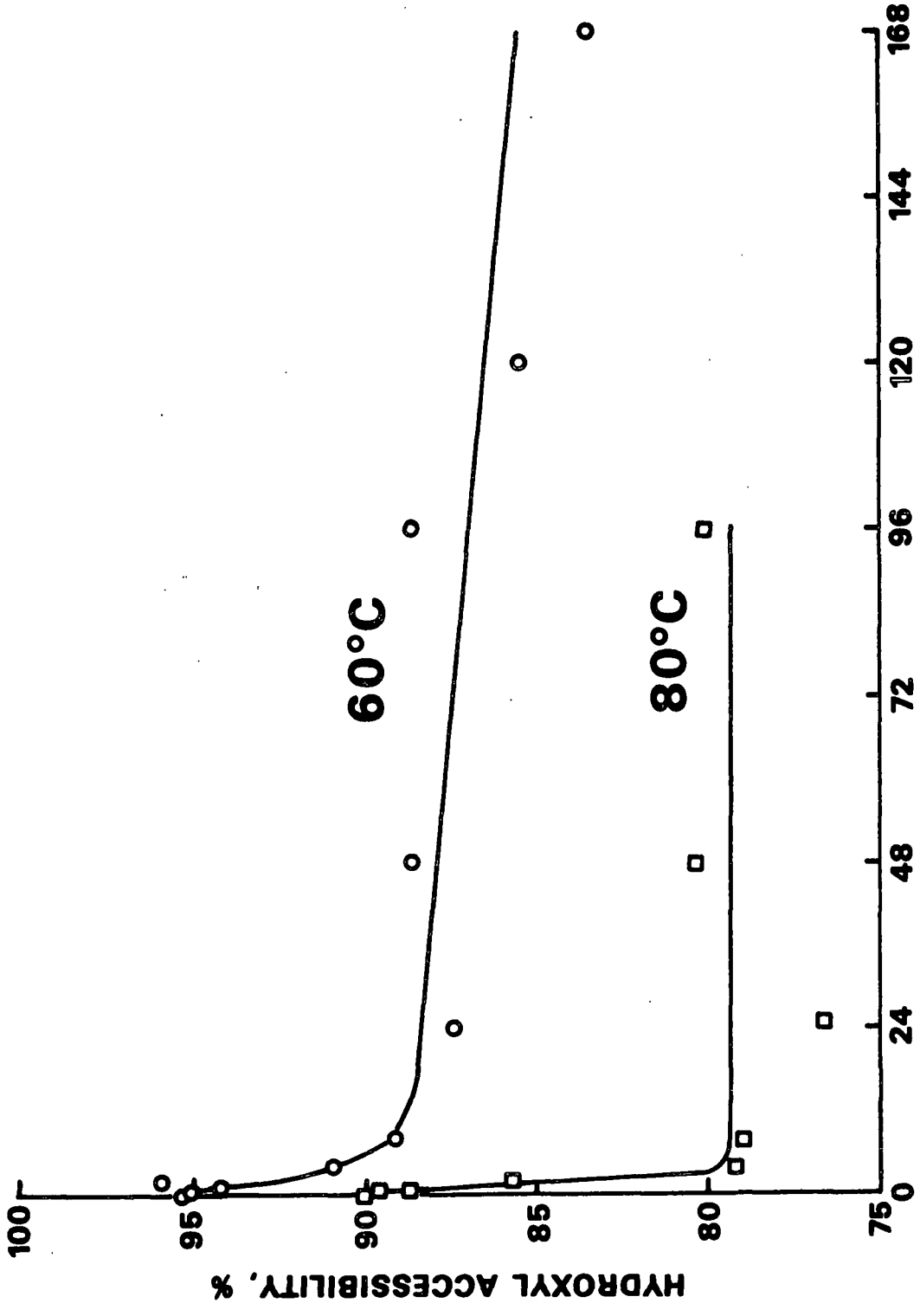

Figure 1. Hydroxyl accessibility of the amorphous hydrocellulose during degradation in 1.0M NaOH.

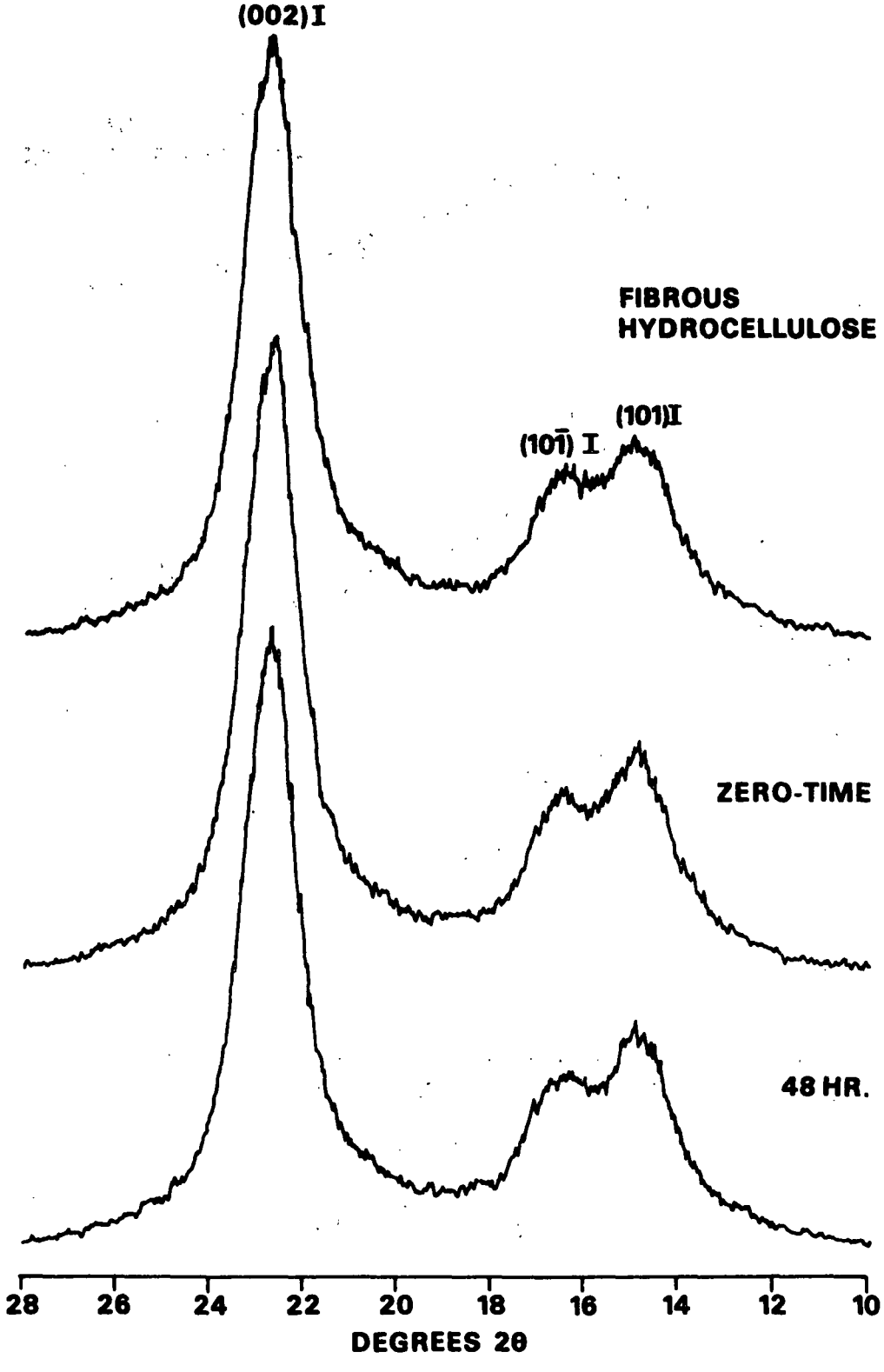

Figure 2. X-ray diffractograms of the fibrous hydrocellulose during degradation in 1.0M NaOH at 80°C.

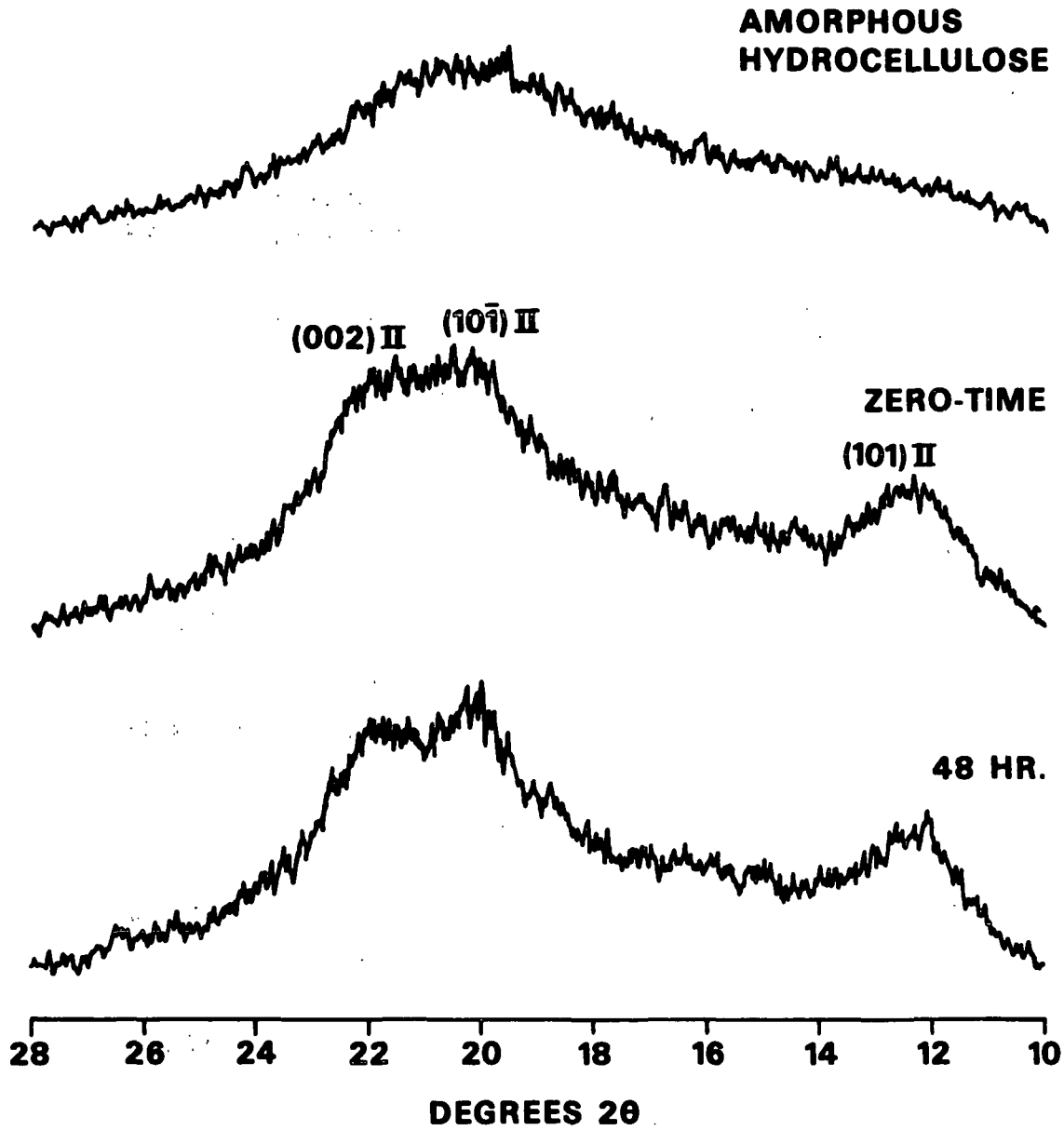

Figure 3. X-ray diffractograms of the amorphous hydrocellulose during degradation in 1.0M NaOH at 80°C.

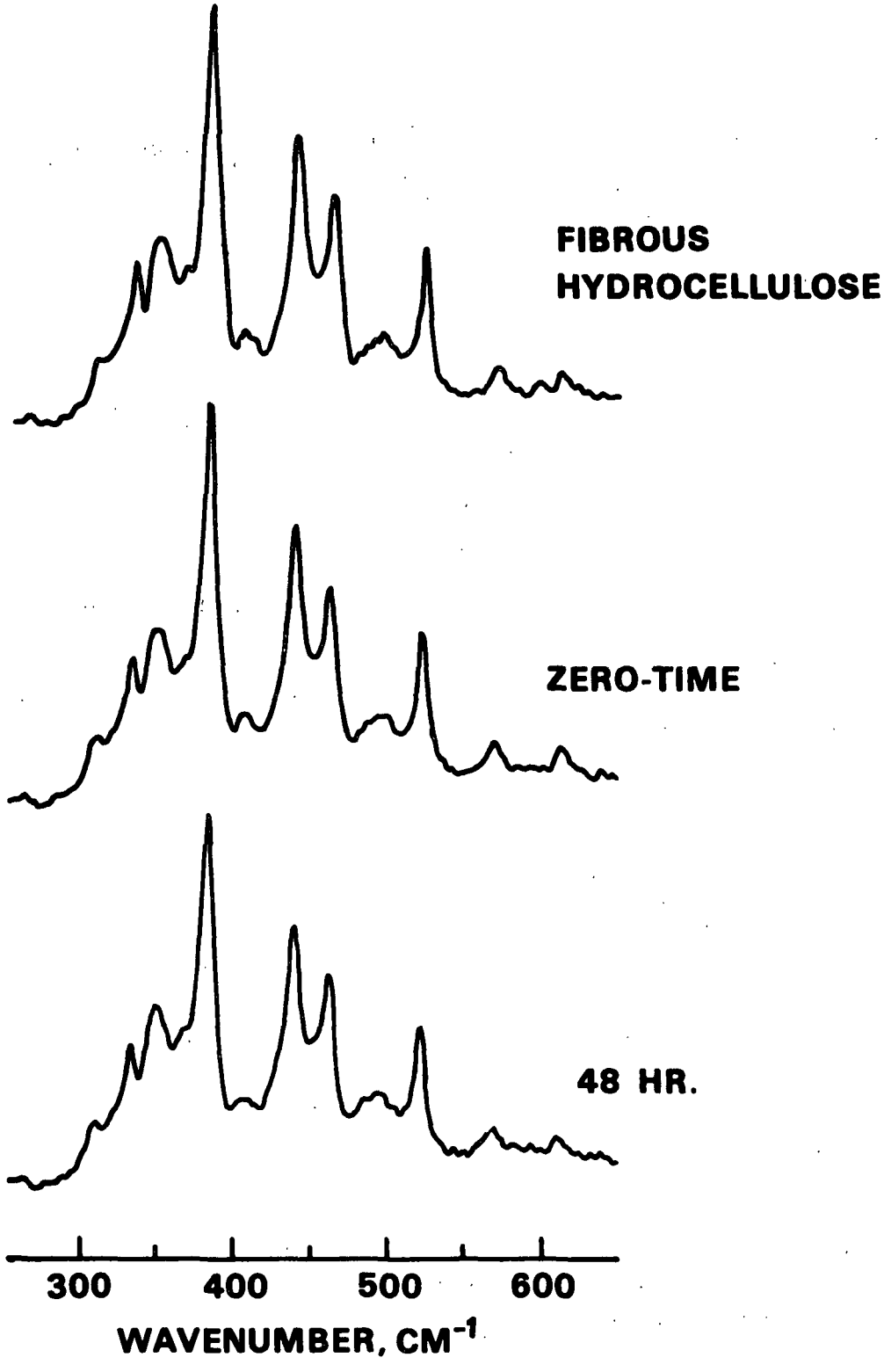

Figure 4. Raman spectra of the fibrous hydrocellulose during degradation in 1.0M NaOH at 80°C.

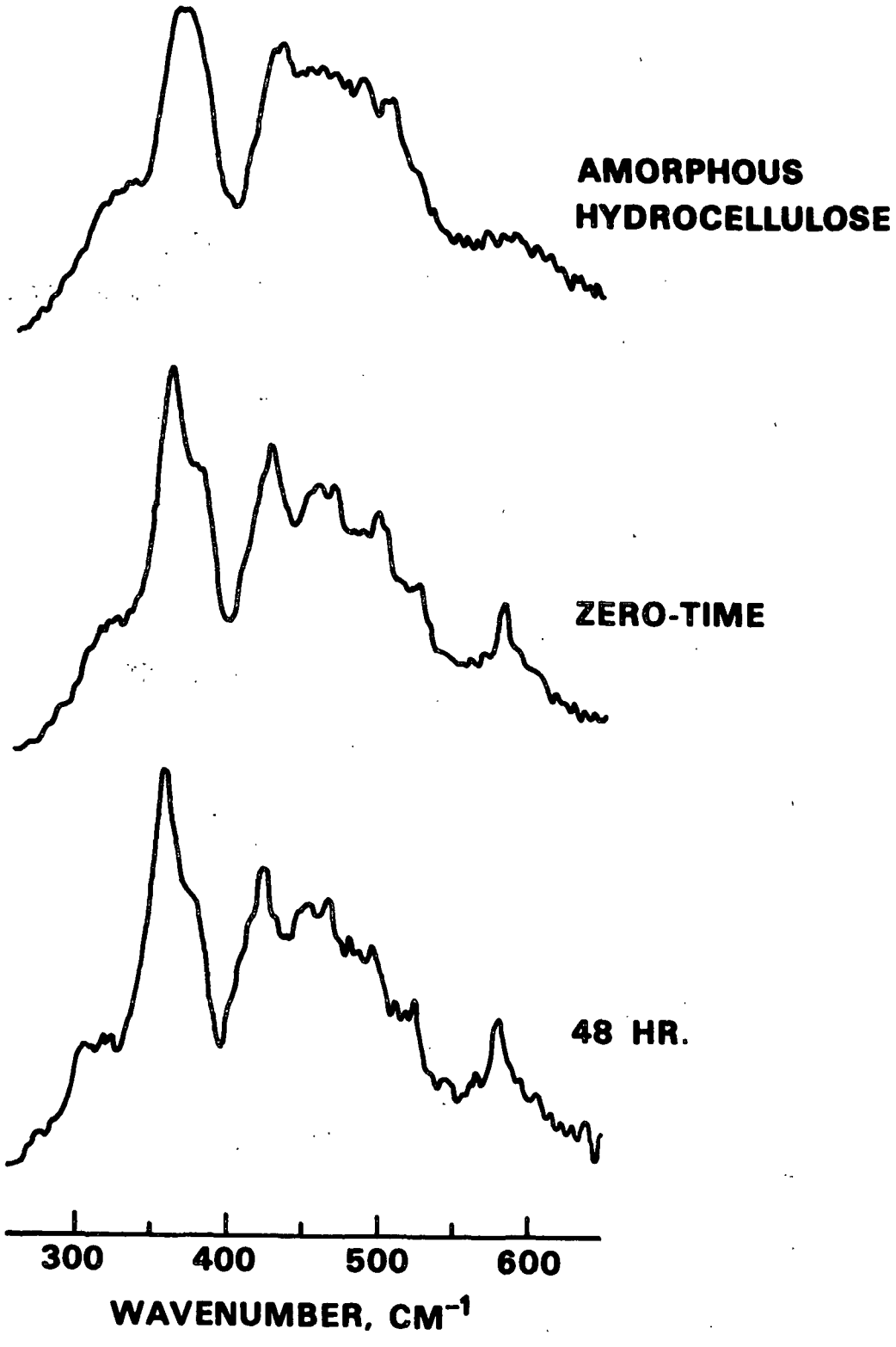

Figure 5. Raman spectra of the amorphous hydrocellulose during degradation in 1.0M NaOH at 80°C.

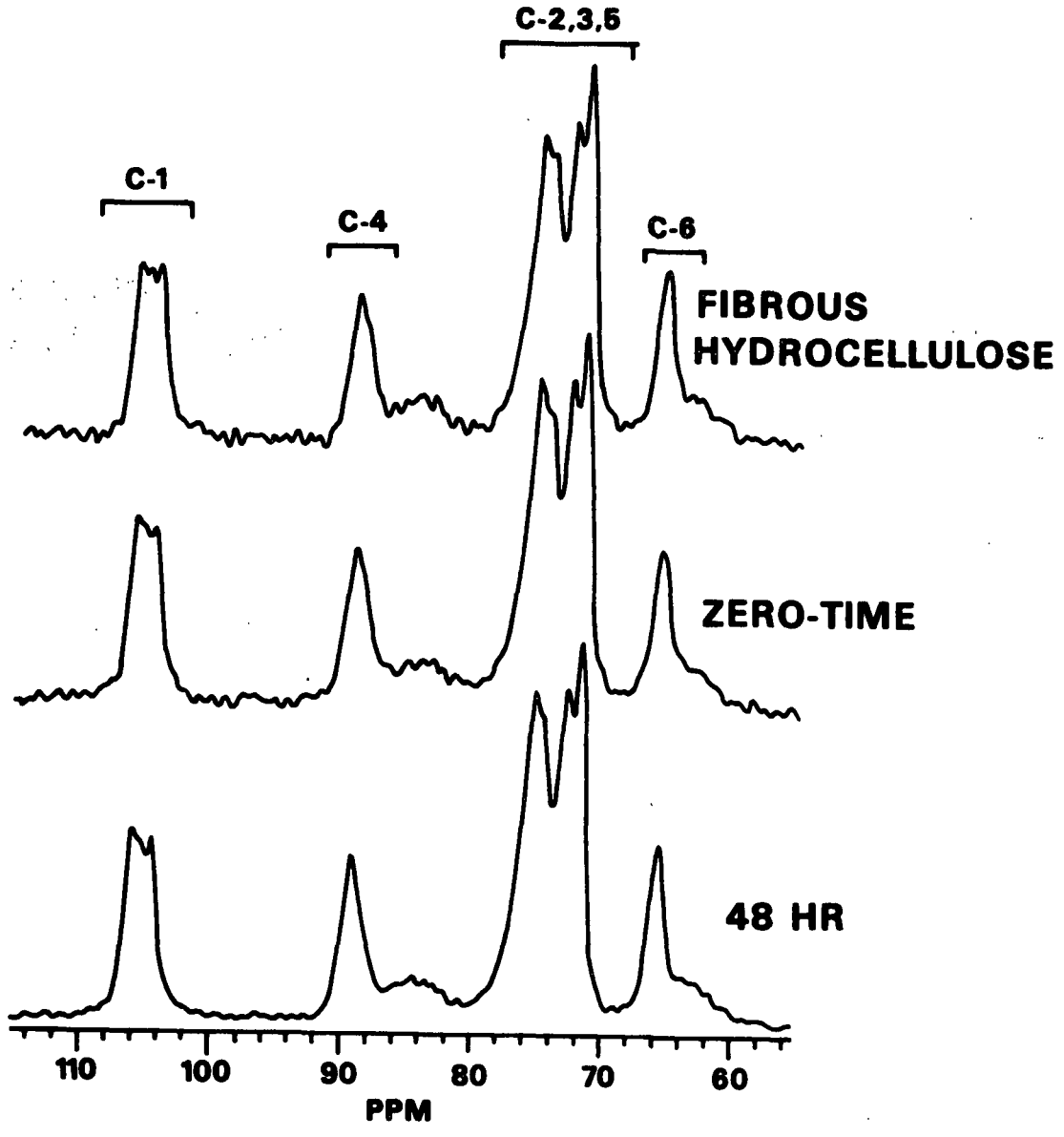

Figure 6. Solid-state ^{13}C-NMR spectra of the fibrous hydrocellulose during degradation in 1.0M NaOH at 80°C.

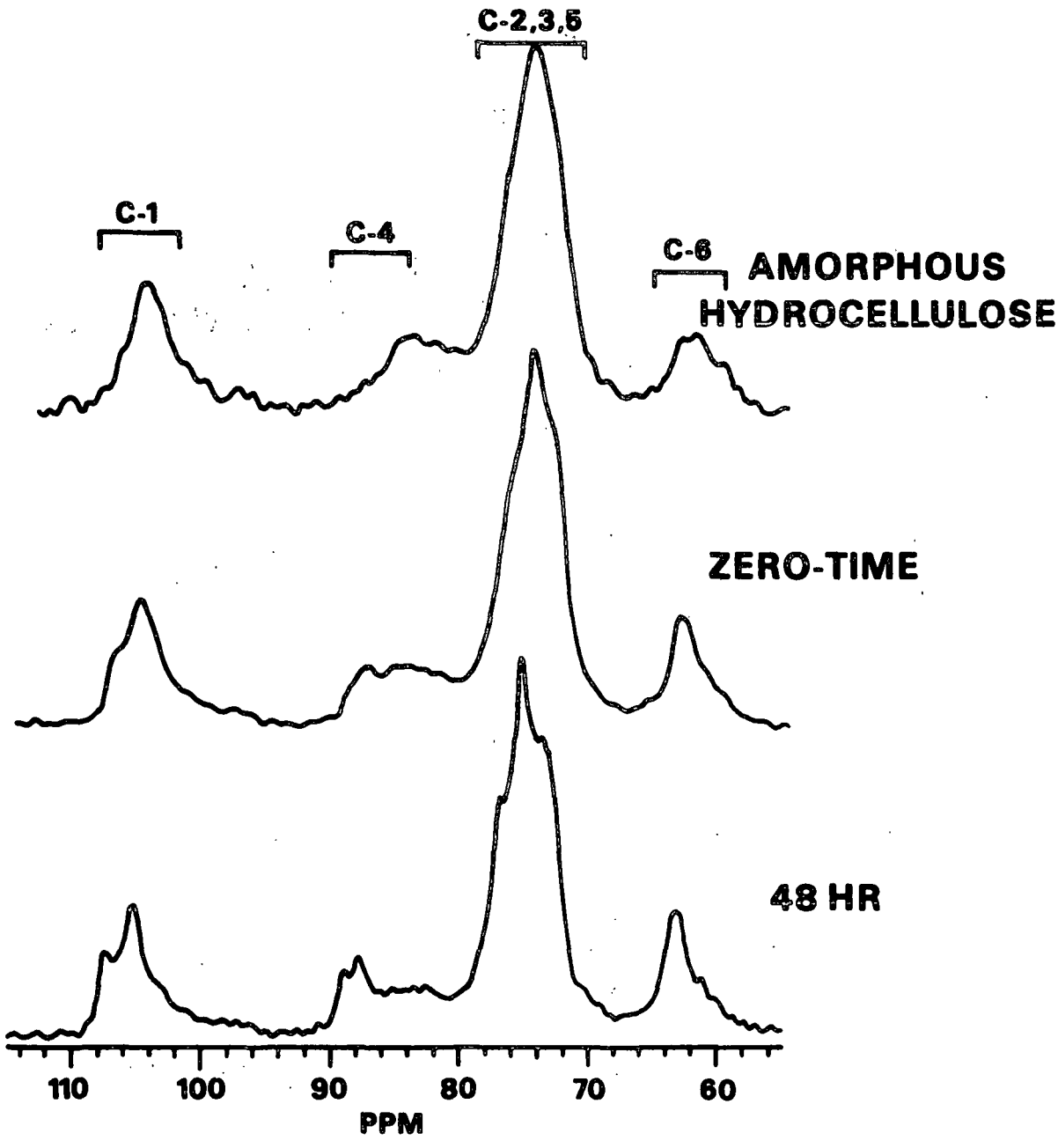

Figure 7. Solid-state ^{13}C-NMR spectra of the amorphous hydrocellulose during degradation in 1.0M NaOH at 80°C.

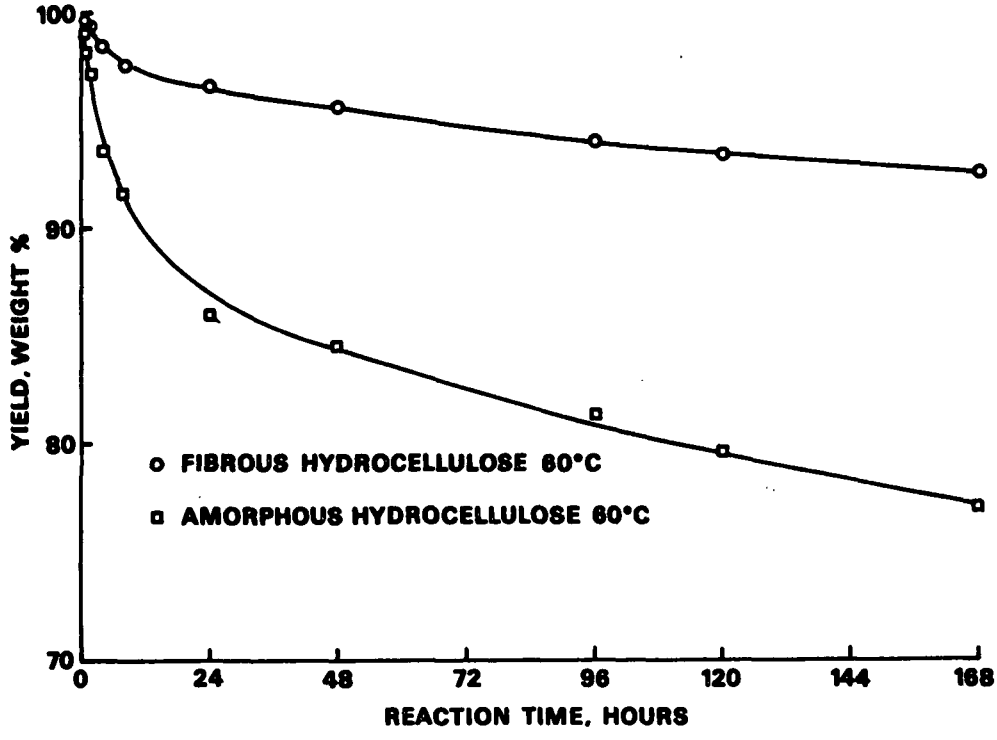

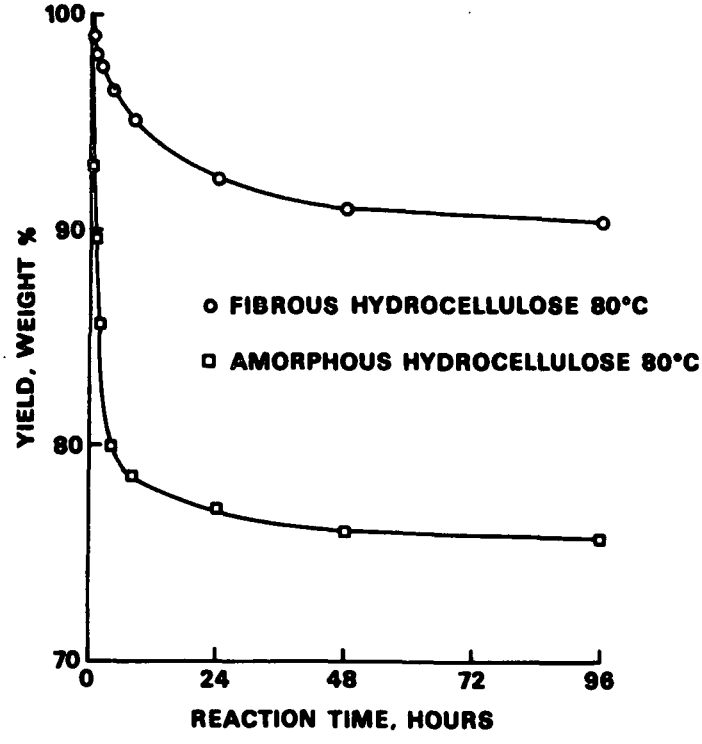

Figure 8. Hydrocellulose yield during degradation in 1.0M NaOH.

Intra- and Intermolecular Hydrogen Bonds in Native, Mercerized and Regenerated Celluloses: Their Reflection in Patterns of Solubility and Reactivity

A. Isogai, A. Ishizu and J. Nakano

Department of Forest Products, Faculty of Agriculture
The University of Tokyo, Bunkyo-ku, Tokyo 113, Japan

Rajai H. Atalla

Division of Chemical Sciences, The Institute of Paper Chemistry
Appleton, Wisconsin 54912, USA

An unusual pattern of dissolution of cellulose and related polysaccharides in the SO_2-amine-DMSO system has been observed and interpreted in terms of distinctive hydrogen bonding patterns. In particular, it was found that only native and mercerized cellulose dissolve in this system, while regenerated celluloses, glucomannan, xylan, starch, pectin and curdlan are insoluble. The pattern for the celluloses has been correlated with relative reactivities of hydroxyl groups in etherification reactions in different environments, and with results of solid state ^{13}C NMR studies on the celluloses and related oligosaccharides and polysaccharides. They suggest that the solvent system acts at particular sites involving cooperative hydrogen bonding, incorporating, among others, the primary hydroxyl group at C6 and the linkage oxygen.

Our proposal has the key implication that regenerated and mercerized celluloses have different patterns of intermolecular hydrogen bonding, even though they may have similar heavy atom lattices. This is analogous to what has been proposed as the key difference between the I_α and I_β forms of native cellulose. Taken together these findings suggest that the organization and packing of the heavy atom lattices in celluloses are dominated by the shapes of the molecules in their different conformations, and that more than one stable pattern of intermolecular hydrogen bonding is consistent with each heavy atom lattice.

The supermolecular structures of cellulose have been investigated extensively by many techniques including x-ray and electron diffractometry, electron microscopy, IR and Raman spectroscopy, broad-line proton NMR and solid-state ^{13}C-NMR. Nevertheless, many questions remain concerning the solid-state structures.

During our studies on cellulose chemistry (1-5), we have encountered an unusual pattern of solubilities of various celluloses and related polysaccharides in one of the nonaqueous cellulose solvent systems we investigated, the SO_2-diethylamine(DEA)-dimethylsulfoxide(DMSO) system. In this paper, we propose an interpretation of this pattern in terms of intra- and intermolecular hydrogen bonds in native, mercerized and regenerated celluloses. We also consider parallels with the relative reactivities of hydroxyl groups in glucose residues of cellulose toward etherification, under basic conditions, and the data from solid-state ^{13}C-NMR reported by Atalla and others (6-9).

Experimental

Sample Preparations. The native celluloses used were Avicel, cotton linters and ramie. Degrees of polymerization of Avicel and the cotton linters determined by the copperethylenediamine viscosity method (10) were 250 and 1360, respectively. Mercerized samples were prepared from these celluloses by stirring in 24% NaOH solution containing 1% NaBH under a nitrogen atmosphere for 20 hrs at room temperature. The samples were washed on a 1G2 glass filter with large amounts of water, dilute acetic acid, large amounts of water again and, finally, acetone. They were dried at 40°C *in vacuo* for 1 day. Regenerated samples were prepared from native celluloses by dissolving in cadoxene (11), and regenerating by dropwise addition to dilute acetic acid. The regenerated cellulose was filtered and washed with large amounts of water. Half of each sample was washed with acetone and dried at 40°C in vacuo for 1 day, and the other half was subjected to lyophilization followed by drying at 40°C in vacuo for 1 day.

Amylose and starch, both derived from potato, were commercial samples. Glucomannan and xylan were isolated from spruce and beech holocelluloses, respectively, and purified by the usual method (12). Pectin was isolated and purified from the midrib of *Nicotiana tabacum* and kindly provided by Dr. Shigeru Eda at The Central Research Institute, Japan Tobacco Inc. (5).

The solubility of the polysaccharides was tested by dispersing 1 g of a dried sample in 42 ml DMSO, and then adding the SO_2/DMSO solution containing 1.19 g of SO_2 (4.09 ml of 0.291 g SO_2/ml DMSO solution) and 1.92 mo DEA, in this order at room temperature. Successful dissolution was judged by visual examination after stirring for 1 day.

Results and Discussion

1. Solubilities of celluloses and other polysaccharides in the SO_2-DEA-DMSO system

In our previous work on the derivatizations of cellulose (1-5), we have found the SO_2-DEA-DMSO system to be the most effective nonaqueous cellulose solvent medium for the preparation of highly substituted cellulose ethers. The solubilities of various cellulosic samples and other polysaccharides in this nonaqueous solvent system were tested in the course of the investigations. As shown in

Table I, native celluloses such as ramie, cotton linters and Avicel, both before and after mercerization dissolved completely in this solvent system. More recently we have established that highly crystalline algal celluloses are also readily dissolved in this system.

Table I. Solubilities of Various Polysaccharides in SO_2-diethylamine-DMSO System

Soluble	Native celluloses (ramie, linter, Avicel) Mercerized celluloses (ramie, linter, Avicel)
Insoluble	Amylose, starch, glucomannan, xylan, pectin Regenerated cellulose (ramie, linter, Avicel)

In sharp contrast, regenerated cellulose samples prepared from ramie, cotton linters and Avicel do not dissolve, even after decrystallization by ball-milling. Furthermore, amylose, starch, glucomannan, xylan and pectin were also found to be insoluble in this system. Our finding concerning regenerated samples is consistent with the report by Yamazaki and Nakao (13) that commercially available rayons, even with DPv as low as 300, are insoluble in all SO_2-amine-organic solvent systems. The patterns of solubility, or lack thereof, are curious because regenerated celluloses generally have lower crystallinities than native ones. Moreover, the other polysaccharides so far examined have lower molecular weights and crystallinities than native celluloses. In addition, amylose and starch are soluble in DMSO alone above 60°C. All the cellulose samples and the polysaccharides used in this work are soluble in other nonaqueous cellulose solvent systems such as paraformaldehyde-DMSO (14), LiCl - dimethylacetamide (15), N-methylmorpholine N-oxide (16) (containing small amounts of water) and others. Thus, the insolubility of regenerated celluloses was observed only for the SO_2-amine systems. We believe that the differences in solubility reported in Table I may reflect different patterns of intra- and intermolecular hydrogen bonding in different celluloses.

In the previous work in which ^1H- and ^{13}C-NMR were used (17), the dissolution of cellulose in the SO_2-DEA-DMSO system has been explained in terms of complex formation between the -OH of cellulose, and SO_2 and DEA, as shown in Figure 1. The pattern of solubilities noted earlier suggests that the complex formation reaction in Figure 1 is specific to particular intra- and/or intermolecular hydrogen bonding patterns peculiar to native and mercerized celluloses.

The dissolution characteristics of native, mercerized and regenerated celluloses and their interpretation in terms of hydrogen bonding differences point to some interesting relationships. Native and mercerized celluloses would seem to have some common hydrogen bonding patterns, although they have different x-ray diffraction patterns. On the other hand, mercerized and regenerated celluloses would differ from each other with respect to intermolecular hydrogen bonds, although they have the same x-ray pattern.

Recently, VanderHart and Atalla (18) proposed,on the basis of CP-MAS ^{13}C NMR of different cellulose samples, that all native celluloses are composites of two crystalline modifications, cell I_α and I_β, even though they have similar x-ray patterns. These have been interpreted in terms of similar heavy atom lattices with different hydrogen bonding patterns (19,20). Thus, it may well be that mercerized and regenerated celluloses differ in the same way and can have different intermolecular hydrogen bonding patterns, which result in differences in their solubility in the SO_2-DEA-DMSO system.

2. Relative reactivities of hydroxyl groups in glucose residues of cellulose toward etherifications under basic conditions

We have previously reported studies on the distribution of substituents in partially etherified celluloses which were prepared from heterogeneous alkali cellulose and from homogeneous nonaqueous cellulose solutions (21). In the latter case, partially substituted cellulose ethers such as methyl- and carboxymethyl-celluloses were prepared from SO_2-DEA-DMSO solutions of cellulose by additions of powdered NaOH as a base.

When the nonaqueous cellulose solvent was used as a medium, the order of reactivities was 6-OH>2-OH~3-OH. This order is similar to observations in the case of simple alcohols. Thus, although the primary hydroxyl group 6-OH has the highest reactivity, and the secondary hydroxyl groups 2-OH and 3-OH have almost equal reactivities, the difference of reactivities between 6-OH, 2-OH and 3-OH is small. On the other hand, when heterogeneous alkali cellulose systems were used, where cellulose was swollen in aqueous alkali rather than being in solution, the order of reactivity was 2-OH>6-OH>>3-OH at all concentrations of aqueous alkali (22). This order is not consistent with the pattern for lower molecular weight compounds and suggests consideration of effects of intra- and intermolecular hydrogen bonds which may remain even in swollen alkali cellulose. The secondary hydroxyl group 2-OH has a higher reactivity than the primary alcohol 6-OH, and there is a remarkable difference in reactivities between the secondary alcohols 2-OH and 3-OH. These results suggest that some of the intramolecular hydrogen bonds between the 3-OH groups and O-5 in the adjacent anhydroglucose residues, known to occur in native celluloses, are retained even in swollen alkali cellulose, and thus have an effect on the etherification process.

The resistance to disruption by alkali also suggests some strong intermolecular hydrogen bonds in cellulose. Such strong hydrogen bonds may well be the key to retention of the fiber form of alkali cellulose at all concentrations of alkali. In the case of most polymers, swelling and dissolution in solvents proceed in sequence. That is, first the accessible parts are swollen by a solvent and this is followed by dissolution. However, in the case of cellulose in aqueous alkali, although it is swollen and undergoes a lattice transformation, it does not dissolve. If the hydroxyl groups are solvated with aqueous alkali and if all intra- and intermolecular hydrogen bonds are cleaved, cellulose fibers cannot be expected to keep their form nor to form a new lattice. This suggests that

some of the strong intermolecular hydrogen bonds in native cellulose may survive in swollen alkali celluloses and contribute to the definition of the new lattice. Such a proposal seems a plausible alternative to that of Na^+ stabilization of the lattice.

It has been proposed that in alkali cellulose, alkali (NaOH) and water bridge the cellulose molecules (23). However, it does not seem likely that all direct intermolecular hydrogen bonds in alkali cellulose are disrupted, inasmuch as the fibrous morphology is retained. Additionally, there have not been any reports of any precipitates of complexes between oligomers and alkali in aqueous solutions.

There has been another proposal that plane-structures consisting of cellulose molecules in the 101 plane of native cellulose are held together by hydrophobic interactions even in the presence of alkali, and that hydrophilic surfaces of the 101 plane-structures are solvated with alkali and water (24). However, if such planar structures were solvated with aqueous alkali, they would be expected to result in the formation of a dispersion of micelles. It seems to us more likely that some strong or sterically protected intermolecular hydrogen bonds of native cellulose survive even in alkali cellulose. On the other hand, since some hydrogen bonds are cleaved by NaOH and water which penetrate into the crystalline lattice of cellulose, new lattice planes can be formed as, for example, in Na-Cellulose I or other soda celluloses.

In assessing the stability of intermolecular hydrogen bonds, the pattern of chemical reactivity of the hydroxyl groups may be an indicator. On the basis of the results of relative reactivities of the hydroxyl groups in the anhydroglucose residues, the more stable intermolecular hydrogen bonds of cellulose appear likely to involve 6-OH, because it often shows lower reactivity for etherifications than the 2-OH.

3. Solid-state 13C-NMR data of various cellulose samples

^{13}C-NMR spectral shifts for cellulose and some oligomers are summarized in Figure 2 (6-9). Horii et al. (9) discussed the chemical shifts of C-6 carbons, and proposed that the difference between Cellulose I and Cellulose II is caused by conformational differences at the 6-OH groups. The shifts in the crystalline parts of Cellulose I were assigned to t-g conformations (ca. 66 ppm for C-6), and those for Cellulose II and the amorphous parts of all celluloses to g-t conformations (ca. 63 ppm for C-6).

In contrast, chemical shifts of the C-4 carbons change largely depending on whether cellulose is in a solid state or in solution (Figure 2). Horii et al. (25) suggested that this change in the chemical shift of C-4 is also caused by conformational difference. However, such a high downfield shift of C-4 carbons (Δ = ca. 10 ppm) seems unlikely to arise from a conformational difference alone. Changes in chemical shifts of carbons in low molecular sugars, which have been reported by Horii et al. (9), were explained mainly in terms of changes in shielding due to different hydrogen bonding patterns associated with different conformations.

The solid-state ^{13}C-NMR spectra of curdlan, amylose and chitin have also been reported (26), and generally C-1 and C-4, or C-3 in

the case of curdlan, have high chemical shifts in their solid states in comparison with shifts in solution. Table II shows the difference (Δ) between the chemical shifts in the solid state and in solution for the above glucans as well as cellulose. The table shows that Δ for C-1 carbons ranges from 1.0 to 3.0 ppm. In the case of amylose and chitin Δ's for C-4, and in the case of curdlan Δ for C-3, are only slightly higher (4.1-4.5 ppm). On the other hand, cellulose has a much larger Δ of 10 ppm for C-4. This exceptionally high chemical shift for C-4 suggests a special difference for solid-state structures of celluloses.

Table II. Difference (Δ, ppm) of ^{13}C-Chemical Shifts Between Solid and Solution States

Sample	Linkages	Δ, ppm C-1	C-3	C-4
Curdlan	(1-3)-β-D-glucan	1.0	4.2	
Amylose	(1-4)-α-D-glucan	2.3		4.5
Chitin	(1-4)-β-D-2-acetamido-2-deoxy-glucan	2.3		4.1
Cellulose	(1-4)-β-D-glucan	3.0		10.0

We propose here a possible explanation for the high value of the chemical shifts of C-4 in crystalline cellulose, namely, as represented in Figure 3, an exceptionally strong intermolecular hydrogen bond between a 6-OH and a glycosidic linkage oxygen atom. We speculate that it is the 6-OH of an adjacent chain because of the anomalously low reactivity of the primary hydroxyls in soda celluloses. Stabilization of such an intermolecular hydrogen bond can be facilitated by a transfer of electron density to the glycosidic oxygen atom from the C-4 carbon. This, in turn, can reduce the shielding at C-4 and result in the downfield shift of its resonance. Electron density at C-1 is clearly too low for it to make a significant contribution because of its anomeric character; this is reflected in its downfield shift beyond 100 ppm. Strong intermolecular hydrogen bonds stabilized by the shift of electron density could be resistant to cleavage even in concentrated aqueous alkali, and thus stabilize the morphology of the fiber.

Discussion

The results discussed in the previous sections suggest one property common to native and mercerized celluloses which is not shared by regenerated celluloses. That is their solubility in the SO_2-amine-DMSO system. On the other hand, mercerized cellulose and regenerated cellulose possess very similar x-ray diffraction patterns, though their response to the solvent system is not the same. These patterns suggest differences between mercerized and regenerated celluloses analogous to the differences between I_α and I_β, among the components of native celluloses. Thus it is proposed that, although

mercerized and regenerated celluloses possess the same or very similar heavy atom lattices, the patterns of hydrogen bonding developed during regeneration are unlike those which result from mercerization. Furthermore, it appears that the system of hydrogen bonds that is the specific site of attack of the SO_2-amine-DMSO system is not formed during the regeneration of cellulose from solution.

Whether the hydrogen bond of the primary hydroxyl to the glycosidic linkage oxygen is a part of this system remains an open question, since the unusually high downfield shift of the ^{13}C-NMR resonance of C-4 also occurs in regenerated cellulose. It seems more likely that this hydrogen bond is part of a system of hydrogen bonds that act in concert and result in a cooperative stabilization of the system for native and mercerized celluloses. Thus, while the C-6 hydroxyl hydrogen bond to the glycosidic linkage may be formed in regeneration, the other components of the cooperative hydrogen bond system do not occur. If the action of the SO_2-amine-DMSO solvent is particularly attuned to the cooperative hydrogen bonding effect, its inability to solubilize regenerated cellulose, or any of the other polysaccharides can be accounted for.

The proposal we make here is a speculative one. We believe it valuable to present it, however, particularly in view of the differences in hydrogen bonding patterns of the I_α and I_β celluloses alluded to above. The implications of our proposal are quite important in the context of structural studies on cellulose in general, for it follows from the proposal that the packing of the heavy atom lattice is determined primarily by the shape of the molecules in their different conformations and that more than one stable pattern of hydrogen bonding is possible for each of the heavy atom lattices.

References

1. Isogai, A.; Ishizu, A.; Nakano, J. J. Appl. Polym. Sci. 1984, 29, 2097.
2. Isogai, A.; Ishizu, A.; Nakano, J. ibid. 1984, 29, 3873.
3. Isogai, A.; Ishizu, A.; Nakano, J. ibid. 1985, 30, 345.
4. Isogai, A.; Ishizu, A.; Nakano, J. ibid. in press.
5. Isogai, A.; Ishizu, A.; Nakano, J.; Eda, S.; Kato, K. Carbohyd. Res. 1985, 138, 99.
6. Atalla, R. H.; Gast, J. C.; Sindorf, D. W.; Bartuska, V. J.; Maciel, G. E. J. Am. Chem. Soc. 1980, 102, 3249.
7. Earl, W. L.; VanderHart, D. L. ibid. 1980, 102, 3251.
8. Kunze, J.; Scheler, G.; Schroter, B.; Phillip, B. Polym. Bull. 1983, 10, 56.
9. Horii, F.; Hirai, A.; Kitamaru, R. ibid. 1983, 10, 357.
10. TAPPI Standard, T 230 om-82 (1985).
11. Jayme, G.; Lang, F. Methods in Carbohyd. Chem., Vol III, Academic Press, New York, p. 80 (1963).
12. Timell, T. E. Methods in Carbohyd. Chem., Vol V, Academic Press, New York, p. 134, 137 (1965).
13. Yamazaki, S.; Nakao, O. Sen-i Gakkaishi 1974, 30, T234.
14. Gruber, E.; Gruber, R. Cellulose Chem. Technol. 1978, 12, 345.
15. Gagnaire, D.; Germain, J. S.-; Vincendon, M. J. Appl. Polym. Sci., Appl. Polym. Symp. 1983, 87, 261.

16. Chanzy, H.; Noe, P.; Paillet, M.; Smith, P. ibid. 1983, 87, 239.
17. Isogai, A.; Ishizu, A.; Nakano, J. J. Appl. Polym. Sci. under contribution.
18. VanderHart, D. L.; Atalla, R. H. Macromolecules 1984, 17, 1465.
19. Atalla, R. H. Proceedings of Paper Making Raw Materials, Vol. III, Oxford p. 59 (1985).
20. Wiley, J. H.; Atalla, R. H. Paper in this ACS Symposium Series.
21. Isogai, A.; Ishizu, A.; Nakano, J. Sen-i Gakkaishi 1984, 40, T504.
22. Rowland, S. P. Cellulose Chem. Technol. 1980, 14, 423.
23. For example, T. Okano and A. Sarko J. Appl. Polym. Sci. 1985, 30, 325.
24. For example, F. J. Kolpak and J. Blackwell Macromolecules 1976, 9, 275.
25. Horii, F.; Hirai, A.; Kitamaru, R. ACS Symposium Series, No. 1984, 260, p. 27.
26. Saito, H.; Tabeta, R.; Hirano, S. Proceedings of the Second International Conference on Chitin and Chitosan in 1982 (Japan), p. 72.

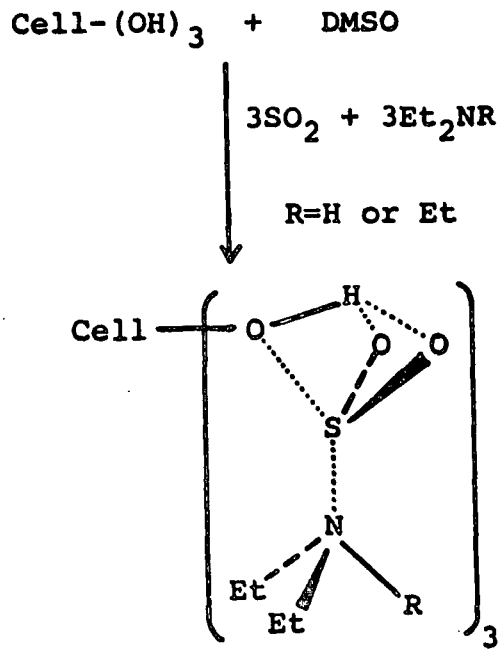

Figure 1. Dissolution mechanism of cellulose in SO_2-amine-DMSO systems.

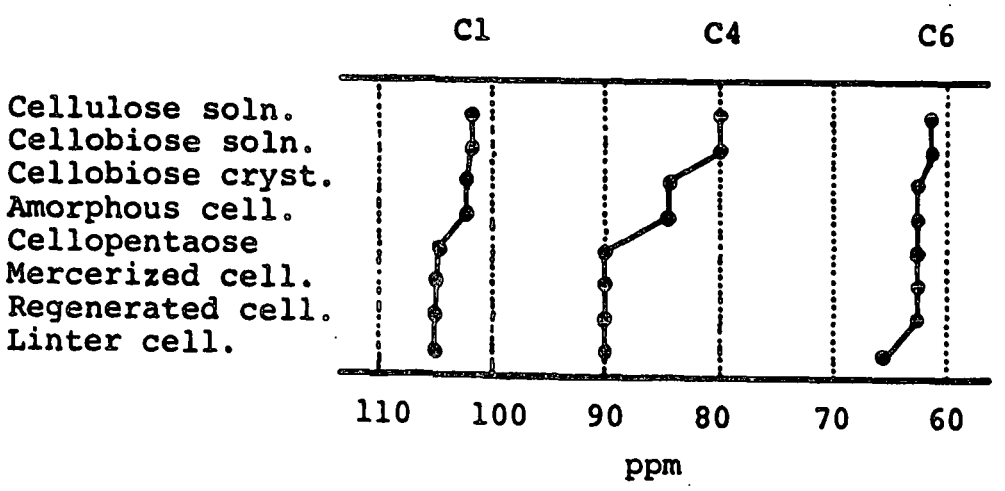

Figure 2. ^{13}C-chemical shifts of carbon in various cellulose samples.

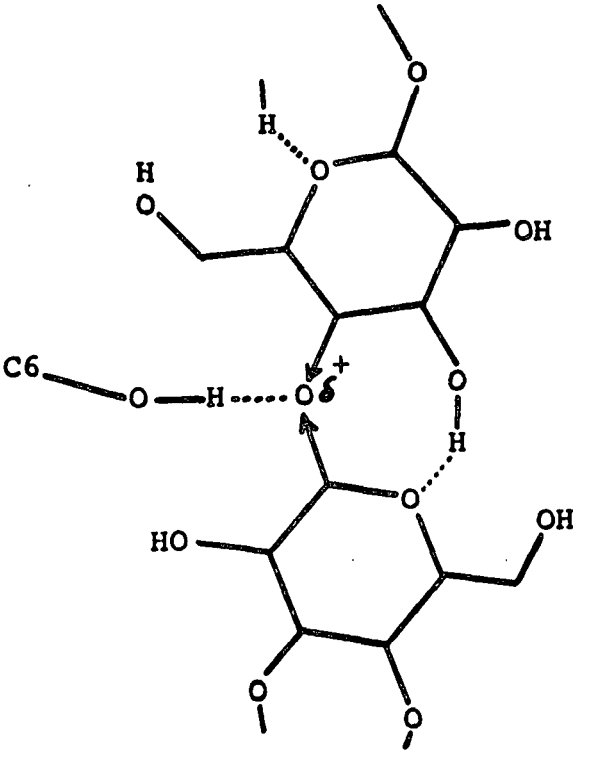

Figure 3. Possible intermolecular hydrogen bond in cellulose.

BAND ASSIGNMENTS IN THE RAMAN SPECTRA OF CELLULOSES

JAMES H. WILEY AND RAJAI H. ATALLA
The Institute of Paper Chemistry, Appleton, Wisconsin 54912 (U.S.A.)
(Received April 22nd, 1986; accepted for publication in revised form, November 10th, 1986)

ABSTRACT

Our investigations of the vibrational spectra of celluloses have been extended by using the Raman microprobe to study the spectra of native celluloses. The microprobe allows spectra to be recorded from domains as small as 1 μm, so that, for fibers of simple morphology, the polarization of exciting and scattered radiation can be defined relative to molecular orientation. Series of spectra in which the polarization of the incident light was varied relative to the fiber axis were recorded from oriented fibers. Analysis of band intensities as a function of polarization revealed new information about the directional character of the vibrational displacements. In addition, a limited study of deuterated celluloses was conducted in order to identify the modes that involve hydrogen motions. The information from the studies of intensities and deuterated celluloses aided in the interpretation of the vibrational spectrum of cellulose. Although a complete assignment of the spectrum was not possible, this new information provides a more thorough characterization of the bands than had been possible in previous studies, and establishes a foundation for future microprobe studies of native tissues.

INTRODUCTION

A variety of spectroscopic and diffractometric techniques has been used to study the structure of cellulose fibers. Vibrational spectroscopy has played a key role in this multifaceted approach. In order to derive structural information from the vibrational spectra of celluloses, the bands in the different spectral regions must be characterized. The large number of vibrational degrees of freedom and the asymmetric structure of the cellulose molecule make interpretation of the spectrum difficult. The group-frequency approach usually used in interpretation of vibrational spectra is not suited to interpretation of the molecular-chain modes of cellulose. With the exception of a few modes associated with highly localized vibrations involving hydrogen atoms, most of the modes are highly coupled and delocalized. This is not surprising, because the pyranose rings and the linkages between them consist of systems of C–C and C–O bonds. These bonds have similar reduced masses and bond energies, so that their frequencies are sufficiently close for a high degree of coupling to occur between their vibrations.

0008-6215/87/$ 03.50

The problem of interpreting the spectrum of cellulose had earlier been approached by us by conducting a series of normal-coordinate analyses of cellulose model-compounds, and using the resulting information as the basis of the analysis. We now report a closely related investigation utilizing a Raman microprobe[1-3] to study the dependence of band intensities on the polarization of the incident light relative to the orientation of the molecules. The study revealed the directional character of many of the vibrational modes, and it serves as a foundation for studies of morphologically complex aggregates of cellulose. In addition, a limited study of carbon-deuterated cellulose was undertaken, in order to identify the bands involving OH and CH motions.

BACKGROUND

Model-compound studies. — A series of normal-coordinate analyses has been undertaken in order to provide a basis for understanding the vibrational spectra of cellulose. The compounds chosen were the 1,5-anhydropentitols[4,5] the acyclic pentitols[6], the pentoses[7], the inositols[8,9] and the hexoses[10]. For each group of compounds, the force constants were refined against the observed frequencies until a satisfactory fit was obtained. The force fields that were derived enabled successful prediction of the spectra of compounds not included in the refinements, and the calculated potential-energy distributions were reasonable in comparison with the group-frequency literature on the carbohydrates. The analyses were thus successful in developing a physically meaningful force-field specifically tailored to the carbohydrates.

The hexose force-field was then used to extend the normal-coordinate method to the cellodextrins[11], whose vibrational spectra more closely resemble the spectrum of cellulose. Because the number of vibrational degrees of freedom greatly exceeds the number of observed bands in the spectra of these compounds, it was neither possible nor meaningful to refine the force constants. Although the calculations predicted many more bands than are actually observed, the distribution of calculated frequencies was in qualitative agreement with the observed spectra. The force field derived appears to provide a good model for understanding the vibrational spectra of the cellodextrins and cellulose.

The potential-energy distributions calculated for the model compounds were quite complex. Except for the internal vibrations of the methylene groups, the modes below 1500 cm^{-1} are delocalized motions involving several internal coordinates. In earlier assignments of the cellulose vibrational spectrum, the modes below 1500 cm^{-1} were assigned to localized group-vibrations[12-15]. Although the potential-energy distributions generally agreed qualitatively with the types of motions suggested in the earlier assignments, the calculations indicated that the motions are often more delocalized than had been recognized in the early assignments. Above 1500 cm^{-1}, the CH and OH stretching modes do behave as relatively pure, group modes.

Raman spectroscopy. — In cellulose, all of the vibrational modes are potentially both infrared- and Raman-active. Raman spectroscopy has, however, some important advantages for recording spectra from cellulosic samples. Highly polar bond systems, which result in intense infrared bands, have relatively low polarizabilities and, hence, weak Raman intensities. Water, therefore, has very weak Raman bands and does not interfere with the spectrum of cellulose. The low-frequency region, which is observed with difficulty in the infrared spectra, is readily observed in the Raman spectra. Finally, cellulosic materials are often optically heterogeneous substrates which scatter light intensely. In infrared spectroscopy, any processes other than absorption which cause attenuation of the incident beam are problematic. Because the refractive index of the sample will often go through large changes in the neighborhood of absorption bands, the scattering losses will vary with frequency over the infrared region. In Raman spectroscopy, refractive index variations are not a problem, as the excitation frequency is far removed from any absorption bands. Therefore, Raman spectra of samples such as cellulose, which scatter light strongly, are more accurate representations of the vibrational motions and the characteristic vibrational transitions.

Raman microprobe. — A recent innovation in Raman spectroscopy was the development of the Raman microprobe[1–3]. The microprobe is a specially designed, optical microscope coupled with a conventional Raman spectrometer. The microscope performs two key functions. It focuses the exciting light on the sample down to a diameter of 1 μm; then, it gathers the scattered light and transmits it to the entrance slit of the spectrometer. Because the microprobe acquires spectra from such small domains, the structural heterogeneity of the domains is greatly lessened relative to the domains examined in conventional Raman spectroscopy. The microprobe makes it possible to identify the morphological features from which spectra are recorded, so that orientation, composition, and structure can be related to morphology.

The spectral attributes of the microprobe make new information available. In the present investigation, the microprobe was utilized to record spectra from morphologically homogeneous, fibrillar domains. The polarization of the Raman scattered light was analyzed to aid in the assignment of the Raman spectrum of cellulose.

EXPERIMENTAL

Sample preparation. — *Valonia* fibers were extracted from the purified cell-walls of *Valonia macrophysa* that was grown in our laboratory. The alga was extracted with chloroform–methanol and boiled in a 1% solution of sodium hydroxide for 6 h under nitrogen, then it was bleached with sodium chlorite following the procedure in Browning[16]. Oriented fibrils were pulled from the cell wall with forceps and mounted on small washers for examination with the microprobe. Scanning electron micrographs of the fibrils showed that they had a high degree of parallel orientation[17].

Deuterated-cellulose fibers were prepared from purified filaments of *Cladophora glomerata* that had been grown in D_2O. The alga was adapted to growth in D_2O following Crespi's methods[18]. The procedure used to purify *Valonia* was followed, except that the bleaching step was omitted. Because the filaments were too small to be mounted on washers, they were stretched across copper specimen-support grids normally used in electron microscopy.

Ramie (*Boehmeria*) fibers were purified by the same method used to purify *Cladophora* cellulose. The fibers were dried under tension, and mounted on small washers. Scanning electron micrographs showed that the fibrils possessed a high level of parallel orientation.

A sample of deuterated, bacterial cellulose was kindly provided by Dr. H. L. Crespi. It was prepared by growing *Acetobacter xylinum* in a deuterated growth-medium[18]. The sample was purified as described for *Valonia,* and then hydrolyzed with acid[17]. The residue was made into the form of a pellet for examination with the conventional Raman system. A detailed description of the growth conditions used for the algae and the purification procedures is given elsewhere[17].

Acquisition of spectra. — Spectra of the *Valonia, Cladophora,* and ramie fibers were recorded with a Raman microprobe developed by Instruments SA. The microprobe system consists of Jobin Yvon Ramanor HG2S coupled with a Nachet optical microscope. Since we wanted to compare the intensities in spectra recorded with different polarizations of the exciting light, special modifications were made to the microprobe in order to avoid problems arising from the dichroism inherent in the optical system of the microscope and the monochromator. First, a polarization scrambler was inserted at the coupling between the microscope and the monochromator. Second, a rotating mechanical stage was installed so that, instead of changing the polarization of the incident light directly, we were able to rotate the sample relative to the plane of polarization of the incident light as shown in Fig. 1. The stage was so aligned that its axis of rotation coincided with the optical axis of the microscope. Therefore, it was possible to rotate the sample without changing the domain being examined.

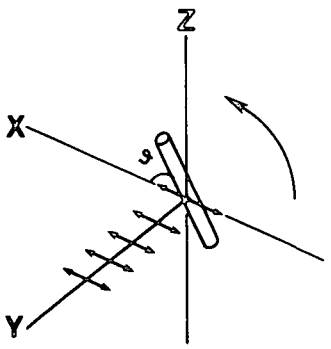

Fig. 1. Representation of the experiment in which the angle between the electric vector of the incident light and the fiber axis was varied from 0 to 90° by rotating the fiber relative to the plane of polarization of the incident light.

The exciting radiation was the 5145-Å line of an argon-ion laser. The power incident on the sample was ~7 mW. A 40-X Nachet objective with a numerical aperture of 0.75 was employed. The spectral slit-width was ~8 cm^{-1}. The acquisition time required for each spectrum was 8 h. Multiple scans were recorded in order to lessen distortion of the relative intensities due to any drift in the laser power during a single scan.

The spectrum recorded from the deuterated, bacterial-cellulose pellet was acquired in the macro chamber of the same Raman spectrometer. The incident laser power was 150 mW. The spectral slit width was 3 cm^{-1}, and the acquisition time was 20 h.

RESULTS AND DISCUSSION

Analysis of band intensities. — Sets of spectra in which the angle between the electric vector of the incident light and the fiber axis (see Fig. 1) was varied from 0 to 90° in 15° increments were recorded from *Valonia* and ramie fibers, and are

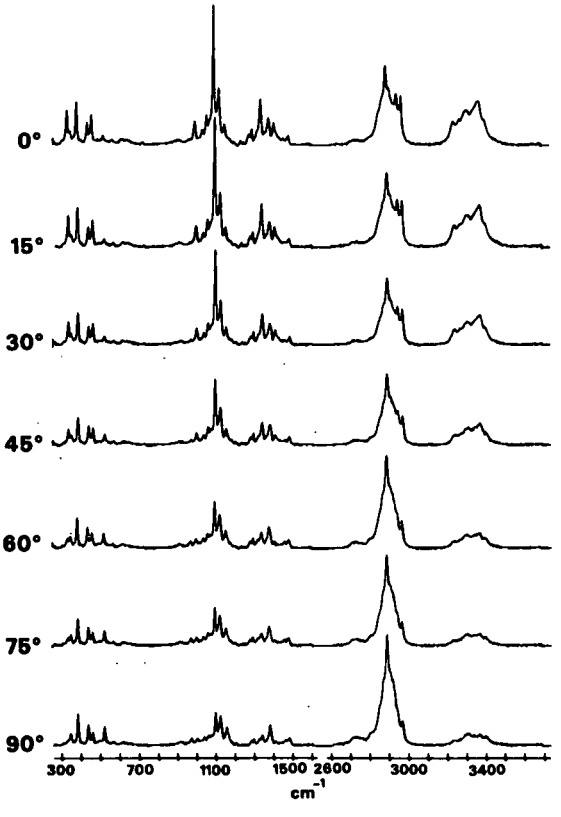

Fig. 2. Polarized Raman spectra of a *Valonia* fiber. [The angle between the electric vector of the incident light and the fiber axis was varied from 0 to 90° in 15° increments.]

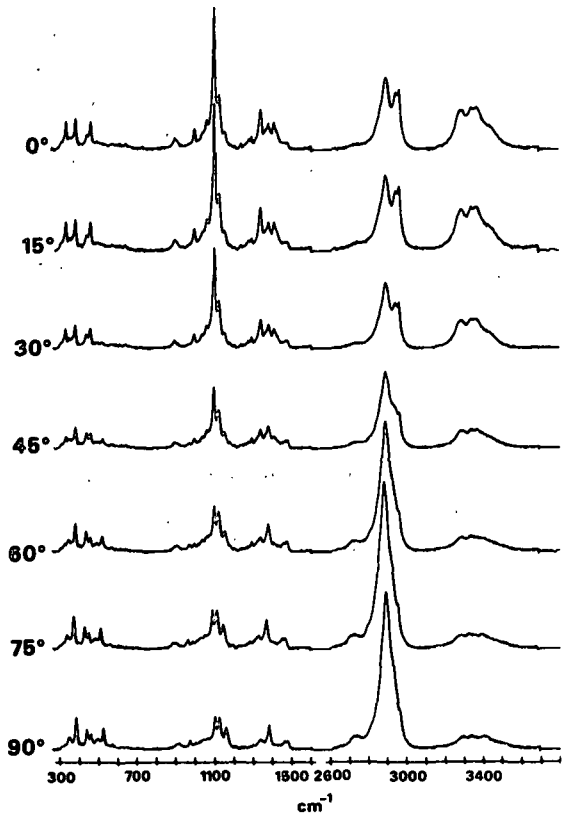

Fig. 3. Polarized Raman spectra of a ramie fiber. [The angle between the electric vector of the incident light and the fiber axis was varied from 0 to 90° in 15° increments.]

shown in Figs. 2 and 3, respectively. Except for the band widths, the spectra of *Valonia* and ramie are very similar to each other below 3000 cm^{-1}, suggesting that the same vibrational modes occur in both celluloses. Above 3000 cm^{-1}, significant frequency differences are observed. The structural implications of these frequency differences will be discussed in a later section. Due to the similarity between the *Valonia* and ramie spectra, they can be compared to check the reproducibility of the band frequencies and the dependence of the band intensities on the polarization of the incident light.

From Figs. 2 and 3, it is clear that the band intensities are strongly dependent on the orientation of the incident electric-vector relative to the fiber axis. The dependence of the band intensities on θ, the angle between the incident electric-vector and the fiber axis, was modeled by the following equation:

$$I = a + b(\cos\theta)^2 + c(\cos\theta)^4, \qquad (1)$$

where a, b, and c are constants related to the derivatives of the polarizability

tensors with respect to the normal coordinates. The equation was derived according to Snyder's treatment of intensities for partially oriented polymers[19]. In the derivation, it was assumed that the cellulose chains are oriented parallel to the fiber axis, and that the microfibrils are oriented randomly around their axes.

Eq. *1* was fitted to the data in Figs. 2 and 3 by a linear-regression technique. The equation provided an adequate model for the dependence of the band intensities on θ for bands which were well resolved. Bands which were weak, or poorly resolved, or both, could not be fitted so well. This approach to classification of the bands in the spectra has been adopted because it is useful as a basis for future applications of Raman microprobe spectroscopy in investigations of molecular organization in native, plant tissue. The advantage of using ramie and algal cellulose spectra as reference spectra is that the organization of molecular chains within the fibrils is known to be simple, and parallel to the fibril axes.

Based on the relationships between the intensities and θ, the bands were divided into four groups. The classification of the bands is summarized in Table I. The first group of bands exhibits a single maximum and minimum in plots of intensity *vs.* θ, as illustrated by curves a and c in Fig. 4. Such curves possess a single inflection point in the range of θ shown. This group of bands is designated group A in Table I. The second group of bands exhibits two maxima, at 0 and 90°, and a single minimum between 0 and 90° (see curves b and d in Fig. 4); these curves possess two inflection points. This group is designated group B in Table I. The multiple maxima may arise from accidentally degenerate modes which have maxima at 0 and 90° or from modes in which some elements of the polarizability tensor decrease during the vibration.

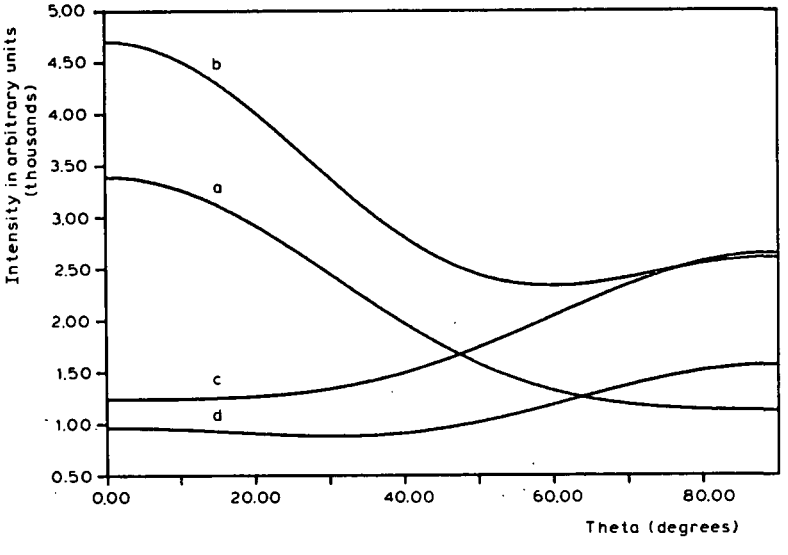

Fig. 4. Plots of intensity *vs.* the angle between the incident electric vector and the fiber axis. (a) A_0 band, (b) B_0 band, (c) A_{90} band, and (d) B_{90} band.

TABLE I

SUMMARY OF INTENSITY MAXIMA, DEUTERATION SENSITIVITIES, AND BAND ASSIGNMENTS FOR THE RAMAN SPECTRA OF *Valonia* AND RAMIE

Band frequency[a] *(cm^{-1})*		*Intensity*	*Deuteration classification*	*Assignment sensitivity*
Valonia	*ramie*			
331	331	A_0	weak	heavy atom bending,
344	344	$B_?$	weak	some heavy atom stretching
381	380	$B_?$	weak	some heavy atom stretching
437	437	$B_?$	weak	some heavy atom stretching
459	458	B_0	weak	some heavy atom stretching
520	519	A_{90}	weak	some heavy atom stretching
913	910	B_0	?	HCC and HCO bending at C-6
968	969	B_{90}	?	heavy atom (CC and CO)
997	995	A_0	?	stretching
1034	1037	A_0	?	stretching
1057	1057	A_0	?	stretching
1095	1095	A_0	weak	stretching
1118	1117	B_0	weak	stretching
1123	1121	A_0	weak	stretching
1152	1151	$B_?$	?	heavy atom stretching plus HCC and HCO bending
1279	1275	A_0	?	HCC and HCO bending
1292	1291	?	?	HCC and HCO bending
1334	1331	A_0	strong	HCC and HCO bending
1337	1337	A_0	strong	HCC, HCO, and HOC bending
1378	1378	$B_?$	strong	HCC, HCO, and HOC bending
1406	1407	A_0	strong	HCC, HCO, and HOC bending
1455	1456	B_{90}	strong	HCH and HOC bending
1477	1475	A_{90}	strong	HCH and HOC bending
2868	2866	B_{90}	strong	CH and CH_2 stretching
2885	2889	B_{90}	strong	CH and CH_2 stretching
2941	2943	$B_?$	strong	CH and CH_2 stretching
2965	2963	B_0	strong	CH and CH_2 stretching
3291	3286	B_0	strong	OH stretching
3334	3335	$?_0$	strong	OH stretching
3361	3363	$?_0$	strong	OH stretching
3395	3402	B_0	strong	OH stretching

[a]Only the bands resolved in both the *Valonia* and ramie spectra are included in this table.

The bands were further categorized by whether they were most intense when θ was 0 or 90°. The bands that are most intense when θ equals 0° are designated by a subscript 0 in Table I. Example plots of intensity *vs.* θ for A_0 and B_0 bands are given by curves a and b, respectively, in Fig. 4. These bands result from vibrations in which the maximum change in polarizability is parallel to the chain axis. Those bands that are most intense when θ equals 90° are designated by a subscript 90. Example plots are given by curves c and d in Fig. 4. For these modes, the maximum change in polarizability is perpendicular to the chain axis. The direction in which the maximum change in polarizability occurs is related to the direction of the

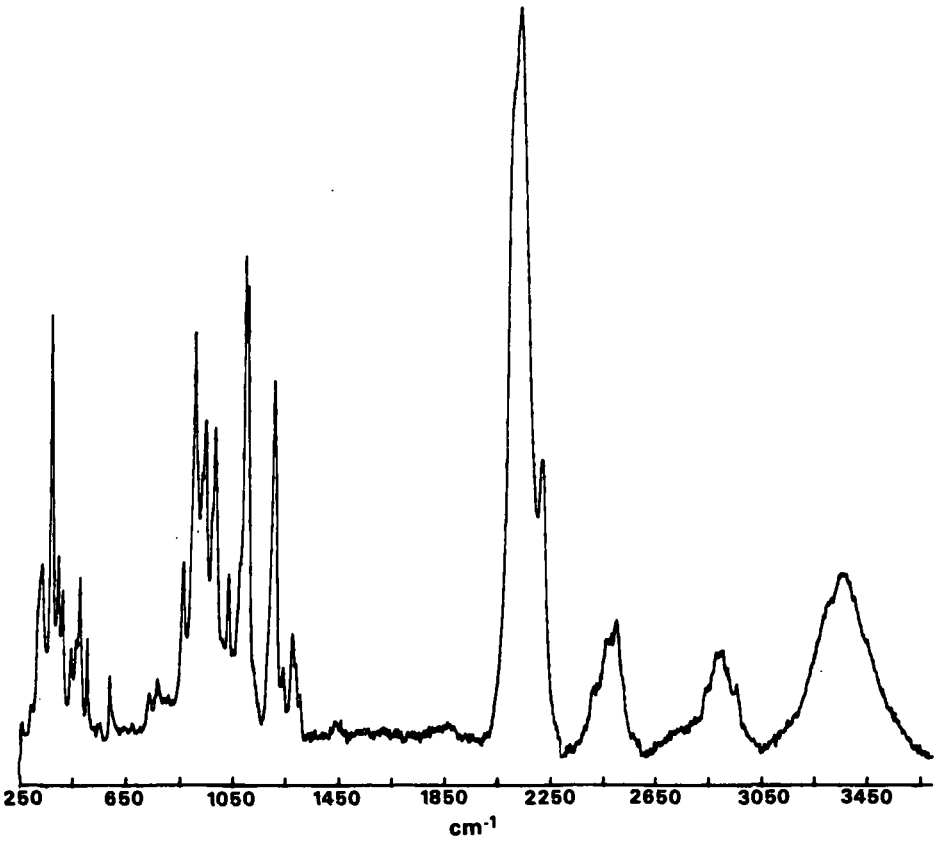

Fig. 5. Raman spectra of a pellet of deuterated, bacterial cellulose.

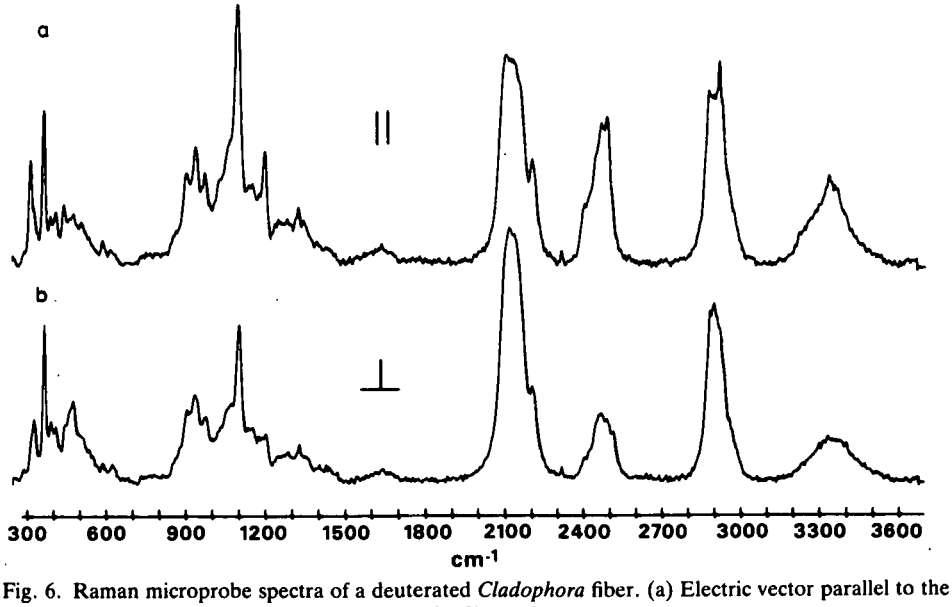

Fig. 6. Raman microprobe spectra of a deuterated *Cladophora* fiber. (a) Electric vector parallel to the fiber axis, (b) electric vector perpendicular to the fiber axis.

vibrational displacements. The intensity study can, therefore, reveal information about the directions of the vibrations. In addition, it provides a more thorough characterization of the bands in the spectrum of cellulose than had been possible in previous studies.

Spectra of deuterated celluloses. — A limited study of deuterated celluloses was conducted in order to identify the modes which involve hydrogen motions. Fig. 5 shows a spectrum from a pellet of deuterated bacterial-cellulose, recorded in the conventional Raman mode. Fig. 6 includes spectra from an oriented sample of deuterated *Cladophora* cellulose recorded with the incident electric-vector parallel to and perpendicular to the fiber axis. The residual intensities in the CH (2800–3000 cm^{-1}) and OH stretching (3200–3500 cm^{-1}) regions indicate that the samples were not fully deuterated. Due to the residual hydrogen present in the samples, the full effect of deuteration on the spectrum of cellulose could not be determined. For most of the bands, however, we were able to determine whether the effect of deuteration was small or large. This information is listed in Table I.

Band assignments. — In previous assignments of the vibrational spectrum of cellulose, it has generally been assumed that the vibrational motions could be described in terms of simple, group motions. The normal-coordinate analyses demonstrated that assignments in the traditional sense are not meaningful. In the region below 1500 cm^{-1}, only the internal motions of the methylene groups can be adequately approximated as group motions. The rest of the modes are delocalized motions involving more than one group or site in the molecule. Furthermore, cellulose possesses many more vibrational degrees of freedom than the number of bands observed in the infrared and Raman spectra. Therefore, it is possible that some modes are accidentally degenerate. The observed bands may actually arise from a composite of several vibrational motions, all having approximately the same frequency.

The assignments to be described are not assignments in the traditional sense, but rather, are descriptions of the types of motions occurring in each region of the spectrum. The types of motions were identified from the potential-energy distributions for the hexoses[10] and the cellodextrins[11], and the study of deuterated cellulose. The assignments also involve a description of the directional character of the vibrations, based on the intensity study. For convenience, the spectrum has been divided into six regions.

Region of 250–550 cm^{-1}. — In the region between 250 and 550 cm^{-1}, several closely spaced, medium-intensity bands were observed in the Raman spectra of *Valonia* and ramie cellulose (see Fig. 2 and 3). A similar pattern had been observed in the infrared spectra of native celluloses[11–15]. The potential-energy distributions are to a large extent delocalized, indicating that the vibrational modes are quite complex. Displacement drawings based on the normal-coordinate calculations for the disaccharides[11] show that almost every atom in the molecule participates in these modes. The predominant motions are skeletal-bending modes involving the CCC, COC, OCC, and OCO internal coordinates. Small amounts of methine

bending (CCH and OCH) and skeletal stretching (CC and CO) contribute in the region. Torsional motions, which are out-of-plane bending about the C–O and C–C bonds, become significant below 300 cm^{-1}. The small sensitivity of the bands to deuteration is consistent with the small contribution of CH coordinates in the potential-energy distributions.

According to the classifications in Table I, the bands at 331, 459, and 520 cm^{-1} are types A_0, B_0, and A_{90}, respectively. The 344-, 381-, and 437-cm^{-1} modes all belong to the B category, but their distribution in groups B_0 and B_{90} is uncertain, due to divergences between the *Valonia* and ramie data. Since the 331- and 459-cm^{-1} modes are most intense when the incident electric vector is parallel to the chain axis, these modes are skeletal-bending modes, where the major change in polarizability is parallel to the chain axis. An accordion-like bending motion of the pyranose rings in the chain is a plausible description of this mode. Since the 459-cm^{-1} band falls in the B category, it may actually be a composite of a motion where the change in polarizability is parallel to the chain axis and a motion where the change in polarizability is perpendicular to the chain axis. Alternatively, some of the polarizabilities may decrease during the vibration. The 520-cm^{-1} mode is most intense when the incident electric-vector is perpendicular to the chain axis.

The normal-coordinate calculations for cellotetraose[11] showed that the frequency distribution below 700 cm^{-1} is sensitive to the dihedral angles at the glycosidic linkages. Raman spectra of various types of cellulose have indicated a sensitivity to the polymorphic form of the cellulose[20,21]. The observed spectral differences are very similar to the differences observed in the frequency distributions for the alternative structures of cellotetraose. This has reinforced the conclusion that cellulose I and II possess different orientations of the glycosidic linkages[20,21].

Region of 550–950 cm^{-1}. — In the region between 550 and 950 cm^{-1} of the Raman spectra of *Valonia* and ramie cellulose (see Figs. 2 and 3), the bands are weak and widely spaced. The region between 750 and 800 cm^{-1} is devoid of any significant features. Infrared spectra of native celluloses differ from the Raman spectra between 550 and 750 cm^{-1}, in that several medium-intensity peaks are observed[11–15]. Between 750 and 850 cm^{-1}, the i.r. spectra are also devoid of any significant features. Both the Raman and i.r. spectra possess a weak, poorly resolved, cluster of bands at ~900 cm^{-1}.

The potential-energy distributions[10,11] indicate that, between 550 and 750 cm^{-1}, the predominant internal coordinates are CCC, COC, OCO, CCO, and OH out-of-plane bending. The OH bending modes are observed in infrared spectra, but are absent from Raman spectra because of the large dipole moment and low polarizability associated with the OH bond. No bands are calculated between 750 and 800 cm^{-1}, which is consistent with the frequency pattern observed. A cluster of peaks is calculated at ~900 cm^{-1} that involves HCC and HCO bending localized at the C-6 atoms.

The deuteration sensitivities of the bands in the Raman spectrum between

550 and 850 cm^{-1} are small. This observation is consistent with the dominance of the CCC, COC, OCO, and CCO internal coordinates in this region. Since the peaks around 900 cm^{-1} primarily involve methine bending coordinates, these bands should be strongly deuteration-sensitive. We were unable to identify a peak in the appropriate region of deuterated-cellulose spectra which could correspond to the 900-cm^{-1} bands. New peaks are shifted into the region at ~900 cm^{-1} by deuteration, so that it is difficult to tell if the 900-cm^{-1} band is still present. It appears, however, that the 900 cm^{-1} band is shifted by much less than would be the case were this a pure CH bending mode[22]. Therefore, it is likely that the bands at ~900 cm^{-1} are more delocalized than was predicted by the cellodextrin calculations.

In assigning the modes at ~900 cm^{-1}, several empirical observations are useful. The band is significantly more intense in the spectrum of ramie than in that of *Valonia* (see Figs. 2 and 3). Below 3000 cm^{-1}, this is the most significant difference between the ramie and *Valonia* spectra. A comparison of the spectra of ramie, cotton, bacterial, algal, and amorphous celluloses suggested that the intensity of the 900-cm^{-1} band is related to the lateral size of the cellulose crystallites. The intensity of the 900-cm^{-1} band was also found to correlate in some instances with the intensity of the broad, upfield shoulders for the C-4 and C-6 atoms in the solid-state, ^{13}C-n.m.r. spectra of native celluloses[23]. The broad shoulders arise from cellulose chains on the crystallite surfaces and in the amorphous regions. These results suggest that the intensity of the 900-cm^{-1} peak is proportional to the amount of disorder in the cellulose. Since the likely sites of disorder in the cellulose molecules are the glycosidic linkages, the C-6 atoms, and the hydroxyl groups, the 900-cm^{-1} band is likely to involve one or more of these sites.

Region of 950–1180 cm^{-1}. — In the region between 950 and 1180 cm^{-1}, several closely spaced, intense bands are observed in both the Raman spectra of *Valonia* and ramie celluloses (see Figs. 2 and 3) and in the infrared spectra of native celluloses reported in the literature[11–15]. The normal-coordinate calculations[11] show that the band density in the 950–1180-cm^{-1} region is very high. The potential-energy distributions are dominated by CC and CO stretching motions. Small amounts of HCC, HCO, and skeletal atom bending also contribute to the bands. The motions are highly coupled, often involving coupling between the D-glucose rings. The high Raman and infrared intensities of the bands are consistent with the large band density and the dominance of CC and CO stretching motions predicted by the normal-coordinate calculations. It is difficult to determine the deuteration sensitivities, because many new bands appear in the region due to deuteration. The 1071-, 1095-, 1118-, and 1123-cm^{-1} bands exhibit very little sensitivity to deuteration, which is consistent with the negligible contribution of CH, CH_2, and OH coordinates to the modes responsible.

The 997-, 1034-, 1057-, 1095-, and 1123-cm^{-1} modes all fall in the A_0 category. The band at 1118 cm^{-1} is a B_0 mode. Since these bands are most intense when the electric vector of the incident light is parallel to the fiber axis, they must result from CC and CO stretching motions which are parallel to the chain axis. The

968-cm^{-1} band is a B_{90} mode. It must result from skeletal stretching motions that are predominantly perpendicular to the chain axis. In addition to 1118- and 968-cm^{-1} bands, the band at 1152 cm^{-1} also belongs in the B category. The ramie and *Valonia* data are not consistent, however, as to whether the 1152-cm^{-1} band is a B_0 or a B_{90} mode. The directionality of the 1152-cm^{-1} mode is, therefore, uncertain.

Region of 1180–1500 cm^{-1}. — Between 1180 and 1270 cm^{-1}, the Raman and infrared spectra of *Valonia* and ramie celluloses exhibit only weak and widely spaced bands. The potential-energy distributions for the cellodextrins indicate that the 1180–1270-cm^{-1} region is a transition region[11]. Below 1180 cm^{-1}, CC and CO stretching coordinates dominate the potential-energy distributions, while, above 1270 cm^{-1}, HCC, HCO, HCH, and COH bending coordinates are most significant. Between 1180 and 1270 cm^{-1}, the modes involve significant amounts of skeletal stretching, as well as methine bending.

The cellodextrin calculations showed that the frequency distribution is sensitive to the orientation of the glycosidic linkages in the 1200–1300-cm^{-1} region[11]. The differences in the frequency distributions correspond closely with the differences observed between the spectra of celluloses I and II. A medium-intensity band is observed in the Raman spectrum of cellulose II at 1261 cm^{-1} that is not observed in the spectrum of cellulose I. This observation lends support to the proposal that celluloses I and II possess different molecular conformations. The sensitivity of the bands to conformation may arise from the nature of the potential-energy distributions. Since the 1180–1270-cm^{-1} region is a transition region, many different types of internal coordinates contribute to the modes, thereby increasing the amount of delocalization.

In the 1270–1500-cm^{-1} region, several closely spaced, medium-intensity bands are observed in both the Raman and infrared spectra of native celluloses. The bands are strongly sensitive to deuteration. The normal-coordinate calculations also predict a high density of bands in the region[11]. The predominant, internal coordinates in the potential-energy distributions are CCH, OCH, COH, and HCH bending. Between 1430 and 1500 cm^{-1}, the major internal coordinate is HCH bending; from 1430 to 1350 cm^{-1}, it is COH bending; and from 1350 to 1270 cm^{-1}, it is HCC and HCO bending. Except for the internal modes of the CH_2OH groups, the motions are quite delocalized. The dominance of CH and OH bending coordinates is consistent with the strong, deuteration sensitivity of the bands.

The Raman bands at 1279, 1334, 1337, and 1406 cm^{-1} are all A_0 modes. Since these modes are most intense when the electric vector of the incident light is parallel to the chain axis, they must result primarily from HCC and HCO bending motions, where the change in polarizability is parallel to the chain axis. Although COH bending coordinates also contribute to the potential-energy distributions above 1300 cm^{-1}, OH bending is very weak in Raman spectra, so that the intensities will be dominated by the motions of CH groups.

The Raman bands at 1455 and 1479 cm^{-1} fall in the B_{90} and A_{90} categories, respectively. The potential-energy distributions show that these bands are HCH

bending modes which contain a very small proportion of COH bending[11]. The bands are most intense when the electric vector of the incident light is perpendicular to the fiber axis. Therefore, the vibrations must be so oriented that the change in polarizability accompanying the vibration is also perpendicular to the chain axis. This can only occur in the so-called *gt* and *tg* rotational orientations for the methylene groups[24]. In the *gt* orientation, the C-6–O-6 bond is *gauche* to the C-5–O-5 bond and *trans* to the C-4–C-5 bond, whereas, in the *tg* orientation, it is *trans* to the C-5–O-5 bond and *gauche* to the C-4–C-5 bond. The Raman spectra do not provide a basis for discriminating between the two forms. Since the 1455-cm^{-1} band is a B mode, it might also be a degenerate vibration, or result from a vibration where elements of the polarizability decrease during the motion.

Region of 2800–3000 cm^{-1}. — Between 2800 and 3000 cm^{-1}, the Raman spectra of *Valonia* and ramie contain several closely spaced, very intense bands. In the infrared spectra, the band structure is very similar, but the bands are not so intense[12,14,15,25]. The bands are strongly deuteration-sensitive. The normal-coordinate calculations predict that the CH and CH_2 stretching vibrations occur in this region. These modes are isolated from the other motions in the molecule and, therefore, behave as group vibrations.

The 2868- and 2885-cm^{-1} bands fall into the B_{90} category in the Raman spectra of both ramie and *Valonia*. The 2965-cm^{-1} band is a B_0 band in both sets of spectra. Although it is difficult to assign the bands in this region, due to the overlapping of the bands and the possibility of Fermi resonance, the most intense band, at 2885 cm^{-1}, is most likely due to the methine protons. The methine CH bonds are perpendicular to the chain axis, and hence would result in stretching bands that are most intense when the electric vector of the incident light is perpendicular to the chain axis. Also, there are more methine protons than CH_2 protons, so that the methine stretch should be the most intense CH band.

The CH_2 group should exhibit both symmetric and antisymmetric stretching bands. The antisymmetric stretching band will be at higher frequency than the symmetric stretching band. Since the symmetric, methylene bending mode is most intense with the incident electric vector perpendicular to the fiber axis, the symmetric methylene stretch is also expected to be most intense in the perpendicular mode, while the antisymmetric stretch is expected to be most intense in the parallel mode. The 2965-cm^{-1} band is most intense with the incident electric vector parallel to the fiber axis, and is a plausible frequency for a CH_2 antisymmetric stretching mode.

Because there are several modes other than the methine stretching band that are most intense when the incident electric vector is perpendicular to the chain axis, the symmetric CH_2 stretching mode is more difficult to identify. As already mentioned, the 2868-cm^{-1} band is a B_{90} mode. The 2848- and 2904-cm^{-1} bands were classified as B_{90} bands based on the *Valonia* data, but they were not resolved in the ramie spectra. The 2941-cm^{-1} band was classified as a B_0 band, based on the *Valonia* data, and as a B_{90} band, based on the ramie data. Since the symmetric CH_2

stretching frequency is usually at least 100 cm^{-1} lower than the antisymmetric stretching frequency[26], either the 2848- or the 2868-cm^{-1} band is most likely to be the CH_2 symmetric stretching mode.

Region of 3200–3500 cm^{-1}. — Between 3200 and 3500 cm^{-1}, the Raman spectra of *Valonia* and ramie contain several closely spaced, medium-intensity bands. In the infrared spectra of native celluloses, the band frequencies are the same as in the Raman spectra, but the bands are much more intense. The bands are strongly deuteration-sensitive. The normal-coordinate calculations[10,11] predict that the OH stretching vibrations occur in this region. As was the case with the CH motions, the OH motions are isolated from the other internal motions of the cellulose molecule. Hydroxyl stretching motions, however, can couple with lattice modes due to their involvement in intermolecular hydrogen-bonds. Since the normal-coordinate calculations are based on an isolated-molecule approximation, they cannot predict the coupling of lattice modes with internal modes in this region.

All of the bands were found to be most intense when the electric vector of the incident light was parallel to the fiber axis, suggesting that the OH groups are predominantly oriented parallel to the chain axis. The bands are not clearly resolved, however, so it is possible that some of the bands might be more intense with the electric vector perpendicular to the chain axis.

Although the OH bands in both the *Valonia* and ramie spectra appear to be most intense with the incident electric vector parallel to the fiber axis, the band frequencies differ significantly. The spectra of *Valonia* have a peak at 3231 cm^{-1} that is not observed in the spectra of ramie. The spectra of ramie, on the other hand, have a peak at 3429 cm^{-1} that is not observed in *Valonia* spectra. The frequency differences suggest that the hydrogen-bonding pattern in *Valonia* cellulose differs from the hydrogen-bonding pattern in ramie cellulose. These differences in the hydrogen-bonding patterns are related to the structural differences between the I_α and I_β forms of native cellulose, which are discussed in more detail elsewhere[17,27].

CONCLUSIONS

Based on the relationships between band intensities and the polarization of the incident light, the bands in the Raman spectrum of cellulose were classified into four groups. The classification of the bands in this manner revealed information about the direction of the vibrational motions in cellulose. The directions of the vibrations are such that the major change in polarizability associated with the motions is either parallel or perpendicular to the chain axis. Raman spectra recorded from deuterated celluloses allowed the vibrational modes involving CH and OH motions to be identified. These spectra demonstrated that most of the modes are complex coupled vibrations. Results from normal-coordinate analyses of cellulose model-compounds were used in order to determine the types of motion most likely to occur in each region of the spectrum. These calculations also

suggested that the vibrational motions are very complex. The information from the normal-coordinate calculations, intensity studies, and spectra of deuterated celluloses aided in the interpretation of the vibrational spectrum of cellulose. The importance of these results, even though they are not complete assignments, lies in the foundation that they establish for microprobe studies of native tissues by providing a thorough characterization of the bands in the vibrational spectrum of cellulose.

ACKNOWLEDGMENTS

The authors thank Dr. H. L. Crespi for furnishing the sample of deuterated bacterial cellulose and for his advice concerning the growth of algae in heavy water, and Drs. U. P. Agarwal and N. S. Thompson for the many helpful discussions they contributed to this work. Portions of this work were used by J. H. Wiley as partial fulfillment of the requirements for the Ph.D. degree at The Institute of Paper Chemistry.

REFERENCES

1 P. DHAMELINCOURT, F. WALLART, M. LECLERCQ, A. T. N'GUYEN, AND D. O. LANDON, *Anal. Chem.*, 51 (1979) 414A–421A.
2 G. J. ROSASCO, in R. J. H. CLARK AND R. E. HESTER (Eds.), *Advances in Infrared and Raman Spectroscopy*, Vol. 3, Heyden, London, 1980.
3 M. E. ANDERSEN AND R. Z. MUGGLI, *Anal. Chem.*, 53 (1981) 1772–1777.
4 L. J. PITZNER, *An investigation of the vibrational spectra of the 1,5-anhydropentitols*, Doctoral Dissertation, The Institute of Paper Chemistry, Appleton, WI, Jan. 1973, 402 pp.
5 L. J. PITZNER AND R. H. ATALLA, *Spectrochim. Acta, Part A*, 31 (1975) 911–929.
6 G. M. WATSON, *An investigation of the vibrational spectra of the pentitols and erythritol*, Doctoral Dissertation, The Institute of Paper Chemistry, Appleton, WI, June 1974, 178 pp.
7 S. L. EDWARDS, *An investigation of the vibrational spectra of the pentose sugars*, Doctoral Dissertation, The Institute of Paper Chemistry, Appleton, WI, Jan. 1976, 245 pp.
8 R. M. WILLIAMS, *An investigation of the vibrational spectra of the inositols*, Doctoral Dissertation, The Institute of Paper Chemistry, Appleton, WI, June 1977, 377 pp.
9 R. M. WILLIAMS AND R. H. ATALLA, *J. Phys. Chem.*, 88 (1984) 508–519.
10 H. A. WELLS, *An investigation of the vibrational spectra of glucose, galactose, and mannose*, Doctoral Dissertation, The Institute of Paper Chemistry, Appleton, WI, Jan. 1977, 431 pp.
11 K. P. CARLSON, *An investigation of the vibrational spectra of the cellodextrins*, Doctoral Dissertation, The Institute of Paper Chemistry, Appleton, WI, Jan. 1979, 153 pp.
12 M. TSUBOI, *J. Polym. Sci.*, 25 (1957) 159–171.
13 C. Y. LIANG AND R. H. MARCHESSAULT, *J. Polym. Sci.*, 39 (1959) 269–278.
14 H. G. HIGGINS, C. M. STEWART, AND K. J. HARRINGTON, *J. Polym. Sci.*, 51 (1961) 59–84.
15 J. BLACKWELL, P. D. VASKO, AND J. L. KOENIG, *J. Appl. Phys.*, 41 (1970) 4375–4379.
16 B. L. BROWNING, *Methods in Wood Chemistry*, Vol. 2, Wiley–Interscience, New York, 1967, p. 295.
17 J. H. WILEY, *Raman Spectra of the Plant Celluloses*, Doctoral Dissertation, The Institute of Paper Chemistry, Appleton, WI, 1986.
18 H. L. CRESPI, *Biosynthesis with deuterated microorganisms*, Technical Committee Meeting on Modern Trends in the Biological Applications of Stable Isotopes., Leipzig, Germany, Dec. 6–10, 1976, pp. 1–15.

19 R. G. SNYDER, *J. Mol. Spectrosc.*, 37 (1971) 353–365.
20 R. H. ATALLA, *Appl. Polym. Symp.*, 28 (1976) 659–669.
21 R. H. ATALLA, *Spectroscopic studies of polymorphy in cellulose: a new structural model,* Proc. Int. Symp. Wood Pulping Chem., Stockholm, June, 1981; SPCI Report No. 38, 1 (1981) 57.
22 S. KRIMM, *J. Chem. Phys.*, 32 (1960) 1780–1783.
23 D. L. VANDERHART AND R. H. ATALLA, *Macromolecules,* 17 (1984) 1465–1472.
24 M. SUNDARALINGAM, *Biopolymers,* 6 (1968) 189–213.
25 C. Y. LIANG AND R. H. MARCHESSAULT, *J. Polym. Sci.*, 37 (1959) 385–395.
26 R. ZBINDEN, *Infrared Spectroscopy of High Polymers,* Academic Press, New York, 1964.
27 J. H. WILEY AND R. H. ATALLA, in R. H. ATALLA (Ed.), *Solid State Characterization of Cellulose,* A. C. S. Symposium Series, 1987, in press.

THE INSTITUTE OF PAPER CHEMISTRY

Appleton, Wisconsin

Status Report

to the

PULPING PROCESSES

PROJECT ADVISORY COMMITTEE

Project 3456-2

SMELT-WATER EXPLOSIONS

August 31, 1987

PROJECT SUMMARY FORM

DATE: August 31, 1987

PROJECT NO. 3456-2: SMELT-WATER EXPLOSIONS

PROJECT LEADERS: T. M. Grace

IPC GOAL:

Increase the capacity potential of processes.

OBJECTIVE:

An increased understanding of the phenomena underlying recovery boiler explosions, and the application of that knowledge to reduce the hazards of operating recovery boilers.

CURRENT FISCAL YEAR BUDGET: $20,000

SUMMARY OF RESULTS SINCE LAST REPORT:

The experiences of the industry with explosions and other issues related to recovery boiler safety continue to be monitored through active participation with the API Recovery Boiler Committee and BLRBAC. Within the past few years we have played a major role in identifying combustible gas explosions originating from black liquor pyrolysis as a distinct hazard and getting the industry to recognize this hazard by working with the API Recovery Boiler Committee and BLRBAC. In this past year, three major smelt-water explosions have occurred. We have had an active role in the investigation of the cause of all three of these incidents. As soon as confidentiality restrictions permit it, the relevant information will be disseminated through API and BLRBAC to help prevent further incidents.

A separate project entitled "Energetics of Smelt-Water Explosions", which was funded by the U.S. Nuclear Regulatory Commission, has just been completed and the final report and papers based on the work are in preparation. The first phase of the study determined the energy conversion efficiency (thermal to mechanical) for some 20 smelt-water explosions. The energy conversion efficiencies for all of the cases analyzed were very low, $< 0.5\%$. Since these cases included most of the major recovery boiler explosions, it appears that energy conversion efficiencies in recovery boiler explosions are inherently very low. These results were reported in an official NRC report, NUREG/CR-4745. The second and final phase of the study attempted to gain insight into the reasons for the low conversion efficiencies in the smelt-water system, and to try to develop scaling criteria for comparing results between different hot-cold fluid pairs and different system sizes. A postdoctoral student, Dr. Niann Shiang, contributed extensively to this second phase of the project. A graduate student under Professor Corradini at UW-Madison was supported on a half-time basis to define the thermodynamic bounds for the smelt-water explosions and to derive scaling criteria based on an explosion model previously developed at Madison.

A salt bridge model, which takes into account mass transfer of components between the two fluids, was developed and proved successful in interpreting the effects of composition on explosiveness in the smelt-water system. The model is based on the fact that the main smelt constituent, sodium carbonate, is not soluble in water at temperatures approaching the critical point, while certain other constituents are soluble. The soluble substances allow a substantial increase in the critical temperature of the solution, which in turn shifts the range of contact interface temperatures (between the spontaneous nucleation temperature and the critical temperature of the coolant) at which spontaneous explosions can occur to higher values. The model was able to provide an explanation of why NaCl, NaOH and Na_2S act as smelt sensitizers and a semiquantitative definition of the concentration ranges in smelt and in the quench solution where spontaneous explosions are likely. A paper describing this work has been drafted but needs to be reviewed by a coauthor at the NRC. It is not ready to be attached to this report, but should be ready by the time of the PAC meeting.

A report on a Swedish study of recovery boiler explosions entitled "Explosion Risk and Protection in Recovery Boilers" has been obtained and translated. The study focused on the possibility for minimizing the effects of an internal explosion in a recovery boiler through relief construction. A theoretical analysis was made of the pressure behavior and the deformation of the enclosing structural parts for various energy releases. The report concluded that pressure relief surface with a size on the order of 30 square meters could provide positive benefits, especially if the relief "gates" were as light as possible.

We continue to keep abreast of the state of knowledge concerning the physical phenomena involved in smelt-water explosions as it is developed at other universities and laboratories.

A high speed motion picture of some test explosions carried out at Sandia National Laboratory using thermite and water, which we obtained from Professor Corradini, has been incorporated into a video tape along with some background information on smelt-water explosions. About 40 copies of this tape have been distributed to various mills. We are charging $80/copy to cover the costs of preparation.

PLANNED ACTIVITY THROUGH FISCAL YEAR 1988:

Explosion monitoring activities and active participation in API Recovery Boiler Committee and BLRBAC will be continued.

The final report and papers based on the NRC study will be issued.

In view of the disastrous experience with smelt-water explosions in the industry this year, we will make a renewed effort to see if there are any reasonable measures that can be taken with regard to recovery boiler operation, furnace construction, or after a smelt-water emergency is recognized, which could reduce either the likelihood or the violence of explosions.

FUTURE ACTIVITIES:

We expect to continue to do whatever we can to reduce the risk and ultimately eliminate smelt-water explosions in recovery boilers.

STUDENT RESEARCH:

In view of the sensitivity of the issues involved, this is not normally a suitable topic for student research.

THE INSTITUTE OF PAPER CHEMISTRY

Appleton, Wisconsin

Status Report

to the

PULPING PROCESSES

PROJECT ADVISORY COMMITTEE

Project 3473-1

FUNDAMENTAL PROCESSES IN ALKALI RECOVERY FURNACES

Fume Generation and Smelt Chemistry

Black Liquor Burning

August 27, 1987

PROJECT SUMMARY FORM

DATE: August 27, 1987

PROJECT NO. 3473-1: FUNDAMENTAL PROCESSES IN ALKALI RECOVERY FURNACES

PROJECT LEADERS: T. M. Grace, J. H. Cameron, and D. T. Clay

IPC GOAL:

Increase the capacity of existing systems.

OBJECTIVE:

A quantitative description of all key processes in the burning of alkaline process black liquor, encompassing reaction paths and rate equations for drying, pyrolysis, gaseous combustion, char oxidation, sulfide production, and fume formation. The overall goal is a comprehensive understanding of black liquor combustion and application of that knowledge to improve recovery boiler performance.

CURRENT FISCAL YEAR BUDGET: $250,000

SUMMARY OF RESULTS SINCE LAST REPORT:

Char Burning:

Greg Aiken completed his Ph.D. thesis on the burning of char in a pile with an air jet directed vertically down onto the surface. He established the factors that govern the ratio of CO to CO_2 in the product gases. His results are in general agreement with the expectations based on the sulfate-sulfide concept. At higher temperatures, the reactions tend to be mass transfer controlled and the sulfur is almost entirely present as sulfide. At lower temperatures, sulfate-carbon reaction rates can be limiting and reduction is not as good. An interesting finding in his work was that the smelt did not penetrate the bed after it was formed but instead remained on the surface. A paper describing this work is attached. Another student, Dan Sumnicht has initiated some char burning experiments in which the air passes horizontally over the surface of the bed. These data have not yet been analyzed.

Fume Formation:

This work is now being carried out entirely as student research. Chris Verrill has developed an apparatus for measuring the production of fume during single-particle burning and will pursue this subject for his Ph.D. research. Kristin Goerg is studying the deposition of fume particles on cooled surfaces for her Ph.D. thesis. An M.S. project on reactions of SO_2 with Na_2CO_3 fume particles has been started by Greg Maule.

Recent movies obtained from Mikko Hupa of Abo Akademi in Finland show intense fume generation during the sulfide reoxidation phase of a single-particle burn. These findings have been confirmed by recent tests at IPC. This means that

oxidation-enhanced fume formation, a phenomenon first recognized as applying to fume formation in kraft furnaces by Cameron, may well be the primary mechanism responsible for fume formation in a recovery boiler.

Single-Particle Burning:

The phenomenological study of black liquor burning behavior using the single particle reactor continues. The reactor has been modified so that the particle can be subjected to radiant heat transfer from hot walls as well as to convection from hot gas. There are two separate studies underway. A Ph.D. thesis by Kathy Kulas (Crane) will acquire detailed experimental burning data and develop a quantitative model of single-particle burning of black liquor. A paper, based on a portion of her work, is attached. The second study is aimed at relating burning behavior to liquor composition and properties. The emphasis of this latter study has shifted from testing of random samples of mill liquor to controlled variations in selected variables.

Formal collaboration on single-particle burning of black liquor with Dr. Mikko Hupa of Abo Akademi in Finland is now underway. Selected films, videos, and liquor samples have been exchanged. A test protocol was developed and carried out. Dr. Clay visited Finland in late August to discuss the first series of results.

Sulfur Release:

A Ph.D. thesis by Frank Harper on sulfur release during pyrolysis and burning of black liquor has been initiated. This work is still in the early stages and no significant results are available yet.

Smelt Reactions with Hydrogen:

The main reactions studied were H_2 reduction of Na_2CO_3 to form NaOH and H_2 reduction of Na_2SO_4 to Na_2S. Hydrogen reduction of Na_2SO_4 is an autocatalytic reaction with Na_2S serving as the autocatalytic agent. The reaction is nearly first order in hydrogen and has an activation energy of 23,000 cal/mol. Hydrogen reduction of Na_2CO_3 is slowed significantly once a few percent of NaOH is formed. Details are given in the attached report.

Corrosion:

Greg Kulas, a Ph.D. student, has developed an apparatus for studying the corrosion of mild steel in molten smelt under conditions where a frozen smelt layer adheres to the steel surface. There are still a few minor problems with the equipment, but he is now at the stage of being able to obtain data.

Drying:

A Ph.D. thesis on drying of black liquor drops by Mark Robinson is essentially complete. His results indicate that although the drying tends to be controlled by heat transfer external to the drop, the droplet expansion that accompanies drying causes an increase in the internal heat transfer resistance. The increased internal resistance counterbalances the increased surface area, which

also accompanies the expansion. The net result is a complex drying behavior that is markedly influenced by the initial liquor solids content. A paper describing some of his results is attached.

DOE Project:

There is a very close tie-in between the DOE-sponsored work on black liquor combustion and this funded research project. Extensive data on drying rates, pyrolysis, carbon fixation, and particle characteristics have been obtained on the in-flight reactor module and are now being analyzed. The in-flight module is now operational in both the upflow and downflow modes. A char bed reactor module has also been installed and is now operational. Preliminary char bed burning tests have been made. A brief status report on the DOE project is included in the attached material.

Liquor Spray Project:

We are cooperating with Dr. Ted Farrington of the Engineering Division on a black liquor spray project. A spray test facility has been constructed which allows testing of spray nozzles using real black liquor at temperatures, pressures and solids contents that are representative of commercial practice. A flash x-ray technique is used to "photograph" the spray patterns. Image analysis techniques can then be applied to determine spray size distributions and the angular distribution of the liquor coming off the nozzle. Further developments of the technique will allow determining the velocity distributions as well. A proposal to the DOE for support for this program has been approved and we expect this support to begin to be available in early 1988.

PLANNED ACTIVITY THROUGH FISCAL YEAR 1988:

Char Burning:

The basic chemistry of char burning is now established. Continuing work will focus on quantification of the mass transfer resistance and the effect of geometry variables. Dan Sumnicht will acquire data in a simple flow-over geometry and continue with modeling of bed burning. A substantial amount of char burning data will be acquired on the DOE reactor. An industrial fellow, Craig Brown, will concentrate on understanding char burning in the DOE reactor. Pat Medvecz will begin a Ph.D. thesis on spectroscopic analysis of selected gases above the char bed in the DOE reactor.

Fume Formation and Deposition:

Chris Verrill will begin his thesis on the quantification of fume formation during single-particle burning. Kris Goerg will continue her work on fume deposition. Greg Maule will complete his M.S. research on reactions between SO_2 and Na_2CO_3 fume. A postdoctoral fellow, Jay Hsu, will implement an *in situ* method of monitoring fume concentration and size distribution in the DOE reactor.

Single Particle Burning:

Kathy Kulas (Crane) will continue her Ph.D. thesis on single-particle burning in combined convective/radiative heat fields. The collaboration with Mikko Hupa will continue.

Sulfur Release:

Frank Harper will continue his Ph.D. thesis on sulfur release in black liquor pyrolysis and burning.

Corrosion:

Greg Kulas will continue his Ph.D. thesis on the corrosion of mild steel in smelt with a frozen smelt layer on the metal surface.

Smelt Chemistry:

The focus of smelt chemistry studies will shift toward reactions of sodium and potassium chlorides. Particular attention will be paid to reactions which may affect deposits and/or create a corrosive environment within deposits. We will also attempt to reach definitive conclusions about the behavior of hydroxides in smelts.

DOE Project:

Data will continue to be obtained from the DOE project. The study of in-flight processes will be completed and reported. The char bed reactor will be used to obtain fundamental data on bed burning rates, structure and behavior. The industrial fellow, Craig Brown, will focus on char bed burning studies and in translating the results of experiments on the laboratory scale reactor to recovery boilers. The Phase-3 equipment to study fume deposition processes in simulated furnace environments will be installed.

Liquor Spray Project:

The black liquor spray and nozzle characterization project will continue and be expanded as DOE funding becomes available. An image analyzer will be obtained at a very early stage to facilitate data analysis.

Synthesis:

Much of the information on black liquor burning now exists as fragments in various stages of completion. We will be examining methods for synthesizing this into a comprehensive theory of black liquor burning. At this stage, we do not know the form that will be used to achieve this goal. It may take the form of a book.

FUTURE ACTIVITIES:

The work already underway to understand black liquor combustion and apply it to recovery boilers will be completed within the next 2 to 3 years.

We will be expanding burning and fundamental smelt chemistry research to include the behavior of chlorine compounds in the system.

Expanded corrosion studies will be carried out in cooperation with the Corrosion Group.

We will initiate studies of the burning behavior of spent liquor from high-yield pulping processes.

STUDENT RESEARCH:

Kathy Kulas (Crane)	Single particle combustion
Frank Harper	Sulfur release
Pat Medvecz	In-situ measurement of gases above char bed
Kristin Goerg	Fume deposition
Chris Verrill	Fume formation during single particle burning
Greg Kulas	Lower furnace corrosion/mild steel
Greg Maule	SO_2-fume reactions

Status Report

FUNDAMENTAL PROCESSES IN ALKALI RECOVERY FURNACES

Fume Generation and Smelt Chemistry

Fume generation research is being conducted entirely as part of the student research program. Three students (2 Ph.D. candidates and 1 M.S. candidate) are involved in this area. Their research projects include fume deposition, fume generation during black liquor combustion, and the reaction between carbonate fume particles and SO_2.

Funded research is focusing on the reactions of hydrogen in the kraft recovery furnace. These reactions include H_2 reduction of Na_2CO_3 forming NaOH and H_2 reduction of Na_2SO_4 to Na_2S. The major portion of this report describes this research.

STUDENT RESEARCH - FUME GENERATION AND CO_2/CO RATIO

Students conducting research under my supervision and their research areas are

1) Gregg Aiken, Ph.D. - Process Controlling CO_2/CO Ratio from Recovery Furnace Char Bed
2) Kristin Goerg, Ph.D. - Fume Deposition
3) Chris Verrill, Ph.D. - Fume Generation During Kraft Char Combustion
4) Gregg P. Maule, M.S. - Preliminary Study of SO_2 Reactions with Na_2CO_3 Fume Particles

Gregg Aiken has recently completed his Ph.D. thesis, which investigated the CO/CO_2 ratio from char combustion. This ratio is critical in determining the amount of O_2 required to burn the carbon content of the char bed and in determining the heat released during char oxidation reaction.

The major conclusions of this study are

1) Carbon monoxide is the major product of char combustion.
2) The CO/(CO + CO) ratio from the char bed is not dependent on temperature, time, or gas O_2 content.
3) Considerable oxidation of CO to CO_2 occurs in the gas phase.

Aiken presented a paper on this research at the AIChE summer meeting in Minneapolis. This paper is attached as an appendix to this report.

HYDROGEN REACTIONS

SUMMARY

This report describes the reactions of hydrogen with alkali carbonate-sulfate-sulfide melts. Based on the off-gas and melt compositions when a Na_2CO_3-Na_2SO_4 melt is contacted with H_2, the following reactions have been identified:

1) hydrogen reduction of sulfate, generating water vapor and sulfide,

$$4H_2 + Na_2SO_4 = 4H_2O + Na_2S \quad (1)$$

2) hydrogen reduction of carbonate, generating sodium hydroxide and carbon monoxide,

$$H_2 + Na_2CO_3 = 2NaOH + CO \quad (2)$$

3) the reaction of the carbon monoxide from hydrogen reduction of carbonate with sulfate forming carbon dioxide and sulfide,

$$4CO + Na_2SO_4 = 4CO_2 + Na_2S \quad (3)$$

4) the reaction between hydrogen, carbon dioxide, water vapor, and carbon monoxide in the gas phase.

$$H_2 + CO_2 = H_2O + CO \qquad (4)$$

INTRODUCTION

Hydrogen may occur in the kraft furnace from either black liquor pyrolysis or from the reaction of CO with H_2O. Borg, A., et al. (1974) reported H_2 concentrations of 3% directly above the bed. Hydrogen may either react with the Na_2SO_4 to form Na_2S and H_2O or it may react with Na_2CO_3 to form NaOH and CO. The objective of this project is to identify the H_2 reactions that are likely to occur within the kraft furnace, and to determine the rate controlling process and significance of these reactions.

PREVIOUS RESEARCH

Little quantitative information is available on the reactions of H_2 with alkali carbonate-sulfate melts. Atomics International (1968) conducted the most extensive research on these reactions. In this research, H_2 reduction of sulfate was studied by bubbling hydrogen through an alkali carbonate-sulfate melt contained in a graphite crucible. The reaction was followed by periodically sampling the melt and analyzing it for sulfide. The melts used for this study consisted of sodium-potassium-lithium carbonates, which form low melting temperature systems and enabled the reaction to be studied over a temperature range of 600 to 840 C. It was believed that at these temperatures the sole reaction that would occur was hydrogen reduction of sulfate. Although carbon dioxide was not normally collected during these experiments, it was sampled during a few experiments and was detected at levels indicating hydrogen reduction

of carbonate was also occurring during these experiments. At these temperatures the reaction was slow, with most reduction experiments requiring 14 to 40 hours. Water was collected during the experiments but was not used to follow the reaction rate.

Hydrogen reduction of sulfate was found to be an autocatalytic reaction with the rate increasing as the sulfide content of the melt increased. The reaction was also catalyzed by iron and tin salts. The reaction was zero order in sulfate and was dependent on the H_2 partial pressure to the 0.65 power at H_2 pressures form 0.25 to 10 atm. Using limited temperature data, the iron catalyzed reaction was determined to have an activation energy of 28.0 kcal/mol. The reaction rate was dependent on the melt-gas interfacial surface area.

EXPERIMENTAL SYSTEM

During our research, the reactions were followed by continuously monitoring the rate of H_2 consumption and CO and CO_2 generation. Water generated from these reactions was collected but was not continuously monitored.

The molten salts were contained in an alumina crucible and heated using a radio-frequency furnace. The reaction of hydrogen with the alkali carbonate-sulfate melts was studied by either bubbling H_2 through the melts or introducing H_2 above stirred melts and monitoring the H_2, CO, and CO_2 content of the off-gas. These experimental systems are illustrated in Fig. 1 and 2. The H_2 and N_2 were metered through the mass flow meters and enter the melt through a ceramic tube. The off-gas from the reactor passed through an adsorbate water trap to a CO_2-CO analyzer. From this analyzer the gases passed through a CO_2 trap

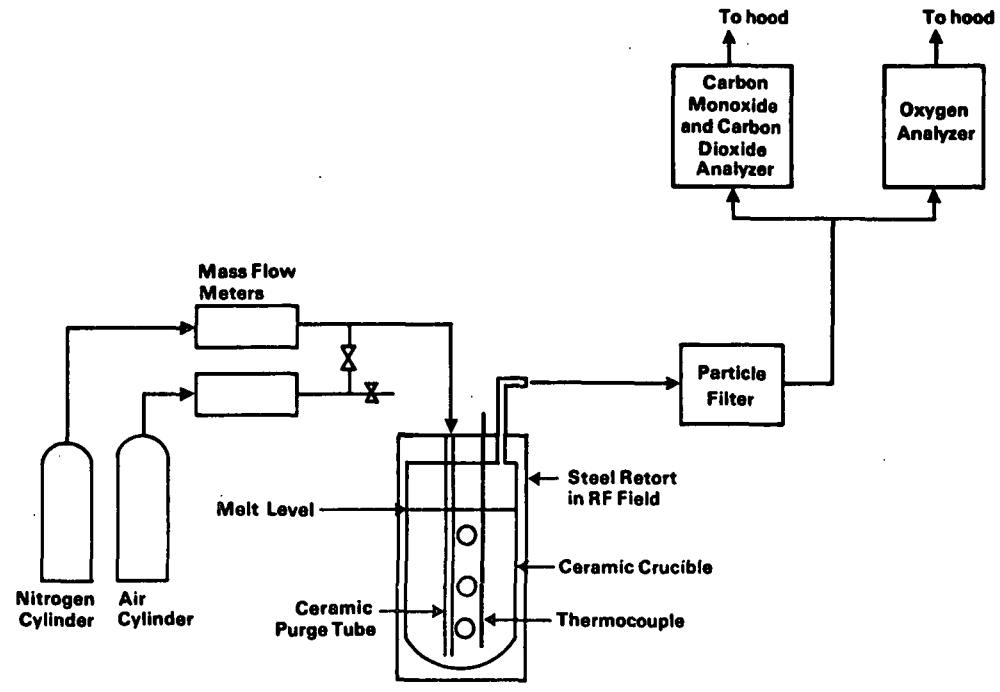

Figure 1. Experimental system with gases introduced below melt's surface.

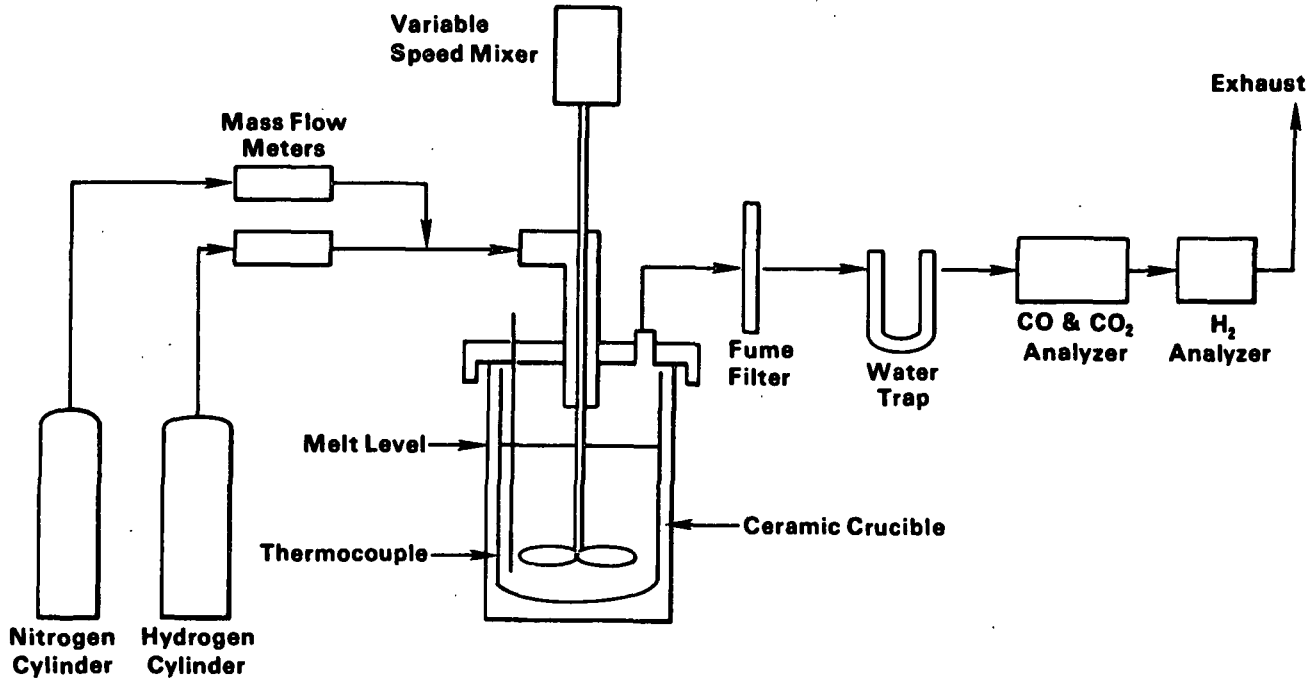

Figure 2. Experimental system with stirred melt and gases introduced above the melt.

before entering an H_2 analyzer. The signals from these analyzers, the mass flow, and the thermocouple in the melt were continuously monitored by a data acquisition system based on an Apple computer. Besides continuously monitoring these instruments, this system also calculated the amount of hydrogen consumed and the amounts of carbon monoxide and carbon dioxide generated.

These experimental systems allowed the effects of the temperature, melt composition, gas composition, and gas flow rate on the reactions to be studied. One deficiency of the system with the purge introduced below the melt's surface is that it does not allow the gas-melt interfacial area to be varied independently from the degree of melt mixing. For example, any change in the purge rate will affect both the interfacial surface area and the degree of mixing in the melt. Therefore, the effect of gas-melt interfacial surface area was studied with the H_2 introduced above the melt's surface.

EXPERIMENTAL RESULTS

REACTIONS IDENTIFIED

The reaction of H_2 with an alkali carbonate-sulfide-sulfate melt produces H_2O, CO, and CO_2. Figure 3 shows the rate of H_2 consumption and CO-CO_2 generation when H_2 is bubbled through a Na_2CO_3-Na_2SO_4-Na_2S melt. After 30 minutes of reaction, the melt in Fig. 3, was cooled under a N_2 purge and analyzed. This analysis and that of a melt from a similar experiment are contained in Table 1.

The standard deviations shown in Table 1 were obtained by dividing the samples into three sections and analyzing each section. Sulfur, hydrogen and oxygen balances were made by comparing the initial melt composition to the final

melt composition and the off-gas generated during the experiments. Generally good agreement was obtained with these balances. Analysis of the melt showed the presence of Na_2SO_3. However, the standard deviation is quite high for this analysis and since Na_2SO_3 is unstable at the temperature of these experiments it is doubtful that it is present.

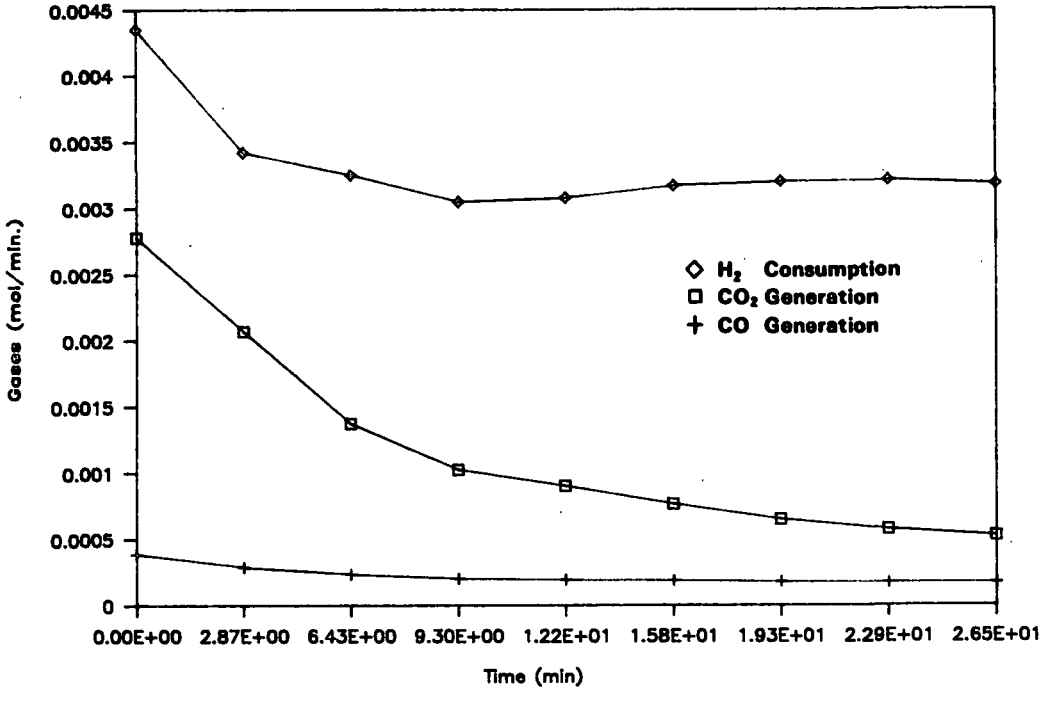

Figure 3. Hydrogen reduction of a sodium carbonate-sulfate-sulfide melt.

AUTOCATALYTIC NATURE OF REACTION

The rate of sulfate reduction with H_2 in a carbonate melt increases as the reaction proceeds. This is shown in Fig. 4, where the hydrogen consumption rate is shown vs. time. In addition to the increase in the rate of H_2 consumption with time, more H_2 is consumed in reducing Na_2SO_4 and less in reducing Na_2CO_3 as the reaction proceeds. Initially, 60% of the H_2 reacts with Na_2CO_3 to form NaOH, as evidenced by the quantities of CO_2 and CO being evolved from the

Table 1. Analysis of melt from hydrogen reduction.

Run 71

Initial Melt Composition:

Compound	Moles
Na_2S	0.024
Na_2SO_4	0.036
Na_2CO_3	0.77

Experimental Conditions:

Temperature: 955°C

Purge Rates N_2 = 1.0 L/min, H_2 = 0.1 L/min (STP)

Results after 30 min reaction

H_2 consumed = 0.097 mol
CO_2 generated = 0.0346 mol
CO generated = 0.0064 mol
H_2O generated = 0.07125 mole

Analyzed Melt Composition

Compound	Moles	SD
NaOH	0.0646	0.018
Na_2S	0.0395	0.006
Na_2SO_3	0.008	0.006
Na_2SO_4	0.013	
Na_2Sx	0.0	
Elemental S	0.0	

Balances

S: S in final melt/S in initial melt = 0.0605/0.06 = 1.0
H_2: (NaOH/2 + H_2O)/H_2 consumed = 0.104/0.097 =1.07
O_2: O_2 in exhaust gases/O_2 lost from melt:
= (H_2O/2 + CO_2 + CO/2)/(NaOH/4 + O_2 lost from sulfur species)
= 0.0734/0.07 = 1.05
C: C in off-gas/C lost from melt = (CO+CO_2)/(NaOH/2)
= 0.041/0.0323 = 1.27

Table 1 (Continued). Analysis of melt from hydrogen reduction.

Run 72

Initial Melt Composition:

Compound	Moles
Na_2S	0.024
Na_2SO_4	0.036
Na_2CO_3	0.77

Experimental Conditions:

Temperature: 1010°C
Purge Rates N_2 1.0 L/min, H_2 = 0.1 L/min (STP)

Results after 30 min reaction

H_2 consumed = 0.123 mole
CO_2 generated = 0.0456 mole
CO generated = 0.00611 mole
H_2O generated = 0.0703 mole

Analyzed Melt Composition

Compound	Moles	SD
NaOH	0.0772	0.015
Na_2S	0.0396	0.003
Na_2SO_3	0.0046	0.002
Na_2SO_4	0.0083	0.0005
Na_2Sx	0.0008	
Elemental S	0.0014	

Balances

S: S in final melt/S in initial melt = 0.055/0.06 = 0.91
H_2: (NaOH/2 + H_2O)/H_2 consumed = 0.109/0.123 = 0.89
O_2: O_2 in exhaust gases/O_2 lost from melt:
= (H_2)/2 + CO_2 + CO/2)/(NaOH/4 + O_2 lost from sulfur species)
= 0.084/0.072 = 1.16
C: C in off-gas/C lost from melt = (CO + CO_2)/(NaOH/2)
= 0.0517/0.0386 = 1.34

melt. After approximately 40 min, the combined CO and CO_2 evolution rates are only 10% of the H_2 consumption, indicating that 90% of the H_2 is consumed in reducing Na_2SO_4 to Na_2S.

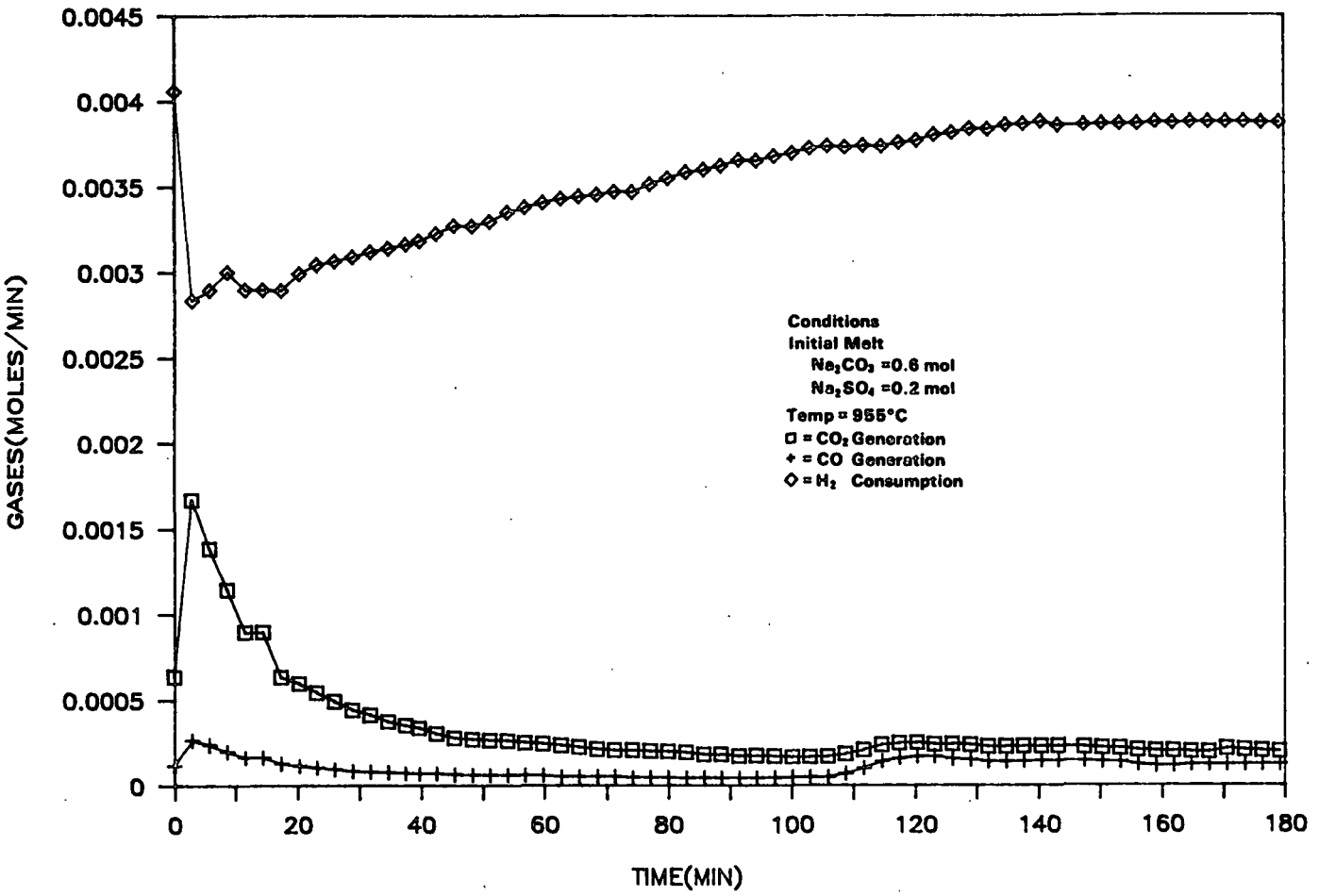

Figure 4. Hydrogen reduction of a sodium sulfate-carbonate melt.

The autocatalytic behavior observed for this reaction results from the increase in sulfide. This is shown in Fig. 5, where the hydrogen consumption rate is shown vs. time under conditions similar to those in Fig. 4, but with the melt initially containing equal moles of Na_2SO_4 and Na_2S. In this experiment the initial H_2 consumption rate is the same as the H_2 consumption rate in Fig. 4

after 2 hr of reaction, and no increase is observed in the consumption rate with time. The H_2 consumption rate in this figure remains constant until all the Na_2SO_4 is reduced, at which time the H_2 consumption rate rapidly decreases.

To determine if the autocatalytic nature H_2 consumption results from a reaction other than Na_2SO_4 reduction, a reduced melt was reoxidized, and again reduced with H_2. During this second reduction experiment little CO or CO_2 was evolved from the melt, but no difference was observed in the shape of the H_2 consumption curve. These experiments show that the autocatalytic nature of this reaction results from increasing sulfide levels and not from the formation of another species.

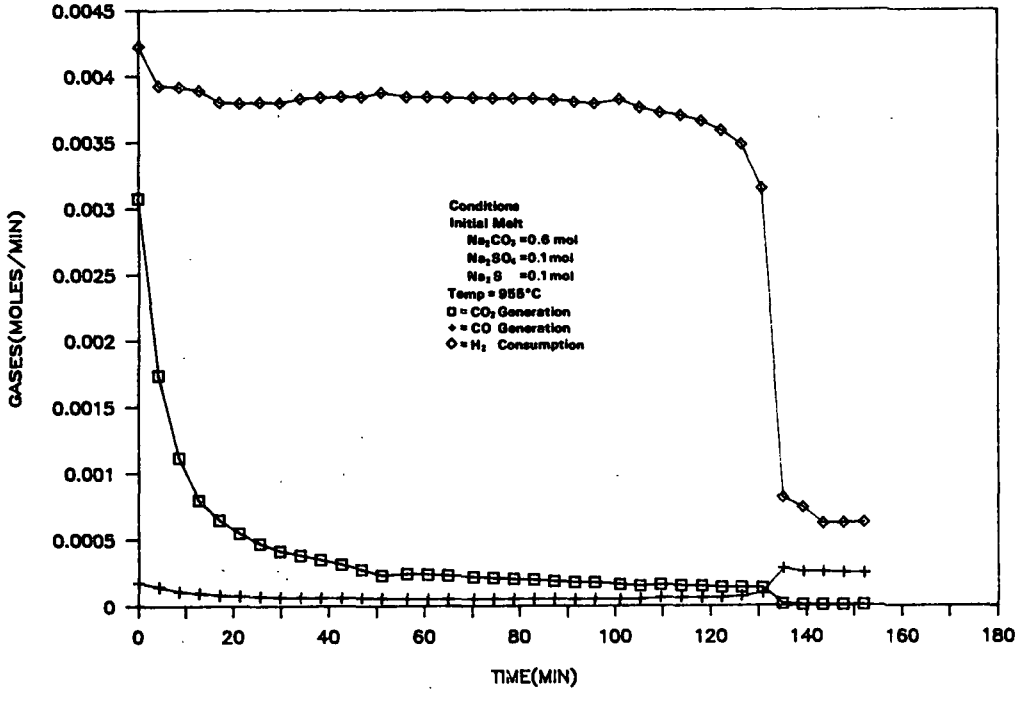

Figure 5. Effect of sulfide on hydrogen reduction of sodium sulfate.

At the temperature of the experiments shown in Fig. 4 and 5 (955°C), the rate of H_2 consumption is quite rapid. With no sulfide present, the initial rate of H_2 consumption is 0.003 mol/min and the reaction is consuming 66% of the H_2 supplied. After two hours of reaction with H_2, the rate is 0.004 mol/min and the reaction is consuming 90% of H_2 supplied. Since the initial H_2 consumption rate is high, the potential rate increase with increasing sulfide level is limited. To expand the potential for an increase in rate with an increase in sulfide content, this reaction was studied at 816 C. The rate of H_2 consumption vs. time at this temperature is shown in Fig. 6. Here, the initial rate is 0.0013 mol/min and the reaction is consuming 28% of the H_2 supplied. After 2 hr the rate is 0.0025 mol/min and the reaction is consuming 54% of the H_2 supplied. This demonstrates that the presence of sulfide in the melt can substantially increase the rate of sulfate reduction.

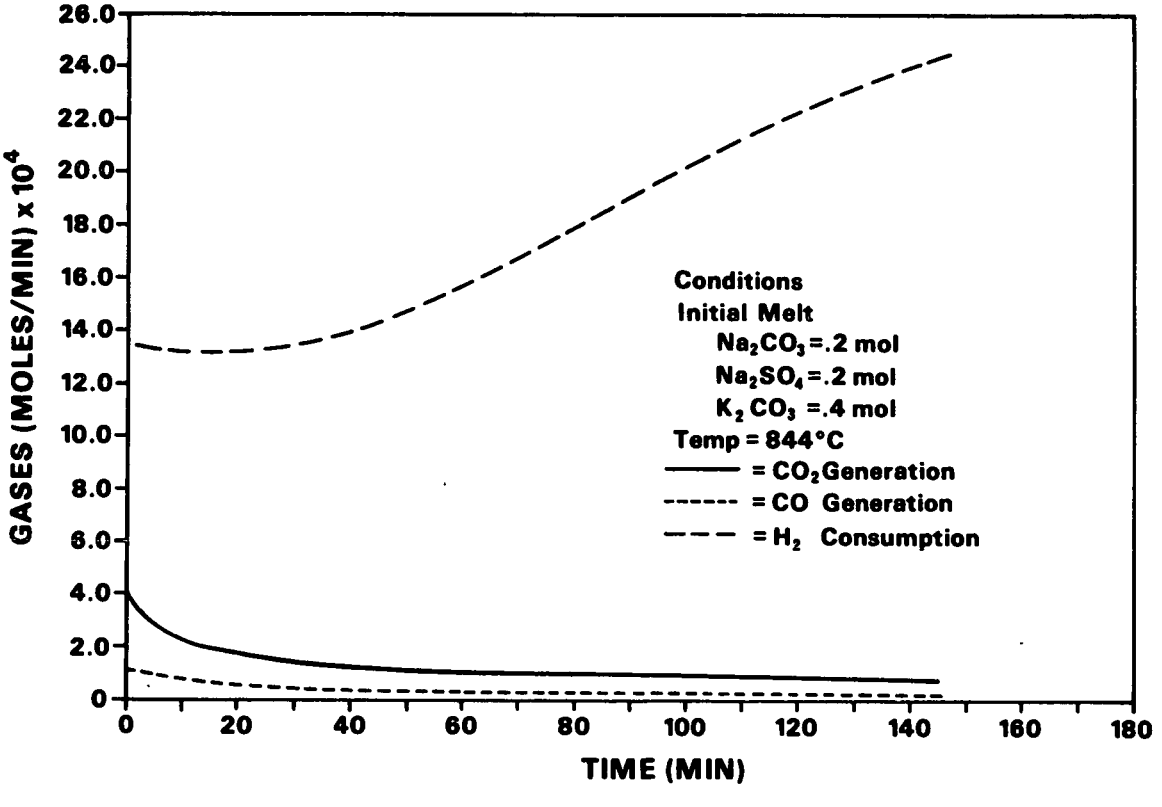

Figure 6. Autocatalytic nature of sulfate reduction with hydrogen.

EFFECT OF EXPERIMENTAL VARIABLES

Experimental results using both experimental systems (that with the H_2 introduced below the melt's surface and that with the H_2 introduced above a mixed melt) are described in this section. These variables include the hydrogen partial pressure, the melt composition, melt quantity, temperature and melt-gas interfacial area. Most of the experimental data were obtained with the H_2 introduced below the melt's surface and the effect of the experimental variables in this mode of gas-melt contact described first.

Purge Introduced below Melt's Surface

1) Sulfate Effect:

To determine the effect of sulfate concentration on the rate of H_2 consumption, the reaction was studied in melts containing Na_2CO_3, Na_2S and different levels of Na_2SO_4. The effect of Na_2SO_4 is shown in Table 2, where the reaction rate was measured with 0.4 mole of H_2 consumed.

Table 2. Effect of sulfate on the rate of hydrogen consumption.

Conditions

Temperature = 955°C

Purge Rates

N_2 = 1.0 L/min
H_2 = 0.1 L/min

Initial Melt Composition
Na_2CO_3 = 0.77 mol
Na_2S = 0.03 mol
Na_2SO_4 = variable

Initial Na_2SO_4, mol	H_2 Consumption Rate, mol/min
0.01	0.00285
0.03	0.00312
0.06	0.00319
0.09	0.0035
0.15	0.00346

As shown in this table, the level of sulfate has little if any effect on the rate of H_2 consumption. Although there is a slight increase in consumption rate with increasing sulfate, this increase is likely a result of increasing melt volume and melt-gas interfacial area.

2) Hydrogen Partial Pressure:

The effect of hydrogen's partial pressure on the hydrogen consumption rate was studied at 816 C. In this experiment, different H_2/N_2 mixtures were bubbled through the melt and the rate of H_2 consumption was measured at 0.01 mole of H_2 consumed. The effect of H_2 on the reaction rate was determined by assuming that the rate of H_2 consumption can be expressed by Eq. (5).

$$\text{Rate of } H_2 \text{ Consumption} = P_{H_2}{}^{n} \times f(\text{temperature and other composition effects}) \qquad (5)$$

To determine the order of reaction with respect to the partial pressure of H_2, the ln of the rate of H_2 consumption was plotted vs. the ln of the average H_2 partial pressure as shown in Fig. 7. The melts in these experiments initially contained 0.03 mole of both Na_2S and Na_2SO_4. Therefore, there was only a small increase in the Na_2S level and the rate of H_2 consumption remained nearly constant over the course of this experiment. The H_2 partial pressure in Fig. 7 is the average of the inlet and exhaust partial pressures. During these experiments approximately 20% of the H_2 supplied to the melt was consumed. Therefore, there was not a large difference between the inlet and exhaust partial pressures of H_2. From the slope of the curve in Fig. 7, the reaction order with respect to H_2 is 0.9. The rate of H_2 consumption is then approximately 1st order in H_2 partial pressure.

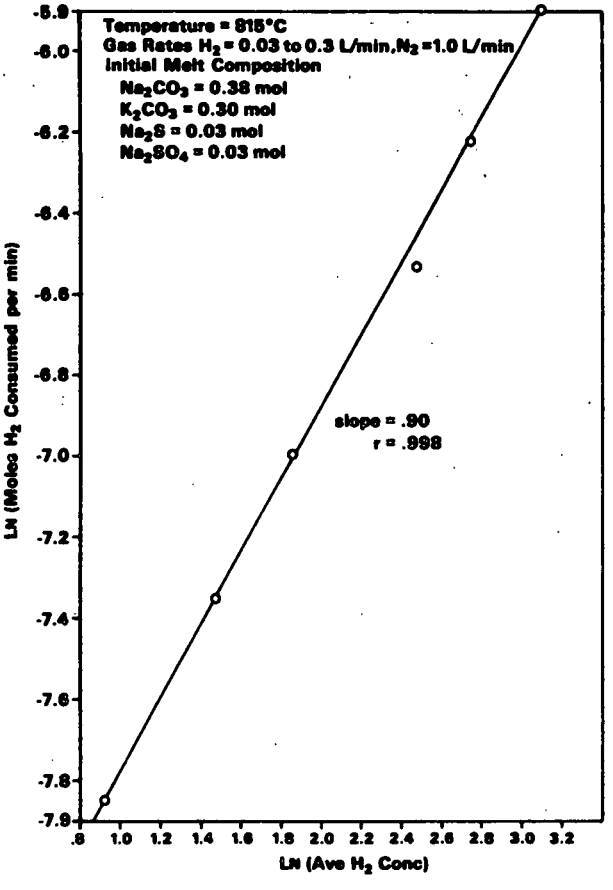

Figure 7. The effect of hydrogen on the rate of hydrogen consumption.

3) Temperature Effect

The effect of temperature on the rate of hydrogen consumption was studied by measuring the rate of H_2 consumption at different temperatures. It was assumed that the temperature effect could be described by the Arrhenius equation as shown in Eq. (6).

$$\text{rate} = f(\text{composition})e^{-\Delta E/RT} \qquad (6)$$

Here, f(composition) is the effect of composition, ΔE is the activation energy, R is the gas constant and T is the absolute temperature.

The activation energy was determined by plotting the ln (of the rate, corrected for difference in H_2 partial pressure) vs. 1/T, °K. as shown in Fig. 8. The reaction rates were measured at temperatures ranging from 770 to 1009°C in alkali carbonate-sulfate-sulfide melts with the melts containing identical levels of sulfide and sulfate. The cation in these melts was either Na or a Na-K mixture. As shown in Fig. 8, the replacement of Na with K had no effect on the reaction rate. Over the temperature range of this study, the consumption of H_2 has an Arrhenius type temperature dependence with an activation energy of approximately 23,000 cal/mol. This activation energy is in the range of kinetically controlled processes.

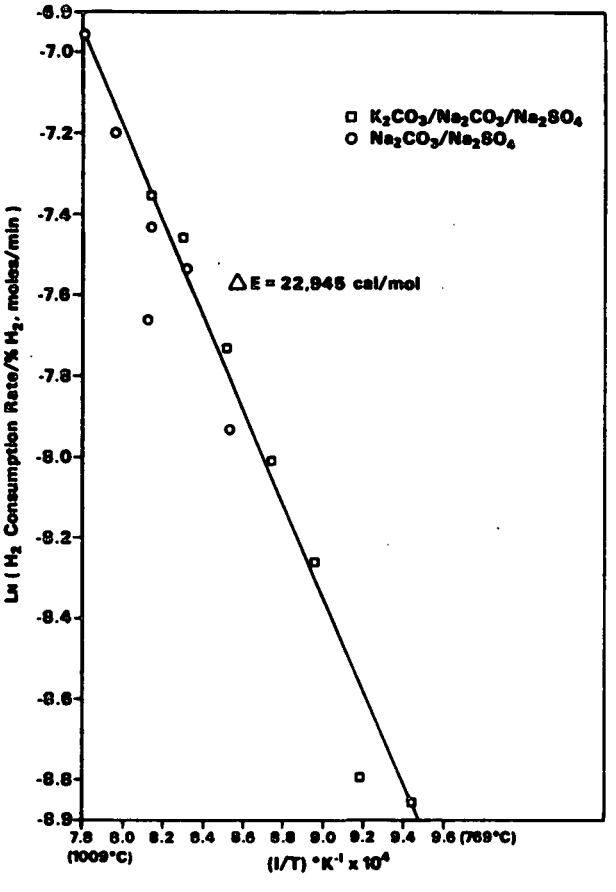

Figure 8. Effect of temperature on hydrogen consumption.

4) Melt Volume:

To determine the kinetic regime for this reaction, the effect of melt volume was investigated. If the reaction occurs through H_2 achieving equilibrium with the melt and then reacting with Na_2SO_4, the reaction rate should be directly proportional to the melt's volume. The effect of melt volume on the rate of H_2 consumption is shown in Table 3.

Table 3. Effect of melt volume.

Conditions:

Temperature 955°C

Initial Melt Composition, wt.%

Na_2CO_3 = 92.5
Na_2SO_4 = 4.8
Na_2S = 2.7

Gas Flow Rates, L/min

N_2 = 1.0
H_2 = 0.1

Melt Wt., g	Melt Volume, mL	H_2 Consumption Rate, moles/min
44.1	23.0	0.00233
66.1	34.5	0.00298
88.2	46.0	0.00314
110.3	57.5	0.00307

As shown in this table, the rate of H_2 consumption is nearly independent of the melt's volume. Although there is a slight increase in reaction rate from 23.0 to 57.5 mL, this is likely a result of the increase in gas-melt interfacial area. This indicates that the reaction is not occurring within the total melt.

STIRRED REACTOR

The stirred reactor, shown in Fig. 2, was used to determine the effects of area and melt mixing on the rate of the reactions. In this reactor the gases were introduced above the melt's surface and the melt was stirred using a variable speed stirrer. The design of this reactor allowed the degree of melt mixing and surface area to be varied independently.

Reactions with Stirred Reactor

Figure 9 shows the rate of CO_2 and CO generation and H_2 consumption vs. time with the H_2 and N_2 introduced above a stirred melt.

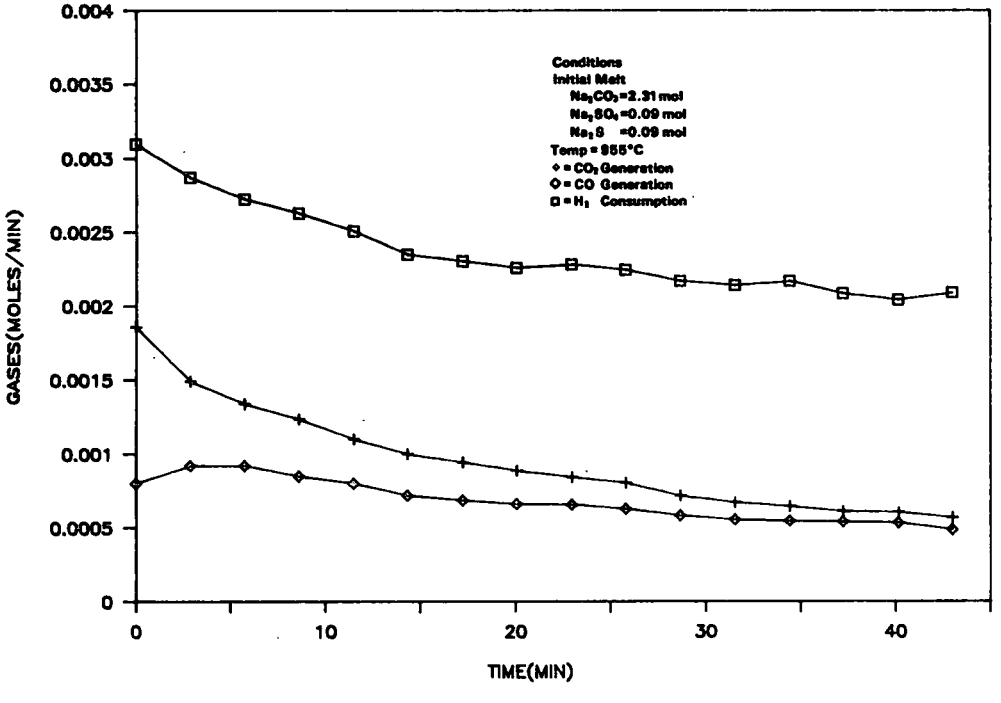

Figure 9. Hydrogen reaction with stirred melt.

As shown in this figure, H_2 reacts with Na_2SO_4 to form Na_2S and with Na_2CO_3 to form NaOH. The fraction of H_2 reacting with each of these species can be calculated from the H_2 consumption rate and the CO and CO_2 generation rates.

The percentage of the H_2 reacting with Na_2CO_3 to form NaOH gradually decreases from an initial level of 80 to 50% at 40 min. This behavior is similar to that observed with the H_2-N_2 purge introduced below the melt's surface. Initially there is a slight decrease in rate as the reaction of H_2 with Na_2CO_3 approaches equilibrium. Since the initial melt contained a relatively high sulfide to sulfate ratio, there was little increase in reaction rate due to increasing sulfide level.

Effect of Degree of Mixing on Reaction Rates

The effect of the degree of mixing on the reactions of H_2 was studied by varying the mixing rate once the reaction reached approximately steady state and monitoring changes in off-gas composition. The effect of the level of mixing on the off-gas composition is shown in Fig. 10. The mixing rate was changed over approximately 15 min. During this time, there was some change in the melt composition which affected these reactions. The duplicate points at a stirring rate of 0 RPM were taken before and after this period. From these duplicate points, it is evident that the effect of composition changes during this time period is small relative to the effect of stirring rate.

As shown in this figure, the degree of mixing has only a small effect on the reactions of H_2 with a Na_2CO_3-Na_2SO_4 melt. The CO generation rate remained constant and there were slight increases in the CO_2 generation rate and the H_2 consumption rate as mixing rate was increased. The increases in the H_2 consumption rate and the CO_2 generation rate were approximately equal. The increase in the H_2 consumption rate then resulted only from the reaction of H_2 with Na_2CO_3, producing CO-CO_2, and the reaction of H_2 with Na_2SO_4 remained constant.

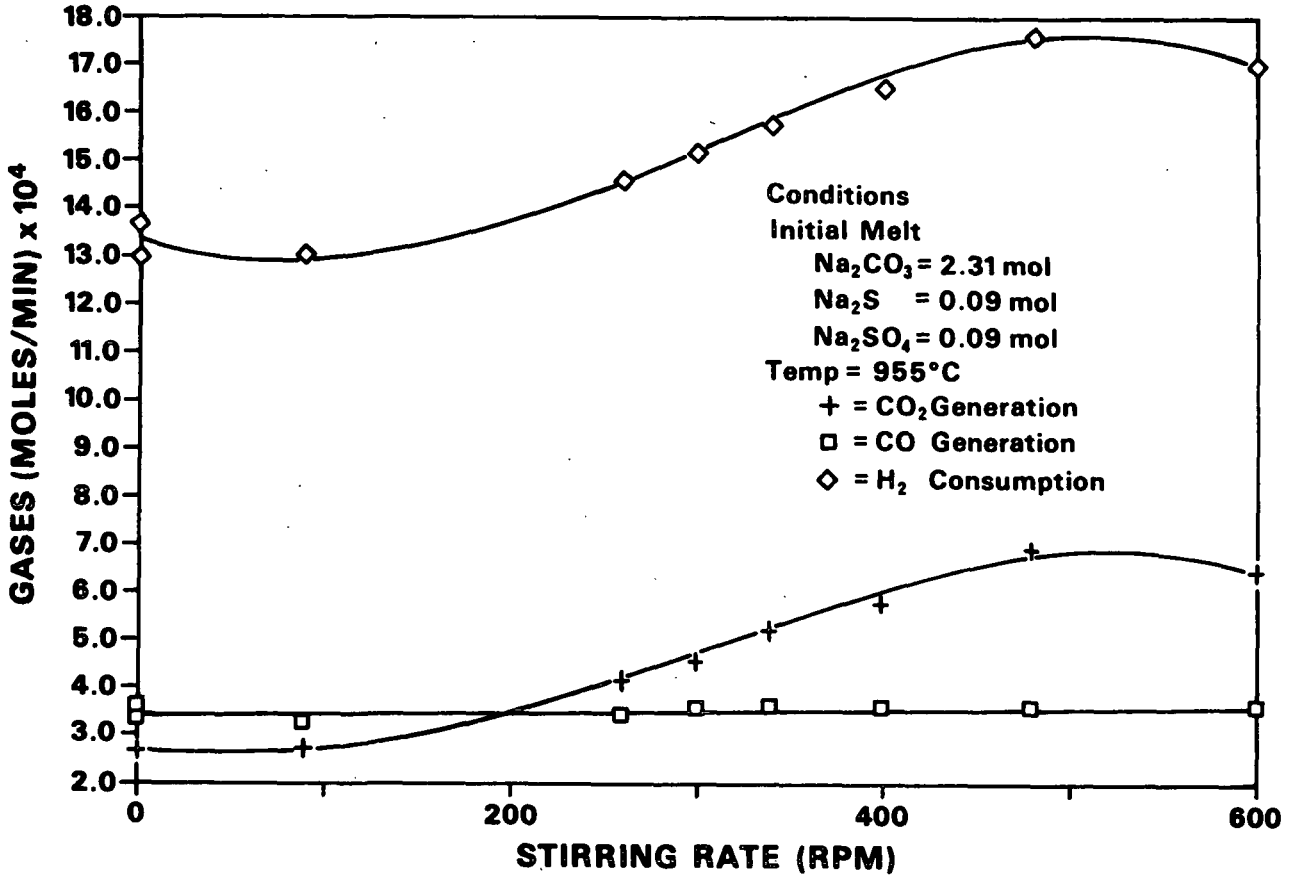

Figure 10. Effect of mixing on hydrogen reactions.

Effect of Surface Area

The effect of gas-melt interfacial area was studied by using two reactors of different cross-sectional areas. Both these reactors were charged with the same amount of melt, and the rate of H_2 consumption was measured with different levels of mixing. The reaction rates for these reactors are compared in Fig. 11.

Although the consumption of H_2 in both reactors increased as the stirring rate increased, the relative rates of H_2 consumption in the two reactors remained approximately constant. For the stirring rates in Fig. 11, the

average rate of H_2 consumption in reactor 1 was 80.6 ± 2.7% of the rate of H_2 consumption in reactor 2, while the surface area of reactor No. 1 was 75% of the surface area of reactor No. 2. This indicates that the rate of H_2 consumption is nearly proportional to the gas-melt interfacial area.

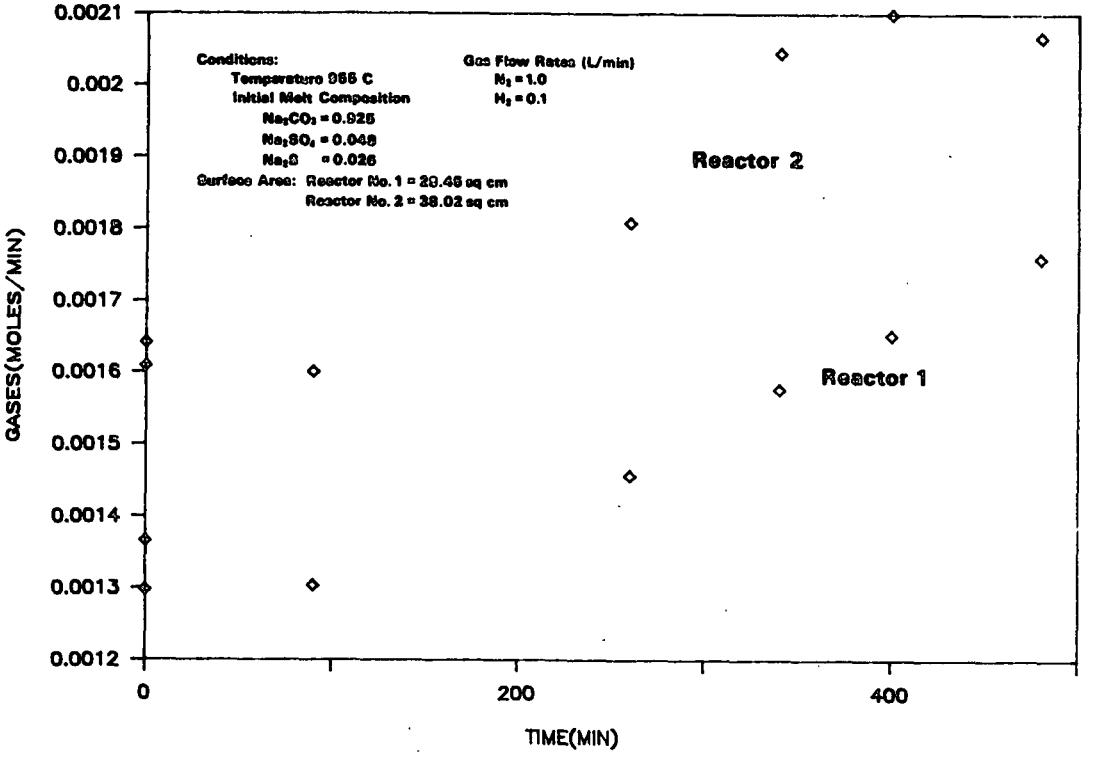

Figure 11. Effect of surface area on hydrogen reactions with melt.

REACTIONS WITH Na_2CO_3

When H_2 is added to an alkali-carbonate-sulfate melt it reacts with both the sulfate to form sulfide and with the carbonate to form hydroxide. The nature of the reaction with sulfate appears to be similar to that reported by Atomics International (1968). However, the reaction with carbonate was not reported by Atomics International. In the H_2 reduction experiments shown in Table 1, approximately 3% of the Na_2CO_3 was converted to NaOH.

Recently, Wensley, D. A. (1986) and Barna, J. L. and Rogan, J. B. (1986) have implicated NaOH as the active agent in composite tube corrosion. Since the conversion of Na_2CO_3 to NaOH was unexpected and may be important in composite tube corrosion, this reaction was examined in greater detail. Experiments were conducted to determine the effects of the experimental variables on the reaction between NaOH and Na_2CO_3.

Hydrogen Reduction of Sodium Carbonate

The reaction of H_2 with a pure Na_2CO_3 melt is shown in Fig. 12. The major gaseous product in this reaction is CO, and analysis of the melt found that it contained 3.8% NaOH. This verifies that the reaction of H_2 with Na_2CO_3 can be described by Eq. (8).

$$H_2 + Na_2CO_3 = 2NaOH + CO \qquad (8)$$

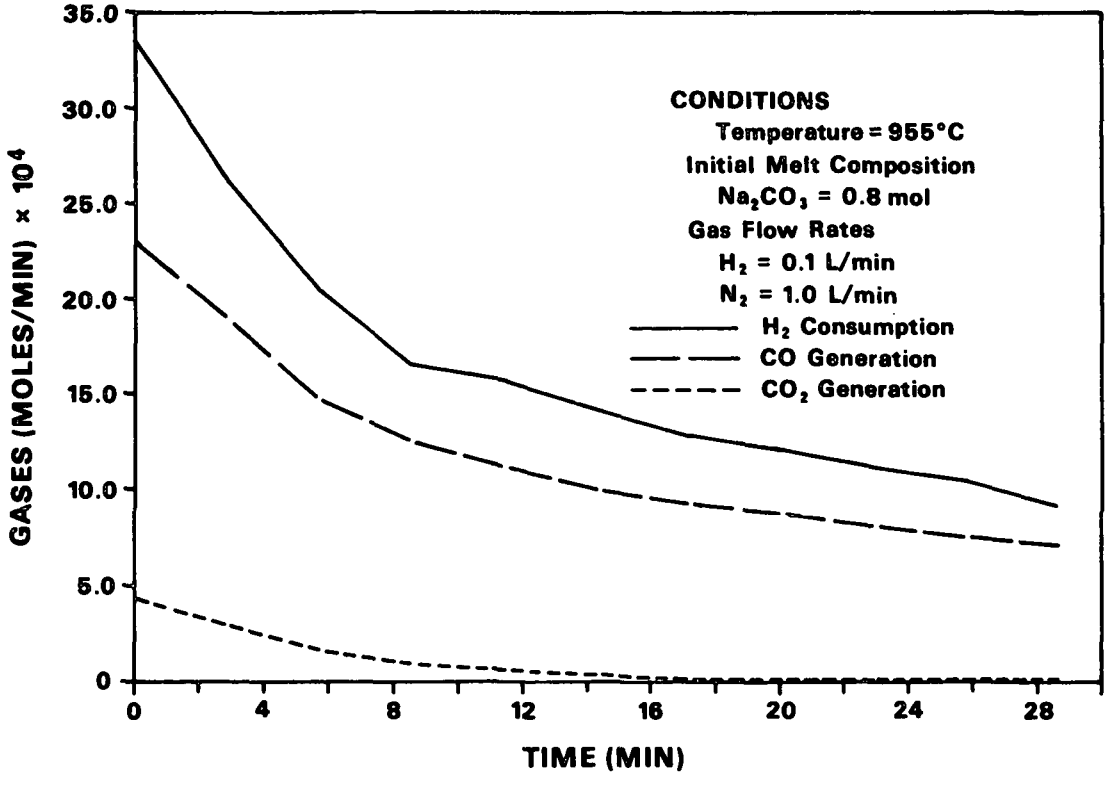

Figure 12. Hydrogen reduction of sodium carbonate.

The effects of the experimental variables on H_2 reduction of Na_2CO_3 were investigated and are described below.

1) Melt Volume

It was previously found that H_2 reduction of a Na_2CO_3-Na_2SO_4 melt did not occur through the melt as a whole but that the reaction occurred at the melt-gas interface. To determine if this was also the situation for H_2 reduction of Na_2CO_3, the effect of melt volume on the consumption of H_2 was determined and is shown in Table 4. Table 4 shows the effect of melt volume on the H_2 consumption rate.

Table 4. Effect of melt volume on H_2 reduction of Na_2CO_3.

Conditions

Temperature = 955°C

Gas Flow Rates:

H_2 = 0.1 L/min
N_2 = 1.0 L/min

Melt Volume, cc	H_2 Consumption Rate, mol/min
22.1	0.00106
33.1	0.00109
44.2	0.00118
55.3	0.00117

To ensure the composition of the melts in Table 4 were the same, the reaction rates were measured at the same relative level of H_2 consumed. As shown in this table, the melt volume had no effect on the rate of H_2 consumption. This demonstrates the reaction is rapid and the H_2 in the gas phase does not reach equilibrium with the melt.

2) Effect of Mixing and Surface Area

The effect of mixing and surface area on the reaction of H_2 with Na_2CO_3 were studied by varying the level of mixing using different gas flow rates. While the total gas flow rate was varied, the H_2-N_2 ratio in the inlet gas was simultaneously adjusted to maintain the same H_2 concentration. The effect of the gas flow rate on the rate of H_2 consumption is shown in Table 5. The H_2 concentration in Table 5 is the average of the H_2 in the inlet gas and exhaust gas.

Table 5. Effect of mixing on the reaction of H_2 with Na_2CO_3.

Conditions:

Temperature = 955°C

Inlet Gas Flow Rate, L/min	H_2 Concentration, %	H_2 Consumption Rate, mol/min
0.55	9.26	0.000689
1.1	8.26	0.00118
1.65	9.6	0.00126
2.2	9.5	0.00144

As shown in this table, the rate of H_2 consumption increases with an increase in gas flow rate. This increase results from both the increase in mixing and the increase in gas-melt surface area as the gas flow rate is increased. Experiments are currently being conducted with the stirred reactor to separate the effects of these variables.

DISCUSSION

REACTIONS IDENTIFIED

The off-gas composition from these experiments and the analysis of these melts indicate that several reactions are occurring in this system. The reactions indicated by these results are

1) Hydrogen Reduction of Sulfate, Eq. (9).

$$4H_2 + Na_2SO_4 = 4H_2O + Na_2S \quad (9)$$

This reaction is indicated from the formation of sulfide in the melt and the presence of H_2O in the off-gases.

2) Formation of Sodium Hydroxide, Eq. (10).

$$H_2 + Na_2CO_3 = 2NaOH + CO \quad (10)$$

This reaction is indicated by CO in the off-gas and the presence of NaOH in the melt.

3) Carbon Monoxide Reduction of Sulfate, Eq. (11).

$$4CO + Na_2SO_4 = 4CO_2 + Na_2S \quad (11)$$

The CO produced in Eq. (6) would react with Na_2SO_4 forming CO_2 and Na_2S. The presence of CO_2 in the off-gas indicates that this reaction is occurring.

4) Reactions of H_2O.

Since H_2O is present in the off-gas from these experiments, reactions of H_2O in either the gas or liquid phases are possible in this system. Two of the H_2O reactions are the reaction of H_2O with Na_2CO_3 to form NaOH, Eq. (12) and the reaction of $H_2O(v)$ with CO_2, Eq. (13).

$$H_2O + Na_2CO_3 = 2\ NaOH + CO_2 \quad (12)$$

$$H_2O + CO = H_2 + CO_2 \quad (13)$$

The reactions of H_2 with a Na_2CO_3-Na_2SO_4 melt were found to generate both Na_2S and NaOH and to be dependent on the gas-melt interfacial area. These reactions likely occur in the interfacial melt without H_2 achieving equilibrium with the melt. Initially both the reduction of Na_2CO_3 to form NaOH and the reduction of Na_2SO_4 to form Na_2S are very rapid with 80% of the H_2 supplied to the melt consumed. Once a few percent of NaOH is formed, the reduction of Na_2CO_3 becomes quite slow. The reduction of Na_2CO_3 with H_2 was studied with no CO_2 added to the supply gas. The addition of CO_2 would be expected to decrease the conversion of Na_2CO_3 to NaOH, and this is currently being studied.

Hydrogen reduction of Na_2SO_4 was found to be an autocatalytic reaction with the autocatalytic behavior due to the formation of Na_2S. It was found to be nearly first order in H_2 partial pressure and to have an activation energy of 23,000 cal/mol.

The results of this study help to determine the importance of the H_2 reactions within the kraft furnace. Two products of these reactions, Na_2S and NaOH, are important to the operation of the kraft furnace. The first, Na_2S, is the desired form of sulfur, and the second, NaOH, has been implicated in corrosion problems within the furnace. Through increased knowledge of how these compounds are formed, it may be possible to control their formation within the furnace.

FUTURE RESEARCH

Sodium and potassium chlorides may significantly affect the nature of the deposits in the kraft recovery. For example NaCl may react with SO_2 to form either $Na_2S_2O_7$ or Na_2SO_4 as shown in Eq. (14) and (15).

$$O_2 + 2NaCl + 2SO_2 + H_2O \longrightarrow Na_2S_2O_7 + 2NaCl \quad (14)$$

$$1/2\ O_2 + 2\ NaCl + SO_2 + H_2O \longrightarrow Na_2SO_4 + 2HCl \quad (15)$$

These reactions may form a corrosive environment within the deposits and/or may result in a harder, more difficult to remove deposit. In this research an experimental system will be developed to study these reactions under conditions similar to those existing within the recovery boiler. The results of this research will enable the significance of these reactions in the kraft furnace to be assessed.

LITERATURE CITED

Atomics International, North American Rockwell. Development of a molten carbonate process for removal of sulfur dioxide from power plant stack gaes. Report Number Two, Part 1, Oct. 27, 1968.

Barna, J. L.; Rogan, J. B. 1986 TAPPI Engineering Conference, 1986:377-85.

Borg, A.; Teder, A.; Warnqvist, B., Tappi 57(1):126-9(Jan., 1974).

Wensley, D. A. 1986 Kraft Recovery Operations Seminar, Orlando, FL, Feb., 1986:231-45.

The Institute of Paper Chemistry

John H Cameron

John H. Cameron
Research Associate
Recovery Group
Chemical Sciences Division

A Study of Factors Affecting the Carbon Monoxide/Carbon Dioxide Ratio in the Exhaust Gases of a Fixed-Bed Char Reactor

Gregg W. Aiken and John H. Cameron

The Institute of Paper Chemistry

Appleton, WI 54912

Prepared for presentation at AIChE Summer National Meeting/
August 16-19, 1987; Advances in Chemical Recovery Technology
Session No. 33

Date August 1987
"UNPUBLISHED"

A Study of Factors Affecting the Carbon Monoxide/Carbon Dioxide Ratio in the Exhaust Gases of a Fixed-Bed Char Reactor

Gregg W. Aiken and John H. Cameron
The Institute of Paper Chemistry
Appleton, WI 54912

ABSTRACT

A kraft recovery boiler has two basic functions. First of all, it burns the organic content of the black liquor to recover the fuel value of the liquor. Secondly, it functions as a chemical reactor where the sulfur species in the liquor sprayed into the boiler are reduced to the sulfide form by the time the inorganic salts flow out of the unit. The char bed of a kraft recovery boiler is where a significant portion of the organic content of the liquor combusts. It is also the place where most of the sulfate reduction to sulfide occurs. The inaccessibility, high temperature and corrosive environment of a char bed make it quite difficult to study in situ.

One pivotal unknown in char bed burning processes is the CO/CO_2 ratio in the char bed off gases. It is important due to its large effects on the energy released during char combustion and also on the air supply required by the bed. The objective of this study was to use a fixed-bed char reactor to determine the effects of supply gas composition and temperature on the CO/CO_2

ratio in the exhaust gases. For the sulfate reduction by carbon portion of this study, an empirical equation was developed relating the CO/CO_2 ratio to the C/O_2 ratio. For the char combustion portion of this study, the primary product of char burning for all experimental conditions investigated was CO. The amount of gas-phase oxidation of CO to CO_2 was in some cases quite significant.

INTRODUCTION

Black liquor burning in recovery boilers is a complex process due to several factors. First of all, the water content of the liquor is typically 30 to 35%. Secondly, the black liquor has a high inorganic salt content. Thirdly, the inorganic salts flowing out of the recovery boiler as smelt must be obtained in a useful form, since the pulping chemicals are regenerated from this smelt.

The char bed is in the hearth zone of a kraft recovery boiler. Char bed temperatures of up to 1422°K (2100°F) have been measured (1); its molten salt content makes the char bed corrosive; the region is also fairly inaccessible. Due to these adverse conditions, char bed sampling surveys reported in the literature are quite limited.

Black liquor combustion is the burning of black liquor to form the combustion gas and inorganic salt products. Three basic

stages are involved in black liquor combustion: drying, volatiles burning and char burning.

During the drying stage, the water content of the black liquor is evaporated. The volatiles burning stage involves two distinct processes: pyrolysis of the black liquor solids and gaseous combustion of the pyrolytic gases. Pyrolysis is the heat-induced transformation of organic compounds yielding combustible gases and a charous residue. The gaseous combustion of the volatile gases will occur simultaneously if an adequate oxygen supply is available. If sufficient oxygen is not available, volatile combustion can be far-removed from the location of pyrolysis. Char burning is the final stage in black liquor combustion. In this stage, the charous residue of pyrolysis is converted to the combustion gases and smelt, the remaining inorganic salts. Since pyrolysis limits oxygen availability, char burning will not commence until pyrolysis is nearly complete.

The simplified composition of the char residue and the smelt given in Table 1 was developed by Grace from an elemental and an inorganic salt analysis of kraft chars (2).

The fixed-carbon concentration of the char, the carbon not in the carbonate form, is the dominant charous species. Char reactions can broadly be defined as either being involved in the

reduction of sodium sulfate to sodium sulfide or involved in the gasification of the fixed-carbon content of the char.

Table 1. Simplified char and smelt compositions (moles/mole/Na_2).

	Char	Smelt
Na_2S	1/6	19/60
Na_2SO_4	1/6	1/60
Na_2CO_3	2/3	2/3
C	3	1/12
H	1	--

Grace suggested that the sulfate/sulfide cycle was the primary means of fixed-carbon combustion (3). Oxygen in the combustion air reacts with the sulfide content of the char to form sulfate. The sulfate is then reduced by carbon to form sulfide and CO and/or CO_2 as the product gas.

The rate of the sulfide oxidation reaction in an alkali carbonate melt was studied by Cameron in a smelt pool reactor (4). He found that the rate of the reaction was limited only by the rate of oxygen supply to the reactor. The rate of the sulfate reduction by carbon reaction, on the other hand, is a strong function of temperature in the temperature range of interest, the 1033 and 1367°K (1400 to 2000°F) range (5,6).

Cameron found that the kinetics of the sulfate reduction by carbon reaction were very dependent upon the carbon source (5). Kraft char, soda char and carbon rods were the carbon sources used. He reported that the CO/CO_2 ratio was at most 1:10. Thorman used activated carbon as the carbon source for his studies of the sulfate reduction by carbon reaction (6). He reported a CO/CO_2 reaction product ranging from 1:1 to 11:1.

The CO/CO_2 product of the sulfate reduction by carbon reaction has a significant effect on the endothermic nature of the reaction, as shown in Table 2.

Table 2. Heats of reaction of sulfate reduction by carbon.

	ΔHr:kJ/kg Na_2SO_4 (Btu/lb)	
	1000°K	1300°K
$Na_2SO_4 + 2\ C \longrightarrow Na_2S + 2\ CO_2$	1261 (542)	1177 (506)
$Na_2SO_4 + 4\ C \longrightarrow Na_2S + 4\ CO$	3667 (1576)	3539 (1521)

The reaction is approximately three times as endothermic with CO as the carbonaceous gas product than with CO_2 as the product.

The CO/CO_2 product also dictates the air supply required during burning. Twice as much oxygen is required if CO_2 is the combustion product, as opposed to CO.

One reaction that complicates CO/CO_2 determinations, for studies involving the oxidation of carbon-containing fuels, is the gas-phase oxidation of CO:

$$CO + 1/2\ O_2 \longrightarrow CO_2$$

It is difficult to determine whether CO_2 in the exhaust gases is a product of this gas-phase reaction or the product of a char pile reaction.

EXPERIMENTAL

A fixed-bed char reactor with an impingement geometry for the supply gases was chosen for this study because it is somewhat analogous to char bed conditions.

Apparatus

A schematic of the fixed-bed char reactor apparatus is shown in Figure 1.

The induction furnace temperature controller compares the temperature of the outside surface of the stainless steel retort, measured by the optical pyrometer, to the set point and adjusts the current supplied to the induction furnace coil accordingly.

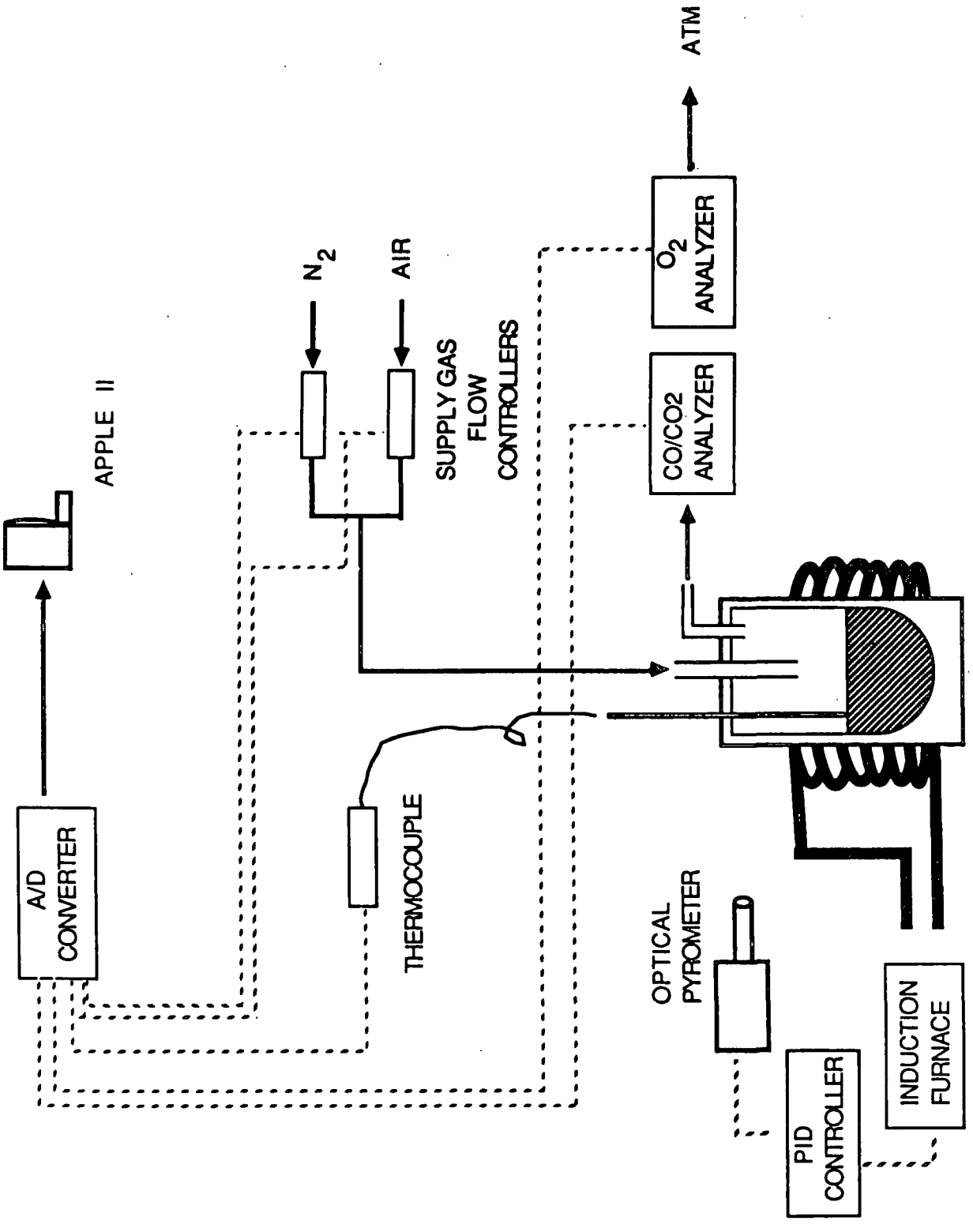

Figure 1. Experimental apparatus.

For most experiments, the stainless steel retort contained an alumina crucible in which the char was placed. For the pyrolysis portion of char preparation, a Hastelloy retort was used without the alumina crucible.

Ports in the reactor head allowed for the insertion of a supply gas tube for the insertion of thermocouples and for the removal of the gases to the gas analyzers.

The supply gas flow rates were monitored by mass flow meters and controlled with appropriate valves. Nitrogen and air were the gases metered into the reactor for most experiments. The supply gas tube was made of 3/16-inch stainless steel tubing and centered 20 mm above the char surface at the beginning of the experiment.

For the sulfate reduction experiments, one 3.2 mm, Type K thermocouple was inserted into the reactor and positioned in the char/salt mixture at the base of the crucible. For the air-termination experiments, two 1.6 mm, Type K thermocouples were inserted into the reactor. One was located at a radial position near the crucible wall. Both were positioned 0 to 2 mm above the char surface at the beginning of the experiment.

Exhaust gas composition was measured using a CO/CO_2 analyzer and an O_2 analyzer. These gas analyzers were calibrated

before each experiment with standard calibration gases and checked afterward to ensure the accuracy of the data.

Temperature measurements, supply gas flow rates and exhaust gas composition data were collected by a data acquisition system attached to an Apple II computer. The data were displayed on the screen and, at the end of an experiment, a hard-copy print-out was obtained. The data were also stored on a floppy disk and transferred to an IBM PC to manipulate the data using Lotus 123 software.

Char Preparation Procedure

A commercial 51% solids kraft hardwood liquor was dried in a vacuum oven at 423°K and 1.67 kPa for at least 16 hours with a slight nitrogen purge. The dry black liquor solids were then coarsely ground and placed in the induction furnace reactor, approximately 80 grams in a 1-liter Hastelloy reactor. The reactor temperature was then increased to 1223°K and held for 10 minutes at this temperature. A nitrogen purge rate of about 300 mL/min was maintained throughout the pyrolysis and cool-down stages. The char remaining was then ground until it could pass through a 10-mesh standard sieve, a 20.32 cm (eight-inch) screen with 2 mm openings.

The fixed-carbon concentration of the kraft char was determined by burning a 1 gram sample of the char in the induction furnace reactor and integrating the amount of CO and CO_2 in the exhaust gases. The carbon concentration measured was 23.4 ± 1.0%.

Procedure for Sulfate Reduction by Carbon Experiments

For the sulfate reduction experiments, kraft char, sodium carbonate and sodium sulfate were ground together so that the fixed-carbon:sulfate ratio was approximately 2:1, 4:1 and 6:1 for Experiments 1, 2, and 3, respectively. A sulfidity of 33% was maintained for all runs. Ten grams of sample were charged to the reactor for each experiment. A nitrogen flow rate of about 0.9 L/min was purged through the reactor for the duration of each experiment. The reactor temperature was rapidly raised to 1077°K (1478°F) and controlled at that target for most experiments. To determine the effect of temperature, experiments with target temperatures of 1033 and 1113°K (1400 and 1543°F) were also run.

The CO and CO_2 concentrations in the exhaust gases were monitored until either the concentrations were negligible or they had leveled at low values (less than 0.5% CO or CO_2).

Experimental Procedure for Air-Termination Experiments

For the air-termination experiments, about 40 mL (18 grams) of char were put in the alumina crucible of the induction furnace reactor. The reactor temperature was then raised to the target temperature for the experiment while nitrogen purged through the reactor at 40 mL/min. After the temperature stabilized, the char burning experiment was initiated when a total flow of about 1.00 L/min of nitrogen and air was introduced to the reactor. The supply gas air concentration was either 10, 20, or 50% air, depending on the particular experiment.

Air flow was stopped at several times during each run to determine whether the CO_2 was a product of a char pile reaction or due to the oxidation of CO. The off char pile CO/CO_2 was calculated after air flow termination when O_2 was no longer detected in the exhaust gases.

RESULTS AND DISCUSSION

Sulfate Reduction by Carbon Experiments

The sulfate reduction by carbon experiments were run to determine the effect of varying the initial fixed-carbon/sulfate ratio on the CO/CO_2 product of reaction. Three different initial 23 ratios were run. The effect of temperature was also investigated.

The results are shown in Figure 2, where the ln C/O_2 is plotted vs. the ln CO/CO_2. The C and O_2 concentrations were calculated by subtracting the amount of C and O_2 measured as CO and CO_2 in the exhaust gases from the initial amounts of C and O_2. A linear regression analysis of the data resulted in the following expression:

$$\ln CO/CO_2 = 0.976 \ln C/O_2 - 1.489$$

The r^2 calculated for the expression was 0.970.

The CO/CO_2 product was dependent upon whether carbon or oxygen was the excess reactant. The oxygen source was the oxygen of the sulfate and any oxygen sorbed by the fixed carbon.

In the excess carbon experiments - the 4:1 and 6:1 carbon: sulfate runs - the CO/CO_2 ratio was high, with the relative amount of CO increasing as oxygen was depleted. In the excess oxygen experiments - the 2:1 carbon:sulfate runs - the CO/CO_2 was low with the relative amount of CO_2 increasing as carbon was depleted.

Also included in Figure 2 are the results of the temperature dependence studies with measured temperatures of 1033, 1077, and 1113°K (1400, 1479, and 1543°F). Temperature does not have a significant effect on the CO/CO_2.

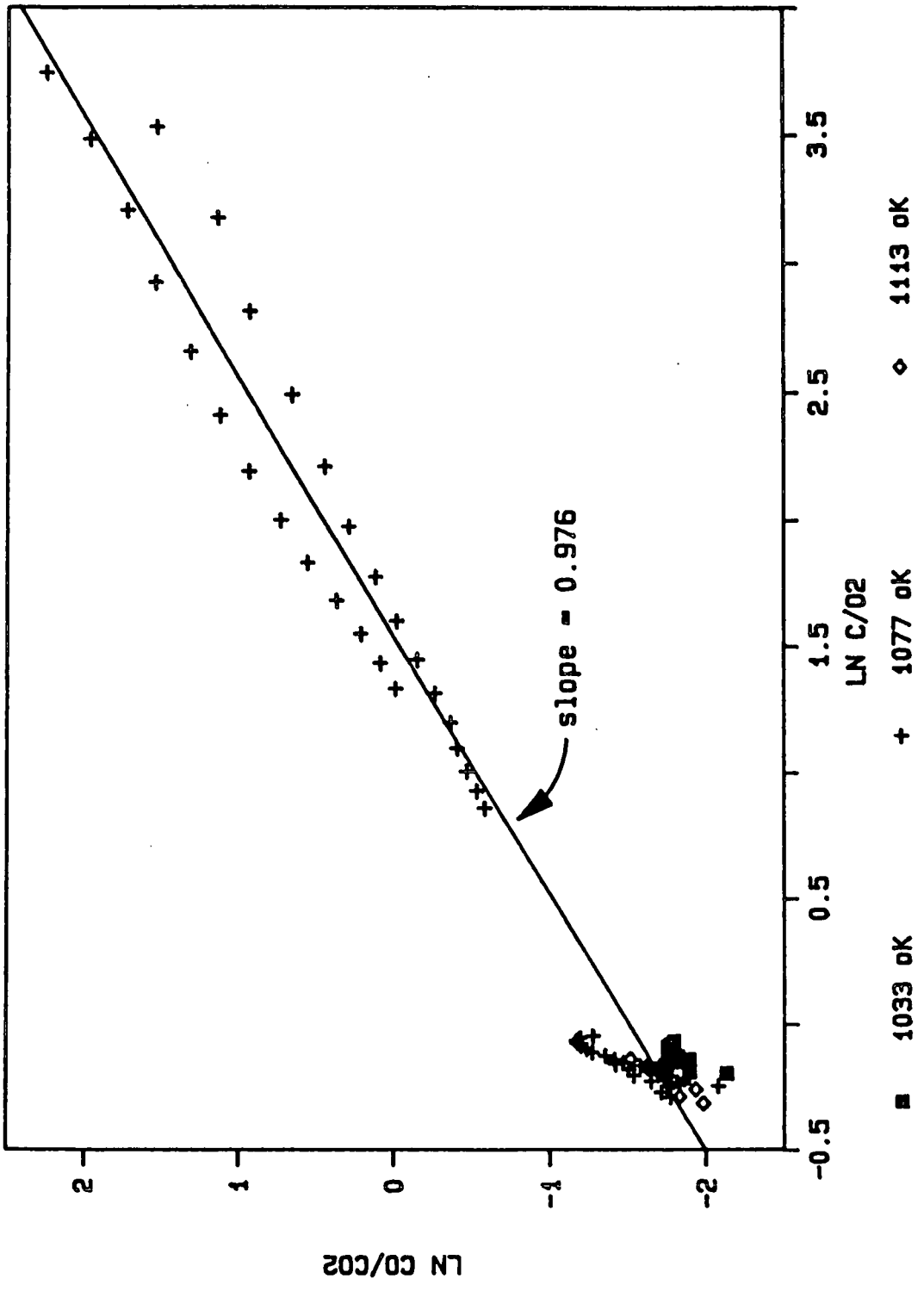

Figure 2. Sulfate reduction by carbon series experimental results - the effect of the C/O_2 of the char on the CO/CO_2 ratio.

Kraft-Char Combustion Experiments

The kraft char combustion experiments were run to determine the CO/CO_2 gaseous product of char burning when an air/nitrogen supply gas stream was impinged on the char surface. This differs from the previous sulfate reduction by carbon study because now oxygen in the supply gases is the oxygen source for fixed-carbon combustion rather than the oxygen in the sulfate. The rate of fixed-carbon burning was measured by integrating the amount of CO and CO_2 in the exhaust gases. Air flow was cut at several times during each experiment to determine whether the amount of gas phase oxidation was changing with time.

Figure 3 shows the effect of cutting the air flow at the 21.92-minute mark of Experiment 4, a 20% air experiment with a measured temperature of 1022°K (1380°F). Prior to the termination of air flow, the CO, CO_2 and O_2 concentrations are fairly constant at 2.1, 1.1, and 1.6%, respectively. After the air flow is cut, the CO_2 and O_2 concentrations drop rapidly. The CO concentration, on the other hand, increases before decreasing slowly with time. The drop in oxygen concentration would reduce the amount of gas-phase oxidation of CO to CO_2. The char pile reactions are initially less affected by the termination of oxygen in the supply gases than the gas-phase reaction. The termination of air flow therefore results in an increase in CO initially due to the

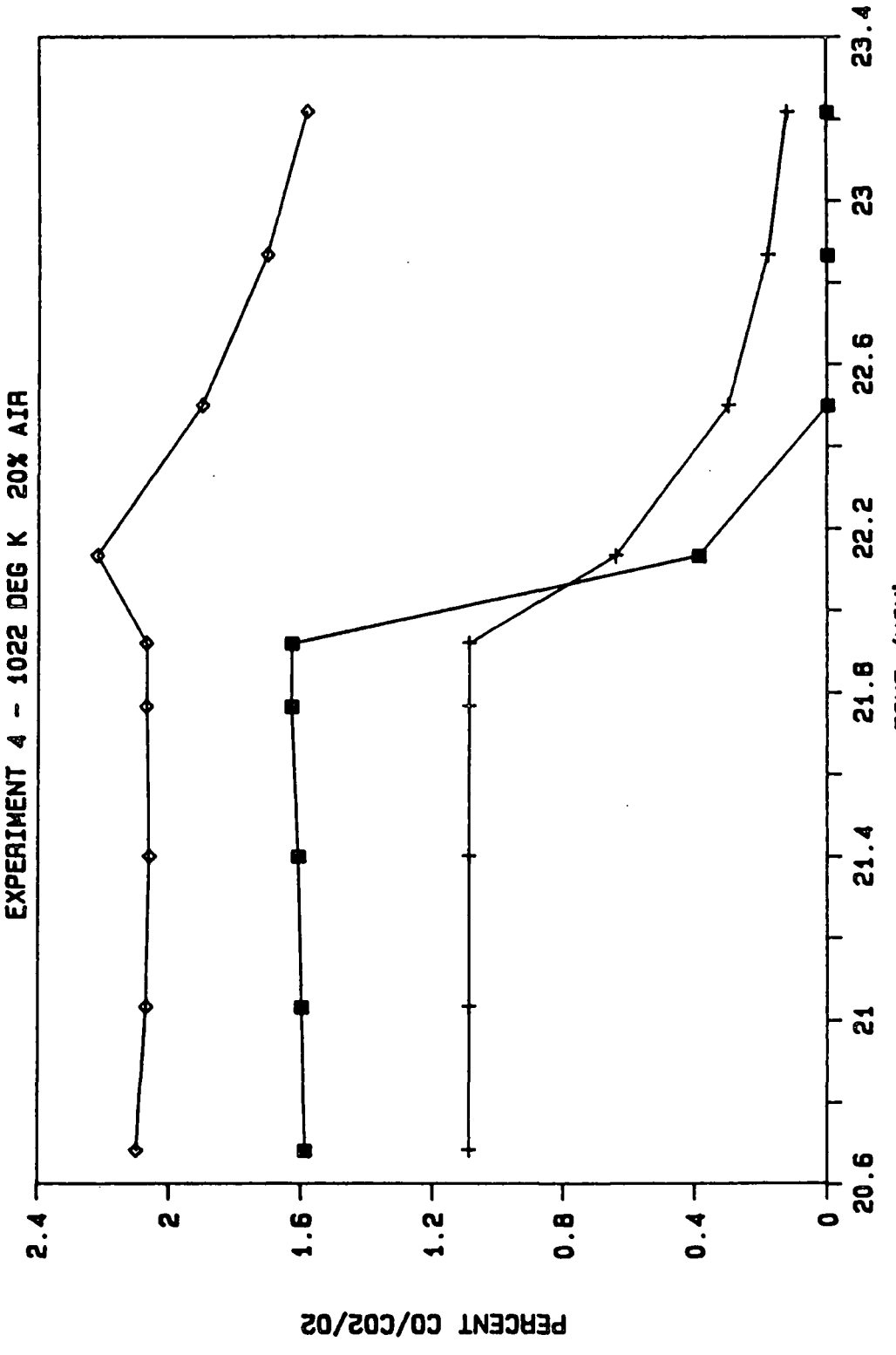

Figure 3. Kraft char combustion - Experiment 4: 1022°K, 20% air.

combined effect of the sudden drop in the CO-consuming, gas-phase oxidation reaction and the buffering capacity of the CO-generating char pile reactions. When these char pile reactions eventually respond to the lack of oxygen in the supply gases, the CO concentration gradually decreases with time.

The $CO/(CO + CO_2)$ measured at the 22.5-minute mark of Figure 3 should be representative of the gaseous product of the char pile reactions without the complications of the gas-phase oxidation of CO. The $CO/(CO + CO_2)$ just prior to the cutting of air flow was 0.66. The $CO/(CO + CO_2)$ measured at the 22.5-minute mark, after air flow termination, was 0.86.

Figure 4 is from Experiment 5, a 50% air run where the air flow was terminated at the 9.1-minute mark, when the measured temperature was 1083°K (1490°F). This cutting of air flow resulted in a dramatic flip-flop in CO and CO_2 concentrations. This is solid evidence supporting the hypothesis that the rapid drop in CO_2 upon air flow termination is due to the stopping of the gas-phase oxidation of CO. The $CO/(CO + CO_2)$ measured in the exhaust gases just prior to air flow termination was 0.06. The off char pile $CO/(CO + CO_2)$ calculated at the 9.8-minute mark was 0.82. The amount of gas-phase oxidation of CO to CO_2 was quite substantial in this instance.

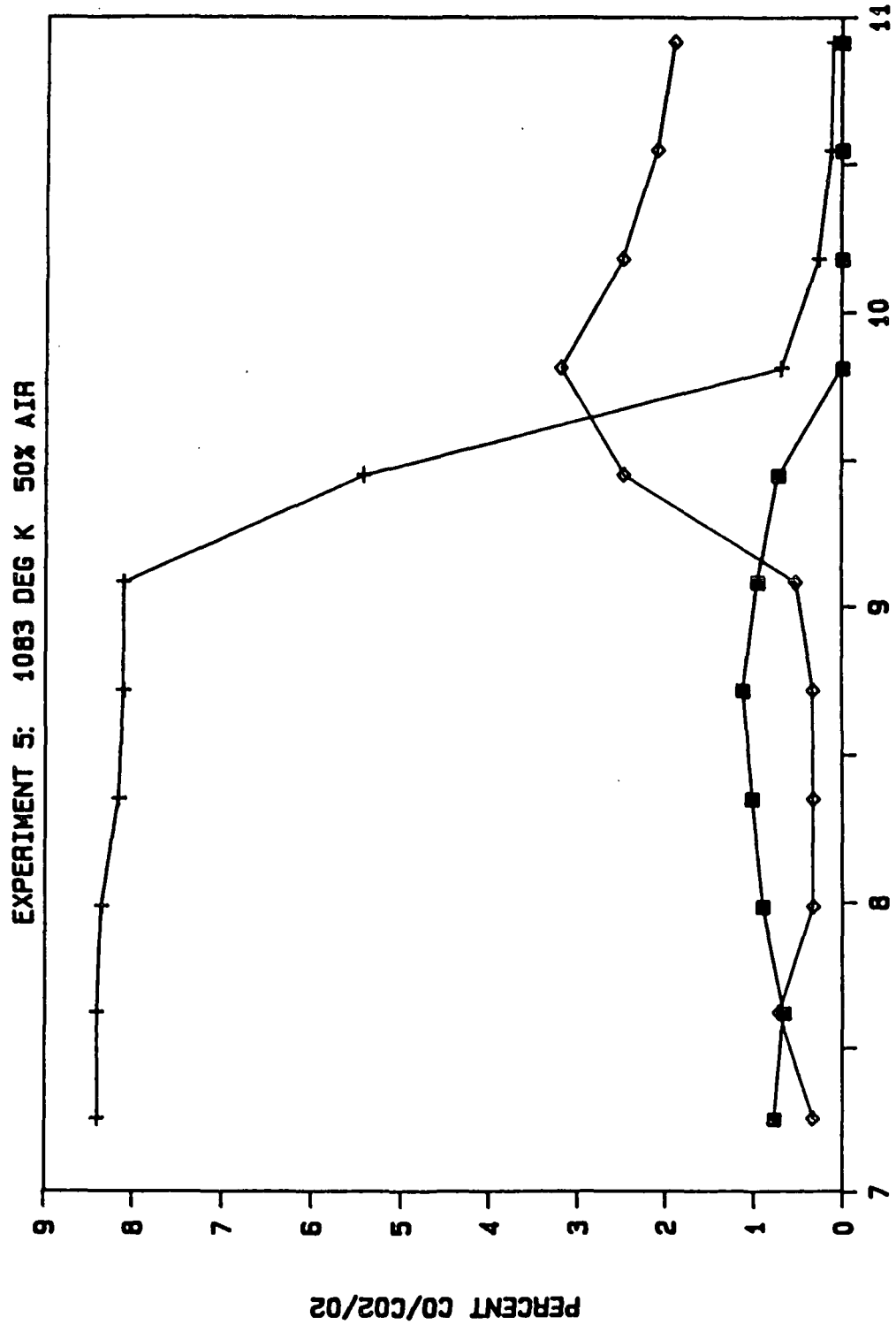

Figure 4. Kraft char combustion - Experiment 5: 1083°K, 50% air.

The results of all the kraft char combustion experiments are listed in Table 3. The $CO/(CO + CO_2)$ recorded just prior to cutting the air flow is given as "exhaust gas." The $CO/(CO + CO_2)$ recorded after air flow termination, when the measured O_2 concentration was less than 0.15%, is listed as "off char pile." The ranges listed for each "$CO/(CO + CO_2)$" and "Temperature" entry represent the range of values recorded for the four to six times during each experimental run that the air flow was cut.

Table 3. Kraft char combustion results.

Temperature, °K	Percent Air, %	$CO/(CO + CO_2)$ Exhaust Gas	$CO/(CO + CO_2)$ Off Char Pile
1004-1012	10	0.78-0.92	0.88-0.92
1019-1024	20	0.65-0.79	0.86-0.90
1049-1083	50	0.06-0.71	0.80-0.86
1089-1093	10	0.74-0.78	0.83-0.94
1076-1082	20	0.77-0.84	0.87-0.90
1097-1100	50	0.72-0.80	0.81-0.90
1098-1111	10	0.83-0.88	0.96
1108-1116	20	0.78-0.82	0.84-0.91
1141-1154	50	0.74-0.82	0.83-0.90

The data given in Table 3 suggest that

1. CO is the primary char pile combustion product for all experimental conditions studied.
2. There is no apparent temperature dependence, time dependence or supply gas oxygen concentration dependence to the off char pile $CO/(CO + CO_2)$ ratio.
3. The amount of gas-phase oxidation of CO to CO_2 can be quite significant.

The results of the sulfate reduction by carbon studies suggest that a high ratio of CO/CO_2 would result only if the C/O_2 ratio is high. Previous research indicated that sulfate reduction by carbon is probably one of the controlling reactions in kraft char burning via the sulfate/sulfide cycle (3). The kraft char combustion experiments, included in this current study, revealed that the $CO/(CO + CO_2)$ of the char pile reactions ranged from 0.80 to 0.95 for all conditions studied. This is equivalent to a CO/CO_2 ranging from 4/1 to 19/1. The C/O_2 required to attain this CO/CO_2 range for sulfate reduction with carbon, according to the empirical expression derived in the sulfate reduction portion of this investigation, is 18/1 to 91/1.

This C/O_2 ratio can be used to estimate the reduction ratio in the char, the ratio of sulfide to sulfide plus sulfate, assuming

1. All the oxygen present in the char is in the sulfate form.
2. The simplified molar composition of char given earlier in this report is accurate; thus the carbon to total sulfur ratio is 9:1.

The reduction ratio calculated ranges from 0.75 to 0.95. So even for relatively low temperature, high supply gas oxygen concentration conditions where low reduction ratios might be anticipated, high reduction ratios were calculated.

CONCLUSIONS

The CO/CO_2 product of sulfate reduction by kraft char carbon is a function of the fixed-carbon:oxygen ratio in the source material. The following empirical expression describes that relationship:

$$\ln CO/CO_2 = 0.976 * \ln C/O_2 - 1.489$$

The air-termination series of kraft char burning experiments revealed that the $CO/(CO + CO_2)$ ranged from 0.80 to 0.95 for all conditions studied.

These data were used to estimate reduction ratios ranging from 0.75 to 0.95 for the air-atmosphere, char burning experiments. These are much higher values than anticipated for the low temperature conditions employed.

ACKNOWLEDGMENT

Portions of this work were used by GWA as partial fulfillment of the requirements for the Ph.D. degree at The Institute of Paper Chemistry.

REFERENCES

1. Richardson, D. L., and Merriam, R. L. Study of cooling and smelt solidification in black liquor recovery boilers. Phase I Report, prepared for The American Paper Institute, New York, NY, Feb., 1977.

2. Grace, T. M., Cameron, J. H., and Clay, D. T. 1985 Intl. Chem. Recov. Conf. Proc., TAPPI Press, Atlanta, GA, 1985:371-9.

3. Grace, T. M., Cameron, J. H., and Clay, D. T. Tappi 69(10): 108-13(Oct., 1986).

4. Cameron, J. H., and Grace, T. M. Ind. Eng. Chem. Fundam. 22(4):486-94(Nov., 1983).

5. Cameron, J. H., and Grace, T. M. Ind. Eng. Chem. Fundam. 24(4):443-9(Nov., 1985).

6. Thorman, R. P., and Macur, T. S. 1985 Intl. Chem. Recov. Conf. Proc., TAPPI Press, Atlanta, GA, 1985:451-8.

7. Cameron, J. H., and Grace, T. M. Ind. Eng. Chem. Fundam. (in press).

Status Report

FUNDAMENTAL PROCESSES IN ALKALI RECOVERY FURNACES

Black Liquor Burning

INTRODUCTION

NEED

There are three main objectives of the kraft chemical recovery cycle. First, to recover and convert spent pulping chemicals into a usable form. Second, to produce the maximum amount of high level energy (steam and electricity) for use throughout the mill. Third, to safely and efficiently process black liquor at solids flow rates at or above equivalent pulping production rates.

The high capital intensity of chemical recovery boilers often results in mill production being limited by the recovery boiler, i.e., the recovery boiler is the pulp mill production bottleneck. Under these circumstances a compromise in objectives must be made. At the present time, situations such as the one above must be made with only limited supporting data on the burning characteristics of black liquor. In addition, extreme conditions such as severe blackouts and pluggage of convective gas passages shut the recovery boiler down regardless of other priorities. These emergency situations are influenced by black liquor burning characteristics.

The present task will document a wide range of black liquor burning phenomena. The resultant data base and supporting interpretation should contribute to improved recovery boiler firing practices.

OBJECTIVE

The objective of this task is to characterize black liquor burning. The burning phenomena will be observed and documented. A battery of analytical

and process related tests will be used and/or developed for this purpose. Finally, the black liquors studied will be a wide variety of mill liquors plus a few synthetic liquors.

BACKGROUND

The burning characteristics of black liquor at a particular mill can significantly vary. For example, the ratio of hardwood to softwood or the ratio of semichemical liquor to kraft liquor are two variables that reportedly influence burning. The most extensive published burning characteristic study to date has been by Hupa (1985). Hupa divides combustion into four stages: drying, combustion of volatiles, char burning, and inorganic reactions. He has shown that the required time for the first three stages varies significantly with initial droplet diameter, liquor type, and initial gas temperature. The char burning stage was the critical one for distinguishing "good" and "bad" burning liquors. Hupa found that increased liquor swelling during formation of volatiles tended to decrease char burning time, i.e., more "good" burning.

The PPPAC report on this task last fall included three technical papers covering specific aspects of black liquor burning. These papers were part of the Fundamental Studies portion of this task and covered the influence of initial moisture content on char reactivity, the influence of composition on swelling during pyrolysis, and sulfur release during burning. All three papers have been presented at professional society meetings. The latter two have been submitted for publication in scientific journals.

The report last fall also contained the preliminary draft of a technical report to the membership on the Survey Studies portion of this task. For

a number of reasons we decided to delay release of this work. One of the reasons was the inability to consistently explain all of the experimental data. Although some progress in this regard has been made, our understanding is still limited. The remainder of this report summarizes the progress in this area and presents additional work in the Fundamental Studies area.

FUNDAMENTAL STUDIES

Two additional papers have been prepared that relate to black liquor burning. These are attached to this report. The paper by Mark Robinson (a soon to be graduated Ph.D. student) covers black liquor drying in air at low temperatures. The paper by Katherine Crane Kulas presents an empirical equation which characterizes mass loss during the volatiles burning region. Both papers have been sent to the membership as part of the IPC Technical Paper Series. They were also presented at the August 1987 AIChE meeting in Minneapolis, MN.

Mark found that black liquor drops dried in air above their boiling points, undergo cycles of inflation and rupture. Contrary to expectation, however, an anticipated increase in drying rate did not occur which one would expect based on the surface area increase. Small vapor bubbles nucleate in the moist droplet shell, creating an internal heat transfer resistance. The increased resistance causes the surface temperature to rise, thereby reducing external heat transfer to the particle. Extension of his findings to higher temperatures implies that significant temperature gradients may exist in black liquor drops as they dry. If inflation and rupture do not mix the drop's contents sufficiently, rapid surface heating will result in simultaneous drying and pyrolysis.

Katherine found that the linear mass loss region during black liquor droplet burning mainly corresponds to the volatiles burning stage. The rate of mass loss during this stage was proportional to the initial surface area of the droplet. The gas phase oxygen content also positively influenced the mass loss rate but was of secondary influence. The developed empirical equation containing these influences correlated the data with an r^2 of 0.85. Her work suggests that the initial droplet surface area, that is, droplet size, is a key factor in determining the mass loss rate during the volatiles burning stage. It is important to recognize that this is the first published quantitative data on black liquor burning mass loss rates.

Quantifying the burning processes is a continuing area of work for Katherine. She initiated a Ph.D. thesis in December 1986 which has as its objective to determine a mathematical model for the overall combustion of a single droplet of kraft black liquor. The proposed model will combine heat transfer, kinetics, and mass transfer to describe the overall combustion of kraft black liquor. One of the critical measurements required to validate such a model is the particle surface temperature history. She has acquired and is implementing a two-color optical pyrometer to obtain such measurements.

A second Ph.D. thesis was initiated by Frank Harper in November 1986. Frank's objective is to develop a quantitative understanding of the factors that affect the release of sulfur to the gas phase during the burning of a black liquor droplet. He will identify during which burning stage or stages sulfur is released, quantify the importance of physical and compositional variables, and develop a model to predict the amount of sulfur released. He will include in his study both oxidizing and nonoxidizing atmospheres. The released gases, be

they TRS (total reduced sulfurs) or SO_2, will be converted to SO_2 and subsequently analyzed with an in-line analyzer. Frank has constructed an electrically heated wire mesh reactor to specifically measure the kinetic effects separate from the mass transfer effects.

SURVEY STUDIES

The fall 1986 PPPAC report described the objective and approach to this portion of the task. A summary of the chemical and combustion characteristics of the 54 tested samples was also presented. I will first summarize the main results from this report, then discuss our present efforts.

One of the main characterizing parameters used for comparing liquor performance differences is the pyrolysis swollen volume. The pyrolysis swollen volume is defined as the stable swollen volume per unit mass of initial black liquor solids reached when a droplet is exposed to a 500°C N_2 atmosphere. Pyrolysis swollen volume variations significantly related ($r^2 = 0.80$) to five measured parameters. There was a positive relationship with the mill-identified kappa number, the liquor chloride content, and the pyrolysis rate. The time from ignition to maximum volume and the contents of Na_2CO_3 and Na_2SO_4 in the liquor had a negative influence on the pyrolysis swollen volume. The most important findings are that pyrolysis swollen volume depends on many compositional variables, it cannot at the present time be explained a priori, and that there is still a significant amount of variation yet unexplained.

One possible source of variation was not accounting for the tall oil content of the liquors. The samples requested in all cases had been taken after the evaporator. The assumption was made that the tall oil content after skimming

would be very low and not contribute to the burning characteristics. Significant levels of tall oil could, however, influence swelling. Paul Miller, in his Ph.D. thesis work, found a significant decrease in pyrolysis swollen volume with only small amounts of extractives in the liquor.

To address the possible influence of tall oil on burning behavior six of the sample liquors were selected for tall oil analysis. Four liquors were high swellers while the others were medium and low swellers. The test data showed that reduction in pyrolysis swollen volume could be explained at the 90% confidence level with only the tall oil variation. Further, the increase in time from ignition to maximum volume (volatiles burning stage) could be explained at the 95% confidence level with only the tall oil variation. We conclude first that tall oil measurements are required even on previously skimmed liquors. Second, tall oil content variations undoubtly contributed significantly to the unexplained variation noted in last fall's PPPAC report. It is important to remember, however, that burning test parameters were included as significant variables. These could possibly account for some of the tall oil variation, since they too should be affected. The possiblity therefore may exist that by including tall oil content, more of the burning variations can be explained a priori via chemical composition than has been done to date.

Additional test work on the survey liquors and further analysis of the database is being delayed. A significant part of the controlled-liquor burning tests and the work with Dr. Mikko Hupa first need to be completed. Many of the discrepancies in the survey work will hopefully be understood when controlled liquors are tested. Both of these efforts will be discussed below.

CONTROLLED LIQUOR STUDIES

The need to conduct burning tests on liquors of known origin became obvious early in the project. We purposely delayed this portion of the study until after the survey liquors had been tested. With the survey liquor database now available we have identified the range of burning characteristics of commerically available liquors. Comparison of this commercial liquor burning database with those of controlled liquors will ensure that realistic phenomena are being studied.

The ten controlled kraft liquors described in the fall 1986 PPPAC have been concentrated and burned under both oxidizing and nonoxidizing conditions. The conditions under which these liquors were generated are given in Table 1. Chemical analyses of these samples have also been completed. Although some of the data have been graphed, an extensive analysis of the data is not yet complete. The observed trends to date appear to show less unexplained variation than the survey liquors. This was one of the main goals of controlled liquor testing. Analysis and interpretation of these data will be one of the main near-term efforts.

COOPERATIVE STUDIES

Dr. Mikko Hupa of the Chemical Engineering Department at Abo Akademi in Turku, Finland is conducting a comparable liquor burning project. The Finnish government and industrial companies sponsor his efforts. We have agreed to cooperate in our efforts to understand more fully the burning processes. The letter agreement between IPC and Abo Akademi was part of the 1986 fall PPPAC report.

Table 1. IPC controlled pulping conditions to generate synthetic black liquors.

Constant Cooking Conditions

16% Effective alkali

25% Sulfidity

12.5% Na_2SO_4 based on Na_2S (as Na_2O)

25% Na_2CO_3 based on NaOH (as Na_2O)

4:1 Liquor:Wood ratio

90 Minutes at 173°C (343°F)

Maximum cooking temperature 173°C (343°F)

Ten Liquors Produced

Wood	H-Factor	Kappa Number
Pine	5500	15.0
Pine	1600	32.2
Pine	690	72.7
Birch	1600	16.6
Birch	971	39.0
Birch	160	79.7
P/B 50/50	4000	17.1
P/B 50/50	947	43.5
P/B 50/50	303	96.5
P/B 50/50	971	41.2

Dr. Hupa visited IPC in January 1987. At that time we exchanged liquor samples. IPC received 8 Finnish liquors and Abo Akademi received 9 U.S. liquors. A work plan was developed for our cooperative efforts.

Our initial efforts focus on comparison of burning characteristics of the two experimental systems. These studies use the above mentioned mill liquors. If possible, the data will be evaluated to see if liquor comparisons can be made. The latter may prove infeasible, given the limited number of liquors and the fact that the chemical composition of the Finnish liquors has not and probably will not be characterized.

Initial burning tests have been completed on the respective samples by both research groups. Ten to twelve replicates of each liquor sample burn have been done to ensure a good estimate of average characteristics of each liquor.

I visited Abo Akademi during August 1987 to discuss the results of our tests and to receive their test results. Although both groups had completed the data generation, neither had had sufficient time to analyze their meaning. Comparing liquor test results between the two systems did not show consistently logical trends. The quick analysis approach was not sufficient. Further separate study of the data will be required.

We extensively reviewed the procedures of both groups. There are apparent differences in burning techniques as well as in sample preparation. There are a number of follow-up items (both calculations and testing) that both groups need to do to resolve these issues. Our intent is to have the required information to complete the analysis of the two combustion systems by January 1988. Dr. Hupa plans to be in the U.S. during this month. Our intent is to ultimately publish a joint paper covering this work.

Another area of cooperation is controlled liquor burning. Dr. Raimo Alen of the Technical Research Centre of Finland, Helsinki, has prepared

approximatley 25 liquor samples for Dr. Hupa. These samples were obtained by both controlled kraft and soda pulping of both pine and birch chips. During the four cooks samples were extracted at selected times. The liquors include not only the cooking liquors but also selected main components of the liquor, separated by Dr. Alen. These liquors will be burned in the Abo Akademi furnace. It will be informative to compare our controlled liquor tests with theirs. We also hope to do this at our January 1988 meeting.

FUTURE DIRECTION

The major tasks in the near term are to analyze the IPC controlled liquor burns and the IPC/Abo Akademi liquor burns. Once this has been completed another look at the IPC survey liquor work would be useful.

In the longer range the fundamental studies of Katherine Crane Kulas, Frank Harper, and Pat Medvecz will expand our understanding of specific aspects of the burning process.

Comparison of the Finnish controlled liquor study with ours should also help explain why variations occur in liquor burning. Placed together, the information developed under this project makes a substantial contribution toward the development of a comprehensive liquor burning databases.

THE INSTITUTE OF PAPER CHEMISTRY

David T. Clay
Associate Professor/Research Associate
Recovery Group
Chemical Sciences Division

An Empirical Equation of the Volatilization of Kraft Black Liquor Droplets During Burning

Katherine A. Crane and David T. Clay

ABSTRACT

Kraft black liquor burning phenomena were studied in a convective single particle reactor. The droplets were suspended from a microbalance in a downward flowing hot gas stream. The linear portion of the mass loss history during the burn mainly corresponded to the volatiles burning stage. An empirical rate equation was determined statistically from the normalized slope of this linear region. Included in the equation were initial droplet size and gas phase oxygen concentration. The mass loss rate was closely proportional to the initial droplet surface area. Gas temperature was not found to be statistically significant.

INTRODUCTION

Chemical recovery is an integral part of the kraft pulping process because it regenerates the cooking chemicals. Pulping produces both pulp and a weak black liquor containing organics and inorganics. The pulp continues on to the papermaking process. The weak black liquor is concentrated into strong black liquor which is then combusted in the recovery boiler. The organic

fraction is oxidized for steam generation which is used millwide. The inorganic fraction is reduced to recover Na_2S, a pulping chemical, and Na_2CO_3, in the form of smelt. The smelt dissolves in an aqueous stream to form green liquor which is then causticized; the conversion of Na_2CO_3 into NaOH. The regenerated cooking chemicals, Na_2S and NaOH, then return to the digester for more pulping.

Very little quantitative information is known concerning the fate of black liquor droplets in the recovery boiler. The stages that the droplet experiences were identified by Hupa (1985) and Grace (1985). The three main burning stages are drying, volatiles burning, and char burning.

The drying stage is evaporation of water in the black liquor as a result of heat transferred to the droplet. The volatiles burning stage consists of three major processes: volatiles evolution, volatiles combustion, and the formation of char in an inorganic matrix. A great deal of swelling and bursting occurs during the drying stage, with sustained swelling only during the volatiles burning stage. The char is then consumed during the char burning stage. When the carbon content is sufficiently low the char structure collapses, and the inorganics, in the form of molten smelt, coalesce. The stages overlap slightly, especially in the larger droplets. For this work, visual events were used to

define the beginning and the end of each stage. These techniques will be discussed later.

Single droplet studies done with black liquor at The Institute of Paper Chemistry (IPC) (Miller 1986, Moreland 1985, and Robinson 1986) suggested several variables important to black liquor combustion. These were droplet temperature, droplet initial size, gas temperature, and gas composition. Research done on single droplets (Hupa 1985) combusted each droplet in a radiantly heated stagnant air environment and measured the times for each stage. Hupa's times will be compared with those from this investigation.

The present investigation had two goals. The first was to determine an empirical equation for the linear region of the droplet mass loss history and the second was to define what occurred in this region.

EXPERIMENTAL

The apparatus used for this work can be seen in Figure 1. It is a convective downflow single particle reactor. The gas is heated in an electrical furnace, travels through an insulated pipe, passes through a flow straightener, and enters the single particle reaction area. The flow rate of the gas is adjustable.

There is a damper to divert the gas flow while the sample is placed in the reactor. The sample is suspended on a wire connected to the electronic microbalance. The microbalance and the gas analyzers are connected to an Apple II+ microcomputer with an analog/digital interface. Heat transfer to the sample is primarily through convection, with some radiative heat transmitted from the surrounding walls. A 16 mm motion picture is taken of each burn through the optical trench. The times for each stage of the burn are obtained from the movies.

(Figure 1 here)

At the start of each burn the kraft black liquor is weighed and wrapped around the wire. The black liquor, from Thilmany Pulp and Paper Co., Kaukauna, WI, had been concentrated to 71.8% solids under vacuum. The black liquor is shaped into an approximate sphere. A wire coil and screen, the basket, surrounds the sample to provide constant drag throughout the burning, as the drop does not swell uniformly. Once the drop has been formed, the reactor is opened by lowering the lower section, the damper is closed to divert the hot gas, the sample in the basket is hooked onto the microbalance wire, the reactor is closed, the 16 mm motion picture camera is started, and the computer is started. The computer causes the damper to open, allowing the hot gas to reach the sample at a defined time zero. The camera runs for up

to 16 seconds, while the data acquisition program runs for 20 seconds.

The experimental design was based upon the central-composite-rotatable three-variable statistical design. This design examined the effects of reactor temperature, T, (660 to 860°C), initial mass of the droplet, M_i, (4 to 41 mg), and oxygen content in the gas stream, O_2, (0 to 21%), on the rate of volatiles evolution. Replications were done at the center point (10.5% O_2, 763°C, 22 mg) to determine the lack of fit and the reproducibility of the data. The design assumes that the lack of fit is constant for all conditions.

RESULTS

Droplet Mass Loss

The plot of the mass of the droplet over time for a typical burn can be seen in Figure 2. The initial rise in the curve is due to the microbalance adjustment to the drag force on the basket and wire assembly. Mass loss data does not reflect the burning process for approximately the first second. The slope of the linear region is the rate of mass loss during the volatiles burning stage, the primary rate measurement used in this work.

(Figure 2 here)

For the purpose of data consistency the following stage transition points were defined. Drying started the moment the droplet was exposed to the hot gases, and ended at the first visual evidence of ignition. The droplet was assumed to be 100% solids at ignition, although residual moisture contents of 5 to 10% are possible. Volatiles burning started at ignition and ended at the point of maximum swollen volume. Maximum volume usually occurred near the end of the linear mass loss. Char burning started at maximum volume and ended at the final collapse of the char structure into a smelt bead.

The points of ignition, maximum volume, and smelt coalescence are noted on the plot. The droplet ignited initially near the wire under all the tests except those at 0% O_2. At 0% O_2 the particle was under pyrolysis conditions and did not ignite or combust. After the volatiles burning stage, mass is continuously lost as carbon is consumed. The weight regain noted prior to the smelt bead formation is due to reoxidation of Na_2S formed during the burning processes (Grace, 1985).

Linear Mass Loss Rate

The slope of the linear region SL, during the volatiles burning stage, was found by linear regression through the included points. It was normalized with respect to initial liquor solids.

$$NSL = SL / (SOL * M_i) \quad (1)$$

where SOL is the initial solids fraction and

M_i is the initial droplet mass in mg.

This was done so that particles of different size could be directly compared. The diameter, D_i, was calculated from the density of black liquor and the mass of the droplet. The droplet was assumed to be a perfect sphere. When data are plotted for a single oxygen content, as in Figure 3 at 10.5% O_2, the plot is linear with minimal scatter. The equation for the line is

$$NSL = 1.04 - 0.242\ D_i \quad (2)$$

with an r^2 of 0.80. A plot of SL vs. diameter was much more scattered. Figure 4 shows the plot of NSL against D_i for all the data. Each of the five gas compositions tested is plotted separately. The scatter is partially due to the variation of temperature in the gas stream, T, in which the burns were done. When all the burns were combined the statistical equation was

$$NSL = \frac{1.634}{D_i} + 0.034\ \frac{O_2}{D_i} - 0.0054\ O_2 - 0.316 \quad (3)$$

with an r^2 of 0.85. O_2 is the percent oxygen in the bulk gas stream. This equation was determined using stepwise linear

regression from a statistical software package for IBM or compatibles. Each variable was entered in the equation depending on its F-test value. New F-test values were calculated after each step. After all the variables with F-test values high enough to enter the equation were entered, the program stepped backward, removing all the variables with F-test values below the F-to remove value. Only one variable was entered or removed from the equation per step. The interaction terms O_2/D_i, D_i*O_2, D_i*T, and O_2*T, were included to test the variable interactions. D_i*O_2, D_i*T, O_2*T, and T were not statistically significant.

(Figure 3 and 4 here)

NSL was obtained according to equation (1) by dividing the rate of mass loss by the initial mass, M_i. This is equivalent to dividing by the cube of the initial diameter, D_i, and a constant. This means that in equation (3), the rate of mass loss is proportional to the square of D_i. In other words, the rate of mass loss during volatiles burning is dependent on the initial surface area of the droplet.

Figure 5 shows the comparision of model to data. The other two levels of oxygen, 4.3% and 16.7%, behaved in a similar manner. They were not included on the plot to improve clarity. Figure 6 shows the agreement between the statistical equation and the data.

(Figure 5 and 6 here)

It was not too surprising that the reactor temperature was not a significant variable. Hupa (1985) had found only a slight influence of reactor temperature on the volatiles burning time. In both this work and that of Hupa the temperature of the particle surface, the reaction zone, was not measured. Its relationship to the volatiles burning rate may be a more significant temperature to measure.

Times

The times for drying, volatiles burning, and char burning are listed in Table 1. Hupa's (1985) times are compared to the ones from this work for a 23 mg droplet, 3.08 mm in diameter, combusted in air. Hupa presented his findings in plots with the largest initial droplet 2.0 mm in diameter. His times were graphically extrapolated and should only be considered as an estimate. The difference in droplet sizes is due to the necessity of comparing burns under similar combustion conditions.

Even though Hupa's times can only be taken as an estimate, they are significantly longer than the present data. One reason for the difference in the drying times is that Hupa had much more water to dry. Hupa's liquor was 60% solids and this

work was at 71.8% solids. Another reason for the difference is that Hupa had a lower heat flux in the furnace than the present work, 76 kW/m^2 compared to 87 kW/m^2 based on rough calculations and experimental verification for IPC's flux (Miller 1986).

Table 1. Comparision of Movie to Hupa Times for the Combustion of a 3.08 mm Diameter Droplet

	Time (sec)	
	Movie	Hupa
Drying	1.7	3.8
Volatiles Burning	2.8	4.2
Char Burning	3.5	5.0
Total	8.0	13.0

The volatiles burning time is 50% longer. The above factors are expected to influence the drying region but do not explain the differences in the volatiles burning region. External diffusion of oxygen through the bulk gas or differences between the liquors may have contributed to the different times. If diffusion was important, then changing the velocity of the gas stream from stagnant (Hupa) to flowing (present) would reduce the times for this stage by having higher net O_2 content at the particle surface. It is not possible at this stage to comment on differences between the two liquors.

DISCUSSION

The present results provide the first data on mass loss rates during the volatiles burning stage for a black liquor droplet. They are, however, insufficient to support a quantitative explanation of the controlling phenomena. The data suggest that the initial droplet surface area is a key factor in the volatiles burning stage. Since the actual surface area is continually changing, the data do not differentiate between external or internal controlling processes. Externally controlled kinetics (i.e., through the gas temperature) had no significant effect. Externally controlled mass transfer (i.e., the O_2 content), or possibly the O_2 concentration effect on the reaction kinetics, did slightly influence the mass loss rate during volatiles burning. Future measurements of dynamic surface area and temperature should help clarify relative rates of external and internal processes.

CONCLUSIONS

Several conclusions can be drawn from this preliminary work. The first is that the linear region in the droplet's mass loss history mainly corresponds to the volatiles burning stage. The second is that the rate of mass loss in the linear region is closely proportional to the surface area of the initial droplet. Quantification of particular rate limiting steps for the volatiles

burning region will require future work. Finally, for closely similar reactor conditions, Hupa's volatile burning times (1985) were longer than those from this work. Differences in air flow rate past the particles appear to be an important difference between these works.

Portions of this work were used by (KAC) as partial fulfillment of the requirements for the Master of Science degree at The Institute of Paper Chemistry.

LITERATURE CITED

Hupa, M; Solin, P. Combustion Behavior of Black Liquor Droplets. TAPPI International Chemical Recovery Conference, Book 3:335-344 (1985).

Grace, T.M.; Cameron, J.H.; Clay, D.T. Role of the Sulfate/Sulfide Cycle in Char Burning - Experimental Results and Implications. TAPPI International Chemical Recovery Conference, Book 3:371-379(1985).

Miller, P.T.; Clay, D.T. Swelling of Kraft Black Liquor During Pyrolysis. AIChE Forest Products Division, 1:152-159 (1986).

Moreland, B.A.; Clay, D.T. The Influence of Water on Black Liquor Combustion. Preprints of TAPPI Pulping Conf., Book 2:389 (Nov. 1985).

Robinson, M. Characterization of Black Liquor Droplet Drying in Air, Steam, and Humid Air. Doctorate Thesis in Progress. Appleton, WI, The Institute of Paper Chemistry, 1986.

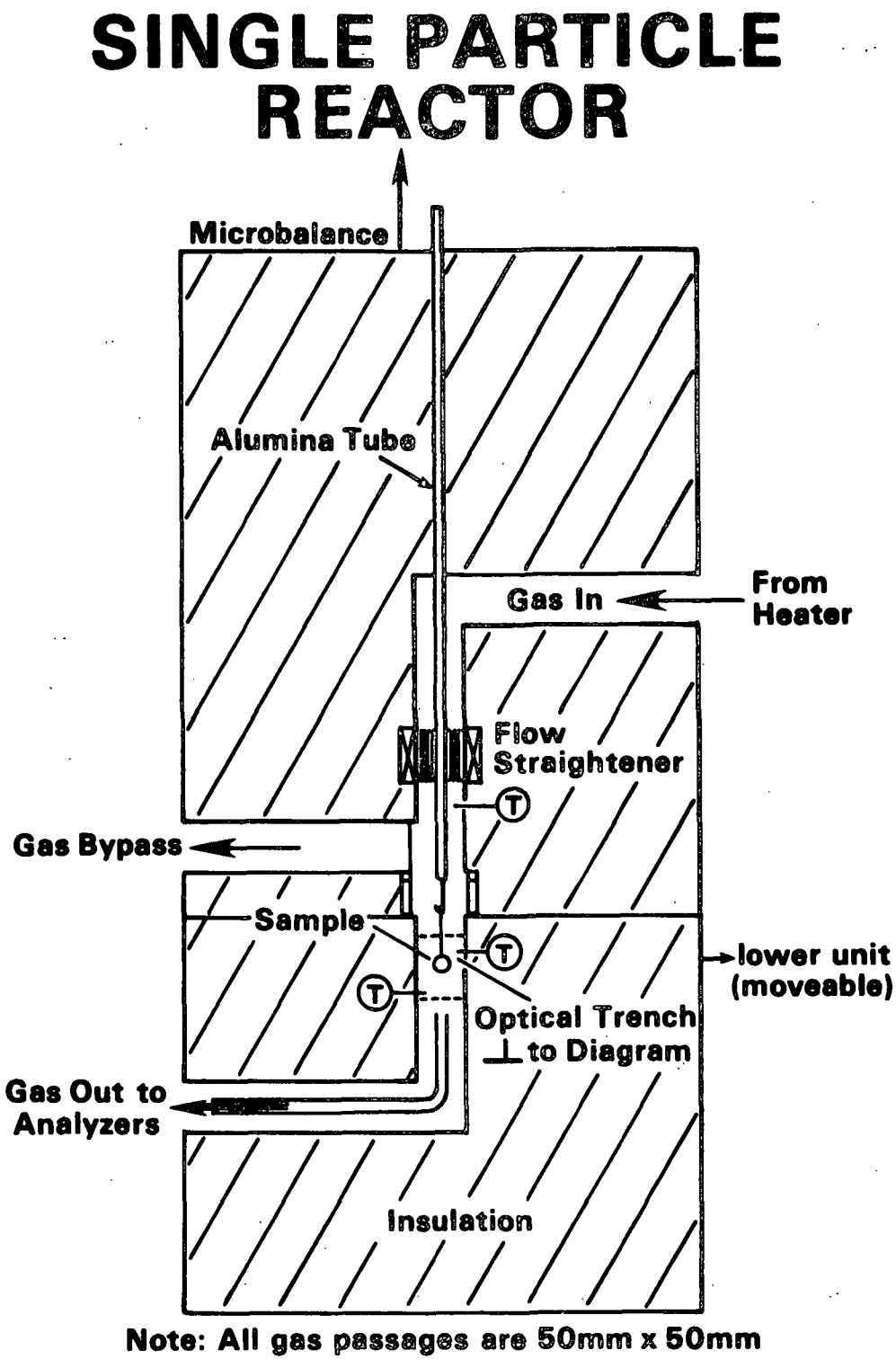

Figure 1. Single Particle Reactor.

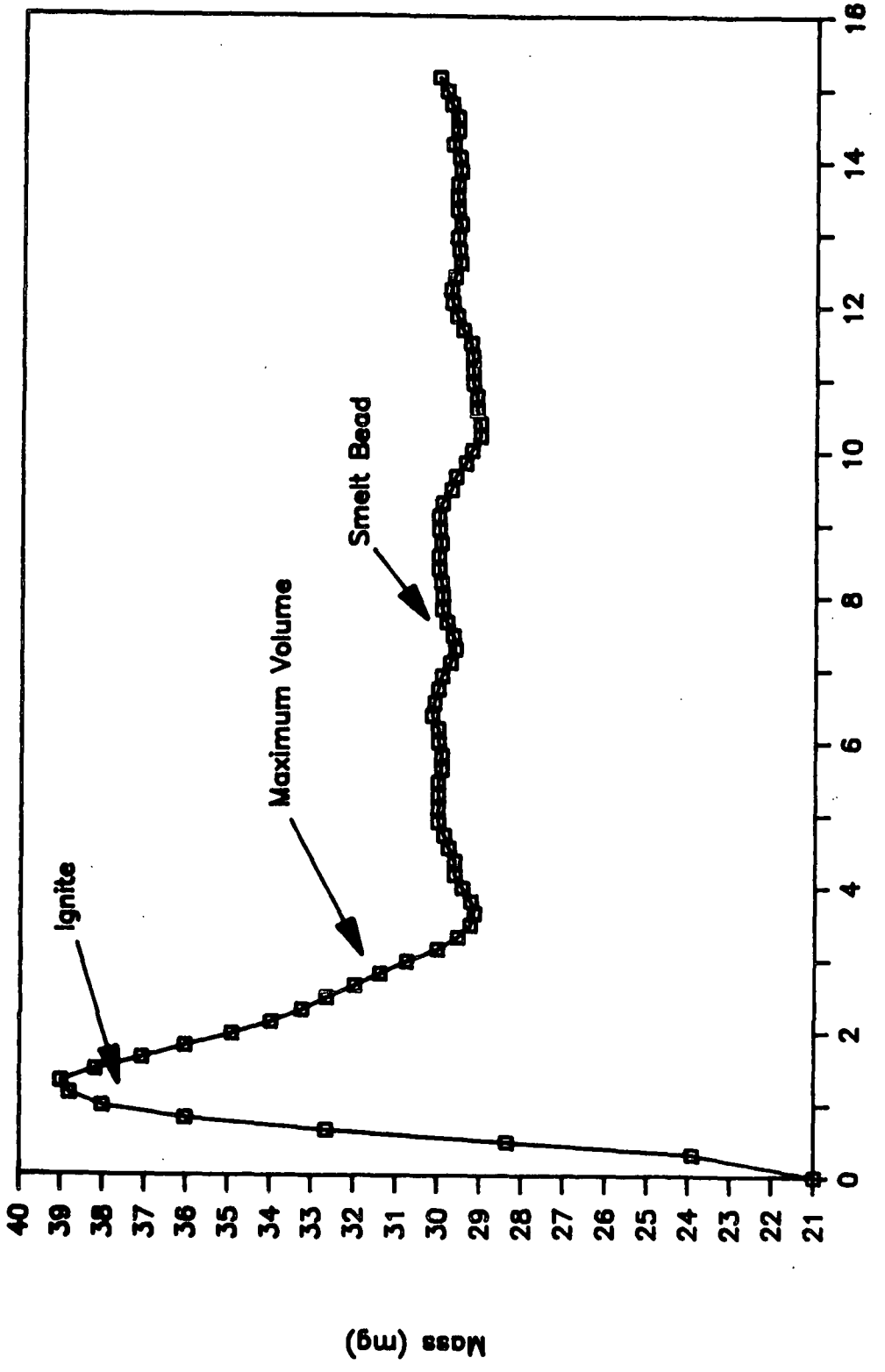

Figure 2. Black Liquor Droplet Mass History. Sample - 21 mg at 71.8% Solids, Gas - 10.5% O_2 Balance N_2 at 763°C.

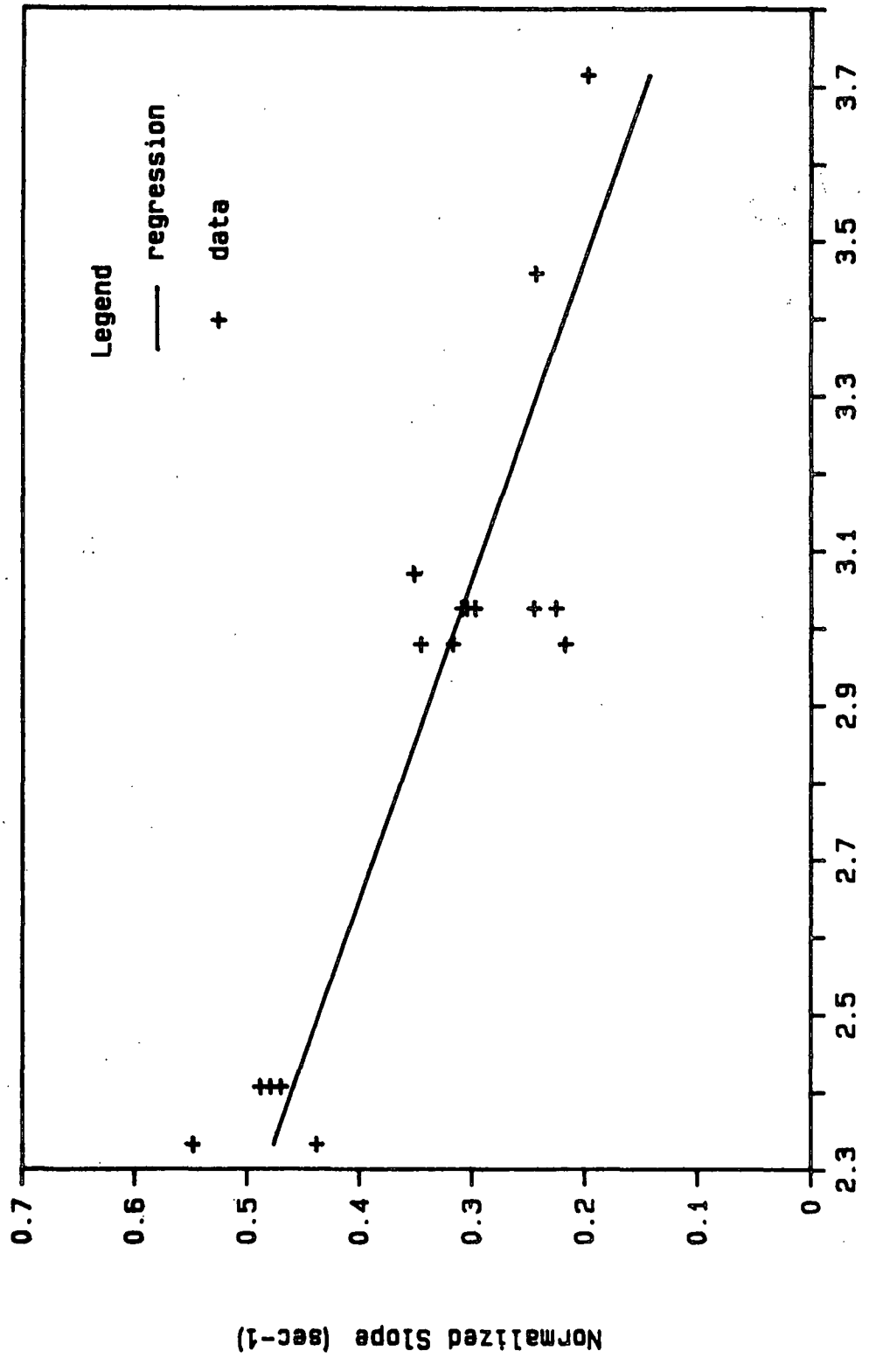

Figure 3. Normalized Rate vs. Initial Diameter for Conditions of 10.5% O_2.

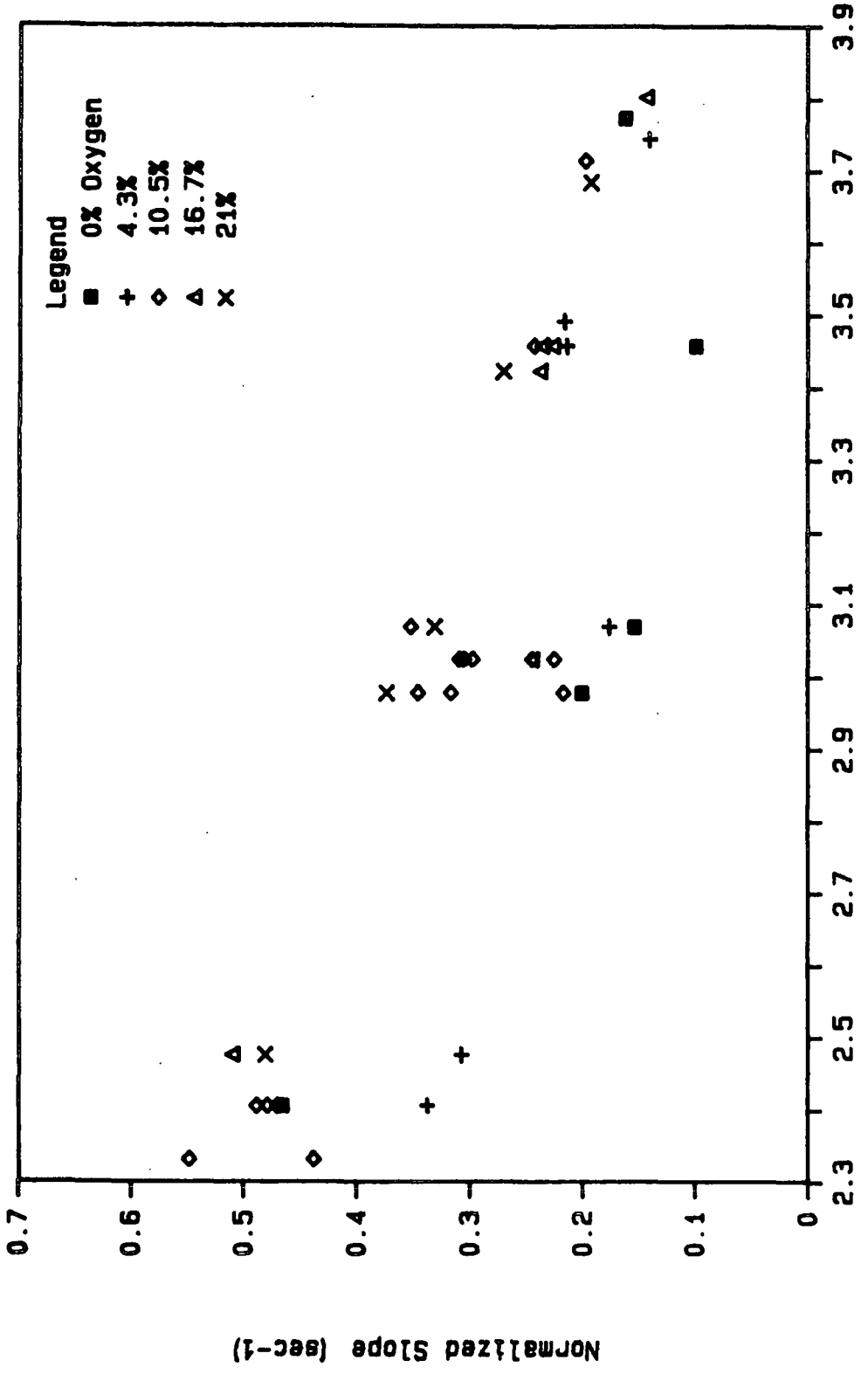

Figure 4. Normalized Rate vs. Initial Diameter for all Data.

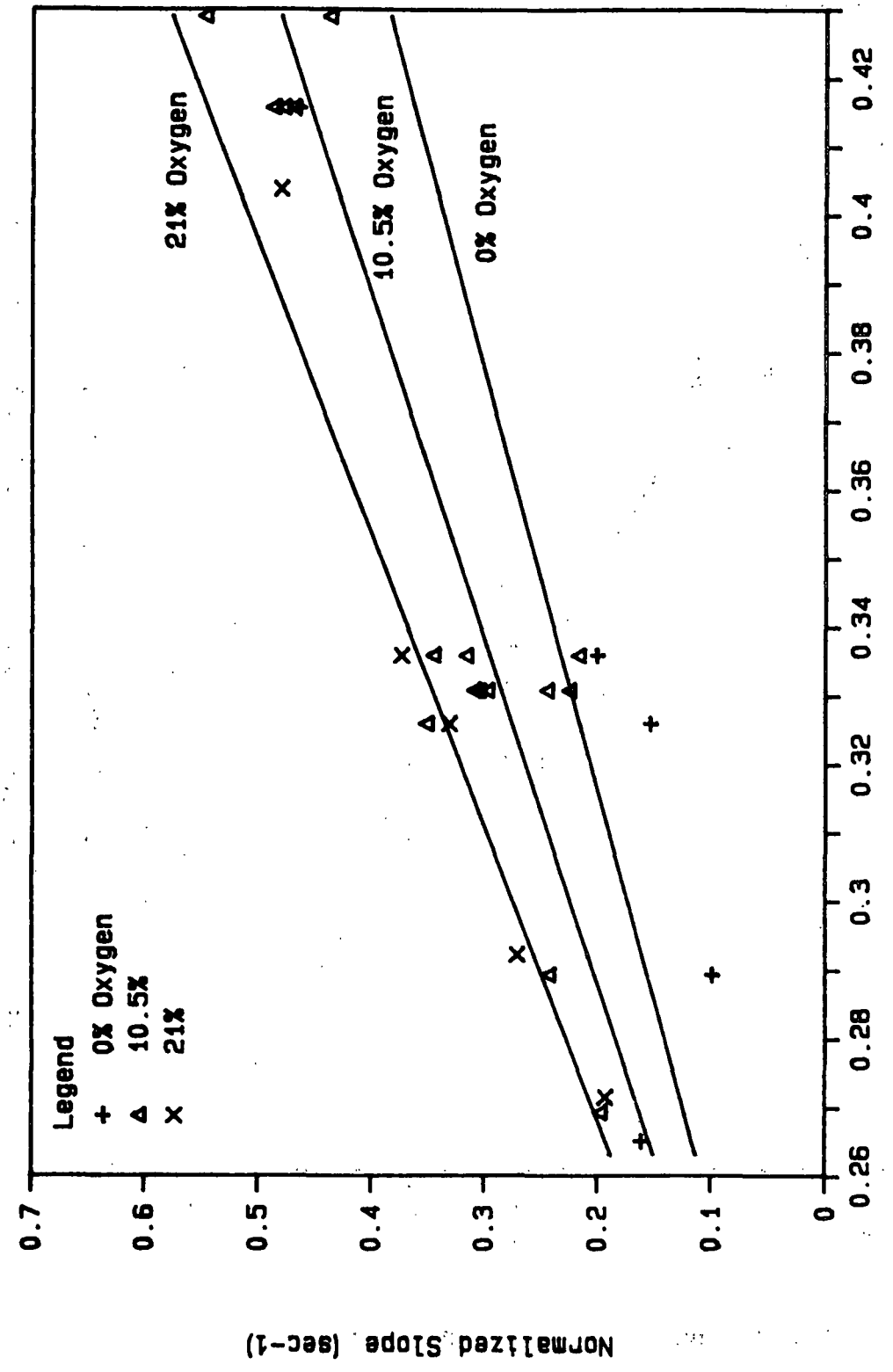

Figure 5. Comparison of Statistical Model (Equation 2) with the Experimental Data at Three Oxygen Levels.

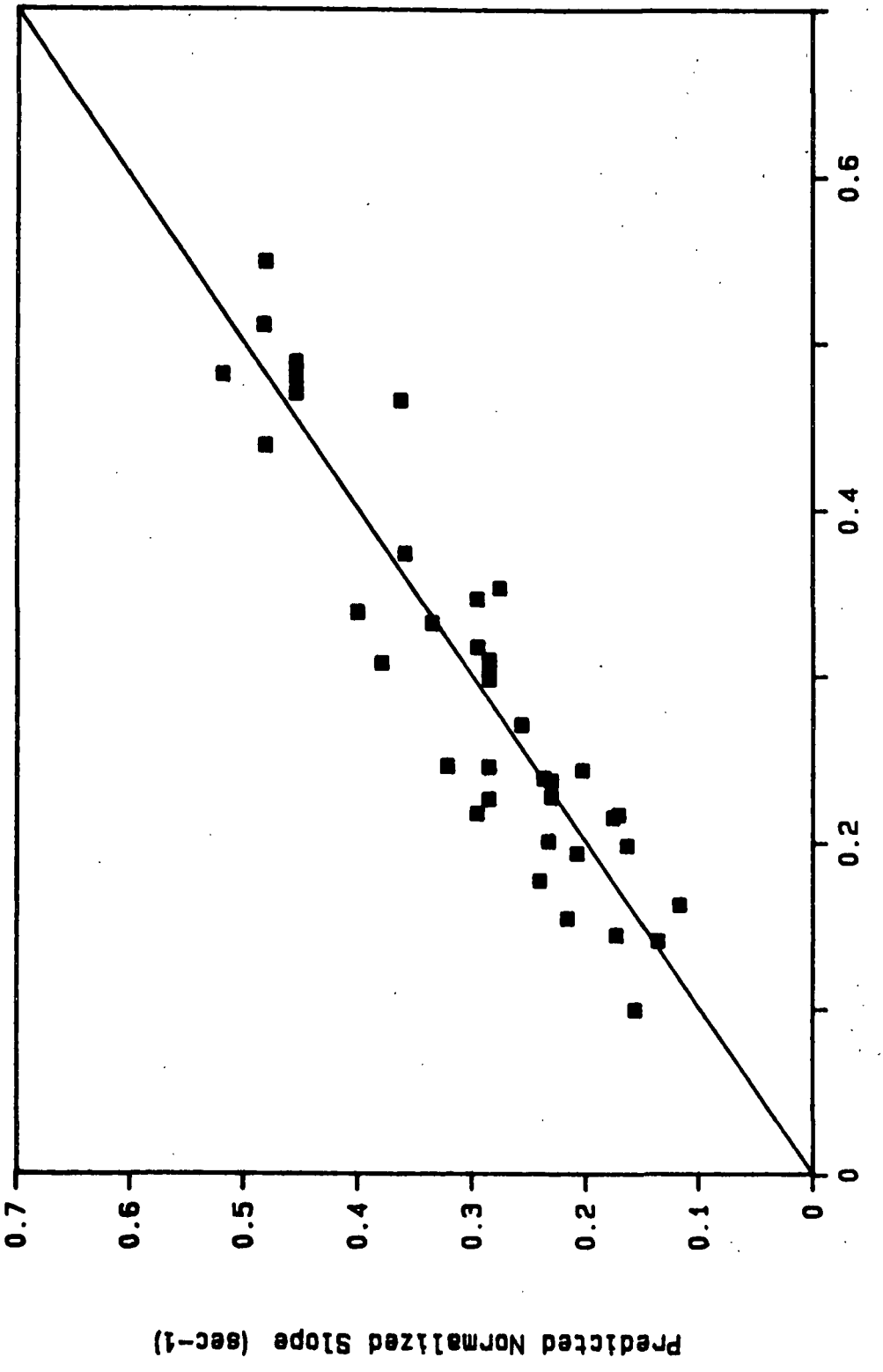

Figure 6. Predicted vs. Observed Normalized Mass Loss Rate.

Characterization of Black Liquor Drop Drying in Air

Mark L. Robinson and D. T. Clay

The Institute of Paper Chemistry

Appleton, WI 54912

ABSTRACT

Forced convective air drying of kraft black liquor drops was studied at temperatures below 200 C to avoid mass loss by pyrolysis. When dried in hot air, black liquor drops form a surface skin and undergo repeated cycles of inflation and rupture. Of particular interest were the influence of surface swelling and rupture on drying rate and drop temperature. Calculations which account for convection, conduction and radiation heat transfer to the drop indicate that increased drying rates should result from inflation. However, experimental drying rates were insensitive to inflation. One explanation is that nucleation of vapor bubbles in the moist drop increases resistance to conduction heat transfer. The subsequent rise in surface temperature reduces the driving force for heat transfer to the drop. The effect of increased surface area is offset by the reduction in temperature driving force. Scanning electron micrographs of dried drops showed multiple voids in the drop shell.

SCOPE

In kraft chemical recovery operations, wet black liquor drops are burned in a hot furnace. Evaporation of moisture is the first step in black liquor combustion. Previous studies of black liquor combustion have focused on subsequent stages, namely pyrolysis (volatiles burning) and char burning. Despite its potential influence on these events, very little information about black liquor drop drying exists in the literature. The purpose of this work is to study black liquor drop drying in air below the pyrolysis temperature. Low temperatures relative to the recovery furnace were chosen so that mass loss was due to drying, not pyrolysis. Certain black liquor physical properties important to drying, such as viscosity, are sensitive to solids content. The influence of initial liquor solids content on drop drying was therefore of interest.

CONCLUSIONS AND SIGNIFICANCE

Black liquor drops dried in air above the boiling point undergo cycles of inflation and rupture. However, an anticipated increase in drying rate due to droplet inflation did not occur. In addition to a large, central void, it appears that small vapor bubbles nucleate in the moist droplet shell, creating an internal heat transfer resistance analogous to a porous insulator. The increased resistance causes the surface temperature to rise. As a

result, the external driving force for heat transfer to the drop decreases and drying rate remains relatively constant. Scanning electron microscopy confirmed the existence of multiple internal voids.

Extension of these results to high temperatures suggests that significant temperature gradients may exist in black liquor drops as they dry in a recovery boiler. If inflation and rupture do not mix the drop's contents sufficiently, rapid surface heating will result in simultaneous drying and pyrolysis.

Drop drying is important to a variety of chemical process industries. Most drying operations are designed to create a dehydrated product for packaging and sale. In kraft pulp mills, however, drop evaporation is the first stage of black liquor combustion -- an essential element of the kraft chemical recovery process.

The economy of kraft pulping depends on a successful scheme for producing energy and recovering pulping chemicals from black liquor -- a "waste" stream from wood pulping (Hough, 1985). In kraft pulping operations, wood chips are "cooked" in sodium hydroxide and sodium sulfide at elevated temperatures to fragment organic binders and liberate their constituent fibers. The fibers are washed and removed. The resulting wash solution, referred to

as black liquor, contains organic material dissolved from the wood as well as the residual inorganic pulping chemicals. After being concentrated from 15% to approximately 65% solids by weight, the black liquor is burned in a special water-walled furnace, called a recovery boiler. Pressure nozzles spray large drops (1 to 5 mm diameter) into the lower part of the furnace where they dry and burn.

Few references to black liquor drop drying exist in the literature (Monaghan and Siddall, 1963; Bjorkman, 1968; Hulden, 1968; Hupa, 1985). With one exception (Hupa, 1985), the results are mainly qualitative.

Black liquor combustion can be described as occurring in three main stages -- drying, volatiles burning, and char burning. The extent to which these events occur simultaneously, and how they influence each other, is presently not well defined. Behavior is specific to each liquor. However, some generalizations can be made. During drying, drops form a surface skin and repeatedly bubble and burst, often violently. Some volume expansion is observed during this stage. Experimental evidence indicates that drying behavior will influence the final size, shape, and porosity of the dried drop. These, in turn, will affect the rate of combustion through their impact on heat and mass transfer within the particle. For example, Hupa (1985) mentions that the

structure and viscosity of the drying particle will have a significant effect on pyrolysis. The influence of particle swelling during the volatiles burning stage on the char burning rate has been clearly demonstrated (Hupa, 1985). In addition, Moreland and Clay (1985) determined that the maximum reactivity of a black liquor char increased with increasing liquor moisture content, probably due to the influence of moisture evaporation on the physical structure of the char.

The goal of this study is to gain quantitative understanding of kraft black liquor drop drying in air. Of particular interest is the possible influence of surface swelling and rupture on drying rate and drop temperature. Final particle structure is also of interest. A suspended-drop drying apparatus with electronic data acquisition equipment was constructed. Drop drying rates and temperatures were measured in an upflowing stream of heated air. Air temperatures were maintained below the pyrolysis range to insure that mass loss by pyrolysis did not occur.

EXPERIMENTAL EQUIPMENT AND OPERATING PROCEDURES

A drawing of the suspended-drop drying apparatus is shown in Figure 1. A sheathed thermocouple was used to hold a black liquor droplet in place in upflowing heated air. The sheath was bent into a hook and hung from an electronic millibalance.

Surrounding the thermocouple was a Pyrex drying chamber supported by a slide valve. A distinguishing feature of the present system is that a simultaneous record of droplet mass and temperature during drying can be obtained by electronic data acquisition.

Figure 1 here

Major components of the experimental system are described below.

Electronic Millibalance

A Cahn Instruments Inc., Model DTL-3 millibalance was used in weigh-below mode to measure the mass of a suspended drop. The balance is accurate to ± 0.2% over the 0-10 mg range used in this study.

Thermocouple Assembly

The thermocouple assembly was constructed from stainless-steel sheathed thermocouple wire. Thermocouples were individually calibrated prior to use. Recorded temperatures are accurate to ± 2 C over the range covered by the experiments. Both the thermocouple assembly and the drying chamber are shown in Figure 2.

Figure 2 here

Drying Chamber

The double walled drying chamber shielded the thermocouple filament, drying gas, and drop from air drafts in the laboratory. Shown in Figure 2, the chamber is similar in concept to one described by Trommelen and Crosby (1970).

Data Acquisition System

Analog signals from the millibalance and thermocouple were sampled and converted to digital form by an ISAAC (Cyborg Corp.) data acquisition system installed on an Apple II+ microcomputer. Signal averaging was used to reduce random noise.

Drop Formation

Drops were formed with a Hamilton microsyringe having a volume of 10 microliters graduated in 0.1 microliter increments. Squarely honed, 26-gage, hypodermic needles were used. In addition to warming the liquor and syringe, higher solids liquors required shorter needles to minimize pressure drop.

Drying Conditions

Temperatures far below the typical 1000 C temperatures in a recovery furnace were used to prolong drying events, avoid pyrolysis, and facilitate observation. Unless indicated otherwise,

drops were dried under the following conditions, referred to as "standard conditions" in the text:

Initial Drop Volume ..... 2.5 µl

Initial Drop Diameter .... 1.68 mm

Drying Air Temp ..... 167 C

Drying Air Velocity ..... 1.5 m/s.

Black Liquor

The kraft black liquor used in this study was produced by pulping loblolly pine chips under the following conditions:

Sulfidity	25%	Eff. Alkali	16%
Liquor/Wood	4	H-Factor	2000
Cooking Temp.	173 C	Time to Temp.	90 min.
Time at Temp.	94 min.		

Calculation of Drying Rates

Mass versus time data from drying experiments were converted into plots of unaccomplished drying (U.D.) as follows:

U.D. = mass moisture (t)/mass moisture (t=0).

This method of presenting the data minimizes the impact of minor variations in initial droplet mass and any spattering which may have occurred (Trommelen and Crosby, 1970). In most cases, three

runs were averaged to obtain a summary curve of unaccomplished drying versus time.

Curvilinear regression was used to fit a second or third order polynomial to the data (Hayek and Cheetham, 1987). Usually the regression understated the actual curve over the first two or three seconds of drying, but was otherwise a good fit. Typical correlation coefficients exceeded 0.99. Once an accurate fit was obtained, the drying rate was computed by differentiating the polynomial and evaluating it at times of interest.

Calculation of Surface Area

The surface area of black liquor drops was estimated from their videotaped silhouettes. Two steps were involved. First, the perimeter of the silhouette was measured. Next, the diameter of a perimeter-equivalent circle was computed. The surface area of the drop was computed from that diameter.

HEAT TRANSFER MODEL

In simplest terms, ignoring such effects as heats of solution, heat transferred to a moist black liquor drop below the pyrolysis temperature either evaporates moisture (supplies latent heat), or raises the temperature of the drop (supplies sensible heat). If heat inputs are correctly accounted for, measured

drying rates should agree with those estimated from heat transfer considerations.

Heat is transferred to a suspended drop by convection from the flowing gas stream, conduction through the thermocouple wires, and radiation from the surroundings. Equations describing each mode have been developed and verified by Trommelen and Crosby (1970). In our work the same equations were built into an electronic spreadsheet model. The primary purpose of the model was to study the effects of drying behavior -- in particular, drop surface area and temperature -- on drying rate.

A second purpose of the model was to test the assumption that temperature gradients inside the drops may be ignored. Based on that assumption, several researchers have justified using an internal thermocouple to estimate drop surface temperature (Sano and Keey, 1982; Trommelen and Crosby, 1970; and van der Lijn, 1976).

Heat transfer by each mode depends on the temperature driving force and the available area for heat transfer. To estimate drying rate, the model equations require that surface area and drop temperature be described as functions of time. Drying rate is then computed by a simplistic energy balance as:

$$\text{Drying Rate} = \left(\text{Rate of Heat Transfer} - \text{Rate of Sensible Heating}\right) / \text{Heat of Vaporization of Water}.$$

As long as physical data required by the equations are accurate, the extent of agreement between experimental results and model computations will depend on how well the input data describe the true surface area and temperature. Combinations of both assumed and experimental surface area and temperature profiles were input to the model to compute drying rates.

Questions about how well the internal thermocouple estimates the true surface temperature, and whether increased surface area due to inflation results in higher drying rates can be answered by comparing the model results to experimental data. For example, early in drying drops shrink as spheres in proportion to mass loss. During that time, if a discrepancy is found between the model calculations which contain input data for area change proportional to mass loss, it follows that the temperature input does not represent the actual surface temperature.

Three calculation options were considered. Each option and its "what if" question are explained below, where T_s is the drop surface temperature, and S.A. refers to the drop surface area. A likely alternative -- that drop surface temperature differs from that measured by the thermocouple, and that the surface area increases due to inflation -- can be evaluated by comparing the results of these three options below with experimental data.

Option 1 "What if" the drop surface temperature is correctly measured by the thermocouple and the drop surface area shrinks as a sphere proportional to mass loss?

Inputs T_s -- as measured by thermocouple
S.A. -- computed from mass loss data assuming spherical shrinkage

Option 2 "What if" the drop surface temperature is correctly measured by the thermocouple and the drop surface area increases due to inflation?

Inputs T_s -- as measured by thermocouple
S.A. -- experimental surface area data

Option 3 "What if" the drop surface temperature differs from that measured by the thermocouple and the drop surface area shrinks as a sphere proportional to mass loss?

Inputs T_s -- assumed temperature profile
S.A. -- computed from mass loss data assuming spherical shrinkage

WATER DROP DRYING

To verify the heat transfer equations, 2-microliter (diameter = 1.56 mm) water drops were dried in air and the

resulting average drying rate curve was compared to model calculations. In the model, the surface temperature was assumed equal to that of the internal thermocouple. The surface area was assumed to be that of a sphere of water whose mass and temperature equalled those measured experimentally.

Results are plotted in Figure 3. The dashed curve represents the expected drying rate if the effect of mass transfer on heat flux is ignored. The fine solid line includes the correction for mass transfer. A maximum discrepancy of 6 percent exists between the corrected model curve and experiment.

Figure 3 here

Good agreement was due to the fact that the model assumptions for surface area and temperature conform to the drying behavior of water drops. First, water drops tend to shrink as uniform spheres in proportion to mass loss. Second, water drops circulate internally, which minimizes any temperature gradients in the drop. Hence, the thermocouple should measure a temperature which approximates the drop surface temperature.

BLACK LIQUOR DROP DRYING

Unlike pure solvents, which tend to dry uniformly, drops containing dissolved solids exhibit a variety of behaviors when

dried above the boiling point. Charlesworth and Marshall (1960) determined that drops of solutions which form a porous crust show little morphology change during drying. Moisture escapes relatively uninhibited through surface pores and interstices. Drops containing skin-forming solutions which inhibit mass transfer will usually inflate and/or rupture, often repeatedly.

Drop Behavior and Surface Swelling

Kraft black liquor is a skin-forming solution. When dried in air on the suspended-drop drying apparatus, black liquor drops initially shrivel and shrink as moisture evaporates. Surface folding develops in drops whose initial solids concentration is less than 50 percent. With continued heat transfer, the internal temperature increases until the drops suddenly inflate and rupture. Inflation increases the available area for heat transfer. If the drop is still moist, some of the contents may be ejected during rupture. Most often, repeated rupture and inflation continue until the drop is nearly dry. A thin, hollow shell is typically found on completion of drying.

Figure 4 shows the relative surface area histories of nominal 2.5 microliter (diameter = 1.68 mm) black liquor drops drying in air under standard conditions. Before inflating, the drops tend to shrink as spheres. Minor deviations from spherical

shrinkage occur for drops with greater than 20% initial solids, probably due to some internal generation of vapor in the drop shell prior to the burst point. The extent of surface swelling after inflation clearly increases with initial solids.

Figure 4 here

Drop Temperature

Initial liquor solids content has a significant influence on the temperature histories of drying black liquor drops. Shown in Figure 5, initially low solids liquors (30% solids and below) experience a constant temperature period whose length decreases with increasing solids content. The availability of surface moisture in the early stages of low solids liquor drying results in a pseudo wet-bulb temperature (approximately 71 C). Above 40% solids, no constant temperature period exists.

Figure 5 here

A second constant temperature period seems to exist near 120 C in Figure 5. Internal pressure relief from repeated rupture produced depressions in the temperature curves. Swings of 2-5 C were typical. As shown in Figure 6, rupture occurred over the range of solids from 55-65% regardless of initial solids content.

Figure 6 here

Drying Rate

Black liquor drops were dried in air under standard conditions. Experimental and calculated drying rates are compared in Figures 7 and 8 for 30% and 50% solids liquors, respectively. The three combinations of surface area and temperature previously described were used as input to the model equations. A small arrow along the abscissa indicates the average time when bursting first occurred (burst point). Inflation usually preceded bursting by one or two seconds.

Figures 7 and 8 here

As indicated in the legend, the heavy solid curve represents the experimental drying rate. Other curves represent model computations using the three input options for surface area and temperature.

The narrow solid line represents the first option; it assumes that the black liquor drop shrinks as a sphere and that the thermocouple measures the surface temperature. The dashed curve represents the second option. It assumes that the thermocouple measures the surface temperature but uses the experimentally determined surface area rather than assuming spherical shrinkage. Because only minor deviations from spherical shrinkage appear prior to the inflation point, this option is applied only

after inflation has occurred. The dotted curve again assumes a shrinking sphere but uses an assumed linear surface temperature which was found to cause agreement with experimental results. The assumed surface temperature is higher than the drop temperature measured by internal thermocouple (Figure 9). The physical basis for assuming a linear temperature profile relates to the rate of surface skin formation on the suspended drop. More details about the assumed profile and the choice of the beginning and end-point temperatures are given in the discussion section.

Figure 9 here

For 30% solids liquor (Figure 7), comparing the experimental and model curves prior to the burst point indicates that assuming spherical shrinkage and that the thermocouple temperature approximates the true surface temperature causes the model to first overestimate and then underestimate the experimental rate of drying (narrow solid curve). After the burst point, the model parallels the experimental drying rate, understating it slightly.

If observed surface swelling is included, the model predicts more rapid drying after the burst point (dashed curve). However, as shown by the heavy solid curve, increased drying rates due to inflation were not obtained experimentally.

An assumed linear increase from an initial surface temperature of 89.5 C to 121 C at the burst point (Figure 9) with

spherical shrinkage gave excellent agreement with the model until the burst point (dotted curve in Figure 7).

For 50% solids liquor (Figure 8), computations which assume that spherical shrinkage and thermocouple temperatures represent the experimental surface area and temperature, respectively, understate the drying rate along the entire drying curve (narrow solid curve). Nevertheless, the curves parallel each other closely after the burst point.

When the actual inflated surface area is included, the model grossly overpredicts the actual drying rate (dashed curve).

An assumed linear temperature increase from an initial temperature of 110 C to 118 C at the burst point causes agreement between model and experiment until the burst point (dotted curve).

DISCUSSION OF RESULTS

Comparing model calculations and experimental results gives valuable insight into black liquor drying behavior and critical factors which influence drying rate. Drop surface area and temperature are considered separately in the following discussion.

Drop Temperature

For 30% solids black liquor, prior to the burst point, surface area decreases approximately proportional to mass loss

(Figure 10). The deviation of the experimental surface area from spherical shrinkage indicates that some internal voids have formed. When compared to other solids levels (Figure 4), this deviation seems exaggerated, probably due to experimental error. Minor change from spherical shrinkage is more likely. Therefore, deviations from spherical shrinkage are probably not responsible for the discrepancy between experimental and predicted drying rates prior to the burst point. It is more likely that surface temperature and the rate of surface temperature change are responsible.

Figure 10 here

In Figure 7, between 0 and 12 seconds, the model which assumes that the thermocouple accurately measures surface temperature and that the drop shrinks as a sphere proportional to mass loss (thin solid curve) overpredicts the actual drying rate. From 12 to 34 seconds the same model understates the drying rate. Local heat transfer considerations may explain why this occurs.

In an upflowing gas stream, a suspended drop will experience greater convective heat transfer coefficients along its lower face (van der Lijn, 1976). Unless circulation is able to mix the contents of the drop, the underside will tend to dry more quickly. Local hot spots may be created where heat transfer is highest, especially if internal bubbles are able to nucleate there

(El-Sayed, 1987). Since the bottom face is the most distant part of the drop from the thermocouple, the thermocouple will approximate the mean surface temperature only if the Biot number is sufficiently low. As shown in Figure 9, early in drying the thermocouple temperature is less than the assumed surface temperature (the temperature which caused agreement between experiment and model). When the thermocouple temperature is used in the model, an exaggerated estimate of the heat transfer driving force results. Therefore, model computations overpredict the initial drying rate.

The role of sensible heating is also important and cannot be ignored. From 4 to 10 seconds, a pseudo-constant temperature period is observed experimentally. During this time, the slopes of the experimental and assumed temperature profiles are similar. The slope determines the amount of sensible heating computed by the model. As mentioned before, in computing model drying rates, sensible heat is subtracted from the total amount of heat available for drying. Between 4 and 10 seconds, the sensible heating rates are similar for both cases. Therefore, the discrepancy between the experimental and model drying rates is primarily due to the difference in surface temperatures.

After about 12 seconds, the temperature difference in Figure 9 steadily decreases with time. However, the slope of the thermocouple-temperature-versus-time curve increases relative to

the assumed temperature curve. As mentioned, a steeper slope implies more sensible heating and a lower drying rate. Therefore, the estimated curve of drying rate falls below the experimental curve.

One reason for the steeper slope may be that heat conducted through the thermocouple dries the mass near the junction instead of heating the entire drop. Abundant nucleation sites on the thermocouple junction promote the formation of vapor bubbles, increasing the thermal resistance to conduction at the thermocouple site. The temperature sensed by the thermocouple will reflect its dry, "insulated" surroundings and increase rapidly. As shown in Figure 9 after 23 seconds, it may even exceed the surface temperature slightly. The mean temperature driving force estimated by thermocouple would then be less than that for the drop as a whole. After that time, heat transfer predictions assuming that the thermocouple measures the surface temperature would tend to slightly understate the actual rate of heat transfer. It follows that drying rate is also somewhat understated. This effect may be a minor one.

The choice of a linear temperature profile to fit the data prior to the burst point was, at first, arbitrary. However, in a solution capable of creating internal heat transfer

resistance, experimental evidence may justify a linear surface temperature increase.

Charlesworth and Marshall (1960) observed that a vertically symmetrical solid phase forms on the bottom of a suspended, drying drop. The crust advances toward the equator. The rate of advance is initially rapid, but slows as the front approaches the equator.

For any spherical drop, the rate of surface area increase with vertical distance from the bottom of the drop is a constant. This implies that, for a relatively constant drying rate, the vertical rate of surface crust advance will decrease linearly as the crust approaches the equator. If vapor bubbles form in the developing crust (or skin) and produce hot spots, the average rate of surface temperature increase should be linear, also.

Beginning and end-point temperatures for the linear interval were chosen as follows. Bursting was assumed to mix the drop's contents and minimize internal temperature gradients. Therefore, at the burst point the thermocouple temperature was chosen to approximate the surface temperature. The starting temperature was then obtained by iterating until model results and experimental data agreed.

Similar results were obtained with 40% solids liquor. Results for 50% solids liquor were not consistent with those of lower solids. The tendency of these very viscous drops to adhere to the side of the thermocouple rather than completely surround it may be responsible.

Surface Area

Inflation of drops would be expected to increase both heat transfer and drying rates (El-Sayed, 1987). To date, no other researchers have attempted to quantify the effect of inflation on drying rates of drops in air. Experiments indicate that inflation does not cause black liquor drying rates to increase significantly. Because the majority of heat transfer in this system is convective, it seems reasonable to seek an explanation based on convective heat transfer considerations.

Convection heat transfer to the drop is calculated by

$$Q_c = h \bullet A(T_a - T_s).$$

The difference between the ambient air temperature and the drop surface temperature is the external driving force for heat transfer to the drop. The influence of drop inflation on each of these factors is considered below.

Inflation can cause dramatic increases in drop surface area. In the commonly used Ranz-Marshall correlation (Ranz and Marshall, 1952)

$$Nu = hD/k = 2 + 0.6Re^{1/2}Pr^{1/3},$$

h decreases with increasing diameter. The product $h^{\bullet}A$ will increase by virtue of the surface area's higher order dependence on diameter. For example, a typical 50% solids drop whose original diameter is 1.7 mm inflates to a maximum near 2.3 mm during air drying at 167 C, a relative surface area increase of about 1.9 times. The ratio of heat transfer coefficients, $h_o^{\bullet}/h^{\bullet}_{infl}$, is approximately 0.8. At the same time, assuming an equal temperature driving force, the relative convection heat transfer, $(h^{\bullet}A)_o/(h^{\bullet}A)_{infl}$, has increased by a factor of 1.5. A proportional increase in drying rate or sensible heating would be expected.

Since the product $h^{\bullet}A$ increases with inflation, for convection heat transfer to remain relatively constant a proportional decrease in temperature driving force must occur. The air temperature is constant. Therefore, it follows that the surface temperature must increase as a result of inflation. Apparently, the increase is not sensed by the internal thermocouple. A probable explanation is that evaporation creates an internal resistance to heat conduction within the drop.

The possibility that vapor bubbles forming inside a drying drop could contribute to local hot spots was mentioned by El-Sayed (1987). A hot spot will result if vapor bubbles nucleate just below the surface and increase local resistance to heat conduction. If adequate conduction paths around a vapor bubble exist, the influence of one or several hot spots on overall heat transfer might not be significant. On the other hand, if multiple small vapor bubbles could form, they would act as a porous insulator. As a consequence, few, if any, good conduction paths would exist within the drop. The surface temperature would rise with increasing vapor bubble volume fraction in the moist drop wall.

Nucleation and growth of multiple vapor bubbles are promoted by low diffusivity and high viscosity (El-Sayed, 1987). Both would be expected in kraft black liquor, especially at solids levels in excess of 50% (Hough, 1985).

Scanning electron microscopy confirmed that multiple small vapor bubbles can form in a black liquor drop drying under standard conditions. Figure 11 shows the cross section of a previously dried, 22% solids black liquor drop magnified 300 times. Two large vapor pockets are evident in the drop wall. Striations on the inner surface of the drop (lower left hand portion of the image) may be the result of vaporization occuring along stress lines caused by inflation and bursting.

Figure 11 here

Further magnification of the upper left-hand corner of the smaller vapor pocket indicates the presence of small vapor bubbles (Figure 12) . Coalescence of many small bubbles appears to be responsible for the presence of larger pockets.

Figure 12 here

Mechanism of Surface Temperature Rise

A mechanism for surface temperature rise during black liquor drop drying is implied from the results above. First, a skin forms on drops exposed to upflowing hot air. The skin eventually covers the drop. Any circulation ceases with the completion of the surface crust. Concentration gradients in the outer shell become steeper as drying continues.

Desorption of air and the presence of inorganic precipitates promote nucleation of vapor bubbles in the moist drop (Greenwald and King, 1982). Once formed, bubbles tend to grow due to further vaporization of water from bordering liquid. Additional drying increases the resistance to moisture movement. As diffusion becomes limiting, multiple small bubbles form in preference to larger single bubbles (El-Sayed, 1987). Even prior to inflation, surface temperature rises as internal thermal resistance grows.

Small bubbles may combine to form larger pockets until high viscosity and low diffusivity prohibit coalescence. Large pockets will eventually burst or become immobilized in the drop shell as it dries (Figs. 11 and 12). If vaporization rates are sufficient, the drop will inflate, increasing the area for heat transfer. Rapid heating results, which quickly dries the outer shell of the drop. The surface temperature increases in response to inflation and the inhibited conduction path to the moist interior.

Bursting will occur when internal pressure from evaporating moisture exceeds the surface strength. For suspended drops under standard conditions, this occurs near 60% solids and 120 C (Figure 6). When deflated, temperature gradients will diminish as conduction within the drop improves. However, this will tend to increase the external temperature driving force, enhance heat transfer, and lead to another round of inflation and bursting.

The overall result of the cycle of inflation (with proportional surface temperature increase) and deflation (with proportional surface temperature decrease) is relatively constant drying rate. No dramatic increase in drying rate due to inflation results.

IMPLICATIONS

Black liquor drops exposed to high temperatures in a typical recovery boiler inflate and burst violently. In contrast to low temperature drying in which the drops tend to vent through one location, at furnace temperatures bursting occurs over the entire surface. Rather than forming a hollow shell typical of low temperature drying, a more homogeneous, porous particle may result. If mixing is able to reduce the temperature and concentration gradients within the particle, it should dry at sufficiently low temperatures to avoid significant surface pyrolysis until the entire particle is dry. On the other hand, if internal voids increase the conduction heat transfer resistance in a way similar to that for low temperature air, even when the majority of the drop is still moist high particle surface temperatures should cause significant simultaneous pyrolysis. In addition, if bursting is forceful enough to expel "fingers" of liquor, these could dry and pyrolyze before surface forces are able to gather them back into the drop. High temperature drying is currently the focus of continuing research.

ACKNOWLEDGEMENTS

The contribution of one of the authors (MLR) is in partial fulfillment of the requirements for the Ph.D. degree. The

financial support of member companies of the Institute of Paper Chemistry is gratefully acknowledged. The assistance of Mr. Orlin Kuehl in assembling the experimental apparatus is also acknowledged.

NOTATION

A = drop surface area, m^2

C_p = average heat capacity of drying medium, J/(kg)(K)

D = average drop diameter, m

h = average heat transfer coefficient between drop and drying medium, W/m^2K

$h^\bullet$ = average heat transfer coefficient between drop and drying medium corrected for mass transfer, W/m^2K

k = average thermal conductivity of drying medium, W/mK

Nu = Nusselt number, hD/k, dimensionless

Pr = Prandtl number, $C_p\mu/k$, dimensionless

Q_c = rate of convection heat transfer to drops, W/s

Re = drop Reynolds number, DV/ν, dimensionless

T_a = temperature of drying air, K

T_s = temperature of drop surface, K

V = average linear velocity of drying air, m/s

ν = average kinematic viscosity of drying air, m^2/s

μ = average viscosity of drying air, kg/(m)(s)

Subscripts

o = initial value (at t=0)

infl = value for inflated drop

LITERATURE CITED

Bjorkman, A., "Pyrolysis of Spent Pulping Liquors," Proceedings of the Symposium on Recovery of Pulping Chemicals, Helsinki, 235 (1968).

Charlesworth, D. H. and W. R. Marshall, Jr., "Evaporation from Drops Containing Dissolved Solids -- Parts I and II," AIChE J., 6, 9 (1960).

El-Sayed, T. M., "Development of Particle Morphology of Drying Drops," Ph. D. dissertation, Univ. of California, Berkeley (1987).

Greenwald, C. G. and C. J. King, "The Mechanism of Particle Expansion in the Spray Drying of Foods," AIChE Symposium Ser. No. 78, 218, 101 (1982).

Hayek, L. and A. Cheetham, "Curvilinear Regression in Release 2," Lotus, 3, No. 5, 78 (1987).

Hough, G. W. ed., "Chemical Recovery in the Alkaline Pulping Processes," TAPPI Press, Atlanta, Ga. (1985).

Hulden, B., "Combustion of Spent Liquor Droplets," Proceedings of the Symposium on Recovery of Pulping Chemicals, Helsinki, 375 (1968).

Hupa, M., P. Solin, and P. Hyoty, "Combustion Behavior of Black Liquor Droplets," TAPPI Proc. 1985 International Chemical Recovery Conf., 335 (1985).

Lijn, J. van der, "Simulation of Heat and Mass Transfer in Spray Drying," Ph. D. dissertation, Agricultural Univ., Wageningen, Netherlands (1976).

Monaghan, M. T. and R. G. Siddall, "Combustion of Single Drops of Waste Sulfite Liquor -- A Preliminary Investigation," TAPPI, 46, 89 (1962).

Moreland, B. and D. T. Clay, "The Influence of Water on Black Liquor Combustion," TAPPI 1985 Pulping Conference, 389 (1985).

Ranz, W. E. and W. R. Marshall, Jr., "Evaporation from Drops," (Part 1) Chem. Eng. Progress, 48, 141 (1952); (Part 2) Chem. Eng. Progress, 48, 173 (1952).

Sano, Y. and R. B. Keey, "Drying of a Spherical Particle Containing Colloidal Material into a Hollow Sphere," Chem. Eng. Sci., 37, 881 (1982).

Trommelen, A. M. and E. J. Crosby, "Evaporation and Drying of Drops in Superheated Vapors," AIChE J., 16, 857 (1970).

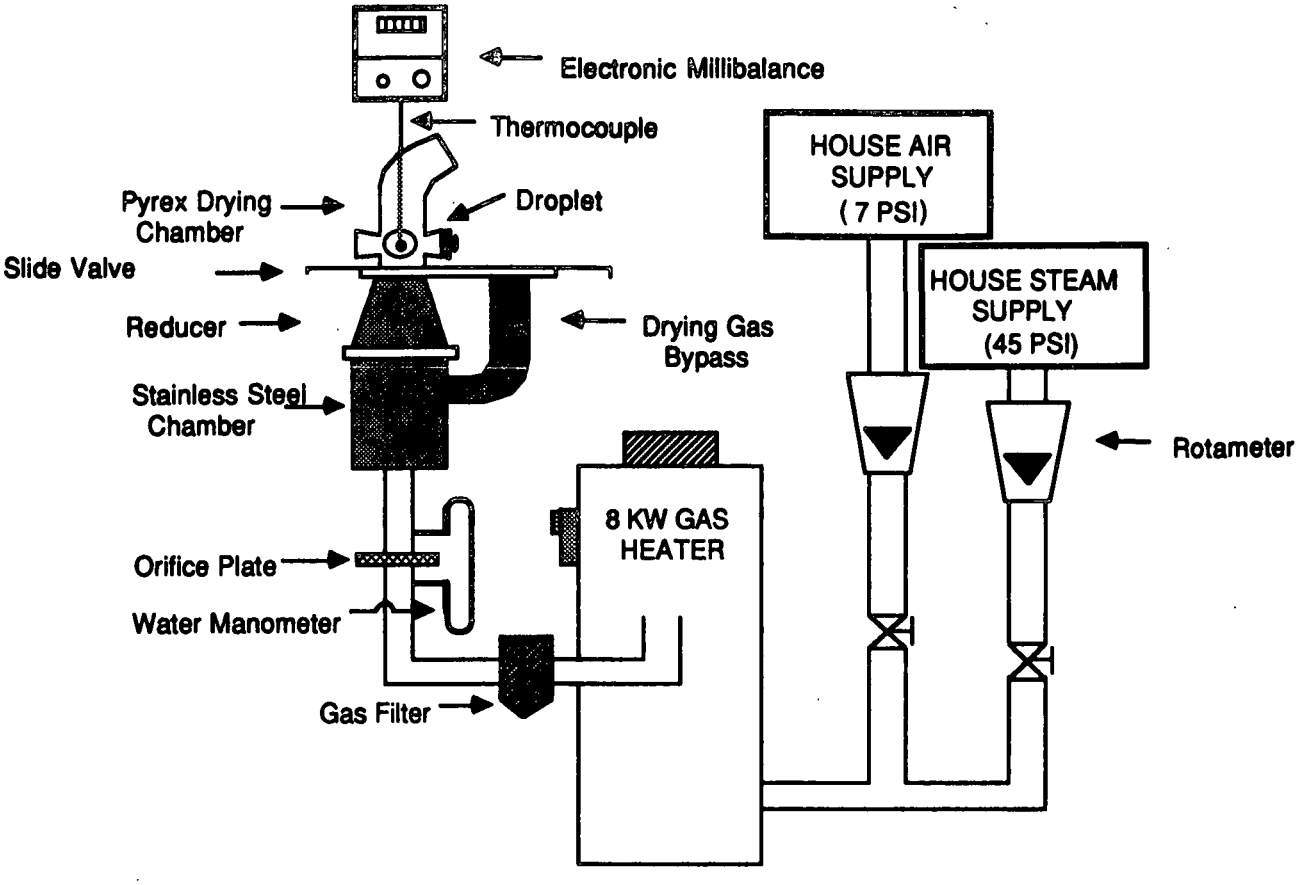

Figure 1. Experimental apparatus used to dry suspended black liquor drops in heated air. Drop temperature and mass during drying were recorded by electronic data acquisition equipment (not shown).

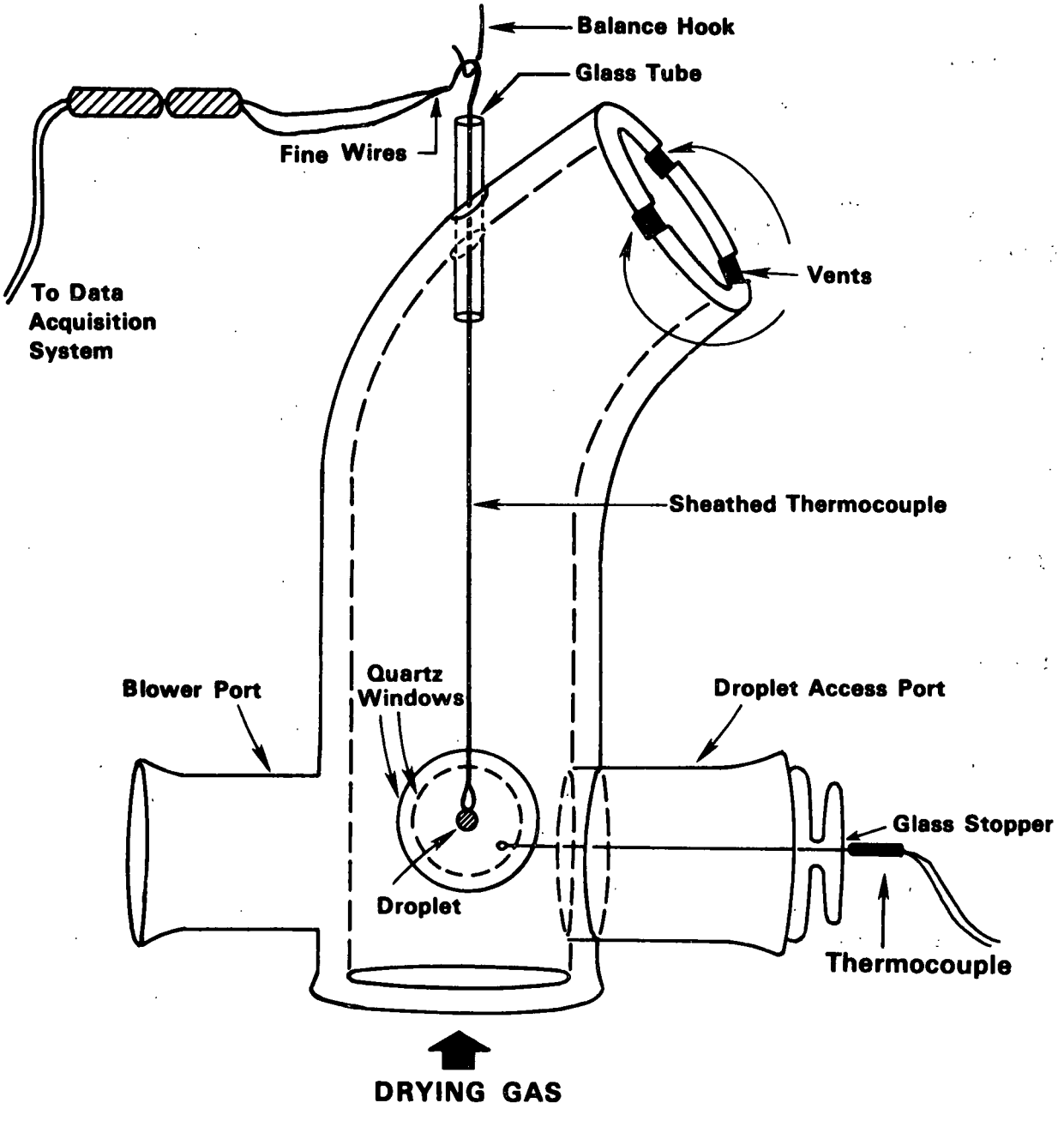

Figure 2. Glass drying chamber and thermocouple assembly.

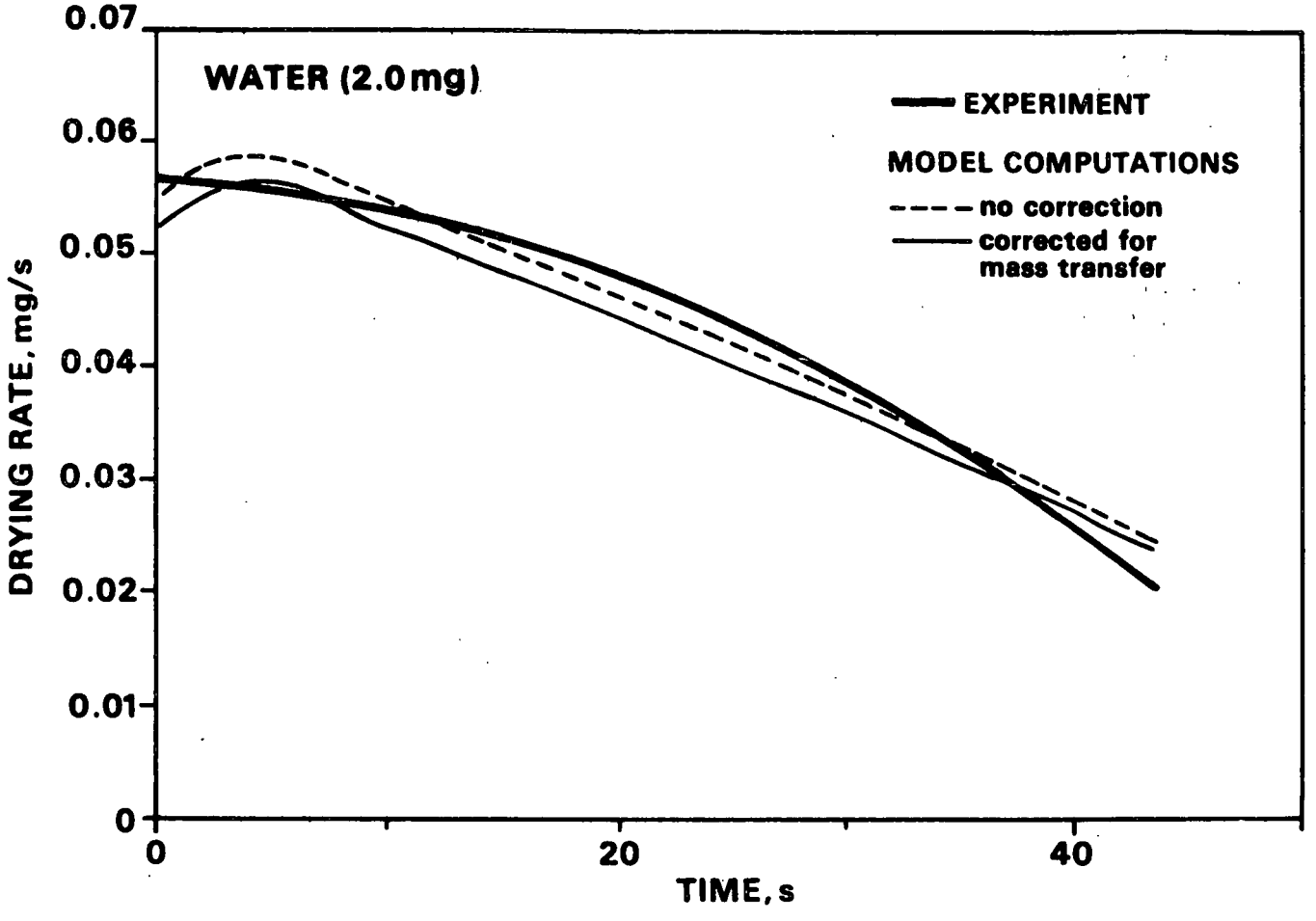

Figure 3. Comparison of water drop drying rate with heat transfer model. In this case, the model assumes that drop surface area shrinks as a sphere in proportion to mass loss by evaporation. It also assumes that the thermocouple measures the surface temperature. [T_a = 167 C, V = 1.5 m/s].

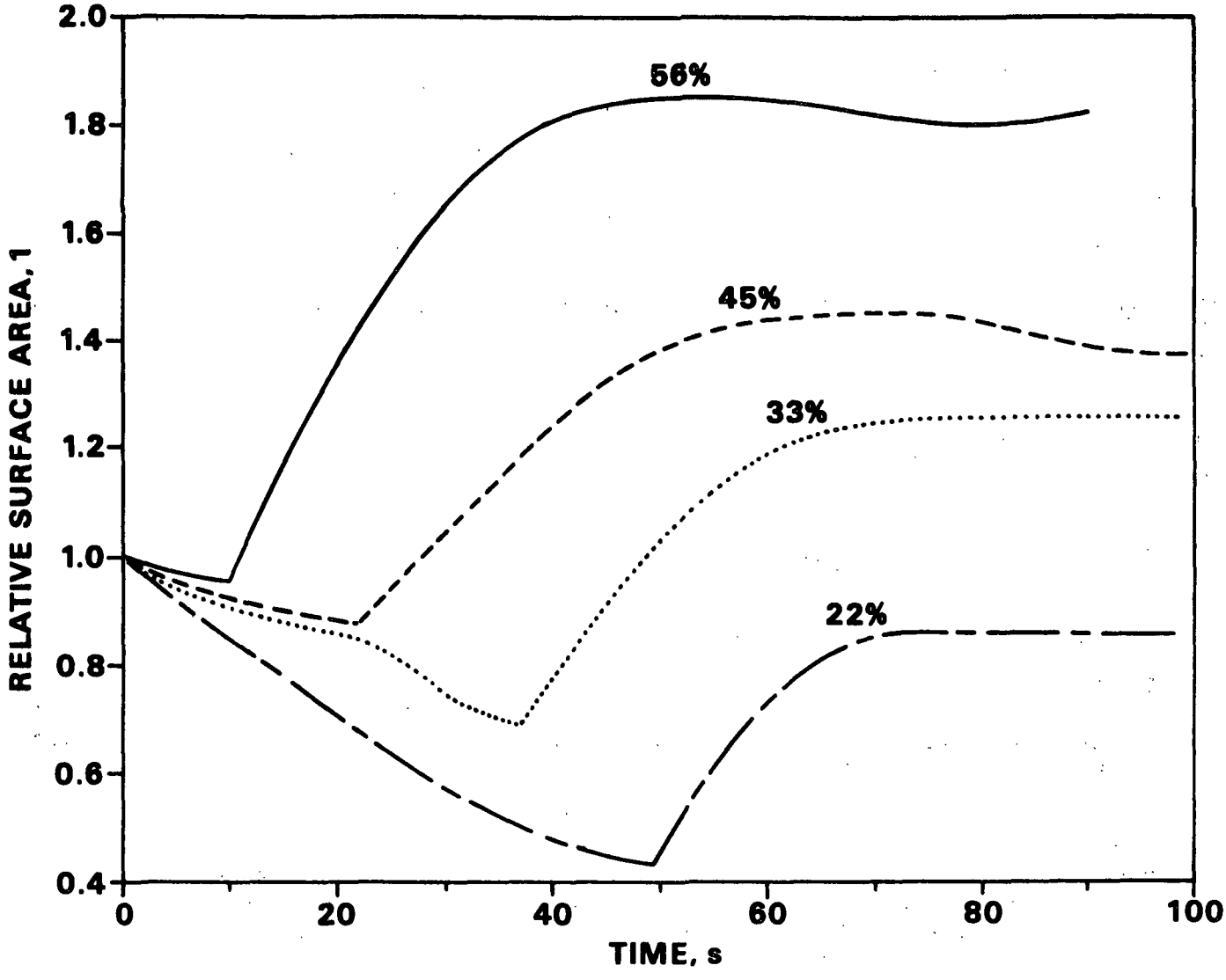

Figure 4. Average relative surface area change of black liquor drops drying in air. [D_o = 1.68 mm, T_a = 167 C, V = 1.5 m/s].

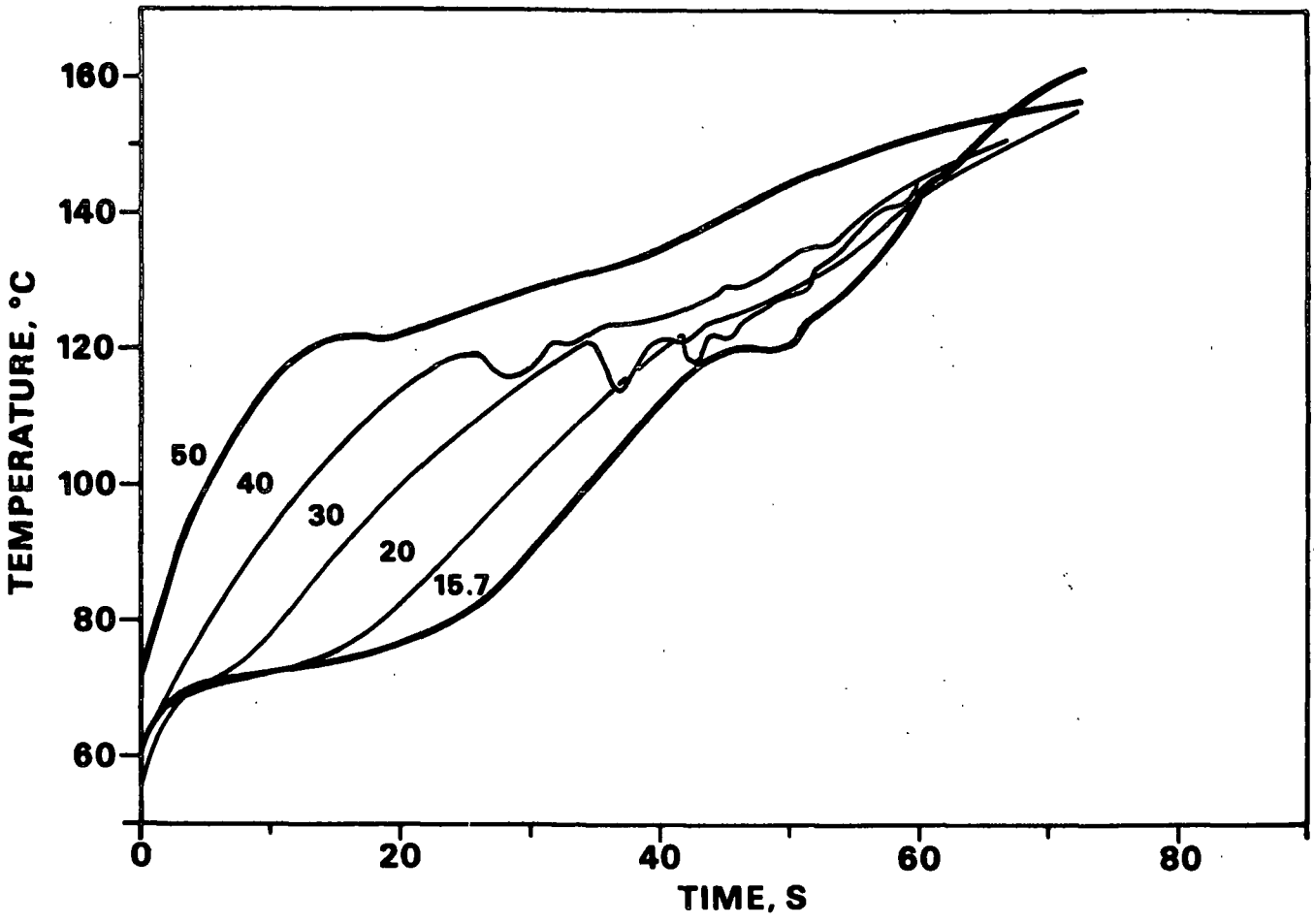

Figure 5. Temperature history of black liquor drops drying in air as recorded by internal thermocouple. Parameter is initial solids content. Bursting of drops is responsible for depressions near 120 C. [D_o = 1.68 mm, T_a = 167 C, V = 1.5 m/s].

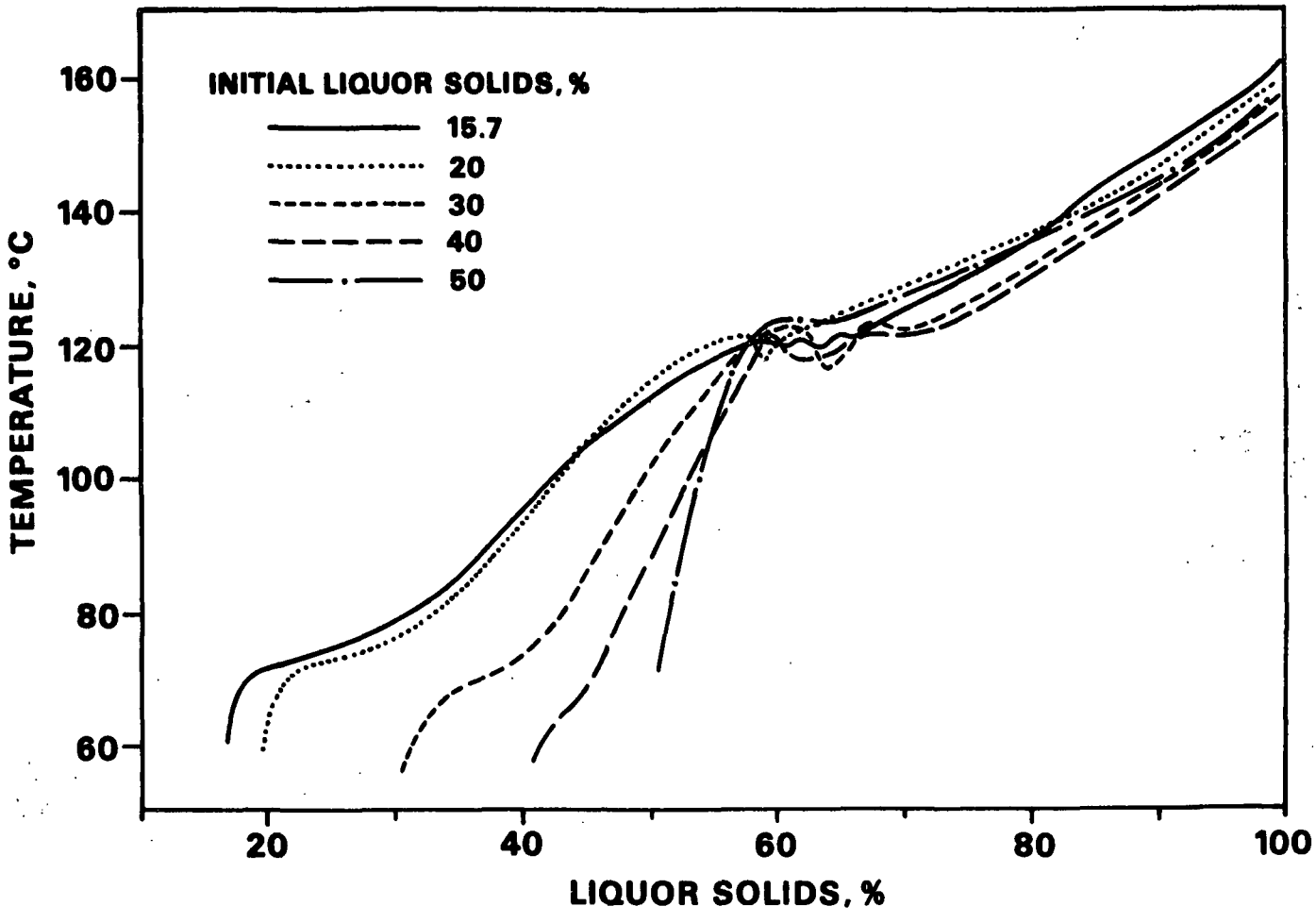

Figure 6. Temperature vs. solids history of black liquor drops drying in air as recorded by internal thermocouple. Bursting occurred near 60% solids, 120 C in all cases. [D_o = 1.68 mm, T_a = 167 C, V = 1.5 m/s].

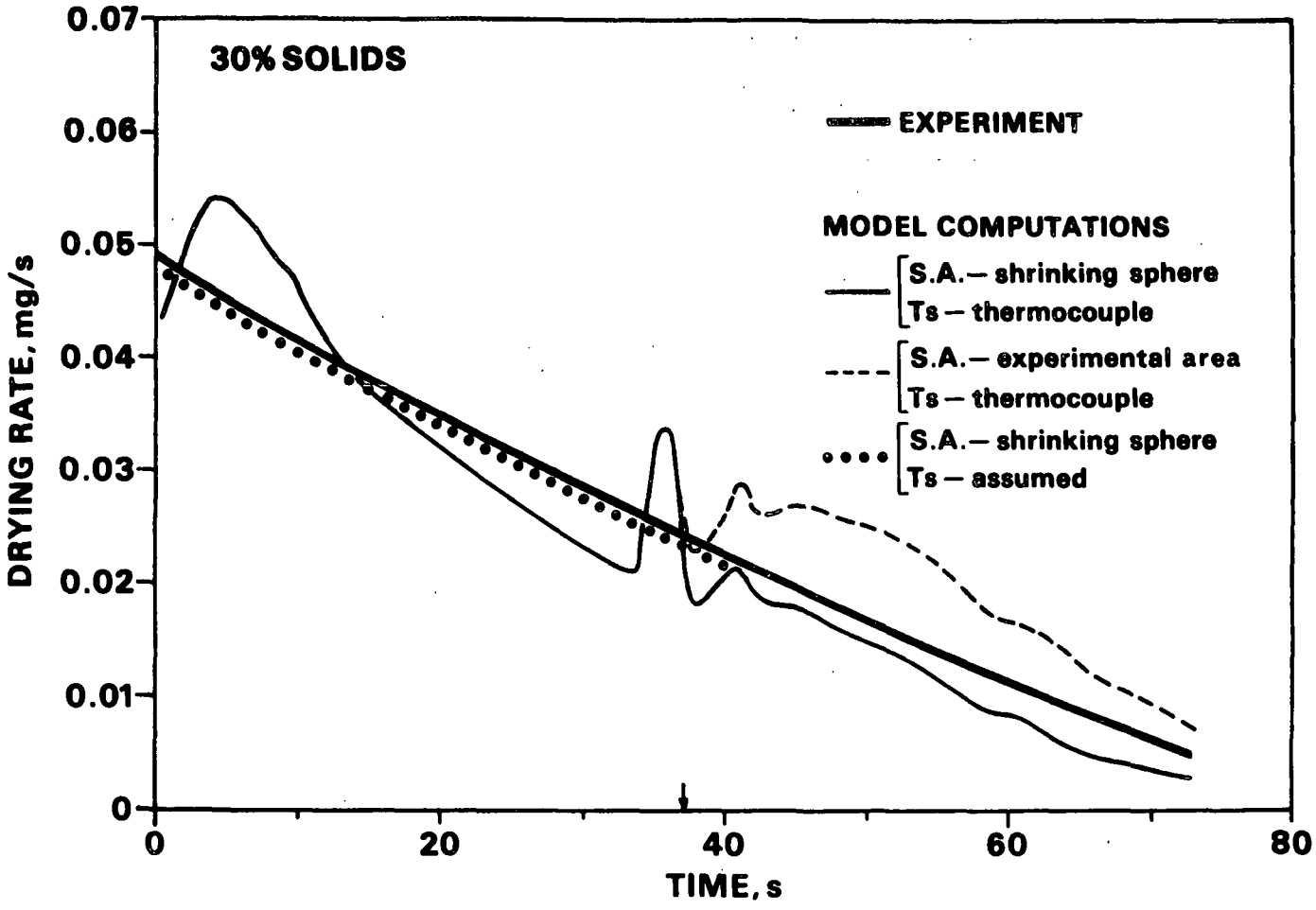

Figure 7. Experimental vs. Model Results for 30% Solids Black Liquor Dried in Air.

Comparison of black liquor drop drying rate with heat transfer model results for three surface area (S.A.) and surface temperature (T_s) input options. Initial liquor solids is 30%. The thin, solid curve results from assuming that the drop surface area decreases as a sphere in proportion to mass loss, and that the internal thermocouple measures the surface temperature. The dashed curve after the burst point (indicated by small arrow along the abscissa) results from including the experimental surface area, and assuming that the thermocouple measures the surface temperature. The dotted curve is obtained by assuming that the surface area decreases as a sphere in proportion to mass loss, and that the surface temperature increases linearly from 89.5 to 121 C at the burst point. The basis for a linear surface temperature rise is explained in the text. [Initial mass = 3.2 mg, T_a = 167 C, V = 1.5 m/s].

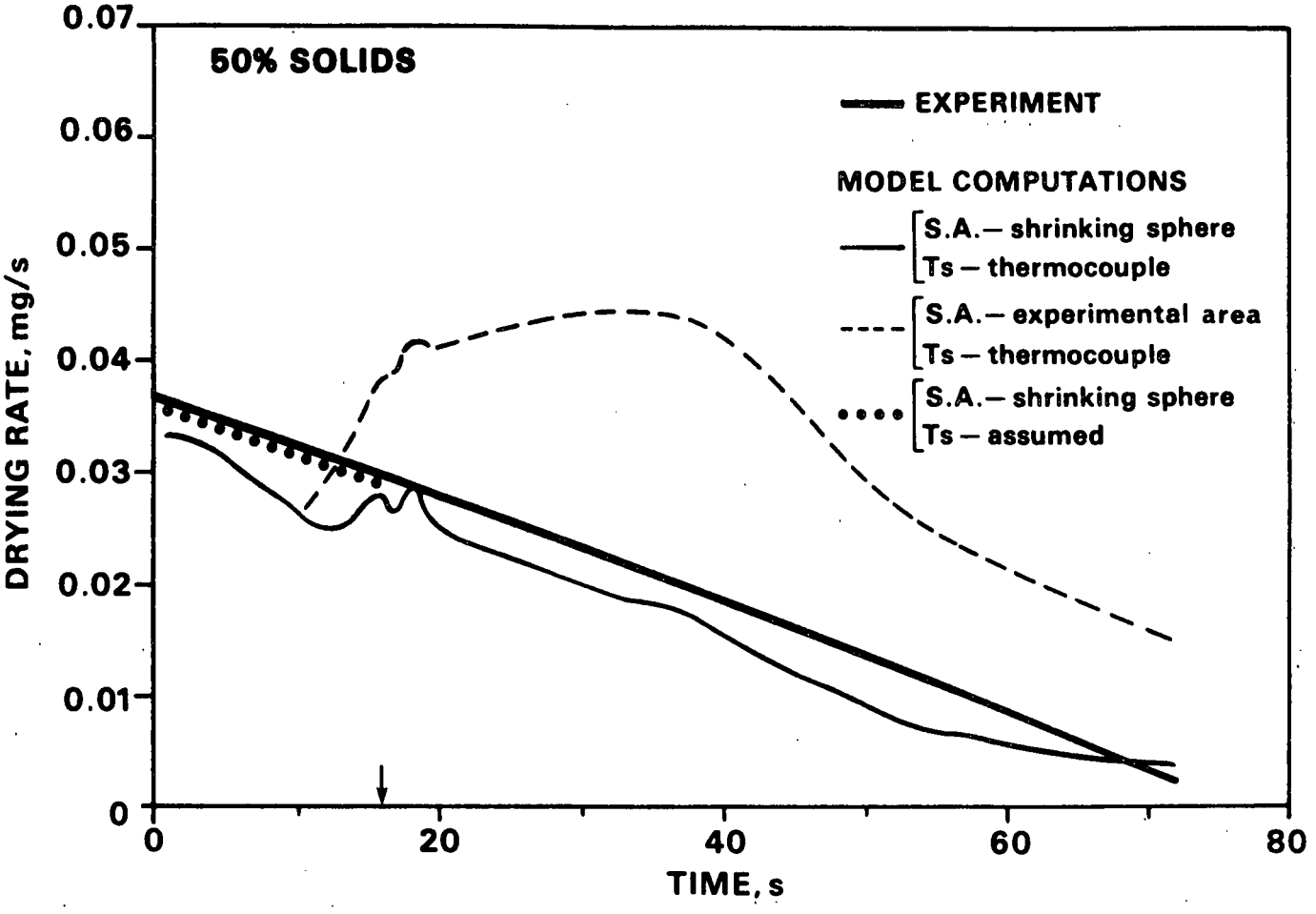

Figure 8. Experimental vs. Model Results for 50% Solids Black Liquor Dried in Air.

Comparison of black liquor drop drying rate with heat transfer model results for three surface area (S.A.) and surface temperature (T_s) input options. Initial liquor solids is 50%. The thin, solid curve results from assuming that the drop surface area decreases as a sphere in proportion to mass loss, and that the internal thermocouple measures the surface temperature. The dashed curve after the burst point (indicated by small arrow along the abscissa) results from including the experimental surface area, and assuming that the thermocouple measures the surface temperature. The dotted curve is obtained by assuming that the surface area decreases as a sphere in proportion to mass loss, and that the surface temperature increases linearly from 110 to 118 C at the burst point. The basis for a linear surface temperature rise is explained in the text. [Initial mass = 3.0 mg, T_a = 167 C, V = 1.5 m/s].

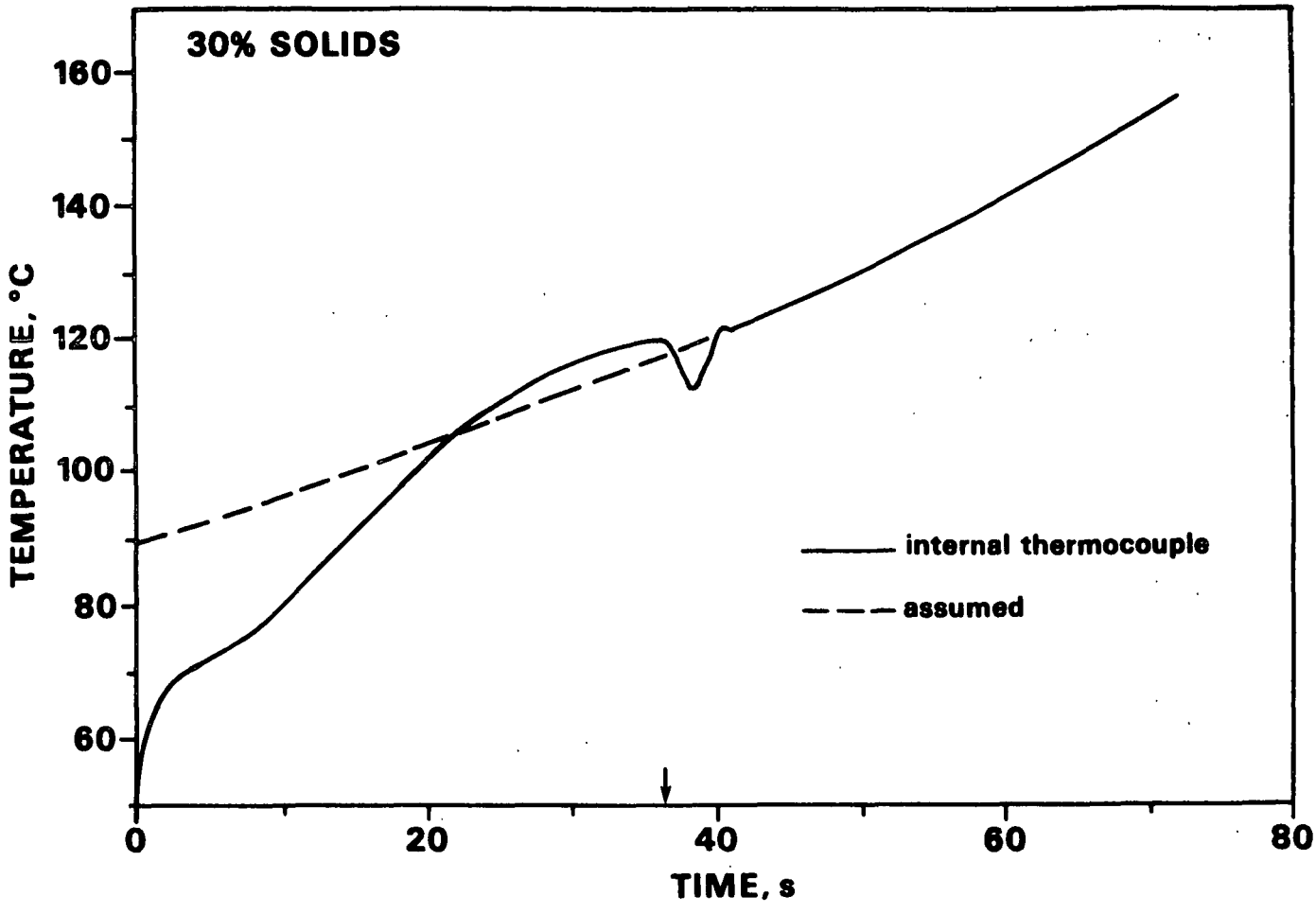

Figure 9. Comparison of drop temperature by thermocouple with assumed linear temperature profile (which caused agreement between model and experiment). [Initial liquor solids: 30%, T_a = 167 C, V = 1.5 m/s].

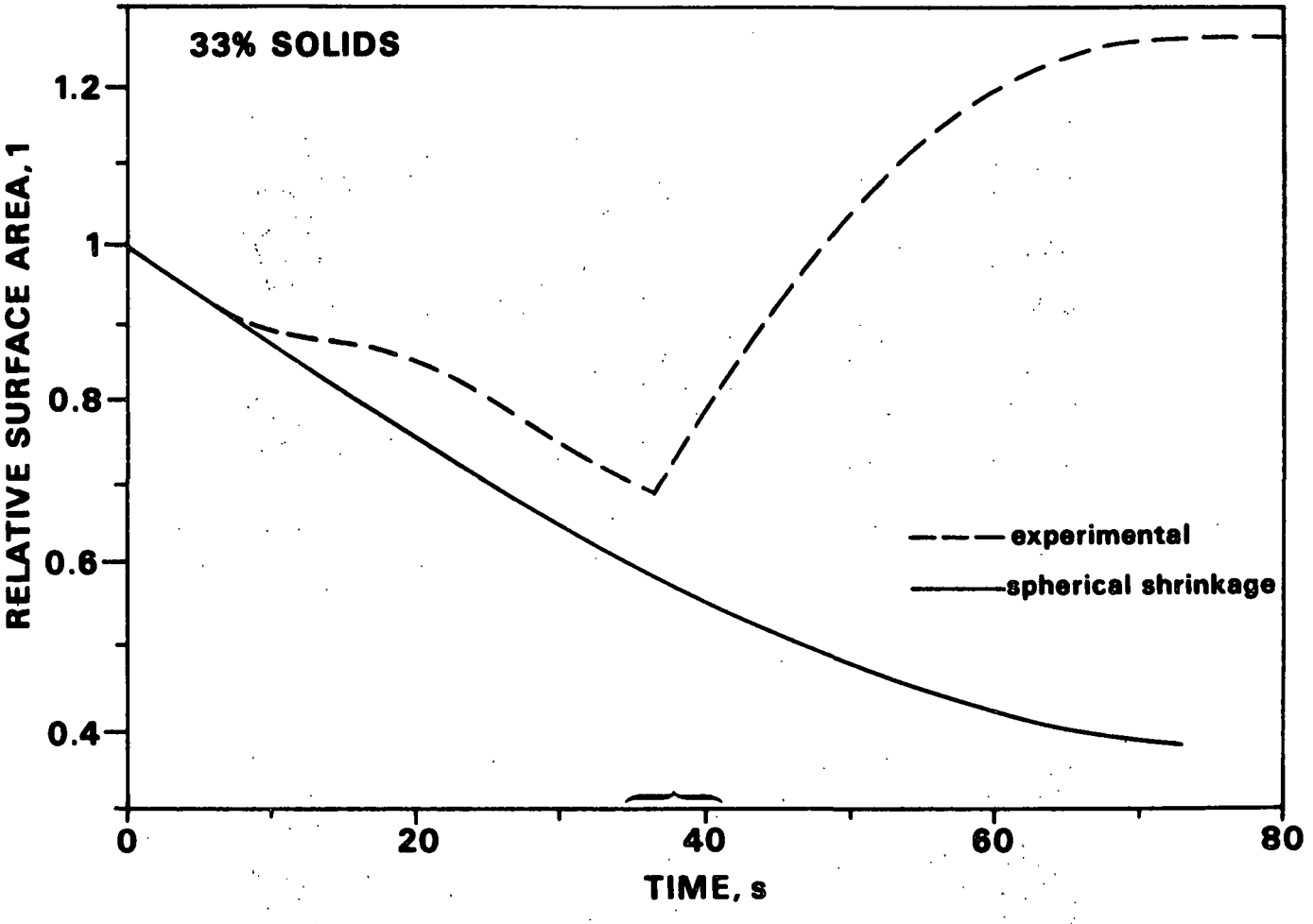

Figure 10. Average relative surface area change of a 33% initial solids drop drying in air. The solid curve illustrates spherical shrinkage proportional to mass loss. The dashed curve represents the surface area of inflated drops from video images. Bracket indicates range of times during which bursting occurred. [D_o = 1.68 mm, T_a = 167 C, V = 1.5 m/s].

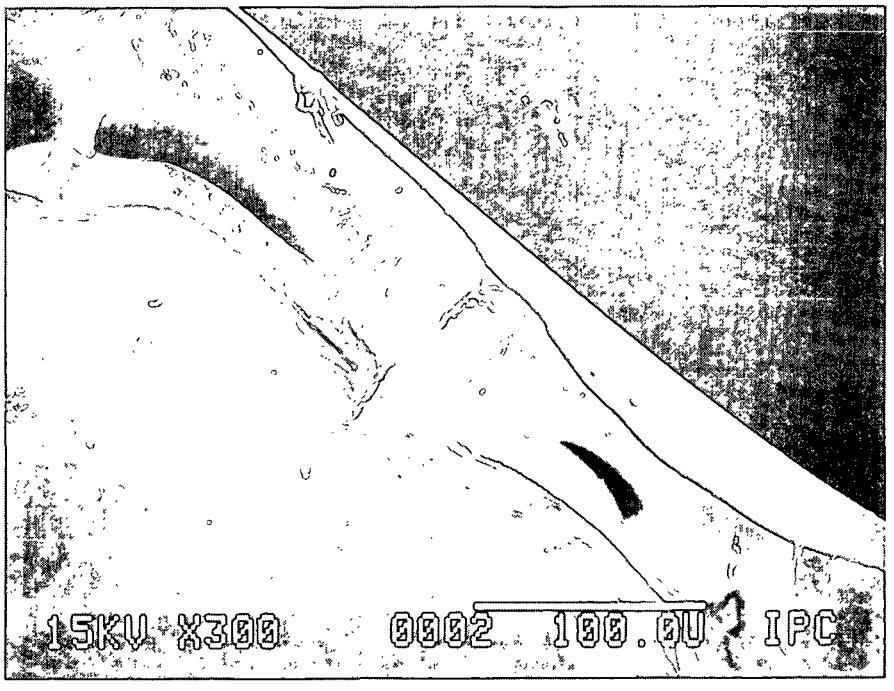

Figure 11. Scanning electron micrograph of the cross section of a hollow black liquor drop. Two vapor pockets are visible in the drop wall which runs diagonally in the figure. Initial solids was 22%. [D_o = 1.68 mm, T_a = 165 C, V = 1.5 m/s].

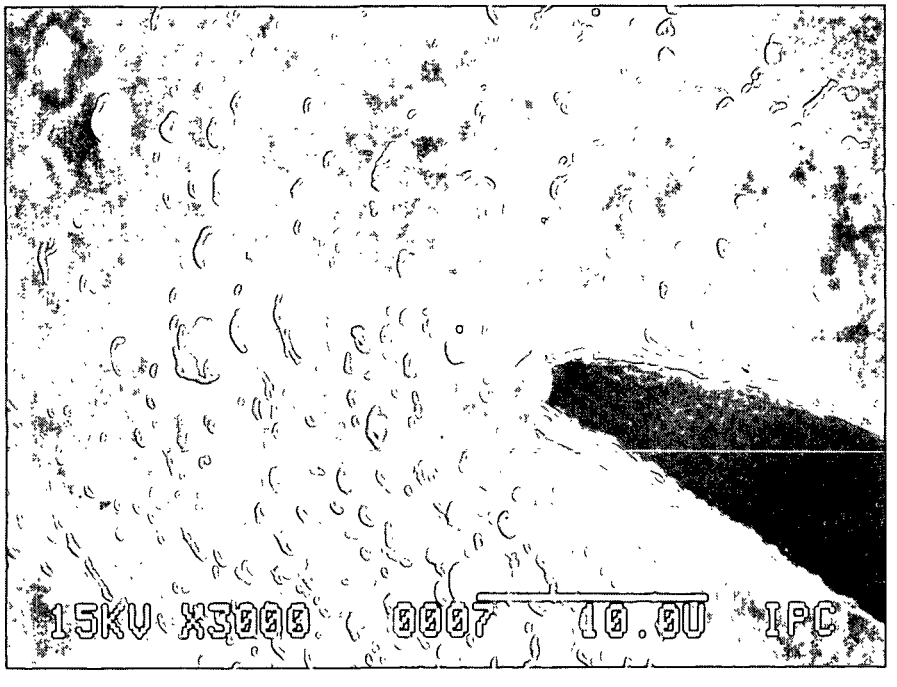

Figure 12. Enlarged view of the upper left hand corner of the smaller vapor pocket from Figure 11 showing what appear to be small bubbles surrounding the larger pocket. Coalescence of many small bubbles may be responsible for the growth of larger vapor pockets.

THE INSTITUTE OF PAPER CHEMISTRY

Appleton, Wisconsin

Status Report

to the

PULPING PROCESSES

PROJECT ADVISORY COMMITTEE

Project 3473-6

FUNDAMENTAL STUDIES OF BLACK LIQUOR COMBUSTION

(DOE FUNDED PROJECT)

September 10, 1987

PROJECT SUMMARY FORM

DATE: September 10, 1987

PROJECT NO. 3473-6: FUNDAMENTAL STUDIES OF BLACK LIQUOR COMBUSTION
(DOE FUNDED PROJECT)

PROJECT LEADER: D. T. Clay
NBS Subcontractor: Dr. H. Semerjian

STAFF: S. J. Lien, O. C. Kuehl, and D. G. Sachs

IPC GOAL:

Develop fundamental data on black liquor combustion which can be used to enhance energy efficiency and productivity of recovery boilers.

OBJECTIVES:

The three main objectives are

a) To develop laboratory scale flow reactor systems which will enable the study of both state-of-the-art and advanced recovery systems

b) To study gas phase and char bed mechanistic processes under realistic and controlled environments with advanced optical and spectroscopic techniques

c) To develop a data base which will bridge the gap between ongoing fundamental research and commercial application of the resultant findings, culminating in increased thermal efficiency, productivity, and capital effectiveness

CURRENT FISCAL YEAR BUDGET (Jan. 1, 1987 through Dec. 31, 1987):

$330,000 (Contract with DOE, OIP) ($130,000 of this is a subcontract to the National Bureau of Standards, NBS)

$150,000 remaining in DOE flow reactor system appropriation as of July 28, 1987.

SUMMARY OF RESULTS SINCE LAST REPORT:

The final draft of the second progress report will be submitted to DOE within two weeks. The report covers the period from January 1985 through January 1987. This completes the majority of work in Phase 1. A paper jointly authored by the principals at IPC and NBS will be presented at the 1987 TAPPI Engineering Conference this month. Intermediate progress reviews have been held with DOE and the ad hoc industry/academic research advisory committee at IPC in October 1986 and at NBS in July 1987.

Included with this report is a copy of the Executive Summary from the second Progress Report Draft. Also included is a copy of the paper to be presented at TAPPI. These summarize the project status and present important findings as of January 1987.

The project progress and current status is shown on the attached milestone chart. The in-flight processes work of Phase 1 is essentially complete. Testing has begun with the char bed burning furnace for Phase 2 studies. Plans are underway to install the fume deposition probe for Phase 3 work. Important aspects of this work are summarized below.

The results from all three test groups of Phase 1 show that the initial droplet size and viscosity are the dominant variables controlling the early in-flight processes. This is the first time that initial liquor viscosity has been tied directly to the burning characteristics.

Dynamic monitoring of droplet size, velocity, and trajectory have been extended to longer times in the NBS Dilute Phase Flow Reactor (DPFR). Despite immediate injection into a furnacelike environment, droplet integrity is maintained. There is, however, a significant amount of swelling (volumetric increases of 5 to 6 times) which occurs during the drying process. The expansion has a significant effect on both the velocity and the trajectory of the resulting particle.

Our findings to date imply that initial control of the droplet characteristics, especially size and viscosity, is a must if optimum recovery boiler operation is to be achieved.

A NBS two-color temperature probe has been successfully used to measure single particle burning temperatures. It is interesting to note that the highest temperatures were recorded during the char burning stage. The success of the technique has lead us to purchase one for detailed studies in this area. The specific work will be done as a part of a PhD thesis by Kathy Kulas (Crane).

The photographs and video records taken to date in the char bed burning furnace demonstrate its similarity to recovery boiler char beds. Particle impingement upon the bed, subsequent ignition and expansion, followed by collapse have been witnessed. Bed growth and burndown have been simulated via regulation of the inlet air jet.

A fume deposition probe has been fabricated. The mounting equipment necessary for installation in the bed burning furnace is complete. Preliminary tests will begin during the next char bed burning tests.

PLANNED ACTIVITY THROUGH FISCAL YEAR 1988:

Issue the second Progress Report and have the third drafted. These will complete Phase 1 and report on the initial work in Phase 2, char burning. The focus of the near term work will be on char bed burning, both process issues and instrumentation diagnostics.

Craig Brown, an Industrial Research Fellow from the Weyerhaeuser Paper Company, and Jay Hsu, a post doctoral fellow who recently completed his Ph.D. at Georgia Tech., will join the project staff. Craig will concentrate on char bed burning studies. Jay will implement an in-situ instrument for measuring fume particle size and concentration for Phase 3 studies in the flow reactor.

A major demonstration of the IPC flow reactor for DOE upper management will be held in October. The next major DOE project review meeting will be in either late winter or spring of 1988.

FUTURE ACTIVITY:

Issue the third Progress Report and have the final report drafted. Complete Phase 4 of the project. Begin to assimilate the fundamental data on this and closely related IPC projects into targeted "best applications" of the findings to commerical practice.

FUNDAMENTAL STUDIES OF BLACK LIQUOR COMBUSTION

Project Milestones

Phase	Milestone	Target	Complete
1	In-Flight Chemical Processes		
	1. Reactor preengineering	Mar '84	X
	2. Preliminary combustion experiments	Sep '84	X
	3. Phase 1 reactor detailed engineering	Dec '84	X
	4. IPC reactor central units and NBS reactor first modules installed	Jun '85	X
	5. Reactor temperature/flow/droplet characterization	Sep '85	X
	6. IPC Phase 1 reactor completely installed	Dec '85	X
	7. NBS Phase 1 reactor completely installed	Aug '86	X
	8. IPC Phase 1 reactor fully operational	Mar '86	X
	9. NBS Phase 1 reactor fully operational	Dec '86	X
	10. Process and diagnostic tests, liquid feed	Sep '86	X
	11. Process and diagnostic tests, solid feed		On hold
	12. Phase 1 Report (draft to DOE)	Dec '86	X

Phase	Milestone	Target	Complete
2	Char Bed Processes		
	1. Design of char chamber	Aug '86	X
	2. Installation of char chamber	Jan '87	X
	3. Char oxidation and reduction tests (IPC)	Oct '87	Started
	4. In-bed and above-bed diagnostics (IPC & NBS)	Nov '87	Started
	5. Phase 2 Report (Draft)	Dec '87	
3	Inorganic Fume Formation Processes		
	1. Conceptual design of fume equipment	Mar '87	X
	2. Installation of initial deposition equipment	Aug '87	X
	3. Preliminary evaluation of fume monitoring equipment (NBS)	Dec '87	
	4. Gas phase reaction tests (NBS)	Dec '87	On hold
	5. Installation of fume monitoring equipment	Apr '88	
	6. Complete evaluation of monitoring techniques (NBS)	Jun '88	
	7. Fume formation tests (IPC)	Jun '88	
	8. Phase 3 Report (Draft)	Aug '88	
4	Recovery Furnace Simulation		
	1. Process modeling concepts	Mar '88	
	2. Process variable interaction tests	Jul '88	
	3. Control strategy tests	Jul '88	
	4. Next generation (gasification) tests	Sep '88	
	5. Final report (draft)	Jun '89	

EXECUTIVE SUMMARY

(From Progress Report Two Draft to DOE)

The efficient recovery of chemicals and high level energy from black liquor contributes heavily toward the dominance of the kraft pulping process. Kraft chemical recovery boilers have been used to burn black liquor for approximately 50 years. Potential still exists, however, for significant improvements in energy recovery and black liquor throughput. This contract addresses both areas.

The identified industry-wide potential energy benefits amount to over 3×10^{13} Btu/year, an approximate value of $100,000,000/year at $\$3.25/10^6$ Btu. Since energy benefits are achieved through process condition changes, these same changes can potentially increase black liquor solids throughput. Pulp production should increase as solids throughput increases for recovery boiler bottlenecked mills. This is especially significant, since the high capital intensity of recovery boilers often results in mill production being limited by recovery boiler solids throughput. Recent practice indicates that production increases of 5% are reasonable with increases above this level being quite likely. An industry wide production increase of 5% corresponds to an approximate value of $500,000,000/year. The combustion research conducted as a part of this DOE contract seeks to provide process understanding that will assist in achieving both energy and productivity benefits.

The contract's three objectives focus on advancing kraft recovery boiler technology. First, develop test systems to study both state-of-art and advanced recovery processes. Second, apply advanced optical and spectroscopic techniques to study the burning processes. Third, develop a data base of process fundamentals which will bridge and enhance prior research findings and their commercial application.

The recovery processes of interest include all those that occur within the recovery boiler. The four burning stages of drying, volatiles burning, char burning, and smelt coalescence are being studied under flowing conditions. Where necessary, this work is supplemented with single particle studies. There are

two distinctive conditions for the flow reactor work. First, reacting particles in flight from liquor injection to the char bed. Second, reacting particles on or within a char bed. These two conditions form the basis for the first two phases of the contract. The last two phases focus specifically on fume processes (both formation and deposition) and simultaneous study of all process steps.

The four phases are specifically:

Phase 1. In-flight chemical and thermal processes
Phase 2. Char bed processes
Phase 3. Inorganic fume formation processes
Phase 4. Recovery furnace simulation

Progress Report 1 (Clay, et al., 1985) reported on the first year of work, the initial part of Phase 1. This report covers the second and third year of the contract. During this time most of Phase 1 was completed and Phase 2 was begun. The remaining Phases of the five year contract are scheduled for completion by September 1988.

Two continuous laboratory-scale flow reactor systems, one at The Institute of Paper Chemistry (IPC) and one at the National Bureau of Standards (NBS), have been operational for most of the last two years. They successfully simulate the in-flight process conditions of interest for Phase 1 tests. A char bed burning furnace has been designed and will be added to the IPC system for Phase 2 studies next year. Instrumentation will be developed by NBS, and subsequently added to the IPC system during Phases 3 and 4, the last year of the contract.

The NBS system, short-height Dilute Phase Flow Reactor (DPFR), is used to study dynamic behavior of falling single droplets of black liquor in varying thermal environments. These have been the first studies to measure velocity and swelling of free falling black liquor droplets in hot environments. Similar tests with the full height of the DPFR will be made in the coming year. Successful development of a droplet injector for black liquor at high temperatures during this report by NBS was essential for both the NBS and the IPC systems. NBS also used a previously developed two-color optical pyrometer to dynamically measure the temperature of a burning single droplet of kraft black liquor.

The IPC flow reactor system is used to study overall process performance with streams of black liquor droplets. Three main test groups have been completed to date. Their overall objective was to evaluate the impact of process variable changes on the chemical and physical characteristics of forming char particles. In addition, droplet drying studies have been completed. These studies are the first to obtain data on intermediate free-falling black liquor droplets as they dry and begin to burn in a hot environment.

To date, both the IPC and NBS systems have been tested in only the gas upflow mode. The remaining Phase 1 tests in the IPC system will be in the gas downflow mode. Single particle pyrolysis and burning tests were also done at IPC to characterize liquor performance via IPC developed tests.

The detailed test results of both groups are contained in Progress Report 2. The project testing to date coupled with supportive research at IPC has begun to expand our knowledge of early in-flight burning of kraft black liquor. A summary of this understanding, at present limited to a specific drop size range (2-4 mm) and the mill liquor tested, is given below.

The early stages of black liquor burning, for conditions similar to recovery furnaces, are dominated by the influence of black liquor droplet characteristics. Heat transfer to and through the droplet is the controlling phenomenon. The three most dominant effects are initial size, initial solids content, and initial viscosity. During drying the droplet swells and collapses in rapid succession, expanding its surface area and mixing the droplet contents. The extent of swelling and the mixing determine the ability of the droplet to absorb heat.

When the droplet viscosity is increased a reduction in swelling and mixing occurs reducing the heat flux to the droplet core. Since the heat flux to the droplet by the environment is initially unchanged the surface temperature will rise. Increasing surface temperature then reduces the heat flux to the droplet. The temperature gradient through the particle will increase. This situation effectively stops rapid drying of the liquor droplet above solids levels of approximately 90-95%. The surface progresses into the volatiles burning stage while the inner core is still drying.

A reduction in initial liquor viscosity improves inner droplet heat transfer, reduces inner droplet temperature gradient, and reaches higher moisture levels before surface burning. The influence of size is analogous to viscosity, with larger droplets developing larger temperature gradients. The influence of solids is first through viscosity, since they are exponentially related. Solids are, however, directly related to the extent of drying. Higher initial solids give products with lower moisture contents.

When the surface temperature of the droplets exceeds approximately 400°F (210°C), thermal degradation (pyrolysis) of the solids will become significant. The gaseous decomposition products will mainly be CO, CO_2, H_2O, hydrocarbons, and reduced sulfur compounds. The solid product will be highly aromatic char carbon, Na_2CO_3, and sodium salts of sulfur in various oxidation states. During pyrolysis the particle undergoes permanent swelling as the generated gases expand the pliable pyrolyzing solids. The outer surface can then rapidly increase in temperature, reaching and exceeding the melting point of the inorganics.

The droplet initial size and viscosity will affect the burning pattern in the early part of the volatiles burning stage. With increasing size or viscosity the outer surface can be fully molten while the inner core is still undergoing pyrolysis. If the particle remains intact while in flight, then pyrolysis gases will contact the molten outer surface. Such a condition is viewed favorably since a major portion of the reduced sulfur gases would react and be retained in the droplet.

The direct link between drying/burning characteristics and initial liquor size and viscosity is extremely important. Droplet size and the viscosity can be controlled as a part of the recovery operations directly at the nozzle. The opportunity therefore exists for on-line control of the initial burning processes. Our work to date further shows that unless these two black liquor characteristics are controlled, optimum furnace control cannot be achieved.

Near-term efforts at IPC will focus on installation of the bed burning furnace and operation of the in-flight section in the downflow gas mode. Testing for Phase 2 will begin. NBS will complete start-up of the full-height DPFR and collect velocity and diameter data at longer residence times. The third progess report will cover this work plus the initiation of Phase 3 work.

BLACK LIQUOR COMBUSTION IN A LABORATORY FLOW REACTOR - STATUS REPORT ONE

D. T. Clay,
Associate Professor
The Institute of
Paper Chemistry
P.O. Box 1039
Appleton, WI 54912

H. G. Semerjian
Group Leader
A. Macek
Research Chemist
National Bureau of Standards
Gaithersburg,MD, 20899

ABSTRACT

The Office of Industrial Programs, U.S. Department of Energy, funds a 5-year research effort at IPC and NBS to study fundamentals of kraft black liquor combustion. Two complementary flow reactor systems, one for process and the other for dilute-phase studies, are now in place. Mill kraft black liquor droplets, nominally 2 mm at up to 68% solids, are continuously fed into simulated furnace environments. These systems have been used to study early in-flight process dynamics, char formation processes, and the physical and chemical characteristics of char and its precursors. This paper discusses significant results to date and summarizes the project's future direction.

INTRODUCTION

The efficient recovery of chemicals and high level energy from black liquor contributes heavily toward the dominance of the kraft pulping process. Kraft pulp represents 74% of North American market pulps (1). Kraft recovery boilers used to burn black liquor have been commercially available for over 50 years. Since the basic process knowledge is only now being developed, the potential exists for significant improvements in energy recovery and black liquor throughput (2,3).

A relatively conservative estimate of the potential improvements results in energy savings of 5×10^5 Btu/adtp and an incremental production increase of 1%. These are equivalent to nominally $200,000,000/yr for the industry (4). Advances to achieve these and hopefully higher benefits can only be done with a fundamental knowledge of the controlling combustion phenomena. Once the controlling phenomena are identified, recovery boilers can be pushed to their ultimate acceptable limits. In practice, the results will also be a starting point for design of equipment, e.g., improved liquor and air delivery systems, to reach and hopefully raise these limits.

The importance of process fundamentals was identified in the American Paper Institute sponsored work of Merriam (5). Two books (6,7) also identify this need. Recent advances have been made to understand kraft black liquor combustion with molten salt and single particle studies (8-13). Four stages of black liquor burning are identified: drying, volatiles burning, char burning, and smelt coalescence. Additional understanding in each one of these stages is needed for application to continuous flowing systems. The increased knowledge should provide a bridge for application of prior or new results to commercial recovery boilers.

The Office of Industrial Programs, U.S. Department of Energy, and The Institute of Paper Chemistry sponsor a project to obtain fundamental data on black liquor combustion. The project began in October 1983 and extends for five years. The three objectives of the project focus on advancing kraft recovery boiler process understanding:

a) Develop continuous flow systems to study both state-of-the-art and advanced recovery processes.
b) Apply advanced optical and spectroscopic techniques to study the burning processes.
c) Develop a data base of process fundamentals which will bridge and enhance the commercial application of prior and new research findings.

These objectives will be accomplished in four phases. These are:

Phase 1. In-flight chemical and thermal processes
Phase 2. Char bed processes
Phase 3. Inorganic fume formation processes
Phase 4. Recovery furnace simulation

Two continuous laboratory scale systems, one at The Institute of Paper Chemistry (IPC) and one at the National Bureau of Standards (NBS), provide the equipment to study the burning processes. The IPC system is used for overall process studies and complete furnace simulation. The NBS dilute-phase system is for instrumentation development and single particle tests.

The work to date has focused on Phase 1, in-flight chemical and thermal processes. The emerging view is that initial liquor characteristics, specifically the droplet size, viscosity and swelling tendency, are major variables affecting both the initial burning processes and particle trajectory. Projects which seek to increase recovery boiler performance need to address these critical issues. This paper will discuss results that lead to this conclusion, the two experimental systems, and future direction of the project.

EXPERIMENTAL

IPC Flow Reactor

Process studies which emphasize the chemical composition of solid, liquid, and/or gaseous products are the focus of the IPC Process Flow Reactor System. Figure 1 shows a schematic of the flow reactor system. Electrical preheaters bring the air, nitrogen, or a mixture of the two to the desired temperature before entry into the reactor base.

The inner fused alumina lining is nominally 4-inch (100 mm) I.D. The entire nominal 14 ft (4.3 m) length of the in-flight section is encased with cylindrical electrical heaters. The gas temperature stays approximately constant over this length. The first and second progress reports to DOE list the system details (4,14).

The Phase 1 system provides for continuous feeding of black liquor droplets at realistic droplet injection temperatures. In this configuration, continuous operation can be achieved within four hours.

All tests covered in this paper were in the gas upflow mode. Table 1 lists nominal test conditions for the results discussed below. Actual operating ranges are wider.

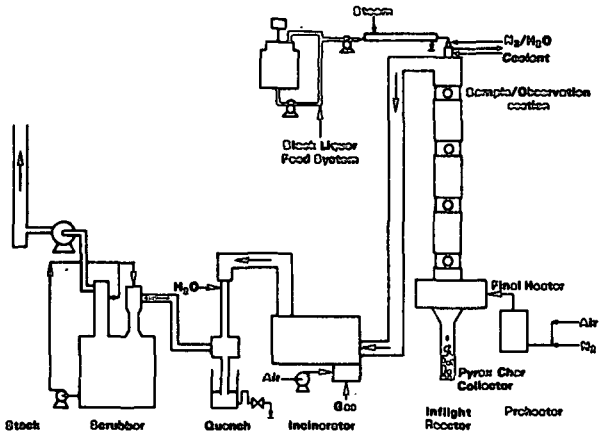

Fig. 1. Upflow mode of IPC Phase 1 system.

Table 1. Test group 1 nominal conditions for the IPC reactor system.

Black Liquor Feed	Flow	1.3 lb solids/h (15 g liquor/min)
	Temperature	200 to 240°F (93 to 115°C)
	Solids	65%
	Droplet size	nominally 2mm
Gas Characteristics	Flow rate	4 scfm (113 std. Lpm)
	Velocity	3 ft/sec (1 m/sec)
	Temperature	1615°F (880°C)
	Oxygen	0 to 21%
Longest Sustained Operating Period	6 hours with liquor feed 10 hours including times without liquor feeding	

NBS Short-Height DPFR

Measurement of size and velocity on free-falling single droplets/particles has been the initial diagnostic work with the short-height dilute-phase flow reactor (DPFR) at NBS. Figure 2 shows a schematic representation of the system. The vertically positioned quartz tube is 4-inch I.D. The system construction details have previously been listed (4).

Hot gases, having the desired temperature and free-oxygen concentration are admitted through the bottom section. Combustion products of a premixed propane/air flame are diluted with the required amount of air or nitrogen. Black liquor droplets form on the tip of the injector at the top of the reactor. The nominal length of droplet fall is 30 inches (760 mm). Since the quartz section is not insulated there is a nominal temperature gradient from top to bottom of 20°F/inch (440°C/m).

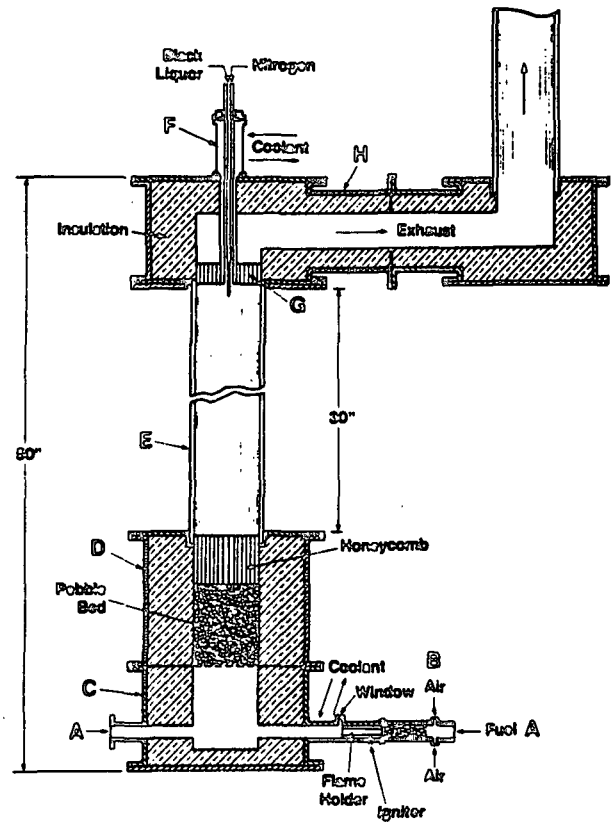

Fig. 2. Dilute phase flow reactor (short-height). A. Dilution air inlet. B. Gas burner. C. Mixing Chamber. D. Flow straightener. E. Quartz tube. F. Droplet injector. G. Flow straightener. H. Exit section.

The operating conditions used in the tests to be discussed below are shown in Table 2.

Table 2. Nominal test conditions for the NBS short-height DPFR.

Black Liquor Feed	Flow	one drop at a time
	Temperature	nominal 195°F (90°C)
	Solids	65%
	Droplet size	nominally 2mm
Gas Characteristics	Flow rate	7 to 16 scfm (200 to 450 std. Lpm)
	Velocities	5 to 14 ft/sec (1.5 to 4.3 m/sec)
	Temperatures	2100 to 1340°F (1150 to 725°C)
	Oxygen	1.5 to 21%

Black Liquor

The black liquor samples used for all the tests reported in this paper came from a north central kraft mill. Normal mill furnish is 57% hardwood and 43% softwood. Continuous digestors are used to cook to a kappa number of 16. Liquor oxidation is practiced at this mill. Samples were collected after the evaporators and after the mix tank near

the recovery boiler. The analysis will be presented in Table 4.

IPC PROCESS STUDIES

Preliminary tests suggested that particle residence times were nominally 1.5 seconds. This is sufficient time to essentially complete drying and initiate the char forming processes. The dynamic increase in specific swollen volume was the major reason for longer residence times than those previously anticipated (4). The influence of upward flowing N_2 was minimal. The early in-flight processes appear dominated by heat transfer to the particle as it dries and pyrolyzes. Virtually all particles impacted the wall. Most bounced off after a short contact time with the wall. The extent of wall impact and subsequent retention depended upon conditions. When the air flow was 4 scfm (113 std. Lpm) or less and the temperature was above 1525°F (830°C) the majority of particles hit but did not stick on the walls.

Approach

The systematic study of the in-flight processes began by studying the influence of six process variables on the chemical and physical characteristics of the produced chars. Three test groups were planned to study two variables each. The variables and their groups were gas phase O_2 content and liquor temperature, gas flow rate and temperature, particle size and liquor solids content. This paper summarizes the results of the first test group.

The objective of test group 1 was to evaluate the effect of gas phase O_2 content and black liquor injection temperature on the chemical and physical properties of the produced chars. A complete factorial with three levels for each variable plus two replicates was planned.

The base operating conditions for the reactor were listed in Table 1. The level for the two variables plus the variation in liquor solids is listed in Table 3.

Table 3. Group 1 test independent variable levels.

Test	Oxygen, % volume	Temperature of Liquor (°F)	(°C)	Feed Solids, % ODS
47	0	199	93	67.4
50	0	207	97	64.8
51	21	200	94	64.8
52	0	215	102	64.0
53	21	217	103	64.0
54	21	217	103	64.0
56	10	221	105	64.0
57	10	239	115	64.0
58	10	203	95	64.0
59	21	219	104	64.0
60	21	241	116	63.6

ODS - Oven dried at 221°F (105°C).

The O_2 level was set by either using N_2, air, or a quantitative blend of the two. The average O_2 level for the 10% and 21% inlet cases was slightly less due to partial combustion. There was some air infiltration due to the slight negative pressure in the reactor and hence, at the 0% O_2 level, some O_2 probably existed. The liquor temperature is the exit injector coolant temperature adjacent to the black liquor feed. The solids variations occurred because of slight water leaks into the liquor supply between tests.

Results

The average and range of the chemical and physical char characteristics produced in the IPC process tests are listed in Table 4. The properties of the initial liquor are also listed for comparison.

Table 4. Average physical and chemical properties of test group 1 product chars.

	Feed Liquor No. 41A	Product Char Average ± 95% CL*	Range
Fixed carbon, % ODS**	0	4.42 ± 1.41	2.65-10.27
Moisture, % ODS	64.4 ± 0.7	1.53 ± 0.45	0.55-2.71
Swollen volume, cc/g-solid	Approx. 1.2	9.8 ± 2.2	4.2-16
Bulk density, g/L	1300	83 ± 17	27-113
Elements (All values, % ODS)			
C	35.7	31.3 ± 1	27.4-33.0
H	3.25	2.59 ± 0.22	1.85-3.10
O	34.3	35.5 ± 0.4	34.5-36.4
S	4.56	4.5 ± 0.3	3.8-5.2
Na	19.8	22.3 ± 0.8	20.2-24.6
K	1.4	2.93 ± 0.12	2.74-3.28
Material balance, %	99	98.5 ± 0.8	96.8-100
Na_2CO_3	7.97	27.8 ± 3.3	22.8-38.0
Na_2SO_4	5.87	8.08 ± 1.11	6.71-11.7
Na_2SO_3	0.96	1.66 ± 0.38	1.01-2.80
$Na_2S_2O_3$	8.19	4.64 ± 0.54	3.27-5.71
Na_2S	0	0.85 ± 0.41	0.14-2.15

*CL - confidence limits.
**ODS - oven dried solids at 221°F (105°C).

Comparison of these data with equilibrium pyrolysis of single particles of the same liquor show that the char is only partially pyrolyzed. It is also interesting to note that moisture still remains in the char even though pyrolysis has begun. This is a good indication that particle temperature gradients exist and that there is overlapping of the burning stages.

Despite the fact that pyrolysis was only partially complete, substantial sustained swelling occurred. The swollen volume increased on average over 8 times and the char bulk density decreased over 15 times. The factors controlling the swelling process (10,11) appear to be mainly operable during the latter phases of drying and the early phases of pyrolysis.

Most of the chemical shifts were as expected. Table 5 lists the percent change of the major components. Based on the change in Na the average solids mass loss was 11%. The major elements lost were C, H, O, and S.

Table 5. Average percent change in chemical components during char forming processes of test group.

	Average ± 95% CL*	Range
Carbon loss, %	22.2 ± 4.9	9.3-33.8
Hydrogen loss, %	33.2 ± 7.6	12.6-46.5
Oxygen loss, %	11.2 ± 3.3	2.0-20.5
Sulfur loss, %	11.9 ± 6.3	0.1-32.8
$Na_2S_2O_3$ loss, %	49.2 ± 7.2	34.6-67.9
Na_2CO_3 gain, %	208 ± 27	170-288
Na_2SO_4 gain, %	23.2 ± 14.7	-1.7-71.9
Na_2SO_3 gain, %	52.7 ± 32	3.1-151
S=/S, %	7.7 ± 3.7	1.5-20.0
FC/C, %	12.7 ± 4.4	7.2-31.7

*CL - confidence limits.

It is interesting to note that there is on average a higher carbon loss than sulfur loss. The tested liquor is an oxidized liquor. A substantial percentage (70%) of the sulfur is as $Na_2S_2O_3$. Sodium thiosulfate showed a 50% loss during these tests. It decomposes rapidly at relatively low temperatures. Literature data (15) support decomposition to Na_2SO_4, Na_2S, and elemental sulfur at temperatures from 433 to 878°F (225 to 470°C). The present data support the reaction products. Note that Na_2S was in the product char. In the cooler regions of the reactor, yellow deposits presumed to be sulfur were found during an inspection following these tests.

The low mass loss, sulfur loss, fixed carbon values, and visual observations support the hypothesis that only relatively low particle temperatures were achieved. Sulfide formation and elemental sulfur release via $Na_2S_2O_3$ decomposition is one of the early in-flight sulfur release processes in the particles.

During these 11 tests the feed solids changed from 67.4 to 63.6%. Feed solids content effectively became a third independent variable. Unfortunately, the unplanned variation in feed solids had a significant trend with liquor temperature. Higher feed solids were present when higher liquor temperatures were tested. This trend makes it difficult to separate the two variables.

Significant effects of the three independent variables on char characteristics were identified with Student's t-test (16). Single and multiple dependencies were tested. The relationships which were significant at the 95% level (t-values > 2.2) are listed in Table 6. Larger t-values imply a higher degree of significance.

The listed t-values are for the single independent variables' relationship with the char characteristic. No multiple relationships were significant.

Table 6. Char characteristics which had a significant relationship with one of the three independent variables.

Char Characteristic	Indep. Variable	t-value*
Swollen volume	Liquor temperature	+2.3
	Feed liquor solids	-2.4
Swollen volume confidence limits	Liquor temperature	+2.7
	Feed liquor solids	-2.9
C/Na_2 percent loss	Liquor temperature	+2.2
CO_3/Na_2 percent gain	Gas phase O_2 level	-2.2
SO_4/Na_2 percent gain	Feed liquor solids	+4.5
SO_3/Na_2 percent gain	Feed liquor solids	+4.2
	Liquor temperature	-2.6
S_2O_3/S percent in char	Liquor temperature	+2.2

*Based on Student's t distribution.

Increased liquor temperature produced larger and more variable swollen volumes, greater carbon loss, less Na_2SO_3 in the char and a higher percentage of the char S as $Na_2S_2O_3$.

Lower liquor solids produced higher and more variable swollen volumes, and less Na_2SO_4 and Na_2SO_3 in the char. As noted above, variations caused by feed solids and liquor temperature may not be completely separable. Fortuitously, the direction of both consistently changes the liquor viscosity, so that at least cancelling effects should not be present.

Lower O_2 levels produced higher Na_2CO_3 levels in the char. It should be noted that the other char analyses had no significant relationship with the three variables.

The changing environment that the particle encounters in the reactor produces significant dynamic changes in its physical as well as its chemical character. The initial results of NBS document these changes.

NBS SIEGLE PARTICLE STUDIES

Approach

In-flight studies of black liquor droplets/particles were done with a high-speed camera, 500 frames per second. The field viewed by the camera was 3.9 inches (100 mm) horizontal by 3.2 inches (80 mm) vertical. Three sets of determinations were made at three locations in the short-height DPFR; top, center, and near the bottom. The initial droplet diameter was determined via a permanently mounted video camera.

To obtain in-flight droplet diameter and velocity a standard reference length is filmed, along

with the droplets, from which a magnification factor is calculated. The droplet velocity is obtained by counting the number of frames of film used by the particle to move over a certain known distance.

Droplet/particle velocity calculations were also made. A computer program calculates particle velocities and distances from the injection point by balancing the gravitational force against buoyant and drag forces due to upward gas flow. Since the calculated velocities are very weak functions of temperature, all calculations were made for gas temperatures of 1560°F (850°C) with virtually no sacrifice of accuracy.

Results

Top of DPFR

The main purpose of high-speed photography, in this section of the reactor, was (a) to observe the process of detachment from the needle and initial trajectories of black liquor droplets, and (b) to measure their velocities. The top of the DPFR is defined as the first 2.8 inches (70 mm) below the injection point.

The process of black liquor droplet detachment from the needle is abrupt. No lingering droplet tails formed. This is advantageous, because it decreases the chances of droplet drying and distortion before detachment. The droplets became spherical immediately after detachment. Finally, the initial droplet trajectories were vertical.

The droplet started at zero velocity and showed rapid acceleration over the viewed segment. The experimental velocities given in Table 7 are the final values before the disappearance of the droplet from the field of view.

Table 7. Velocities at the top of DPFR.

d, mm	U_g	U_p (exp)	U_s (exp)	U_s (calc)	U_t (calc)
1.7	4.36 (1.33)	4.00 (1.22)	8.36 (2.55)	7.93 (2.42)	29.2 (8.91)
2.1	5.15 (1.57)	3.54 (1.08)	8.69 (2.65)	8.75 (2.67)	36.1 (11.00)

Velocity Units, ft/sec (m/sec).
exp = experimental calc = calculated.

U_g - upward gas velocity from measured volumetric rates and local temperature.
U_p - particle velocity relative to laboratory coordinates.
U_s - particle velocity relative to gas (slip velocity).
U_t = particle terminal velocity relative to gas.

The agreement between the experimental and calculated U_s values is good. Table 7 also gives the computed terminal (settling) velocity, U_t, which U_s would approach at long times if the droplet remained physically unchanged. The droplets are still accelerating in the top of the DPFR. Another aspect of the experimental and calculated results in the top of DPFR is that they give a good definition of initial conditions. The nominal residence time from injection to leaving this field of view was 0.10 second.

Center of DPFR

The camera was centered at 16 inches (400 mm) below the injector. At this height there is not one-to-one correspondence between the droplets at injection and droplet/particles measured by high-speed films. The procedure adopted in these studies was to relate the properties of droplets/particles observed by high-speed photography (shapes, sizes, and velocities) to average initial diameters from VCR measurements. Most falling particles were still nearly spherical and were almost always falling vertically near the center of the reactor. Moderate expansion of particles was observed. This implies density decreases. In addition, there may or may not have been mass losses due to vaporization.

Table 8 gives the data for four individual particles at a fixed set of test conditions. The format is similar to that in Table 7, with two differences. First, the ratio d/d_o is given, because it is a parameter necessary for calculation of velocities. The second difference, also due to the lack of continuous recording, is that the calculation of U_s is not straightforward, but requires some assumptions, as discussed below.

Table 8. Velocities at the center of the DPFR.

	Experimental			Calculation A		Calculation B	
	d/do	U_p	U_s	U_s	U_t	U_s	U_t
	1.6	6.92 (2.11)	16.9 (5.16)	15.0 (4.57)	16.8 (5.11)	12.7 (3.88)	12.4 (3.79)
	1.4	7.25 (2.21)	17.2 (5.26)	15.7 (4.78)	19.0 (5.81)	14.1 (4.31)	14.1 (4.31)
	1.6	6.92 (2.11)	16.9 (5.16)	15.0 (4.57)	16.8 (5.11)	12.7 (3.88)	12.4 (3.79)
	1.6	7.25 (2.21)	17.2 (5.26)	15.0 (4.57)	16.8 (5.11)	12.7 (3.88)	12.4 (3.79)
Average:	1.55	7.02 (2.14)	17.1 (5.21)	15.1 (4.62)	17.3 (5.28)		12.8 (3.92)

Velocity units = ft/sec (m/sec).

Calculation A - no drying assumed.
Calculation B - complete drying assumed.
Conditions: d_o = 1.6 mm, U_g = 10.0 ft/sec (3.05 m/sec).

Analysis of high speed films yields two experimental quantities: the particle diameter d and the particle velocity U_d, relative to laboratory coordinates. The latter is then converted to the experimental slip velocity U_s (exp) by means of the known upward gas velocity U_g. While all three measurements - d, U_p, and U_g - are subject to experimental errors, their determination does not require the knowledge of the initial diameter d_o. It is important to note that the calculations of terminal velocities, U_t, are also independent of

d_o, being determined only by the particular diameter which is measured, and the particle density which must be assumed. Therefore, for the purpose of data analysis, it was useful to calculate two sets of U_t values with different particle densities: one for no mass loss from the original droplets (assumption A) and the other for complete drying, i.e., 35% mass loss (assumption B).

The experimental and calculated velocities are given in Table 8. Inspection of the columns which are based only on measurements of expanded particles (i.e., independent of numerical values of d_o), show good agreement between the experimental U_s and the U_t calculated on the assumption of no drying. This shows that the assumption of any degree of drying would give two low values of calculated U_s and U_t. Thus the data are consistent with the concept of expanded particles, with little or no mass loss, settling against the upward gas flow.

In contrast to the experimental U_s and the calculated U_t values, the calculated U_s values depend not only on the extent of mass loss, but also (a) on the value of d_o and (b) on assumptions regarding the expansion history of the droplets. A reasonable choice regarding the expansion history was to break up the calculation of the two parts: one up to 2.8 inches (70 mm) of travel with the initial droplet diameters and densities, and the second with final particle diameters d. As in the case of U_t calculations, two sets of U_s values were obtained (assumptions A and B). A comparison of these with the experimental U_s, again, shows that the assumption of drying is not at all reasonable. In fact, it can be seen that even the assumption of no drying yields calculated U_s values at or about 13% low. This difference can probably be ascribed to the uncertainties in calculation assumptions and to experimental errors.

Bottom of DPFR

The most extensive set of data was obtained in the bottom of the DPFR, centered at 29 inches (740 mm) below the point of droplet injection. The data were taken in a series of 14 runs, each lasting about 10 seconds, during which period about 30 to 50 black liquor droplets were released from the injector.

The analysis of high-speed records revealed that most of the falling particles were again nearly spherical. Table 9 lists the average values of the initial droplet diameters, d_o, in each of fourteen runs, and the corresponding average values, d, of particles at the bottom.

Each of these average values is the arithmetic mean of at least ten individual readings. Table 9 shows that the average linear expansion, d/d_o, is about 1.5. There is substantial scatter. The tested levels of oxygen concentration had no noticeable effect. Another effect which may be expected is that smaller initial droplet diameters should have a longer residence time between injection and observation. This is not apparent from the data.

Table 9. Initial black liquor diameter, and expanded diameter at the bottom of the DPFR.

O_2 in Gas, %	Initial Dia d_o, mm	Expanded Dia d, mm	Ratio, d/d_o
1.5	1.7	2.6	1.5
2.2	1.6	2.1	1.3
5.1	1.7	2.5	1.5
8.4	1.7	2.4	1.4
9.4	1.3	2.2	1.1
9.5	1.7	2.2	1.3
9.7	1.6	2.5	1.6
9.8	1.6	2.7	1.7
9.8	1.7	2.7	1.6
10.1	1.5	2.1	1.4
10.3	1.6	2.9	1.8
16.7	1.4	2.4	1.7
16.9	1.6	2.0	1.3
20.9	2.0	3.1	1.6

Gas Conditions: upflow at 8.3-12.8 ft/sec (2.5-3.9 m/sec) 1740°F (950°C)

The velocity results are shown in Table 10 in the same format as Table 8. This table also includes a calculated estimate of the residence time. The experimental U_s and calculated U_t are based only on direct velocity and diameter measurements, while the calculated U_s and t_R were determined in two stages.

Table 10. Droplet velocities and residence times near bottom of DPFR.

Experimental			Calculation A			Calculation B		
d_o, mm	d/d_o	U_o	U_o	U_t	t_R, sec	U_o	U_t	t_R, sec
1.62[a]	1.52[a]	19.4[a] (5.91[a])	16.6 (5.07)	18.4 (5.60)	0.56	13.7 (4.19)	13.8 (4.20)	0.66
1.7	1.5	17 (5.1)	16 (4.8)	19 (5.9)	0.49	13 (4.1)	14 (4.4)	0.57
1.6	1.3	17 (5.3)	17 (5.1)	21 (6.5)	0.49	15 (4.5)	16 (4.8)	0.57
2.0	1.6	20 (6.0)	18 (5.4)	21 (6.4)	0.51	15 (4.6)	16 (4.8)	0.61
1.7	1.6	20 (6.1)	17 (5.2)	18 (5.6)	0.62	14 (4.2)	14 (4.2)	1.05
1.4	1.7	19 (5.8)	14 (4.3)	14 (4.3)	0.82	11 (3.4)	11 (3.4)	>5

[a]Average of 14 experimental tests shown in Table 9.

t_R = particle residence time estimate from injection until it leaves the bottom field of view.
U_g = 10 ft/sec (3.06 m/sec).
Velocity units ft/sec (m/sec).

The height in the reactor at which droplet expansion begins is unknown. The transition between the two stages is assumed to take place 2.8 inches (71 mm) below the injector. The position assumed does not have a major effect on the calculated velocities or residence times.

Table 10 consists of two parts. The first line is based on an overall average of experimental data of 14 runs, listed in Table 9. These original data show initial diameter variations from 1.3 to 1.8 mm and final diameter variations from 2.0 to 3.1 mm. The average gas velocity was U_g = 3.06 m/sec. The second part of Table 10 gives the results of several individual runs.

Inspection of the first line (experimental averages) appears to show a contradiction: even on the assumption of no drying (calculation A), the calculated U_t is lower than the observed U_s. These results illustrate the problem of measurement accuracy. For example, if the measured d/d_o were 6% lower (i.e., if the measured value of d were 2.32 rather than 2.46 mm), U_t would exceed the measured U_s, removing the contradiction. The same would be true, of course, if the measured U_s were 6% lower. Experimental errors of this magnitude are to be expected. On the other hand, experimental errors of 40% would have to be postulated to bring calculation B into agreement with the experiment. The reasonable conclusion, therefore, is that even at the bottom of the DPFR, little mass loss occurred from the particles.

Inspection of results from individual runs in Table 10 provides further illustration of the correctness of the main conclusion: limited drying, if any, after 0.6 second residence in the reactor. On the basis of no drying (calculation A), terminal velocities are seen to exceed U_s, providing the initial diameters are not too small and the measured expanded diameters not too large (expansion ratios not exceeding 1.5 or 1.6). Large expansion ratios, especially when combined with small d_o values, lead to results which can be explained only by invoking inadequate measurement accuracy. The fault, most likely, is with the assignment of d_o which, even for a single line in Table 10, is a calculated average of several individual particles.

Other Observations

The high-speed films show upward moving particles at all locations in the DPFR. Most of these particles had reached the bottom of the reactor, where they either ignited or shattered (or both). In either case they have the potential to be entrained either because of increased diameter or decreased density. The upward moving particles usually had irregular shapes and moved in random trajectories, sometimes hitting the reactor walls and sticking to them. They also had widely different velocities. A few particles had gas flames on top; they were in the volatiles burning stage. In addition, a very few particles were seen to enter the view at low downward velocities, decelerating further, igniting, and reversing their direction of motion (upward). Since average droplets reached the bottom of the short-height DPFR before ignition, it is concluded that these isolated observations of particle ignition were abnormally small.

CONCLUSIONS

Flow reactor systems to study the burning phenomena of kraft black liquor are successfully operating at IPC and NBS. Initial studies have focused on in-flight drying and the early phases of the volatiles burning stage. Overlap between these two stages exists for the nominal 2 mm size particle tested; residual moisture was present even though pyrolysis was well underway.

Both the drying stage and the volatiles burning stage are characterized by droplet/particle swelling. Particle velocity, trajectory, and heat flux to the particle are influenced by swelling. Swelling in the drying stage consists of rapid swelling, bursting, and collapsing. Initiation of swelling comes before significant mass loss. The swelling in the volatiles burning stage continually increases.

Initiation of the volatiles burning stage results in losses of carbon, hydrogen, oxygen, and sulfur. Transitions in the nonvolatile sulfur species also occur in the early phases. Formation of Na_2S was noted despite implied low particle temperatures. Higher feed temperatures and lower feed solids (i.e., lower droplet viscosities) increased the extent of particle reaction. There is minimal effect of the gas-phase oxygen content during these first burning stages.

The data collected to date support the premise that external heat transfer to the particle and the initial liquor conditions, e.g., droplet mass and liquor viscosity, have the greatest influence on the initial burning stages of drying and volatiles burning. The practical significance of this premise is that heat release, black liquor viscosity and spray size need to be controllable parameters for optimum recovery boiler performance.

FUTURE DIRECTION

The in-flight processes studies will continue at both IPC and NBS with emphasis on intermediate sampling at IPC and longer flight times at NBS. Smaller initial droplet sizes will also be tested at IPC with the flow reactor in the gas downflow mode. A two-color pyrometer developed by NBS will be used to measure the particle surface temperature during the burning processes.

The Phase 2 char burning studies will involve construction of a bed burning furnace to replace the Pyrex char catcher on the IPC system. The configuration will allow either batch char bed burning or steady-state bed burning studies.

Phases 3 and 4 will complete this project with work on fume formation and an experimental simulation of simultaneous recovery furnace processes.

ACKNOWLEDGEMENTS

The authors want to thank The U.S. Department of Energy, Office of Industrial Programs, especially program manager Mr. Stanley F. Sobczynski, for support and guidance of this project. The Institute of Paper Chemistry and its member companies also contributed to this project. The support staffs at IPC and NBS, especially Orlin Kuehl, Steve Lien, and N. Amin are responsible for much of the experimental systems and their operation.

7

LITERATURE CITED

1. Mies, W. E., Allen, D. R., Pollitzer, S., Adams, D., and Espe, C., Pulp and Paper '84, '85 North American Fact Book, Miller Freeman Publications, San Francisco, CA, 1985:237.

2. Grace, T. M., Improved energy efficiency, safety likely in future recovery systems, Pulp Paper, p. 90, October (1981).

3. Grace, T. M., Increasing recovery boiler throughput, Tappi J., 67(11): 52(1984).

4. Clay, D. T., et. al., Fundamental Studies of Black Liquor Combustion Report No.1 - Phase 1 (October 1983-September 1984), U.S. Department of Eneregy Report DOE/CE/40637-T1 January (1985).

5. Merriam, R. L., Simulation analysis of liquor-firing and combustion processes in kraft recovery furnaces, Tappi J., p. 112, September (1982).

6. Blackwell, B., King, T. K., Chemical Reactions in Kraft Recovery Boilers, Sandwell & Company Ltd. (1985).

7. Hough, G., ed., Chemical Recovery in the Alkaline Pulping Processes, TAPPI Press (1985).

8. Grace, T. M., Cameron, J. H., Clay, D. T., Role of the sulfate-sulfide cycle in char burning: experimental results and implications, Tappi J., p. 108, October (1986).

9. Cameron, J. H., Clay, D. T., Grace, T. M., Oxidative fuming - the phenomenon and possible interpretations, 1985 International Chemical Recovery Conference Preprints, Book 3, p. 435 (1985).

10. Miller, P. T., Clay, D. T., Swelling of kraft black liquor during pyrolysis. Applications of Chemical Engineering Principles in the Forest Products and Related Industries, Volume 1, p. 152, (1986).

11. Miller, P. T., Clay, D. T., Lonsky, W. F. W., The influence of composition on the swelling of kraft black liquor during pyrolysis, TAPPI Engineering Conference Preprints, Book 1, p. 225 (1986).

12. Cantrell, J. G., Sulfur gas release during black liquor burning, M.S. Thesis, Georgia Institute of Technology School of Chemical Engineering, March (1986).

13. Hupa, M., Solin, P., Hyoty, P., Combustion behaviour of black liquor droplets, 1985 International Chemical Recovery Conference Preprints, Book 3, p. 335 (1985).

14. Clay, D. T., et. al., Fundamental Studies of Black Liquor Combustion Report No. 2 - Phase 1 (October 1984-December 1986), U.S. Department of Energy Report DOE/CE/40637-T2 In press (1987).

15. Kubelka, V., Jr., Votoupal, J., Chemical recovery in kraft pulp mills. The chemistry of the recovery process and the design of the recovery unit, Sbornik Vyzkum. Praci z Oboru Celulozy a Papiru 2: 49-73(1957).

16. Hogg, R. V., Craig, A. T., Introduction to Mathematical Statistics, The Macmillan Company, New York (1969).

THE INSTITUTE OF PAPER CHEMISTRY

Appleton, Wisconsin

Status Report

to the

PULPING PROCESSES

PROJECT ADVISORY COMMITTEE

Project 3474

IMPROVED PROCESS FOR BLEACHED PULP

Low-Lignin Pulps

Nonchlorine Bleaching

September 16, 1987

THE INSTITUTE OF PAPER CHEMISTRY

Appleton, Wisconsin

Status Report

to the

PULPING PROCESSES

PROJECT ADVISORY COMMITTEE

Project 3475

FUNDAMENTALS OF SELECTIVITY IN PULPING AND BLEACHING

Delignification Reactions

Carbohydrate Reactions

September 14, 1987

PROJECT SUMMARY FORM

DATE: September 14, 1987

PROJECT NO. 3475: FUNDAMENTALS OF SELECTIVITY IN PULPING AND BLEACHING

PROJECT LEADER: D. R. Dimmel

IPC GOAL:

Improved process for bleached chemical pulps

OBJECTIVE:

Provide a fundamental understanding of the chemical and physical reactions that control both:

(1) the rate of lignin removal, hemicellulose dissolution, and cellulose degradation, and
(2) the structures of the lignin, hemicelluloses and cellulose that remain in the pulp after pulping and bleaching.

CURRENT FISCAL YEAR BUDGET: $150,000

SUMMARY OF RESULTS SINCE LAST REPORT:

Lignin Reactions

Anthraquinone (AQ) pulping exhibits higher selectivities than that shown by the other major commercial alkaline pulping processes. Why? Studies in our laboratory over the last several years indicate that the chemistry associated with the AQ process may be unique. We have evidence from model studies that anthrahydroquinone (AHQ), a reduced form of AQ, can single electron transfer (SET) to quinonemethides (QMs); the latter are important intermediates in lignin reactions. Following electron transfer, the generated QM radical ions have been shown to fragment at their β-aryl ether linkages - a process synonymous with delignification. These findings were arrived at by a combination of studies with low temperature electrochemical experiments in organic solvents and high temperature reactions of model compounds in aqueous alkali.

Recent studies have focused on examining the suitability of using high temperature aqueous electrochemistry to demonstrate the existence of SET reactions under pulping conditions with wood and wood components. An electrochemical cell has been constructed which has provided data in aqueous alkali up to a temperature of 165°C. We have examined the electrochemistry of NaOH, Na_2S, AQ, AMS (sulfonated AQ), AHQ, simple phenols, carbohydrates, wood meal, bleached kraft pulp and some combinations of these.

Studies have continued toward developing insoluble lignin model compounds which could be used to determine the importance of "physical" effects associated with

typical delignification reactions. The binding of a lignin model to polystyrene via a trityl ether bond does not provide a linkage which stands up to pulping conditions. Attaching lignin models to the polymer via benzyl ether linkages using allyl ether protecting group methodologies appears feasible. Separate experiments aimed at producing a ligninlike model which would demonstrate the possible rapid rates associated with SET delignification reactions have been unsuccessful; the model synthesis has been difficult.

Carbohydrate Reactions

Work is being directed at answering two important questions: Does AQ cause significant carbohydrate chain cleavage reactions in cellulose samples (reactions which cause losses in pulp viscosity) and to what extent does the physical nature (crystalline or amorphous) affect the degree of chain cleavage reactions? We have repeated some earlier project work and verified that AQ causes only a slight drop in viscosities in soda "pulping" of cotton linter samples, both with and without AQ. Experiments with high levels of AQ did not, however, give the anticipated result, namely, large losses in viscosities.

We have experienced significant problems in preparing a high viscosity, stabilized amorphous cellulose sample; however, we have recently prepared such a sample. The amorphous cellulose sample is quite reactive, losing 75% of its initial viscosity in 10 minutes at 150°C in 1M NaOH.

The thesis work of M. Bovee has produced a polymer supported cellulose model compound. Recent efforts within this project have involved synthesizing more polymer supported model, attempting to characterize the degree of model-to-polymer loading, and performing soda degradations of the insoluble cellulose model. The preliminary results from these degradations indicate that the polymer supported model is suitable for studying physical effects and is behaving differently than the analogous unsupported model with regard to reaction rates and the formation of a new type of product.

PLANNED ACTIVITY THROUGH FISCAL YEAR 1988:

Our electrochemical studies will focus primarily on improving the cell sensitivity, correlating electrochemical behavior with delignification rates, and assessing the potential of these techniques. Selected mechanistic studies aimed at better understanding delignification chemistry will be used to fill in the time gaps during electrochemical cell development.

A systematic study of the reactivity differences between crystalline and amorphous cellulose will begin. The loading of cellobiitol on the polystyrene of our insoluble cellulose model will be determined; degradations of the model and characterization of the products (both liberated into solution and remaining on the polymer) will commence.

FUTURE ACTIVITY

The high temperature electrochemical studies will be expanded into evaluating methods to monitor pulping and promoting (probably indirectly) beneficial pulping reactions. As new information on SET reactions becomes available, we will examine novel ways to promote these reactions in an economical manner.

The synthesis and reactions of an appropriate insoluble lignin model compound will be pursued; a comparison of the chemistries of soluble and insoluble lignin model reactions will (1) clarify the suitability of the former model studies and (2) provide data on "physical effects."

Methods which have been developed for determining cellulose molecular weight distribution will be applied to assess the effect of carbohydrate physical structure (crystalline vs. amorphous) on the extent of chain cleavage reactions. The methods will also be used to systematically study how changes in pulping and bleaching conditions affect carbohydrate chain cleavage reactions. For example, studies of cellulose chain cleavage in alkaline pulping indicate that increased ionic strength accelerates the cleavage reaction. Thus the effect of "dead load" (increased ionic strength) on cellulose chain cleavage during pulping could be examined.

Further applications of insoluble cellulose models will be explored; degradations of the models at different temperatures, alkalinities, and ionic strengths, in the presence of strong nucleophiles and/or labeled water, will provide valuable information on the mechanisms of chain cleavage reactions with a model that should closely mimic that of cellulose in wood.

STUDENT RESEARCH

J. Leege, M.S.-1987; P. Sands, M.S.-1987; P. Medvecz, M.S.-1987; M. Bovee, Ph.D.-1987; G. Reed, Ph.D.-1988; W. Molinarolo, Ph.D.-1988; R. Barkhau, Ph.D.-1988; J. Wozniak, Ph.D.-1988.

Status Report

FUNDAMENTALS OF SELECTIVITY IN PULPING AND BLEACHING

Carbohydrate Reactions

OBJECTIVE

The goal of chemical pulping is to liberate, without degradation, carbohydrate fibers from wood through delignification. Unfortunately, alkaline pulping processes are not very selective for delignification. For example, in kraft pulping the loss of carbohydrate material may be comparable to, or even exceed, the lignin removal.[1-2] In addition, reduction of the carbohydrate chain length, leading to decreased pulp viscosity and product strength, also occurs.[1-3]

The objective of this project is to elucidate the mechanisms of carbohydrate and lignin degradation reactions which occur during pulping and bleaching. A better understanding of the chemistry involved will ultimately facilitate better control of pulping and bleaching selectivities. The fact that anthraquinone (AQ) and its reduction product anthrahydroquinone (AHQ) increase pulping selectivities has stimulated interest in its chemistry. Recent research has been directed toward understanding the role of "physical effects" in lignin and carbohydrate reactions and looking toward using electron transfer chemistry as a means of improving pulping selectivities.

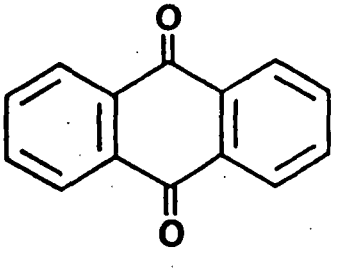

AQ

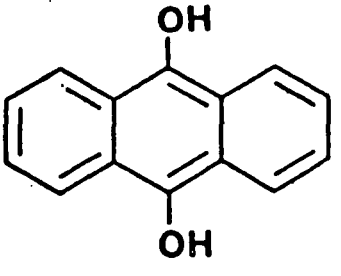

AHQ

LIGNIN REACTIONS

Most wood chemists would agree that pulping chemicals, such as NaOH, NaSH, Na_2SO_3, and AHQ, act in a similar ionic fashion, adding to reactive lignin subunits known as quinonemethides (QMs) and then generally assisting in the cleavage of ether linkages which hold lignin units together. While this view may be correct for many pulping reagents, we feel that it is probably not accurate for explaining the rapid delignification associated with AQ pulping. Single electron transfer (SET) mechanisms[4] probably account for the effectiveness of AHQ as a delignification aid.

Differentiation between pure ionic and SET mechanisms has not been easy. Often the results of carefully planned experiments have provided ambiguous answers.[5] The results have been compatible with the SET mechanism and, in at least two cases, an electrochemical study[6] and the thesis work of IPC student Dean Smith,[7] have left no doubt that such reactions occur between AHQ and QMs. Also, recent project research has demonstrated that AHQ is much more effective than NaSH (the active ingredient in kraft pulping) at promoting a fragmentation of a lignin model compound which has a built in "clock."[8]

Based on the assumption that SET reactions can be very beneficial toward producing highly selective pulping processing, we have been examining the possibility of using high temperature electrochemical techniques for detecting and promoting SET reactions in aqueous alkaline solutions. Work in this area, along with attempts to develop an insoluble lignin model compound, have been the focus of the research conducted in this project over the last year.

ELECTROCHEMICAL STUDIES

The area of high temperature aqueous electrochemistry in a corrosive environment is truly an exploratory research area. There are very few literature citations of research in this area. Much of our research has focused on electrochemical cell development. Our first cell employed a rotating platinum disk working electrode and a mechanical means for cleaning the electrode. After many trials, this cell was eventually abandoned. We encountered two principal problems: (1) absorption of hydrogen on the platinum surface, from electrolysis of water, which created a large amount of interference and (2) constant leaks as a result of stirring with an external shaft.

Our second cell was vastly different from the first one. It used a magnetic stirring bar for agitation, a glassy carbon working electrode, a counterelectrode made of platinum wire, and an external reference electrode of the silver-silver chloride type, containing a Teflon double junction. This cell provided enough encouraging results that a modification which added five more glassy carbon working electrodes was incorporated. The working electrodes were arranged in a circle around the reference and counter electrodes; when one working electrode became dirty, we just switched to another. This modified second cell has provided some exciting data. Eventually we found epoxies and materials that would allow us to increase the temperature of the electrolysis up to roughly pulping temperatures without serious degradation of the electrodes and contact points.

Our experiments have involved an electrochemical technique known as cyclic voltammetry. Figure 1 illustrates the technique. The system typically has three electrodes, namely, counter, working, and reference electrodes; the

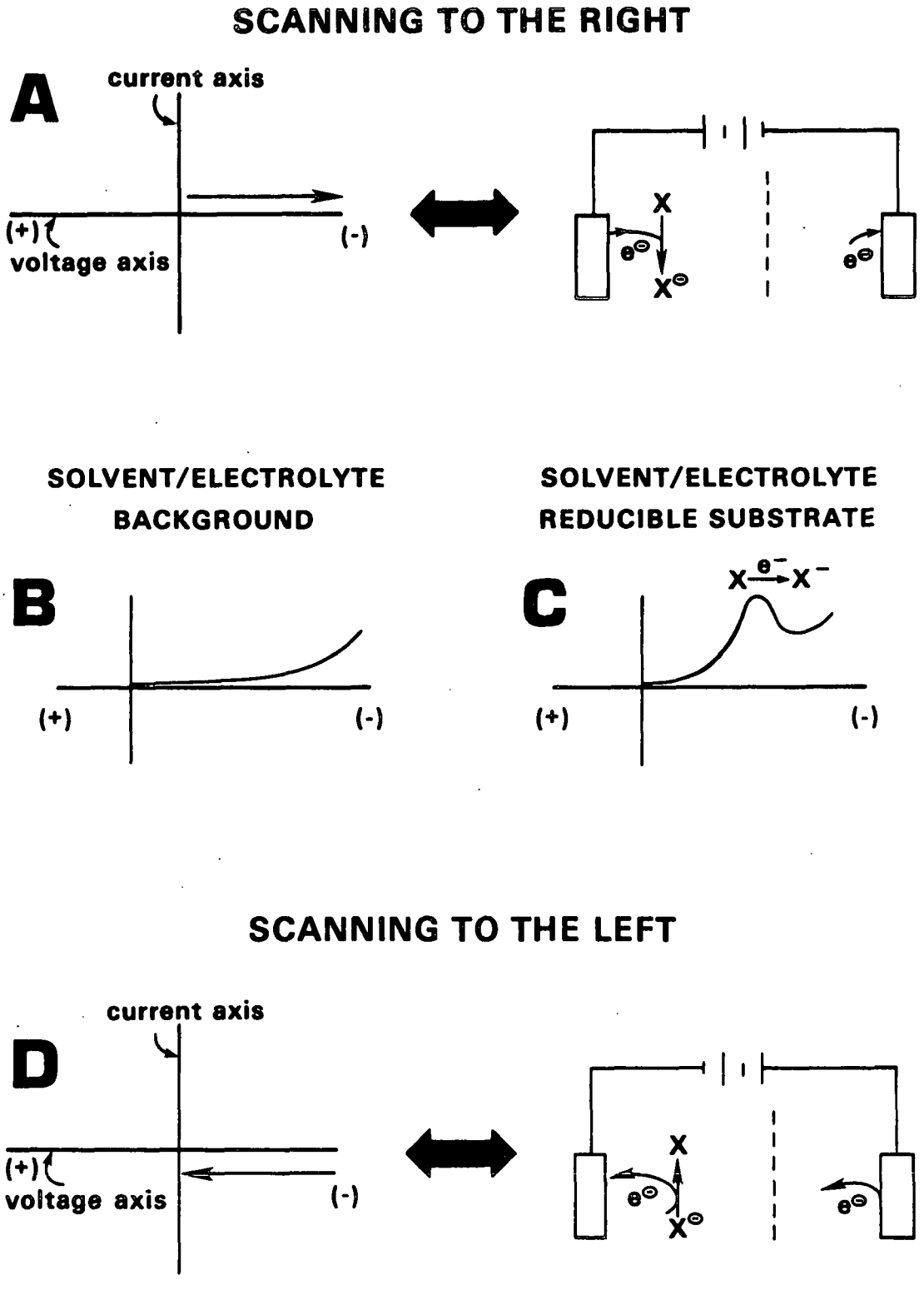

Figure 1. Cyclic voltammetry - crude theory.

latter is not shown in Fig. 1. The three electrodes are connected to a potentiostat which allows the potential of the working electrode to be set relative to the reference. The counterelectrode supplies sufficient current to maintain the working electrode potential regardless of the redox reactions occurring at its surface.

In the cyclic voltammetric technique a constantly changing potential is applied to the working electrode. On the forward sweep (Fig. 1A) reduction of the solvent begins, resulting in a small current flow (Fig. 1B). If a reducible substrate (X) is present in the solution, a significant current will flow when the redox potential of the substrate is reached (Fig. 1C). As the substrate is depleted near the electrode surface, the current wave peaks, and the current falls off, approaching a diffusion-controlled value. If the direction of the scan is reversed, one can expect to see the reduced species being reoxidized on the return sweep (Fig. 1D); an example is shown in Fig. 2C.

Figure 2 presents some examples of cyclic voltammograms. Comparison of the top two voltammograms shows that a solution containing a phenol has a cyclic voltammogram very similar to that of the 1M NaOH background voltammogram with the addition of a negative peak (anodic current) at a positive potential. This negative current is associated with phenol ions giving up electrons to the working electrode. The fact there is no positive current peak (cathodic wave) indicates that the oxidation of the phenol leads to species which rapidly undergo chemical reaction (i.e., an irreversible system).

Previous studies[6] have produced the data shown in Fig. 2C. The cyclic voltammogram of anthraquinone, dissolved in acetonitrile containing tetrabutylammonium perchlorate electrolyte, shows one cathodic wave and one

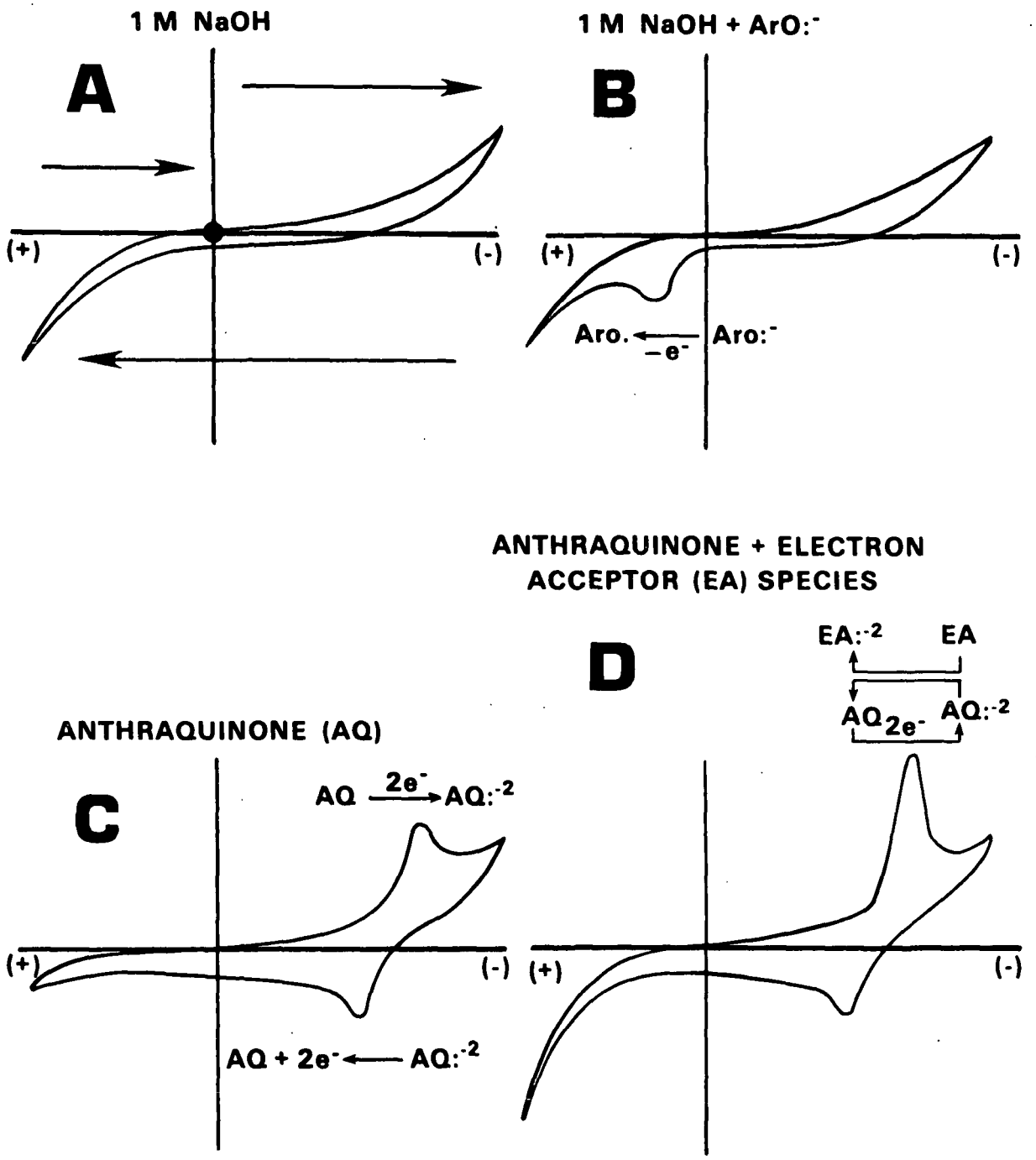

Figure 2. Example cyclic voltammograms.

anodic wave. The two waves have equal peak currents for the reversible AQ redox couple. [It should be noted, that for simplicity reasons, the reduced form of AQ is shown in Fig. 2 as $AQ:^{-2}$ rather than the usual notation, which is AHQ^{-2}].

If an electron acceptor species is present in the AQ solution, one can get the voltammogram shown in Fig. 2D. The fact that the forward (reductive) wave has a larger current than the reverse (oxidative) wave in this instance indicates that AQ is acting as a homogeneous redox catalyst for the electron acceptor substrate. A cyclic voltammogram of this type (Fig. 2D) has been observed by us[6] for a solution of anthraquinone and lignin model quinonemethide in acetonitrile with the appropriate electrolyte at room temperature.

With our new, second generation electrochemical cell we have now been able to obtain cyclic voltammograms at high temperatures in 1M NaOH. Figure 3 shows cyclic voltammograms of mixtures of anthraquinone in 1M NaOH with either bleached kraft pulp or wood meal. Each experiment begins with the cell at low temperature and the temperature is increased gradually up to 165°C. [The temperature indicated is that of the oil bath on the exterior of the cell and may not accurately describe the temperature for the solution inside the cell.] In both experiments the appearance of the anthraquinone signals occurred once 140°C is reached.

The bleached kraft pulp experiment (first column, Fig. 3) shows the reversible anthraquinone cyclic voltammogram at the higher temperatures, with roughly the same intensity for the cathodic and anodic wave from start to

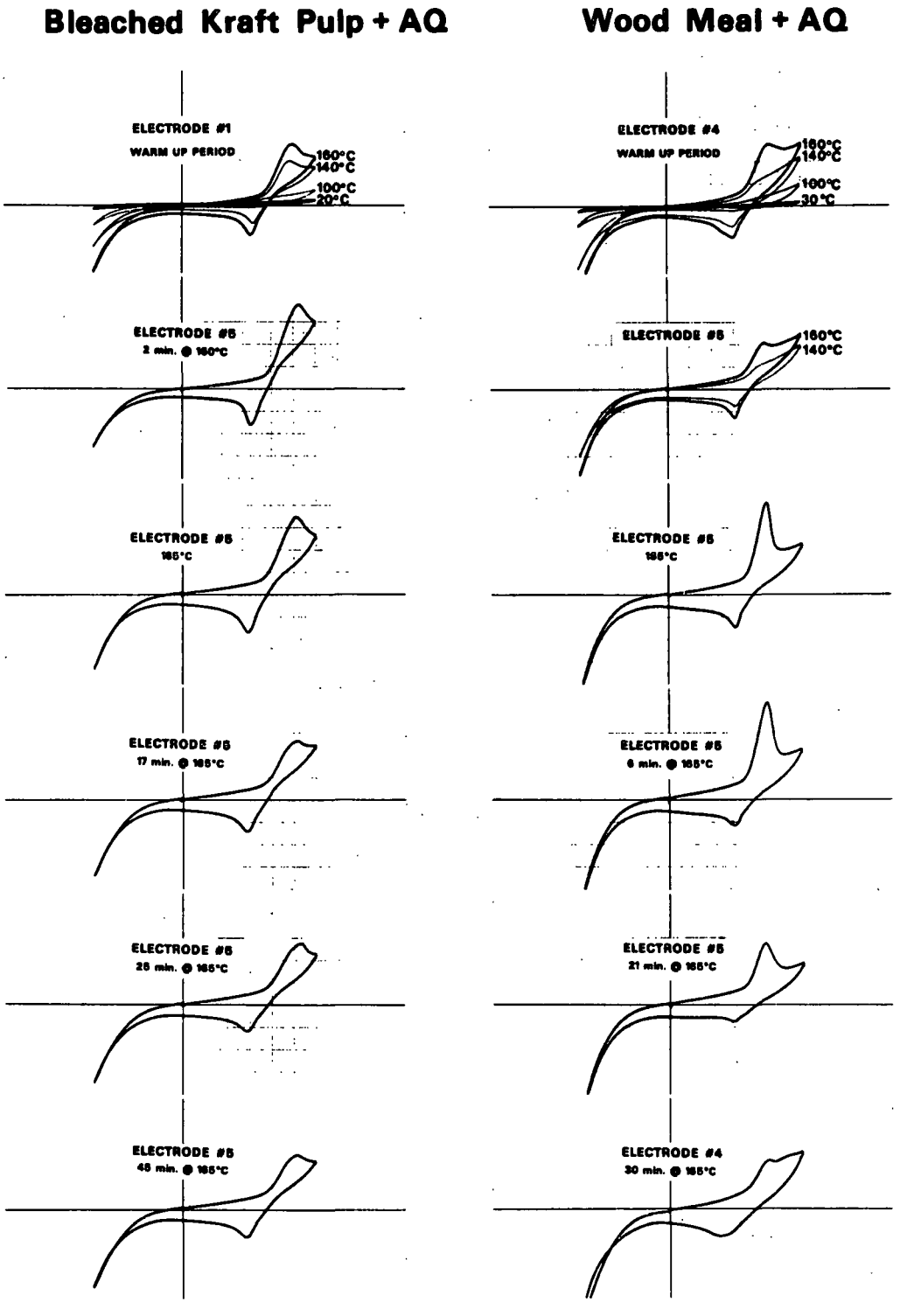

Figure 3. A comparison of the high temperature electrolyses of bleached kraft pulp and wood meal in the presence of anthraquinone.

finish. In contrast, the experiment with the wood meal shows, at the early part of the 165°C temperature range, an enhancement in the cathodic signal. This current enhancement is associated with the lignin component of the wood meal being an electron acceptor compound for the reduced anthraquinone species and signifies the occurrence of a redox cycle. It appears that anthraquinone's delignification effects do not last long into the cook; in other words, the cyclic voltammograms are indicating that anthraquinone's main effect may only be in the initial delignification phase.

These are exciting results! We are observing the action of a pulping catalyst in situ during the pulping experiment. There are, however, many refinements and challenges ahead. We in essence have done our "last experiment" first, without doing several needed controls.

What problems do we face and how do we intend to tackle them? We need to correlate the observed redox chemistry with actual lignin removal from the wood meal. This means that we need to develop a way of sampling the pressure vessel during the course of our pulping experiments and determine residual lignin levels in the wood. [We would welcome suggestions on how to pull a solid sample from a small pressure vessel.] Our latest electrochemical cell has now been equipped with a thermal couple (to measure internal temperatures accurately) and a device for sampling the liquor in the cell. With these modifications, we hope to be able to follow the course of a lignin model fragmentation reaction as a function of time, temperature, and the redox chemistry which is occurring with the anthraquinone.

One of our biggest problems at this point is the low sensitivity of the electrochemical cell. The levels of AQ employed to generate the data shown in

Fig. 3 are substantially above those typical in a pulping experiment. This means that we need to develop better ways of cleaning the electrode surfaces, redefining electrode geometries, and modifying the solution interface between the cell and the external reference electrode. Our goal is to not only increase the sensitivity enough to see AQ at 0.1% levels but also to observe phenols and quinonemethides in pulping liquors; the concentration of quinonemethides will be low. Changes in concentrations of quinonemethides and phenols will serve as possible accurate indicators of pulping progress.

The research team in this area has changed over the last few months. We will greatly miss the contributions of research assistant Lois Bovee (formerly Lois Schuller/Lois Perry). However, the electrochemical experience of postdoctoral fellow Mike Van Lente will be invaluable to future developments in the electrochemical pulping area. The change in personnel, and the time gap between the changes, momentarily slowed progress in this and allied research areas in Project 3475.

INSOLUBLE LIGNIN MODELS

The 1986 Ph.D. thesis of P. Apfeld concerned the synthesis, characterization, and preliminary reactions of a polymeric insoluble lignin model compound. Our interest in this model stems from the realization that pulping chemistry involves the degradation of an **insoluble** lignin to soluble lignin particles. Studies involving degradation of **soluble** lignin model compounds may not accurately describe the importance of "physical" effects associated with typical delignification reactions. Yet, soluble studies are the best we can presently do; detailed studies of actual lignin reactions are very complex due to the structural complexities of lignin.

Apfeld's thesis left many unanswered questions concerning the usefulness of his insoluble lignin model. We have taken up studying his model, since an understanding of the applicability of models of this type is needed to define the scope of other student thesis work and will guide us in future research directions.

Research on Apfeld model 1 has demonstrated that the model-to-polymer trityl ether linkage is not very stable. It is apparent that the model, when subjected to pulping conditions, gets converted into an ionized form 2 which undergoes an intramolecular displacement reaction between the α oxyanion and the ε carbon. This popping off of the model from the polymer is favored by the close proximity of the α oxygen and the ε carbon.

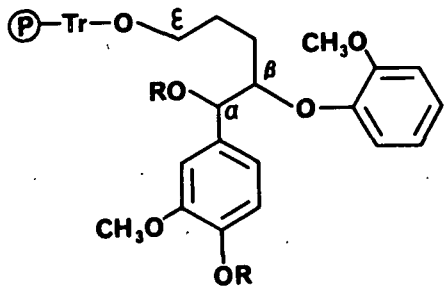

1, R = H
2, R = :—

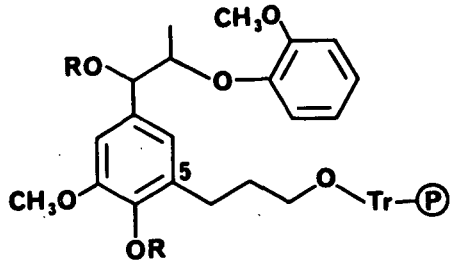

3, R = H
4, R = :—

Models of the type 3 were also considered by Apfeld; however, he was unable to synthesize such structures. Insoluble 3-type models were expected to be more stable than 1-type models because an intramolecular displacement reaction involving a phenolate oxyanion 4, which would pop the model of polymer, would be less likely to occur. Consequently, we have reinvestigated the synthesis of 3-type models. Most of our synthetic efforts have involved work with analogous models 5 and 6, plus model 7.

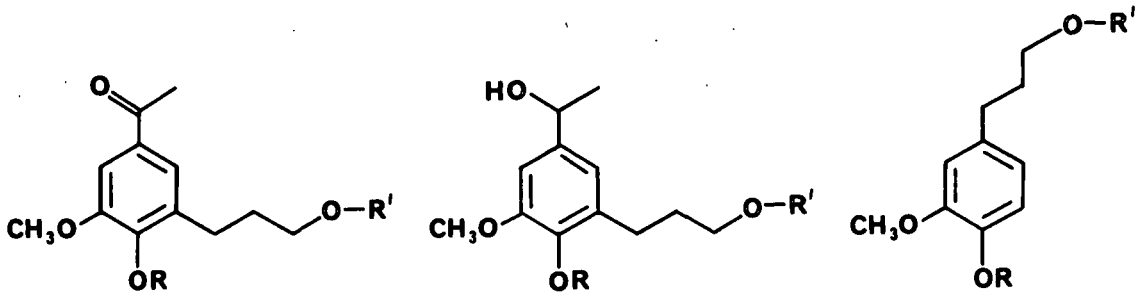

5 6 7

A, R = H, R' = H
B, R = H, R' = Tr—Ⓟ
C, R = H, R' = Bn—Ⓟ
D, R = protecting group, R' = H
E, R = protecting group, R' = Tr
F, R = protecting group, R' = Bn
G, R = H, R' = Tr
H, R = H, R' = Bn

SEM = 
allyl = 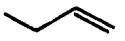
propenyl = 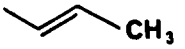
trityl = Tr = CPh_3
benzyl = Bn = CH_2Ph
Ⓟ = polymer backbone

The synthetic efforts were aimed at converting the A series of compounds 5, 6, and 7 to the polymer bound B or C series. The preliminary synthetic work, however, focused on converting the A series to either the G or H series; the latter have the same ether linkages that might exist in a polymer-bound model. The methodology involved putting a protecting group on the phenolic oxygen, then placing either a trityl or benzyl group on the side chain oxygen, and finally removing the protecting group; in other words going from the A series to the D series, then to either the E or F series, and finally to the G or H series. The protecting groups employed were either an SEM group[9] or an allyl group.[10] The SEM protecting groups can be removed selectively by treatment with tetrabutylammonium fluoride[9] and the allyl protecting groups are removed by first isomerization to a propenyl substituent and then hydrolysis.[10]

Our synthetic work taught us a great deal. For example, we learned that SEM protecting groups are not easily removed once they are put in place. We also learned that phenolate ions appear to be more reactive than alkoxy ions; for example, benzylation of **5A** under a variety of conditions gives primarily attachment of the benzyl group unto the phenolic oxygen and not the side chain oxygen. We eventually made tritylated model **6G** via the SEM protecting group route. By analogous chemistry it should be possible to make the polymer-bound model.

Simultaneous with our synthesis studies, Ph.D. student Bob Barkhau was studying the stability of tritylated polymer-bound model **7B**. He found that this model was not very stable to alkaline pulping conditions and suggested that we abandon the trityl ether linkage as a way of binding the model to the polymer. In subsequent work, Barkhau and our project team have established that the best method of attaching a model to a polymer is by use of an allyl protecting group and a benzyl ether linkage to the polymer. Additional work in this area is being carried on by Barkhau.

MISCELLANEOUS

Most of the compounds we deal with and refer to as "starting materials" cannot be purchased directly but are generally made in multistep syntheses; these include **4A**, **5A**, **6A**, tritylated polystyrene, iodobenzyl polystyrene, and our typical lignin model dimer (**3** without the C_5 side chain). Many hours of project time go into the preparation of such compounds. There are also occasional synthetic efforts that don't succeed. For example, we recently tried to prepare a β-butenyl lignin model compound via a butenyl trifylate alkylating agent and the two attempted reactions were unsuccessful.

Several experiments have been done over the past year which were aimed at answering questions associated with previously collected data and at exploring new areas. With regard to the latter point, for example, we have used the electron detector compound developed by Dean Smith[7] to study whether methyl mercaptan is capable of electron transferring to quinonemethides. Methyl mercaptan interestingly promotes pulping by as yet some unexplained chemistry.[11] Preliminary model degradations by sulfite, anthraquinone/sulfite, and mixtures of sulfite, sulfide, and AQ have been investigated. The aim of this research was to try to better understand the apparent synergistic affects that exist between these various pulping additives.[12] We have also briefly examined the affects of Smith's electron detector compound[7] on the degradation rates of a lignin model compound.

CARBOHYDRATE REACTIONS

One of the ways to improve the selectivity of pulping and bleaching reactions is to prevent, or lessen the amount of, unfavorable carbohydrate degradation reactions. In order to do this, we must first understand the fundamental underlying chemistry that exists. Considerable research by M.S. and Ph.D. students at the Institute and the research staff involved in Project 3475 has been directed toward this end. The focus of recent project research has been to determine the extent to which the physical nature of the carbohydrate (crystalline or amorphous) affects the degree of chain cleavage reactions which are occurring during pulping. Carbohydrate chain cleavage reactions have a significant effect on yield losses of hemicelluloses and on viscosity losses in cellulose.[1-3]

The fact that anthraquinone causes extensive degradation of amylose but appears to have little effect on crystalline cellulose has been taken to mean

that the physical state of the carbohydrate is a very important factor with regard to chain cleavage reactions.[13] Amylose differs from cellulose in that it has α linked monomers instead of β linked monomers and it is soluble in water. Earlier project studies with model compounds have demonstrated that the nature of the linkage, be it α or β, is not the cause of the differences between cellulose and amylose.[13] Thus, it appears that the main factor is one of solubility differences (the crystalline cellulose is not soluble in water). The hypothesis which we have developed is that the main carbohydrate degradation reactions of wood are occurring with amorphous or soluble carbohydrates. In order to test this hypothesis, we have been pursuing studies involving a polymer supported cellulose model compound and studies involving a comparison of the reactions of amorphous and crystalline cellulose.

AMORPHOUS CELLULOSE

We have had considerable difficulties preparing a high viscosity, stablized amorphous cellulose sample. In broad terms, the precedure for preparing an amorphous cellulose sample consists of dissolving a crystalline cellulose sample in a cellulose solvent, precipitating the cellulose, washing thoroughly, reducing with sodium borohydride to stabilize the carbohydrate end groups, washing again, and drying. Of the two cellulose solvent systems examined, we have found that the SO_2/diethylamine/DMSO system[14] generally gives higher viscosity amorphous cellulose in much less time than the DMSO/paraformaldehyde system.[15]

The method of precipitation of the amorphous cellulose and the amount and type of washings performed play a significant role in the final viscosity of the amorphous cellulose sample. Without proper washing, an amorphous cellulose sample can lose half its viscosity in just a matter of a few days. Besides

these problems, we were experiencing difficulties obtaining reproducible viscosity values for identical samples. We have subsequently resolved this problem by using larger sample sizes and a different procedure.

After much experimentation, we have recently produced an amorphous cellulose with a viscosity of 45 cps which holds this viscosity upon storage. Portions of this amorphous cellulose have been placed, along with 1M NaOH, in small pressure vessels, sealed, and heated at 150°C to produce the data shown in Fig. 4. As can be seen, the amorphous cellulose sample rapidly loses its viscosity under these conditions. We suspect that a crystalline, stabilized cellulose sample will not degrade nearly as fast as this amorphous cellulose sample; experiments to establish this point are presently underway.

We are now poised to do several interesting experiments with this high viscosity amorphous cellulose. These experiments will basically compare the reactivity of an amorphous cellulose sample with that of a crystalline cellulose sample under varying conditions, such as soda pulping, anthraquinone pulping, sulfite pulping, oxygen bleaching, peroxide bleaching, and so forth.

AN INSOLUBLE CELLULOSE MODEL

The Ph.D. thesis work of recently gradated IPC student Matt Bovee has produced a polymer supported cellulose model compound which should be suitable for studying "physical" effects. Dr. Bovee has successfully grafted a 1,5 anhydrocellobiitol structure onto a polystyrene matrix by way of a benzyl ether linkage.[10] He has also established the extent of "loading" of the model onto the polymer surface by two different techniques. Chemical studies of the model have been taken up by Project 3475 personnel. Preliminary reactions of the insoluble model

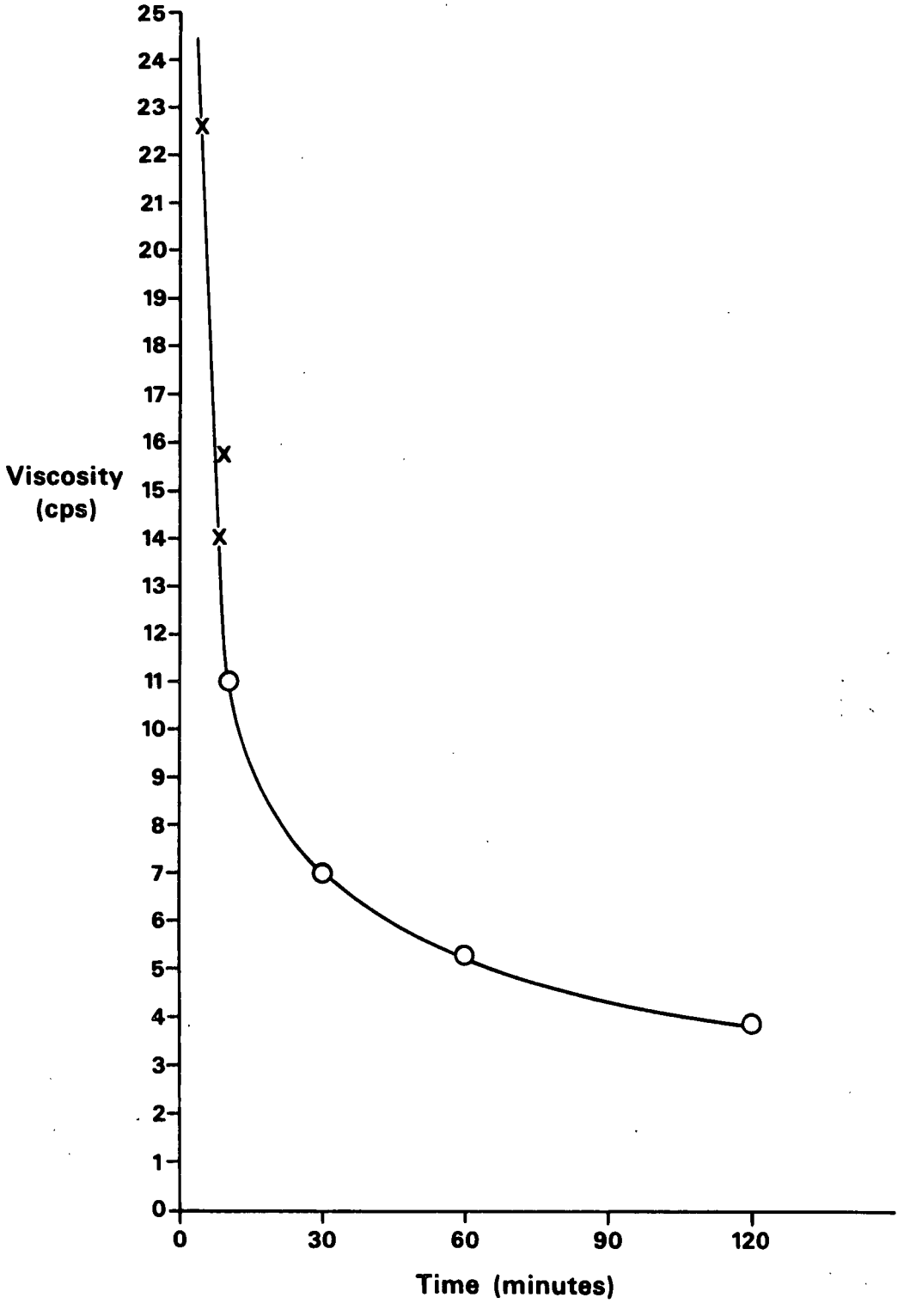

Figure 4. Changes in viscosities of a 45 cps amorphous cellulose sample upon heating in 1M NaOH at 150°C for various time periods.

at 170°C in the presence of aqueous sodium hydroxide indicate that the model will be a suitable substrate for studying glycosidic bond cleavage chemistry.

Only a small amount of insoluble model was available from the work of Bovee. Because of the potential high value of this model and because of the complexity of the synthesis of the model, we asked Bovee to direct us in the synthesis of a larger quantity of this model. The preparation, which was rather time consuming, followed a ten step synthesis to get an allyl "protected" carbohydrate dimer (8), a two step synthesis to prepare the polymer (9) for reaction, the coupling of the model unto the polymer (to give 10), and finally removal of the protecting groups (Fig. 5).

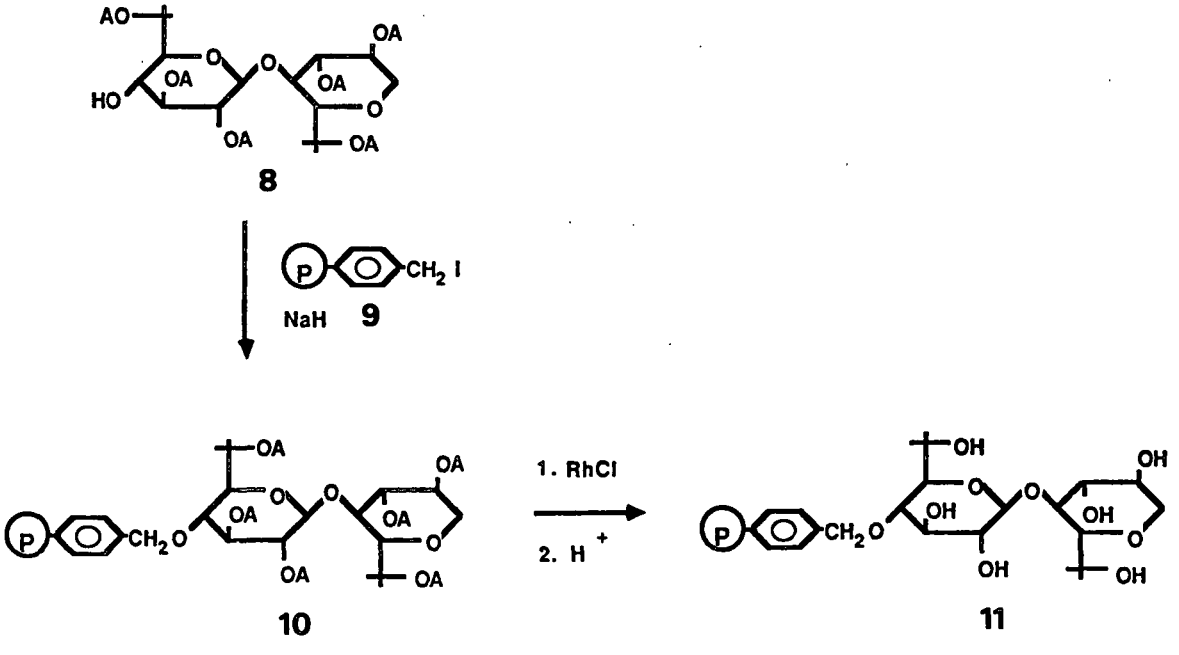

Figure 5. The final steps in the synthesis of a polymer-bound cellulose model; A = allyl group ($-CH_2CH=CH_2$), Ⓟ = polystyrene.

The coupling step was done in a somewhat different way than Bovee had used in his thesis work; consequently, we had to determine the degree of loading

of the model unto the polymer. Knowing the loading value was necessary in order to determine reaction conditions to be used in degradation studies and to define the starting concentrations for the future kinetic experiments. Establishing the degree of loading has proven to be a difficult task.

Bovee determined his loading by two techniques. The first involved measuring the increase in weight of the allyl protected insoluble model 10 upon treatment with osmium tetraoxide, which presumably reacts quantitatively with the double bond of the allyl groups (Fig. 6). His second method involved hydrolysis of the unprotected model 11 in aqueous ethanol with hydrochloric acid; this method cleaves the glycosidic bond and releases 1,5-anhydro-D-glucitol (12) into the solution which is then quantitatively determined by GC techniques (Fig. 7). The agreement between the two methods was fairly good - only about a 10% difference between the absolute numbers.

We have employed the same two methods that Bovee used plus a third one, acetolysis. The latter method involves treating polymer supported model 11 with a mixture of acetic anhydride, acetic acid, and sulfuric acid, and heating at 70°C for several hours. These conditions were expected to both cleave the carbohydrate completely from the polymer and cleave the carbohydrate glycosidic linkage, resulting in a molecule of acetylated glucose and molecule of acetylated 1,5-anhydro-D-glucitol. This method not only has the potential for determining the loading of the carbohydrate on the polymer but also to determine the residual carbohydrate on the polymer after, for example, a pulping degradation experiment. We found, however, that the severity of the conditions that were needed to get the carbohydrate off the polymer also caused the glucose to degrade; consequently the acetolysis method will only allow us to quantitate the liberated 1,5-anhydro-D-glucitol.

Osmylation – Degree of Loading

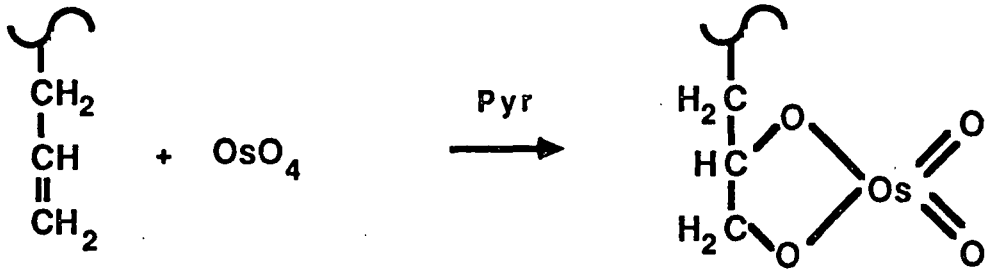

Figure 6. Determination of the degree of model loading on the polymer by osmylation of the allyl protecting groups.

Ethanolysis – Degree of Loading

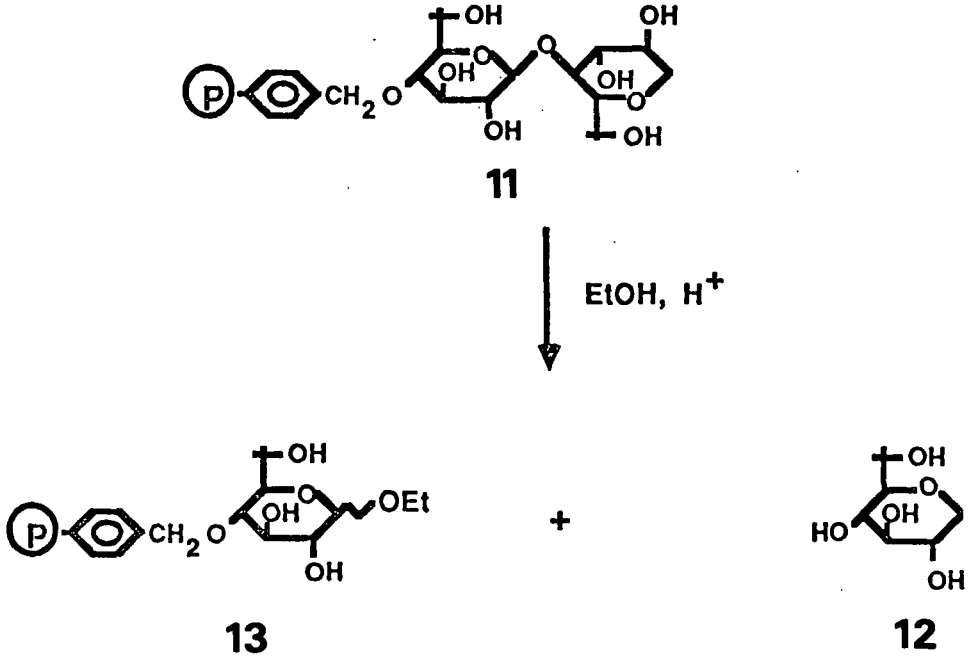

Figure 7. Determination of the degree of model loading on the polymer by osmylation of the allyl protecting ethanolysis.

Application of the three methods, osmylation, ethanolysis, and acetolysis, has led to three different values for the loading of the recently prepared insoluble model compound. The differences between the methods are considerable; for example, the acetolysis gives a value of loading which is four times that suggested by the osmylation method. The ethanolysis method gives a value somewhere in between the two. We have done considerable work perfecting the conditions of the ethanolysis and acetolysis methods; trials with the unsupported model, 1,5-anhydrocellobiitol, have shown that these two methods are reliable and consistent. The methods give reproducible results when duplicates and triplicates are run on the polymer supported sample using both low and high reaction times. Yet, at this time, we do not understand why there are differences in the loading value obtained by these methods and which method is the most reliable. Additional work is being done in this area to sort out these problems.

FUTURE STUDIES

Several immediate goals have already been mentioned. Longer range goals in the lignin area involve evaluating methods to monitor pulping and to promote beneficial pulping reactions by means of high temperature electrochemical techniques and to examine ways to further detect and promote single electron transfer reaction during pulping; SET reactions hold great promise for improving the selectivity of pulping systems. The longer range goals on the carbohydrate side involves systematically studying how changes in pulping and bleaching conditions affect carbohydrate chain cleavage reactions of amorphous and crystalline cellulose samples and studying how variations in temperature, alkalinity, ion strength, presence of nucleophiles, and labeled water will affect the degradation of an insoluble cellulose model. When completed we should have

a much more thorough understanding of both the chemical and physical aspects of chain cleavage reactions.

STUDENT RESEARCH

There is considerable student research activity in the wood chemistry area related to this project work. Briefly listed below are the students and their research topics. All of the Master's students and Ph.D. student Matt Bovee graduated this last spring. The remaining four Ph.D. students are expected to be graduated within a year from now.

M.S. STUDENTS

Leege, Joseph C.

A characterization of the thermodynamic functions of activation for 1,5-anhydromaltitol under alkaline conditions.

Sands, Peggy D.

Mechanism of methyl mercaptan delignification.

Medvecz, Patrick J.

Determination of o-quinone structures by reactions with phosphite compounds.

Ph.D. STUDENTS

Reed, Gregg A.

Nucleophilicities of hydroxide, hydrosulfide, and anthrahydroquinone ions toward saturated and unsaturated carbon centers at high temperatures.

Molinarolo, Wm. E.

High temperature alkaline degradation of phenyl beta-D-glucopyranoside.

Barkhau, Robert A.

Anthraquinone inhibited lignin condensation.

Wozniak, John. C.

Preparation and reactions of Diels-Alder adducts of lignin-derived quinones.

Bovee, M.

The synthesis and characterization of a polymer-supported cellulose model.

REFERENCES

1. Matthews, C. H., Svensk Papperstid. 77:629(1974).
2. Schroeder, L. R., Project 3284 Interim Report to the Program Committee, March 17, 1986.
3. Schroeder, L. R.; Wabers, B. A., Project 3475-1 Interim Report to the Program Committee, Sept. 10, 1982.
4. Dimmel, D. R., J. Wood Chem. Technol. 5:1(1985).
5. Dimmel, D. R.; Schuller, L. F., IPC Technical Paper Series Number 159, 160, and 165; J. Wood Chem. Technol., accepted for publication.
6. Dimmel, D. R.; Perry, L. F.; Chum, H. L.; Palasz, P. D., J. Wood Chem. Technol. 5:15(1985).
7. Smith, D. A.; Dimmel, D. R., Internat. Symp. on Wood and Pulping Chem., Vancouver, B.C., Canada, August 28, 1985; Project 3475-2 Interim Report Sept. 5, 1985; Ph.D. Thesis, June, 1986; J. Org. Chem., submitted.
8. Dimmel, D. R.; Schuller, L. F.; Apfeld, P. B., J. Wood Chem. Technol. 7: 97(1987).
9. Lipshutz, B. H.; Pegram, J. J., Tetrahedrom Letters 21:3343(1980).
10. Bovee, M. J., Ph.D. Thesis, The Institute of Paper Chemistry, June, 1987.
11. Ohara, S.; Meshitsuka, G.; Nakano, J., J. Japan Wood Res. Soc. 29:611(1983).
12. Olm, L.; Teder, A., Svensk Papperstid. 89(16):20-2, 25-6(1986).
13. Schroeder, L. R.; Lingnowski, H. J, Project 3475-1 Interim Report, Sept. 5, 1985.
14. Isogai, A.; Ishizu, A.; Nakano, J., J. Appl. Polym. Sci. 29:2097(1984).
15. Schroeder, L. R.; Gentile, V. M.; Atalla, R. H., J. Wood Chem. Technol. 6:1(1986).

THE INSTITUTE OF PAPER CHEMISTRY

Donald Dimmel

Donald R. Dimmel
Senior Research Associate
Wood Sciences
Chemical Sciences Division

Holly J. Willenbrink
Research Assistant

THE INSTITUTE OF PAPER CHEMISTRY

Appleton, Wisconsin

Status Report

to the

PULPING PROCESSES

PROJECT ADVISORY COMMITTEE

Project 3477

DEVELOPMENT AND APPLICATION OF ANALYTICAL TECHNIQUES

Determination of Lignin in Wood Pulp by Diffuse Reflectance Fourier Transform Infrared Spectrometry
(Continued under FKBG Sponsorship: On-line Lignin Sensor)

Analysis of Pulping and Bleaching Liquors by Ion Chromatography

Pyrolysis Gas Chromatography

August 31, 1987

PROJECT SUMMARY FORM

DATE: August 31, 1987

PROJECT NO. 3477: DEVELOPMENT AND APPLICATION OF ANALYTICAL TECHNIQUES

PROJECT LEADER: D. B. Easty

IPC GOAL: N/A

OBJECTIVE:

Evaluate and/or develop analytical techniques which are required to meet demands of both Institute and member company activity.

CURRENT FISCAL YEAR BUDGET: $60,000

SUMMARY OF RESULTS SINCE LAST REPORT:

Determination of Lignin in Wood Pulp by Diffuse Reflectance Fourier Transform Infrared Spectrometry

A manuscript describing the method developed for estimating lignin in unbleached pulps by FTIR has been accepted for publication in Tappi Journal.

This investigation was continued under FKBG sponsorship. Results indicated that diffuse reflectance FTIR measurements can be made on papers and that IR band areas correlate with lignin content. Regression lines for data on handsheets were not significantly different from those on the pulps from which the handsheets were made. Results obtained on smooth and rough sides of handsheets also did not differ significantly.

The use of near-infrared reflectance measurements for estimating lignin content is currently being investigated.

Analysis of Pulping and Bleaching Liquors by Ion Chromatography

Earlier findings on determination of sulfide and sulfate were published in the March, 1987 issue of Tappi Journal.

A suggestion that three guard columns in series would separate sulfoxy anions efficiently was evaluated and confirmed; the thiosulfate retention time was reduced from 35 to 13 minutes with adequate resolution of sulfite and sulfate. Further increases in separation efficiency are achievable by use of gradient elution. This requires a new generation ion chromatograph which is not available at the Institute.

The performance of columns and eluents not formerly used at the Institute was assessed to obtain data for the revised TAPPI test methods on ion chromatography. Review of the test method revisions by officers of the Process and Product Quality Division was conducted in August. The methods should be approved momentarily.

Pyrolysis Gas Chromatography

A manuscript on identification of polymers in paper by pyrolysis gas chromatography has been accepted for publication in Journal of Chromatography. The paper is based on the M.S. research of Tom Crockett. Samples were subjected to low-temperature pyrolysis at 400°C to char the paper; subsequent pyrolysis at 850°C produced characteristic pyrograms of polymers with minimal interference from the paper substrate.

PLANNED ACTIVITY THROUGH FISCAL YEAR 1987:

The thrust of this work will continue to be development of improved techniques for analysis of pulp, paper, and relevant process streams.

Of interest in FKBG-sponsored future work on the FTIR method for estimating lignin will be learning whether the method measures lignin in the bulk sample or only on the surface. Diffuse reflectance spectra obtained on fibers lumen-loaded with TiO_2 may indicate whether materials within the fibers are sensed by the technique. Mixtures of cotton linters and high lignin-content fibers will be studied to detect a possible effect of sample inhomogeneity. The investigation of near-infrared for estimating lignin content will be continued if the results of orienting studies are favorable.

Additional studies on ion chromatography will be directed at increasing the accuracy and efficiency of analysis, within the limits of our instrumentation, and solving problems as they arise. The stability or instability of the anions of interest in pulping liquors has not been adequately documented; it will be studied further.

An inductively coupled plasma spectrometer has been purchased, and it should be in operation in September. Before submitted samples can be run, optimized conditions for measuring the elements of interest in various types of samples must be developed. This preliminary work will be essential in order to assure the quality of the data obtained with the new instrument.

Student research will continue on: (a) development of techniques for quantitative determination of volatiles in paper by headspace analysis, and (b) evaluation of the CIRCLE cell for infrared analysis of aqueous solutions.

FUTURE ACTIVITY:

Future work will involve continued studies of pulp, paper, and liquors by chromatographic and spectrometric techniques.

Status Report

DEVELOPMENT AND APPLICATION OF ANALYTICAL TECHNIQUES

Determination of Lignin in Wood Pulp by Diffuse Reflectance Fourier Transform Infrared Spectrometry

(Continued under FKBG Sponsorship: On-line Lignin Sensor)

INTRODUCTION

The ultimate objective of this project is the development of an on-line lignin sensor. Intermediate tasks involve evaluation of infrared and Raman spectrometry for estimating the lignin content of pulp and paper. Raman spectrometry should be useful for analysis of wet samples, such as pulp slurries. The strong absorption of infrared energy by water restricts infrared analysis to dry samples, such as handsheets. Thus, infrared is likely to remain principally a laboratory technique. However, findings from the investigation of lignin estimation via infrared should aid subsequent studies employing Raman.

An earlier study has revealed the existence of linear relationships between the area of the 1510 cm^{-1} infrared band of unbleached pulps, measured on diffuse reflectance difference spectra, and kappa number and Klason lignin.[1] These relationships serve as calibration lines for lignin estimation. An unknown pulp's 1510 cm^{-1} band area is referred to the line to estimate its lignin content. This method is nondestructive, requires no sample preparation other than drying, employs no calculations, and may be used on pulp samples as small as 0.5 mg.

The current investigation was undertaken to evaluate diffuse reflectance Fourier transform infrared (FTIR) spectrometry for estimating the lignin content of paper. Specific questions to be answered by this work include: Can

diffuse reflectance FTIR measurements be made on paper? Does the area of the 1510 cm^{-1} band correlate with the paper's lignin content? What effect does sample surface (pulp vs. paper, rough vs. smooth paper) have on the measurements?

EXPERIMENTAL

Pulps were selected for this study from those used in the earlier investigation on determination of lignin in wood pulp by diffuse reflectance FTIR.[1] The principal criterion for selection was that enough pulp must be available for the preparation of at least one handsheet. Fourteen pulps were disintegrated and made into single handsheets of basis weight approximately 60 g/m^2 on the British sheet mold. The sheets were pressed and air dried with one side of each sheet against a polished plate. Thus each handsheet had a smooth side and a rough side. A cork borer was used to cut 8-mm diameter disks from each handsheet to fit the diffuse reflectance attachment.

Spectra were collected on a Nicolet 7199 FTIR spectrometer equipped with a liquid nitrogen-cooled MCT detector and a Harrick Praying Mantis diffuse reflectance attachment. Maximum spectral resolution was 2 cm^{-1}. Five hundred scans for each sample were accumulated in approximately nine minutes.

The disks from the handsheets were placed in the diffuse reflectance attachment where the IR beam was focused for maximum signal output. Infrared spectra were recorded for both surfaces of each handsheet and for cotton linters. Each spectrum was ratioed against a background of potassium chloride before baseline correction. The reference cotton linters was subtracted from each pulp sample by manually obtaining the best baseline subtraction in the aliphatic C-H stretch region (2800-3000 cm^{-1}). To determine the best subtraction factor, the spectrum of the cotton linters was overlaid on the pulp

spectrum on the computer screen. The area of the lignin band at 1510 cm^{-1} was integrated and recorded for data analysis. Determinations were performed in duplicate.

RESULTS AND DISCUSSION

Infrared band areas (1510 cm^{-1}) were measured by diffuse reflectance FTIR on each side of handsheets made from 14 kraft pulps. The pulps represented a range of kappa numbers from 11 to 65 and Klason lignin from 0.9 to 8.7%. Data are shown in Fig. 1 and 2.

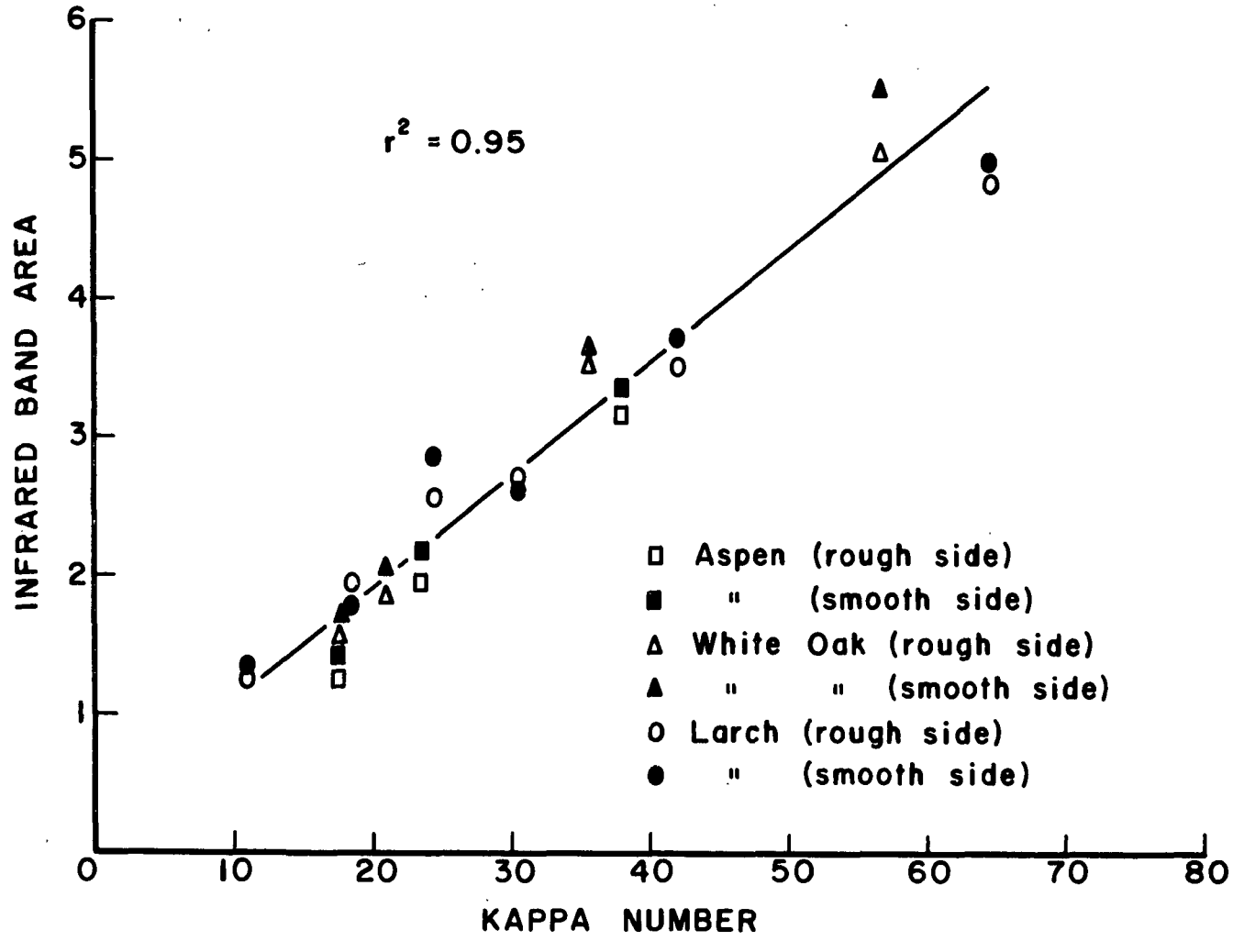

Figure 1. Diffuse reflectance FTIR band area (1510 cm^{-1}) measured on handsheets vs. kappa number.

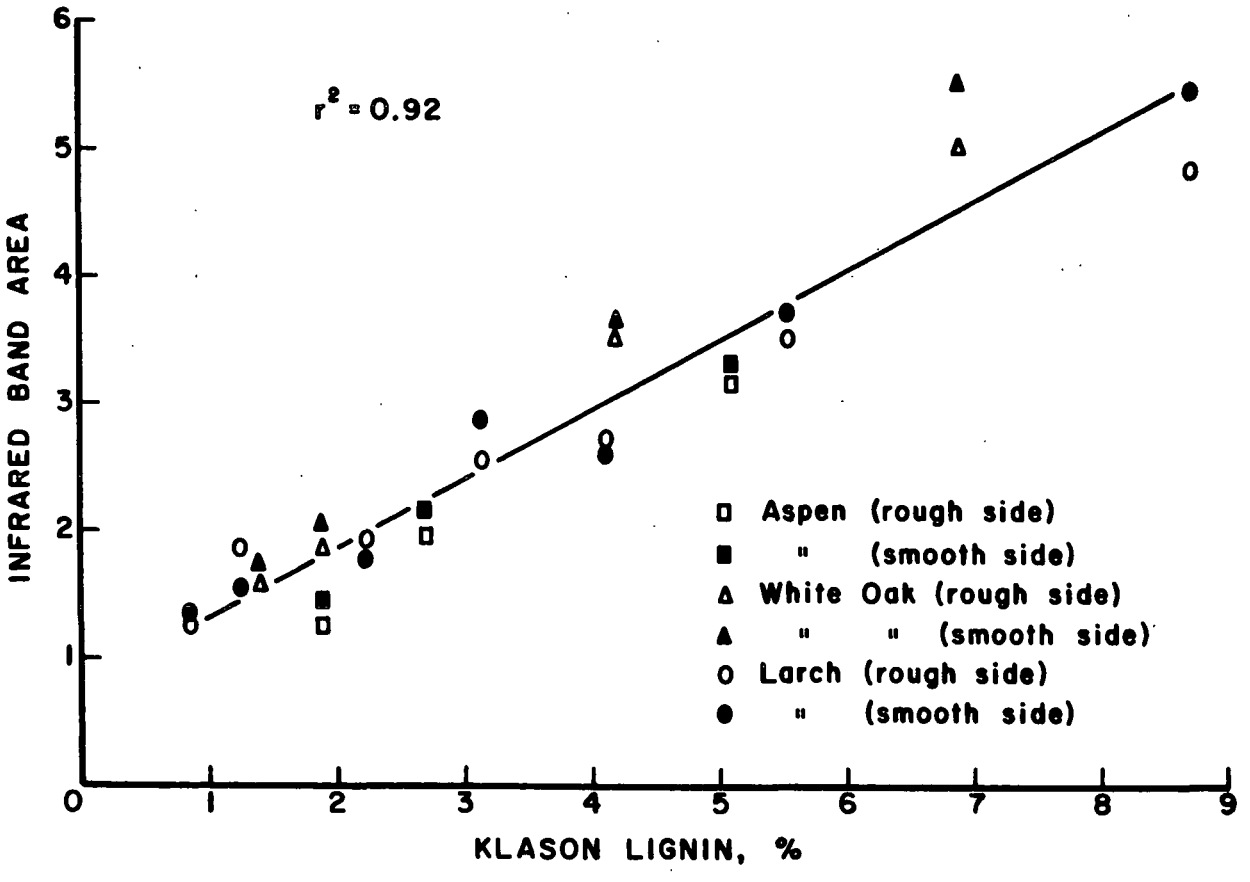

Figure 2. Diffuse reflectance FTIR band area (1510 cm^{-1}) measured on handsheets *vs.* Klason lignin.

Results indicate that diffuse reflectance FTIR measurements can be made on papers and that IR band areas correlate with lignin content. Infrared band areas measured on the smooth side of most of the handsheets appeared to be greater than those measured on the rough side. However, slopes and intercepts of regression lines for data from smooth and rough sides of the handsheets did not differ significantly. Furthermore, regression lines for data on handsheets were not significantly different from those on the pulps from which the handsheets were made. Thus, it appears that the physical character of the sample surface has little effect on the measurement of "FTIR lignin."

Diffuse reflectance is, by definition, radiation which emerges from a bulk sample after penetrating one or more particles.[2] It has been used to analyze granular solids, powders, and polymer foams.[2-4] Thus its utility for analysis of clumps of pulp fibers was anticipated, but we were concerned about its application for the analysis of paper with a smooth surface. Radiation which undergoes reflections from particle surfaces, but never actually penetrates the surface, constitutes specular reflectance.[2] This type of reflectance is a more likely occurrence with smooth samples. Data collected in the present investigation were probably comprised of specular as well as diffuse reflectance, even though the instrument component used was the diffuse reflectance accessory. This would seem to be a reasonable explanation for the insensitivity of the lignin estimation method to the nature of the sample surface.

FUTURE WORK

An attempt will be made to estimate the depth of penetration of diffuse reflectance measurements into pulp and paper. This result will indicate whether the method is measuring surface or bulk lignin. Also included in future work will be a study of the possible effect of sample inhomogeneity.

LITERATURE CITED

1. Berben, S. A.; Rademacher, J. P.; Sell, L. O.; Easty, D. B. Determination of lignin in wood pulp by diffuse reflectance Fourier transform infrared spectrometry. IPC Technical Paper Series Number 210. January, 1987.

2. Suzuki, E. M.; Gresham, W. R., J. Forensic Sci. 31(3):931(1986).

3. Suzuki, E. M.; Gresham, W. R., J. Forensic Sci. 31(4):1292(1986).

4. Suzuki, E. M.; Gresham, W. R., J. Forensic Sci. 32(2):377(1987).

THE INSTITUTE OF PAPER CHEMISTRY

Sally A. Berben
Sally A. Berben
Research Assistant
Analytical Sciences
Chemical Sciences Division

Dwight B. Easty
Dwight B. Easty
Group Leader
Analytical Sciences
Chemical Sciences Division

Status Report

DEVELOPMENT AND APPLICATION OF ANALYTICAL TECHNIQUES

Analysis of Pulping and Bleaching Liquors by Ion Chromatography

INTRODUCTION

Earlier work in this project has documented the validity of ion chromatography (IC) for the analysis of pulping liquors[1] and bleaching liquors.[2] Additional investigations led to improved methods for determining sulfide and sulfate.[3] Efforts during the past year have been devoted to revising the TAPPI test methods on ion chromatography and to improving the accuracy, precision, and efficiency of ion chromatographic analysis of pulping liquors in our laboratory. This report describes our recent findings and our proposed changes in methods for ion chromatography.

RESULTS AND DISCUSSION

ACCURACY, PRECISION, AND INSTRUMENT STABILITY

It became evident over a year ago that the sensitivity of the ion chromatograph was increasing during a day's running of samples. This occurred in the determination of sulfoxy anions and chloride, separated by conventional IC, and it was even more pronounced in determinations of carbonate, analyzed by ion chromatography exclusion (ICE). Because the day-to-day response of sulfoxy anions did not vary greatly, an analyst who injected standards only in the morning might overlook the effect. We do not know whether this is a widespread problem or whether it occurs only with our instrument.

Several actions were taken to minimize the effect of varying instrument response on our data. Our normal procedure for sulfoxy anions and chloride had

been to calibrate the Hewlett-Packard 3390A integrator by injection of a standard mixture in the morning. The frequency of standard injection and recalibration was increased to three times per day. Carbonate is normally calculated from a calibration line based on standards of 5, 10, and 15 ppm. After response variations were detected, injection of one of the standards before each sample and preparation of three new calibration lines each day became normal practice. Some typical calibration lines are shown in Fig. 1.

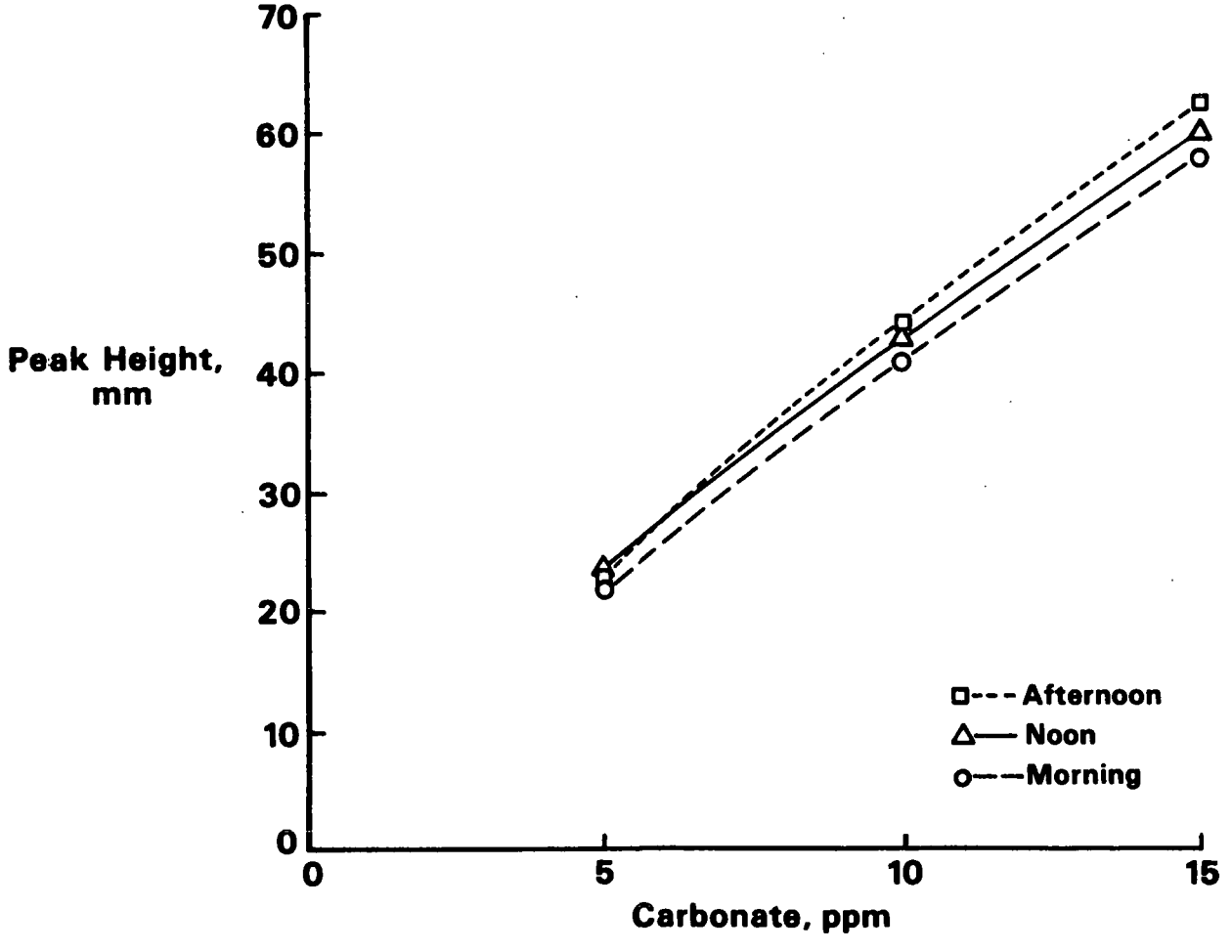

Figure 1. Carbonate calibration lines from data of August 19, 1987.

When uncompensated response variations occur, duplicate samples injected in succession can yield results with good precision but poor accuracy. The running of randomized replicates, i.e., injection of duplicates not in succession, alerts the analyst to this problem when duplicate values do not agree. Duplicates are now run in random order in our laboratory.

Likely sources of changing ion chromatograph response are variations in room temperature and instrument baseline. The temperature effect occurred despite room air conditioning and temperature compensation in the conductivity detectors. Baseline stability has been significantly improved by installation of an eluent degassing module and use of a micromembrane suppressor in place of a fiber suppressor. An additional benefit of the micromembrane suppressor is that it produces a stable baseline soon after start-up. This permits analysis of samples to begin earlier in the day.

An internal standard was desired to more fully compensate for variations in instrument response. A known amount of the internal standard would be added to each sample; its response would serve as the basis for quantitation of the sulfoxy anions. To be an acceptable internal standard, the added species would have to be stable in all samples and would have to be resolved from all other peaks on the ion chromatograms of the samples. The following anions were tested and found not to be acceptable as internal standards: fluoride, bromide, iodide, phosphite, phosphate, nitrite, nitrate, tartrate, and biphthalate. Fortunately, the improved stability provided by the micromembrane suppressor reduces the need for an internal standard.

An improvement in the stability of the carbonate response was sought by changing the eluent. The eluent normally used for carbonate is distilled water,

which doesn't require a suppression device. Octanesulfonic acid (1mM) was tried as the new eluent; it was used with the AFS-2 suppressor and ammonium hydroxide as suppressor regenerant. The new eluent yielded higher sensitivity for carbonate in green and white liquors. This eluent cannot be used with black liquors because it separates organic acids, one of which interferes with carbonate. Unfortunately, the new eluent did not solve the problem of increasing carbonate response.

Within-laboratory precision of ion chromatographic analysis of pulping liquors is shown by the repeatability data in Table 1, prepared for the revised TAPPI test method on IC. For most ions, repeatabilities are in the 10-15% range. Values were computed from data from randomized duplicate runs, and a test result is considered to be a single determination. Repeatabilities are not reported for sulfide because a UV detector was not available at the Institute when this work was done. Our earlier work on sulfide employed a UV detector loaned to us by Dionex Corporation; the detector was returned to Dionex early in 1986. We now determine sulfide by potentiometric titration.

Table 1. Repeatability values for ion chromatographic analysis of pulping liquors.[a]

	Carbonate	Sulfate	Chloride	Sulfite	Thiosulfate	Sulfide	Organic Acids
Black liquor	10	12	15	30	16	NA[b]	15
Green liquor	15	10	10	25	7	NA	--
White liquor	12	10	12	30	15	NA	--
Smelt	NA	NA	NA	NA	NA	NA	--

[a]Repeatability expressed as percentage of mean.
[b]NA = not available.

COLUMNS, ELUENTS, AND RETENTION TIMES

When the proposed revision of the TAPPI test method on IC was reviewed by the Chemical Properties Committee, addition of a table of retention times with different columns and eluents was proposed. Table 2 was then compiled, based upon data from our laboratory. The retention time of thiosulfate was about one-half hour or longer for all column-eluent combinations in the table.

Table 2. Some typical retention times: chloride, oxalate, sulfoxy anions.

Guard Column	Separator Column	Eluent	Flow Rate, mL/min	Retention Time, min[a] Chloride	Sulfite	Sulfate	Oxalate	Thiosulfate
HPIC-AG3	HPIC-AS3	3.0 mM $NaHCO_3$ +2.4 mM Na_2CO_3	2.3	2.0	5.7	8.6	12.0	40.9
HPIC-AG4A	HPIC-AS4A	2.0 mM Na_2CO_3 +0.75 mM $NaHCO_3$	2.0	1.8	6.1	7.8	9.8	27.4
HPIC-AG4	HPIC-AS5	1.0 mM Na_2CO_3 +5.0 mM NaOH +0.8 mM p-cyano-phenol	1.6	1.8	5.8	6.9	8.1	29.6
HPIC-AG4	HPIC-AS5	3.0 mM $NaHCO_3$ +2.4 mM Na_2CO_3 +0.8 mM p-cyano-phenol +2% CH_3CN	1.8	1.6	5.5	6.1	6.9	26.0

[a]Approximate times with new columns. Retention times decrease with column use.

Because the slow elution of thiosulfate limits the number of samples that can be run in a day, conditions were sought which would yield faster ion chromatograms without losing resolution of ions of interest. Replacing the 25-cm long separator column with three guard columns in series (15 cm effective length) was suggested.[4,5] This was tested using three AG3 columns with carbonate-bicarbonate eluent at 2.3 mL/min. Figure 2 shows that the thiosulfate

retention time was reduced to about 13 minutes with adequate resolution of sulfite and sulfate. Use of this column arrangement should significantly increase a laboratory's sample throughput.

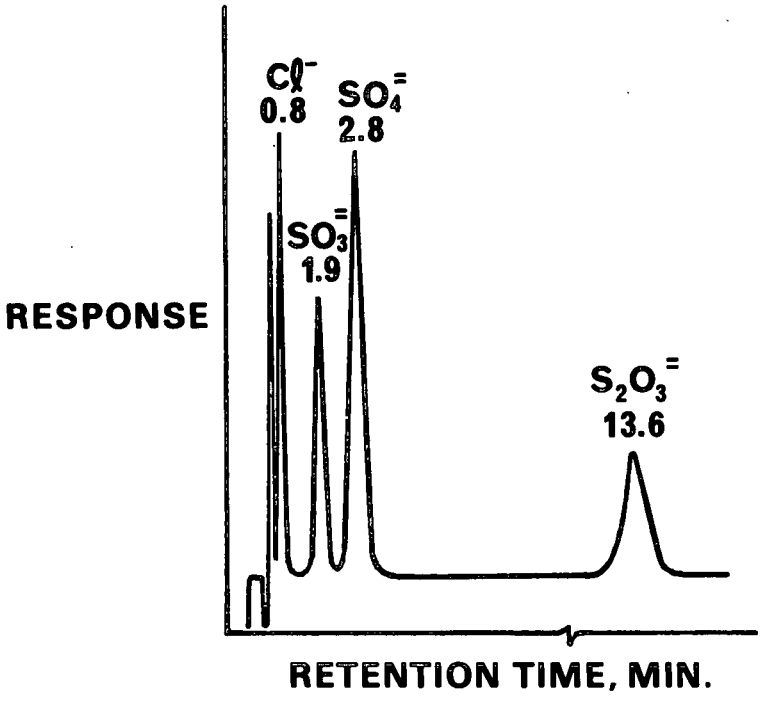

Figure 2. Ion chromatogram using three guard columns in series.

Further increases in separation efficiency by use of gradient elution have been reported.[6] A complete determination of sulfoxy anions can be achieved in 11 minutes. This requires a new generation ion chromatograph (Dionex 4000i) which is not available at the Institute.

CONCLUSIONS AND FUTURE WORK

The time required for ion chromatographic determination of sulfoxy anions in pulping liquors can be significantly shortened by use of three guard columns in series (or a shortened separator column) in place of the normal

separator column. Variations in response of the ion chromatograph can be reduced somewhat by installation of an eluent degassing module and use of a micromembrane suppressor. The frequent running of standards can lessen the impact of residual response variations on analytical results.

Work will continue on increasing the accuracy and efficiency of ion chromatographic analysis. The stability of the ions of interest in liquor samples during storage before analysis will receive further study.

ACKNOWLEDGMENT

The receipt of guard and separator columns from Dionex Corporation for evaluation of retention times is gratefully acknowledged.

LITERATURE CITED

1. Easty, D. B.; Borchardt, M. L.; Webb, A. A., Paperi Puu 67(9):501(1985).
2. Easty, D. B.; Johnson, J. E.; Webb, A. A., Paperi Puu 68(5):415(1986).
3. Easty, D. B.; Johnson, J. E., Tappi J. 70(3):109(1987).
4. Douek, M.; Pulp and Paper Research Institute of Canada, Personal Communication, 1987.
5. Goss, J.; Westvaco Corp., Personal Communication, 1987.
6. Falleur, G. C.; Longview Fibre Company, Personal Communication, 1987.

THE INSTITUTE OF PAPER CHEMISTRY

Connie L. Weber /dc.

Connie L. Weber
Research Assistant
Analytical Sciences
Chemical Sciences Division

Dwight B. Easty

Dwight B. Easty
Group Leader
Analytical Sciences
Chemical Sciences Division

Status Report

DEVELOPMENT AND APPLICATION OF ANALYTICAL TECHNIQUES

Pyrolysis Gas Chromatography

INTRODUCTION

A study of the identification of polymers in paper by pyrolysis gas chromatography has been performed by Tom Crockett as partial fulfillment of the requirements for the M.S. degree from the Institute. This work is described in the enclosed manuscript, IPC Technical Paper Series 239, which has been accepted for publication in Journal of Chromatography.

Identification of polymers in paper by pyrolysis gas chromatography. Reduction of paper interference by prepyrolysis.

THOMAS D. CROCKETT,‡ ARTHUR A. WEBB, LEROY G. BORCHARDT and DWIGHT B. EASTY*

*Chemical Sciences Division, The Institute of Paper Chemistry, P. O. Box 1039, Appleton, WI 54912 (U.S.A.)

A sequential pyrolysis procedure has been developed to facilitate the identification of polymers in paper by pyrolysis gas chromatography. The sample was subjected to low-temperature pyrolysis (prepyrolysis) at 400°C to char the paper; subsequent pyrolysis at 850°C produced characteristic pyrograms of polymers with minimal interference from the paper substrate. Of twenty-one polymers added to paper, twelve yielded identifiable "fingerprint" pyrograms by employing the prepyrolysis-pyrolysis sequence.

‡Present address: Westvaco Corp., N. Charleston, SC (U.S.A.)

INTRODUCTION

Pyrolysis gas chromatography (PGC) has been used extensively for the analysis of polymers [1], but its application to the identification of polymers in paper has been rather limited [2-8]. Polymer-containing papers are most often analyzed to determine the additives used in a product, or to identify deposits and contaminants inadvertently picked up during paper manufacturing, especially from recycled fiber [7,8].

Pyrograms of polymer-paper combinations are complex, because they contain peaks representing pyrolysis products of the paper as well as the polymer. As a result, identification of the polymer of interest is often extremely difficult. This is especially true for small amounts of polymer because the pyrolysis products of the paper dominate the pyrogram. Some investigators have pyrolyzed paper without polymer and then have attempted to subtract visually the peaks due to the paper from the pyrogram of the mixture [2,6]. Such an approach is difficult under the best of conditions, and it is likely to fail when there are secondary pyrolysis reactions between the pyrolysis products of the polymer and the paper. Furthermore, a paper identical to that in the polymer-paper combination is not always available.

Whenever possible, the polymer is removed from the paper prior to analysis. Coatings and saturants are extracted with solvents, and deposits and discrete plastic fragments are lifted from the paper surface [7,8]. However, a preliminary separation of polymer and paper is not feasible for all analyses. Crosslinked polymers cannot be extracted, and small polymer specks often cannot be dissolved in solvents or removed without paper contamination. A technique is needed to enhance the response of the polymer in PGC relative to that of the

paper. This has been achieved with styrene-containing polymers [4]. Low-temperature (600°C) prepyrolysis decomposed the paper, and its products were vented; subsequent pyrolysis at 725°C yielded pyrograms used to determine styrene-butadiene.

The current investigation was undertaken to more fully evaluate the prepyrolysis technique for identification of polymers in paper. Sufficient quantities of a large number of polymers were found to survive prepyrolysis to be identified by subsequent pyrolysis at higher temperature. Optimized pyrolysis and gas chromatographic (GC) conditions were developed to permit characterization of the polymers via "fingerprint" pyrograms or mass spectral (MS) analysis of pyrolysis products.

EXPERIMENTAL

PGC and PGC/MS instrumentation and conditions

Pyrolyses were performed with a CDS Pyroprobe 120 (Chemical Data Systems, Oxford, PA, U.S.A.). For prepyrolysis, the sample probe was inserted into a 15-cm x 12-mm Pyrex tube closed at both ends with silicone septa and caps. One septum was bored out to admit the probe. After purging with nitrogen for 1 min, the tube was capped and the sample was prepyrolyzed for 2 min at 400°C. The probe was withdrawn from the tube and inserted into the GC interface mounted on a Hewlett-Packard 5890A GC.

Pyrolysis was performed at 850°C for 10 s with the ramp setting on the pyrolyzer in the "off" position. The GC interface was maintained at 200°C. Products of pyrolysis were separated on a 6-ft. x 2-mm I.D. glass column packed with 1% SP1000 on 60/80-mesh Carbopak B. Column temperature was programmed from

40 to 200°C at 8°C/min, and the helium carrier gas flow rate was 20 ml/min. Injector temperature on the GC was 250°C, and the flame ionization detector temperature was 300°C. Data were recorded on a Hewlett-Packard 3388A integrator.

A Hewlett-Packard 5985B GC/MS was used for identification of pyrolysis products. All conditions were the same as on the 5890A GC, except that a higher carrier gas flow rate, 30 ml/min, was required for proper operation of the jet separator. This reduced retention times by about 1 min. Pyrolysis products were identified by comparing their mass spectra, via computer, with those in the Wiley Library.

Pulps, papers, and polymers

One sample each of bleached hardwood kraft, unbleached softwood kraft, and thermomechanical pulp (TMP) was selected for study. Laboratory-made papers were prepared from the bleached kraft pulp.

Polymers typical of those used in paper saturation, coating, sizing, and as dry- and wet-strength additives were studied (Polymer Sample Kit, Scientific Polymer Products, Ontario, NY, U.S.A). The polymers were pyrolyzed alone and after addition to the paper as a solution or a melt. Samples for pyrolysis weighed 1 mg or less. A semimicro balance was used for weighing the samples.

RESULTS AND DISCUSSION

Removal of paper matrix by prepyrolysis

Low-temperature pyrolysis (prepyrolysis) conditions were sought which would substantially destroy the paper and leave intact the polymeric additives and coatings. The paper's contribution to a subsequent higher temperature

pyrogram would thus be minimized. Because cellulose has been shown to undergo pyrolysis at 300-500°C [9], prepyrolysis of the pulp samples was studied in that range.

The prepyrolysis temperature was increased in increments above 300°C; 400°C was found to be the lowest temperature at which most of the pulp was charred. At prepyrolysis temperatures above 400°C, significant additional changes in the pulp were not observed. Figure 1 shows pyrograms (850°C) of the bleached hardwood kraft pulp with and without prepyrolysis at 400°C. It is evident that most of the pulp was pyrolyzed at 400°C, leaving little to contribute to the high-temperature pyrogram. Similar results were obtained on the unbleached softwood kraft and the TMP pulps. The area of the major peak in the high-temperature pyrogram of bleached, unbleached, and TMP pulp was reduced by 97, 91, and 80%, respectively, after prepyrolysis.

(Fig. 1 here)

Effect of prepyrolysis on polymers

Twenty-one polymers were subjected to pyrolysis (850°C) and to the prepyrolysis (400°C) - pyrolysis sequence. The area of the major peak in the high-temperature pyrogram of the 12 polymers in Table I was reduced by almost one-half or less as a result of prepyrolysis. Thus, sufficient quantities of these polymers, when added to paper, would be expected to survive the paper's charring in prepyrolysis to be identified by subsequent pyrolysis at higher temperature. An example of the performance of these polymers is shown in Fig. 2; the pyrogram of polyvinyl butyral was virtually unchanged by prepyrolysis. Additional examples of fingerprint pyrograms obtained after prepyrolysis are shown in Fig. 3.

(Table I and Fig. 2 and 3 here)

Because substantial reductions in peak areas were sustained in prepyrolysis, the nine polymers in Table II are less likely to be identifiable in paper by the sequential pyrolysis technique. Despite large peak area reductions, four of the polymers, polyvinyl chloride, methyl and ethyl cellulose, and polyacrylamide, exhibited characteristic high-temperature pyrograms after prepyrolysis. Later work showed, however, that these materials could not be readily determined in paper by PGC.

(Table II here)

Compilation of library of pyrograms

The polymers listed in Table I were found to yield characteristic "fingerprint" pyrograms with well resolved peaks. In uncomplicated samples these materials should be identifiable from their pyrograms by inspection. As a further aid to polymer identification, the pyrolysis products represented by the principal peaks on the pyrograms were identified by PGC/MS. Peak identifications are listed in Table III. These data should faciliate use of PGC/MS to analyze polymer mixtures which yield pyrograms too complex for visual interpretation.

(Table III here)

Identification of polymers in paper

Each of the polymers listed in Table I was added to paper and subjected to sequential pyrolysis. The resulting pyrograms matched the library pyrograms of the polymers, as is illustrated by the example in Fig. 4. Amounts of polymer in the polymer-paper combinations ranged from 18 to 81%; the higher amounts were those polymers added as melts. A high polymer-to-paper ratio would be typical of a deposit or a polymer-paper laminate but not of a pigment-coated paper with a polymer binder.

(Fig. 4 here)

As a final test of the PGC procedure, sequential pyrolysis was used to analyze a commercially-prepared wrapping paper (polyethylene-coated freezer wrap). Pyrograms from the coated paper and the library, shown in Fig. 5, display some differences in peak heights, but the match between the polyethylene in the paper and in the library is quite evident.

(Fig. 5 here)

Results of this study show that prepyrolysis can be used to minimize the contribution of the paper matrix and simplify the identification of many polymers in paper by PGC.

ACKNOWLEDGMENT

Portions of this work were used by TDC as partial fulfillment of the requirements for the Master of Science degree at The Institute of Paper Chemistry.

REFERENCES

1 W. J. Irwin, Analytical Pyrolysis, Marcel Dekker, New York, 1982, Ch. 6.
2 M. Chene, O. Martin-Borret, O. Bollon and A. Perret, Papeterie, 88 (1966) 1587.
3 A. Seves, A. Groce and P. Brizzi, Ind. Carta, 10 (1972) 271.
4 C. G. Smith and R. Beaver, Tappi, 63(8) (1980) 93.
5 E. J. Levy and T. P. Wampler, J. Forens. Sci., 31(1) (1986) 258.
6 T. P. Wampler and E. J. Levy, LC·GC, 4 (1986) 1112.
7 L. Sjöström and M. Kjellman, Proc. Int. Process and Materials Quality Evaluation Conf., Atlanta, GA, September 21-24, 1986, TAPPI, Atlanta, 1986, p. 179.
8 N. Dunlop-Jones and L. H. Allen, Proc. Int. Process and Materials Quality Evaluation Conf., Atlanta, GA, September 21-24, 1986, TAPPI, Atlanta, 1986, p. 183.
9 F. Shafizadeh, R. H. Furneaux, T. G. Cochran, J. P. Scholl and Y. Sakai, J. Appl. Polym. Sci., 23 (1979) 3525.

TABLE I

EFFECT OF PREPYROLYSIS ON POLYMERS*

Sample	Retention time of major peak (min)	Reduction of peak area (%)
Styrene butadiene	27.84	4
Polybutyl acrylate	13.09	13
Polyethyl acrylate	17.08	53
Polyethylene	15.54	50
Polypropylene	10.10	29
Polyvinyl butyral	10.26	15
Styrene maleic anhydride	27.84	51
Polyamide resin	15.53	4
Acrylonitrile styrene butadiene	28.22	13
Styrene isoprene	27.99	25
Ethylene vinyl acetate	6.46	3
Polystyrene	27.83	10

* The area of the major peak in the high-temperature pyrogram of these polymers was reduced by about one-half or less in prepyrolysis.

TABLE II

EFFECT OF PREPYROLYSIS ON POLYMERS*

Sample	Retention time of major peak (min)	Reduction of peak area (%)
Polyvinyl alcohol	13.18	96
Melamine formaldehyde resin	No characteristic pattern	--
Polyvinyl acetate	12.27	90
Polyvinyl chloride	14.97	88
Polyvinylidene chloride	Very low response	--
Methyl cellulose	9.22	68
Cationic starch	5.95	78
Ethyl cellulose	4.23	61
Polyacrylamide	6.58	72

* These polymers experienced substantial pyrolysis under prepyrolysis conditions.

TABLE III

PYROLYSIS PRODUCTS IDENTIFIED BY PGC/MS

Sample	Retention time of main peak (min)	PGC/MS identification*
Styrene butadiene	6.46	1,3-butadiene
	9.11	1,3-cyclopentadiene
	14.93	benzene
	21.19	toluene
	24.23	ethylbenzene
	27.84	styrene
Polybutyl acrylate	5.53	isobutene
	10.15	butyraldehyde
	13.09	butyl alcohol
	25.92	butyl acrylate
Polyethyl acrylate	4.39	ethanol
	15.79	benzene
	17.08	ethyl acrylate
	21.32	toluene
Polyethylene	5.44	2-methyl propene
	6.61	1,3-butadiene
	9.01	cyclopentene
	9.27	1,3-cyclopentadiene
	10.36	1,1-dimethylcyclopropane
	12.61	1-pentyne
	13.41	1,3-pentadiene
	14.66	cyclohexene
	15.13	benzene
	15.54	1,4-cyclohexadiene
	20.47	1-heptene
	21.44	toluene
Polypropylene	5.28	isobutane
	5.85	isobutene
	6.42	1,2-butadiene
	9.07	1,3-cyclopentadiene
	10.10	1,1-dimethylcyclopropane
	10.89	2-methyl-2-butene
	11.22	N-pentane
	11.44	cyclopentene
	14.81	1-hexene
	15.19	1,4-cyclohexadiene
	16.50	1,4-dimethyl-1,3-pentadiene
	17.83	2,4-dimethyl-1-pentene
	18.19	2-methylfuran
	18.75	2-methyl-1,5-hexadiene
	21.20	toluene
	26.85	2-ethyl-1-butanol

* See end of table for footnotes.

TABLE III (Continued)

PYROLYSIS PRODUCTS IDENTIFIED BY PGC/MS

Sample	Retention time of main peak (min)	PGC/MS identification*
Polyvinyl butyral	5.32	1-butene
	5.81	acetone
	6.48	1,2-butadiene
	9.12	1,3-cyclopentadiene
	10.26	butyraldehyde
	13.16	2-butenal
	14.96	benzene
	21.26	toluene
Styrene maleic anhydride	15.15	benzene
	21.40	toluene
	24.53	ethylbenzene
	28.28	styrene
Polyamide resin	5.43	isobutene
	6.22	propenitrile
	6.59	1,3-butadiene
	9.26	1,3-cyclopentadiene
	10.35	1,1-dimethylcyclopropane
	11.41	isoprene
	15.10	benzene
	15.53	1-hexane
	16.62	N-hexane
	20.45	1-heptene
	21.40	toluene
	25.27	1-octene
Acrylonitrile styrene butadiene	6.66	1,3-butadiene
	15.15	benzene
	21.43	toluene
	24.52	ethylbenzene
	28.22	styrene
Styrene isoprene	5.85	isobutene
	6.52	1,2-butadiene
	11.60	isoprene
	15.02	benzene
	15.27	cyclohexadiene
	21.27	toluene
	24.36	ethylbenzene
	27.99	styrene
	29.44	xylene

* See end of table for footnotes.

TABLE III (Continued)

PYROLYSIS PRODUCTS IDENTIFIED BY PGC/MS

Sample	Retention time of main peak (min)	PGC/MS identification*
Ethylene vinyl acetate	5.32	2-butene
	6.46	1,2-butadiene
	9.12	1,3-cyclopentadiene
	10.21	ethylcyclopropane
	11.14	acetic acid
	13.21	cyclopentene
	14.93	benzene
	15.36	1-hexene
	20.28	1-heptene
	21.22	toluene
Polystyrene	14.98	benzene
	21.17	toluene
	24.18	ethylbenzene
	27.83	styrene

*Identifications are based on the best match of an unknown spectrum with spectra in the Wiley Library.

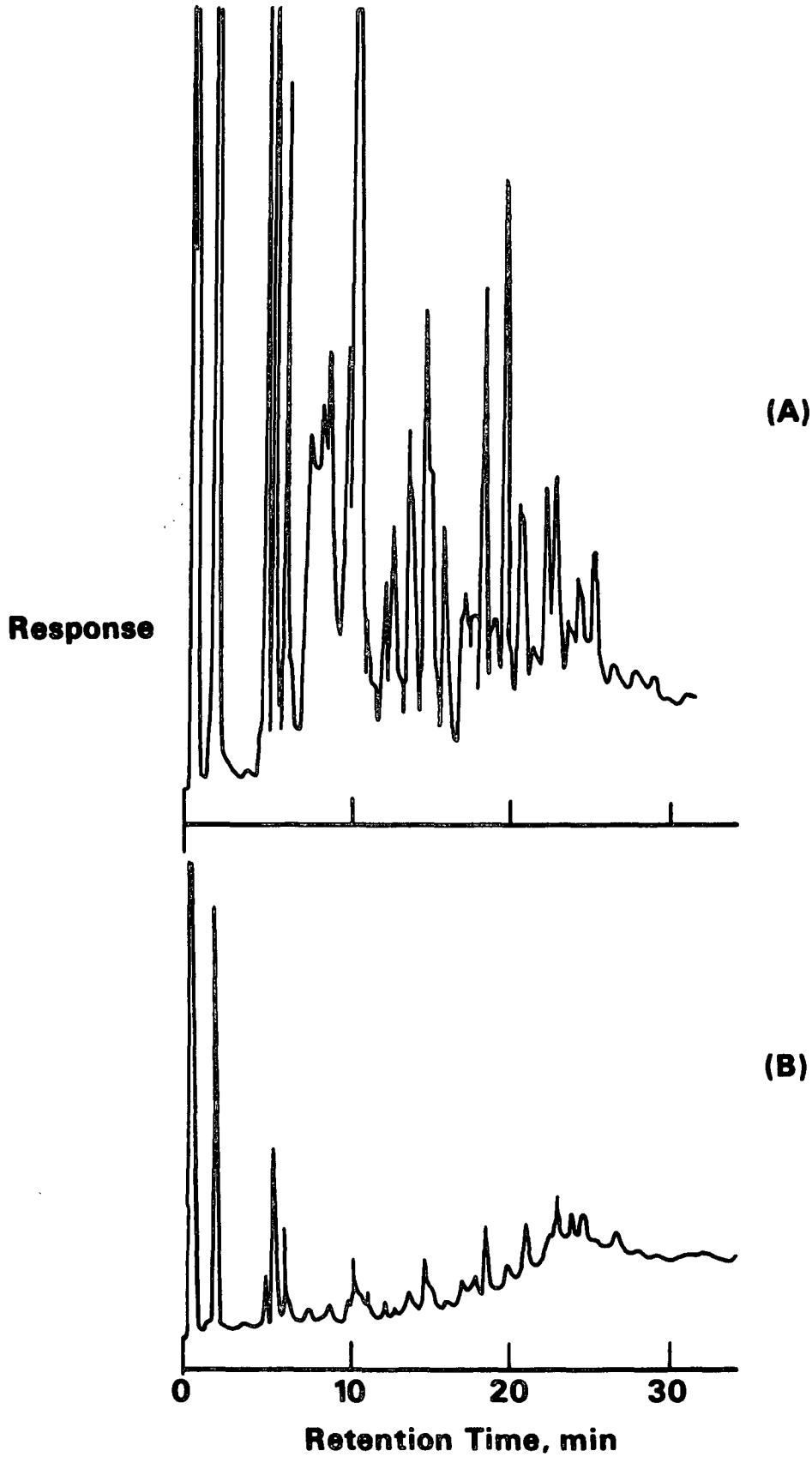

Fig. 1. Pyrogram of (A) bleached hardwood kraft pulp and (B) same after prepyrolysis.

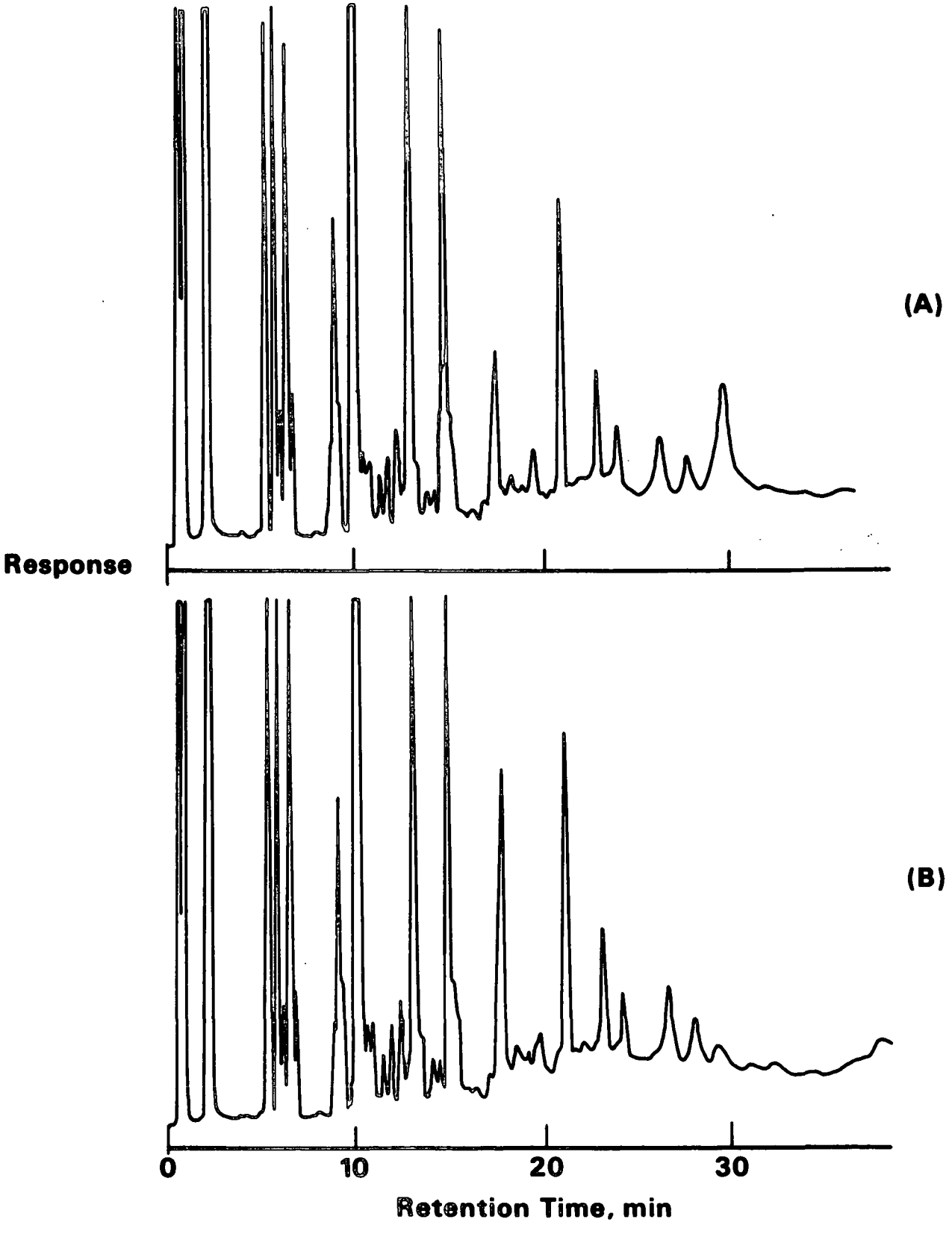

Fig. 2. Pyrogram of (A) polyvinyl butyral and (B) same after prepyrolysis.

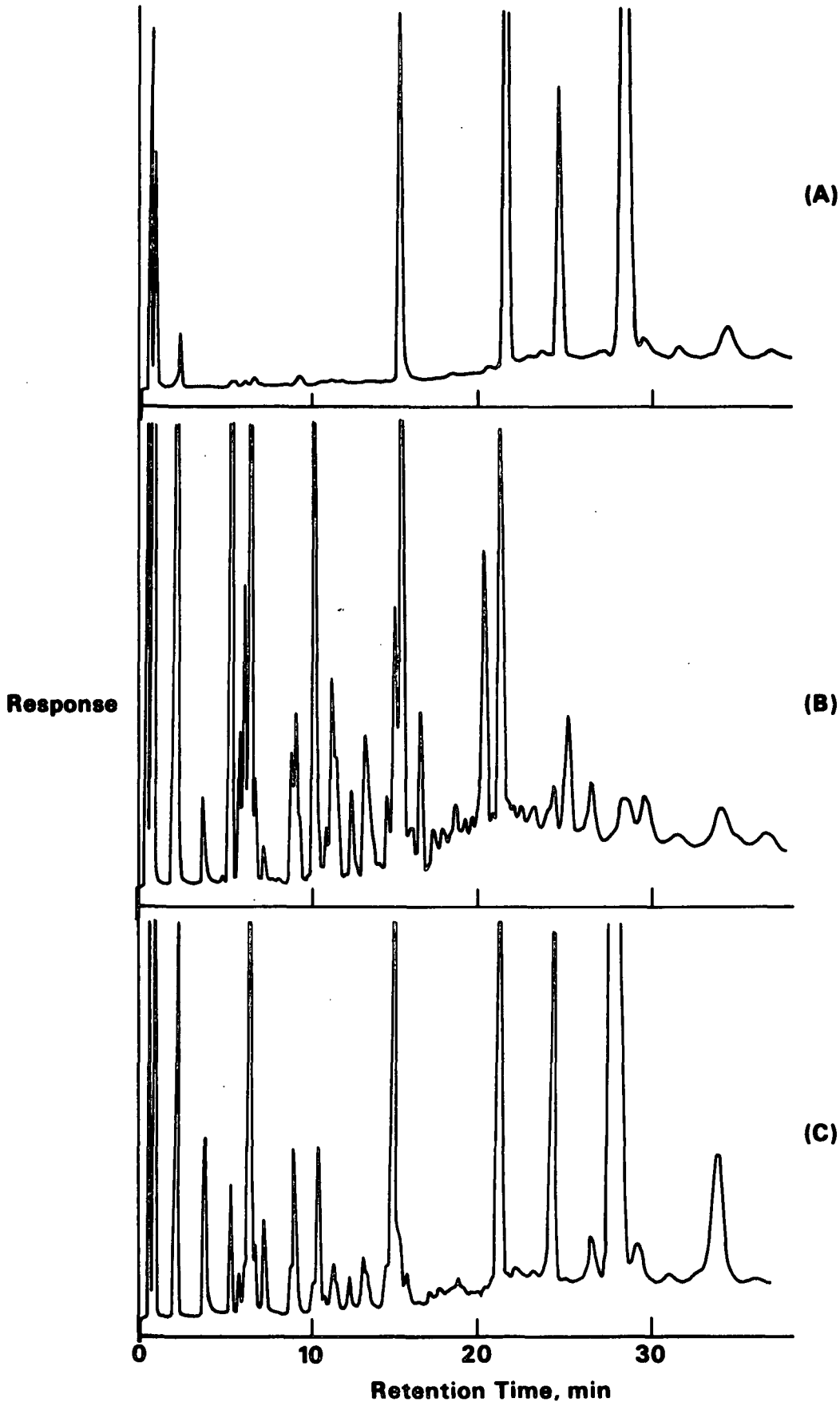

Fig. 3. Pyrograms of (A) styrene maleic anhydride, (B) polyamide resin, and (C) acrylonitrile styrene butadiene, all after prepyrolysis.

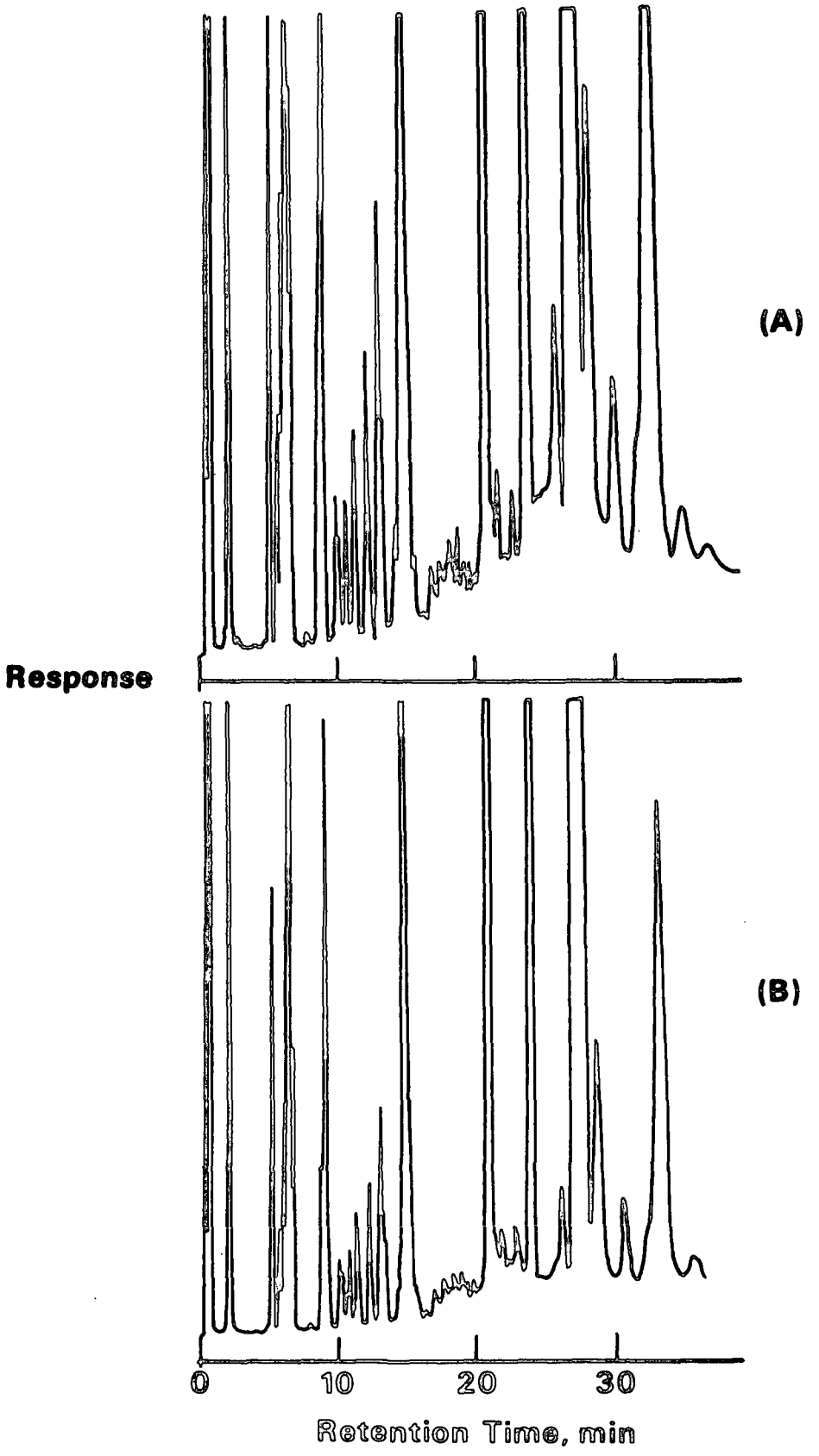

Fig. 4. Pyrogram of (A) styrene butadiene alone and (B) after addition to paper, both after prepyrolysis.

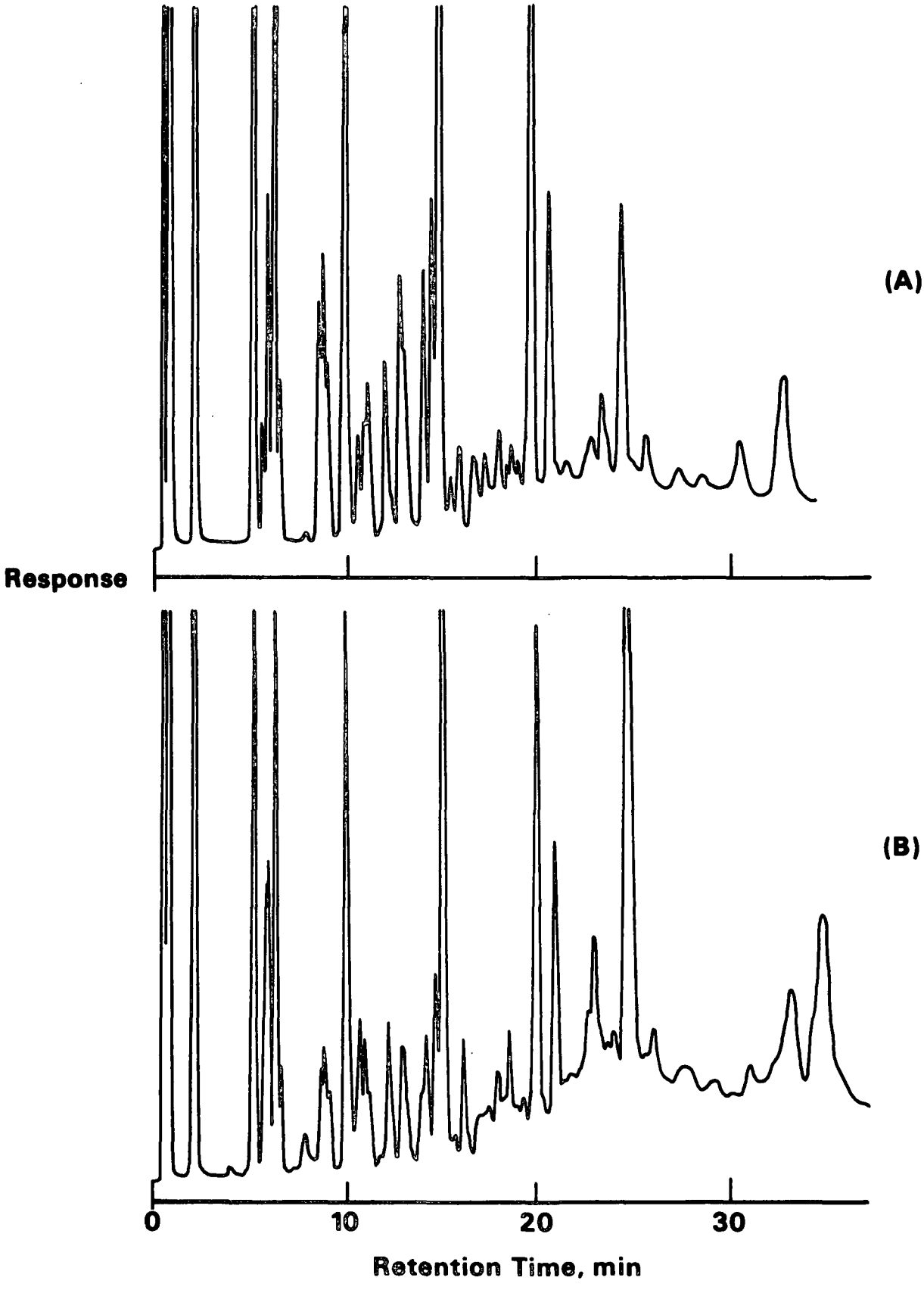

Fig. 5. Pyrogram of polyethylene (A) from library and (B) in commercially prepared freezer wrap paper, both after prepyrolysis.

THE INSTITUTE OF PAPER CHEMISTRY

Appleton, Wisconsin

Status Report

to the

PULPING PROCESSES

PROJECT ADVISORY COMMITTEE

Project 3524

FUNDAMENTALS OF BRIGHTNESS STABILITY

September 15, 1987

PROJECT SUMMARY FORM

DATE: September 15, 1987

PROJECT NO. 3524: FUNDAMENTALS OF BRIGHTNESS STABILITY

PROJECT LEADER: U. P. Agarwal

IPC GOAL:

A significant increase in yield of useful fibers.

OBJECTIVE:

Elucidate mechanism for brightness loss in high-yield pulps.

CURRENT FISCAL YEAR BUDGET: $140,000

SUMMARY OF RESULTS SINCE LAST REPORT:

Optical equipment has been put in place to evaluate both color development and photobleaching. This has been used to arrive at a comprehensive theory for color change on exposure to light. The kinetics of the yellowing reaction have been established and comparisons made between bleached and unbleached, hardwood and softwood, sheets. Laboratory results have been verified by outdoor exposure to sunlight.

Bleached sheets yellow at a faster rate than unbleached. Heavy metals do not have a major effect on light-induced yellowing. Direct reaction with singlet oxygen suggests that singlet oxygen is not directly involved in the yellowing reaction. We have support, but no positive proof, that photobleaching is a result of triplet oxygen interaction with the quinone triplet state. ESR work has confirmed the presence of radicals generated in the sheet on exposure to light.

Acetylation has been used to give sheets with greatly reduced yellowing. Mechanistic implications are being considered.

The Raman equipment necessary to study the initial photochemical reactions is installed. Equipment evaluation trials are in progress.

An IPC Ph.D. thesis by S. Lebo entitled "Formation of ortho-quinonoid structures in high-yield pulp lignins" has been completed. The contribution of ortho-quinonoid lignin structures to the absorbance of yellowed spruce pulp has been quantified. A novel method based on formation of the phosphite ester and subsequent ^{31}P NMR analysis was developed to aid in the quantification. While the o-quinonoid lignin structures are a major reason for color development on exposure to light, other colored structures are present. These may originate in the carbohydrate component of the pulp.

Preliminary model compound studies aimed at establishing the initial photochemical pathway for yellowing have been completed. The relative occurrence of fluorescence vs. phosphorescence is being investigated.

Color Reversion

Yellowed as well as unyellowed sheets from white spruce RMP were subjected to Raman investigation using the oxygen flushing method. Raman spectrum from the yellow material could only be obtained after prolonged flushing. The acquired spectrum matched that of ferulic acid quite well. Other lignin model compounds were also studied and compared. The control, on the other hand, gave the usual lignocellulosic spectrum containing features of both cellulose and lignin.

Further studies to reveal the nature of the ferulic acid and its interactions within the lignocellulosic matrix are currently underway.

Woody Tissue Luminescence

Further studies have been carried out to understand the nature of luminescence from wood tissue. Results obtained earlier indicated that luminescence intensity is sensitive to both water and molecular oxygen. Although excited by a much longer wavelength, luminescence showed characteristic behavior of room temperature phosphorescence (RTP). In our case, phosphorescence contributions to the luminescence intensity from lignin structural units are being considered.

Quenching of background by molecular oxygen has been beneficially used to obtain better spectra. When experiments were run over an extended period of time (> 2.5 days) under an oxygen atmosphere, the irradiated area of Black spruce cross sections was found to have yellowed. Under similar circumstances, however, longitudinal sections did not yellow. We feel further studies are warranted on this topic in order to gather important information. If it turns out that the same excited states are involved in the two kinds of yellowing processes, insights gained from the study on wood will richly contribute to the understanding of color reversion in high yield pulps.

PLANNED ACTIVITY THROUGH FISCAL YEAR 1988:

Continue work on yellowing mechanism. Emphasis will be on initial photoactivation using laser-Raman spectroscopic studies of model compounds. Establish pathways for decay of energy of photoexcitation, identify mechanisms which can cause irreversible changes, and seek ways to block these pathways. Once staffing is back to full strength, more emphasis will be given to chemical modification to block selected points in the overall reaction pathway. Specific work will include:

1. Study yellowed and unyellowed handsheets made from RMP of hardwoods.

2. Establish the roles of detected compound in the photoinduced yellowing.

3. Study to determine reaction pathways that lead to formation of ferulic acid and its counterpart in hardwoods.

4. Study effects of various pretreatments of pulp, e.g., metal ions, bleaching chemicals, reducing agents, radical scavengers, etc.

5. Study photoexcitation and decay processes in lignin and its model compounds.

6. Investigate contributions of lignin phosphorescence, lifetime of excited states, and wood yellowing.

FUTURE ACTIVITY:

As we become more knowledgable with regard to yellowing processes, means will be looked for to inhibit color reversion in high-yield pulps.

Status Report

FUNDAMENTALS OF BRIGHTNESS STABILITY

INTRODUCTION

Photoinduced color reversion of high-yield pulps has been an area of active research for quite some time. Although significant progress has been made over the years, many areas are not well understood. Lack of understanding is in part due to the experimental problems encountered while dealing with complex heterogeneous samples. As a result, a large number of studies have been carried out on lignin model compounds. Results of such work may or may not be applicable to lignin in the complex biological matrix of wood.

In this report, we describe the results of our in situ Raman studies carried out to identify various chromophores in the yellowed and nonyellowed samples of high-yield pulps. The work reported here is limited to the handsheets made from refiner mechanical pulp of white spruce, but in the future, sheets made from hardwoods will also be subjected to similar spectral studies.

PROCEDURE

The handsheets used in this study were the same as used by Mr. S. Lebo in his doctoral thesis work. These sheets were made from white spruce RMP, and a few were yellowed for 20 hours using a solar simulator.

Raman spectra were obtained on an Instruments S.A. Ramanor HG2S system. The 514.5 nm line of a Spectra Physics 2025-05 laser was used as the excitation frequency. The laser radiation was focused on the samples, which were mounted in homemade cells through which oxygen could be flushed. The laser power at the

samples was approximately 250 mW. The scattered light was collected in the 90 degree mode. In order to obtain Raman spectra of the samples background contribution to the total signal had to be reduced.

The method of oxygen-flushing which we have previously developed to accomplish the same purpose in the studies of other lignocellulosic materials was used to quench the background. In view of very high background counts from the yellow sample, extended flushing was carried out in this particular case. Unyellowed sample was also flushed with gaseous oxygen, but the duration was not as long.

RESULTS AND DISCUSSION

Yellowed handsheet gave the spectrum shown in Fig. 1. The spectrum did not change at all over the next 24 hr, as was evident from several spectral acquisitions over that period. However, as expected, background did diminish somewhat. This indicates that the acquired spectrum was not of a product that resulted from a chemical reaction of oxygen with the yellow sheet components. Had the spectral contribution been due to a reaction product, features in the spectrum would have changed with time.

A typical lignocellulosic spectrum was obtained from the control sheet as is shown in Fig. 2. The experimental conditions were identical to those used in the case of the yellow sample. A comparison of the two spectra clearly indicates that the yellow sheet spectrum does not have any features which can be assigned to lignin or cellulose. On the contrary, it suggests the presence of new species.

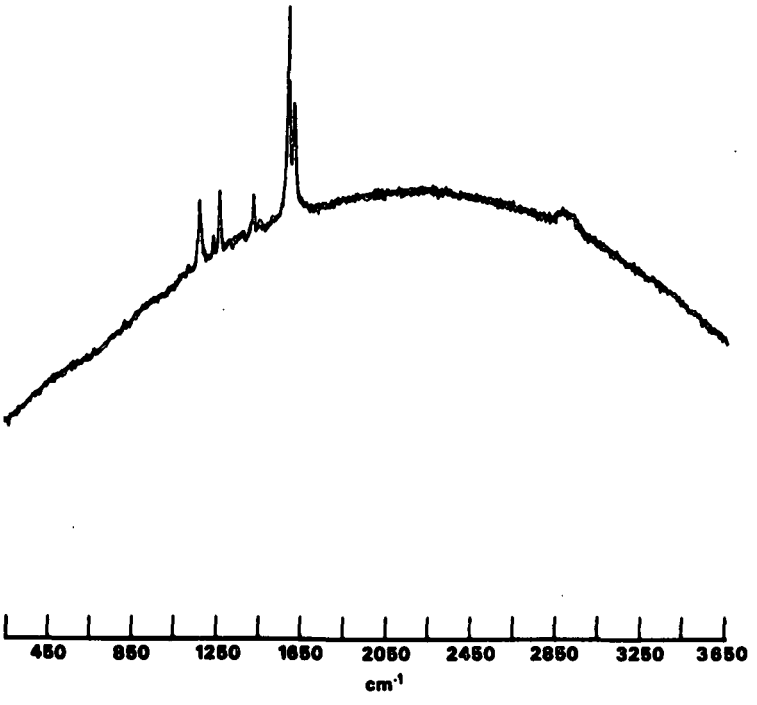

Figure 1. Raman spectrum of the yellowed handsheet made from white spruce RMP.

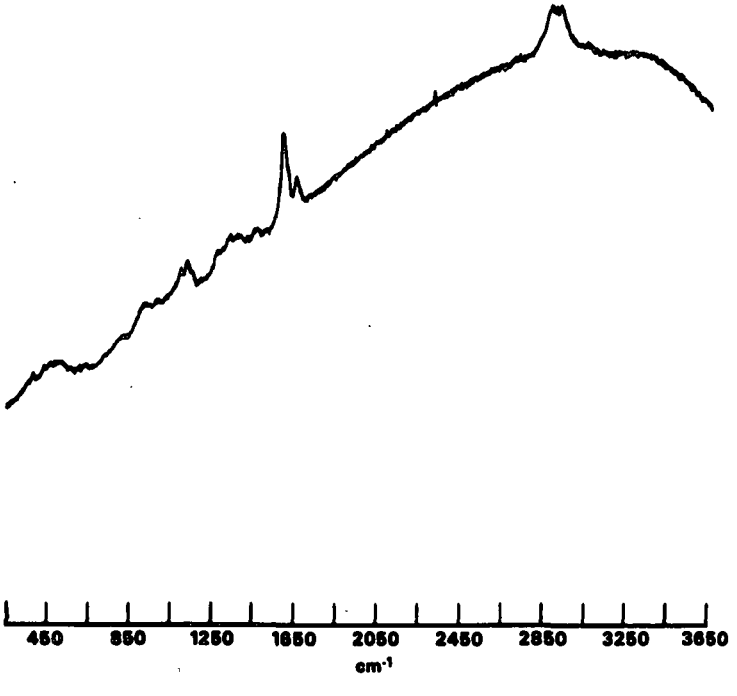

Figure 2. Raman spectrum of the unyellowed handsheet used as control.

In order to assign the Raman spectrum of Fig. 1, a number of lignin model compounds were subjected to analysis by Raman spectroscopy. Upon comparison of such spectral data a remarkable match between Fig. 1 and the ferulic acid spectrum was obtained (see Fig. 3).

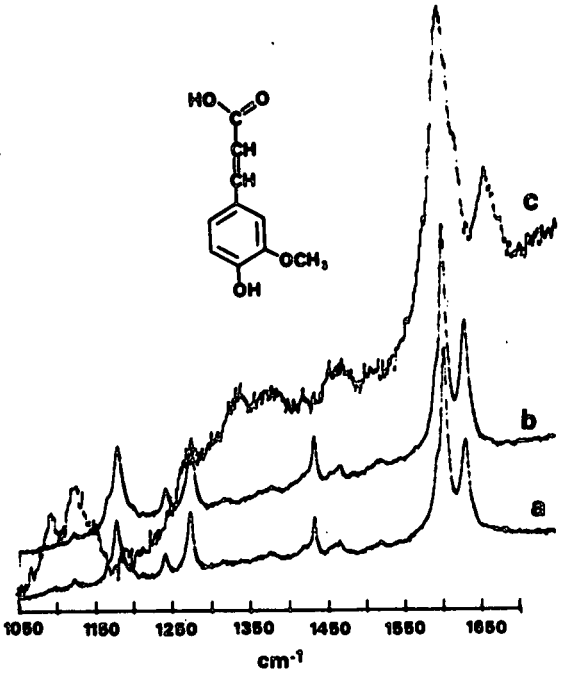

Figure 3. Spectra plotted on expanded frequency scale; (a) yellowed sheet, (b) ferulic acid (molecular structure shown); (c) control.

The spectral features in the two spectra [Fig. 3(a) and (b)] are almost identical. This seems to rule out the possibility of contributions from additional compounds. However, additional chromophores may be present in the yellow sheet.

The next question that we have to address is if the yellow color is produced by ferulic acid. This compound shows an absorption maximum at 321 nm and is not colored by itself. Moreover, it is soluble in alcohol. When the yellow sheet is immersed in ethanol, no evidence of solubility of ferulic acid is found. Hence, it appears that ferulic acid molecules may be interacting with

various species in the lignocellulosic matrix. Perhaps, such perturbation forces are strong enough to cause a red shift in the absorption band of ferulic acid and produce the yellow color. We are presently looking for evidence of such interactions.

In summary, a structure similar to ferulic acid has been detected on the yellowed sheet of a high-yield pulp. Further studies are planned in order to understand its interactions within the lignocellulose matrix.

WOODY TISSUE LUMINESCENCE

AN OVERVIEW

Fluorescence vs. Phosphorescence

When we first started recording Raman spectra on woody tissue, the efforts were often frustrated by high levels of background contributions. Such radiation was called luminescence due to the fact that we did not know if it was fluorescence and/or phosphorescence. Soon after that, working with water immersed samples, we observed that the background reduced significantly - so much indeed that we could obtain Raman spectra. Since then, we have also shown that the oxygen interaction accomplishes the same purpose. Although we have not been able to come up with an explanation for these observations, some progress has been made.

Quite a bit is published on the quenching of excited states by molecular oxygen. It is known, for example, that molecular oxygen is capable of quenching both singlet and triplet states in simple systems. However, in view of shorter life times of fluorescing states and diffusion controlled nature of the deactivation processes, quenching in solid, polymeric, and complex matrices generally

occurs in the excited triplet. Considering the complex lignocellulosic nature of our system, it is highly likely that such quenching takes place in the triplet. However, the molecules, in our case lignin structural units, would have to be excited to the triplet states. There are different pathways to accomplish this, but the one operating in our case is direct or indirect excitation by 514.5 nm wavelength laser radiation. Singlet <——> triplet transitions are spin forbidden, however, the presence of heavy atoms and the usage of an intense laser beam are two factors which may give direct excitation. Indirect excitation to the triplet will only be possible when there are entities which absorb (allowed single <——> singlet) at 514.5 nm. Assuming that there are no such units in lignin and/or in the lignocellulosic matrix, we are left primarily with the possibility of direct population of triplet states.

It is well known that a number of nonphosphorescent compounds when adsorbed on filter paper give rise to strong phosphorescence signal at room temperature. Under such conditions, deactivation processes are unable to operate and the phosphorescence signal can be detected. Moreover, these analytes give much weaker signals when moisture/water is present. Although, the mechanism of the water effect is not known, the H-bonding capability of water and the resulting loosened cellulosic matrix structure are two important factors generally cited in order to explain this observation. Woody tissue behaves analogously, and we believe, similar factors are responsible for reduction of its luminescence signal. In any event, we plan to carry out studies of excited state lifetimes in the future, which will help us conclude one way or another.

Yellowing of Woody Tissue

During Raman experiments on dry woody tissue, it was noticed that when the experiments were run for a long duration under O_2 atmosphere the exposed

area turned yellow. The cause of this yellowing is not clear. Nevertheless, it is possible that when lignin molecules are excited, they interact with oxygen in a fashion similar to that involved in color reversion in high-yield pulps. In the latter case, lignin structural units once in higher singlet states drop down to corresponding more stable triplet states from which further chemistry ensues. In the case of 514.5 nm excitation, on the other hand, such triplets are directly populated. The rest of the processes are envisioned to be identical.

THE INSTITUTE OF PAPER CHEMISTRY

Umesh Agarwal
Research Fellow
Wood Sciences
Chemical Sciences Division

THE OCCURRENCE AND LIGHT INDUCED FORMATION OF ORTHO-QUINONOID STRUCTURES IN HIGH YIELD PULP LIGNINS

A thesis submitted by

Stuart E. Lebo, Jr.

B.A. 1981, Shippensburg State University

M.S. 1983, Lawrence University

In partial fulfillment of the requirements
of The Institute of Paper Chemistry
for the degree of Doctor of Philosophy
from Lawrence University
Appleton, Wisconsin

July, 1987

ABSTRACT

"Yellowing" upon exposure to light is a major problem associated with the use of high-yield pulps, both bleached and unbleached. Because of this problem, the use of high-yield pulps as substitutes for fully bleached chemical pulps has been severely limited. Although various model studies have indicated that colored quinonoid lignin structures are formed when such pulps are exposed to light, the light induced formation of these structures in situ has not been extensively studied. The occurrence and light induced formation of quinonoid lignin structures, particularly ortho-quinonoid lignin structures, is the subject of this investigation. Specifically, work was aimed at determining if such structures occur and/or are photochemically generated in white spruce refiner mechanical pulp sheets, and, if photochemically generated, what the quantum yield of their formation is.

Diffuse reflectance UV-visible, diffuse reflectance Fourier transform infrared, and solid state ^{31}P NMR spectroscopy were the major investigative tools used to follow the formation of quinonoid lignin structures during light induced yellowing. These methods were also the major investigative tools for determining if unirradiated pulp contained these structures. The results obtained when irradiated white spruce refiner mechanical pulp (RMP) sheets were examined before and after reaction with sodium dithionite, sulfur dioxide and trimethyl phosphite showed that approximately five ortho-quinonoid lignin structures were formed when white spruce sheets were irradiated for 20 hours with simulated sunlight. These results were confirmed by comparison with simple model quinones and with sheets formed from an ortho-quinone enhanced white spruce pulp. In subsequent studies with "monochromatic" UV light, the quantum yield for the

312.5 nm light induced formation of such structures was determined to be 8.0 x 10^{-2} moles of ortho-quinonoid lignin structures per mole of adsorbed photons.

The results obtained when irradiated white spruce refiner mechanical pulp (RMP) sheets were examined showed that this pulp also contained ortho-quinonoid lignin structures. As in the analysis of the irradiated pulp, these results were confirmed by comparison with simple models and with an ortho-quinone enhanced white spruce pulp. Quantitative analysis of this irradiated refiner pulp indicated that it contained approximately six ortho-quinonoid lignin structures per 100 C_9 lignin units.

In both the irradiated and unirradiated cases, ortho-quinonoid lignin structures are major contributors to the absorbance of these pulps. Based on Kubelka-Munk measurements, the contribution of these structures to the absorbance of the unirradiated pulp was estimated to be 47% at 415 nm, 73% at 457 nm, and 75% at 520 nm. The contribution of these structures to the absorbance of the sunlight irradiated pulp was estimated to be 68% at 415 nm, 75% at 457 nm, and 79% at 520 nm. While the nature of the other major contributor was not determined, it was shown that this product has an absorption maximum at 395 nm and that this product is not easily reduced by sodium dithionite, sulfur dioxide or trimethyl phosphite. It was also shown that rate at which this product is formed depends on the wavelength of the light incident upon the pulp with the maximum rate occurring around 312.5 nm.

Thus, it was shown that ortho-quinonoid lignin structures are present in high yield pulps. Their presence is partly responsible for the low brightnesses of these pulps. It was also shown that more of these structures are formed when high-yield pulps are exposed to light. They are not, however, the only colored structures formed.

THE INSTITUTE OF PAPER CHEMISTRY

Appleton, Wisconsin

Status Report

to the

PULPING PROCESSES

PROJECT ADVISORY COMMITTEE

Project 3566

STRONG, INTACT, HIGH-YIELD FIBERS

September 10, 1987

PROJECT SUMMARY FORM

DATE: September 10, 1987

PROJECT NO. 3566: STRONG, INTACT, HIGH-YIELD FIBERS

PROJECT LEADERS: T. J. McDonough, S. Aziz

IPC Goal:

Significant increase in the yield of useful fibers.

OBJECTIVE:

Develop methods of wood fiber separation which will allow the production of separated fibers having the same physical strength and geometrical form possessed when bound in the original wood matrix.

CURRENT FISCAL YEAR BUDGET: $175,000

SUMMARY OF RESULTS SINCE LAST REPORT:

Experimental work has centered upon the effects of fiber separation on fiber strength, and how they depend on fiberization conditions, and on the degree to which separated fibers of high strength can be bonded to form strong sheets.

Fibers of white spruce were separated, without refining, at temperatures representing atmospheric, thermomechanical and high-temperature thermomechanical pulping processes. All fibers had comparable strength, suggesting that the expected beneficial effect of lignin softening on fiber strength retention is either nonexistent or masked by thermal degradation of fiber strength. Shorter fibers were weaker than long ones, a difference which may reflect simultaneous weakening and shortening of the fibers during separation.

Kraft fibers made from white spruce were much stronger than the corresponding mechanical pulp fibers, a situation which is the reverse of that previously observed for southern pine. Work is in progress to resolve this paradoxical result, in the hope of gaining insight into the nature of fiber strength losses during pulping.

Lignin softening by sulfonation before refining, unlike thermal softening, increased fiber strength, suggesting that fibers are weakened by work done to overcome the resistance to fiber separation and that thermal weakening also occurs.

Efforts to effectively bond unrefined fibers of known high strength have employed chemical posttreatments, additives, and press drying. To date the sheet strengths obtained have been high by high-yield pulp standards (8 km breaking length at 90% yield), but are well below the theoretical value calculated from single fiber strength measurements.

Related student research has addressed the nature and significance of cell wall sulfur distribution and has explored a new chemimechanical pulping concept based on hemicellulose modification.

PLANNED ACTIVITY THROUGH FISCAL 1988

The observed differences in behavior between pine and spruce will be delineated and experiments done to explain them. Study of the factors governing fiber strength retention will be completed.

The maximum sheet strength that can be realized when bonding unrefined, high-yield fibers of known strength will be determined. The effects of fiber modification and the mechanism of sheet failure will be investigated.

STUDENT RESEARCH:

T. Heazel, Ph.D.-1986; E. Byers, Ph.D.-1986; C. Nordberg, Special Student-1985; T. Cornbower, M.S.-1987.

Status Report

STRONG, INTACT, HIGH-YIELD FIBERS

OBJECTIVES

The ultimate objective of this project is to develop methods of wood fiber separation that give fibers with the the same strength and dimensions they had in the wood. The medium term goals are to identify the factors governing retention of fiber strength and integrity and to develop methods of controlling them. The specific objectives of the work described here are:

1. to determine the effect of fiberization temperature on the strengths of the separated fibers,
2. to compare the strengths of fibers in different length fractions and thereby infer something about the effect of fiberization on fiber strength,
3. to determine the effect of wood presulfonation on the strength of the separated fibers,
4. to investigate various methods of bonding in an attempt to realize the very high strength potentials apparent in the fibers of some of our pulps,
5. to characterize and investigate the reasons for the observed distribution of sulfonate groups across the fiber wall in chips subjected to a simulated chemimechanical pulping pretreatment stage,
6. to compare the strengths of kraft fibers with those of mechanical and chemimechanical fibers from the same wood supply, and

7. to investigate a new concept of chemimechanical pulping based on modification of hemicellulose, not lignin, prior to fiberization.

INTRODUCTION

In an effort to better understand the relationship between high-yield fiber strength and the conditions of fiberization, we have prepared coarse mechanical pulps at various temperatures in a pilot scale disk refining system. The resulting fibers were characterized, with emphasis on fiber strength. Similarly, to assess the effect of presulfonation on fiber strength, sulfonated wood was fiberized in the laboratory, and the strengths of the resulting fibers compared with those of the fibers separated by purely mechanical means. The results of both sets of experiments are among those summarized in the present report.

Since this research is aimed at making stronger high-yield fibers, it assumes that loss of fiber strength during separation is at least partially responsible for the inferior strength of ultrahigh yield pulps, as compared to kraft pulps. This assumption is justified by the fact that it is possible with existing technology to make high-yield pulp sheets whose strength is limited by the strength of their fibers, and by the likelihood that the large amount of energy expended during fiberization results in weakening of fibers in addition to the breakage that obviously occurs. Further justification was sought in the present work by fractionating several pulps on the basis of fiber length and determining the strengths of fibers in the respective fractions. It was reasoned that if strength reduction does occur during fiberization, it should be most evident in the fractions containing shortened fibers; fibers that are broken are

likely to have experienced more violent events during refining than fibers that escaped the refining zone intact.

The current approach also assumes that fibers separated with little or no strength loss can be made to bond to one another so well that their high strength is reflected in the strength of the resulting sheet. This is made plausible by the growing store of experience with bonding improvement in mechanical pulps by chemical modification of the fibers, but will require further experimental validation. As further described in this report, we have taken a step in this direction by exploring various methods of bonding very strong fibers prepared by coarsely fiberizing sulfonated sprucewood. The results of related student research on sulfur distribution in sulfonated wood are also relevant to the bonding question, inasmuch as sulfonate profiles may be expected to impact fiber conformability and fiber surface bonding potential. Accordingly, recent results in that area are included in the present report.

Learning how to separate and effectively bond high-yield fibers without strength loss is equivalent to learning how to make the strongest possible pulp at that yield level. How the resulting ultrastrong pulp fares in the inevitable comparison with the corresponding kraft pulp then depends only on the efficiency of fiber strength retention and bonding development in the kraft process. If it turns out that kraft fibers suffer extensive strength loss during pulping, the high-yield pulp sheet may be expected to be as strong or stronger than the kraft sheet. Such a finding would lend additional importance to the current research. If, on the other hand, the load bearing ability of the kraft fibers is unaffected by pulping, then the strength of the high-yield sheet can never approach that of a kraft sheet, other things being equal, because of the fiber number

disadvantage of the high-yield pulp. This finding would suggest that factors other than fiber strength, such as interfiber bonding, should be studied instead. Because of these implications of the comparison with kraft it has also been one of our experimental objectives.

The last research area to be discussed in the present report concerns the development of a new chemimechanical pulping concept based on the modification of hemicellulose prior to fiber separation. This work, done as academic research, showed that partial hemicellulose removal can significantly improve pulp properties after subsequent fiberization.

RESULTS AND DISCUSSION

EFFECT OF FIBERIZATION TEMPERATURE ON FIBER STRENGTH

Preparation of Pulps

Pulps were produced at three different preheating/fiberization temperatures to determine the effect of this variable on fiber strength. The refiner system used was a Sunds Defibrator two-stage pilot unit with a pressurized 300CD unit as the primary refiner. The pilot plant is located in Chillicothe, Ohio at the Central Research Laboratories of Mead Corporation. Freshly cut white spruce was chipped at IPC and the chips were screened at Chillicothe. Chips passing through 1-1/8 inch diameter holes and retained on a plate with 1/4 inch diameter holes were used.

For these trials the 300CD refiner, which normally has both flat and conical refining zones, was fitted with 12 inch flat single rotating disc plates only. Experiments were conducted at 120°C, 160°C and atmospheric conditions. For the runs at 120 and 160°C, the chips were steamed at atmospheric pressure

for approximately 15 minutes prior to passing through a 4:1 compression ratio screw feeder into the preheater, where they were retained at the appropriate temperature for 10-15 minutes before fiberizing. Deionized water was added at the feed screw to prevent burning of the pulp; the consistency calculated from the chip and dilution water flows was 16%. The actual consistency in the fiberizing zone was higher because of steam generation.

Because our goal was to isolate fiberization from refining, the objective of the refiner runs was to produce fibers which had been just separated, and subjected to the least possible additional mechanical action. Accordingly, power input to the primary refiner was kept low, and the secondary was operated with a wide plate gap. It did little or no refining and was used merely to pump the fiber out of the system.

In each case, pulp collection was begun after steady operation had been achieved. When a sample of sufficient size had been obtained, the run was interrupted and operating conditions were changed to produce pulps for Mead's use. When these were completed, the operating conditions were returned as nearly as possible to their original values, and pulp collection was begun again. Thus, each run was replicated and the samples from replicate runs were kept and analyzed separately to provide an estimate of experimental error.

Screening and Characterization of the Fibrous Fractions

A necessary consequence of low specific energy input is a high content of screen rejects (Table 1). Screening was done in two stages, the first at Mead on a 0.014 inch cut screen plate and the second at IPC on a 0.006 inch cut screen. The final accepts levels were roughly similar for the three sets of operating conditions, averaging 35-45%. The low coarse screen rejects' levels in

the 120° pulps reflect the lower plate gap used for these runs, but the effect did not extend into the finer fractions, as indicated by the similar fine screen rejects' levels for all three pulps. Within sets, the runs reproduced fairly well. An inverse relationship was observed between temperature and energy consumption. This is to be expected, since fiber separation, not refining, dominates under these conditions, and the resistance to fiber separation decreases as the temperature approaches and then surpasses the glass transition temperature of lignin.

Table 1. Disk refiner fiberization of white spruce.

Run	Preheater Temp, °C	Primary Refiner Plate Clearance, nm	Specific Energy Consumption HPD/ODT	0.014 Inch Cut Screen Rejects, %[a]	0.006 Inch Cut Screen Rejects, %[b]
775-1	29	0.80	55.7	12.9	44.4
775-2	57	0.80	48.0	15.0	59.5
Average			51.8	14.0	52.0
773-1	120	0.40	21.4	2.8	50.4
773-2	121	0.40	22.6	4.7	55.8
Average			22.0	3.8	53.1
774-1	160	0.60	7.6	11.2	61.3
774-2	160	0.60	10.2	12.1	58.9
Average			8.9	11.6	60.1

[a]Based on combined o.d. weight of accepts and rejects; fines loss neglected.
[b]Based on o.d. weight of unscreened pulp.

Table 2 shows that this decrease in resistance to fiber separation is paralleled by an increase in fiber length, although the effect observed upon increasing the temperature from 120 to 160° was small and was not apparent in

the classification data. The pulps fiberized under pressure had high average fiber lengths and low contents of material passing through a 100 mesh screen.

Table 2. Accepts fiber length and classification data.

Run	Preheater Temperature °C	0.006 Inch Cut Screen Accepts, %[a]	Fiber Length,[b] mm	% Retained on Screen of Mesh Size 14	28	48	100	Remainder, %
775-1	29	48.4	0.96	4	30	27	15	24
775-2	57	34.4	1.26	7	37	31	13	13
Average		41.4	1.11	6	34	29	14	17
773-1	120	48.2	1.73	27	33	18	5	16
773-2	121	42.1	1.68	24	37	21	6	12
Average		45.1	1.70	26	35	20	6	14
774-1	160	34.4	1.96	20	37	20	6	16
774-2	160	36.1	1.76	22	43	20	7	9
Average		35.2	1.86	21	40	20	6	12

[a]Based on o.d. weight of pulp out of refiner.
[b]Length-weighted average; analysis by Kajaani FS-100.

None of the fiber samples exhibited appreciable bonding ability, as indicated by the low degrees of consolidation and low strengths of standard handsheets (Table 3). This is to be expected of unrefined fibers and indicates that we were successful in achieving fiber separation without appreciable additional mechanical action in the refining zone. The very high freeness of all three fiber samples is consistent with this view. These observations notwithstanding, the fibers separated under atmospheric conditions did exhibit slightly but significantly higher bonding ability than any of those separated at higher temperatures, all of which were similar.

Table 3. Unrefined long fiber[a] handsheet properties.

Sample Identity	Preheater Temperature, °C	CSF, mL	Zero Span BL, km	Tensile Index N·m/g	Tear Factor	Density, g/cm^3
775-1	29	750	6.9	3.8	16.3	0.17
775-2	57	N.D.[b]	6.9	2.4	16.2	0.14
Average			6.9	3.1	16.2	0.16
773-1	120	760	6.8	0.7	9.6	0.13
773-2	121	N.D.	6.1	0.7	10.5	0.12
Average			6.4	0.7	10.0	0.12
774-1	160	750	5.5	0.4	9.1	0.13
774-2	160	N.D.	6.5	0.6	8.1	0.14
			6.0	0.5	8.6	0.14

[a]Combined 14, 28, and 48 mesh fractions.
[b]N.D. - Not determined.

The atmospheric fibers also differed from the others in ease of surface development. Table 4 contains data on the properties of handsheets made after disintegration for 3 hours in a standard TAPPI disintegrator. This treatment caused substantial surface development and concomitant improvement in the strength properties of all samples, but the response of the atmospheric samples was markedly better than that of the others. This behavior is probably due to loosening of the wall structure associated with separating fibers that are strongly bonded together by unsoftened lignin. At higher temperatures, softening of the lignin allows the fibers to be separated without disrupting the wall structure to as great a degree. As in the case of the unrefined fibers the refined 120° and 160° fibers were remarkably similar, which suggests that the well known effect of fiberization temperature over this range is primarily associated with refining and not with fiber separation. Alternatively, the apparent

absence of the temperature effect over this range may be a result of the long preheating times used in the present study in the atmospheric samples.

Table 4. Refined[a] long fiber[b] handsheet properties.

Sample Identity	Presteaming Vessel Temperature, °C	CSF, mL	Zero Span BL, km	Tensile Index N•m/g	Tear Factor	Density, g/cm^3
775-1	29	350	8.9	22.4	53	0.21
775-2	57	N.D.[c]	8.7	24.7	55	0.23
773-1	120	660	7.7	13.1	60	0.17
773-2	121	N.D.	7.6	14.4	49	0.17
774-1	160	720	7.1	12.4	41	0.18
774-2	160	N.D.	7.8	12.2	50	0.19

[a]Three hours in standard TAPPI disintegrator.
[b]Combined 14, 28, and 48 mesh fractions.
[c]N.D. - not determined.

Effect of Fiberization Temperature on Fiber Strength

The zero-span tensile strength of handsheets made from unrefined fibers, also shown in Tables 3 and 4, was low in relation to the zero-span of kraft pulps from the same species (about 20 km) and exhibited a pronounced dependence on handsheet density. These observations indicate that at the low levels of bonding that characterize these pulps, zero-span does not provide a valid estimate of fiber strength. To assess effects of fiberization variables on fiber strength, it is necessary to resort to measurements of the load-elongation characteristics of individual fibers.

These measurements may be summarized by recording, for each fiber tested, the breaking load, the compacted fiber cross-sectional area, the breaking stress calculated from these two quantities, and the initial modulus. Approximately fifty fibers were randomly selected from each sample and tested.

Table 5 contains the average breaking loads obtained in this way for each of the samples discussed above. (Data are also shown for a kraft pulp prepared from the same wood supply, and for fractions obtained by Bauer-McNett classification; these are discussed in subsequent sections.) The average breaking loads for fibers selected from samples produced at all three temperatures were very similar, the only exception being a suspiciously low value obtained for one of the 120° samples. This indicates that the load bearing ability of fibers is independent of the temperature at which they were separated from the wood. This result is mildly surprising, in view of the expectation that fibers torn from the wood surface at low temperature, when the lignin is hard and offers much resistance, will undergo more damage than those separated at high temperature, when the softened lignin offers little resistance to separation. A possible explanation is that fibers preheated and separated at higher temperatures undergo thermal degradation that reduces their strength. Experiments are planned to test this hypothesis.

Table 5. Average fiber breaking load[a].

Sample Identity	Preheater Temperature, °C	Breaking Load (g) of Fibers from Whole Pulp	14 Mesh Fraction	28 Mesh Fraction	48 Mesh Fraction
775-1	29	18.0	23.4	16.1	13.4
775-2	57	17.1			
773-1	120	13.9	27.0	18.9	10.8
773-2	121	16.4			
774-1	160	16.1			
774-2	160	18.5			
Kraft		17.5	17.6	14.3	10.0

[a]Least significant difference approximately 3.4 at 95% confidence level.

An alternative hypothesis is that fibers separated at higher temperatures somehow undergo a reduction in cross-sectional area. That this is not the case is apparent from the measurements of this quantity contained in Table 6. No difference can be associated with differences in fiberization temperature. The observed cross sectional areas are about one-third of those previously observed for the corresponding southern pine fibers.[1]

Table 6. Average fiber cross-sectional area.[a]

Sample Identity	Preheater Temperature, °C	Cross-sectional Area (μm^2) of Fibers from Whole Pulp	14 Mesh Fraction	28 Mesh Fraction	48 Mesh Fraction
775-1	29	204	239	182	172
775-2	57	186			
773-1	120	209	250	219	161
773-2	121	190			
774-1	160	196			
774-2	160	212			
Kraft		89	98	85	78

[a]Least significant difference approximately 34 at 95% confidence level.

As expected on the basis of the above results, the calculated breaking stresses show no significant temperature effects (Table 7). Similarly, there were no effects of temperature on average fiber modulus (Table 8).

Comparison of Strengths of Fibers in Different Size Classes

It is apparent from Table 5 that shorter fibers have markedly lower breaking loads than those in longer size classes. Table 6 shows that the difference can be at least partially attributed to the more slender nature of the shorter fibers, but calculation of the breaking stresses (Table 7) reveals that

the differences in breaking load cannot be accounted for on the basis of cross-sectional area alone; the shorter fibers are inherently weaker. This is paralleled by a correlation of modulus with fiber length, as shown in Table 8.

Table 7. Average fiber breaking stress.[a]

Sample Identity	Preheater Temperature, °C	Breaking Stress (kg/mm^2) of Fibers from Whole Pulp	14 Mesh Fraction	28 Mesh Fraction	48 Mesh Fraction
775-1	29	93	108	94	92
775-2	57	93			
773-1	120	76	111	88	68
773-2	121	90			
774-1	160	91			
774-2	160	89			
Kraft		201	190	177	138

[a]Least significant difference at 95% confidence level.

Table 8. Average fiber modulus.

Sample Identity	Preheater Temperature, °C	Modulus (kg/mm^2) of Fibers from Whole Pulp	14 Mesh Fraction	28 Mesh Fraction	48 Mesh Fraction
775-1	29	1045	1445	1265	1110
775-2	57	1200			
773-1	120	920	1220	920	765
773-2	121	1060			
774-1	160	1080			
774-2	160	980			
Kraft		3070	3235	2701	2567

[a]Least significant difference approximately 290 at 95% confidence level.

The lower breaking stress of fibers in the shorter fractions is an observation which is open to at least two possible interpretations. One is that

the shorter fractions have lower strength by virtue of the broken fibers they contain and that these are weak as a result of the same events that shortened them. If true, this would support the view that fibers are weakened as a result of the damage they suffer during separation. Another interpretation is that the shorter fractions are weaker by virtue of morphological differences that existed before separation. This would support the view that fiber damage during separation is confined to fiber breakage and that prefailure weakening does not occur to a significant extent. In an effort to distinguish between the two interpretations, we plan to make measurements of the proportions of broken fibers and of fibril angles in the various fractions.

Comparison with Kraft Fiber Strength

The average breaking load of fibers randomly selected from a laboratory made white spruce kraft pulp was remarkably similar to those of the mechanical pulps discussed above, as shown in Table 5. Their average cross-sectional area was, however, markedly different from those of the mechanical pulp fibers, having undergone a 55% reduction during kraft pulping (Table 6). As a result, the kraft fibers exhibited an average breaking stress that is more than twice as high as that of the mechanical pulp fibers (Table 7). As shown in Table 8, the superior strength of the kraft fibers relative to those of the mechanical pulps is accompanied by much higher average modulus values.

Classified kraft fibers showed a pronounced reduction in breaking load with decreasing fiber length (Table 5) that was only partly attributable to reduced fiber cross-section (Table 6). The resulting dependence of strength on fiber length (Table 7) was similar to that found earlier for the mechanical pulp fibers, am observation that suggests that morphological factors are responsible in both cases.

Effect of Presulfonation on Fiber Strength

The trials that produced the mechanical pulps already described did not include runs involving chemical treatment of the wood prior to fiberization. Nevertheless, such pretreatments, which result in lignin softening, may be expected to affect the mechanical properties of the separated fibers and therefore merit investigation as part of the present study. Accordingly, pulps were prepared from sulfonated wood in our laboratory and compared with those prepared from untreated wood at the Mead pilot plant. The procedure used to prepare the laboratory pulp employed the Asplund Mill for fiberization and has been described in detail in an earlier report.[1] It involved sulfonation to 94% yield with liquor containing 120 g/L Na_2SO_3 and 5 g/L NaOH.

The results of this comparison are shown in Table 9. In general, the sulfonated fibers were stronger and more slender than those of the control. The strength difference was concentrated in the 28 mesh and 48 mesh fractions. These results are consistent with the hypothesis that the fibers suffered less weakening because less work was done on them during separation, but other interpretations are possible.

Table 9. Comparison of fibers from sulfonated and unsulfonated white spruce wood.

		Whole Pulp	14 Mesh Fraction	28 Mesh Fraction	48 Mesh Fraction
Breaking load, g	Unsulfonated	15.2	27.0	18.9	10.8
	Sulfonated	17.5	18.9	17.8	13.4
Cross-sectional area, μm^2	Unsulfonated	200	250	219	161
	Sulfonated	164	186	147	172
Breaking stress, kg/mm^2	Unsulfonated	83	111	88	68
	Sulfonated	117	107	123	94
Modulus, kg/mm^2	Unsulfonated	990	1220	920	765
	Sulfonated	1355	1120	1175	1040

Correlations Between Fiber Properties

In an effort to find the reasons underlying the observed differences in fiber properties, correlations between them were sought. As shown in Fig. 1, initial modulus and breaking stress were strongly correlated for all fiber samples tested. This suggests that weaker samples fail early in the loading cycle because of nonuniform stress distribution.

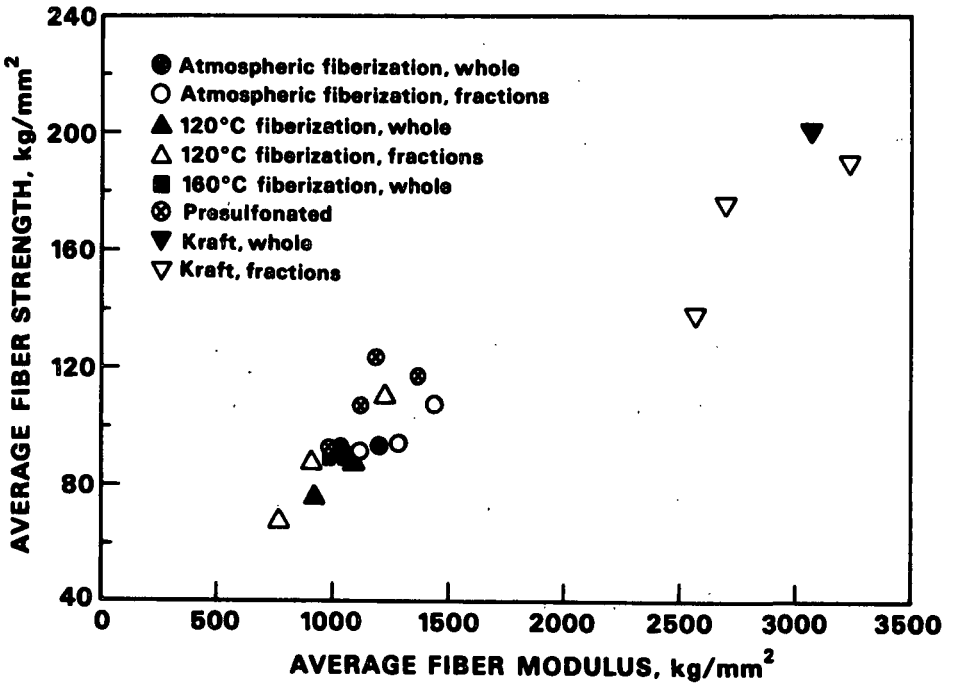

Figure 1. Correlation between fiber modulus and fiber strength.

A less straightforward correlation was observed between breaking stress and fiber cross-sectional area (Fig. 2). Within the group of purely mechanical pulps, coarser fibers tended to be stronger. The same was true of the kraft fiber samples, except that the dependence of strength on area was stronger.

There was no corresponding relationship for the sulfonated pulps, which also lacked the direct relationship of fiber length to cross-sectional area exhibited by the kraft and mechanical pulps.

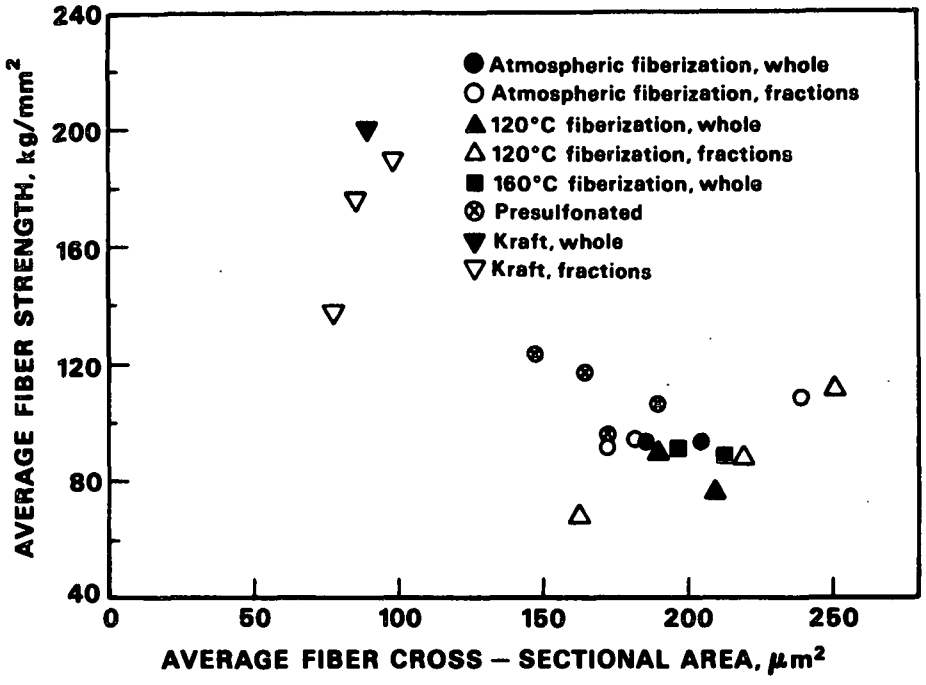

Figure 2. Correlation between cross-sectional area and strength.

Fiber Wall Sulfur Profiles in Sulfonated Wood

Wood sulfonation prior to fiberization improves pulp properties by softening the lignin in both the interfiber middle lamellar region and in the fiber wall. Middle lamella softening affects the site of fiber separation and also reduces fiber breakage. Fiber wall softening affects the conformability of the separated fibers. Since the degree of softening may be expected to be proportional to the concentration of sulfonate groups introduced, it is apparent that, at a given average concentration of such groups, their distribution will have a major effect on pulp properties.

A Ph.D. candidate, T. Heazel, has investigated the factors affecting this distribution by using scanning transmission electron microscopy-energy dispersive spectrometry to measure it in southern pine latewood sulfonated under various conditions. Common features are a steady decrease in sulfur content from the S3 layer (adjacent to the lumen) to a region in the S2 layer near the middle lamella and high values in the middle lamella and cell corners (Fig. 3). Within a given cell wall, the distribution can be characterized by the x-ray intensity (proportional to sulfur concentration) at the lumen (A), at the minimum (B) near the middle lamella, and in the cell corners (CC) where the value is similar to that found in the middle lamella. Average values are shown in Table 10, from which it is apparent that the general shape of the distribution is not sensitive to reaction time or sulfite concentration in a vapor phase pretreatment.

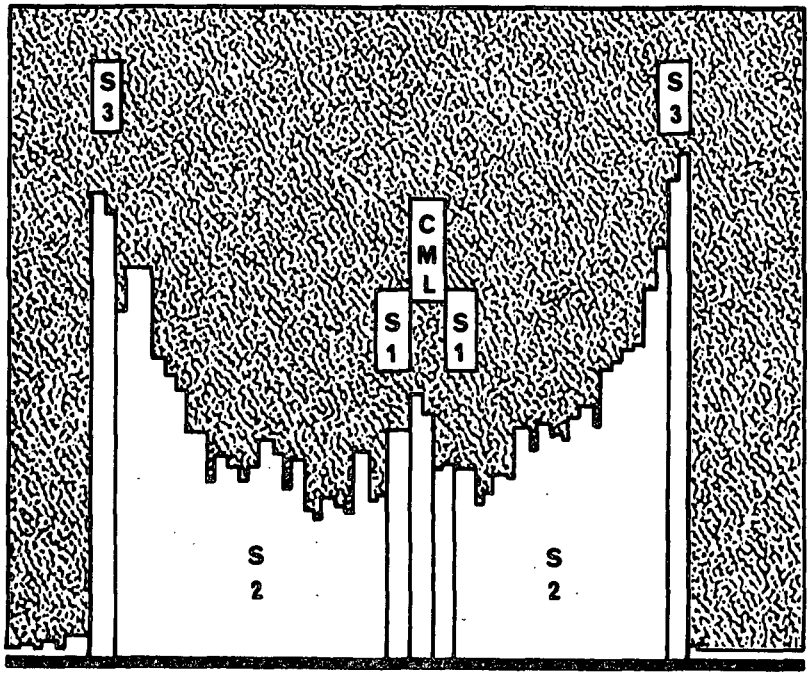

Figure 3. Extreme example of net sulfur count histogram from double-wall linescans.

Table 10. Treatment means for various parameters used to describe the degree of sulfonation of different cell wall layers.

Time, min	Na_2SO_3 Concentration, g/L liquor	Net Sulfur Counts[a]					
		A	B	CC	A/B	CC/B	S
20	60	288	188	530	1.65	2.97	225
20	130	393	262	773	1.49	2.89	304
20	200	672	398	1177	1.70	3.01	474
40	60	270	185	537	1.59	3.18	212
40	130	433	277	799	1.68	2.84	343
40	200	913	640	1733	1.42	3.08	722
Mean ± 95% conf. int.:					1.59 ± 0.15	2.98 ± 0.22	

[a] A = maximum near lumen; B = minimum in S2; CC = cell corner; S = mean secondary wall (S_2 + S_3).

More recently, Heazel has shown that in liquid phase cooks there is a significant effect of liquor pH on the A/B ratio, lower values being obtained under alkaline conditions. The CC/B ratio decreased with increasing cooking time. In addition, he has constructed a mathematical model of the relevant transfer phenomena to test the hypothesis that the observed gradients are the combined result of variations in lignin concentration across the double cell wall and limitations on the rate of diffusion of sulfite ion into the cell wall from the lumen. Initial simulations of the process have given calculated distributions similar to the observed ones (Fig. 4).

A New Approach to Chemimechanical Pulping

The use of chemical treatments of wood prior to mechanical pulping is based on the supposition that lignin softening is necessary to improve pulp

properties by reducing fiber damage and enhancing fiber flexibility. With the help of a Master's candidate, T. Cornbower, we have explored the possibility that hemicellulose modification and/or removal can have similar effects in the absence of lignin softening. Duplicate samples of both acid hydrolyzed and untreated chips were fiberized and refined and the properties of the resulting pulps were compared.

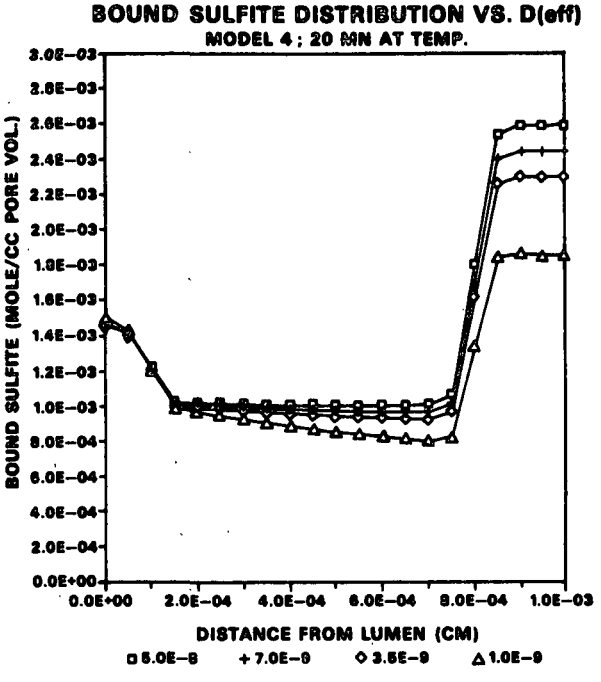

Figure 4. Bound sulfur profiles obtained from a 20 minute cook by integrating partial differential equations describing diffusion of sodium sulfite and its simultaneous chemical reaction with lignin in the cell wall. The distance represented on the x-axis is along a straight line from the lumen-S3 interface to the center of a lignin-rich intercellular region at the cell corner.

Although the small scale of the experiments necessitated the use of refining equipment that was less than optimal, the results (Table 11) clearly indicated a beneficial effect of the hydrolytic pretreatment. A patent disclosure has been prepared and larger scale experiments are planned.

Table 11. Simulated thermomechanical pulping of hydrolyzed chips.

	Hydrolyzed Chips		Control Chips	
Lignin, %	29.7	31.0	30.0	29.7
Xylan, %	5.1	4.6	9.8	10.0
Mannan, %	10.4	10.3	16.2	16.2
CSF	89	105	111	106
PFI rev.	1140	985	1750	1730
Density, g/cc	0.60	0.58	0.46	0.46
Burst index, $KPam^2/g$	2.26	2.13	1.34	1.20
Tensile index, $N \cdot m/g$	48.7	44.0	34.4	33.7
Tear index, $mN \cdot m^2/g$	4.42	5.06	3.51	3.26

BONDING STRONG, HIGH-YIELD FIBERS

In the previous status report we stated our intent to study the bonding characteristics of high yield pulps (a) to test the hypothesis that high-yield fibers separated without strength loss can subsequently be made to bond to one another to such a degree that fiber strength controls sheet strength and (b) to provide a method of making well bonded sheets for meaningful zero-span tensile strength measurements. Accordingly, we had begun a series of experiments to determine the extent to which fibers separated from a 93% white spruce pulp can be converted to sheets with strengths similar to that of the corresponding kraft pulp. A large quantity (several kg) of fiber was prepared in the laboratory; the details are documented in the September 10, 1986 Status report. The zero-span breaking length of sheets formed from this fiber source might be expected to be 29 km (this value is obtained by multiplying the single fiber breaking length of 78 km for the whole pulp by 3/8).

The bonding study, as outlined in Fig. 5, uses three different approaches. They are (a) modification of the high-yield fibers by subsequent chemical treatment, (b) using different drying techniques and (c) use of additives to improve bonding of these fibers. To date, we have completed most of the work except a detailed analysis of impulse drying of high yield fibers. Each of the three procedures is discussed below.

Chemical Modification

Two methods were used to modify the fibers: ozone treatment and chlorine dioxide followed by caustic extraction. Ozone treatment: Sixty gram samples were treated with 2.3, 4.4, and 8.6% ozone at 34% consistency and pH 3.8, 3.2, and 2.8 to give ozonated pulp yields of 98.7, 91.7, and 85.7%, respectively. Samples were subjected to secondary refining in the PFI mill and physical properties were evaluated. Figure 6 relates the tensile strength to density for the chemically treated and untreated refined pulps.

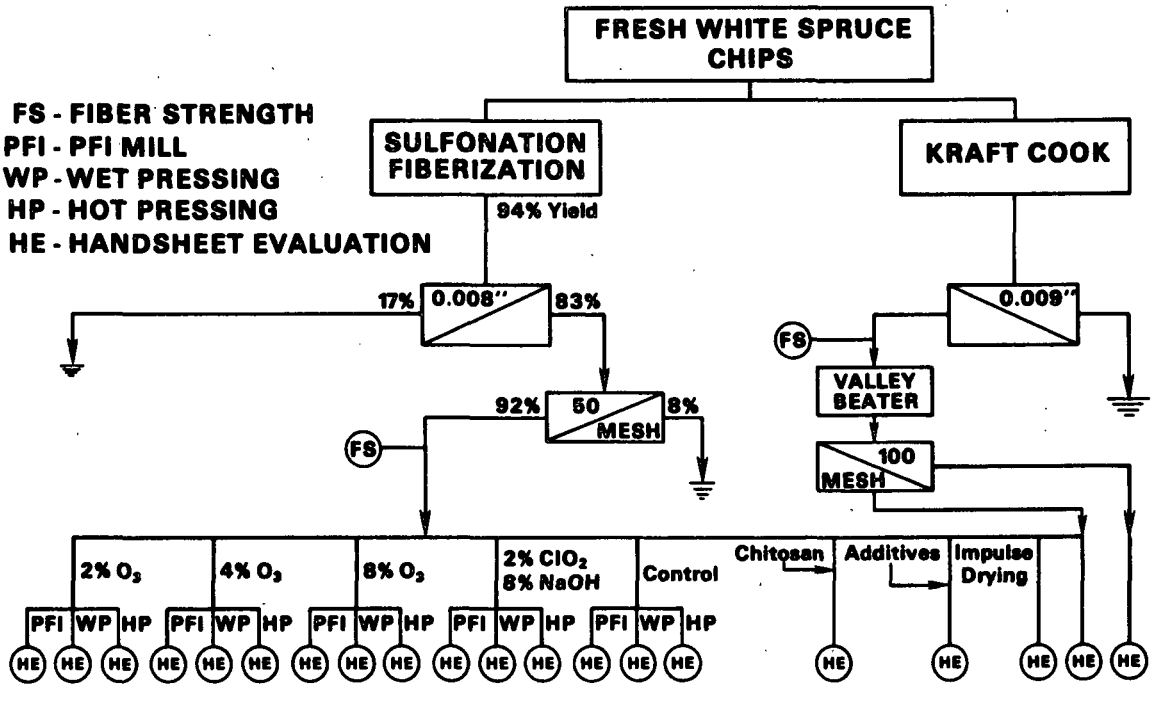

Figure 5. Experimental plan for bonding strong high-yield fibers.

Pulp strengths improve with refining and with the degree of ozonation. At a sheet density of 0.6 g/cc the zero-span breaking lengths of the 8.6 and 2.3% ozonated CMP pulps are 40 and 36% lower than the kraft pulp, while the tensile strengths are only 14 and 23% lower (Table 12). This suggests that the specific bond strength of CMP pulp is greater than the kraft pulp. The burst index for the 8.6% ozone level is 7% higher than the kraft pulp and 22% lower for the 2.3% ozonated pulp. Pulp yields from the 8.6 and 2.3% ozone treatment are 85.7 and 98.7% of the original pulp charged, resulting in chemical yields of 81 and 93%, respectively, compared with about 48% for unbleached spruce kraft pulp. Tear strength of the ozonated pulp decreased dramatically with refining from 155 units at a freeness level of 740 to 65 units at a freeness level of 605 for the 2.3% ozone treated pulp. Ozonation of the CMP pulps improved the strength of the resulting sheets considerably, with some loss in pulp yield especially at the 8.6% ozonation level.

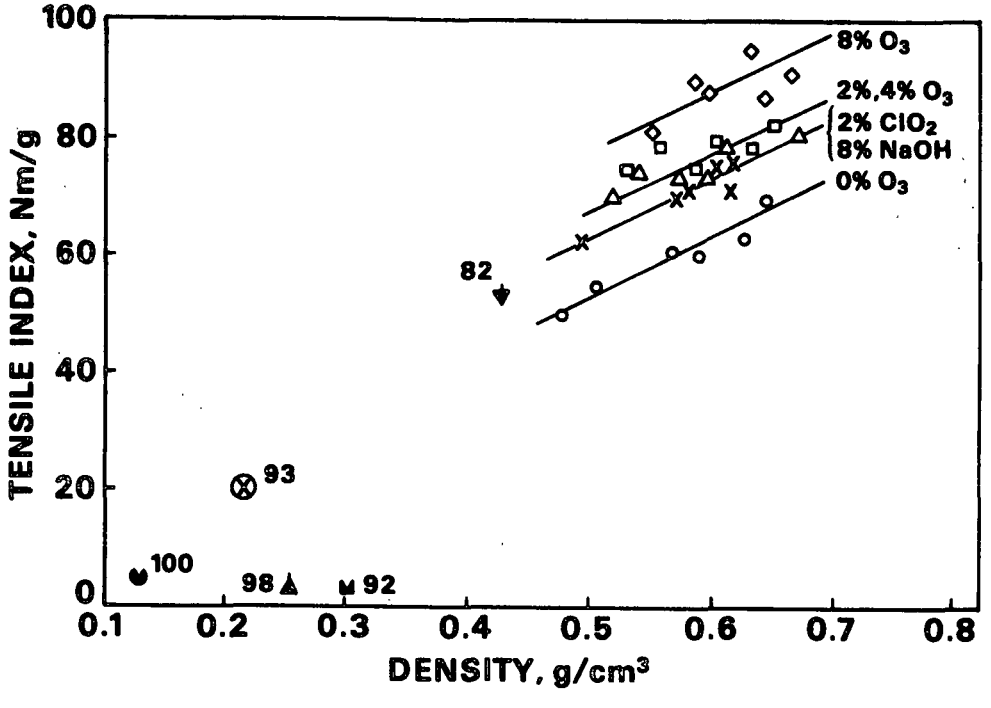

Figure 6. Effects of chemical treatments and refining on tensile strength of CMP.

Table 12. Effect of chemically posttreating CMP pulp on sheet properties.

Sample ID	PFI Counts	CSF, mL	TEA Index	Tensile Index, Nm/g	Burst Index, kPa m^2/g	Tear Factor, gF/100 g	Tensile Stiffness Index, Nm/g	Zero-span Index, Nm/g	Density, g/cc	Stretch, %	Thwing Formation, unit	Bendtsen Porosity, mL/min
1	0	740	25	5.5	NA	50.2	802	80	0.128	0.8	31.3	> 3000
1	1000	595	439	50.0	2.5	60.2	5739	121	0.480	1.4	63.5	3291
1	1250	520	544	53.5	2.7	60.1	5858	132	0.507	1.6	63.7	2092
1	1500	395	613	60.0	3.2	49.0	6564	131	0.569	1.7	51.8	715
1	1750	340	316	59.6	3.2	49.3	6405	129	0.592	1.8	57.5	375
1	2000	230	573	62.2	3.4	41.2	6875	141	0.627	1.5	55.9	98
1	2500	165	681	69.1	4.0	41.5	5313	139	0.644	1.7	52.9	40
2	0	740	397	3.9	2.5	154.7	3362	105	0.255	1.7	44.4	> 3000
2	750	605	886	69.9	4.5	65.0	6443	137	0.518	2.1	50.3	2811
2	875	535	984	73.3	5.0	63.7	6359	125	0.537	2.2	50.6	1783
2	1000	420	906	72.3	5.0	61.6	6817	135	0.576	2.0	40.8	710
2	1250	355	884	72.7	5.3	56.1	6899	135	0.598	2.0	41.7	276
2	1500	240	924	77.5	5.3	55.8	7169	141	0.609	1.9	39.2	134
2	2500	95	808	80.0	6.0	43.6	7582	142	0.676	1.7	36.4	< 12
3	0	740	383	3.9	2.8	152.0	3448	113	0.300	1.7	38.3	> 3000
3	550	570	994	74.5	6.0	80.6	6508	140	0.527	2.2	33.3	2352
3	700	515	958	78.7	6.0	72.8	6990	140	0.554	2.1	32.3	1320
3	1000	302	902	73.1	6.1	66.9	6792	145	0.586	2.1	37.3	401
3	1250	270	1057	79.5	6.1	66.0	6853	130	0.608	2.1	32.3	156
3	1500	160	903	77.5	6.1	54.2	7274	135	0.637	2.0	28.7	< 5
3	1800	125	969	81.5	6.9	54.5	7098	144	0.649	2.0	27.2	< 5
4	0	740	692	53.7	4.0	128.9	5267	134	0.426	2.0	42.4	> 3000
4	250	600	1053	80.8	6.5	82.1	7194	149	0.550	2.1	35.6	2076
4	375	500	1227	89.0	6.8	74.2	7468	129	0.585	2.2	33.6	748
4	500	430	1241	86.9	7.3	72.7	7188	135	0.595	2.3	31.8	681
4	750	330	1338	94.4	7.6	66.5	7842	152	0.632	2.3	31.6	111
4	1000	190	1048	86.7	7.9	63.9	7947	151	0.641	2.0	28.2	32
4	1200	135	1085	90.8	8.0	57.8	8092	156	0.663	1.9	25.5	< 5
5	0	740	113	20.7	1.2	184.2	2548	109	0.212	1.0	24.5	> 3000
5	1300	605	702	61.5	4.1	76.2	5884	120	0.491	1.9	53.0	2373
5	1800	475	885	70.0	5.2	63.9	6283	141	0.569	2.1	46.7	588
5	2250	380	875	70.7	5.3	61.3	6610	130	0.575	2.1	44.1	292
5	2700	320	909	74.3	5.5	54.8	6694	129	0.602	2.1	42.0	118
5	3280	240	958	75.3	5.7	55.9	6848	134	0.629	2.1	41.3	54
5	4200	160	765	69.1	5.4	57.6	6541	127	0.617	1.9	36.4	20
6				101.0	6.8			222	0.608			
6				126.0	9.8			202	0.748			

Sample Identification:
1. Untreated CMP
2. 2% OZONE (97.7% yield)
3. 4% OZONE (91.7% yield)
4. 8% OZONE (85.7% yield)
5. ClO_2-NaOH EXTRACTED (93.4% yield): 2% ClO_2-8% NaOH
6. White spruce Kraft pulp

The pulps produced are still weaker than the spruce kraft pulp in tensile strength at the same sheet density (0.6 g/cc) but compare favorably if one considers the higher yield obtained by the CMP-ozone system. Dramatic improvement in sheet stiffness, stretch, TEA and formation occur after refining the CMP pulps to a freeness level of 600 csf. Minor improvements are obtained in these properties by further refining. A maximum sheet zero-span breaking length of 15.7 km was obtained at an ozone treatment of 8.6%, far short of the calculated zero span breaking length of 29 km based on the single fiber measurements.

Chlorine dioxide followed by alkali extraction: This procedure was chosen for its desirable effect on both fiber conformability and specific bond strength. Ozone is known to have a greater effect on specific bond strength than on fiber conformability. On these bases one should expect substantially higher sheet strengths. As shown in Table 12 and Fig. 6 the properties obtained after refining were comparable with the 2.3 and 4% ozone treated pulps. The chemical yield after this treatment was 88% of the original pulp charged. As shown in Table 12, this pulp was harder to refine to a given freeness than the control or the ozone treated pulps. A maximum zero-span breaking length of 14 km was obtained, again significantly lower than that expected on the basis of single fiber measurements.

The chemically modified CMP pulps improved significantly in pulp properties when compared with the untreated CMP pulp, although not to the level of a kraft pulp. The breaking length differential between the single fiber measurement and the sheet zero span values suggests improved bonding is required. Further improvement in bonding will be sought by hot pressing or impulse drying the refined ozone treated sheets. Zero-span breaking length and tensile strength

measurements for CMP pulp at sheet density of 0.75 g/cc will be compared with spruce kraft pulp for testing the observation that the specific bond strength of the CMP pulp is greater than the kraft pulp at the same sheet density.

Drying techniques: To improve sheet densification and bonding, wet pressing at elevated pressures, hot pressing, and impulse drying techniques were considered. To date we have completed work on wet pressing and hot pressing of chemically treated and untreated unrefined stock. The wet pressing technique involves pressing handsheets in a Carver press in the pressure range of 1000 to 9000 psi, while hot pressing involves heating the sheet to 177°C under the same pressures. Figure 7 and Table 13 relate the strength to density of the various pulps, showing the effects of refining, wet pressing, and hot pressing. Substantial strength increases were achieved by hot pressing the sheets. Wet pressing improved the tensile strength but not as dramatically as the hot pressing. Also, higher sheet densities were obtained by the hot pressing technique. The hot pressing technique in such sheets probably works through two different mechanisms: (a) increased bonded area as a result of fiber wall softening and subsequent fiber collapse under applied pressure, and (b) enhancement of bond strength per unit of bonded area through flow and cohesion of lignin on adjacent fiber surfaces. In the hot pressing of CMP handsheets, increasing the pressure beyond 1000 psi gives little or no improvement in zero-span breaking length (ZSBL). For example at a pressure of 2000 psi the ZSBL is 101 units, while at a pressure of 9000 psi the ZSBL is 91 units.

Additives for improved fiber bonding: This approach for increasing fiber bonding and formation involved using compounds which had been previously reported in the literature such as chitosan, Kymene, CMC, viscose treatment and kraft fines.

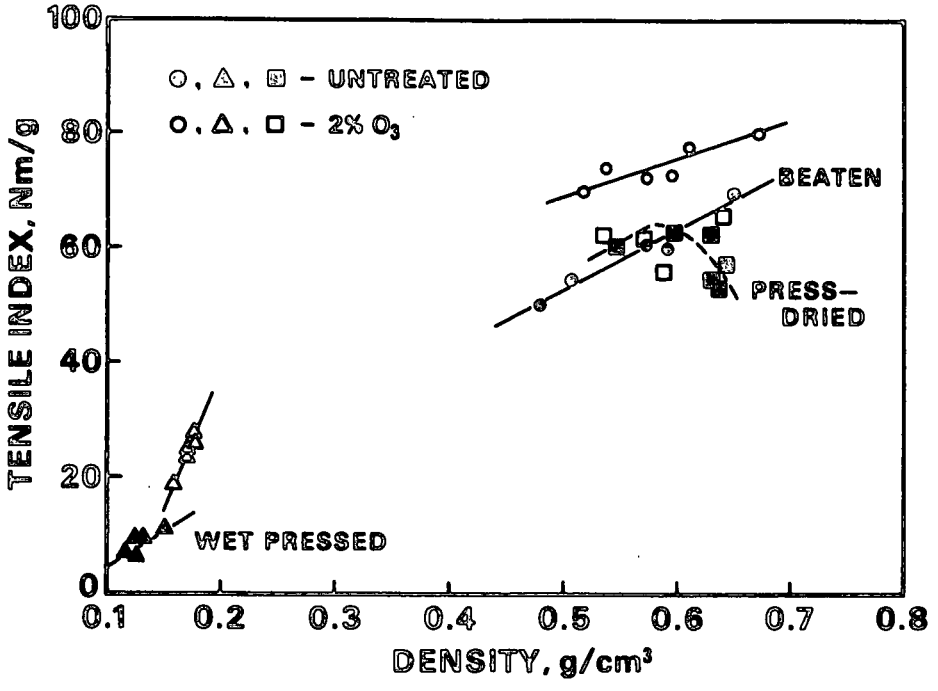

Figure 7. Effects of pressing, press-drying, and refining on tensile strength of untreated and ozone treated CMP.

Table 14 shows the effect of spraying chitosan on sheets of different stocks. For comparison purposes, commercial spruce MP, commercial sulfite, and spruce kraft pulp were used. As shown in Table 14, the properties of the CMP pulp improve with chitosan addition, especially tear, stiffness and stretch, but there was no improvement in ZSBL. The most noticeable improvement is for the sulfite pulp, where fourfold increases in tensile and burst strength are obtained. The sheet density of the sulfite pulp increased from 0.47 to 0.64 g/cc after the chitosan treatment. The spruce kraft pulp improved twofold in burst strength but suffered a 36% loss in sheet formation and also losses in ZSBL and stretch.

Table 13. Effect of pressing on pulp strength of CMP fibers.

Sample ID	PFI Counts	Pressure, psi	CSF, mL	TEA Index	Tensile Index, Nm/g	Burst Index, kPa m^2/g	Tear Factor, gF/100 g	Tensile Stiffness Index, Nm/g	Zero-span Index, Nm/g	Density, g/cc	Stretch, %	Thwing Formation, unit	Bendtsen Porosity, mL/min
1	0	--	740	25	5.5	NA	50.2	802	80	0.128	0.8	31.3	> 3000
1	1000	--	595	439	50.0	2.5	60.2	5739	121	0.480	1.4	63.5	3291
1	1250	--	520	544	53.5	2.7	60.1	5858	132	0.507	1.6	63.7	2092
1	1500	--	395	613	60.0	3.2	49.0	6564	131	0.569	1.7	51.8	715
1	1750	--	340	316	59.6	3.2	49.3	6405	129	0.592	1.8	57.5	375
1	2000	--	230	573	62.2	3.4	41.2	6875	141	0.627	1.5	55.9	98
1	2500	--	165	681	69.1	4.0	41.5	5313	139	0.644	1.7	52.9	40
2	--	1000	740	30	6.5	NA	57.9	884	81	0.123	0.9	33.7	> 3000
2	--	2000	740	30	6.9	NA	54.5	948	82	0.118	0.9	36.0	> 3000
2	--	4000	740	42	8.2	NA	68.0	1071	82	0.125	1.0	33.7	> 3000
2	--	6000	740	48	8.7	NA	67.3	1071	85	0.133	1.1	NA	> 3000
2	--	9000	740	72	11.1	0.6	80.1	1160	88	0.148	1.2	34.5	> 3000
3	--	1000	740	532	59.7	3.3	56.8	4936	96	0.542	1.6	33.5	> 3000
3	--	2000	740	618	63.0	3.6	51.5	5056	101	0.598	1.7	28.6	3251
3	--	4000	740	292	53.8	4.3	44.5	5255	94	0.628	1.1	29.1	2241
3	--	6000	740	239	52.5	4.4	40.2	5399	92	0.635	0.9	32.2	1851
3	--	9000	740	273	56.4	4.6	34.1	5586	91	0.642	1.0	28.7	1690
4	--	1000	740	730	63.5	4.1	64.4	6981	99	0.530	1.8	31.1	> 3373
4	--	2000	740	440	60.1	4.4	55.1	7624	99	0.570	1.2	30.0	3260
4	--	4000	740	268	55.3	4.9	44.5	8150	96	0.615	0.9	28.4	2296
4	--	6000	740	168	48.8	5.1	41.8	8478	94	0.633	0.7	24.5	1724
4	--	9000	740	197	52.5	5.0	35.2	8708	95	0.627	0.8	31.9	1377

Sample Identification
1. Untreated CMP fibers
2. Wet Press - no heat
3. Wet Press - heated to 177°C
4. Wet Press - heated 177°C 2% ozone

Table 14. Effect of adding chitosan on sheet properties of CMP pulp.

Sample ID	CSF, mL	TEA Index	Tensile Index, Nm/g	Burst Index, kPa m^2/g	Tear Factor, gF/100 g	Tensile Stiffness Index, Nm/g	Zero-span Index, Nm/g	Density, g/cc	Stretch, %	Thwing Formation, unit
1	740	25	5.5	NA	50.2	802	80.0	0.128	0.8	31.3
2	740	65	12.2	0.7	74.6	1535	80.2	0.146	1.0	NA
3	740	102	13.5	1.0	80.4	1630	75.7	0.144	1.3	NA
4	740	55	10.0	0.5	79.3	1388	74.7	0.143	1.0	35.5
5	740	419	35.3	2.2	219.5	5235	169.6	0.378	1.8	43.9
6	740	367	38.7	5.3	201.5	5728	149.3	0.408	1.4	28.1
7	740	598	34.9	2.1	79.1	3151	84.5	0.283	2.5	36.0
8	740	482	39.9	2.8	69.0	3960	87.5	0.315	1.9	30.3
9	740	130	16.4	0.8	86.0	2832	95.0	0.474	1.3	30.3
10	740	483	65.9	4.4	34.6	4704	95.0	0.640	1.9	30.3

Sample Identification
1. CMP untreated
2. CMP + 1% chitosan
3. CMP + 2% chitosan
4. CMP + 1% chitosan; cold pressed at 4000 psi
5. Spruce kraft - untreated
6. Spruce kraft 1% chitosan
7. Consolidated spruce MP
8. Consolidated spruce MP - 1% chitosan
9. Sulfite softwood
10. Sulfite softwood - 1% chitosan

Kymene and CMC treatments produced a slight increase in sheet properties at dosage levels between 0.2 and 2.0% (Table 15). A sample of CMP pulp treated with 0.2% Kymene was sent to a member company for viscose treatment. The treatment involved saturation of the pulp with dilute viscose solution followed by regeneration with dilute sulfuric acid for a viscose pickup of 2.5-3.0%. These additives did not improve sheet formation or zero span strength. Viscose treatment improved the tensile, tear, and stiffness properties but had a negative effect on zero-span breaking length and water absorption capacity. Figure 8 is a plot of tensile strength versus sheet density of the various additives used for bonding the CMP pulp. The data indicate that increasing sheet density should increase tensile index. Further improvement in sheet densification will be explored by beating in a PFI mill and by hot pressing the sheets in a Carver press. Another additive being used at present is xyloglucan (molecular weight 1.3×10^6) isolated by Susan Molinarolo for her thesis project. Use of a CMC and Kymene combination previously investigated by R. Stratton will also be explored.

Kraft fines addition showed slight improvement in zero-span breaking length at a 30% fine addition level (Table 16). Sheet formation declines with fines addition, which can result in lower zero span values. Increasing fines addition improves properties affected by bonding but also improves the tear strength from 50 to 96 units. The increase in tear by displacing long fibers by kraft fines is at first surprising, but can be explained in terms of the high strength and poor bonding characteristics of the fibers. When fiber strength is high, increased bonding (as achieved, for instance, with kraft fines) will continue to increase tear strength up to high levels before the onset of fiber breakage causes further increase in bonding to decrease tear. Fines addition

Table 15. Effect of additives on sheet properties of CMP pulp.

Sample ID	Tensile Index, Nm/g	Burst Index, kPa m^2/g	Tear Factor, gF/100 g	Tensile Stiffness Index, Nm/g	Zero-span Index, Nm/g	Density, g/cc	Stretch, %	Thwing Formation, unit	Bendtsen Porosity, mL/min	Water Absorption, s
1	5.5	NA	50.2	802	80.0	0.128	0.8	31.3	> 3000	NA
2	10.8	NA	47.0	1322	83.7	0.121	1.1	31.8	> 3000	17.6
3	13.6	0.6	61.1	1350	77.3	0.125	1.3	33.2	> 3000	50.8
4	14.0	0.7	64.2	1519	78.6	0.128	1.1	28.5	> 3000	37.0
5	16.4	0.8	61.2	1619	81.4	0.127	1.3	23.2	> 3000	44.2
6	16.3	0.8	66.3	1604	85.5	0.128	1.3	26.3	> 3000	38.0
7	7.4	NA	38.1	1092	74.5	0.121				
8	9.1	NA	37.3	1206	81.2	0.132	1.0	33.6	> 3000	19.4
9	7.9	NA	35.5	1184	93.2	0.127	0.9	33.2	> 3000	15.5
10	7.5	NA	40.5	1145	81.4	0.124	0.9	29.8	> 3000	8.5
11	7.1	NA	37.3	1067	79.5	0.119	0.9	30.9	> 3000	23.4
12	45.5	3.0	62.3	5111	72.9	0.309	1.3	27.3	> 3000	67.0

Sample Identification

1. Untreated CMP
2. CMP 0.2% Kymene 557
3. CMP 0.4% Kymene 557
4. CMP 0.6% Kymene 557
5. CMP 1.2% Kymene 557
6. CMP 2.0% Kymene 557
7. CMP 0.2% CMC
8. CMP 0.4% CMC
9. CMP 0.6% CMC
10. CMP 1.2% CMC
11. CMP 2.0% CMC
12. CMP viscose treated

improves the stretch characteristics of the sheet from 0.8 to 3.8 units at a stiffness index of 4225. The stretch obtained (3.8 units) is higher when compared with 1.8 for spruce kraft pulp. Although the increase of sheet density from 0.13 to 0.29 g/cc obtained for the 30% fines addition level was modest, there was a dramatic improvement in sheet properties. To determine the maximum extent of improvement in sheet properties, sheet density will be increased by refining and hot pressing at pressures lower then 2000 psi at 177°C.

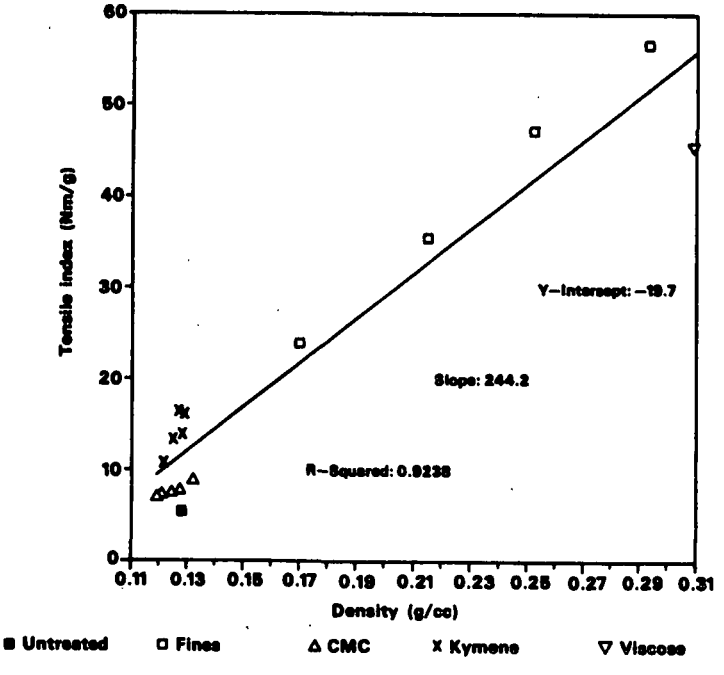

Figure 8. Effect of additives on tensile strength of CMP.

ACKNOWLEDGMENTS

We thank the Mead Corporation for making available to us their pilot-scale refining facilities. The skilled experimental assistance of Harry Grady, Amy Malcolm, and Kristie Rankin is also gratefully acknowledged.

Table 16. Effect of adding kraft fines on sheet properties of CMP pulp.

Kraft Fines, %	Tensile Index, Nm/g	Burst Index, kPa m^2/g	Tear Factor, gF/100 g	Tensile Stiffness Index, Nm/g	Zero-span Index, Nm/g	Density, g/cc	Stretch, %	Thwing Formation, unit	Bendtsen Porosity, mL/min	Water Absorption, s
0	5.5	NA	50.2	802	80.	0.128	0.8	31.3	> 3000	NA
5	24.0	1.3	74.2	2553	86.	0.170	1.7	27.6	> 3000	17.2
10	35.6	2.2	89.2	3388	89.	0.215	2.1	28.5	> 3000	3.4
20	47.3	3.4	96.1	3708	89.	0.252	3.3	25.6	> 3000	18.0
30	56.9	4.2	96.0	4225	96.	0.293	3.8	24.8	1072	84.2

REFERENCE

1. Status Report, Project 3566, Sept. 10, 1986.

THE INSTITUTE OF PAPER CHEMISTRY

Thomas J. McDonough
Group Leader, Pulping/Bleaching
Pulping Sciences
Chemical Sciences Division

Salman Aziz
Supervisor, Pulp Laboratory
Pulping Sciences
Chemical Sciences Division

THE INSTITUTE OF PAPER CHEMISTRY

Appleton, Wisconsin

Status Report

to the

PULPING PROCESSES

PROJECT ADVISORY COMMITTEE

Project 3605

COMPUTER MODEL OF RECOVERY FURNACE

August 31, 1987

PROJECT SUMMARY FORM

DATE: August 31, 1987

PROJECT NO. 3605: COMPUTER MODEL OF RECOVERY FURNACE

PROJECT LEADERS: T. M. Grace

IPC GOAL:

Increase the capacity potential of processes.

OBJECTIVE:

Develop a comprehensive, three-dimensional, mathematical model of the fireside processes in a kraft recovery furnace. The model would be based on first principles and would incorporate and integrate the results of ongoing fundamental studies of black liquor combustion.

CURRENT FISCAL YEAR BUDGET: $40,000

SUMMARY OF RESULTS SINCE LAST REPORT:

This project was initiated in the Fall of 1986 as three concurrent Ph.D. theses. The concept is a three-dimensional model of the processes going on in the furnace cavity (up to the entrance into the screen or superheater section). This model is envisioned as an effective way of translating the fundamental knowledge of black liquor combustion being obtained in other research programs into improvements in recovery boiler performance. The modeling effort is divided into three distinct parts (each a thesis);

1. A model of the char bed
2. A model of liquor supply and in-flight behavior
3. An overall model integrating the other two models along with air/flue gas flow patterns, gaseous reactions, and heat transfer.

The overall model provides the core and structure for the entire effort. It is formulated in an Eulerian coordinate frame using a cellular description of the furnace space. After a period of examining different options, we have decided to base the furnace model on the FLUENT software package. This is basically a finite difference package for modeling fluid flows. Additional features of FLUENT include a six-flux radiation model, the PSI-CELL model for two-phase flow, a combustion model, and a number of turbulence models. The initial modeling effort was directed toward predicting cold-flow behavior in recovery boiler geometries. This was done for two reasons; first it is the least complicated situation we need to deal with, and second, data were available from cold-flow tests on scale-model furnaces to check the model predictions. A 10,000 node version of the FLUENT program was used for this stage of the effort. The results are described in a paper which is attached. In general, the bulk flow behavior, particularly in the upper furnace, matched the experimental data reasonably well. It is clear however, that 10,000 nodes is insufficient for a proper description, particularily near the bed and when focusing on individual

air jet behavior. Steps are being taken to upgrade software and hardware capability so that we can run with 50,000 nodes. This will be sufficient to give reasonable results. Initial attempts at including temperature dependence and combustion have been made, and this has been found to be a tractable problem.

The liquor supply and inflight model is formulated partially in a Lagrangian reference frame (moving with the particle). Trajectory equations are formulated based on Newtons Law and include mass changes, gravity and aerodynamic drag. For each particle, drying, pyrolysis and volatiles burning, char burning and smelt reoxidation are modeled in a Lagrangian frame. The PSI-CELL (Particle Source in Cell) subprogram is used to transform the information from the Lagrangian frame to the Eulerian frame required by the main model. This part of the effort is highly coupled with the overall model, because gas flow patterns and temperatures will have a major influence on droplet trajectories and behavior. The procedure that will be used will be to first converge the cold flow case, then make appropriate adjustments for gas temperature, and then introduce the particles, calculate the source terms in the gas flow equations and iterate. Preliminary tests indicate that this approach will work. At the present time, the trajectory equations have been checked out and the drying model is being tested against its ability to predict drying in the DOE reactor.

The char bed mathematical model is not as far along because we are still trying to find a conceptual framework for modeling the bed. Neither a plug flow reactor nor a well mixed reactor appears to be an adequate description. The fact that the bed modeling is trailing the other models does not slow down the overall effort because the bed model enters the overall model essentially as a boundary condition, and so the other efforts can proceed by making assumptions about the bed. Recently we have decided to obtain some experimental bed burning data in a very simple geometry, O_2/N_2 mixtures passing horizontally over a layer of char in a partially filled pipe. Modeling of this experimental data will provide a basis for subsequent modeling of bed burning in the DOE reactor. These two will then provide the base for the model of the bed in the furnace. We expect to treat the bed as psuedo-dynamic. Any imbalance between the rate at which material is falling on the bed and the rate at which it is burned (or smelted) will be used to determine an accumulation (depletion) term. This can be used to predict bed growth or decay rates and as input for selecting different bed geometries for subsequent iterations.

PLANNED ACTIVITY THROUGH FISCAL YEAR 1988:

Most of the development of the model is expected to be completed within the current fiscal year. Within the next few months we will expand our capability so that we will be able to run cases with 50,000 nodes. The overall model will be stepwise augmented to handle combustion, temperature gradients, heat transfer, and source terms from the PSI-CELL model. Convergence problems will be examined and convergence techniques determined. The complete Lagrangian burning model will be developed and evaluated. At that point we will begin the integration of the inflight model into the overall model. Considerable effort will need to be devoted to the question of how many particles and trajectories are needed to reasonably define the situation, and how to model the spray itself. Bed interactions will be handled by assumption at this stage.

By the end of December we expect to be done with the simple char burning experiments and the modeling of those experiments, and the effort will be mainly focused on modeling burning rates in the DOE reactor. In the early part of the next calendar year we will develop the mathematical model for the bed in the recovery furnace, and in late spring will be interfacing that model with the rest of the burning model. The goal is to have the entire model put together and have at least one complete, converged case done by the end of June.

A considerable part of the effort over the next 10 months will be devoted to finding appropriate graphical methods of displaying the information developed by the model. We feel that this will be a very important part of the overall product.

FUTURE ACTIVITY:

The model will be used to run a large number of simulations. These do not always have to be fully-crunched, complete solutions. Often the information sought can be found from less comprehensive simulations. We want to use this to find out the optimum way to set up the liquor sprays and air flows in recovery boilers to maximize thoughput without plugging and to enhance other performance criteria.

STUDENT RESEARCH:

This entire effort is being done through student research. The three Ph.D. students are:

Andy Jones - overall model
Allan Walsh - in-flight model
Dan Sumnicht - char bed model

Status Report

COMPUTER MODEL OF RECOVERY FURNACE

A COMPARISON OF COMPUTATIONAL AND EXPERIMENTAL DETERMINATIONS OF GAS FLOW PATTERNS IN THE KRAFT RECOVERY BOILER

ABSTRACT

Computational fluid dynamics is applied to the kraft recovery boiler and the results compared to experimental results obtained by B&W. The recovery furnace used for comparison is a 1/8th scale replica of a B&W unit located in DeRidder, LA. The computational modeling of the furnace is successful in reproducing many of the characteristics of the flow seen experimentally. The main problem with the computational models is a lack of nodes; more nodes are needed to describe the finer details of the bed and air jets. With 50,000 nodes (5 times the number used in this study), it should be possible to accurately reproduce the results found experimentally.

INTRODUCTION

This paper describes the first stage in the development of a three-dimensional recovery furnace model, namely, the simulation of cold flow in an existing furnace design. The recovery furnace simulated was of B&W design, chosen because of data available for comparison.[1] B&W measured the velocity profiles in a 1/8th scale replica of this furnace design, under a number of flow conditions. This paper examines five computationally developed flow patterns in this recovery furnace, obtained by using FLUENT (a commercially available computational fluid flow program), and two experimentally determined flow patterns. The five analytical cases were set up as a means to investigate the agreement that is possible

between experimental and analytical flow patterns, and to find if FLUENT can be used to model the recovery boiler.

A DESCRIPTION OF FLUENT

The main tool used in this investigation is FLUENT, a finite difference package for the modeling of fluid flows. The program is flexible and comprehensive, permitting its use in a wide variety of flow situations, including two or three dimensional flows, laminar or turbulent flows, and swirling flows. Additional features of FLUENT include a six-flux radiation model, the PSI-CELL model for two-phase flow,[2] a combustion model, a number of turbulence models, and a porous flow model; this is not a complete list.

The variables that are solved for in the simplest three-dimensional case are u-velocity, v-velocity, w-velocity and pressure. If temperature effects are added, the enthalpy and the radiative heat fluxes are also determined. If the K-n turbulence model is used, then the kinetic energy of turbulence and the dissipation rate are found. If combustion is included, the mole fractions of combustibles (C), oxygen (O), and products (P) must be calculated in each cell. The maximum number of finite element cells that can be solved for in the version of FLUENT (version 2.8) used thus far is 10,000.

The advantages of FLUENT are (1) interactive input; (2) flexibility - almost any type of flow can be modelled; (3) internally generated relaxation coefficients, which usually result in stable iterations; and (4) excellent graphics for viewing the results.

The process of setting up a fluid flow simulation is straightforward, as the description of a flow is done interactively. Cartesian or cylindrical regions

can be described. In a Cartesian description the cells are rectangular parallelpipeds that can be different lengths in each coordinate direction. A number of different cell types can be specified. Typically five different types are used: (1) live cells - the variables in these cells are solved for at each iteration; (2) inlet cells - the values of the flow variables are specified for these cells and remain the same throughout the calculation; (3) wall cells - these cells act as barriers to the flow and are used to describe the flow geometry; (4) outlet cells - the value of the flow variables are solved for, but these cells are placed on boundaries of the flow; (5) symmetry cells - they define lines or planes of symmetry in the flow, which reduces the number of cells necessary to describe a given flow geometry.

In addition to a description of the flow geometry, it is necessary to specify the physical properties of the fluid and the boundary conditions in the wall and inlet cells. The mass flow rates in the inlet cells are controlled by varying the gas velocity or the distance between adjacent nodes.

THE COLD FLOW SIMULATION

The numerical simulation of cold flow in the B&W 1/8th scale furnace was done as accurately as possible; this justifies comparison between the experimental and analytical cases. The upper limit of 10,000 nodes makes it necessary to use some approximations. An isoparametric view of the furnace is shown in Fig. 1 and 2. Due to the symmetry involved, it is necessary to describe only half of the furnace. The flow patterns in the other half of the furnace will be a mirror image of the area of the furnace modeled. The symmetry plane is parallel to the side walls and cuts the bullnose and bed in half. The furnace cavity is 10 meters wide, 5 meters in depth, and 30 meters high. The bullnose extends 5 meters across the furnace top, leaving the other half as outlet. The bullnose

was described as being parallel to the floor of the furnace; it actually slopes slightly downward to the back of the furnace, but this was ignored to reduce the nodes used. The resulting effect on the gas flow patterns should be negligible.

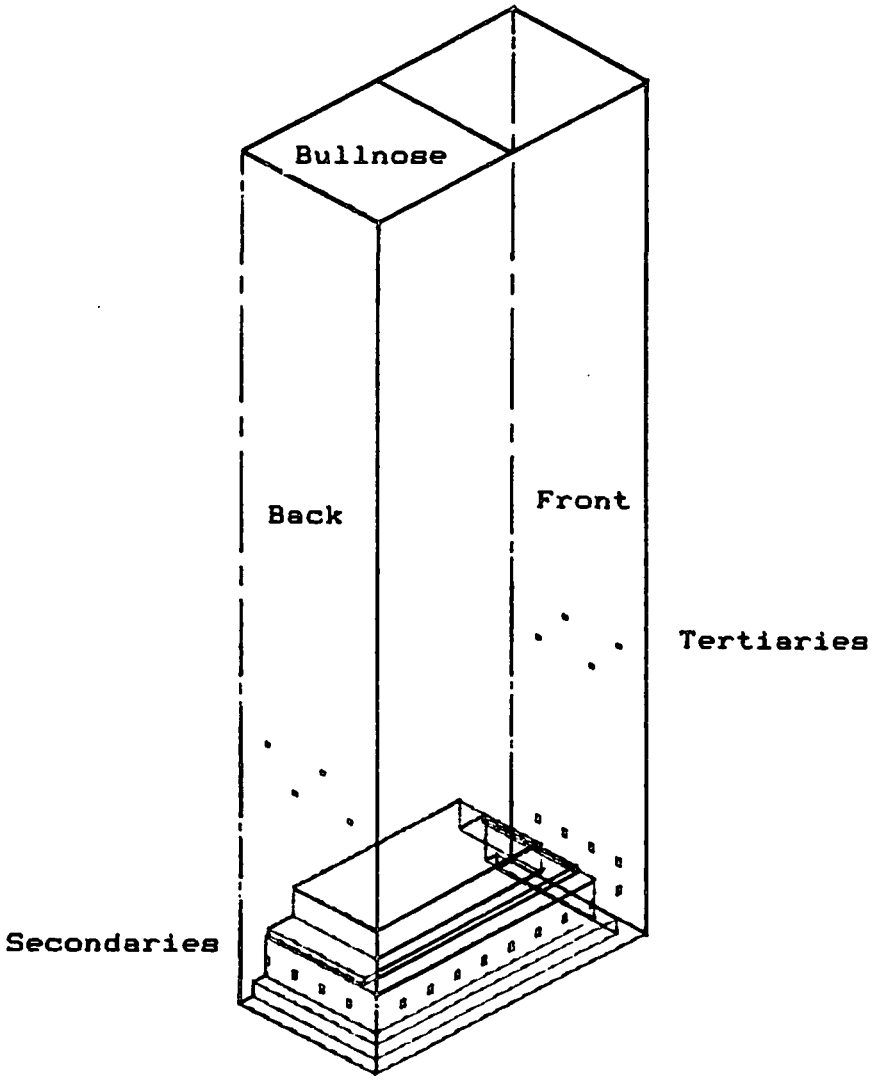

Figure 1. Isoparametric view of analytical model showing high bed and high velocity tertiaries.

The air inlets were modeled in the following manner:

Primary air - a row of nodes along the walls was designated as inlets. The distance between the inlet nodes and the nodes above and below was adjusted in order to satisfy the volumetric flow rates. This

treats the primary air as if it were a planar jet completely encircling the furnace. A shortage of nodes made description of individual primary ports impractical. The primary air was injected 1 meter above the furnace floor at a velocity of 40 meters/sec.

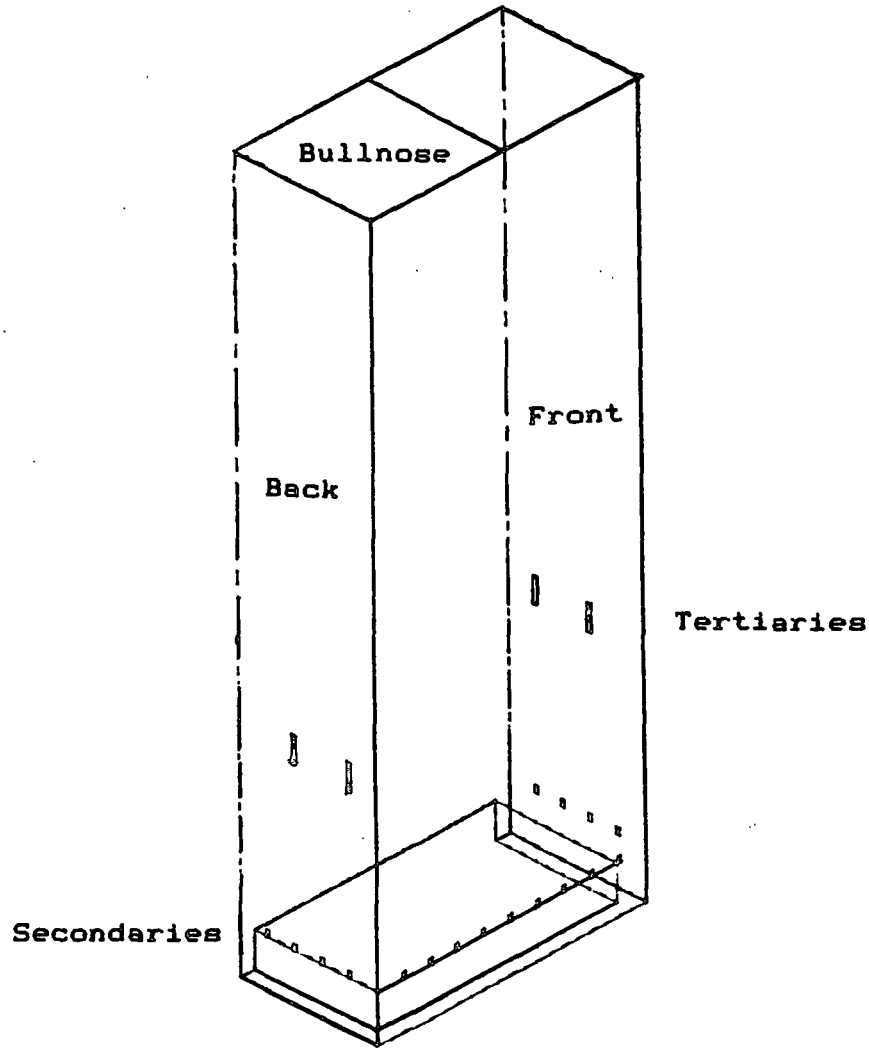

Figure 2. Isoparametric view of analytical model showing low bed and low velocity tertiaries.

Secondary air - separate air ports of the same dimensions as the ports in the actual furnace were used for the secondary air. The half of the furnace modeled had 16 secondary ports, each with an inlet

velocity of 36 meters/sec (identical to the B&W case). The injection level was 3 meters above the furnace floor.

Tertiary air - separate air ports on the walls were used, once again of the same shape as in the actual furnace. Three configurations were examined; in the first, 4 ports at 10 meters above the furnace floor were used, two on each the front and back walls, with an inlet velocity of 10 meters/sec, (identical to the B&W case), as shown in Fig. 3; in the second configuration, 8 smaller ports with an inlet velocity of 77 meters/sec were used, four on each the front and back walls. Two closely spaced levels of tertiary air were used (at 9.5 and 10.5 meters above the bed); this is shown in Fig. 4. In the third configuration eight tertiary jets are added to the side walls with the same geometry as seen in Fig. 4; this is in addition to the jets already on the front and back walls.

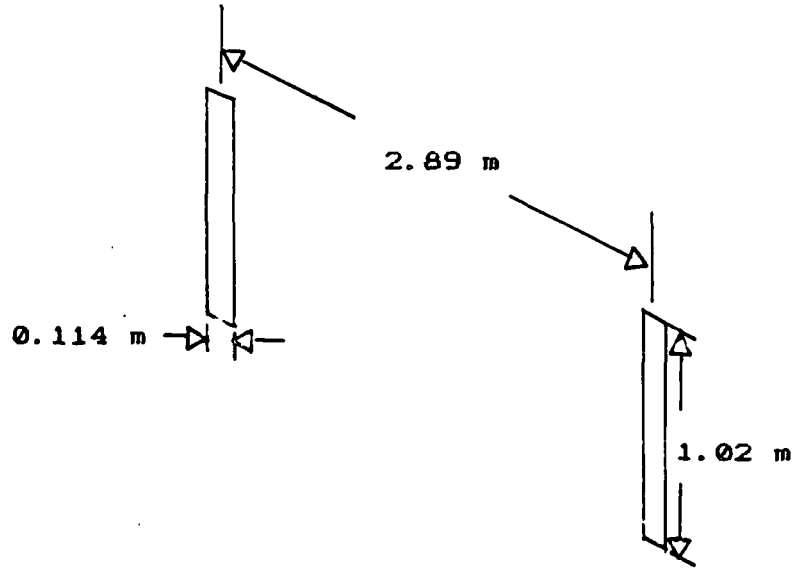

Figure 3. Low velocity tertiaries.

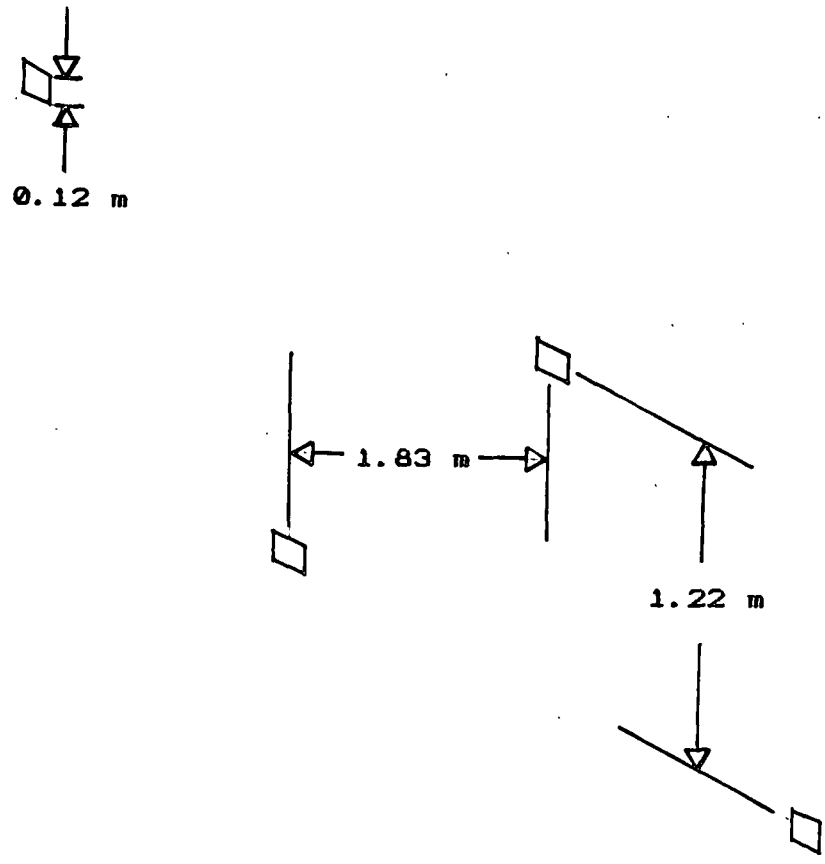

Figure 4. High velocity tertiaries.

Two different smelt bed shapes were examined; in both a staggered shape is used. The limitations of version 2.8 of FLUENT necessitate the use of a staggered bed outline. The use of body fitted coordinates would eliminate the staggered bed shape and the resulting numerical problems, leading to a more accurate description of the flow around the bed. The first bed shape used (Fig. 1) corresponded as closely as possible to the one used in the experimental work (Fig. 5) with the top of the bed extended slightly above the secondary air ports; the second bed peaked below the secondary jets (Fig. 2). The fluid used in all cases was air.

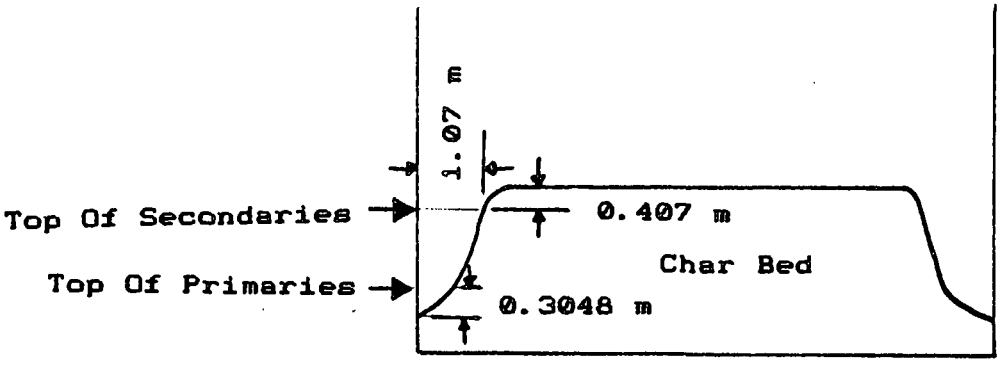

Figure 5. Char bed used in experimental model of furnace.

A number of cases may be modeled, using different combinations of bed shapes and tertiary jet configurations described above. The five cases examined were as follows:

1) High bed, low-velocity tertiaries - the bed that extends above the tertiaries is used, along with the large, low-velocity tertiary air ports;

2) High bed, high-velocity tertiaries - same bed, but the tertiary jets are replaced with an increased number of smaller jets;

3) Low bed, low-velocity tertiaries - same tertiary jets as in case 1, but the lower bed is used;

4) Low bed, high-velocity tertiaries - same tertiary jets as in case 2, but the lower bed is used;

5) Low bed, four wall high-velocity tertiaries - high velocity tertiary jets on all four walls, with the lower bed being used.

The mass flow rates were the same as the experimental cases (except for case 5); the total flow rate for the half of the furnace modeled was 48 kg/sec (380,000 lbs/hr). In cases 1 and 3 the flow was split into 50% primary, 40% secondary and 10% tertiary air. In cases 2 and 4 the flow was split into 46% primary, 36% secondary and 18% tertiary air. In case 5 the split was 39% primary, 31% secondary and 30% tertiary air with the total flow rate increased to 56.6 kg/sec due to the additional tertiary ports.

EXPERIMENTAL DATA

The data used to test the analytical cold flow models are part of a B&W investigation.[1] The furnace examined was the Boise Cascade Process Recovery Boiler, located in DeRidder, LA. This furnace was experiencing excessive particulate carryover and inadequate excess air flow. The problem was believed to be due to insufficient breakup of a high velocity core of gas by the existing tertiary air jets.

A number of changes in the tertiary air system were considered. These changes were evaluated by constructing a 1/8th scale replica of the DeRidder recovery furnace and conducting cold flow measurements in this replica. The velocities within the scaled-down furnace were measured with a hot film anemometer at two traverse planes, T1 located halfway between the secondary and tertiary air ports, and T2 located about halfway between the tertiary air ports and the bullnose. Isovelocity plots were constructed using these data.

The two cases that were simulated were the as-is design and the recommended design. In both cases a bed was included in the bottom of the furnace; the shape of this bed is shown in Fig. 5. The isovelocity plots obtained in these two cases are presented in Fig. 6, 8, 12, and 14.

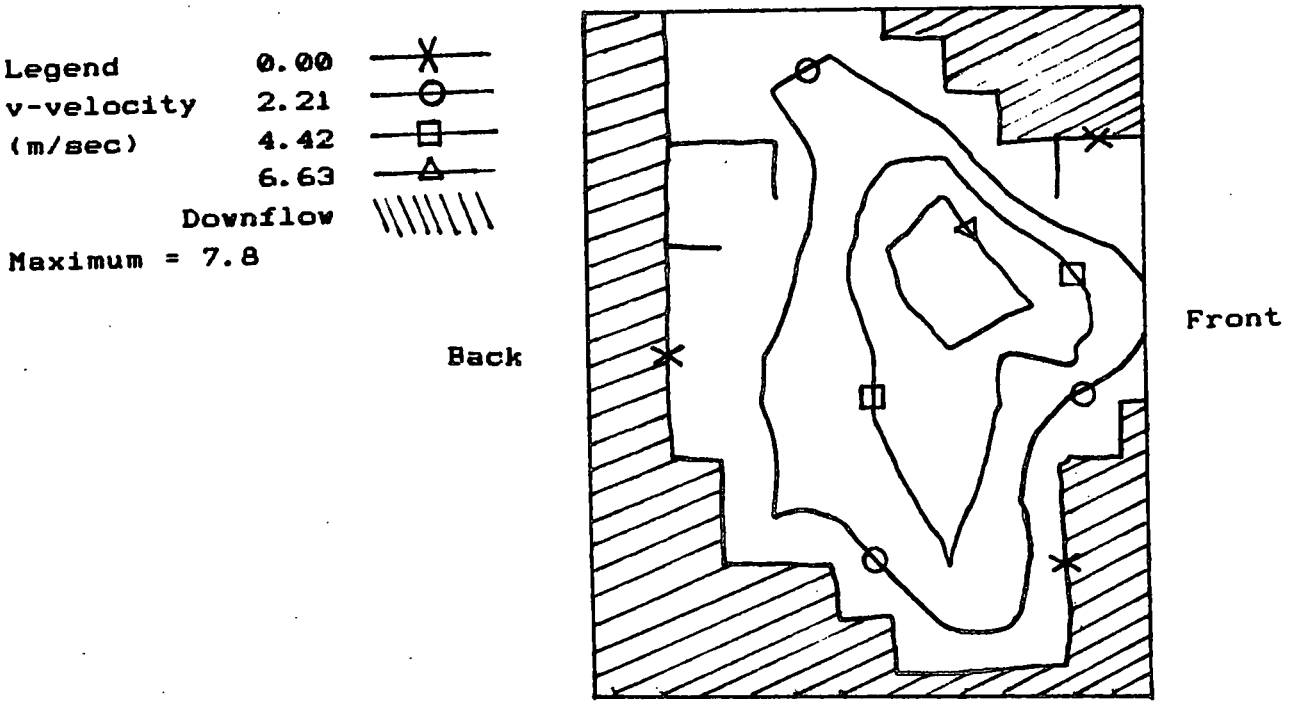

Figure 6. T1 traverse case 1 experimental.

THE ANALYTICAL MODEL

This section will describe in detail the results of modeling with FLUENT the five cases described earlier.

Case 1 corresponds to the B&W as-is case. The T1 and T2 traverses are shown in Fig. 7 and 9. The experimental results and the results obtained with FLUENT show good overall agreement at the T2 traverse. The large region of stagnation and downflow on the bullnose side of the furnace is quite apparent in both situations. The experimental results show a peak velocity of 4.5 meters/sec, which is found closer to the front of the furnace than the FLUENT peak velocity of 1.9 meters/sec. The difference in peak velocity may be due to slightly higher temperatures in the experimental case, by errors in the hot wire anemometer, or inaccuracies in the furnace simulation.

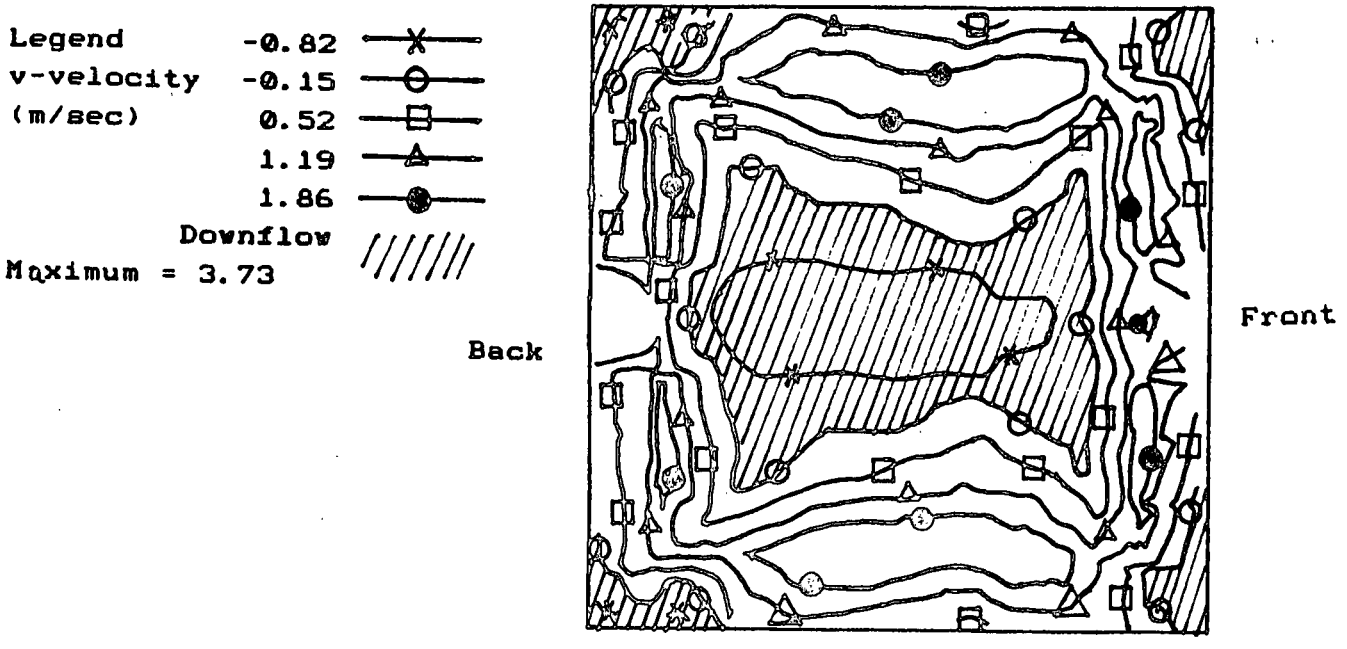

Figure 7. T1 traverse case 1 analytical.

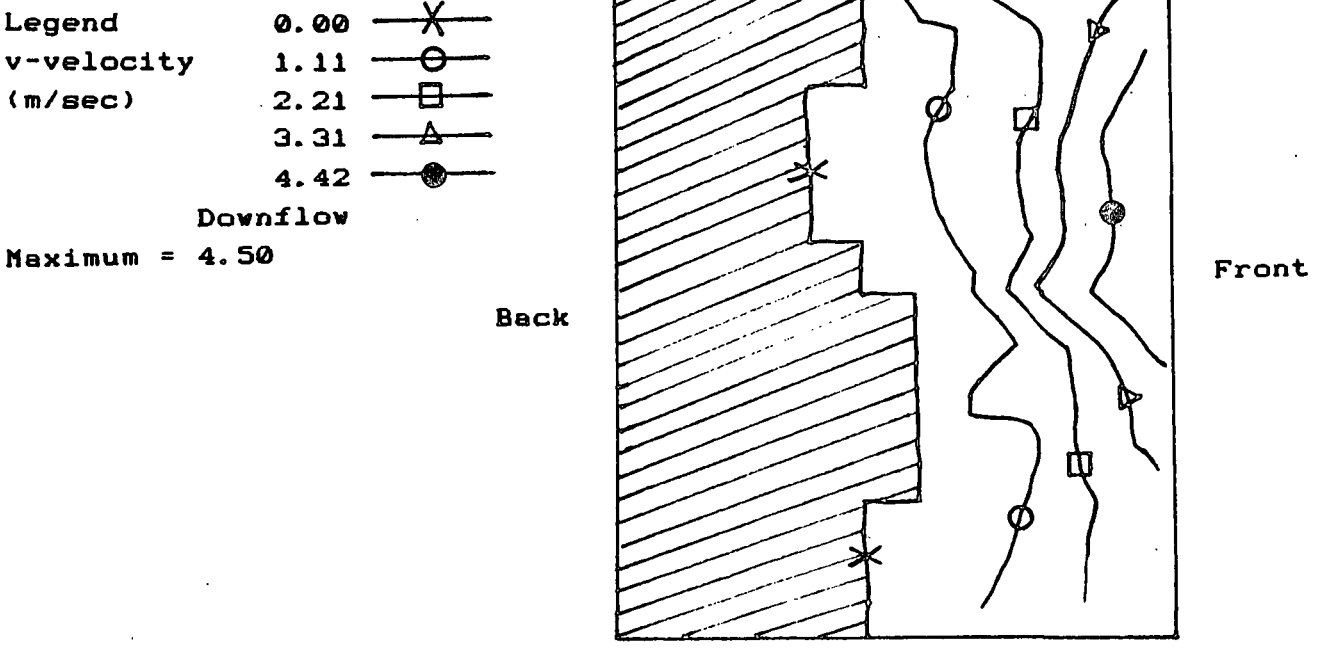

Figure 8. T2 traverse case 1 experimental.

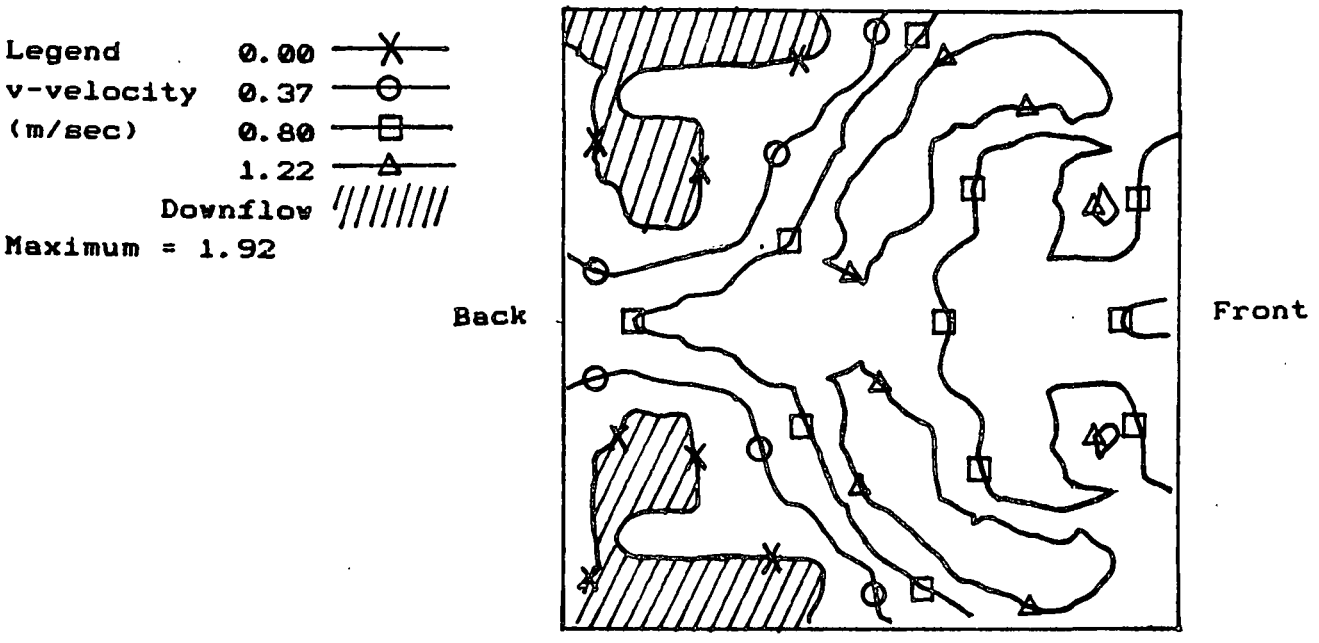

Figure 9. T2 traverse case 1 analytical.

The T1 traverse shows quite different results in the experimental and analytical versions of case 1. The experimental version shows a high velocity core in the center of the furnace with a peak velocity of 7.8 meters/sec. The FLUENT results show the peak velocities directly above the edges of the bed. This is due to numerical problems; these edge effects are caused by the staggered bed shape. The peak velocity of 3.7 meters/sec is about half of the experimental result; the areas of downflow close to the walls are similar in the FLUENT and experimental cases.

Additional contour plots are included to provide improved visualization of this case. Figure 10 shows the v-velocity profile at the midpoint of the furnace. The main feature of this plot is the large stagnant region over the bed; this is due to the edge effects described earlier, which prevent the secondary jets from reaching the center of the furnace. The jets can be seen hitting the edge of the bed and bending straight upward. Figure 11 shows the penetration of the tertiary jets. This is a contour plot of the u-velocities at the level of the

tertiary jet inlets. The low inlet velocity of 10 meters/sec is insufficient to allow interpenetration of the jets. The jets do not appear to spread as they enter the furnace; this is due to the jets bending upward and spreading in a plane above the one viewed.

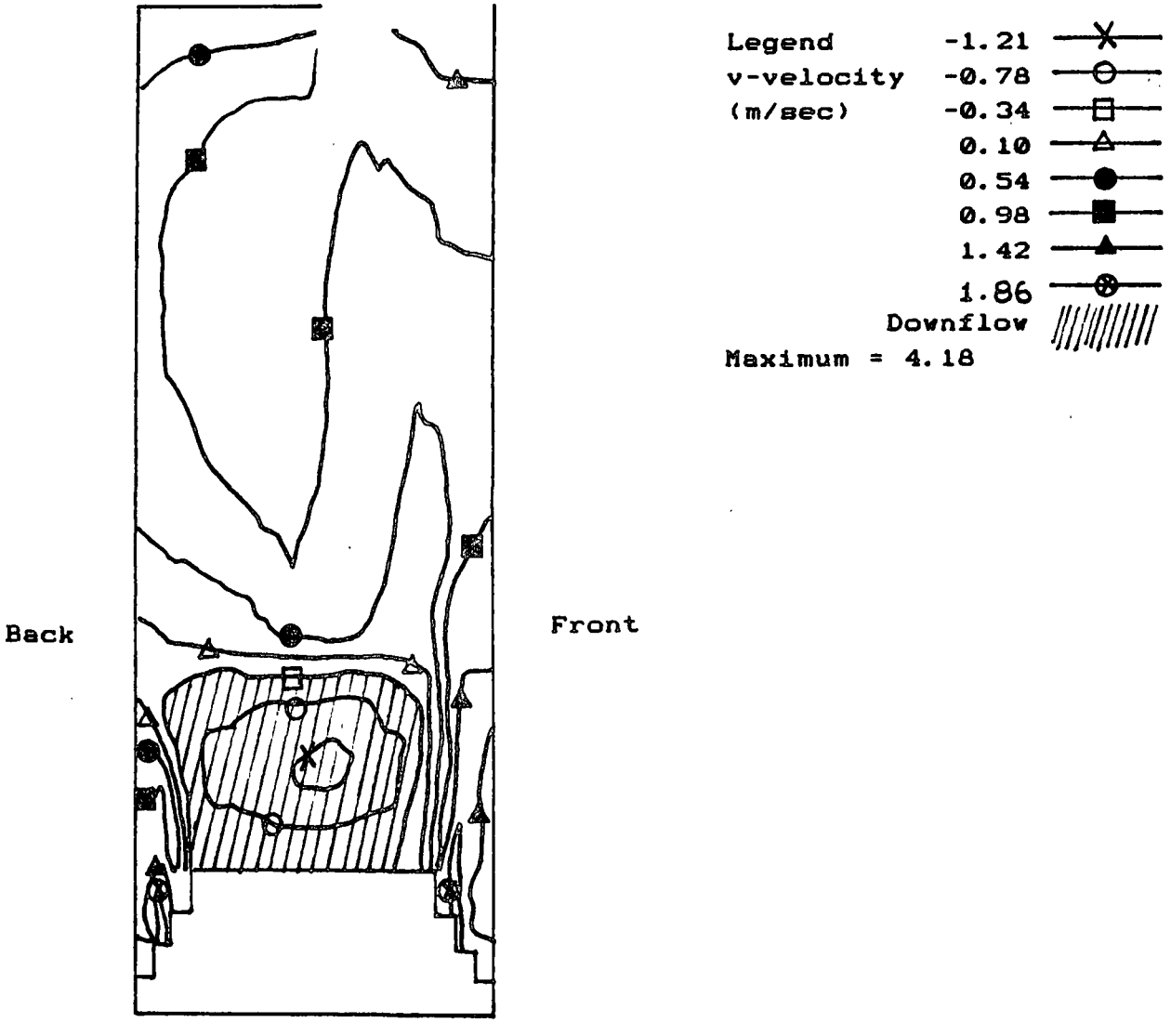

Figure 10. Vertical slice at furnace midpoint case 1 analytical.

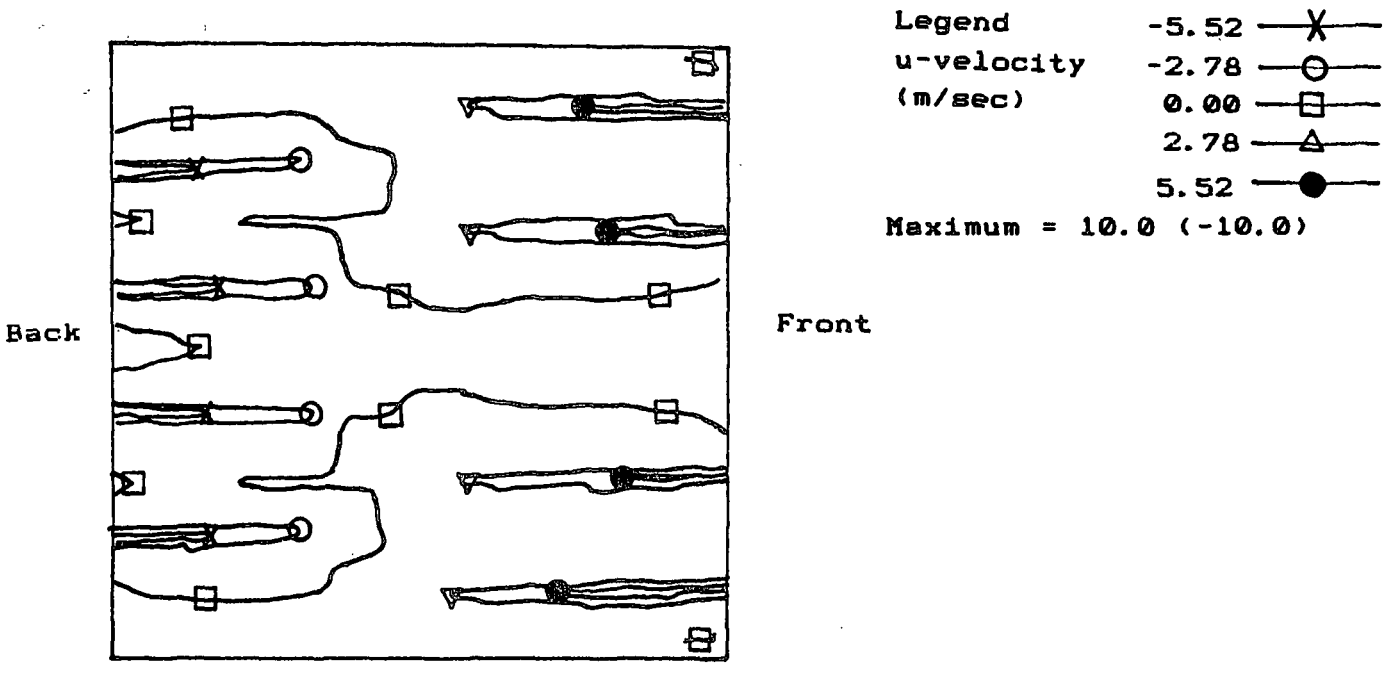

Figure 11. Penetration of tertiary air jets case 1 analytical.

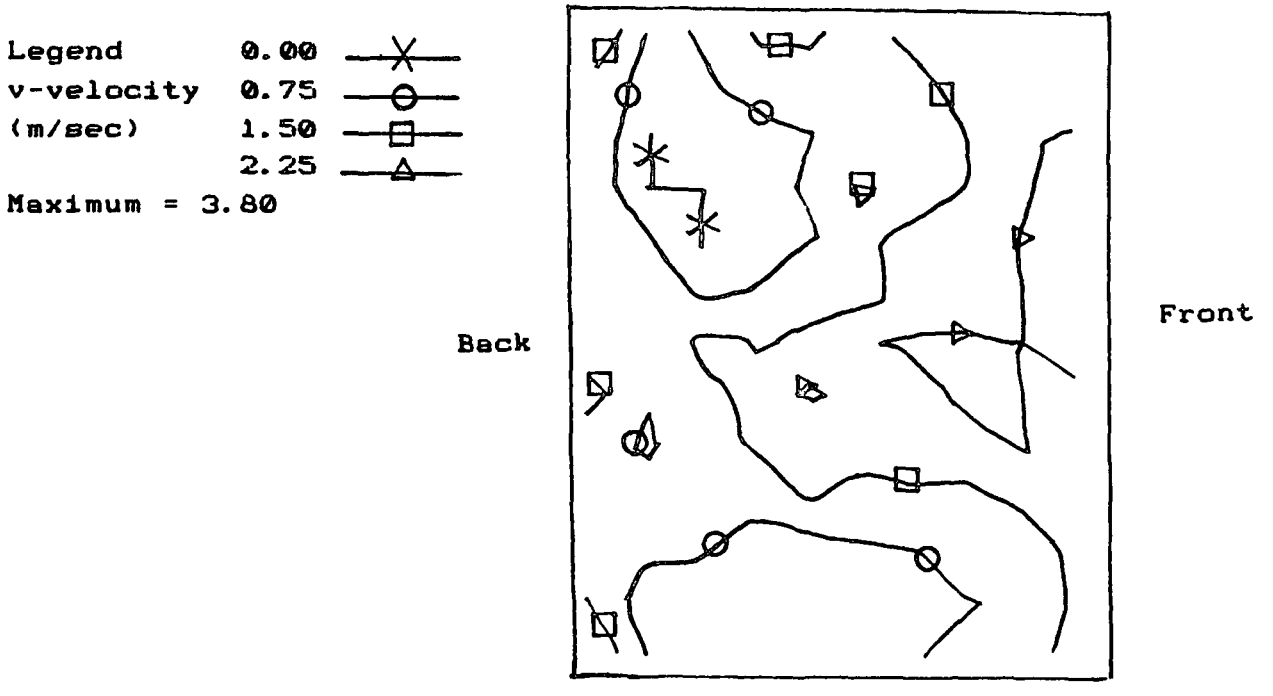

Figure 12. T2 traverse case 2 experimental.

Case 2 corresponds to the B&W recommended design. The T1 traverse is almost identical to the as-is cases, as only minor changes were made with the secondary jets. The experimental and analytical results are essentially the same as case

1 for the T1 traverse; however, the T2 traverse is radically different. The experimental results show that the downflow region has been essentially eliminated. The peak velocity has dropped to 1.2 meters/sec. The analytical results (Fig. 13) also show an elimination of the downflow region, and a reduced peak velocity of 3.8 meters/sec. The reason for this change is readily apparent if Fig. 15 is examined. The high velocity tertiary jets interpenetrate, creating a highly turbulent region; this provides mixing and helps to eliminate the stagnant region below the bullnose.

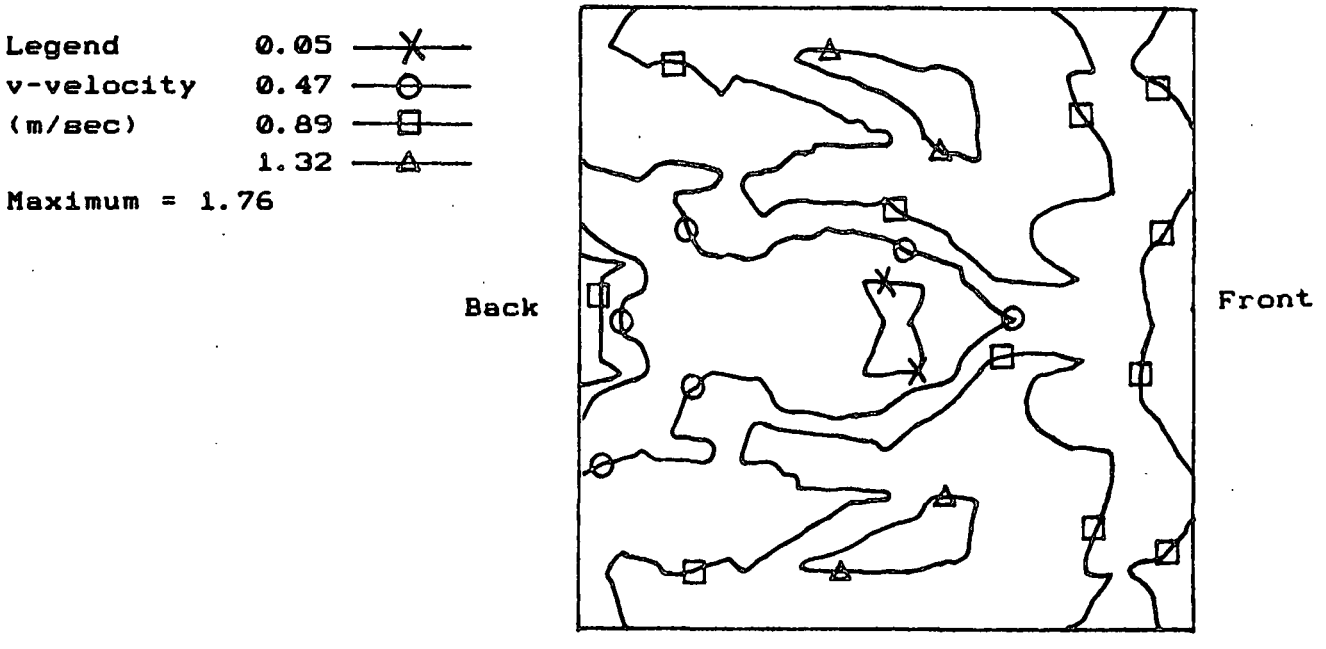

Figure 13. T1 traverse case 2 analytical.

Figure 16 shows the v-velocities at the midpoint of the furnace. The velocities above the tertiary jets are all between 0.4 and 1.3 meters/sec in the upward direction. The stagnant region above the bed has been reduced.

In order to get better agreement between the analytical and experimental results at the T1 traverse the bed shape was changed. Instead of extending the bed above the secondary jets, it was cut off just below the secondary jets. Cases 3

order to break up this center core. The agreement at the T2 traverse between the experimental and analytical results is not as good as was observed in cases 1 and 2. The removal of the top part of the bed seems to create a more persistent center core of gas.

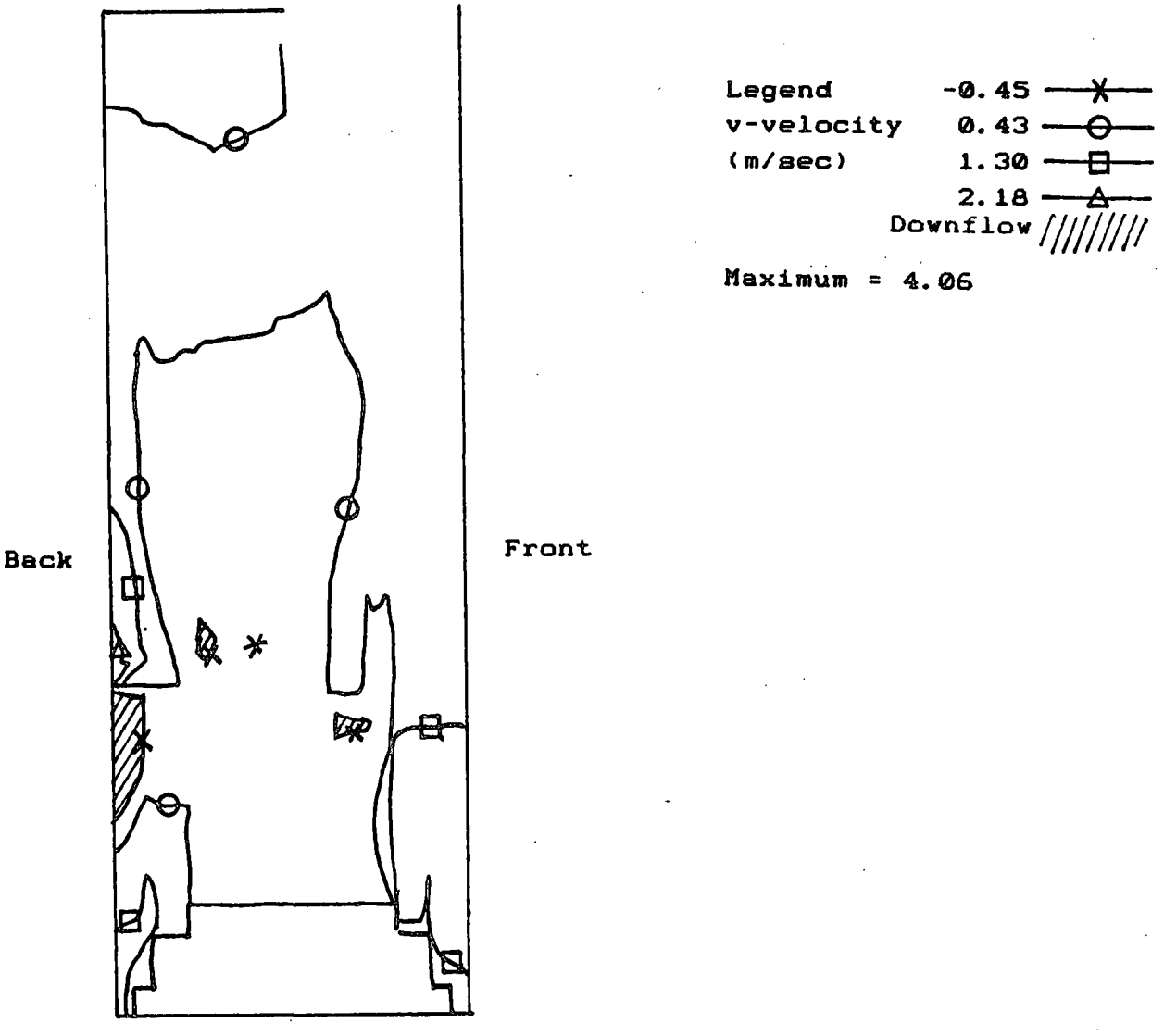

Figure 15. Vertical slice at furnace midpoint case 2 analytical.

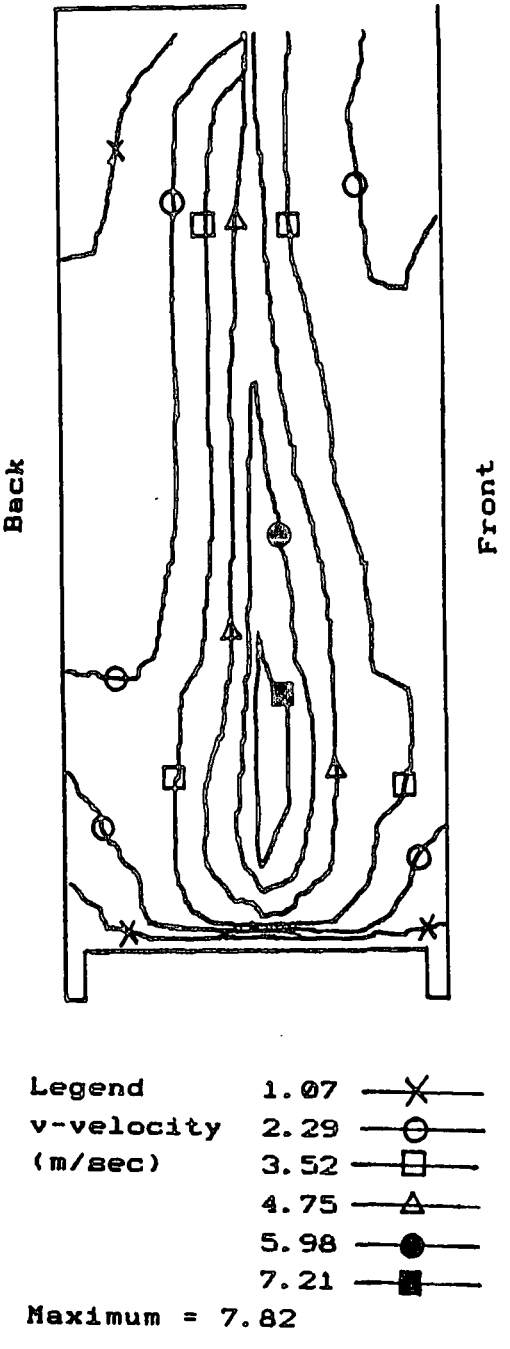

Figure 16. Vertical slice at furnace midpoint case 3.

Case 5 examines the effect of adding tertiary jets to the side walls, in the same arrangement as those in cases 3 and 4. This was done in an attempt to break up the center core of high velocity gas observed in case 4.

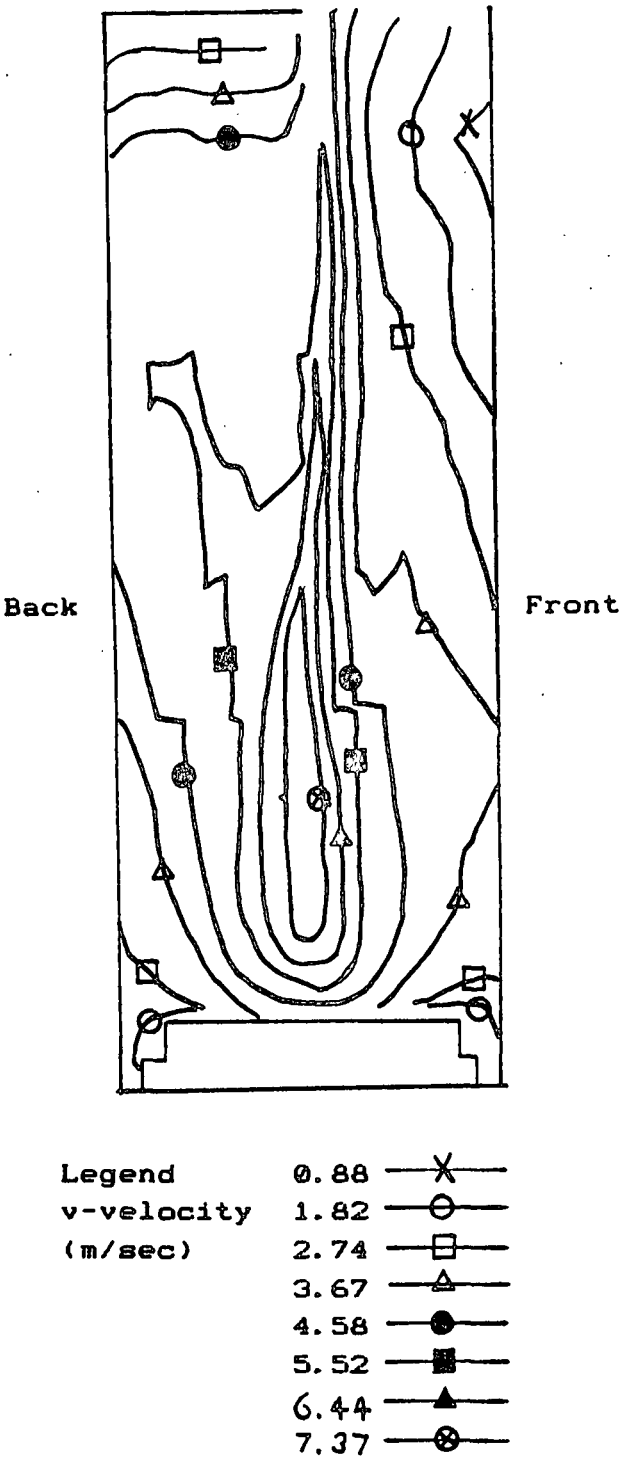

Figure 17. Vertical slice at furnace midpoint case 4.

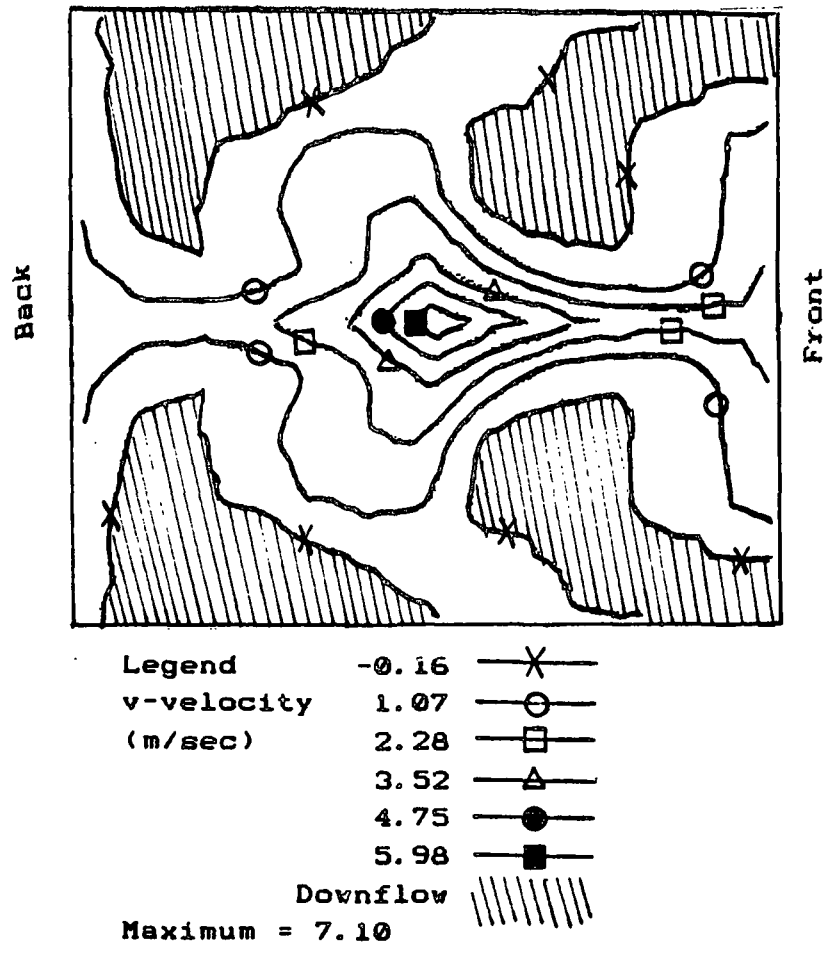

Figure 18. T2 traverse case 3.

The tertiary jets on the side walls do a good job of breaking up the high-velocity core of gas seen in case 4. The T2 traverse (Fig. 22) has a peak velocity of 4.1 meters/sec, well below the 7.1 meters/sec peak velocity in case 4. The region of downflow has been almost eliminated. Figure 23 shows how the center core is broken up above the tertiary air level; this is due to a greater number of tertiary jets and twice the tertiary volumetric flow rate of case 4.

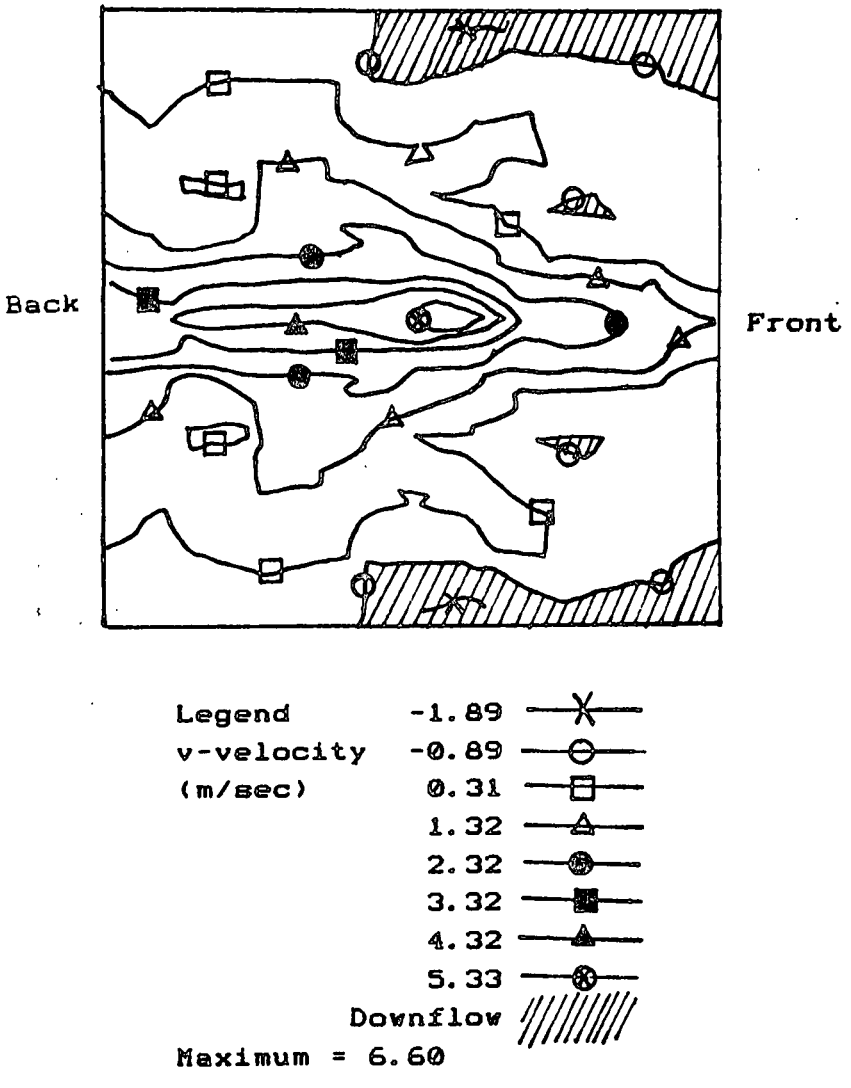

Figure 19. T2 traverse case 4.

DRAWBACKS OF NUMERICAL MODELING

Numerical modeling of fluid flows can be effective and provide valuable results if the limitations of this technique are kept in mind. The main limitations are (1) the need to use staggered nodes to describe a diagonal surface (i.e., bed surface); (2) the empiricism of built-in turbulence models; (3) the large amount of computer time required to converge complex problems (a typical

problem takes about 1 day of CPU time to converge); (4) the difficulty in deciding when a flow pattern has converged; and (5) the limitation in the number of nodes, making it impossible to describe fine details of the flow around the bed and in jets. Considerable improvements in the recovery boiler model should be possible with a 40,000 or 50,000 node version of FLUENT.

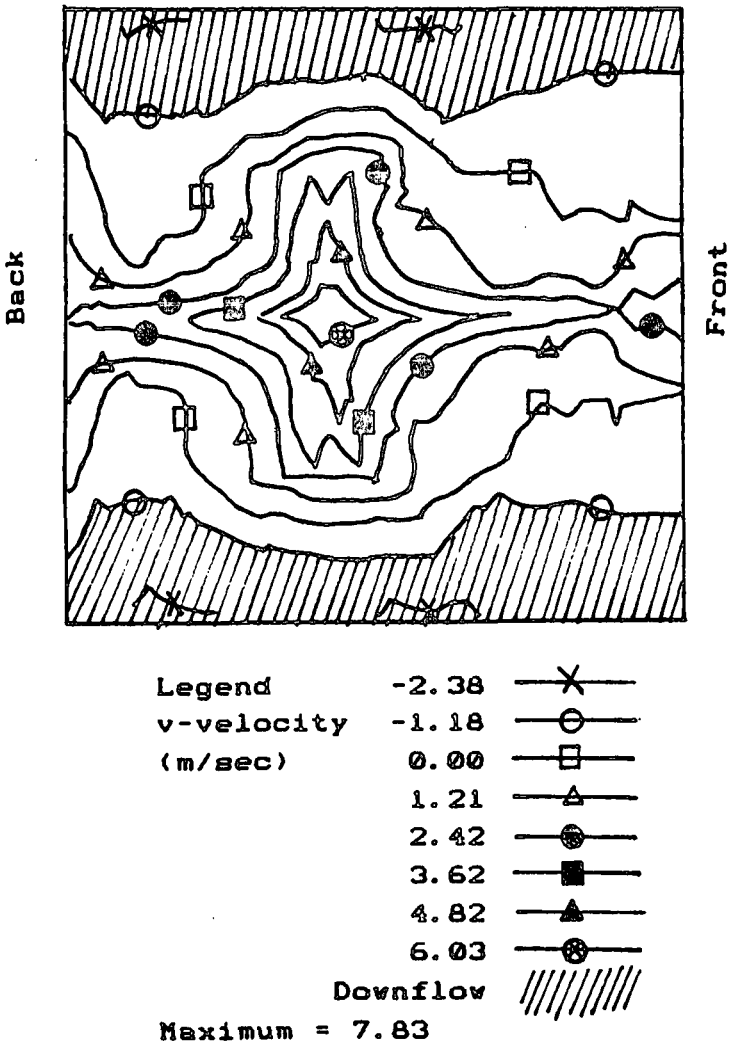

Figure 20. T1 traverse case 3.

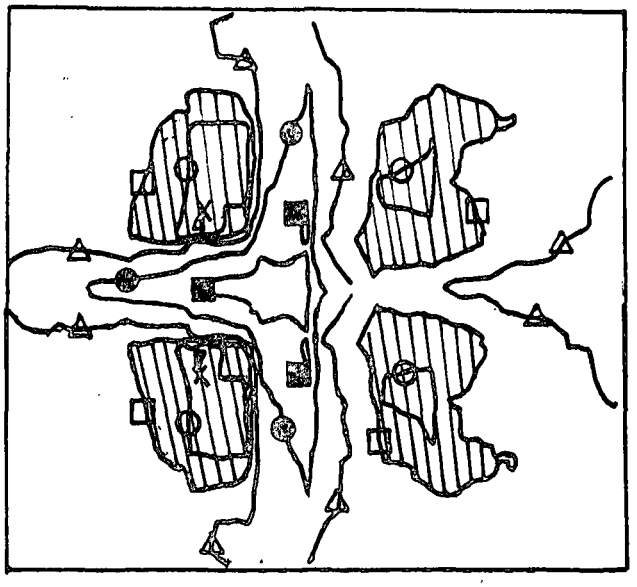

Figure 21. T1 traverse case 5.

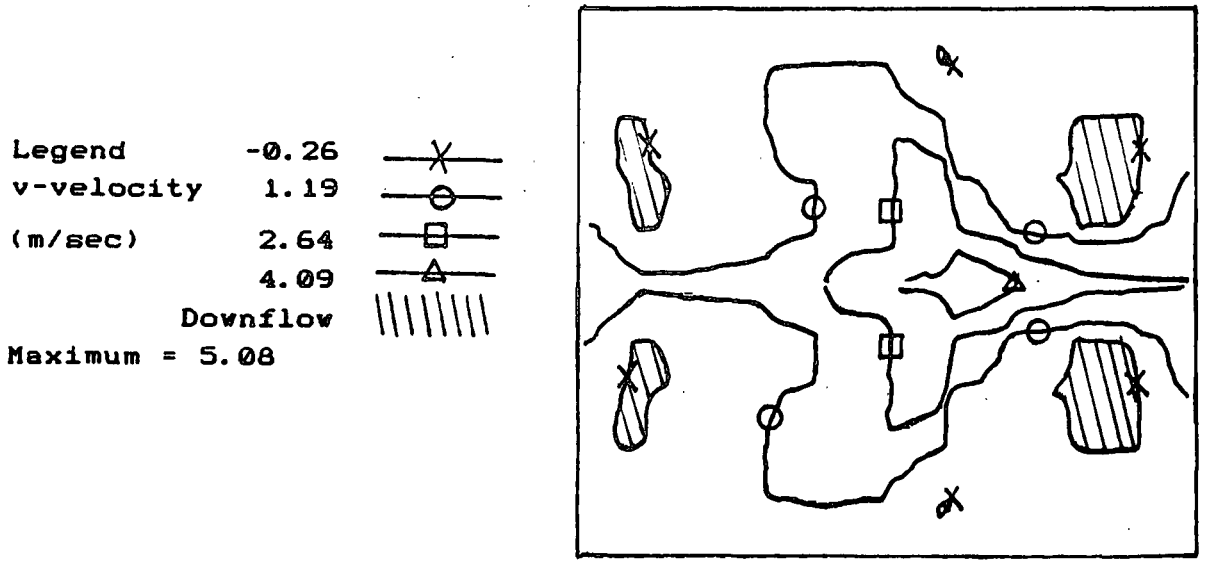

Figure 22. T2 traverse case 5.

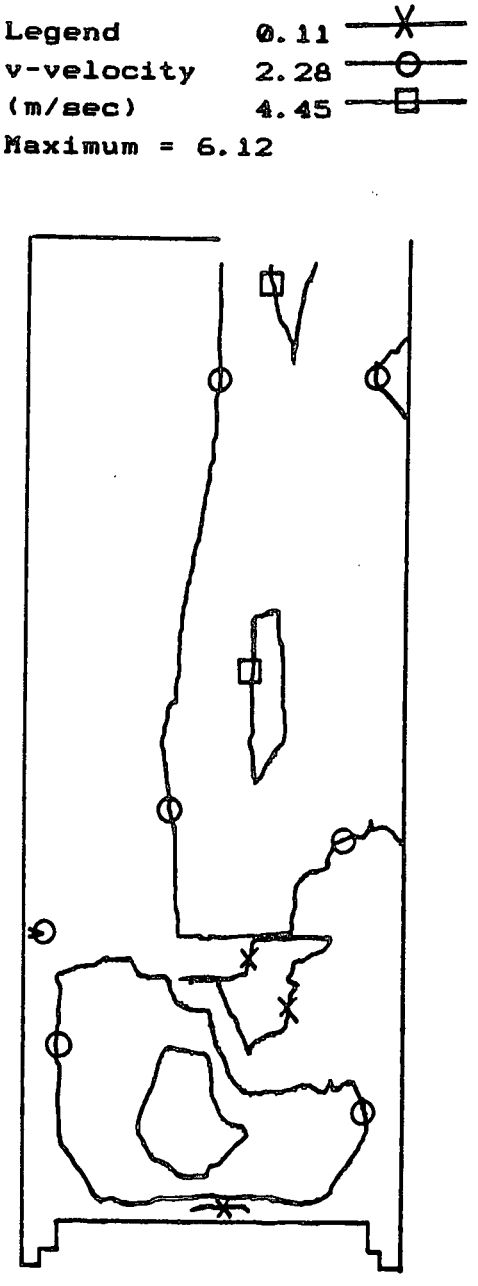

Figure 23. Vertical slice at furnace midpoint case 5.

SUMMARY

The main conclusions that can be drawn from this study thus far are

1. The benefit of modifying the tertiary jets in the B&W furnace can be observed by the use of FLUENT, in agreement with experimental results.
2. FLUENT can be used effectively to simulate the flow patterns in the kraft recovery boiler. The main factor preventing better agreement is the limitation on the number of nodes in the FLUENT version being used. Additional nodes will allow for a better description of the bed geometry and result in improved modeling of the air jets. The use of 50,000 nodes should result in an analytical model that gives essentially the same flow pattern as obtained experimentally.

REFERENCES

1. Dykshoorn, P.; Process Recovery Boiler Flow Model Tests; RDD:87:6940-01-01:01, (July 1986).
2. Crowe, C.T., Sharma, M.P.; The Particle-Source-In-Cell (PSI-CELL) Model for Gas-Droplet Flows; Journal of Fluids Engineering, 99:325-32(July, 1977).